BESSY - Annual Report

2002

Berliner Elektronenspeicherring-Gesellschaft für Synchrotronstrahlung m.b.H.

Published by:
Berliner Elektronenspeicherring-Gesellschaft
für Synchrotronstrahlung m.b.H. (BESSY)

Albert-Einstein-Str.15
12489 Berlin
Tel. +49 30 6392 2999
Fax +49 30 6392 2990
info@bessy.de
www.bessy.de

Edited by :
Dr. Kai Godehusen

Dear users and friends

The new version of our annual report, the BESSY Highlights, including a CD covering all the activities and publications for the year is now published for the second year. We were overwhelmed by the positive feedback on our first Highlights edition which ran out of print only after 6 months, and we feel encouraged to keep on informing you in this new style.

Last year witnessed a novelty for synchrotron radiation sources around the world – the generation of stable, broadband THz-radiation and its application in a unique experiment at BESSY. This achievement is a result of three years development on accelerator operation and beamline construction thus expanding the use of SR beyond the far-infrared into the THz gap.

Together with eight other large scale research projects, the BESSY soft X-ray FEL has been evaluated by the German Science Council (Wissenschaftsrat). Our scientific case has been awarded a rating of “excellent” and at the forefront of international research. We are encouraged to complete the technical design as planned by the end of 2003.

The traditional users meeting in the beginning of December with some 250 participants, 100 posters and a large industrial exhibition was preceeded by an FEL-workshop focusing on experiments and beamline development. During the user meeting Fabrice Wilhelm (FU Berlin) and Tobias Lau (Universität Hamburg) were awarded the “Ernst-Eckhard-Koch” Prize and Ralf Röhlsberger (Universität Rostock) received the BESSY Innovation Prize for his “Nuclear Lighthouse Effect”.

In 2002, user services were improved substantially. Starting in August, BESSY now offers 24 hours user support for the more than 40 beamlines in operation. We are progressing in improving on laboratory facilities. To keep pace with the growing user community, a new guest house is now under construction and will be ready for occupancy by end of the year. User access to the experimental hall has been significantly simplified with the construction of cages around the first mirror boxes to the beamlines: The radiation safety authorities approved an almost complete elimination of the control area in the experimental hall.

With the operational beamlines of the Protein Structure Factory, biology is becoming a more important research field at BESSY, offering already six experimental stations with several more to come. Two additional members from this community have been appointed to the beamtime committee to account for the raising numbers of biological proposals.

BESSY again has been a magnet for many visitors throughout the year with prominent guests such as the King and Queen of Jordan and the President of Malaysia. Events from ”breakfast lectures” to art exhibitions have caught visitor interest. At the “Lange Nacht der Wissenschaft” about 6,000 people took the opportunity to obtain an inside view of the goings on here. BESSY was for a second time in sequence the institution with the largest number of visitors.

The successful operation and further development of BESSY would not be possible without the excellent work of our users and the enthusiasm and competence of our staff. We would like to thank all people involved for their dedication and our funding agencies for their support.

Enjoy reading the Highlights

The BESSY Board of directors
Berlin, February 2003

Sensor Chips for Measuring the Antioxidative Capacity of Polydispersive Systems like Novel Food Products and Beauty Treatment

T. Wegwerth, B. Löchel, BESSYmbH, Albert-Einstein-Str.15, 12489 Berlin
O. Pulz, E. Kurth, Institut für Getreideverarbeitung, Arthur-Scheunert-Allee 40/41; 14558 Bergholz-Rehbrücke
F. Lisdat, Uni Potsdam, Institut für Biochemie und Biologie, PF 601553, 14415 Potsdam
H.-J. Just, H. Adamzig, Elektronik Bauelemente GmbH, Darßer Bogen 19, 13156 Berlin
W. Berthold, EKF-Diagnostic GmbH, Ebendorfer Chaussee 3, 39179 Barleben
H. Pfeiffer, Bio Sensor Technologie, Buchholzer Str. 55-61, 134156 Berlin

Introduction

BESSY is partner in the BMBF InnoRegio project “Measurement of the antioxidative capacity of polydispersive systems like novel food products and beauty treatment”. It is planned to fabricate a bio chip in co-operation with the other project partners. Main part of the chip is a fluidic system. This system contains channels of different form and length. One of the access channels is widened to a chamber and includes the reservoir of the oxidase, a component of the biochemical reaction that should take palace at the chip. Via the second channel the sample (antioxidase) is applied. Both channels merge in a mixer. After leaving the mixer the liquids will pass a measurement chamber containing special electrodes for the detection. A final waste drain connects the measurement chamber with the outer supply system.
The optimisation of the bio chip and its components was planned to be a three cycle process. All work for generating the fluidic system on the chip will be done at the BESSY Application Center for Microengineering in Berlin.

Design and Fabrication

The fundamental chip design was defined in a discussion with the project partners. Following basic approach was fixed:

- the volume mixer should be spherical
- the feeding in of the antioxidases and the oxidase shall be realised via channels
- into the feeding in of the flowing medium (**Di****M**ethyl**S**ulf**O**xid) there should be a reservoir to activate it
- the detector chamber should be placed close behind the mixer
- the detector chamber should contain a cavity for mounting the electrode chip
- the electrode chip should be fabricated in thick layer technology
- the material of the carrier should be PMMA (high chemical resistance for DMSO)

First prototyps of the bio chip should be realised by precise cutting. Later versions will then be fabricated by LIGA techniques. The first version of the chip consists of two parts, a base plate and a cover part. Both were realised in PMMA. Outer dimensions of the plates are 23 x 54 x 5 mm. A three dimensional view of the chip is given in fig. 1.
The cover plate contains a cavity for the xanthine oxidase (XOD), which generates peroxide ions, and the electrode-chip. Silicone sealing material is used to prevent leakage from the channels and chambers. The drawing in fig. 2a gives details for the cavities in the cover part of the bio chip. The two drill holes are necessary for mounting the cover part and the basic plate of the chip precisely. The realised channel diameter for the prototype is 0.7 mm.

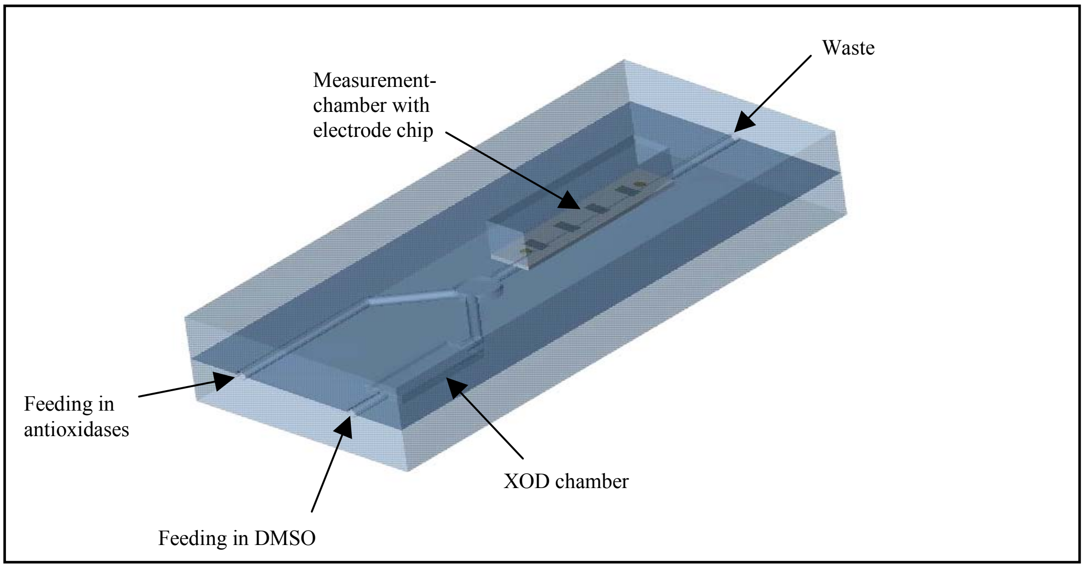

Figure 1: Principle assembly of the AO chip

The base plate of the chip contains the same channels and cavities as the cover part but as an inverted version.

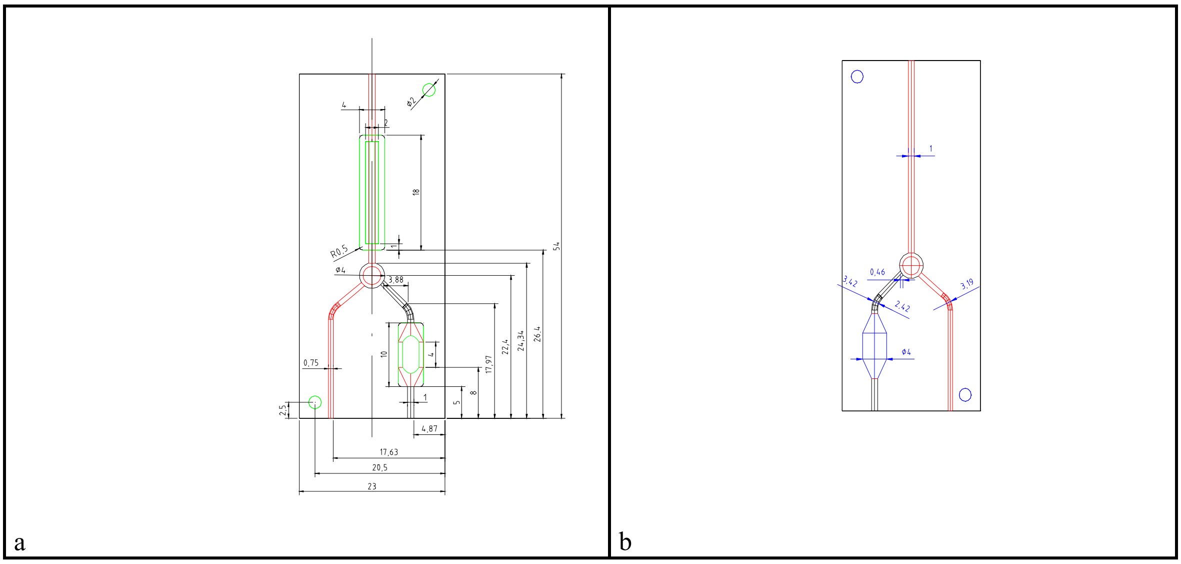

Figure 2: First layout of the AO-chip-design (a cover part, b base plate)

The fabrication of both plastic parts of the chip were realised by precision milling at BESSYs Application Center. After milling both parts of the chip were measured with the co-ordinates measuring system and the results were used for a redesign.

In the next step the two parts were bonded with special glue. For better alignment two pins were used for mechanical guidance.

Two different glues, UV sensitive glue (Viralit 1505) and silicone glue (DL 3145 RTV Silicon + Primer 1200 DS), were tested for mounting. Only the silicone based glue met the process requirements

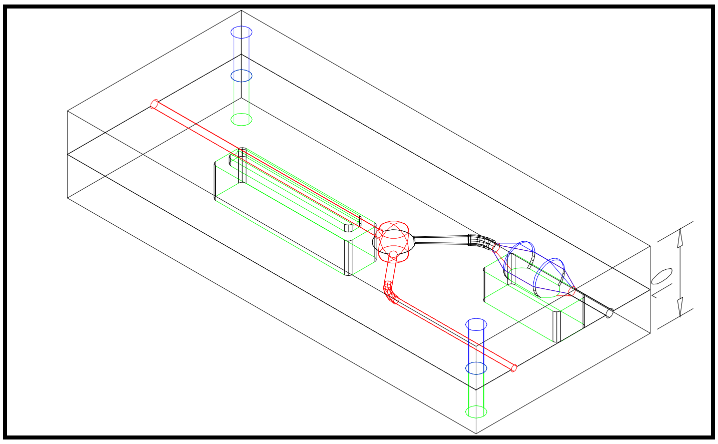

Figure 3: Wireframe graphics of the AO-chip

For leakage tests a chip was completely mounted (see fig 4). The separate electrode chip was built in and sealed with silicone. The cavity for the XOD chip was closed by a silicone plug and the fluid was fed via cannulas.

The chip was found leak proof. Some problems occurred with the electrode chip. Its outer dimension did not fit into the opening of the base plate. The problem could easily be overcome by adapting the opening for the chip to the chip size.

A second problem was caused by the glue applied for mounting. Small amounts of permeated glue blocked the channels. In order to prevent this effect, small additional trenches beside the channels were introduced into the design and realised. Now permeated glue fills up the trenches before entering the channels.

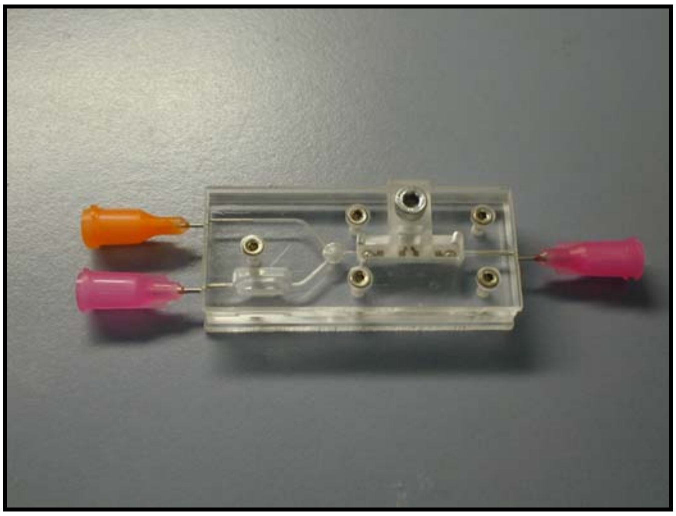

Figure 4: Completly mounted AO-chip

Conclusion and outlook

A first version (prototyp) of a fluidic system for a bio chip was realised using precision cutting. The two parts of the chip were assembled and stuck by special glue in order to meet the demands concerning leakage, adhesive strength, and chemical resistance. Presently first investigations for testing the electrochemical properties of the chip take place at the University of

Potsdam. Furthermore the properties of the liquid system will be checked and on the base of these results a redesign for the chip is planned.

Fresnell Lenses for Synchrotron Radiation

A. Firsov, I. Wichert, BESSY Anwenderzentrum Mikrotechnik, Albert-Einstein-Strasse 15, 12489 Berlin

The challenge to develop electron beam lithography at BESSY is connected with a need to have various diffractive structures – gratings, focusing elements (zone plates, Bragg-Fresnell elements), X-ray holograms, test objects, gauges of X-ray position and so on available for scientific investigations at BESSY. Since the start-up of the BESSY Application Center for Microengineering in October 2001, technical requirements can be fulfilled and processes are installed.
As a lithographic tool a scanning electron microscope LEO1560 equipped with an image pattern generator and a software package of the Interface Ltd., Moscow is available.
At the beginning of our investigations the development was focused on the fabrication of focusing elements for "soft" X-ray radiation.

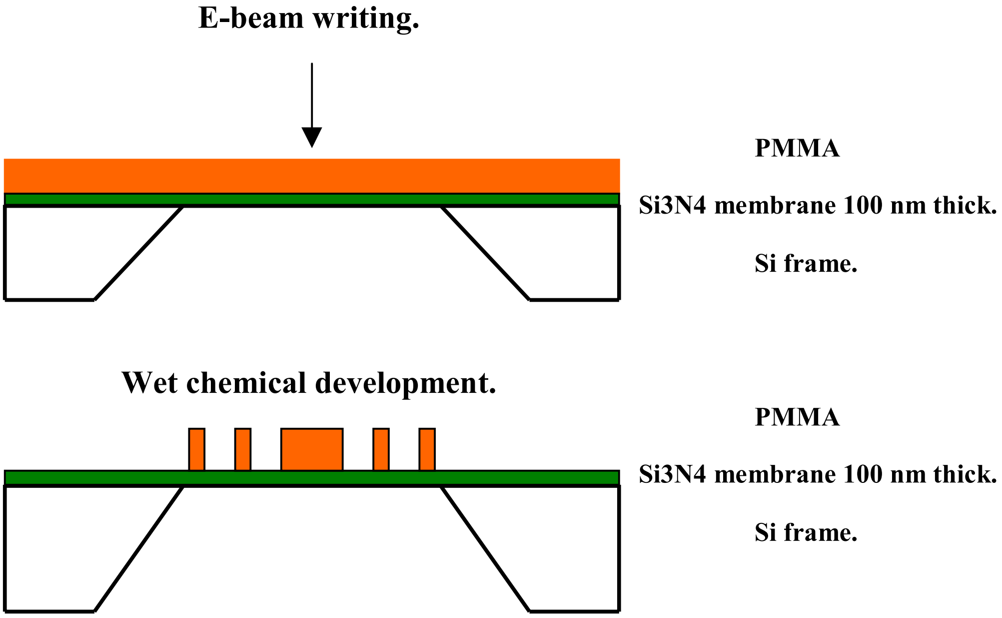

Figure 1: Flow chart for the fabrication of diffractive elements

In figure 1 a sequence of technological steps for the fabrication of such elements is depicted. The electron beam sensitive resist itself is used as a phase shifting material for the diffractive elements. Figures 2a and 2b show SEM pictures of focusing elements designed to focus a radiation of 786 eV energy. The diameter of this lens is 625 µm and size of the last zone 0.24 micron.

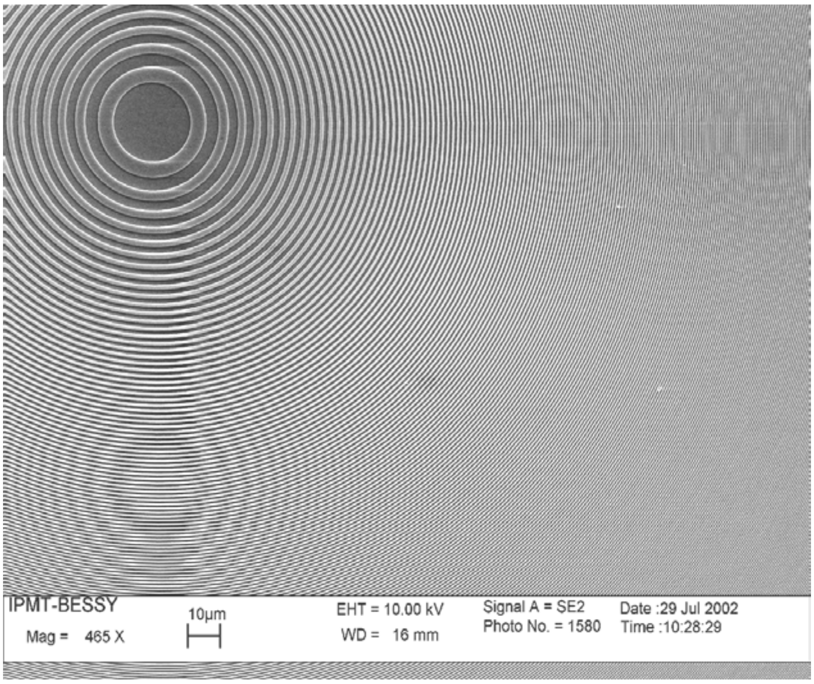

Figure 2a: Pattern structure of a Fresnell lens

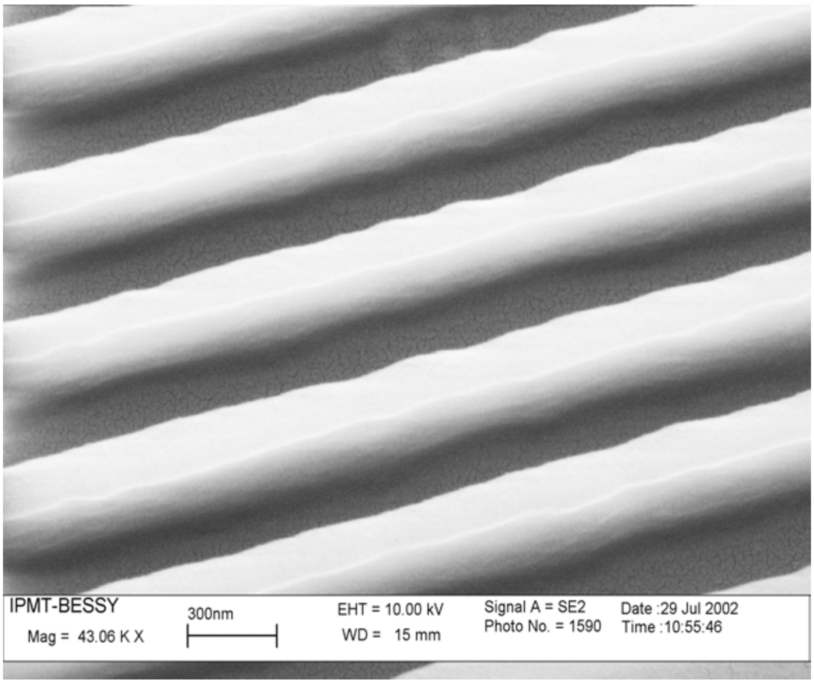

Figure 2b: Detailed view of Fresnell patterns showing lines and spaces

One of the future projects carried out at BESSY, is the creation of holograms for “hard” X-ray radiation lithography. Such holograms can be created at a surface of a silicon substrate and are under preparation for 8 keV and 10 ke. As phase shifting material gold patterns with a thickness of 0.12 µm were used. In figure 3 fragments of such a hologram are depicted. The hologram itself has a dimension of 961 µm by 239 µm and minimal pattern size of 0.3 µm.

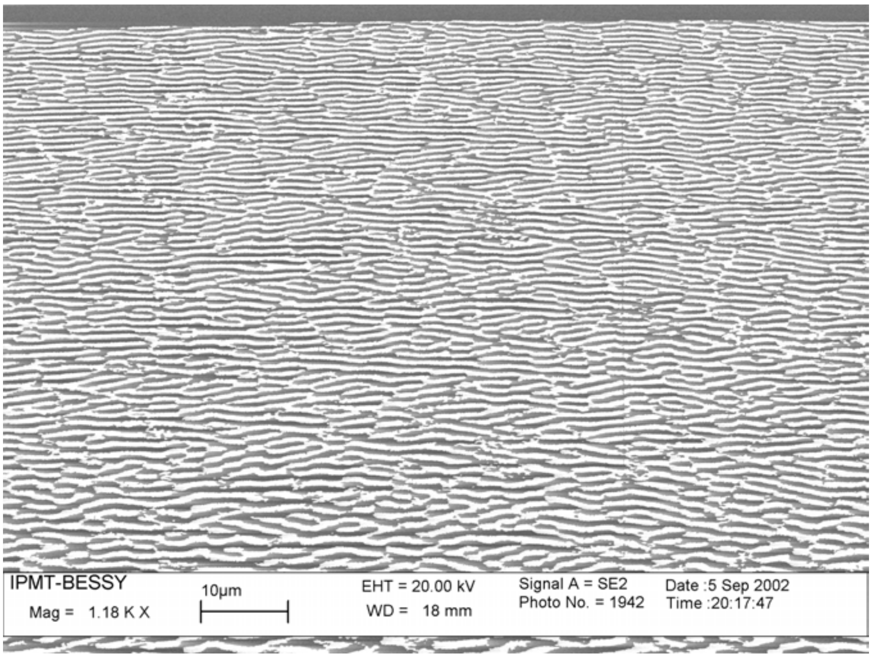

Figure 3: Gold patterns of X-ray hologram for 8 keV radiation

It is planned for the future to equip an electron microscope with a laser interferometer stage. The new stage will allow to fabricate diffractive elements with large apertures like Bragg-Fresnel lenses for microfluorescence analysis and diffraction gratings.

Continuous Operation of the 4 T Wave Length Shifter – Fabrication of Extreme High Micro Patterns

H.U. Scheunemann, H. Köhrich, A. Barth, A. Firsov, B. Löchel
BESSY GmbH, Anwenderzentrum Mikrotechnik, Albert-Einstein-Strasse 15, 12489 Berlin

Presently at BESSY two of the beamlines are under operation for X-ray lithography. They are designed for different applications. One of them is connected with a standard bending magnet (1.3T) and is in use for standard deep X-ray lithography (Resist deep: PMMA 0.6 mm, SU 8 2 mm).

The second one offers the possibility of multiple use. It is connected with a straight section of the BESSY store ring. This section is equipped with a wave length shifter (WLS) and correction magnets. Typically, the WLS will be operated at a magnetic field of 4Tesla. Due to the higher magnetic field of 4Tesla the critical photon energy is shifted to 7.7 keV compared to a standard BESSY dipole magnet with 2.5 keV. This configuration is mainly used for ultra deep X-ray lithography (UDXRL) for resist thickness up to 1 cm (PMMA).

Beside the UDXRL mode the same beamline can also be used in a soft radiation mode. For this mode only the correction magnets (~0.4T) of the WLS (steerer magnets) will be switched on while the WLS magnet is switched off. For this soft operation mode the critical photon energy is 0.8 keV. The light generated from steerer magnets is best qualified for high precession patterning of thin resist layers < 100 µm and will be used especially for masks copying.

Both beamlines are provided with two beryllium windows of 200 µm thickness in all. These windows separate regions of different vacuum conditions and are transparent for photons of higher energy (> 1.5 keV) only. Beryllium absorbs low energy photons which do not contribute to the resist exposure but charge mask and sample thermally.

Different spectral intensity distributions are shown in figures 1 and 2 for different running modes. The high intensity of the soft mode is due to the contribution of effective 3 steerer magnets as sources. Figure 1 show the "pure" spectral distributions without any window. The beryllium windows influence the spectral composition and decrease the contribution of low energy photons (fig.2).

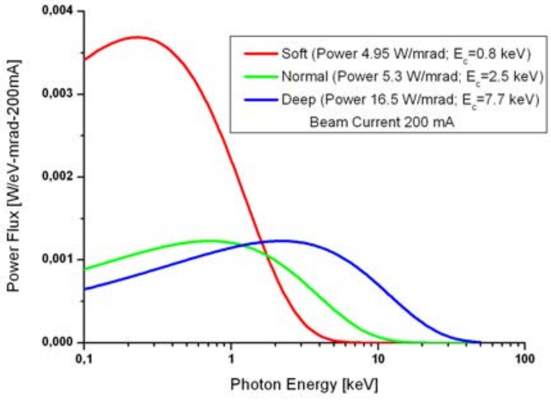

Figure 1: White light power spectra for different X-ray sources, 200 mA beam current, no windows

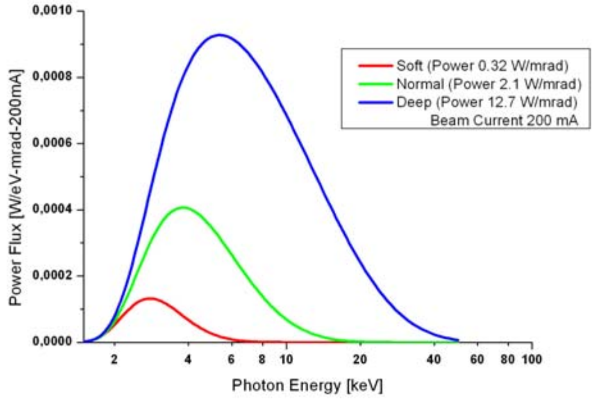

Figure 2:White light power spectra for different X-ray sources, 200 mA beam current, window: 200 µm Beryllium

The normal and soft operation mode was installed in 1999 and was available since this time, while the test of the WLS mode started in November 2002.

At the beginning of our investigations we measured the laterally intensity profile of the X-ray beam in the exposure chamber at the end of the beamline. This measurements were performed with an X-ray sensitive diode mounted at an xy-table. In figure 3 and 4 the lateral intensity distribution over the beam is depicted. The integration of the measured intensity distribution in vertical direction with regard to the beam width (horizontal direction) shows a very homogeneous character (fig. 5). In an area of 85 mm the homogeneity is better than ±2%. The measurement was done at low beam current (< 20 mA).
This integration of the intensity distribution complies with the situation during the scanning of a sample through a synchrotron beam while exposing.

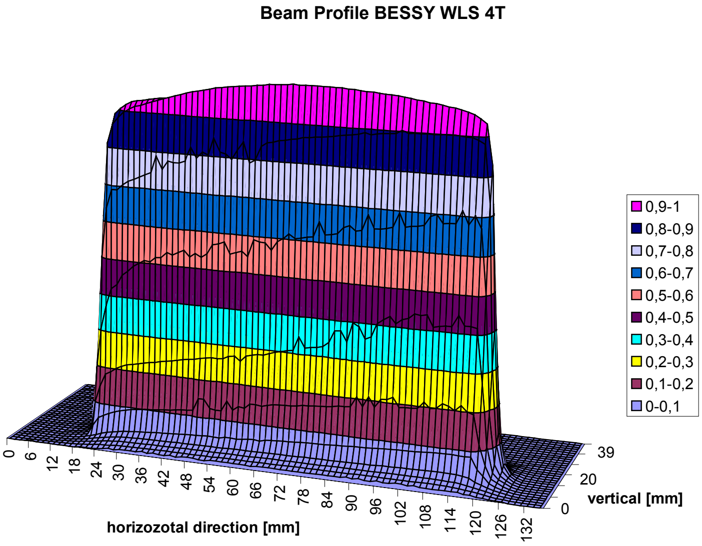

Figure 3: Intensity profile of the WLS beamline

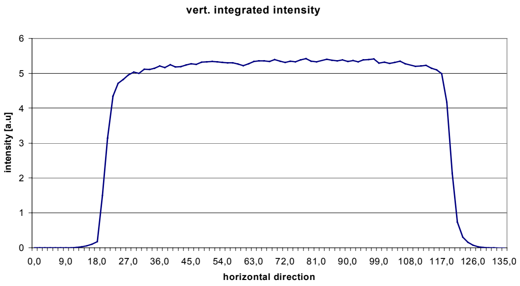

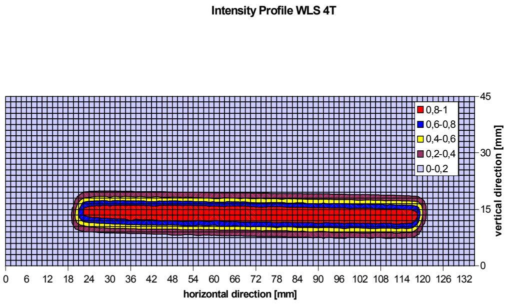

Figure 4: Contour lines of the intensity
profile of the WLS beamline

Figure 5: Vertical integrated intensity
distribution of the WLS 4T

In table 1 the variable offer for using BESSY synchrotron light for X-ray lithography exposures is outlined.

The exposure times per 1 cm height vary between 1 min for the high sensitive resist SU-8 up to 2 ½ h for the low sensitive PMMA by using the normal bending magnet respectively the WLS 4T. Due to the extreme high, structures (> 2 mm) are only used for special applications. When using the WLS for patterning extreme thick PMMA layers, exposure times shorten and the acceptance of the process will increase. Calculated exposure times for the different exposure modes offered at the BESSY lithography beamlines are given in figure 6.
Using these variable modes, different types of resist with varying thickness can be exposed under tailored conditions in reasonable exposure times.

Table 1: Options for use of the BESSY lithography beamlines

Mode	**Device**	**Magn. Field**	**Beamline**	**Application**		**Resist Thickness**		**Exposure Time (ca.)**
SOFT	Steerer	~ 0.4 T	ID 06	SXRL	Mask Copy	PMMA	~ 30 µm	15 min/cm
						PMMA	< 100 µm	40 min/cm
NORMAL	Dipol	1.3 T	DI 06 1A	DXRL	Standard Application	PMMA	< 600 µm	45 min/cm
						SU 8	< 2 mm	1 min/cm
DEEP	WLS	4 T	ID 06	UDXRL	Special Application	PMMA	> 1mm	15 min/cm
						PMMA	< 10 mm	2 ½ h/cm

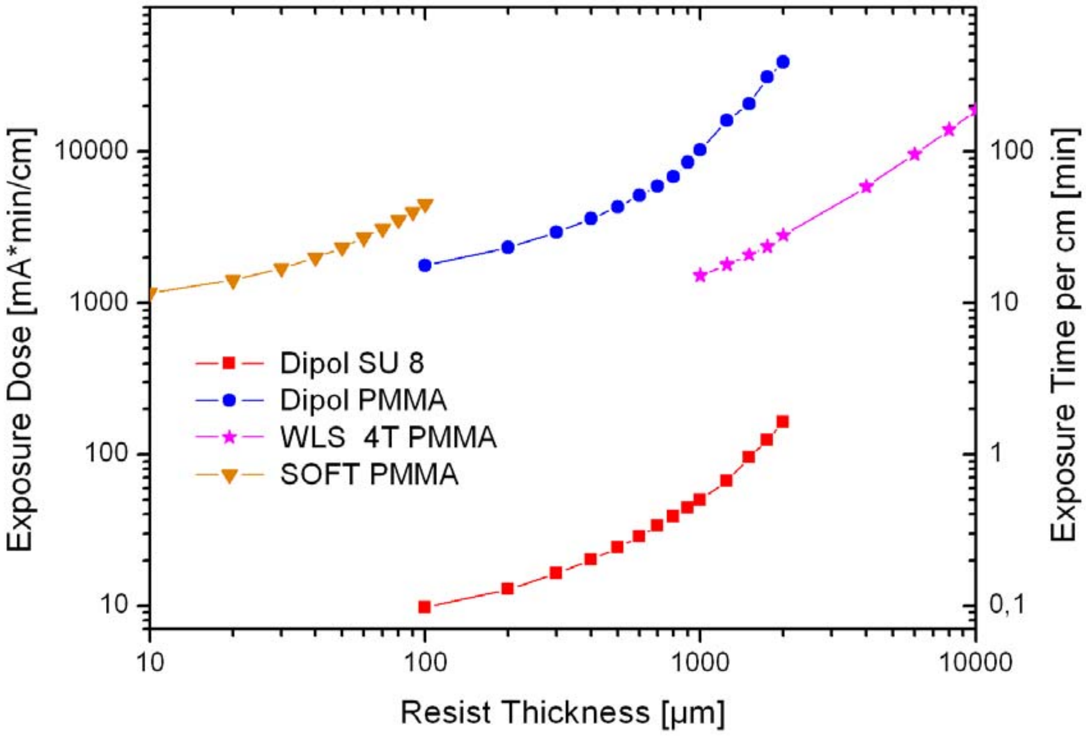

Figure 6: Exposure Time at BESSY facilities for different sensitive resist material

First test exposures using 2 mm and 4.5 mm PMMA resist have been carried out at the WLS beamline (figure 7 and 8). Preliminary inspection proved excellent pattern fidelity and steep side walls.

Comprising present results one can say that the WLS beamline, now available at BESSY, is an unique tool for soft and hard X-ray exposure. This beamline expends BESSY's service activities for LIGA technique towards ultra-high and ultra-precise microstructure fabrication.

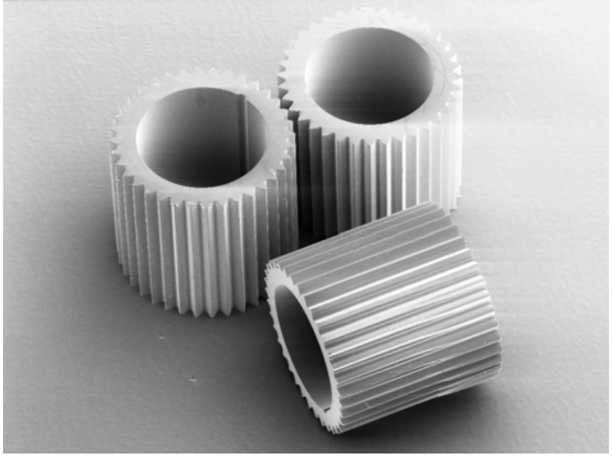

Figure 7:Micro gears made by Ultra Deep X-Ray Lithographie (UXRL) produced with the BESSY 4Tesla Wave Length Shifter (WLS) height 2 mm, diameter 2 mm

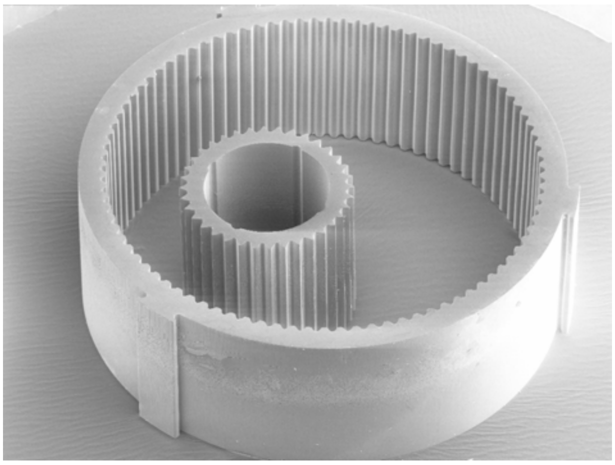

Figure 8: Part of a micro gear, PMMA 2 mm high

Fabrication of Masks for Deep X-ray Lithography at BESSY

LINKE JIAN, MARTIN BEDNARZIK, HEINZ-ULRICH SCHEUNEMANN, DANIEL SCHONDELMAIER,
INGRID WICHERT, ALEXANDRE FIRSOV, IVO RUDOLPH, BERND LOECHEL
BESSY GmbH, Anwenderzentrum Mikrotechnik, Albert-Einstein-Strasse 15, 12489 Berlin

The mask fabrication is the key technology in the fabrication of HARMS through X-ray lithography. Mask membrane for X-ray lithography may include polyimide, diamond, silicon carbide, silicon nitride, boron nitride, silicon, titanium, graphite or beryllium. Various mask fabrication techniques based on different membrane materials have been developed for LIGA technology [1]. For these different membrane materials, titanium and silicon compound membranes are just a few micrometers and have a high X-ray transparency but are expensive and difficult to handle. Beryllium is the most favorable material due to the high X-ray transparency but the potential toxicity is a limitation. At BESSY, we have developed the technologies which use the graphite, glass carbon or glass as the membrane material to fabricate the X-ray masks [2].

The specifications are:

- Mask size: 4 inch diameter, similar to 4 inch silicon wafer.
- Design area: 80 mm diameter.
- Minimum feature size: 5-10 microns.
- Membrane materials: 150 or 200 um graphite or 30 um glass
- Gold thickness: up to 35 um
- 4 inch support ring

The process of the x-ray mask includes the following steps, as shown in Figure 1.

1. ***Optical Lithography***

In this step, the designed microstructures pattern on an optical mask are transferred to a thick resist layer by optical lithography. SU-8, a negative resist, is used for the fabrication of x-ray masks. Thick resist layers up to 50 µm are applied on the graphite or glass membranes. The resist layers are patterned by use an optical mask and UV aligner. Development is carried out by immersion into SU-8 developer.

2. ***Gold Electroforming***

A gold electroplating solution, BTD200, from OMI Ethone, is used to electroform gold on the patterned graphite membranes. The growth rate of gold is approximately 10 -15 µm/hr.

3. ***Mask Mounting***

After electroforming, the mask is mounted on the 4 inch steel support ring. The SU-8 layer can be simply left in place and will not affect the irradiation process significantly.

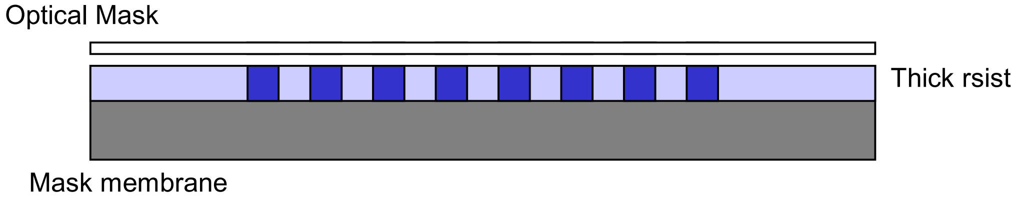

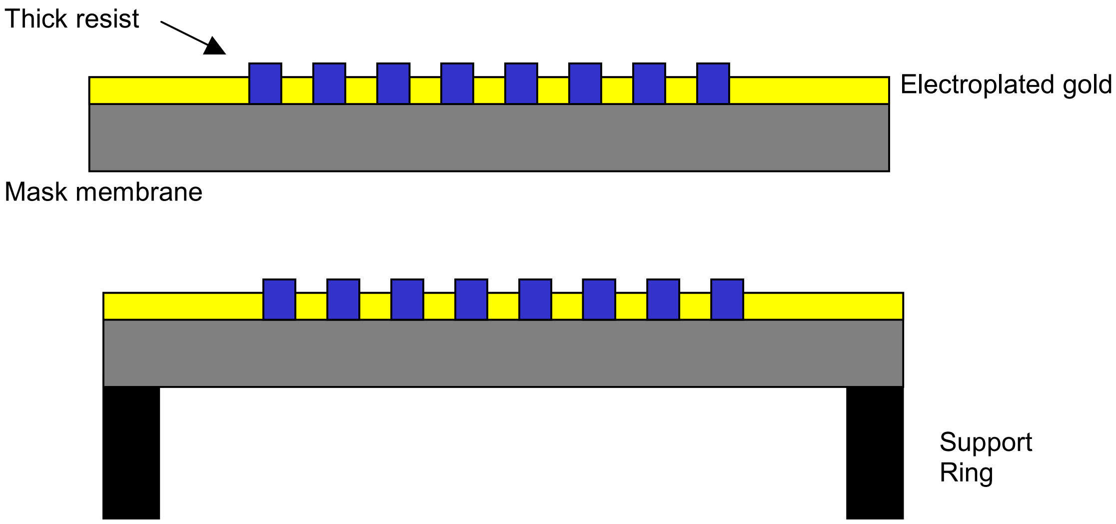

Figure 1 Main process steps for the production of an x-ray mask

Masks fabricated with graphite substrate as membrane include (Figure 2), Micro Motion project; Mold-LIGA project; Optic Bench project; Test pattern masks.

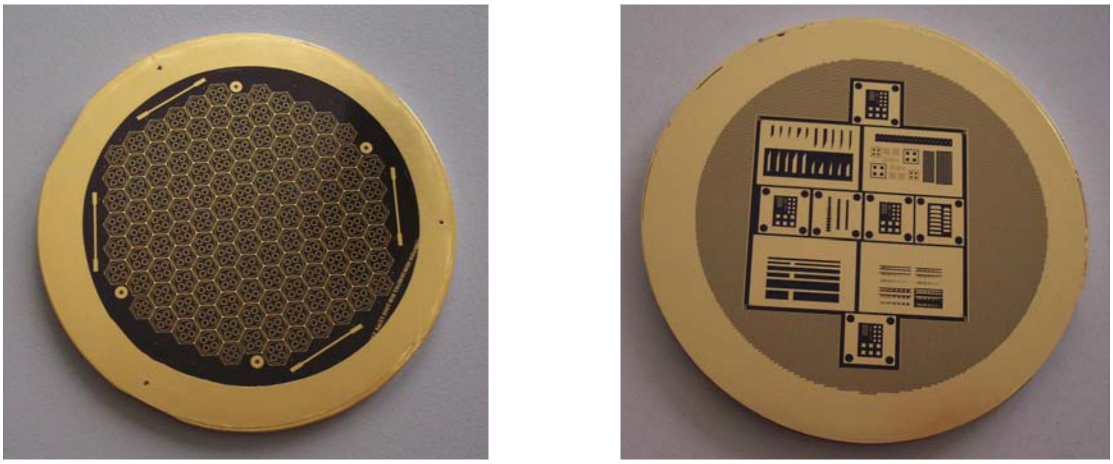

MicroMotion project   Mold-LIGA project

Optic Bench project   Test pattern

Figure 2 Examples of x-ray masks made in BESSY-- Graphite membrane X-ray masks

Masks fabrication process with thin glass as membrane has been developing, masks from MicroMotion project, Mold-LIGA project, Optic Bench project, and Test pattern masks have been made in BESSY (Figure 3, Figure 4).The optic transparency of glass membrane provides the advantage in making X-ray masks with alignment marks (Figure 4), especially with conductive and transparent ITO film as plating base (Figure 5).

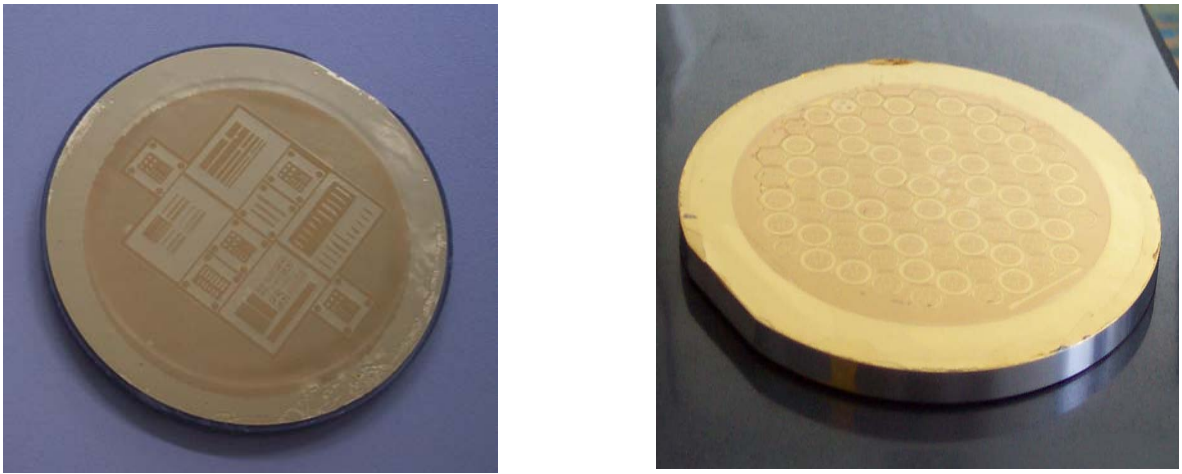

MiMo project Mold-LIGA project

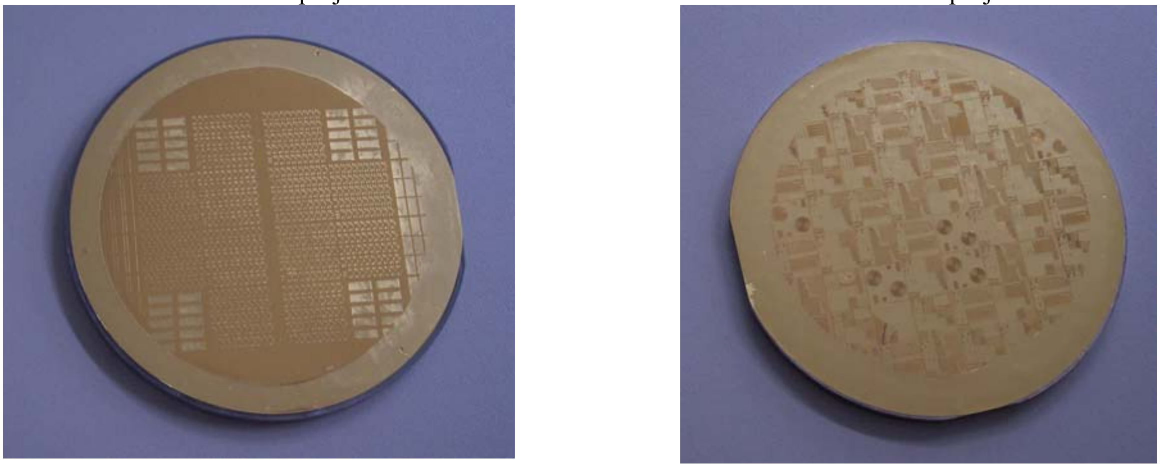

Optic Bench project Test pattern

Figure 3 Examples of x-ray masks made in BESSY -- Glass membrane X-ray masks

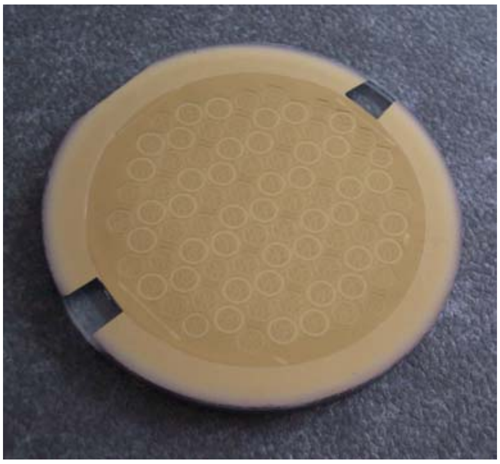

Figure 4 Glass membrane supported by glass ring, the two optic transparency windows for alignment marks

Figure 5 Gold plating on glass substrate with ITO as plating base

For these three different membrane X-ray masks, graphite membrane mask is cost-effective and easy handle in fabrication[3] but the high roughness on sidewall of the patterned resist structures limited its application in high precision structures; glass carbon membrane has not only the same advantages as graphite but also overcome the disadvantage regard of the roughness on sidewall of the resist structures; glass membrane is thin and fragile and difficult handle, but its optic transparency provides the advantage in making X-ray masks with alignment marks, especially with conductive and transparent ITO film as plating base.

Reference

1. Yohannes M. Desta, Bernd Loechel, Overview on X-ray Mask Fabrication for HARMST, HAMST'03, Monterey, California, USA
2. Linke Jian, Martin Bednarzik, Heinz-Ulrich Scheunemann, Daniel Schondelmaier, Ingrid Wichert, Alexandre Firsov, Ivo Rudolph, Bernd Loechel, Improvement in Cost-Effective X-Ray Mask Fabrication, HAMST'03, Monterey, California, USA
3. Yohannes M. Desta, Jost Gottert, Linke Jian, Georg Aigeldinger, Michael C. Murphy, Phil Coane, Graphite Membrane X-ray Masks for Rapid and Inexpensive Prootyping of LIGA Structures, HAMST'01, Baden-Baden, Germany, 2001

Photoionization cross sections of Kr and Xe from threshold up to 1000 eV

M. Richter, A.A. Sorokin, G. Ulm
Physikalisch-Technische Bundesanstalt, Berlin, Germany

Chr. Gerth, K. Tiedtke
Deutsches Elektronensynchrotron, Hamburg, Germany

S.V. Bobashev
Ioffe Physico-Technical Institute RAS, St.Petersburg, Russia

In atomic and molecular physics, photoionization (PI) is a fundamental process. The knowledge of absolute PI cross sections with low uncertainty is crucial for the understanding of photon-atom interaction. Moreover, accurate PI cross sections of rare gas atoms are needed in many fields of applied research, for example, when the absolute photon intensity of sources of VUV and soft X-ray radiation is measured using an ionization chamber. In this paper we propose recommended data for absolute total PI cross sections of Kr and Xe with a relative standard uncertainty of 3 %. The experiments are based on the accurate measurement of ratios of total cross sections for PI and electron-impact ionization (EI) followed by a normalization procedure. The apparatus used for the cross-section ratio measurements has been discussed in detail previously [1,2].

The measurements refer to the successive ionization of a target gas by electrons with known energy as well as by monochromatized synchrotron radiation. While the current of impact electrons is measured using a Farday cup the photon flux is determined with the help of a calibrated semiconductor photodiode as detector standard. Ions produced in these processes are collected and recorded by a microchannel plate (MCP) detector operated in the counting mode. In order to obtain the same collection and detection efficiency for differently charged ions, the latter are accelerated in a constant electric field up to kinetic energies of 13 keV for single charged ions. The measurements were performed at the SX700 and NIM beam lines for detector calibration and reflectometry in the Radiometry Laboratory of the Physikalisch-Technische Bundesanstalt [see, e.g., Ref. 3 and references therein]. Relative standard uncertainties as low as 1.3 % to 1.9 % for the cross-section ratios were achieved [2].

Based on the cross-section ratio measurements, total PI cross sections of Kr and Xe were determined in a two-step procedure. In the first step values for the total EI cross sections at 1000 eV electron energy were derived from the measured ratios using absolute total PI cross sections as reported in the literature by different experimental groups [4-8] with relative uncertainties quoted being smaller than 7 %. The relative uncertainties for these values arise from the relative uncertainties of the measured ratios and the relative uncertainties of the absolute total PI cross sections claimed by the groups. This step enabled us to examine different sets of PI cross-section data, to choose the most reliable of them and to derive an average value $\sigma_e(E = 1000\text{ eV})$ for the total EI cross section [2]. The corresponding values for Kr and Xe were determined with a relative standard uncertainty of 2 % by averaging the data obtained in the VUV spectral range below 25 eV photon energy using the PI cross sections reported in Ref. 4 with a quoted relative uncertainty of 0.8 %.

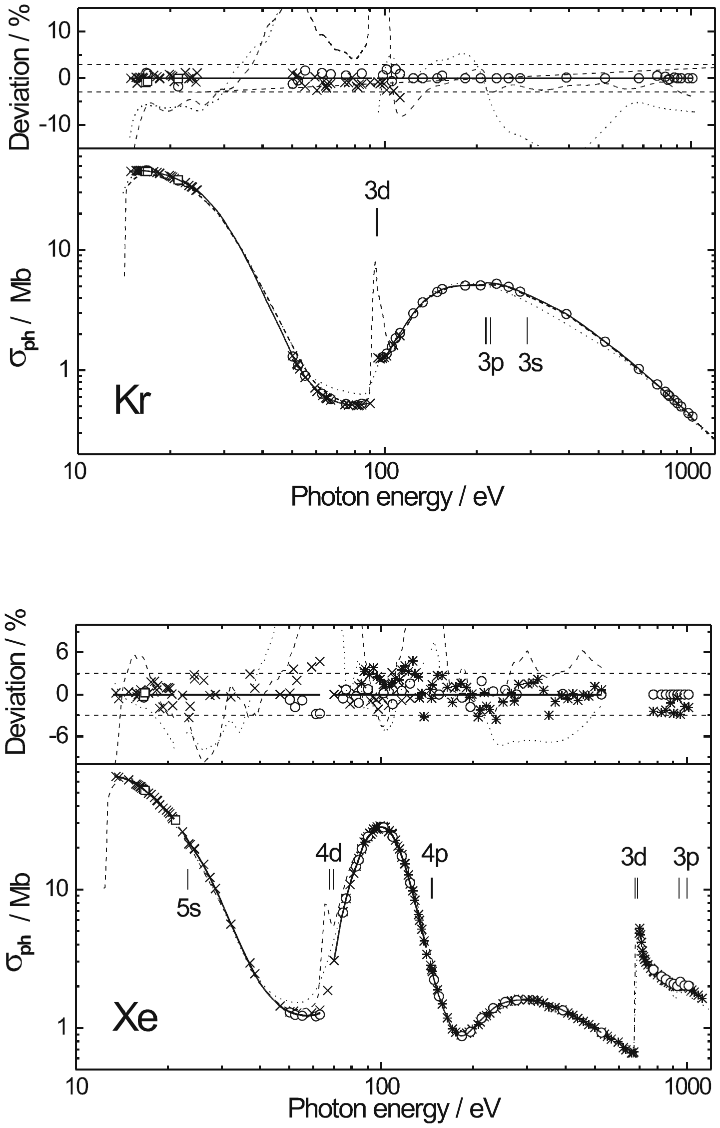

FIG. 1. Total photoionization cross sections of Kr and Xe: present experimental data (o), Samson and Yin [4] (□), Samson et al. [5] (×), Saito and Suzuki [12] (✻), present recommended data (—), Henke et al. [11] (----), Marr and West [9] and West and Morton [10] (····). The upper plots show the fractional deviation of the experimental and preceding recommended data from the present recommended data. In the case of Xe, in the spectral range above the 3d thresholds, the fractional deviation of the experimental data [12] from the present experimental data are shown.

In the second step, taking the measured values for the cross-section ratios and the values for $\sigma_e(E = 1000\ \mathrm{eV})$, we derived total PI cross sections for Kr and Xe in the photon energy range from 50 eV to 1012 eV with relative standard uncertainties of 2.4 % to 2.7 %, i.e. with uncertainties which are smaller than those reported in the literature for this spectral range in the past. The present total PI cross sections of Kr and Xe are shown in Fig. 1 together with the experimental data of Samson and coworkers obtained with quoted relative uncertainties of 0.8 % to 3 % [4,5]. Also shown are recommended values for absolute total PI cross sections proposed in this paper with a relative uncertainty of 3 % as well preceding recommended data [9-11] and absolute total PI cross sections of Xe recently measured with a quoted relative uncertainty of 1 % [12]. The present recommended values were obtained for Kr and Xe in the spectral range below the 2p and 3d thresholds, respectively, from a polynomial fit to our experimental values and to the experimental values reported in Refs. 4 and 5 by the least-squares method, taking into consideration the relative cross-section dependence of the preceding recommended data [9-11]. In the spectral range where the two data sets overlap, the two polynomial fits were averaged. No polynomial fit was performed in the spectral intervals containing absorption edges and resonance structures in the photoionization spectrum. The present experimental and recommended data for Xe are in good agreement with the data obtained in Ref. 12, while significant discrepancies occur between our recommended data and those published in Refs. 9-11.

The present total PI cross section data have been used for the absolute calibration of a recently developed gas-monitor detector [13]. The detector, which is based on atomic photoionization at low target gas density, allows for a quantitative characterization of sources of extremely intense and pulsed VUV and soft X-ray radiation, like the VUV free electron laser (FEL) at the TESLA Test Facility (TTF) at DESY which emits up to about 10^{14} photons within a pulse of 100 fs duration. First promising results from the gas-monitor detector were obtained recently during phase 1 of the TTF project. Fig. 2 shows an example of a pulse measurement at a photon energy of 14.3 eV about one order of magnitude below saturation of the FEL. Single-pulse readout was realized by photoelectron detection.

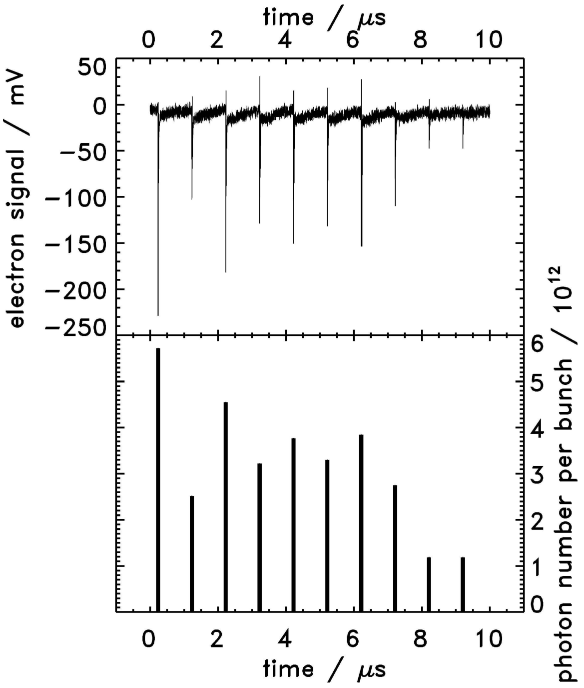

FIG. 2. Photoelectron signal of a FEL bunch train filled with 10 bunches (top) and evaluated photon numbers per bunch (bottom), measured at a photon energy of 14.3 eV at the TTF-FEL with a recently developed gas-monitor detector using Xe as the target gas [13].

[1] A.A. Sorokin, L.A. Shmaenok, S.V. Bobashev, B. Möbus, G. Ulm, Phys. Rev. A. **58**, 2900 (1998).

[2] A.A. Sorokin, L.A. Shmaenok, S.V. Bobashev, B. Möbus, M. Richter, G. Ulm, Phys. Rev. A. **61**, 022723 (2000).

[3] M. Richter, G. Ulm, J. Electr. Spectrosc. Relat. Phenom. **101-103**, 1013 (1999).

[4] J.A.R. Samson, L. Yin, J. Opt. Soc. Am. B **6**, 2326 (1989).

[5] J.A.R. Samson L. Lyn, G.N. Haddad, G.C. Angel, J. Phys. IV **1**, C99 (1991).

[6] B.L. Henke, R.L. Elgin, R.E. Lent, R.B. Ledingham, Norelco Reporter **14**, 112 (1967).

[7] F. Wuilleumier, Ph. D. Thesis, Université de Paris, 1969 (unpublished).

[8] J. Lang, W.S. Watson, J. Phys. B **8**, L339 (1975).

[9] G.V. Marr, J.B. West, At. Data Nucl. Data Tables **18**, 497 (1976).

[10] J.B. West, J. Morton, At. Data Nucl. Data Tables **22**, 103 (1978).

[11] B.L. Henke, E.M. Gullikson, J.C. Davis, At. Data Nucl. Data Tables **54**, 181 (1993); (see also E.Gullikson, http://www-cxro.lbl.gov/optical_constants/).

[12] N. Saito, I.H. Suzuki, Nucl. Inst. Meth. A **467-468**, 1577 (2001).

[13] M. Richter, A. Gottwald, U. Kroth, S.V. Bobashev, A.A. Sorokin, L.A. Shmaenok, J. Feldhaus, Ch. Gerth, K. Tiedtke, “ Verfahren und Monitordetektor zur Bestimmung der Intensität von gepulster VUV- oder EUV-Strahlung sowie Verwendung eines derartigen Monitordetektors”, Deutsches Patent- und Markenamt, Aktenzeichen: 102 44 303.3, München (2002)

This work is funded by the Deutsche Forschungsgemeinschaft (DFG RI 804/3-1; 436 RUS 113/581/3-1) and the Russian Basic Research Foundation (RBRF 01-02-04001).

Stability of an ECR source as transfer standard for the VUV spectral region

A. Gottwald, S. Appelfeller, M. Richter
Physikalisch-Technische Bundesanstalt, Abbestr. 2-12, 10587 Berlin, Germany

U. Schühle
Max-Planck Institut für Aeronomie, Max-Planck-Str. 2, 37191 Katlenburg-Lindau, Germany

One of the basic tasks of the PTB radiometry laboratory at BESSY II is the development, characterization and calibration of VUV radiation sources for radiometric applications in industry and basic research. The electron storage ring is a primary source standard in this spectral region [1], i.e. its spectral radiant power can be calculated within the framework of fundamental principles of electrodynamics from a set of geometrical and storage-ring parameters. Established transfer standards such as deuterium lamps, Penning- and hollow cathode discharge sources suffer from their limited spectral range and, in particular, their limited lifetime and stability due to electrode erosion. To overcome this limitations, a radiation source based on the principle of Electron Cyclotron Resonance (ECR) had been developed and intensively characterized at PTB [2,3].

Recently, the emission of the ECR source operated with neon in the wavelength interval between 50 nm and 75 nm has been investigated concerning stability and reproducibility. Based on the former measurements, the cavity of the ECR source has been tuned to parameters which allow for long-term stable operation of the source. The neon gas pressure was stabilized at 1.7×10^{-4} mbar and the microwave heating at about 11 W at 9.94 GHz resonance frequency.

The measurements were performed at a normal incidence monochromator for the 40 to 400 nm spectral range. The emission of the ECR source was compared to a hollow cathode transfer standard source (Fig.1) previously calibrated at the source calibration beamline in the PTB radiometry lab [4]. Therefore, measured spectral radiant intensities are traceable to the primary source standard BESSY II. For the stability measurements, the ECR source was operated over a 40 day time period, with a longest non-disturbed run of 7 days. To investigate the reproducibility, the plasma was ignited several times. Wavelength scans of the emission spectrum were performed as well

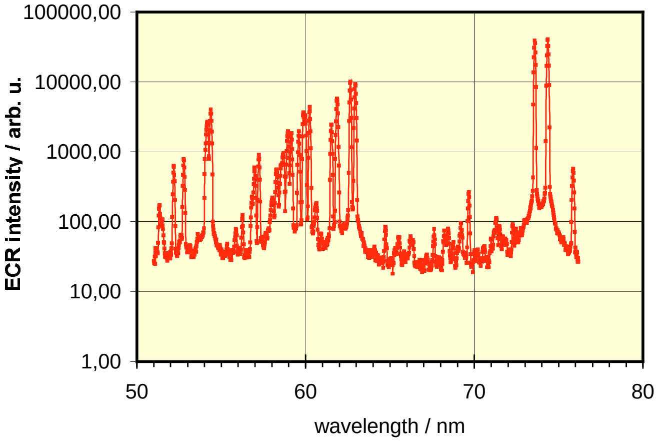

FIG. 1. ECR spectrum of the Ne plasma emission.

as continuously monitoring of the line intensity at the selected Ne I emission line at a wavelength of 61.9 nm, and stability has been determined from both kind of spectra (Fig. 2). During operation, input parameters for the ECR (Ne gas pressure and microwave power) were controlled and kept stable better than 1 %. The stability of the monochromator and detector was checked by regular re-calibrations with the hollow cathode transfer standard.

From the results shown in Fig. 2, the relative standard uncertainty (σ=1) of the spectral radiance at the 61.9 nm Ne I emission line is deduced to be about 4 %. The recorded spectra over the whole 50 to 75 nm range show no significant changes of the spectral distribution, or shifts between line intensities, so that the result shown for this selected wavelength can be regarded as representative.

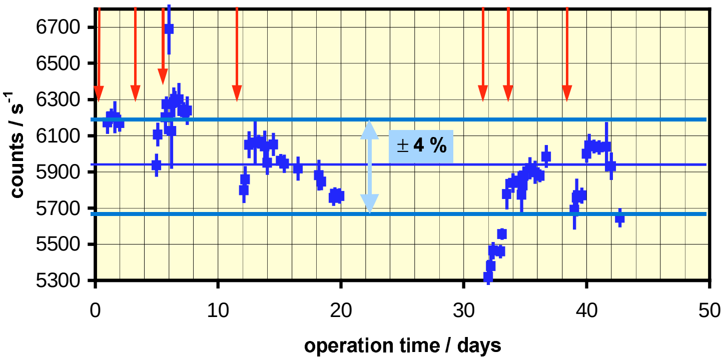

FIG. 2. Stability and reproducibility of the ECR emission, measured at emission wavelength of 61.9 nm. Red arrows indicate new ignitions of the source plasma.

In conclusion, the emission of the ECR plasma is comparable to the hollow cathode as established transfer standard, i.e. lower but still sufficient intensity at the bright Ne I lines that dominate the hollow cathode spectrum but significant higher intensities at other lines. The stability demonstrated here is even better than the hollow cathode which showed a stability of about 6% to 10% during the measurement period, mainly due to degradation caused by cathode erosion, whereas the ECR source showed no such degradation effects. The measurements implicate that after ignition, the relaxing time for the source is in the order of about 24 h. Drifts within the continuos operation might arise from the non-linear response of the emission on small changes of the sources' input parameters, which might be further stabilized by technical improvements.

[1] R. Thornagel, R. Klein, G. Ulm, Metrologia **38**, 385 (2001)

[2] P. Grübling, J. Hollandt, B. Möbus, G. Ulm, BESSY Annual Report 1998, 110 (1999)

[3] P. Grübling, J. Hollandt, G. Ulm, Rev. Sci. Instrum. **71**, 1200 (2000)

[4] M.Richter, J. Hollandt, U. Kroth, W. Paustian, H. Rabus, R. Thornagel, G. Ulm, Metrologia **40** (2003), in press

Irradiation of blood samples with monochromatic X-rays

M. Krumrey, M. Hoffmann, P. Müller and G. Ulm
Physikalisch-Technische Bundesanstalt, Abbestraße 2-12, 10587 Berlin, Germany

Breast cancer is the most frequent type of cancer for women and X-ray mammography is the most commonly used method for its detection. On the other hand, every mammography is associated with a dose delivered to the breast which can induce radiation effects. To estimate these effects, the relative biological effectiveness (RBE) is used, where relative refers to hard γ-rays, because most data for late radiation effects in humans are available for atomic bomb survivors for which the incident radiation can be approximated by ^{60}Co γ-rays. It is currently assumed that all X-rays have the same effectiveness as γ-rays, thus an RBE of 1. However, in recent publications an RBE of up to 8 has been claimed for mammography spectra generated with X-ray tubes using a W anode and Rh filtration [1]. Lower RBE values have been found for typical mammography spectra, generated with a Mo anode and Mo filtration [2]. These spectra are dominated by the K_α peak at 17.4 keV and the K_β peak at 19.6 keV (Fig. 1). The spectral shape especially at low energies can have a significant influence on the RBE as a large fraction of the dose is due to low energy photons.

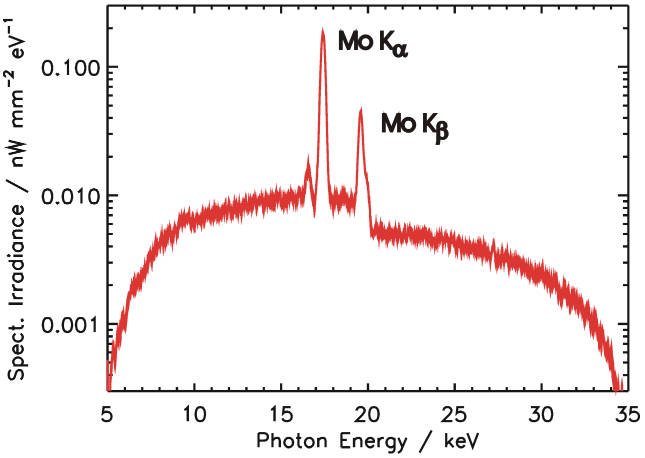

Fig. 1: Typical mammography spectrum, produced with a Mo anode at 35 kV and a Mo filter

In co-operation with the GSF-National Research Center for Environment and Health, a program has been started to determine the RBE as a function of the photon energy. Blood samples are irradiated with monochromatic X-rays and the induced chromosome aberrations in lymphocytes are analyzed. In a first step, irradiations at 17.4 keV and 40 keV were performed at the BAMline [3], the wavelength shifter beamline jointly operated by the Bundesanstalt für Materialforschung und –prüfung (BAM) and the Physikalisch-Technische Bundesanstalt (PTB). At both energies, doses between 0.25 Gy and 2 Gy were applied. The dosimetry is based on a disk-shaped transmission ionization chamber, produced by the Department of Dosimetry for Radiotherapy and Diagnostic Radiology of the Physikalisch-

Technische Bundesanstalt (PTB) in Braunschweig. The radiation passes the chamber on its central axis perpendicularly through the front and back electrodes and the central measuring electrode, all consisting of 25 μm thick graphitized polyethylene foils. The central electrode has an active circular area of 50 mm diameter. The spectral responsivity *s* of this detector has been determined with monochromatized synchrotron radiation at the same beamline by calibration against a plane-parallel free-air ionization chamber, a primary standard detector for dosimetry [4].

The disk-shaped blood samples have a diameter of 23 mm. Due to the limited opening angle of synchrotron radiation in the vertical plane, it is not possible to irradiate a large area with a homogeneous beam. While most synchrotron radiation beamlines are even designed to focus the radiation onto an area of well below 1 mm^2, the BAMline can provide a horizontal stripe which can be up to 35 mm wide at a distance of 10 m behind the monochromator. The homogeneity has been verified by scanning a vertical slit through the beam and additionally by taking pictures with an X-ray sensitive CCD camera system. The obtained variations were below 3%. A large area can be irradiated by scanning the sample vertically through this stripe. To eliminate the effect of the beam decay in the electron storage ring where the lifetime is about 7 h, the sample is scanned back and forth with the two-fold speed. The time to deposit e.g. 1 Gy in the blood sample varied between 2 min at 17.4 keV and 50 min at 40 keV.

These observed RBE, obtained from the induction of acentric and dicentric chromosomes at low radiation doses, is only about half of the values reported earlier for exposure of blood from the same donor with the broad energy spectra of 29 kV X-rays (mean energy of 17.4 keV) and 60 kV X-rays (mean energy of 48 keV) [2,5]. This confirms the assumption that a large fraction of the effects should be attributed predominately to photons with energies well below the mean energy. Further experiments with monochromatic X-rays at lower photon energies are being performed.

References

[1] D. Frankenberg, K. Kelnhofer, K. Bär and M. Frankenberg-Schwager, Radiat. Res. **157,** 99-105 (2002)

[2] E. Schmid, D. Regulla, H.M. Kramer and D. Harder, Radiat. Res. **158**, 771-777 (2002)

[3] W. Görner, M.P. Hentschel, B.R. Müller, H. Riesemeier, M. Krumrey, G. Ulm, W. Diete, U. Klein and R. Frahm, Nucl. Instr. and Meth. **A 467-468**, 703-706 (2001)

[4] B.-A. Engelke, W. Oetzmann und G. Struppek, PTB-Report Dos-16, Braunschweig (1988)

[5] E. Schmid, M. Krumrey, G. Ulm and D. Regulla, submitted to Radiat. Res.

Characterization of thickness standards with X-ray reflectometry

M. Krumrey, M. Hoffmann and G. Ulm
Physikalisch-Technische Bundesanstalt, Abbestraße 2-12, 10587 Berlin, Germany

High accuracy film thickness measurements in the range below 100 nm can be made by various complex methods like spectral ellipsometry (SE), scanning force microscopy (SFM), grazing incidence X-ray reflectometry (XRR) or X-ray fluorescence analysis (XRF). A key question in nanotechnology is to achieve consistent results on a level of uncertainty below one nanometer with different techniques. In the framework of a project funded by BMBF, reference standards for the thickness of films have been developed, evaluated and tested [1]. Two different types of thickness standards have been realized:

- Metal layer standards consist of a fused silica substrate with a Pt layer or a C-Ni-C system with nominal thickness values of 10 nm and 50 nm. The carbon coatings are protective layers with thickness values of about 2 nm to 3 nm to prevent oxidation of the Ni film and to suppress diffusion into the substrate.
- Silicon dioxide layer standards have been produced on Si wafers. Different oxide layer thicknesses between 6 nm and 1 μm have been realized. A structure produced by direct electron beam writing allowed the measurement of the film thickness as a step height with an AFM.

Both types of standards have been calibrated by XRR with monochromatized synchrotron radiation at the PTB four-crystal monochromator beamline [2] in combination with a high-precision reflectometer [3]. The thickness is obtained by fitting the measured reflectance at a fixed angle as a function of the photon energy (fig. 1) or for a $\Theta/2\Theta$-scan at fixed photon energy (fig. 2). The data analysis using the program IMD (Bell Labs, USA) is based on the Fresnel equations and takes into account surface and interface roughness effects [4].

For the metal film standards the $\Theta/2\Theta$-scans have been performed at 8048 eV, the energy of Cu K_α radiation which is used in commercial X-ray tube based diffractometers. The results obtained at four different facilities show excellent agreement. For the SiO_2 on Si standards a photon energy of 1841 eV, just above the Si K-edge, has been chosen to obtain pronounced interference effects. With the exception of the 6 nm SiO_2 film, relative uncertainties of 1% have been achieved for the layer thickness.

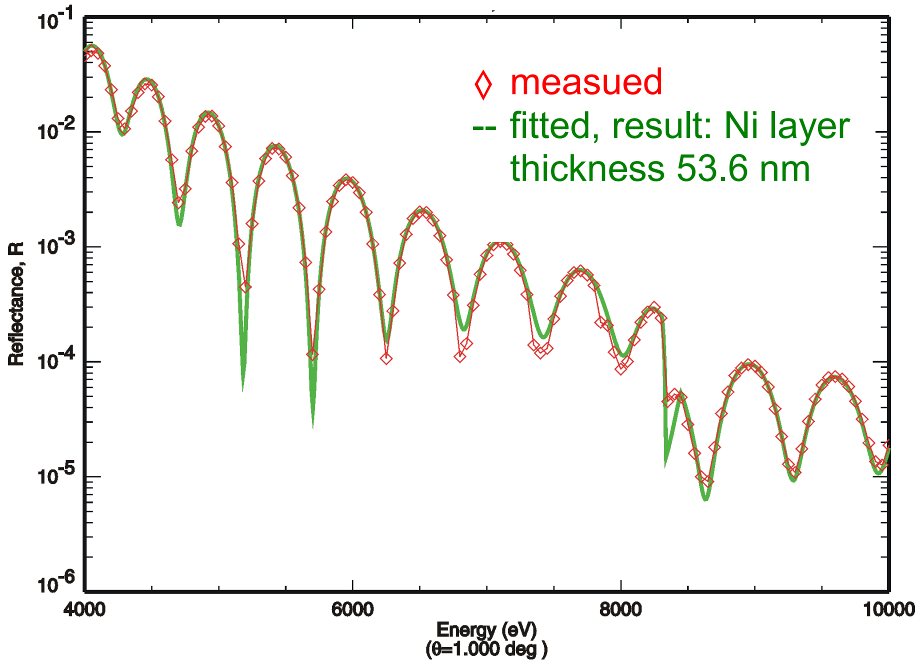

Figure 1:

Reflectance of a C-Ni-C layer system on a fused silica substrate at fixed angles. The structure at 8333 eV is due to the Ni K edge.

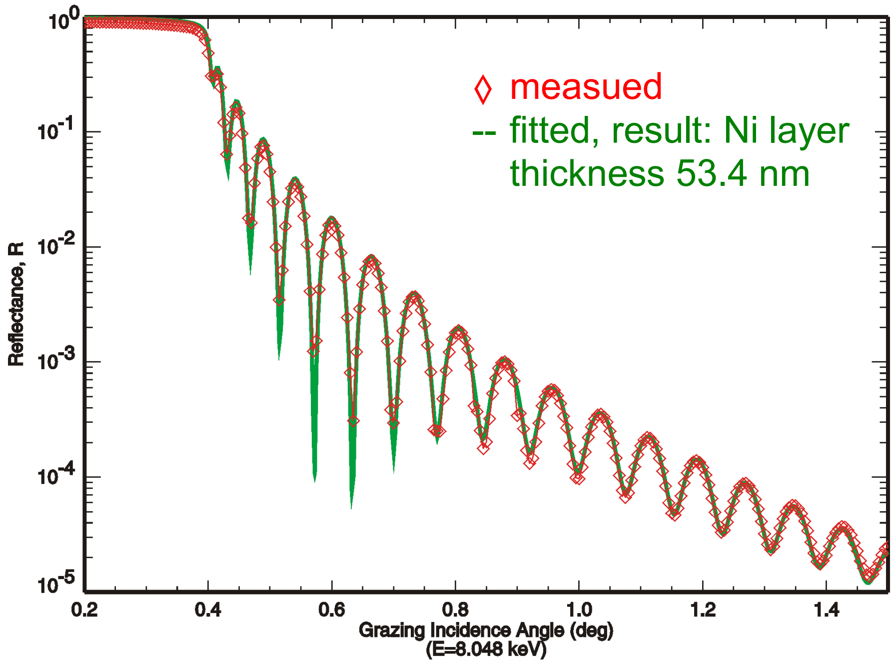

Figure 2:

Reflectance of a C-Ni-C layer system on a fused silica substrate at fixed photon energy

References

[1] K. Hasche, G. Ulm, K. Herrmann, M. Krumrey, G. Ade, J. Stümpel, I. Busch, P. Thomsen-Schmidt, S. Schädlich, A. Schindler, W. Frank, M. Procop and U. Beck Proc. of 3rd euspen Int. Conference – Eindhoven 2002, 549 - 552

[2] M. Krumrey and G. Ulm
Nucl. Instr. and Meth. A **467-468**, 1175 - 1178 (2001)

[3] D. Fuchs, M. Krumrey, P. Müller, F. Scholze and G. Ulm
Rev. Sci. Instrum. **66**, 2248 - 2250 (1995)

[4] D. L. Windt, Computers in Physics **12,** 360 – 370 (1998)

High-accuracy radiometry for EUV source calibration at PTB

F. Scholze, J. Tümmler, and G. Ulm.

Physikalisch-Technische Bundesanstalt, Abbestraße 2-12, 10587 Berlin, Germany

A major challenge for EUV lithography is the development of suitable radiation sources for the production process[1]. Radiometry is needed to characterize these sources regarding their in-band power, spectral distribution, spatial distribution of emitting volume, and angular distribution of the emission. At PTB, radiometry for EUV sources is based on detectors. Photodiodes are calibrated as transfer detector standards[2] with a relative uncertainty of u=0.26% by comparison to a cryogenic electrical substitution radiometer[3]. With these high-accuracy calibrations, PTB serves the EUVL source program within in the European MEDEA+ framework[4] and international benchmarking efforts like the 'flying circus'[5].

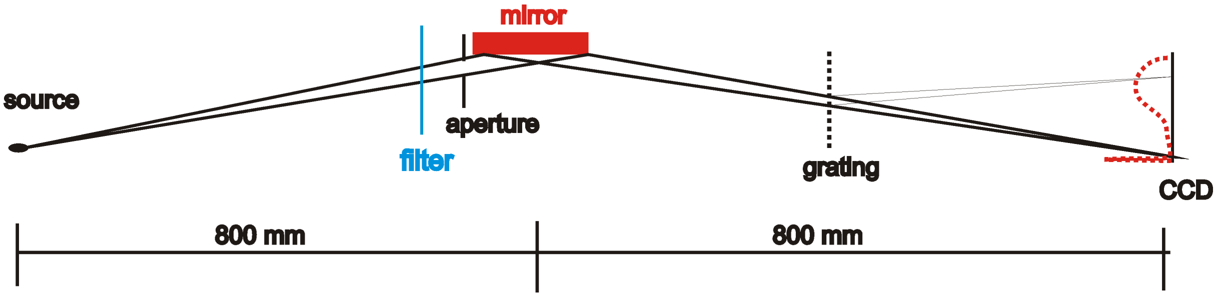

Figure 1 Scheme of an imaging spectrometer used to characterize the spectral distribution of EUV radiation and the spatial distribution of emitting volume.

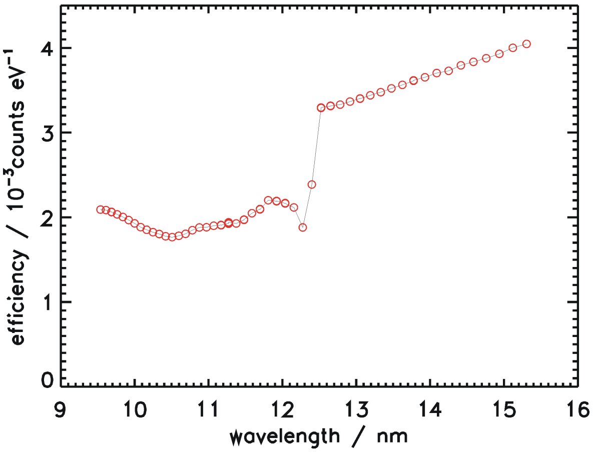

Figure 2 Spectral detection efficiency of grating plus CCD, measured by direct comparison to a photodiode using monochromatized radiation at the soft X-ray radiometry beamline. Measured points are shown as open circles, the line is only to guide the eye.

For the characterization of a (LPP)-source, developed at the Max-Born-Institute[6], an imaging spectrometer has been set-up for the characterization regarding spectral photon flux, source size and source point stability. The optical scheme of the spectrometer is shown in Figure 1. The main components are a solid angle defining aperture, a grazing incidence mirror which is used to obtain an image of the source over a broad spectral range, the dispersing grating and a CCD as the image detector. For source size measurements, a filter is used to reduce the intensity at the CCD and the grating is removed.

Figure 2 shows the spectral efficiency of the spectrograph as counts at the CCD with respect to the total energy of the photons incident at the grating. At 13 nm, the energy per photon is about 100 eV, thus one count at the CCD corresponds to between two and five photons. In the range from 10 nm to 15 nm, the spectrometer efficiency varies by about a factor of two. The reason for this rather strong spectral dependence is the efficiency of the CCD-chip as shown in Figure 3. The diffraction efficiency of the grating, see Figure 4, shows a rather smooth spectral behaviour. Thus, the main source of the spectral dependence is the CCD which clearly shows the need for absolute detector calibration for the characterization of spectrometers.

With this device, we characterized a gold target LPP source to be used in a laboratory based EUV-reflectometer[7]. We obtained a source size of 30 µm by 55 µm (horizontal by vertical) and a stability of better than 5 µm, horizontally and 9 µm vertically. The spectral photon flux was $1*10^{14}$ /(s sr 0.1 nm) at 13.4 nm at a laser pulse energy of 650 mJ. The shot-to-shot stability of the EUV flux is about 5% (1σ) for laser pulse energies above 200 mJ. In this range, a linear relation between laser pulse energy and EUV output was obtained.

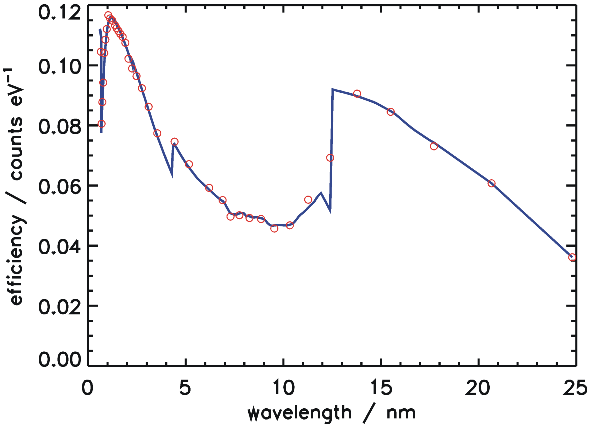

Figure 3 Detection efficiency of a backside illuminated CCD, measured by comparison to a photodiode using monochromatized radiation at the soft X-ray radiometry beamline. Measured points are shown as open circles, the line is an interpolation using a responsivity model developed for photodiodes.

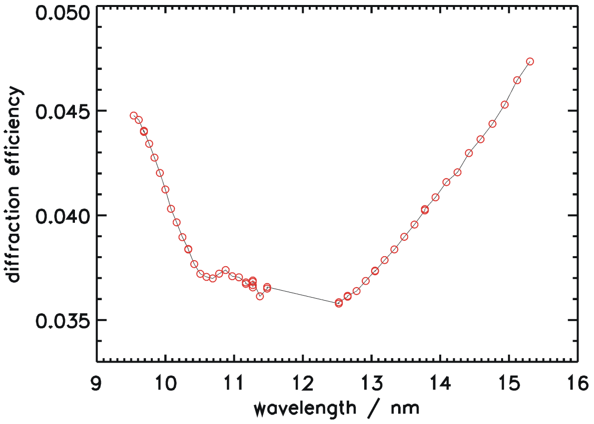

Figure 4 Absolute diffraction efficiency of a free-standing gold transmission grating. The efficiency is the ratio of the intensity diffracted into the first order of the grating normalized to the radiation incident at the grating.

References

1 U. Stamm, H. Schwoerer, R. Lebert, *Phys. Journal*, **1 Nr. 12**, 33-39 (2002)

2 F. Scholze, J. Tümmler, and G. Ulm, Metrologia **40** (2003) in print

3 H. Rabus, V. Persch, and G. Ulm, Appl. Optics **36**, 5421-5440 (1997)

4 G. Schriever, M. Rahe, U. Rebhan, D. Basting, W.J. Walecki, H. Layuth, R. Lebert, K. Bergmann, D. Hoffmann, O. Rosier, W. Neff, R. Poprawe, R. Sauerbrey, H. Schwoerer, S. Düsterer, C. Ziener, P. Nickles, H. Stiehl, I. Will,. W. Sandner, G. Schmahl, D. Rudolf, *Proc. SPIE,* **4146,** 113-120 (2000)

5 R. Stuik, F. Scholze, J. Tümmler, F. Bijkerk, Nucl. Instrum. Meth. **A492**, 305-316 (2002)

6 L. van Loyen, T. Böttger, S. Braun, H. Mai, A. Leson, F. Scholze, J. Tümmler, G. Ulm, H. Legall , H. Stiel , C. Rempel, A. Schulze, J. Brutscher , F. Macco,
"A New Laboratory EUV Reflectometer for Large Optics using a Laser Plasma Source,"
accepted for SPIE 'Microlithography', Santa Clara 2003

7 F. Scholze, F. Scholz, J. Tümmler, G. Ulm, H. Legall, P.-V. Nickles, W. Sandner, H. Stiel, L. vanLoyen,
"Characterization of a laser produced plasma source for a laboratory EUV reflectometer,"
accepted for SPIE 'Microlithography', Santa Clara 2003

Comparison of Extreme Ultraviolet Reflectance Measurements at CXRO and PTB

F. Scholze [a], J. Tümmler [a], E. Gullikson [b], A. Aquila [b]

[a] Physikalisch-Technische Bundesanstalt, Abbestraße 2-12, 10587 Berlin, Germany

[b] Center for X-Ray Optics, Lawrence Berkeley National Laboratory,
Berkeley, California 94720

The semiconductor industry has pushed linewidths on integrated-circuit chips down to 100 nm. To pattern ever-finer lines by use of photolithography, the industry is now preparing the transition to extreme ultraviolet lithography (EUVL) at 13 nm by 2007. Reflectometry is an essential metrology of the multilayer coatings of masks and optics for EUV lithography. A high absolute accuracy and worldwide traceability of reflectance measurements is mandatory for a worldwide system development. As EUVL matures[1], the requirements for the accuracy of reflectivity and wavelength measurements are becoming tighter. In response to this demand, there have been substantial improvements of measurement precision and accuracy at the facilities in Europe and the US. Achieving high accuracy involves quantifying and reducing all the sources of systematic measurement uncertainties. We report the results of a cross-calibration study between the Physikalisch-Technische Bundesanstalt (PTB) at BESSY II[2] which serves the European EUVL program and the Center for X-ray Optics (CXRO) at the ALS[3] which serves the US EUVL program. A direct comparison of EUV reflectance measurements at the ALS CXRO and PTB yielded perfect agreement within the mutual relative uncertainties of 0.14% for reflectance and 0.014% for wavelength. A broader round-robin series of measurements including the other reflectometry facilities around the world is in progress and will be reported on in the near future.

At PTB, reflectometry[4] is performed at the soft X-ray radiometry beamline[5], a bending magnet beamline equipped with a plane grating monochromator in the radiometry laboratory at BESSY II. The monochromator uses a 1200 line/mm grating for the whole spectral range from 0.6 nm to 65 nm. The beamline is optimized to deliver radiation of high spectral purity. The deflection angle at the grating is optimized for third and higher order suppression, and additionally edge filters are used for the suppression of remaining second order contributions. The relative higher order contributions to the radiant power are below 1% for all wavelengths between 0.65 nm and 25 nm and below 0.03% in the EUV spectral range[5,6]. Another critical issue for the spectral purity is the presence of diffusely scattered radiation. An upper bound for the total contribution of diffusely scattered radiation of less than 0.2% has been derived for the wavelength of the Si L_3-edge at 12.42 nm and the Be K-edge at 11.08 nm[6].

The Center for X-Ray Optics (CXRO) maintains a beamline at the Advanced Light Source (ALS) dedicated to accurate calibrations of optics in the EUV and soft x-ray[3] . The beamline uses a varied line spacing (VLS) plane grating monochromator and a three mirror order suppressor to achieve high spectral purity[7]. The higher order radiation from the monochromator is reduced to a negligible level (0.0002%) using a transmission filter and the three-mirror order suppressor. The main source of spectral impurity[3] is scattered radiation which is measured to be 1.3% of the incident intensity at a wavelength of 13.4 nm. A correction has been applied to the reflectivity measurement for the scattered radiation. The uncertainty in the amount of scattered radiation (0.12%) is the main source of reflectance uncertainty.

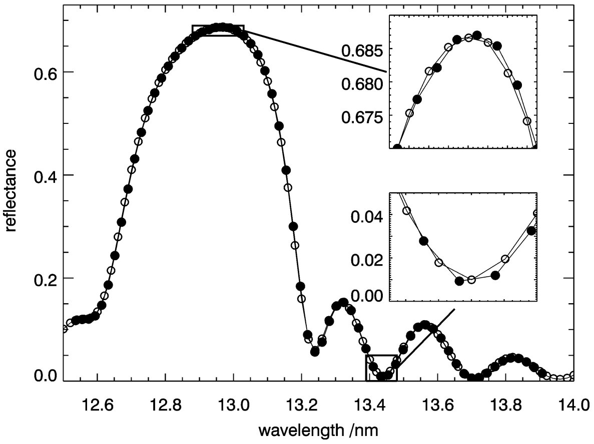

Figure 1 Measured reflectance of a Mo/Si multilayer mirror. Measurements at PTB are shown solid circles and at the CXRO data as open circles. The insets show details at the reflectance peak and a side minimum.

	PTB	CXRO
quantity	**relative uncertainty contribution u /10 $^{-3}$**	
peak reflectance		
stability of normalized intensity	0.3	0.2
inhomogeneity of the detector	0.6	0.7
higher diffraction orders	0.3	0.002
diffuse scattered radiation	1.2	1.2
total relative uncertainty of peak reflectance	**1.4**	**1.4**
peak wavelength		
Kr $3d_{5/2}$-5p resonance wavelength	0.12	0.12
repeatability of wavelength	0.08	0.08
total relative uncertainty of peak wavelength	**0.14**	**0.14**

Table 1 Compilation of the uncertainty contributions for the measurement of the reflectance at a wavelength around 13 nm. For the peak reflectance, the dominant contribution is diffuse scattered radiation outside the mirror bandwidth which is incident on the detector in the direct beam and not reflected. The main uncertainty for the wavelength is the uncertainty in the reference wavelength.

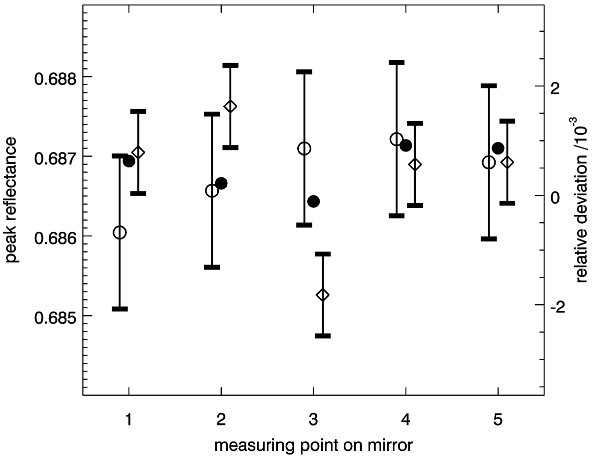

Figure 2 Peak reflectance measured at five points of the mirror. Shown are the initial measurement at PTB (open circles) the measurement at CXRO (closed circles) and the final measurement at PTB (diamonds). Error bars are shown for the initial measurement, representing the full 0.14% uncertainty, while the error bars at the final measurement are 0.075% without the systematic contributions from the spectral purity.

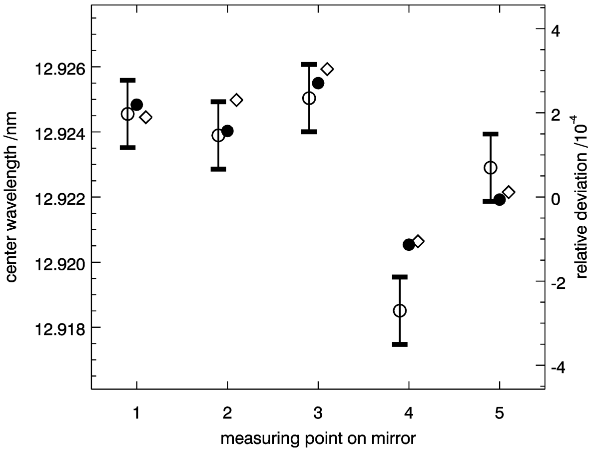

Figure 3 Center wavelength measured at five points of the mirror. Shown are the initial measurement at PTB (open circles) the measurement at CXRO (closed circles) and the final measurement at PTB (diamonds). Error bars are shown for the initial measurement, representing the relative repeatability of the wavelength of 8·10 $^{-5}$.

The uncertainties for peak reflectance and center wavelength obtained by CXRO and PTB are compiled in table 1. In both laboratories, the systematic uncertainty caused by spectral impurities of the monochromatized radiation dominates the total uncertainty of the peak reflectance. The wavelength is normalized to the Kr $3d_{5/2}$ -5p resonance[8] in both laboratories.

The measurements were performed on a Mo/Si multilayer coated one-inch diameter optical flat supplied by the FOM institute in the Netherlands. The sample was first measured by the PTB then sent to CXRO and finally re-measured by PTB. Measurements were made at the sample center and at four points located 5 mm from the center. The measurements at the sample center are shown in fig. 1. The agreement is practically ideal at the peak as well as in the region of the side wiggles.

The results are shown more quantitatively in figs. 2 and 3. Figure 2 shows the peak reflectance for all 5 points. For the initial measurement of PTB, the total uncertainty ($u=1\sigma$) is shown. All other but the second measurement of PTB at point 3 are within this rage. There is no systematic difference between CXRO and PTB values. The repeatability of the measurements is shown for the second measurement of PTB. Comparing initial and final measurement, again all but point 3 are within in that range. The change of the reflectance at point 3 is therefore attributed to the sample.

Figure 3 shows the center wavelength at half maximum. The error bars shown represent only the repeatability because the Kr $3d_{5/2}$ -5p resonance is used for reference at both laboratories. Therefore, the systematic uncertainty cancels in the comparison. The spread of the measured values exceeds the width of the error bar only for point 4. Point 4, however, also deviates significantly in wavelength from the other points. So, the explanation is most probably an inhomogeneity of the mirror.

Acknowledgements

We would like to thank Fred Bijkerk for providing the multilayer sample used for these measurements. The work at CXRO was supported by the Extreme Ultraviolet Limited Liability Company.

References

1 P. Gargini; Proc. SPIE **4688**, 25 (2002)

2 G. Ulm, B. Beckhoff; R. Klein, M. Krumrey, H. Rabus, R. Thornagel; Proc. SPIE **3444**, 610 (1998)

3 E.M. Gullikson, S. Mrowka, B.B. Kaufmann; Proc. SPIE **4343**, 363 (2001).

4 J. Tümmler, F. Scholze, G. Brandt, B. Meyer, F. Scholz, K. Vogel, G. Ulm, M. Poier, U. Klein, W. Diete; Proc. SPIE **4688**, 338 (2002)

5 F. Scholze, B. Beckhoff, G. Brandt, R. Fliegauf, A. Gottwald, R. Klein, B. Meyer, U. Schwarz, R. Thornagel, J. Tümmler, K. Vogel, J. Weser, and G. Ulm; Proc. SPIE **4344** , 402 (2001)

6 F. Scholze, J. Tümmler, and G. Ulm; Metrologia **40** (2003) in print

7 J.H. Underwood, E.M. Gullikson; J. Electr. Spectrosc. Relat. Phenom. **92**, 265 (1998)

8 G.C. King, M. Tronc, F.H. Read, R.C. Bradford; J. Phys. **B10,** 2479 (1977)

A New Reflectometer for Large EUVL Optics

J. Tümmler, F. Scholze, H. Blume, G. Brandt, J. Eden, B. Meyer, S. Plöger, H. Scherr, F. Scholz, G. Ulm

Physikalisch-Technische Bundesanstalt, Abbestraße 2-12, 10587 Berlin, Germany

Extreme Ultraviolet Lithography (EUVL) holds the key to the next generation of computer technology. EUVL imaging requirements demand multilayer mirror optics to be manufactured with extreme accuracy to ensure uniform illumination of the wafer plane and optimized throughput. As EUVL matures,[1] the requirements for the accuracy of reflectivity and wavelength measurements are becoming tighter. Specially, the wavelength for the peak mirror reflectivity should be matched to better than 0.02 % and the uniformity of reflectivity should be better than 0.2 %. In response to this demand, there have been substantial improvements of measurement precision and accuracy at the PTB. PTB with its laboratory at BESSY II, is the European center for EUV radiometry and supports the national and European industry with high accuracy at-wavelength measurements in the EUV spectral region.

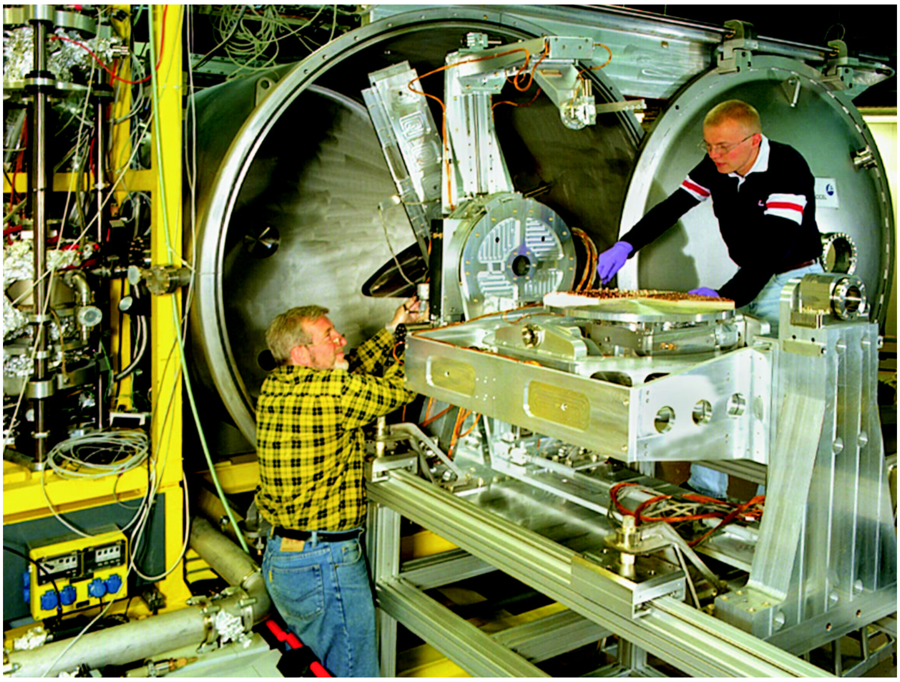

Figure 1. Picture of the reflectometer sample stage in front of the vacuum chamber during the set up at the PTB soft x-ray radiometry beamline

For the investigation of the large optical components for EUV lithography tools, PTB has designed a new reflectometer. It allows the investigation of samples with 550 mm in diameter and a weight of 50 kg.[4] The reflectometer has been set up at the soft x-ray radiometry beamline[2] in the shutdown period of BESSY II in October 2002. Already in November 2002 reflectance measurements for industry partners could be performed with the usual low uncertainties.[3]
The new reflectometer system consists of a cylindrical vacuum chamber with a diameter of 1.9 m and a length of 2.1 m. Inside this vacuum chamber the sample stage is mounted. Fig. 1 shows

the reflectometer sample stage in front of the vacuum chamber during set up.

The complete sample stage is motorized in vacuum. The sample can be translated in x, y, and z direction (for orientation see Fig. 2). The incidence and reflection angle can be adjusted via θ and 2θ, for the sample and the detector, respectively. The $\theta\,/\,2\theta$ axis is in the horizontal plane, parallel to the electric field vector of the linear polarized synchrotron radiation. For aligning the sample and to account for a curved sample surface, a tilt around the y-axis is possible. A rotation around the surface normal (ϕ axis) allows to perform a raster scan in spherical coordinates. With movements in ϕ and y, every point of the sample surface can be positioned into the photon beam. The additional x axis allows to raster the surface of smaller samples in cartesian coordinates, which is a necessary feature for the measurement of e.g. gratings or grazing incidence mirrors.

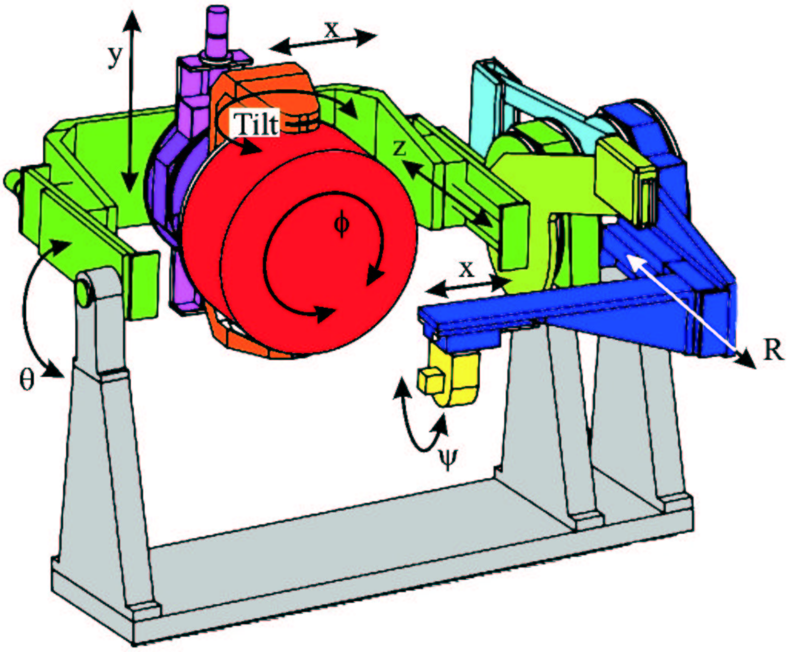

Figure 2. Sketch of the reflectometer system showing all degrees of freedom

In addition to the 2θ movement the detector can be moved in x direction for the measurement of bi-directional scattering. Furthermore, the distance between the sample surface and the detector can be varied to account for the different beam divergence when reflected from a curved surface. For reference measurements of the direct beam, the detector can be rotated around the ψ axis by 180°. This avoids large movements of the sample and the detector.

For stray light suppression, a cross slit aperture is installed at a distance of about 0.5 m from the sample surface. The cross slits are fully motorized and can be opened with a resolution of 1 μm.

The construction work and manufacturing of the reflectometer system is done by ACCEL, Bergisch-Gladbach, Germany.

The large sample weight necessitates a handling robot to set the samples into the measuring chamber. The sample is held by a sample holder that fits exactly onto the sample stage inside the reflectometer chamber. The holder is transferred into the reflectometer chamber by the robot. For different sample sizes individual holders can be used. A taper key guarantees that the sample holder is centered onto the stage. During the mounting of the sample the complete front

	Axis	Range	Positioning Accuracy
Sample	x	$-90\,\text{mm}$ to $90\,\text{mm}$	$10\,\mu\text{m}$
	y	$-10\,\text{mm}$ to $300\,\text{mm}$	$10\,\mu\text{m}$
	z	$-15\,\text{mm}$ to $140\,\text{mm}$	$10\,\mu\text{m}$
	ϕ	$0°$ to $360°$	$0.01°$
	tilt	$-10°$ to $10°$	$0.01°$
	θ	$-30°$ to $95°$	$0.01°$
Detector	2θ	$-5°$ to $190°$	$0.01°$
	x	$0\,\text{mm}$ to $120\,\text{mm}$	$10\,\mu\text{m}$
	R	$150\,\text{mm}$ to $550\,\text{mm}$	$100\,\mu\text{m}$
	ψ	$0°$ to $180°$	$0.01°$

Table 1. Sample and detector movements of the EUV reflectometer

of the reflectometer chamber is opened. A cleanroom in the front of the reflectometer chamber avoids the contamination with dust particles. It allows working conditions of class 1000 or better. Here the samples are mounted onto the sample holder. The reflectance measurement must be performed in vacuum. A set of four dry compressing vacuum pumps (4 x $48\,\text{m}^3/\text{h}$), a turbo pump (680 l/s N_2), and a cryo pump (10000 l/s N_2) work to evacuate the reflectometer chamber within 1 h to a working pressure of $9 \cdot 10^{-7}$ mbar. The venting of the vacuum chamber takes less than 30 min.

With the new measuring station PTB is prepared best for the measurement of full-size EUVL optical components. According to our partner Carl Zeiss SMT AG, for the next couple of years the EUV mirror size will not exceed the maximum possible sample size which is the largest sample size that can be investigated at-wavelength, worldwide.

ACKNOWLEDGMENTS

The EUV reflectometer has been financially supported by the Bundesministerium für Wirtschaft und Arbeit (BMWA) and Carl Zeiss SMT AG. At Carl Zeiss M. Wedowski is responsible for the project.

REFERENCES

1. Gargini, P. Worldwide technologies and the ITRS in the current economic climate. *Proc. SPIE* **4688** (2002), 25 – 28.
2. Scholze, F., Beckhoff, B., Brandt, G., Fliegauf, R., Gottwald, A., Klein, R., Meyer, B., Schwarz, U., Thornagel, R., Tümmler, J., Vogel, K., Weser, J., and Ulm, G. High-accuracy EUV metrology of PTB using synchrotron radiation. *Proc. SPIE* **4344** (2001), 402 – 413.
3. Scholze, F., Tümmler, J., and Ulm, G. High-accuracy rediometry in the EUV range at the PTB soft x-ray beamline. *Metrologia* **40** (2002), in press.
4. Tümmler, J., Scholze, F., Brandt, G., Meyer, B., Scholz, F., Vogel, K., Ulm, G., Poier, M., Klein, U., and Diete, W. New PTB reflectometer for the characterization of large optics for the extreme ultraviolet spectral region. *Proc. SPIE* **4688** (2002), 338 – 347.

Characterization of High-Resolution Superconducting Tunnel Junction Detectors

B. Beckhoff, R. Fliegauf and G. Ulm
Physikalisch-Technische Bundesanstalt
Abbestraße 2-12, 10587 Berlin, Germany

The energy resolution of conventional semiconductor detectors is insufficient for simultaneously separating the leading fluorescence lines of low Z and medium Z materials in the soft X-ray regime. It is therefore important to investigate alternative detection instruments offering higher energy resolution and evaluate their applicability to soft X-ray fluorescence (XRF) analysis. Here, some results of the characterization and evaluation of a cryogenic superconducting tunnel junction (STJ) detector, which was provided to the Physikalisch-Technische Bundesanstalt (PTB) by the Lawrence Livermore National Laboratory (LLNL), are given with respect to both detector response functions and XRF. For this investigation, monochromatized undulator radiation of high spectral purity, available at the PTB PGM beamline[1] at BESSY II, was employed, by which it was possible to record the STJ response functions at various photon energies of interest ranging from 180 eV to 1600 eV. By scanning the effective detector area and the adjacent substrate and leads, relevant artefacts of the detector response were identified. The best way to obtain reliable detector response functions is to illuminate the detector with monochromatic radiation of high spectral purity, which is crucial for avoiding interference from possible source artefacts in the detector response. A drawback of this approach is that the high photon flux of a beamline has to be adapted to the count rate capability of the STJ detector. However, this can be achieved in a reliable manner by severely reducing the stored electron beam current by several orders of magnitude, which the PTB can take advantage of during special operation shifts at BESSY II.

The cryogenic STJ detector system[2-4] employed in the present invesitgation is based on a two-stage adiabatic demagnetization refrigerator (ADR). The STJ is operated at temperatures between about 70 mK and 400 mK at the end of a cold finger inside a liquid He- and a liquid N_2-cooled shield. As the STJ chip is located at the end of this doubly-shielded cold finger, an effective fluorescence detection in a UHV environment can be achieved by placing the cold finger as close as possible to the irradiated specimen. In the present snout design, the solid angle of acceptance for thermal noise is about two orders of magnitude higher than in older cryostat designs, where the STJ detector chip is located in the center of the cryostat. Thus, by using appropriate entrance windows[2], infrared noise can be blocked. The most important advantage of using STJ detectors, as opposed to conventional semiconductor detectors such as Si(Li) detectors, is the improved higher energy resolution. The reported energy resolution for Nb based STJs[5] is 6 eV FWHM at a photon energy of 277 eV and for Al based STJs[6] is 12 eV FWHM at a photon energy of 5.9 keV. STJ detectors can be operated at count rates of at least up to 10000 cps with only moderate degradation of the energy resolution[5]. Evaluating the performance of STJs for XRF analysis requires an investigation of the origins and magnitude of the various artefacts that appear in the STJ pulse height spectra. In the experimental results below, we shall see that some of the sources for artefacts are due to photons being absorbed in the substrate or in the Nb contact leads. Additionally, the probability of line splitting increases as the energy of the incident photon increases because the absorption capability of the top Nb layer and of the Al layers generally decrease, allowing the photon to reach the bottom Nb layer. As the response of the bottom Nb layer may be slightly different than that of the top Nb layer, line splitting can occur when both responses superimpose.

For the investigation of detector response functions, a closer look at the STJ with an edge length of 141 µm was taken. A photograph of this STJ, taken through a microscope, is shown in fig. 1. The contacts connecting the STJs from the left and from the right are clearly visible. The STJ detector chip was investigated using an uncollimated beam at the PTB plane grating monochromator beamline and then with a collimated beam smaller than the STJ. The situation involving the uncollimated beam agrees quite well with the one when detecting X-ray fluorescence radiation, since here the entire chip is illuminated. Response functions were obtained for both of these beams at 929 eV and again at 1547 eV, corresponding to the copper L_α and almost to the aluminum K_β fluorescence line energies (see fig. 2).

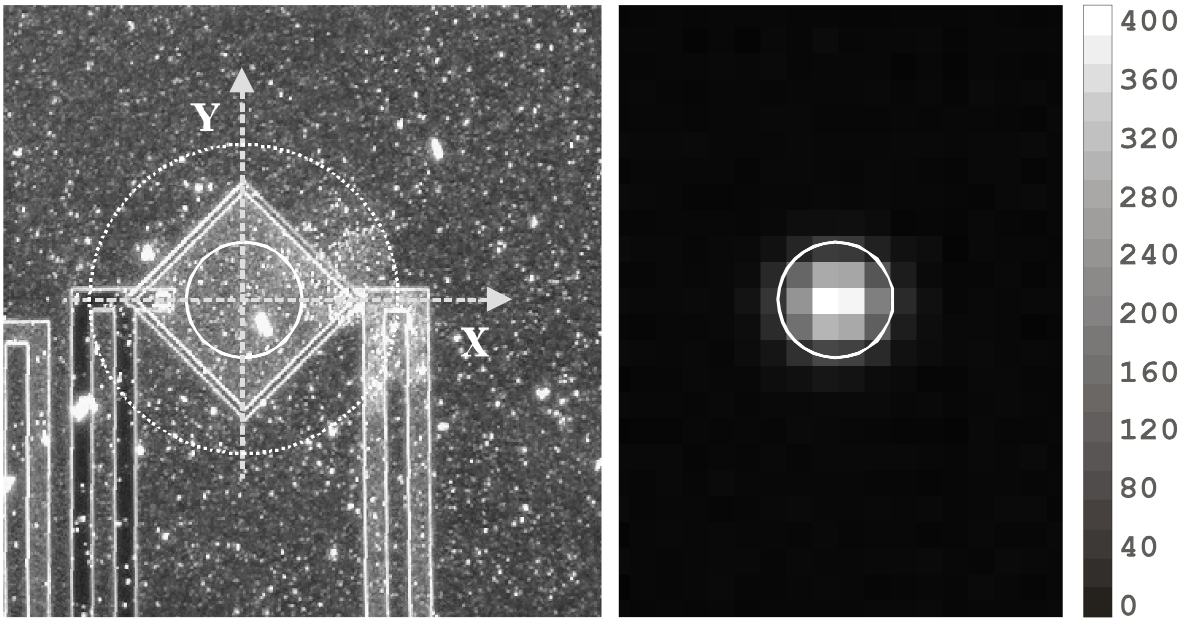

Fig. 1: Picture of a 141 x 141 µm² STJ detector investigated at various photon energies below 2 keV with a collimated beam of about 105 µm diameter (solid circle) and with a larger beam profile (dotted circle) to the left. Prior to the STJ investigations, the collimated beam profile was recorded during a special operation shift at BESSY II by a CCD camera as shown along with its depicted intensity scale to the right.

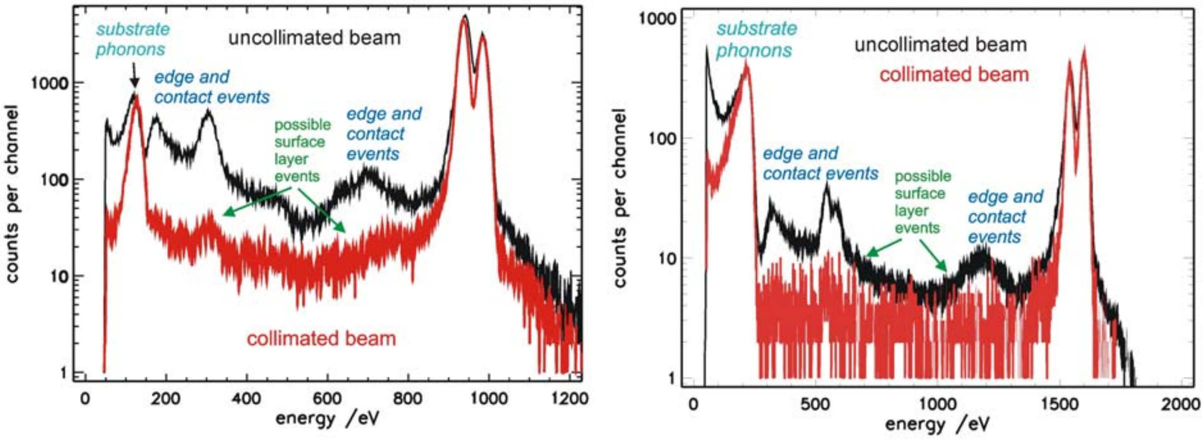

Fig. 2: Response functions of a 141 x 141 µm² STJ detector recorded with a collimated and an uncollimated beam of high spectral purity radiation at the photon energies of 929 eV (left) and 1547 eV (right).

At 929 eV, three different types of artefacts are visible: the adjacent substrate events, contact events in the uncollimated case, and substrate phonons originating from the substrate underneath the STJ. Because the collimated beam in the present arrangement may not have been small enough to fully exclude a non-desired illumination of the STJ edge regions, it is possible that a certain fraction of the above artefacts may also be associated with surface layer events caused by oxide clusters on the top Nb layer. The same types of artefacts occur at higher energies, for example at 1547 eV (cf. right of fig. 2), when comparing the collimated and uncollimated cases. The fig. 3 shows the STJ response function in the collimated case at two different energies, one just above and one just below the aluminum K-edge. Due to the increased X-ray absorption in the Al trap layer of the STJ at the higher energy, the probability of bottom layer events decreases considerably. For the same reason, the probability of substrate phonons is drastically reduced, allowing us to identify the origin of these events underneath the detector.

Fig. 3: Response functions of a 141 x 141 µm² STJ detector recorded with a collimated beam of high spectral purity radiation at 1547 eV and 1567 eV just below and above the Al-K edge.

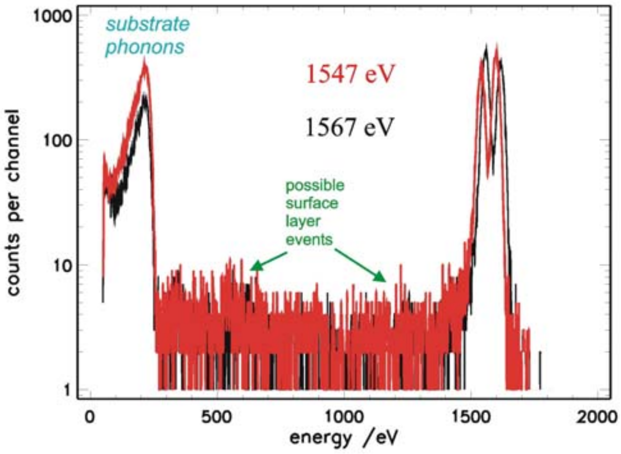

The STJ artefacts observed in the present investigation are an obvious restriction to both the detection sensitivity and the elemental quantification when using these detectors in X-ray fluorescence analysis. Optimized high-resolution detectors should contribute effectively to industrial and fundamental research in EDXRF analysis.

Acknowledgements

The authors would like to thank M. Frank, S. Friedrich and S.E. Labov (LLNL) for the excellent construction of the cryostat for STJ detectors, for debugging and setting up the system in the PTB laboratory lab at BESSY II, and for many fruitful discussions on STJs.

References

1. F. Senf, F. Eggenstein, U. Flechsig, W. Gudat, R. Klein, H. Rabus, and G. Ulm, J. Synchr. Rad. **5**, 780-782 (1998).
2. S. Friedrich, L.J. Hiller, M. Frank, G.B. le Grand, C.A. Mears, B. Nideröst, S.E. Labov, A.T. Barfknecht, M. LeGros, S.P. Cramer, J. El. Spectrosc. Relat. Phenom. **101**, 891 (1999).
3. S. Friedrich, T. Niedermayr, O. Drury, M.F. Cunnigham, M.L. van den Berg, J.N. Ullom, A. Loshak, T. Funk, S.P. Cramer, J.D. Batteux, E. See, M. Frank, S.E. Labov, Nucl. Instr. Meth. A **467-468,** 1117 (2001).
4. M. Veldkamp, B. Beckhoff, R. Fliegauf, G. Ulm, M. Frank, S. Friedrich, S.E. Labov, Nucl. Instr. Meth. A **487,** 182 (2002).
5. M. Frank, L. J. Hiller, J. B. le Grand, C. A. Mears, S. E. Labov, M. A. Lindeman, H. Netel, D. Chow, A. T. Barfknecht, Rev. Sci. Instrum. **69**, 25 (1998).
6. G. Angloher, P. Hettl, M. Huber, J. Jochum, F. v. Feilitzsch, R. L. Mößbauer, J. Appl. Phys. **89**, 1425 (2001).

TXRF analysis of low Z elements on silicon wafer surfaces excited by monochromatized undulator radiation

B. Beckhoff [1], R. Fliegauf [1], G. Ulm [1], J. Weser [1],
G. Pepponi [2], C. Streli [2], P. Wobrauschek [2],
T. Ehmann [3], L. Fabry [3], C. Mantler [3],S. Pahlke [3]

[1] Physikalisch-Technische Bundesanstalt, Abbestraße 2-12, 10587 Berlin, Germany
[2] Atominstitut der Österreichischen Universitäten, Stadionallee 2, 1020 Wien, Austria
[3] Wacker Siltronic AG, 84479 Burghausen, Germany

Total reflection X-ray fluorescence spectroscopy (TXRF) using high flux synchrotron radiation (SR) as the excitation source is a powerful technique for the non-destructive analysis of very small amounts of both metal and low Z elements on silicon wafer surfaces. Several different TXRF experiments were conducted at the plane grating monochromator (PGM) beamline[1] for undulator radiation of the Physikalisch-Technische Bundesanstalt (PTB) at BESSY II. The lower limits of detection (LOD) of TXRF analysis were investigated for some low Z elements[2,3] such as C, N, Na, Mg and Al in two different detection geometries for various excitation modes. For the sake of an application-oriented TXRF approach, droplet samples on silicon wafer surfaces were prepared by Wacker Siltronic and investigated in the TXRF irradiation chamber of the Atominstitut (ATI). Using the vacuum chamber of the ATI, the wafer samples could be mounted horizontally. The fluorescence radiation was recorded in a vertical geometry with respect to the incident photon beam and the electron orbit by means of a down-looking HPGe detector. Turning the irradiation chamber 90°, allowing for the insertion of a horizontally movable Si(Li) detector towards a vertically oriented wafer sample, the polarization vector of the incident radiation is parallel to the detector axis. In this arrangement, the wafer samples were located about 1.5 m behind the PGM focal plane, offering a beam profile of about 1.0 mm x 0.5 mm. The irradiation chamber was protected by a class 100 cleanroom in order to reduce the risk of cross-contaminations of the wafer samples.

A direct comparison of both detection geometries was performed by means of a standard reference droplet sample containing 1 ng of Na, Mg and Al, which was prepared by the Central Analytical Laboratories of Wacker Siltronic. The droplet was deposited on a monocrystalline Si wafer having a diameter of 100 mm. Figure 1 shows the respective TXRF spectra for an excitation energy of 1700 eV. As continuous background contributions in TXRF are very small, absolute detection limits in the lower pg to higher fg range could be found for the selected low Z elements between C and Al using various prepared droplet samples. Table 1 shows both the detection sensitivities and detection limits achieved in these experiments. The VPD-LLD values given in table 1 are derived from the assumption that the sample is a VPD (Vapor Phase Decomposition) droplet collected from a wafer with a diameter of 200 mm.

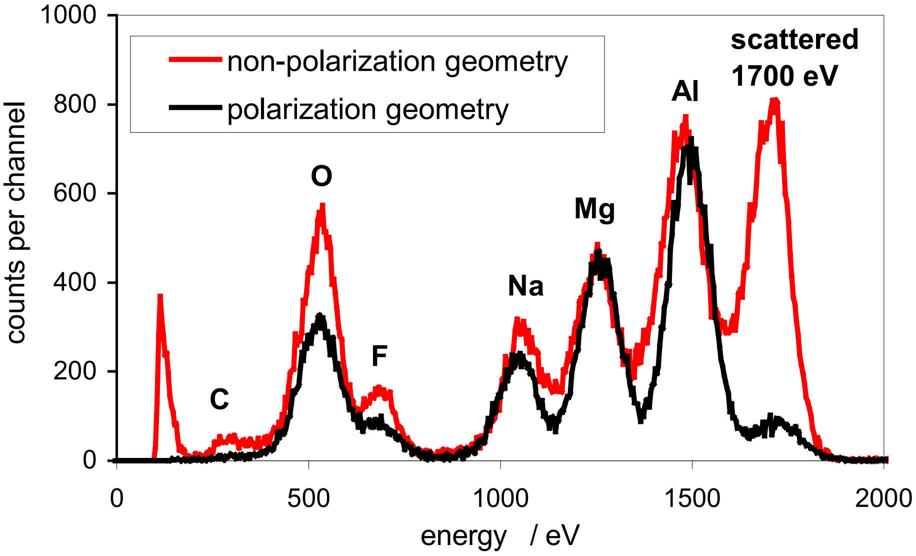

Figure 1: Comparison of two different detection geometries by means of a droplet sample containing 1 ng of Na, M and Al on a silicon wafer surface. In the 'non-polarization geometry' an HPGe and in the 'polarization geometry' a Si(Li) detector were employed. At low photon energies, the lower detection efficiency of the Si(Li) prevents similar count rates from being obtained.

Tab. 1: Detection limits (LLD viz. LOD) and sensitivities extrapolated for a counting time of 1000 s and an electron beam current of 100 mA as deducted from several measurements with the ATI irradiation chamber using the HPGe detector for C and N and the Si(Li) detector for Na, Mg and Al:

Exciting photon energy / eV	Element	sensitivity / cps/ng	LLD viz. LOD / pg	VPD-LLD / atoms/cm²
357	C	1200	0.5	1 10^8
511	N	1100	0.8	1 10^8
1600	Na	110	1.3	1 10^8
1600	Mg	210	0.5	4 10^7
1600	Al	305	0.3	2 10^7

Synchrotron radiation based TXRF analysis offers absolute detections limits in the lower pg to higher fg range for selected low Z elements between C and Al. Vapor phase decomposition (VPD) detection limits calculated for 200 mm silicon wafers range from 2 10^7 atoms / cm^2 to about 10^8 atoms / cm^2 for Na, Mg and Al, thus fulfilling current requirements of the semiconductor industry according to the SEMATECH roadmap. All investigations are going to be continued in a new TXRF set-up of the PTB suited for the off-line routine analysis of 200 mm and 300 mm silicon wafers, including a state-of-the-art wafer handling system.

References

1. F. Senf, F. Eggenstein, U. Flechsig, W. Gudat, R. Klein, H. Rabus, and G. Ulm, J. Synchr. Rad. 5, 780-782 (1998).
2. C. Streli, P. Wobrauschek, B. Beckhoff, G. Ulm, L. Fabry, S. Pahlke, X-Ray Spectrom. 30, 24-31 (2001).
3. B. Beckhoff, R. Fliegauf, G. Ulm, G. Pepponi, C. Streli, P. Wobrauschek, L. Fabry, S. Pahlke, Spectrochim. Acta Part B 56, 2073-2083 (2001).

Lithography with EUV: First successful exposure in Europe at the PTB Laboratory at BESSY II

E. Sohmen, V. Kießling, U. Müller, T. Ihl, A. Dallmeyer, P. Kürz
Carl Zeiss SMT AG, 73446 Oberkochen, Germany
R. Müller, A. Gottwald, R. Klein, F. Melchert, U. Schwarz, G. Ulm
Physikalisch-Technische Bundesanstalt, Abbestr. 2-12, 10587 Berlin, Germany

During the last decades, owing to a gradual reduction of the circuit size, electronic chips have become ever more powerful and more compact with the cost being lowered at the same time. The optical lithography techniques used for their production have however been pushed to the possible extent. It is expected that using radiation 157 nm in wavelength, a feature size of 65 nm can be achieved as the ultimate limit in the year 2007 (according to the International Technology Roadmap for Semiconductors [1])

Extreme ultraviolet (EUV) lithography is an attractive next generation lithographic technology since it will support imaging dense 1:1 line-space features smaller than 50 nm. EUVL uses radiation of about 13 nm wavelength. Similar to optical lithography, the patterns of a mask are demagnified by projection onto a semiconductor wafer covered with a photo resist. The mask and the entire projection optics have to be reflective and the required specifications for mask making, mirror shaping and wafer handling are unprecedented.

Crucial for the successful fabrication of EUV optics is the development of EUV system metrology. For testing and demonstration of the measurement methods a so-called Small Field Metrology Tool was set up in cooperation with Carl Zeiss Semiconductor Manufacturing Technology AG (SMT AG) at the PTB-undulator beamline [1]. The main item of this set-up is the Micro Exposure Tool (MET) projection optics built by Carl Zeiss in collaboration with the Lawrence Livermore National Laboratory (LLNL). At 13.4 nm wavelength, two multilayer mirrors reduce reticle structures by a factor of five onto the wafer plane. An illumination system allows efficient coupling of the 13 nm radiation emitted by the PTB undulator to the projection optics.

At the BESSY II electron storage ring, the Physikalisch-Technische Bundesanstalt (PTB) operates a laboratory [2] with several beamlines for high-accuracy at-wavelength metrology in the EUV spectral range using synchrotron radiation from bending magnets and from the PTB-undulator [3]. Many companies such as Carl Zeiss, Jenoptik Mikrotechnik GmbH, Infineon Technologies AG and Schott ML GmbH as well as many research groups rely on PTB's work.

In February 2002, a first print in photoresist of the Micro Exposure Tool at the PTB laboratory at BESSY II was obtained. Figure 1 shows an image of this print. Structures with a size of about 50 nm could be printed using EUV radiation for the first time in Europe. The result shows that the modern optical components for EUVL like the MET have the potential to fabricate electronic chips for next generations. Recently, the international board of the semiconductor industry, SEMATECH, has ordered a Micro Exposure Tool for an new EUVL-Tool.

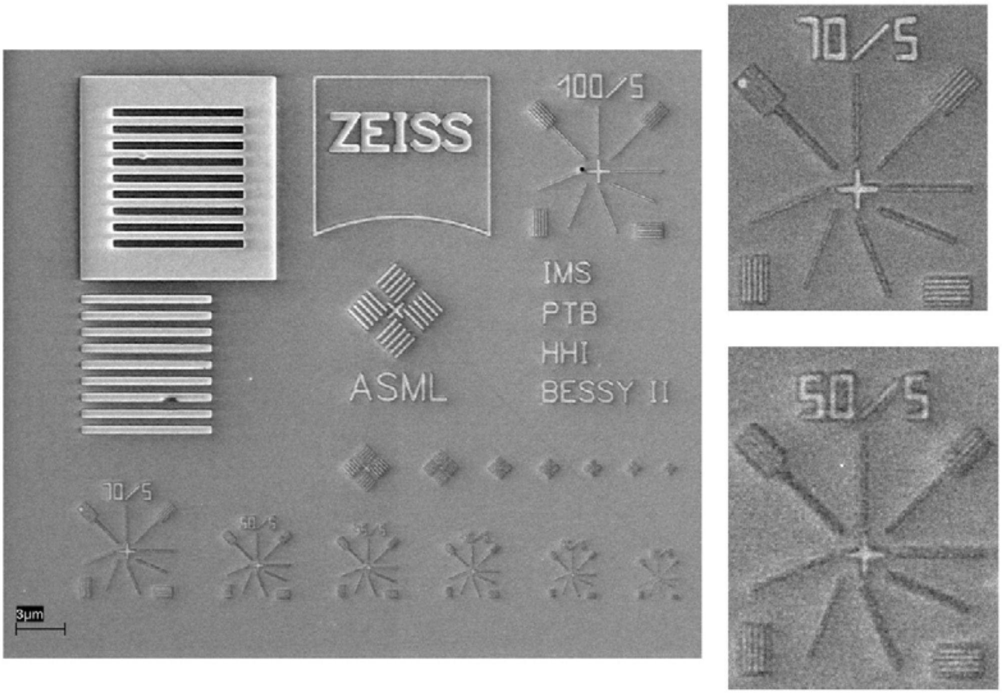

FIG. 1. First successful 50 nm print obtained in 2002 at the PTB-laboratory at BESSY II. The print is an image in the photoresist of the Micro Exposure Tool (MET). The MET is implemented in the Small Field Metrology Tool of Carl Zeiss SMT AG at the undulator -beamline ID13.

EUVL is considered a lithography generation which will last many decades. The resolution obtainable will be gradually pushed to ist theoretical limits, provided the necessary metrology keeps pace. The PTB low energy compact storage ring (200 MeV up to 600 MeV electron beam energy) planned in close cooperation with BESSY GmbH and scheduled to be put into operation in 2007, will be an ideal platform for investigating EUVL metrology questions of prime importance.

ACKNOWLEDGEMENTS

The following are gratefully acknowledged for their contributions: R. Steingrüber (HHI Berlin), H. Tierock and M. Schmidt (AZM Bessy, Berlin), M. Dierichs and K. v. Ingen-Schenau (ASML). The EUV program at Zeiss is supported by the Bundesministerium für Bildung und Forschung (Project 13 N8088). Part of the MET work has been funded by International SEMATECH Project Lith-112.

[1] H. Meiling, I. Benschop, R. Hartmann, P. Kürz, P. Hoghoj, R. Geyl, N. Harned, Proc. SPIE 4688, 52 (2002)

[2] R. Klein, M. Krumrey, M. Richter, F. Scholze, R. Thornagel, G. Ulm, Synchrotron Radiation News 15, 23 (2002)

[3] R. Klein, F. Melchert, F. Scholze, R. Thornagel, J. Thümmler, G. Ulm, BESSY-Highlights 2001

HIGH RESOLUTION PHOTOABSORPTION SPECTROSCOPY OF THE METHYL HALIDES. TESTS AND FIRST RESULTS.

R. Locht[1], H.W. Jochims[2] and H.Baumgärtel[2].
[1]Département de Chimie, Université de Liège, Institut de Chimie, Bât. B6c,
Sart-Tilman par B-4000 Liège 1, Belgium..
[2]Institut für Physikalische und Theoretische Chemie, Freie Universität Berlin,
Takustrasse 3, D-14195 Berlin, Germany.

The most recent investigations of the photoabsorption and photoionization of the methyl halides (CH_3X with X= F, Cl, Br and I) were performed on a 1.5m-NIM monochromator at the BESSY I facility [1] . The results on CH_3F and CH_3Cl (CD_3Cl) have been published fairly recently [2-5]. Even though the analysis of the Rydberg series observed in CH_3Br (CD_3Br) and CH_3I (CD_3I) is fairly obvious, several new assignments should be proposed. A deeper fine structure analysis prescribed a monochromator characterized with a higher resolution.

The main aim of the measurements reported in this contribution is the search and test of an instrument allowing us to achieve this goal. At the BESSY II facility the most suitable instrument is a 3m-NIM monochromator and is presently available for this purpose (the 3m-NIM-2 beamline). Transferred from BESSY I, its reassembling and commissioning at BESSY II have been achieved very recently [6].

It is equipped with a 600 l/mm (Al/MgF_2 coated) and a 2 400 l/mm (Pt coated) grating. Only the latter has been used. Slit widths of 50µm were used and an MgF_2 window is available for second order suppression. A photoabsorption cell of 30 cm optical pathlength is mounted on the monochromator together with a two stages differential pumping system to obtain the allowed working pressure in the monochromator. The standard procedure to obtain the absorbance $\log_{10}(I_0/I)$ was to scan successively the absorption spectrum and the transmission spectrum of the monochromator. In the present contribution we present the first results on the investigation of the photoabsorption of the methyl bromide (CH_3Br) and iodide (CH_3I). The corresponding perdeuterated isotopomers as well as CH_2DI have also been investigated. Most of the spectra have been recorded in the 5-25 eV photon energy range.

Above the 10 eV photon energy range the VUV photoabsorption spectrum of CH_3I shows only a few broad bands, whereas below this energy narrow atomic-like structures are observed [1]. A congested fine structure is observed in the 9.3-10.0 eV photon energy range [1] and is shown in fig.1. As expected, it is obvious from this picture that an

important increase of resolution is obtained with the present monochromator. However, problems remain and have to be solved in the future, particularly in the low photon energy range (5-10 eV) where photon beam instabilities are noticable in the transmission curve. These are probably related to both mechanical and optical insufficiencies from the monochromator and the focussing mirrors.

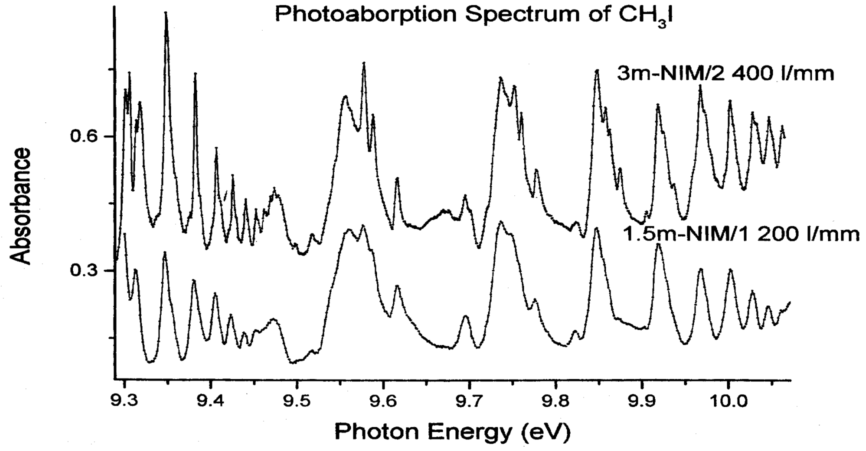

Fig.1 The absorption spectrum of CH_3I as recorded between 9-10 eV.

Acknowledgement.

R.L. gratefully acknowledges the financial support of the European Community under the contract n° HPRI-1999-CT-00028 and the valuable technical assistance of Dr. G. Reichardt.

References.

[1]. R. Locht, B. Leyh, A. Hoxha, K. Hottmann, H.W. Jochims and H. Baumgärtel, BESSY Jahresbericht, **1997**, 160; **ibid. 1998**, 169; **ibid. 1999**, 147.

[2]. R. Locht, B. Leyh, A. Hoxha, D. Dehareng, H.W. Jochims and H. Baumgärtel, Chem.Phys. 257 (**2000**) 283.

[3]. R. Locht, B. Leyh, A. Hoxha, D. Dehareng, H.W. Jochims and H. Baumgärtel, Chem.Phys. 272 (**2001**) 277.

[4]. R. Locht, B. Leyh, A. Hoxha, D. Dehareng, K. Hottmann, H.W. Jochims and H. Baumgärtel, Chem. Phys. 272 (**2001**) 293.

[5]. R. Locht, B. Leyh, A. Hoxha, H.W. Jochims and H. Baumgärtel, Chem. Phys. 272 (**2001**) 259.

[6]. G. Reichardt, T. Noll, I. Packe, P. Rotter, J.-S. Schmidt and W. Gudat, Nucl.Instr. Meth.Phys.Res. A 467-468 (**2001**) 458.

Structural investigations of square-planar Ni(II)-complexes by XANES and EXAFS spectroscopy

Martin P. Feth[1*], *Markus Kreitmeir*[1], *Venkata Krishnan*[1], *Helmut Bertagnolli*[1],
Alexei Erko[2], *Martin Fieber-Erdmann*[2] *and Axel Klein*[3*]

[1]Institut f. Phys. Chemie, Univ. Stuttgart, Pfaffenwaldring 55, 70569 Stuttgart
[2]Berliner Elektronenspeicherring-Gesellschaft für Synchrotronstrahlung m.b.H. (BESSY),
Albert-Einstein-Straße 15, 12489 Berlin
[3]Institut f. Anorg. Chemie, Univ. Stuttgart, Pfaffenwaldring 55, 70569 Stuttgart

* correspondig authors. e-mail: m.feth@ipc.uni-stuttgart.de
aklein@iac.uni-stuttgart.de

Organonickel(II) complexes are widely used in organometallic catalysis [1], especially nickel complexes of the type [(diimine)Ni(R)X] (R = alkyl or aryl; X = Cl or Br) are promissing catalysts for olefin polymerization reactions. For a better understanding of the mechanism of catalytic reaction it is necessary to know about the structure of the catalytic active species and possible intermediate compounds. In this report we present EXAFS and XANES studies on several amorphous square-planar nickel(II)-complexes in the solid state, which we investigated for the structural influence of different diimine ligands as well as the structural properties of dimeric species in comparison to monomeric analogues.

The measurements were performed at the XAFS beamline KMC-2 of BESSY II at the Ni K- (8333.0 eV) and Br K-edge (13473.7 eV). Data were analysed with the program packages described in [2] and [3]. The EXCURV92 module of CERIUS^2 was used for curve fitting.

Figure 1 illustrates the Ni K-edge XANES spectra for [(bpz)Ni(Mes)Br], [(bpym)Ni(Mes)Br] and [(μ-bpym){Ni(Mes)Br}$_2$]. In each spectrum the typical two pre-edge peaks of square planar Ni(II) complexes can be observed [4]. The pre-peak at about 8333 eV can be assigned to a 1s→3d electron transition, while the second peak, which occurs at about 8337 eV, is due to a 1s→4p$_z$ transition [5]. These typical fingerprints of square planar Ni(II) complexes can be observed in all investigated complexes.

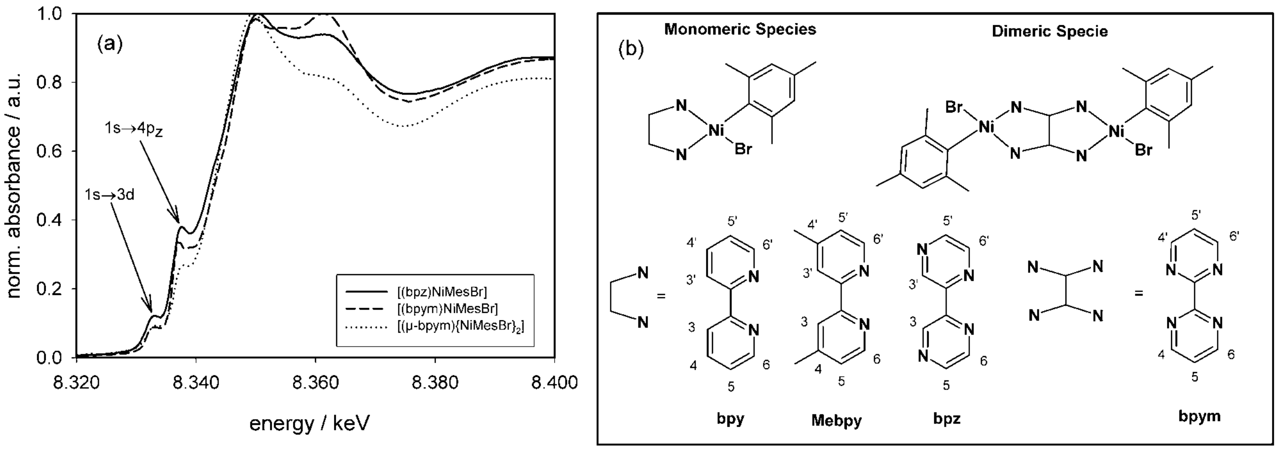

Figure 1:
(a) Comparison plot of the Ni-K edge XANES spectra of [(bpz)Ni(Mes)Br], [(bpym)Ni(Mes)Br] and [(μ-bpym){Ni(Mes)Br}$_2$].
(b) Molecular formulae of the investigated Ni(II)-complexes.

The obtained structural parameters of the investigated complexes determined by curve fitting analysis of the EXAFS spectra at the Ni K- and Br K-edge are summarized in Table 1.

The complexes, [(Mebpy)Ni(Mes)Br], [(bpym)Ni(Mes)Br] and [(bpz)Ni(Mes)Br] show very similar EXAFS functions at the Ni K- and Br K-edge, leading to almost identical structural parameters, which are in very good agreement with values found from the EXAFS analysis of the complex [(bpy)Ni(Mes)Br] [4]. As an example, Figure 2 (a + b) shows the k^3-weighted EXAFS spectra coupled with the magnitudes of the Fourier transforms of [(bpz)Ni(Mes)Br] at the Ni K-edge. The fitting of the Ni K-edge EXAFS spectra was performed with a 3 shell model, in which the first coordination shell at about 1.9 Å consists of the two coordinating nitogen atoms of the diimine ligand and the carbon atom of the mesitylene group, the second shell at about 2.3 Å of the bromine backscatterer and the third coordination shell at about 2.8 Å of the further backbone-carbon-backscatterers of the mesitylene- and diimine ligand. Due to nearly same distances and similar backscattering behaviour of the nitrogen and carbon backscatterers, the first coordination shell was fitted as a combined shell with nitrogen amplitude- and phase-functions. The Br K-edge EXAFS spectra were fitted with one coordination shell of nickel at about 2.3 Å.

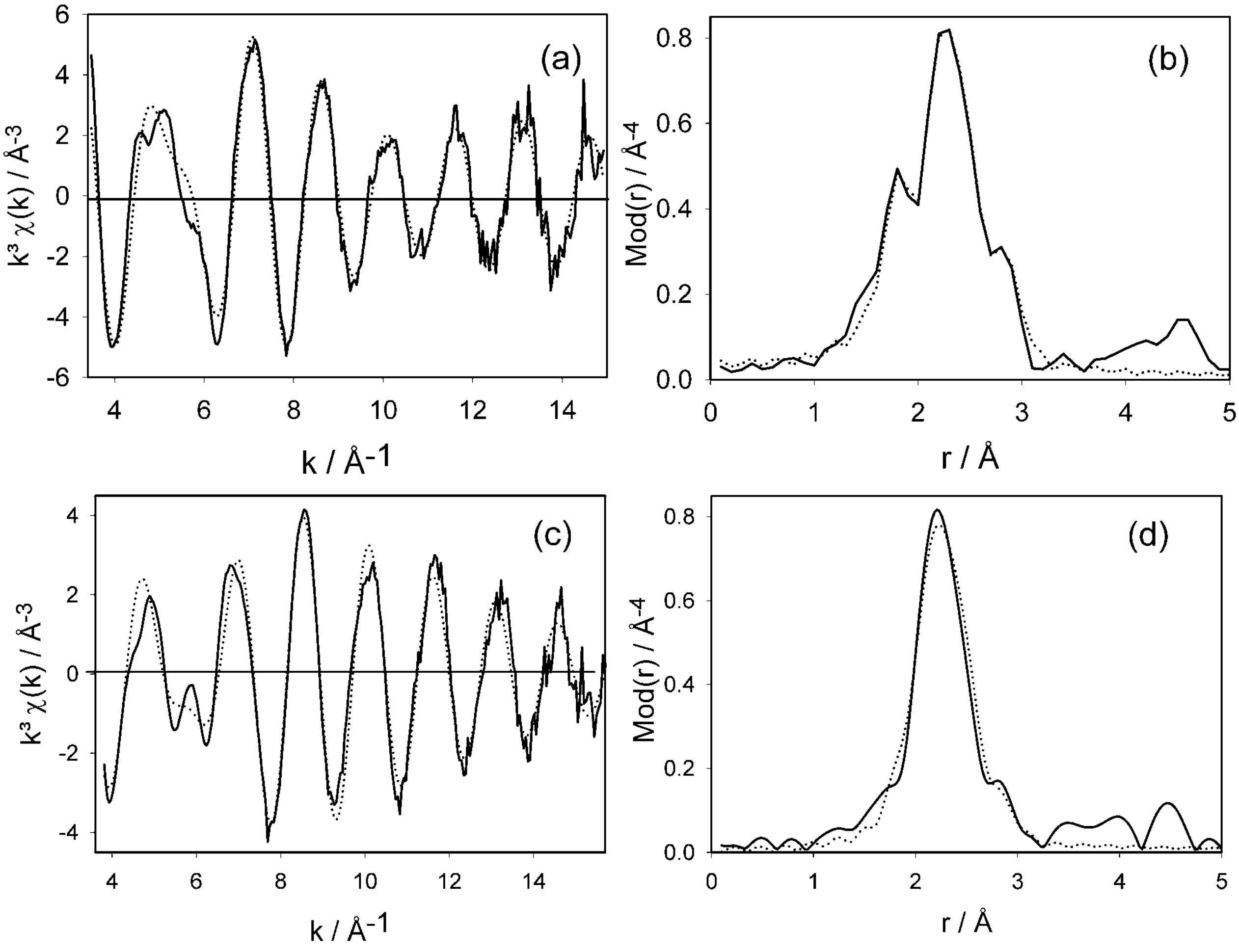

Figure 2:
Comparison plot of the experimental (solid line) and calculated (dotted line) EXAFS spectra (a,c) and its Fourier Transforms (b,d) of [(bpz)Ni(Mes)Br] (top) and $[(\mu\text{-bpym})\{Ni(Mes)Br\}_2]$ (bottom) at the Ni K-edge.

Significant structural changes were found from the analyses of the Ni K-edge EXAFS spectra of the dimeric complex $[(\mu\text{-bpym})\{Ni(Mes)Br\}_2]$ compared with the monomeric species [(bpym)Ni(Mes)Br]. In the dimeric complex (Figure 2(c) + 2(d)) the Ni-C/N distances of the first coordination shell is 0.12 Å longer than in the monomeric species. This can be seen evidently in the Fourier transformed Ni K-edge EXAFS spectrum of $[(\mu\text{-bpym})\{Ni(Mes)Br\}_2]$ (Figure 2(d)), where the peaks of the first (carbon and nitrogen backscatterers) and second (bromine backscatterer) coordination shells are no longer separated like in the Fourier-Transformed spectra of [(bpym)Ni(Mes)Br], [(Mebpy)Ni(Mes)Br] and [(bpz)Ni(Mes)Br]. The increase in the Ni-C/N distance of the first coordination shell can be explained due to the difficulties of the bpym bridging ligand to coordinate with two metal atoms in an optimal way. Such results were also reported earlier for similar dimeric complexes [6, 7].

Table 1 Structural parameters of the solid complexes determined from the Ni K- and Br K-edge EXAFS spectrum.

	[a]	r [Å]	N	σ [Å]	ΔE_0 [eV]	k-range [Å^{-1}] Fit-Index
[(Mebpy)Ni(Mes)Br]	Ni-C/N	1.93 ± 0.02	3.1 ± 0.3	0.093 ± 0.006	25.6	3.70 – 13.00
	Ni-Br	2.29 ± 0.02	0.9 ± 0.2	0.062 ± 0.008		27.6
	Ni-C	2.79 ± 0.03	3.8 ± 1.1	0.099 ± 0.019		
	Br-Ni	2.29 ± 0.02	1.0 ± 0.1	0.064 ± 0.007	18.5	4.40 – 13.40 47.8
[(bpym)Ni(Mes)Br]	Ni-C/N	1.91 ± 0.02	2.8 ± 0.3	0.056 ± 0.006	27.6	3.70 – 12.50
	Ni-Br	2.29 ± 0.02	1.2 ± 0.2	0.054 ± 0.008		23.7
	Ni-C	2.82 ± 0.03	2.8 ± 0.8	0.063 ± 0.019		
	Br-Ni	2.29 ± 0.02	0.9 ± 0.1	0.051 ± 0.007	13.5	4.00 – 12.50 30.6
[(bpz)Ni(Mes)Br]	Ni-C/N	1.92 ± 0.02	3.3 ± 0.3	0.093 ± 0.009	25.1	3.70 – 15.00
	Ni-Br	2.29 ± 0.02	0.8 ± 0.1	0.058 ± 0.008		25.5
	Ni-C	2.80 ± 0.03	4.6 ± 1.4	0.090 ± 0.027		
	Br-Ni	2.29 ± 0.02	1.0 ± 0.1	0.064 ± 0.006	16.5	3.70 – 14.00 30.6
[(μ-bpym){Ni(Mes)Br}$_2$]	Ni-C/N	2.03 ± 0.02	2.6 ± 0.3	0.097 ± 0.009	22.3	3.65 – 15.80
	Ni-Br	2.30 ± 0.02	0.8 ± 0.1	0.063 ± 0.009		26.2
	Ni-C	2.82 ± 0.03	1.7 ± 1.4	0.092 ± 0.027		
	Br-Ni	2.30 ± 0.02	1.0 ± 0.1	0.077 ± 0.008	15.7	3.70 – 15.00 47.0
[(bpy)Ni(Mes)Br], EXAFS [3]	Ni-C/N	1.92 ± 0.02	3.1 ± 0.3	0.081 ± 0.008	28.0	3.60 – 14.90
	Ni-Br	2.30 ± 0.02	1.0 ± 0.2	0.062 ± 0.011		21.8
	Ni-C	2.81 ± 0.03	5.6 ± 1.7	0.110 ± 0.030		
	Br-Ni	2.30 ± 0.02	0.9 ± 0.1	0.060 ± 0.006	14.5	3.60 – 11.30 23.5

[a] absorber-backscatterer distance r, coordination number N, Debye-Waller factor σ with their calculated deviation, shift of the energy threshold ΔE_0 and the fit-index R.

References

[1] S. Mecking, A. Held, F.M. Bauers, *Angew. Chem., Int. Ed. Engl.* **2002**, *41*, 4, 544.

[2] T. S. Ertel, H. Bertagnolli, S. Hückmann, U. Kolb, D. Peter, *Appl. Spectrosc.* **1992**, *46,* 690.

[3] S.J. Gurman,, N. Binsted, I. Ross, *J. Phys. C* **1986**, *19*, 1845.

[4] M.P. Feth, A. Klein, H. Bertagnolli, *Eur. J. Inorg. Chem.*, in press.

[5] G.J. Colpas, M.J. Maroney, C. Bagyinka, M. Kumar, W.S. Willis, S.L. Suib, N. Baidya, P. K. Mascharak, *Inorg. Chem.* **1991**, *30*, 920.

[6] W. Kaim, R. Reinhardt, S. Greulich, M. Sieger, A. Klein, J. Fiedler, Coll. Czech. *Chem. Commun.* **2001**, *66*, 291.

[7] A. Dogan, M. Wanner, A. Klein, I. Tiritiris, T. Schleid, D. J. Stufkens, T. L. Snoek, E. J. L. McInnes, J. Fiedler, S. Zališ*, Inorg. Chem*. **2002**, *41*, 4139.

Spin Polarization Transfer for the resonant Kr 3d^{-1} 5p Auger Decay

T. Khalil, M. Drescher, N. Müller, S. Fritzsche[*]*, N. M. Kabachnik and U. Heinzmann*
Universität Bielefeld, Fakultät für Physik, 33615 Bielefeld
[*]*Universität Kassel, Fachbereich Physik, 34132 Kassel*

We have measured the transferred spin polarization of the resonantly excited $3d_{5/2}^{-1}5p$ and $3d_{3/2}^{-1}5p$ Auger electrons of krypton. The resonant Auger transitions correspond to the excitation of an inner 3d shell electron to an unoccupied 5p Rydberg orbital. The two fine-structure components of the core $3d_{3/2}$ and $3d_{5/2}$ have a separation of about 1 eV and can be discriminated with moderate photon bandwidth (Fig. 1), while the corresponding splitting in the Rydberg state is not resolved (Fig. 1). The inspected resonant Auger spectrum is characterized by a strong final-ionic-state interaction [1] . Correlation satellites (V in Fig. 3 and 4) result from a strong mixing of the final-state configurations $4s^{-1}4p^{-1}np$ of the diagram transitions with $4s^{-2}4p^{-3}$ mdnp configurations. Shake-up satellites (IV in Fig. 3 and 4) result when the spectator 5p electron is shaken up to an upper orbital in the Auger decay.

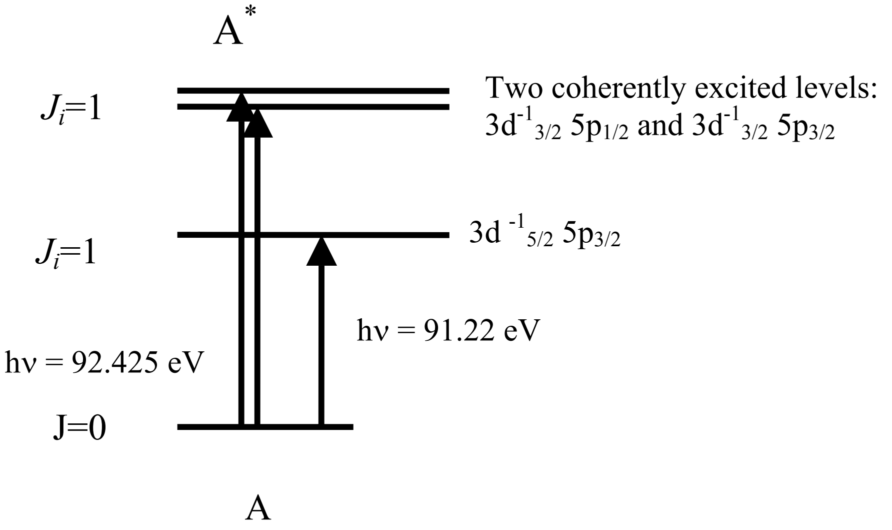

Figure (1). The dipole excitation of resonantly excited Kr 3d^{-1} 5p leads to three initial resonances with $J = 1$.

The transferred spin polarization component [4] of the resonantly excited Kr 3d^{-1} 5p was measured in the electron-fixed frame shown in (Fig. 2) at Θ = 90°; with

$$P_x = -(1 - 1/2\,\alpha_2 A_{20})^{-1}\,\xi_1 A_{10}, \qquad (1)$$

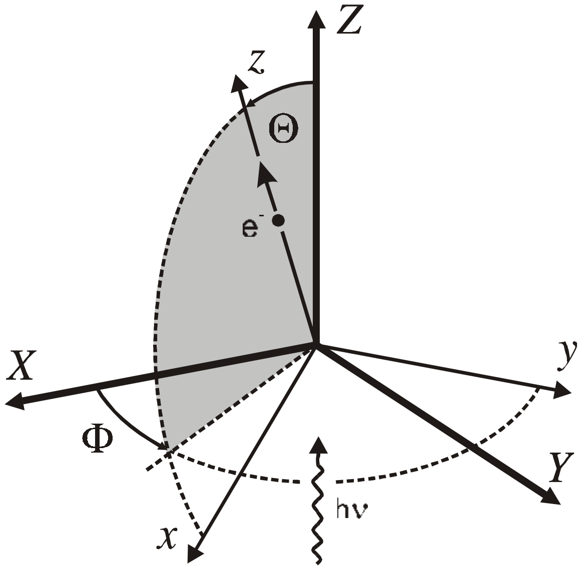

Figure (2). The Z-axis of the laboratory coordinate frame (X, Y, Z) is oriented along the photon beam whereas the electron-fixed frame (x, y, z) is oriented along the direction of the Auger electron.

where A_{10} and A_{20} are the orientation and alignment of the resonance, respectively and α_2 is the intrinsic anisotropy parameter which determines the angular intensity distribution of Auger electrons. The intrinsic parameter ξ_1 characterizes the spin polarization component P_x, which corresponds to the spin polarization transfer to the electron in this geometry.

Figures 3 and 4 present the measured spin polarization for the $3d_{5/2}^{-1}$ 5p and $3d_{3/2}^{-1}$ 5p excitation, respectively. The experimental uncertainty includes the statistical error but is dominated by the uncertainty due to the analyzing power S_{eff} of the Mott polarimeter.
The large value of the transferred spin polarization is partially due to the large value of the orientation $A_{10} = \sqrt{(3/2)}$ [2 , 3]. Comparison with the calculation based on the multiconfiguration Dirac-Fock approach taking into account both initial state and final ionic state configuration interactions reveals excellent agrement.

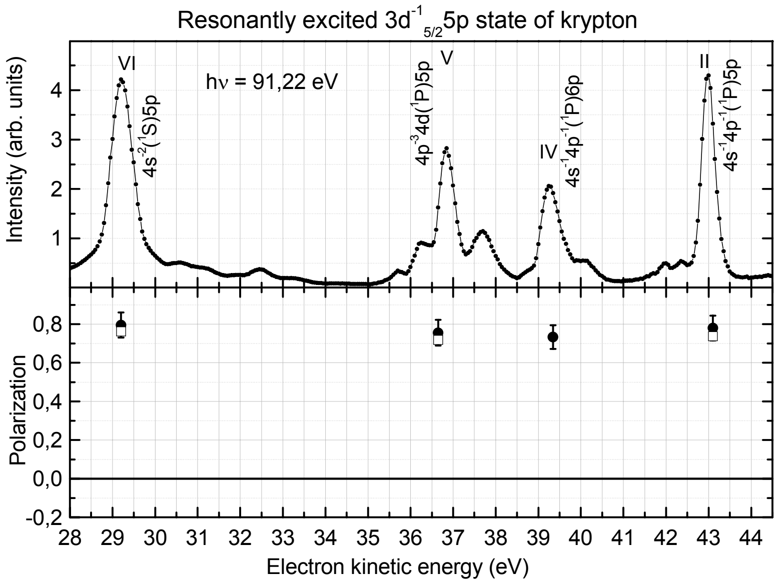

Figure (3). The measured transferred spin polarization of the resonantly excited $3d^{-1}_{5/2}$ 5p state of Krypton [circles] and the calculated values [open squares].

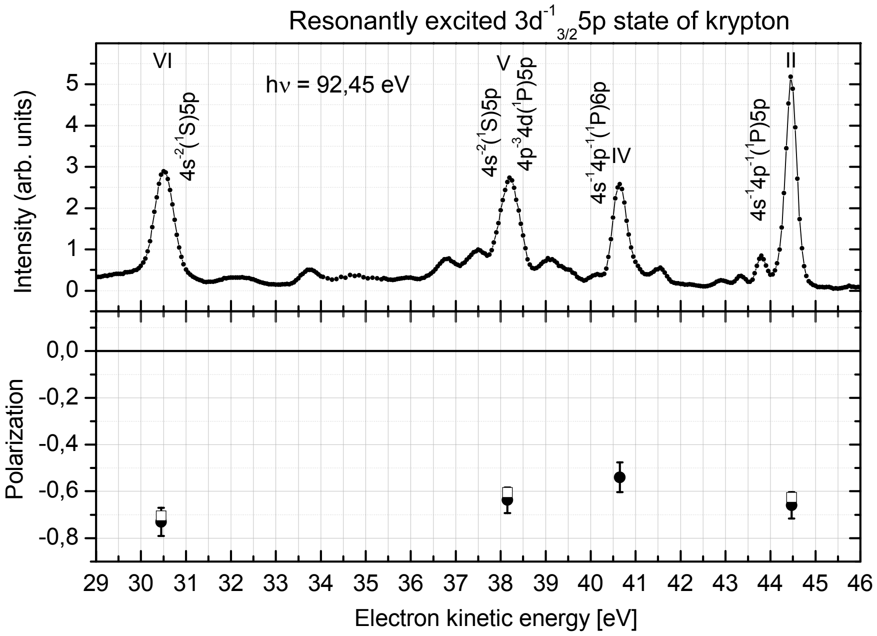

Figure (4). The measured transferred spin polarization of the resonantly excited 3d$^{-1}_{3/2}$ 5p state of Krypton [circles] and the calculated values [open squares].

References

1. J. Mursu , J Jauhiainen, H Aksela and S Aksela *J. Phys. B: At. Mol. Opt. Phys*. **31,** 1973 (1998)

2. V. V. Balashov, A. N. Grum-Grzhimailo, and N. M. Kabachnik 2000 Polarization and correlation Phenomena in Atomic Collisions. A Practical Theory Course (New York: Kulwer Academic) p59.

3. N. M.Kabachnik and I. P.Sazhina *J. Phys. B: At. Mol. Opt. Phys.* **35,** 3591(2002).

4. B.Lohmann, U. Hergenhahn and N. M. Kabachnik *J. Phys. B: At. Mol. Opt. Phys.* **26** 3327 (1993).

Study of the dynamics of the doubly excited states of H_2

M. Glass-Maujean, S. Klumpp, L. Werner*, A.Ehresmann* and H. Schmoranzer**
Laboratoire de Dynamique des Ions Atomes et Molécules, Université P. et M. Curie /CNRS, 4, pl Jussieu, F-75252 Paris Cedex 05, France
* Fachbereich Physik, Technische Universität Kaiserslautern, D-67653 Kaiserslautern, Germany
HPP contract: HPP18/130801

Correlations between electrons have been neglected in most of the classical approaches of atomic or molecular physics. Calculations of these correlations are now possible for simple systems. Doubly excited states are systems in which correlations are especially important. The doubly excited states of molecular hydrogen constitute one of these calculated simple systems [1].

The dynamics of the H_2 doubly excited states are very sensitive to the electronic correlations as several processes are in competition with each other: autoionization ($H_2^{**} \to H_2^+ + e^-$), dissociative ionization ($H_2^{**} \to H + H^+ + e^-$) and dissociation into neutral atoms ($H_2^{**} \to H + H^*$ or $H^* + H^*$)[2,3].

The photon excitation of these doubly excited states out of the ground state in the 25-50eV energy range is allowed only through electron correlations, so that their absorption cross sections are very low (10^{-19} cm^2). The absolute values of the absorption cross sections are also of interest in the correlation study.

We are interested in the process of dissociation into neutrals. The dissociation yield is a few percent of the global excitation. Such dissociation leads to excited fragments which may radiate. The atomic radiation wavelength is characteristic of the principal quantum number of the excited state, and its decay times are characteristic of the orbital momentum states of the atomic fragment.

Fluorescence radiation of the atomic H(n=2) fragments was detected through Lyman–α (121 nm). Time analysis of the fluorescence decay was performed using the single-photon technique.

The H(n=2) states are of 2s or 2p configuration where the 2s atoms, being metastable, may radiate only by collisions so that the 2s fluorescence has to be slow and pressure-dependent [4, 5].

In the 25-50eV energy range, several doubly excited states excited by photons out of the ground state may lead to dissociation followed by Lyman–α fluorescence. They belong to the configurations (in the Franck-Condon region) 2snℓ (Q_1 states) or 2pnℓ (Q_2 states). The excitation threshold of the Q_2 states lies by 3eV higher than the Q_1 state threshold so we can distinguish the relative contributions. The Ly–α fluorescence may also originate from cascades following the process: $H_2 + h\nu \to H(3^2S) + H(1s) \to H(2^2P) + H(1s) + h\nu$ [6]. An excitation spectrum of the Ly–α fluorescence had been published a quite long time ago (see figure 1) showing the different contributions [3].

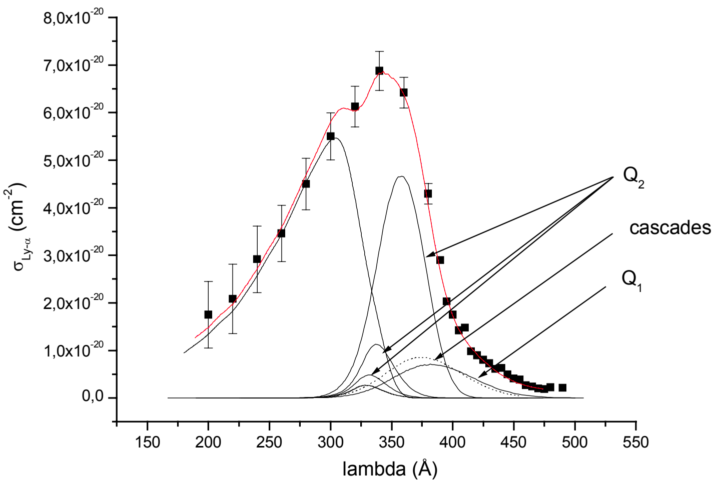

Figure (1): *Ly-a excitation spectrum. Experimental points with fitted theoretical curves.*

The Q_1 states excited by photons and leading to H(n=2) atoms may be Q_1 $^1\Pi_u(1)$ or Q_1 $^1\Sigma_u(2)$ yielding 2^2P or 2^2S, respectively[6]. The H(2^2S) to H(2^2P) ratio will give the ratio of the dissociation cross section of the Q_1 $^1\Sigma_u(2)$ to Q_1 $^1\Pi_u(1)$ states.

The Q_2 states lead to H(2^2P) atoms + H(nℓ). The lowest one identified as the Q_2 $^1\Pi_u(1)$ yields H(2^2S) + H(2^2P) [6,7]. The Q_2 $^1\Pi_u(2)$ yields H(2^2S) + H(2^2P) [6], its energy range is the same as for the Q_2 $^1\Pi_u(3)$ and Q_2 $^1\Pi_u(4)$ states yielding H(2^2P) + H(n=3). The experimental value of the H(2^2S) to H(2^2P) ratio will give a value of the Q_2 $^1\Pi_u(2)$ dissociation cross section.

The decay due to the H(3^2S) cascade process is slow (the lifetime of the H(3^2S) atoms is expected to lie between 150 and 50 ns depending on the pressure[8]).

We analyzed the decay at 12 different energy values between 28 and 45 eV (or 44.3 to 27.5 nm) for at least four pressure values from 3 to 15 μbars. Each Ly–α decay curve is analyzed as a double-exponential decay function. The fast exponential component is assigned to the P signal, the slow one to the S signal or to cascades. The signal to noise ratio does not allow us to fit each decay curve with a three-exponential function with varying widths. The cascade could only be distinguished from the H(2^2S) collision-induced fluorescence through its pressure dependence.

The populations at t_0=0 of the initial atomic states are proportional to the area of the exponentials of their decay component.

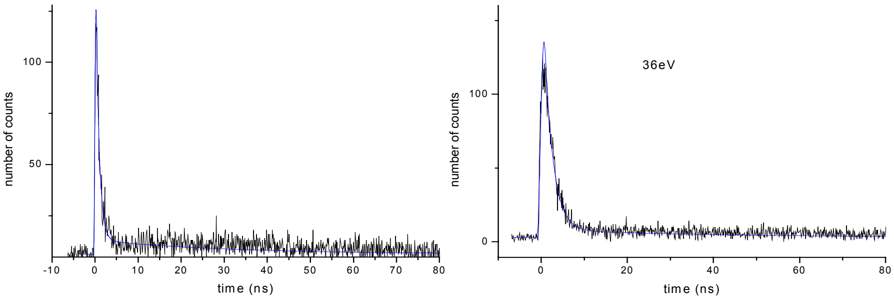

Figure 2: *Ly-α decay curve for an excitation energy of 30eV (left curve) and 36 eV (right curve) and a pressure of 7 microbar*

The fast component lifetime is found to be much shorter than the theoretical H(2^2P) one at low energy values (E<32eV) and longer than the theoretical one at high energy (figure 2). No explanation has been found yet.

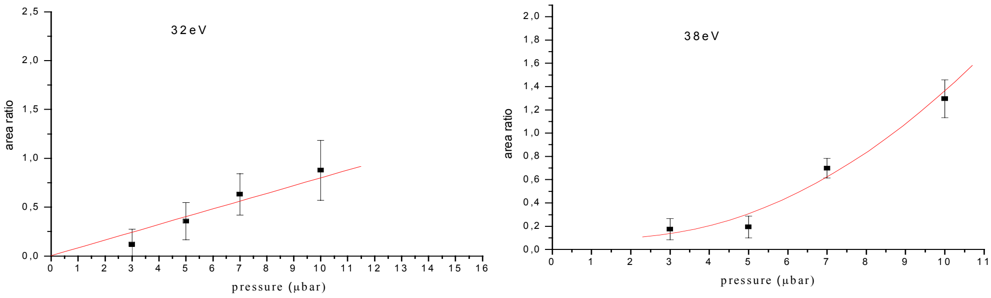

Figure 3 : *pressure dependence of the slow to fast component ratio for two values of the incident energy.*

At low excitation energy, the slow component area presents a quasi linear pressure variation, indicating H(2^2S) atoms formation, and a quadratic behavior at high energy, typical of a pure H(2^2P) formation (figure 3). This result has to be confirmed. The full analysis of the experimental data is not achieved yet. It seems that both $Q_1\ {}^1\Pi_u(1)$ and $Q_1\ {}^1\Sigma_u(2)$ states dissociate into neutral atoms.

References:

[1] F. Martin J. Phys. B, 32 (1999) R197; I Sanchez and F. Martin J. Chem. Phys. 160 (1977) 7720; I Sanchez and F. Martin J. Phys. Rev. A 60 (1999) 2200.
[2] M. Glass-Maujean J. Chem. Phys. 85 (1986) 4830
[3] M. Glass-Maujean J. Chem. Phys. 89 (1988) 2839
[4] M. Glass-Maujean, S. Lauer, H. Liebel and H. Schmoranzer J. Phys. B 33 (2000) 4593
[5] S. Lauer, H. Liebel, H. Schmoranzer and M. Glass-Maujean J.Phys.B 34 (2001) 5121.
[6] M. Glass-Maujean, H. Frohlich and P. Martin J. Phys. Rev. A 52 (1995) 4622.
[7] S. Arai, T. Kamosaki, M. Ukai, K. Shinsaka, Y. Hatano, Y. Ito, H. Koizumi, A. Yagishita, K. Ito and K. Tanaka J. Chem. Phys. 88 (1988) 3016.
[8] S. Lauer, H. Liebel, F. Vollweiler, O. Wilhelmi, R. Kneip, E. Flemming, H. Schmoranzer and M. Glass-Maujean J.Phys.B 31 (1998) 3049.

Photofragmentation and charge transfer processes in Cs halide molecules

M. Martins
Universität Hamburg, Institut für Experimentalphysik
Luruper Chaussee 149, D-22761 Hamburg

K. Godehusen,
BESSY GmbH, Albert-Einstein-Str. 15, D-12489 Berlin

T. Richter, and P. Zimmermann
Technische Universität Berlin, Institut für Atomare Physik
und Fachdidaktik, Hardenbergstraße 36, D-10623 Berlin

Photofragmentation of small molecules is studied in general for covalent bound molecules. Fragmentation studies on molecules like Cs halides CsX, which are prototype molecules of ionic bonding have not been done up to now. Cs halides are known to produce almost only monomeric vapours on heating which are free from small clusters $(\mathrm{CsX})_n$ [1]. First experiments on the photoabsorption of CsCl have been done by Radler et. al [2] in the region of the Cs $4d \rightarrow (4\epsilon)f$ excitation showing a close correspondence between the photoabsorption of atomic Cs and molecular CsCl. First experiments in photoemission were done using helium discharge lamps and synchrotron radiation [3, and references therein]. Spectra from all diatomic species have been observed and spectra have been successfully interpreted in terms of simple ionic models [3].

In CsCl and $\mathrm{BaCl_2}$ crystals inter-atomic processes in the form of cross luminescence are observed. To investigate these decay processes we have studied the photofragmentation of the molecules CsF, and CsBr in the region of the Cs $4d$ giant resonance and the Cs $3d$ and F $1s$ excitation. The experiments have been performed at the U125/2-SGM (BUS) beamline and the U49/2-PGM1 beamline, respectively using a small time-of-flight (TOF) mass spectrometer.

In atomic Cs the $4d \rightarrow (4\epsilon)f$ photoabsorption is dominated by a strong shape resonance, due to the non-collapsed $4f$ wavefunction. Therefore in partial ion yield spectra one observes ionized ions from Cs^{2+} up to Cs^{4+} [4]. In the case of a collapsed $4f$ wavefunction, where the excitation has be to described as a resonant excitation into the $4f$ orbitals, this will result in lower ionization stages [5, 6]. The collapse of the $4f$ wavefunction depends strongly on the charge of the ion, which has been shown the first time for Ba atoms and ions by Lucatorto et. al [7], and has recently been observed for Cs ions by Cummings et. al [8]. Now the question arises in which way the charge of the Cs ion in the molecule will influence the $4f$ wavefunction and the decay of a core hole.

Figure 1 shows the partial ion yield of free CsBr molecules in the region of the $4d \rightarrow (4\epsilon)f$ excitation, which is very similar for all Cs halide molecules. The shape of the resonance is very similar to atomic Cs, however in contrast to atomic Cs only the lower ionization stages photofragments Cs^{+} and Cs^{+2} are observed. This is an indication for a collapsed $4f$ wavefunction, however in this case a different shape of the resonance is expected. In the atomic ion this collapse shows up by sharp Rydberg like resonances. Thus, in the molecule

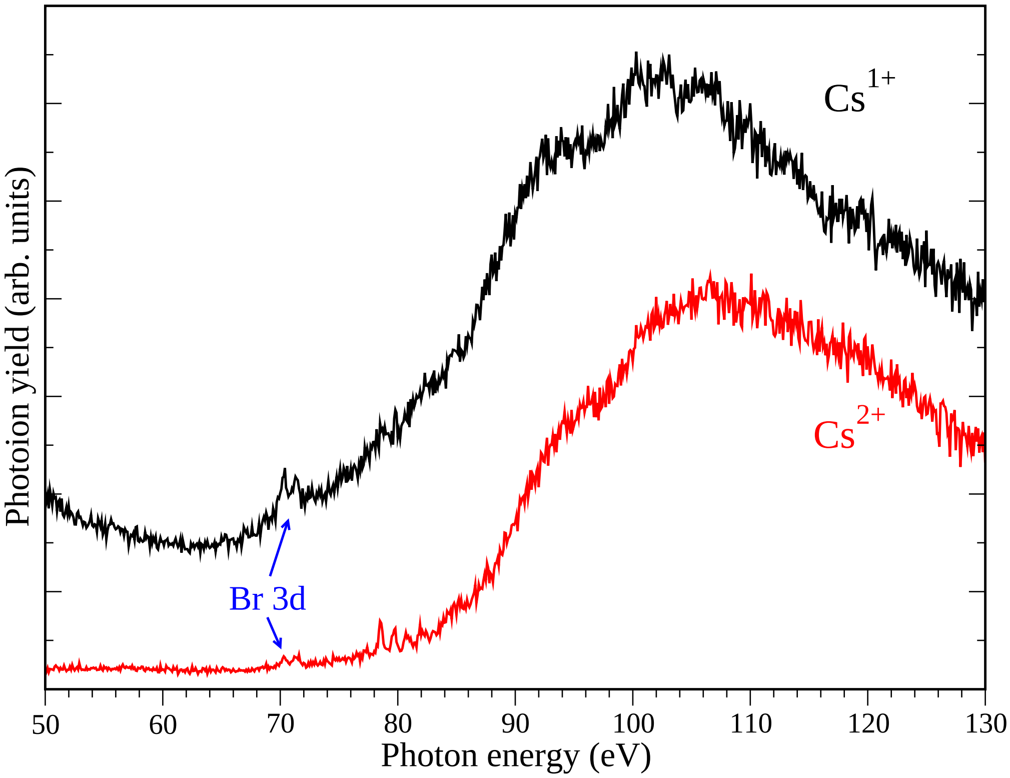

Figure 1: Partial ion yield of free CsBr molecules in the region of the Cs 4d excitation.

the fragmentation has to be explained in a different way. The $4f$ wavefunction still has to be treated as uncollapsed, however due to the halide ligand the $4f$ electron will now be bound in the molecular field. Therefore the decay of the Cs $4d$ hole can be explained more like a resonant excitation, which results in the low ionization stages for the Cs ion photofragments.

Another interesting point is a charge transfer subsequent to a core hole excitation. To shed some light into this problem we have also measured the Cs $3d$ and F $1s$ excitation of CsF molecules. Here in almost the same energy range a core hole excitation of both compounds Cs and F is possible. The partial ion yield for the different observed Cs ions is shown figure 2. In the Cs^+ channel the F $1s$ excitation shows up as a small resonance at 685 eV photon energy. This results from a simply fragmentation of the molecule after the F $1s$ excitation. However, the F $1s$ excitation is also observed in the Cs^{2+} channel, but with a different energy dependence. Here a very broad resonance structure between 685 and 700 eV photon energy is measured. This enhanced Cs^{2+} signal already at the F $1s$ edge indicates a charge transfer from the Cs side to the F side of the molecule.

The authors would like to thank the BESSY staff for their support during the beamtimes.

References

[1] J. Berkowitz, C. Batson, and G. Goodman, in *ACS Symp.*, *179*, edited by J. Gole and W. Swalley (1982).

[2] K. Radler and B. Sonntag, Chem. Phys. Lett. **39**, 371 (1976).

[3] J. M. Benson, I. Novak, and A. W. Potts, J. Phys. B **20**, 6257 (1987).

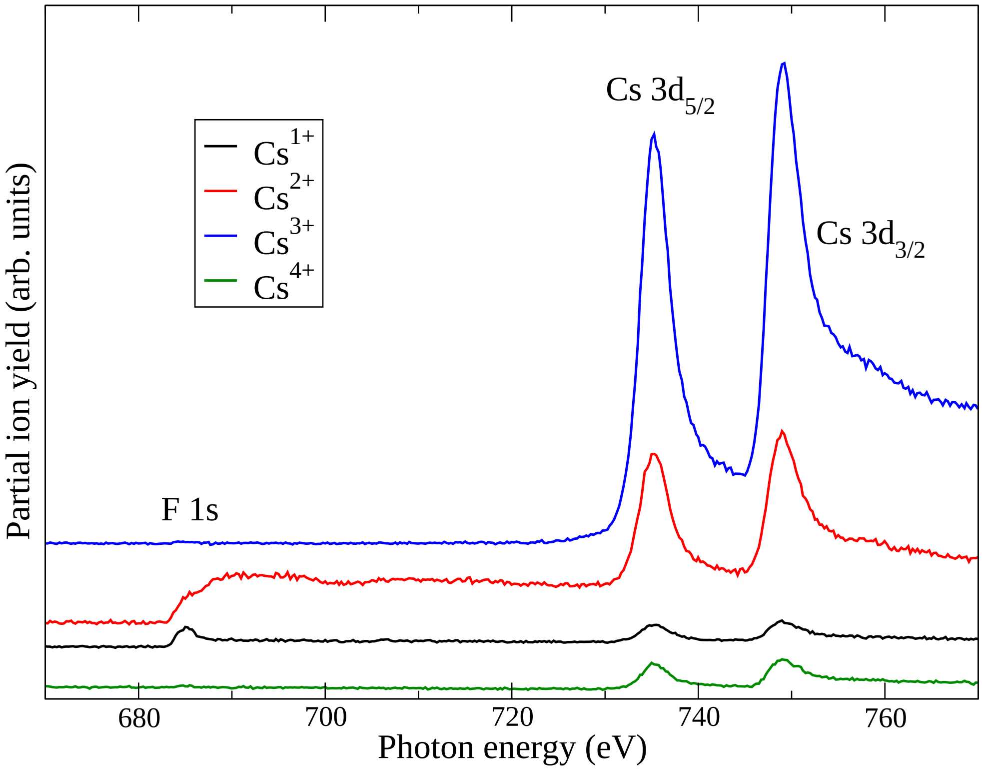

Figure 2: Partial ion yield for the Cs ion channels of free CsF molecules in the region of the Cs $3d$ and F $1s$ excitation.

[4] T. Nagata *et al.*, J. Phys. B **22**, 3865 (1989).

[5] C. Dzionk, W. Fiedler, M. von Lucke, and P. Zimmermann, Phys. Rev. Lett. **62**, 878 (1989).

[6] C. Dzionk, W. Fiedler, M. v. Lucke, and P. Zimmermann, Phys. Rev. A **41**, 3572 (1990).

[7] T. B. Lucatorto, T. J. McIlrath, J. Sugar, and S. M. Younger, Phys. Rev. Lett. **47**, 1124 (1981).

[8] A. Cummings *et al.*, Phys. Rev. A **63**, 022702 (2001).

High resolution studies of the photoionization excitation of Ne and Ar satellites incuding the partical wave analysis for the autoionization of doubly excited states

B. Zimmermann, S. Kammer, S. Mickat, R. Schill, K.-H. Schartner
I. Physikalisches Institut, Justus-Liebig-Universität, D-35392 Giessen

A. Ehresmann, H. Schmoranzer, Y. Schutov, L. Werner, S. Klumpp
Fachbereich Physik , Universität Kaiserslautern, D-67663 Kaiserslautern

The photoionization of the rare gas valence shells at threshold energies of excited ion states is a clear demonstration of electron correlations. Close to the thresholds it is strongly enhanced by autoionization of doubly excited states. Direct excitation is a comparably weak channel with the consequence of absorption type resonance profiles. Due to the open mp^4 shell of the ion core with its three LS-coupled states (^{3}P, ^{1}D, ^{1}S) a correspondingly large number of Rydberg series can be excited producing a complicated overlap of autoionization resonances. This became already evident in the pioneering absorption studies by Madden et al. for Ar [1]. The corresponding experiments for Ne by Codling et al. [2] showed a clearer separation of Rydberg series favouring Ne for the analysis of doubly excited states [3,4], while for Ar one has to confine the experiments to the lowest excited ion states in order to avoid the complexity of classification [5].

We have studied the Ne$^+$ $2p^4$ (^{3}P) 3p ^{2,4}P, (^{1}D) 3s ^{2}D- and the Ar$^+$ $3p^4$ (^{3}P) 4s ^{2,4}P-satellite production using the method of photon induced fluorescence spectroscopy (PIFS) [5]. Fluorescence spectra in the spectral range of the visible and the VUV were accumulated as function of the energy of the exciting photons. Their energy was varied between 52.0 eV and 55.5 eV for Ne and 32.4 eV and 34 eV for Ar, respectively. The bandwidth of excitation was 4.5 meV.

In fig. 1 we present the cross sections for populating the Ne$^+$ (^{3}P) 3p ^{2}P- and ^{4}P-states as well as the Ne$^+$ (^{1}D) 3s ^{2}D-states. The threshold energies (≈ 52.1 eV) for the (^{3}P) 3p ^{4}P- and

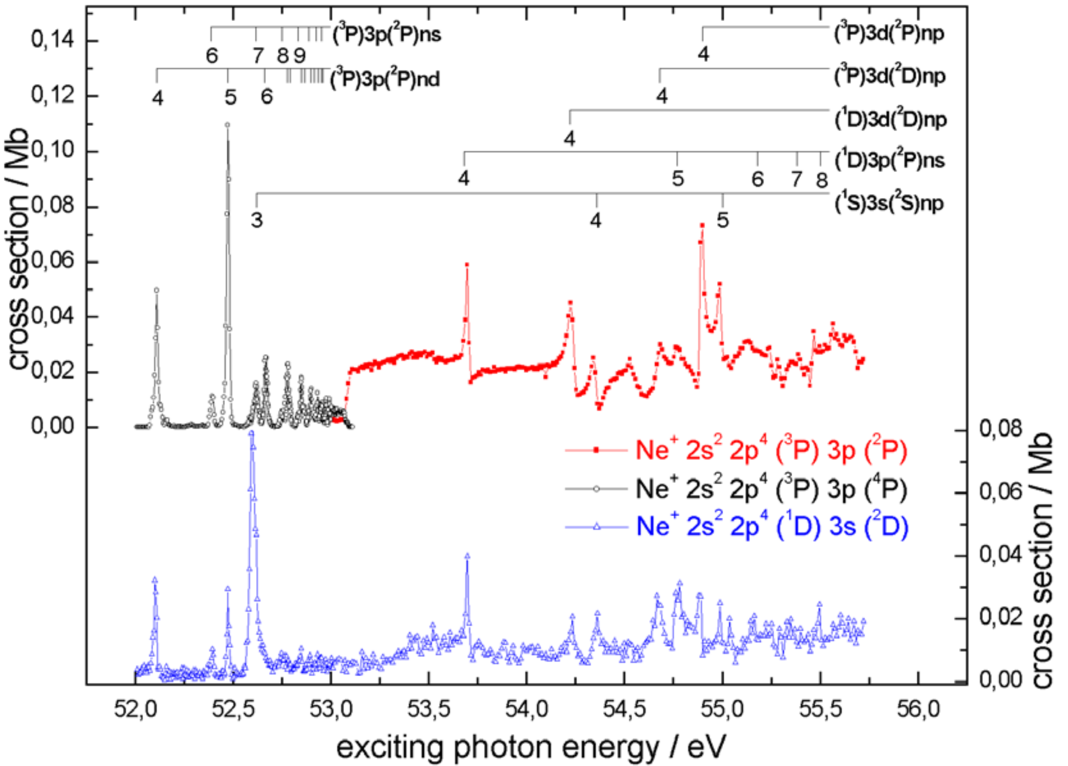

Fig. 1: Photon induced satellite production cross sections for the Ne$^+$ (^{3}P) 3p ^{2,4}P- and Ne$^+$ (^{1}D) 3s ^{2}D-states as function of the exciting photon energy.

the (^{1}D) 3s ^{2}D-states are practically degenerate, i.e these states are not separable by PES. Included in fig.1 are Rydberg series of doubly excited states classified by Codling et al [2] and by Schulz et al [3]. For Ne, satellite production is favoured by a 6 % admixture in the ground state of the 2p^5 3p configuration. In consquence, the (^{3}P) 3p ^{2}P-states can be populated by dipole allowed one electron transitions, while the direct population of the ^{4}P component is forbidden in LS coupling: The experiment shows direct excitation of the ^{2}P-states and Fano type interference profiles caused by the autoionization while the ^{4}P-states are populated exclusively through autoionization. This holds also for the (^{1}D) 3s ^{2}D-states for energies below 53.3 eV. Above 53.3 eV the direct excitation process becomes visible. At this energy, also the cross section for the (^{3}P) 3p ^{2}P-state – and here especially for the J = 1/2 state – shows a shoulder which is unexplained. Calculations for the cross sections in fig.1 have not been published so far.

For a sensitive test of initiated future calculations, the results presented in fig.2 are certainly of interest. The cross section for populating the J = 3/2 fine structure component of the (^{3}P) 3p ^{4}P-state is shown in the energy range of the higher n–members of the (^{3}P) 3p (^{2}P$_{3/2,1/2}$)ns, nd Rydberg series. In the lower part the angular anisotropy parameter ß$_{fl}$ for the Ne$^+$ 2s^2 2p^4 (^{3}P) 3p (^{4}P$_{3/2}$) $\longrightarrow$ (^{3}P) 3s (^{4}P$_{3/2,1/2}$)-transitions as function of the photon energy are reproduced. These data can be interpreted with respect to the contribution of the three allowed electron partial waves with j$_{el}$ = 5/2, 3/2, 1/2: On the ns–resonances, the s$_{1/2}$ partial wave dominates, the decay of the nd – resonances seems to favour the d$_{5/2}$ partial wave i.e. the total angular momentum of the Rydberg electron is nearly conserved in the autoionization process. We add, that for the (^{3}P) 3p ^{4}P$_{5/2}$-fine structure component, no energy dependence of ß is observed with ß$_{fl}$ values supporting a preference of j$_{el}$ = d$_{5/2}$.

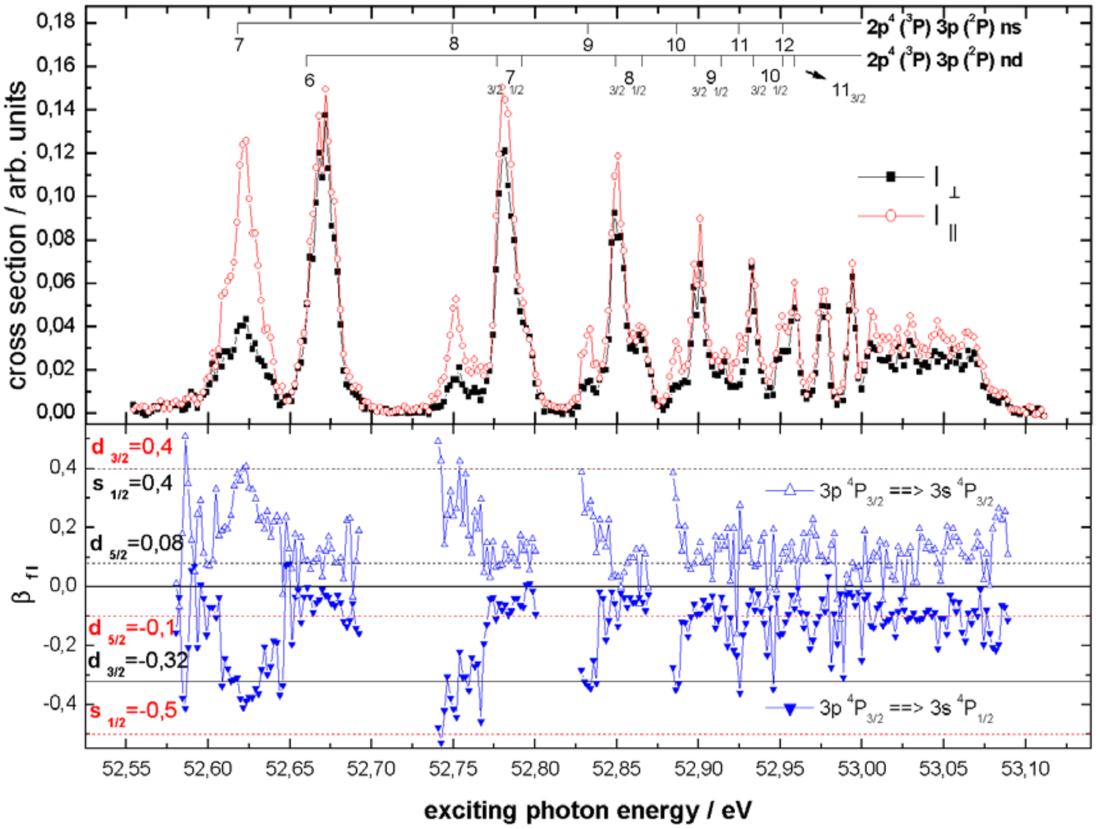

Fig. 2: Cross section for the Ne$^+$ (^{3}P) 3p ^{4}P$_{3/2}$-state and angular anisotropy parameter ß$_{fl}$ for the Ne$^+$ 2s^2 2p^4 (^{3}P) 3p (^{4}P$_{3/2}$) $\longrightarrow$ (^{3}P) 3s (^{4}P$_{3/2,1/2}$)-transitions as function of the exciting photon energy.

For Ar as target gas, the high resolution experiments concentrated on the Ar$^+$ 3p^4 (^{3}P) 4s ^{2,4}P-states. In the earlier results [6] only two broad peaks were observed at 32.5 eV and 32.8 eV. The present result is reproduced in fig. 3 which shows the resonance enhancement in this

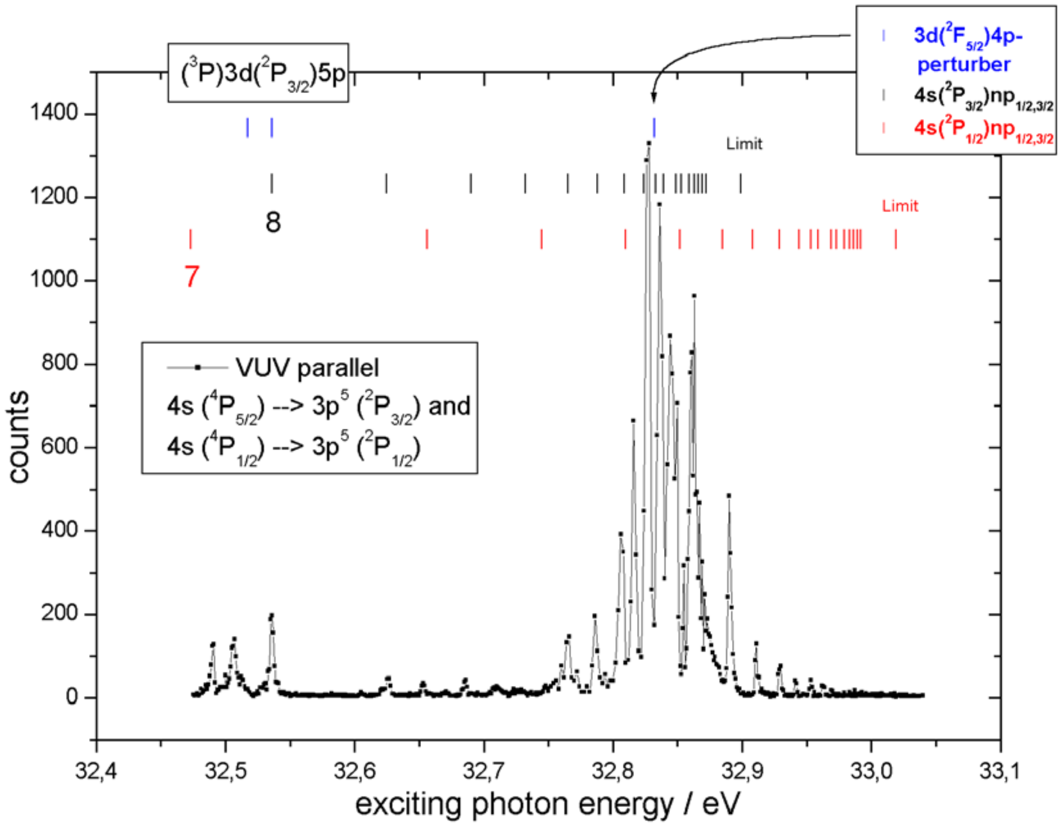

Fig. 3: Intensity of the Ar$^+$ 4s $^4P_{5/2,1/2}$ satellites as function of the exciting photon energy.

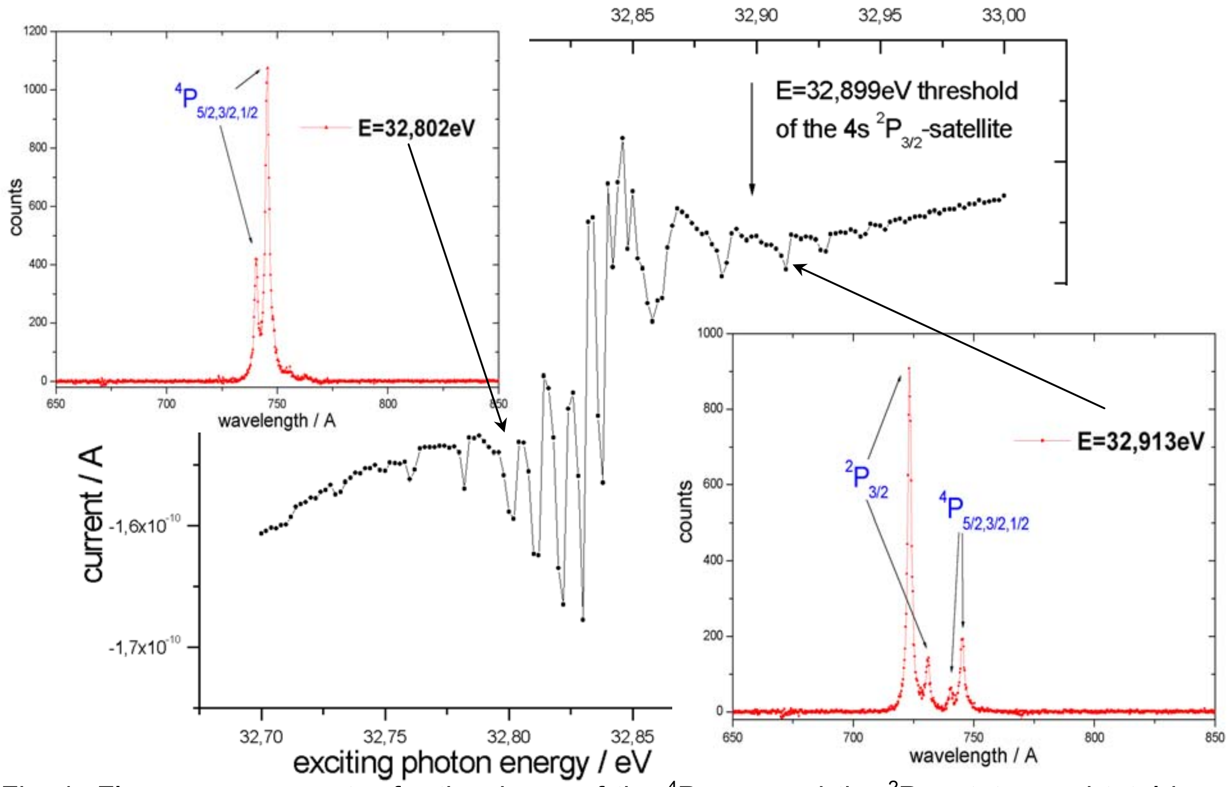

Fig. 4: Fluorescence spectra for the decay of the $^4P_{5/2,3/2}$- and the $^2P_{3/2}$-states and total ion yield as function of the exciting photon energy.

range as it was measured using the BESSY II U125/1-PGM beam line. Included in fig.3 are the energies of the 4s ($^2P_{3/2,1/2}$) np$_{3/2,1/2}$ Rydberg states. The thresholds of the 4s ^4P_J fine structure component have values between 32.99 eV and 32.57 eV, while the 4s $^2P_{3/2}$-state and the 4s $^2P_{1/2}$-states can be populated from 32.9 eV and 33.08 eV upwards. The intensity increase of the higher n-members is due to a perturber identified by Baig et al [7] as (^3P) 3d ($^2F_{5/2}$)4p doubly excited state. We have additionally measured the total ion yield, and the result for the 32.8 eV range is shown in fig. 4. in connection with fluorescence spectra observed at the indicated energies below and above the 4s $^2P_{3/2}$ threshold.

While the Ne results are already on an absolute cross section base, the Ar data are still relative but can be normalized in further experiments on the Ar 3s electron ionization cross section. In order to determine the energy positions of the Rydberg states the satellite intensity as function of the photon energy seems to be better suited than the ion signal which has to be analyzed by Fano profiles. While the 4s ($^2P_{3/2}$)np$_{3/2,1/2}$ series has been modelled [7], the 4s ($^2P_{1/2}$)np$_{3/2,1/2}$ series been omitted. The analysis of the resonance enhancement of the 4s $^2P_{3/2}$-state by the 4s ($^2P_{1/2}$)np$_{3/2,1/2}$ series is in progress and should help in measuring the energy positions for the higher n members of this Rydberg series.

Funded by the Deutsche Forschungsgemeinschaft under contract numbers Scha 235/16 and Schm 379/12.

References

[1] R.P. Madden et al., Phys. Rev. 177 (1969) 136

[2] K. Codling et al., Phys. Rev. 155 (1967) 29

[3] K. Schulz et al., Phys. Rev. A 54 (1996) 3095

[4] T.W. Gorczyca et al., Phys. Rev. A 58 (1998) 3661

[5] G. Mentzel et al., J. Phys. B 31 (1998) 227

[6] K.-H. Schartner et al., Phys. Lett. A 128 (1988) 374

[7] M.A. Baig et al., Phys. Rev. A 45 (1992) 7963

Photodissociation of CO and O_2 Rydberg states into neutral fragments at exciting-photon energies of about 20 eV investigated by fluorescence spectroscopy

M. Schlüter, L. Werner, S. Klumpp, Ph.V. Demekhin, A. Ehresmann, H. Schmoranzer,
Fachbereich Physik, Universität Kaiserslautern, D-67653 Kaiserslautern

S. Kammer, S. Mickat, B. Zimmermann, K.-H. Schartner
I. Phys. Institut, Justus–Liebig–Universität, D–35392 Giessen, Germany

Motivation. Photon-induced fluorescence spectroscopy (PIFS, Schmoranzer et al. 2001), recording dispersed fluorescence radiation from excited fragments as a function of the energy of the exciting-photons, has proven to be a valuable tool for the investigation of photodissociation processes of small molecules into neutral fragments. Using beamlines at third generation synchrotron radiation sources it is possible to combine narrow bandwidth of the exciting-photons and high flux, which enables the use of high resolution fluorescence spectrometers to measure the dispersed fluorescence. Therefore this technique has been used a few years ago to experimentally prove that the O_2 vibronic Rydberg states $(c^4\Sigma_u^-)\, ns\sigma\ {}^3\Sigma_u^-$ $(v = 1)$ and $(c^4\Sigma_u^-)\, nd\sigma\ {}^3\Sigma_u^-$ $(v = 1)$ prefer to dissociate into fragment pairs $OI + OI(^4S^o)ns/(n\text{-}1)d$ and $OI + OI(^4S^o)nd/(n+1)s$, respectively, whereas the corresponding states with $v = 0$ show a very weak dissociation only (Ukai et al. 1995, Liebel et al. 2000). Since these superexcited Rydberg states are test cases to study the competition between dissociative decay and autoionization, a new set of experiments have been carried out.

In case of CO the photodissociation into neutral fragments has been investigated previously by (undispersed) fluorescence ($\lambda_{fl} = 105nm – 200nm$) excitation spectroscopy after excitation by narrow bandwidth photons ($\Delta E = 13meV$ at 23.4eV, Ehresmann et al. 1997). There, new Rydberg series converging to the CO^+ D state have been tentatively assigned in the exciting-photon energy range between about 21eV and 23.4eV. In a parallel investigation (Ehresmann et al. 1996) dispersed fluorescence ($\Delta\lambda_{fl} = 1.3nm$) has been recorded as a function of the exciting-photon energy with a bandwidth of $\Delta E = 40meV$ at 20eV to disentangle the dissociation of these Rydberg states into specific neutral fragments. Although some general features have been observed, the bandwidth and fluorescence resolution have not been sufficient to allow detailed conclusions. Here it has been found necessary to carry out additional experiments to verify the previous assignments of the vibronic molecular Rydberg states and to investigate whether there are preferred dissociation channels.

Experimental. In the experiments on O_2 and CO, monochromatized synchrotron radiation of energies around 24eV with very narrow bandwidth of about $\Delta E = 1meV$ from beam line U125/1-PGM at BESSYII was used to excite CO or O_2 gas in a target cell at room temperature. In case of O_2, the impinging photons excite the above mentioned Rydberg states which subsequently decay via (pre-)dissociation or autoionization. Since the dissociation process forms excited OI fragments the spectroscopy of fluorescence in the wavelength range between $\lambda_{fl} = 91$nm and 105nm with a resolution of $\Delta\lambda_{fl} = 0.2$nm was used for the determination of dissociation probabilities into fragment pairs with an excited OI fragment. Simultaneously the yield of positive ions was measured as a function of the exciting-photon energy. For CO, the probabilities to form excited CI fragments were measured through the intensities of dispersed fluorescence in the wavelength range between 115nm and 135nm and the ones to form excited OI fragments through fluorescence in the wavelength range between 91nm and 105nm as a function of the exciting-photon energy. The bandwidth of the exciting photons was set to 2meV and the fluorescence resolution to $\Delta\lambda_{fl} = 0.2$nm.

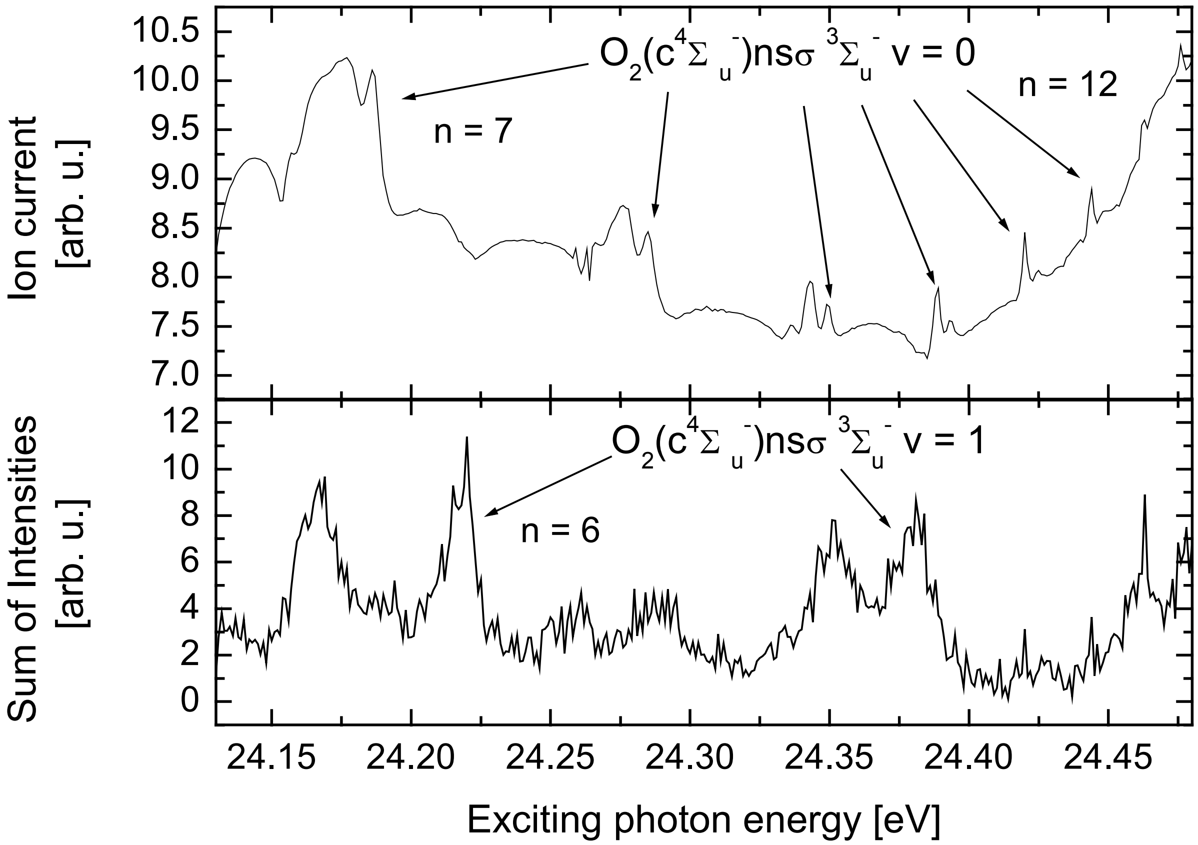

Fig. 1:Ion current (top panel) and fluorescence intensities summed between wavelengths of 91nm and 105nm (bottom panel) as a function of the energy of the exciting photons, both normalized to the flux of the incoming photons.

Results. Fig.1 shows a part of the results for O_2 in the exciting-photon energy range between 24.1eV and 24.5eV. The vibronic Rydberg states with v = 0 show a strong photoion signal, whereas they are only weakly seen in fluorescence. This implies that these vibronic bands preferentially autoionize rather than dissociate. In contrast, the vibronic Rydberg states with v = 1 do dissociate strongly, whereas they practically cannot be identified in the photoion yield signal, i.e. these bands prefer to dissociate rather than to autoionize. With the narrow bandwidth of the exciting photons it was even possible to observe the envelope of single rotational branches of the autoionising Rydberg states with v = 1. The profile of the branches is determined by the rotational constants of the involved electronic states and the type of electronic transition in the excitation. In this case the excitation is a Σ-Σ transition and correspondingly only P and R branches are expected. Simulations show that the P branch is sharp with high intensity, whereas the R branch is smeared out over a wider exciting-photon energy range. The two closely lying sharp peaks in the ion current at energies of the vibronic Rydberg states with higher n therefore do not represent the P and R branches rather than the P branches of the two Rydberg states (c$^4\Sigma_u^-$) nsσ $^3\Sigma_u^-$ (v = 0) and (c$^4\Sigma_u^-$) ndσ $^3\Sigma_u^-$ (v = 0). As accompanying theoretical estimates show, the natural widths of the rovibronic Rydberg states with v = 0 are decreasing as n increases, which is easily seen in Fig.1 as well through the narrowing of the P-branch peaks in the ion current.

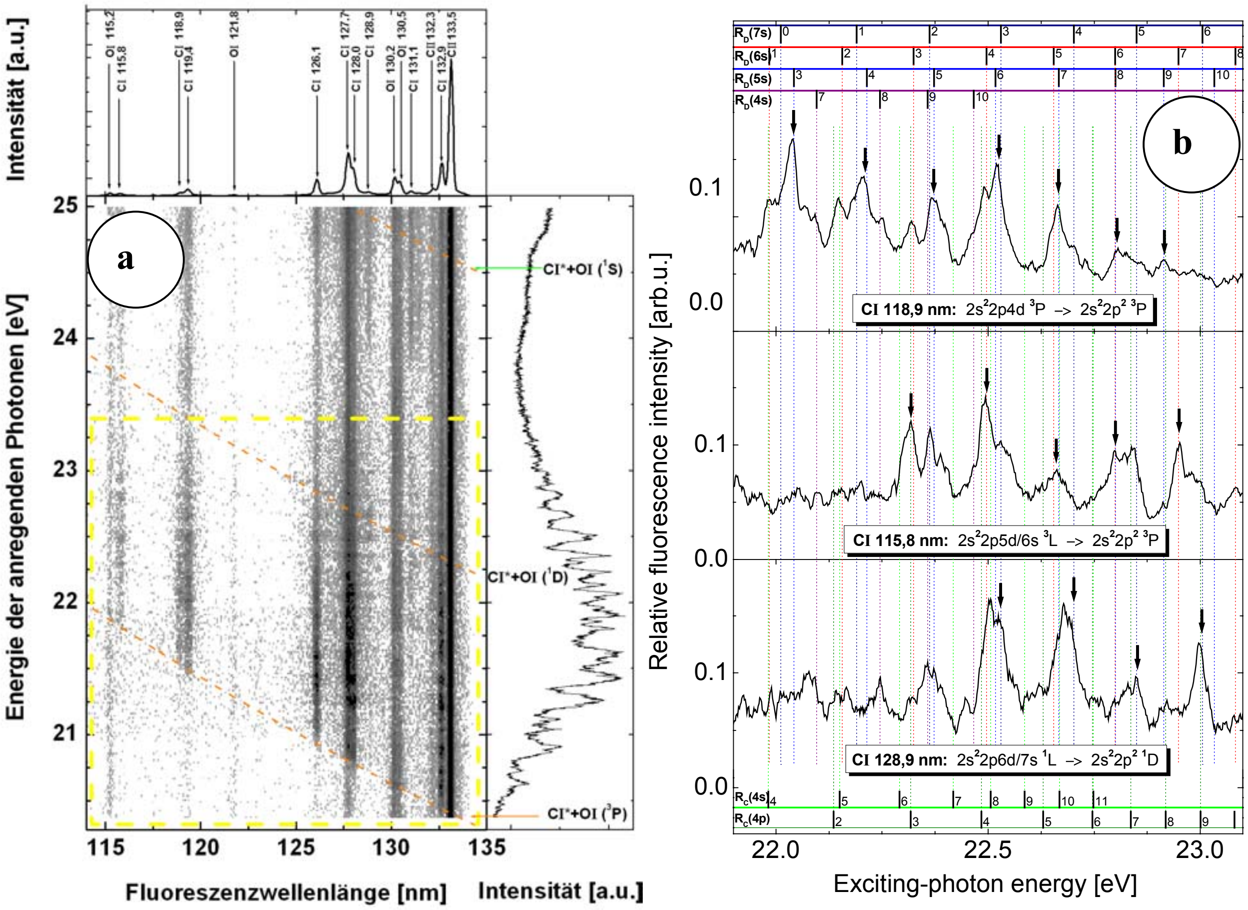

Fig.2: a) Two-dimensional grey scale plot of intensities of the dispersed fluorescence as a function of fluorescence wavelength and exciting-photon energy. Top panel: fluorescence intensities summed over the whole exciting-photon energy range and assignment of peaks to fluorescent species (numbers correspond to the approximate transition wavelength). Right panel: excitation spectrum of undispersed fluorescence between 115nm and 135nm.

b) Comparison of CI fragment fluorescence excitation spectra for fragments with outer 4d, 5d/6s, and 6d/7s electrons, representing the population probabilities of the corresponding excited fragments after dissociation. Highest intensities (see arrows) are observed after (pre-) dissociation of superexcited molecular Rydberg states where the Rydberg electron possesses approximately the same effective principal quantum number as the Rydberg electron of the excited CI dissociation fragment.

For CO the observed dispersed fluorescence as a function of the exciting-photon energy is shown in Fig.2a in a two-dimensional plot where the intensities are plotted as grey scales as a function of both the fluorescence wavelength and the exciting-photon energy. This data was used to check the previous assignments of dissociating molecular Rydberg states. Most of the assignments of spectral features to dissociating vibronic Rydberg states given in Ehresmann et al. (1997) were verified and a yet unknown series could additionally be assigned.

In the fluorescence wavelength range between 91nm and 105nm, where only excited OI atoms fluoresce, practically no fluorescence was observed. Intensities of OI fluorescence observed in the spectral range between 115nm and 135nm (see Fig.2a) are mainly due to higher-order exciting photons. Therefore it is concluded that excited oxygen atoms will be formed only very weakly by the dissociation of the superexcited Rydberg states. Practically only excited carbon atoms emerge from the dissociation of these Rydberg states. Evidence was found that the vibronic states of the Rydberg series $R_D(n_m s\sigma, v)$, converging to the CO^+ D state, preferentially dissociate into fragment pairs where excited carbon fragments of the electron configuration $1s^2 2s^2 2p^1 n_f s$ are formed (i.e. the principal quantum number n_f of the carbon Rydberg electron has the same value as the principal quantum number n_m of the Rydberg electron in the dissociating molecular state).

Acknowledgements. The authors are grateful to the BESSY staff, particularly to Dr. G. Reichardt, for their support. Financial support by the Deutsche Forschungsgemeinschaft is gratefully acknowledged.

References

A. Ehresmann, S. Machida, M. Ukai, K. Kameta, M. Kitajima, N. Kouchi, Y. Hatano, K. Ito, T. Hayaishi, J. Phys. B: At. Mol. Opt. Phys. **29**, 3629-50 (1996)

A. Ehresmann, S. Machida, M. Ukai, K. Kameta, M. Kitajima, N. Kouchi, Y. Hatano, K. Ito, T. Hayaishi, J. Phys. B: At. Mol. Opt. Phys. **30**, 1907-26 (1997)

H. Liebel, S. Lauer, F. Vollweiler, R. Müller-Albrecht, A. Ehresmann, H. Schmoranzer, G. Mentzel, K.-H. Schartner, and O. Wilhelmi, Phys. Lett. A **267**, 357 (2000)

H. Schmoranzer, H. Liebel, F. Vollweiler, R. Müller-Albrecht, A. Ehresmann, K.-H. Schartner, B. Zimmermann, Nucl. Instr. Meth. in Phys. Res. A **467-8** 1526 (2001)

M. Ukai, S. Machida, K. Kameta, M. Kitajima, N. Kouchi, Y. Hatano, and K. Ito, Phys. Rev. Lett **74**, 239 (1995)

The 3p giant resonances of atomic Manganese: Energy dependent investigation of the fine structure resolved photoelectron spectra

T. Richter, T. Wolff, Th. Ryschawy, P. Zimmermann
Institut für Atomare Physik und Fachdidaktik, Technische Universität Berlin

K. Godehusen
Berliner Elektronenspeicherring-Gesellschaft für Synchrotronstrahlung mbH

M. Martins
Institut für Experimentalphysik, Universität Hamburg

The photoabsorption spectrum of atomic Mn shows pronounced resonances in the region of the 3p excitation at about 48–55 eV. The reason for this is a large overlap of the 3p and the 3d orbitals which channels the majority of the oscillator strengths into discrete transitions Mn $3p^63d^54s^2$ $\rightarrow$ Mn $3p^53d^64s^2$ of the 3p electrons into the unfilled 3d subshell and also causes the subsequent autoionization of these states Mn $3p^53d^64s^2 \rightarrow \mathrm{Mn}^+3p^63d^44s^2 + \epsilon p, f$.
As the half filled 3d subshell forms the rather stable ground state Mn $3d^54s^2\ {}^6S_{5/2}$ (the level with the next lowest energy is more than 2 eV away) the main resonances are due to the transitions Mn $3p^63d^54s^2\ {}^6S \rightarrow$ Mn $3p^53d^64s^2\ {}^6P$. The main photolines are caused by the autoionization decay Mn $3p^43d^64s^2\ {}^6P \rightarrow \mathrm{Mn}^+3p^63d^44s^2\ {}^5D + \epsilon p, f$. This was already studied in detail by Witfield in [1].
The experiments were carried out at the beamline U125/2-SGM-1 (BUS beamline). The atomic beam was produced by thermal evaporation of the metal at temperatures of about 1200 K. The atoms were crossed by a monochromatized photon beam and the resulting photoions and photoelectrons were analyzed by a time-of-flight spectrometer or electron analyzer (Scienta SES 2002).

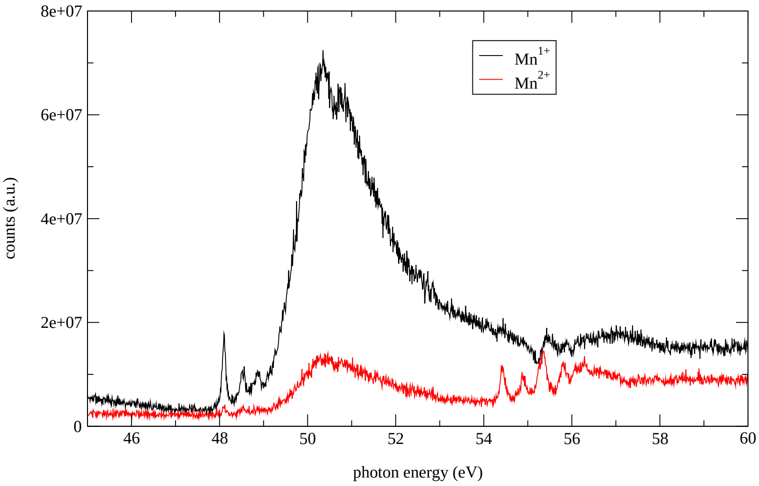

Figure 1: *partial ion yield for* Mn^{1+} *and* Mn^{2+}

In figure 1 the partial ion yield for Mn^{1+} and Mn^{2+} is presented. The giant resonance can easily be seen in the 1+ ion yield starting at about 48 eV. With higher photon energies the creation of doubly charged Manganese becomes possible for example via $3p \rightarrow 5s, 4d$ excitation and decay, seen between 54 and 56 eV in the 2+ channel.

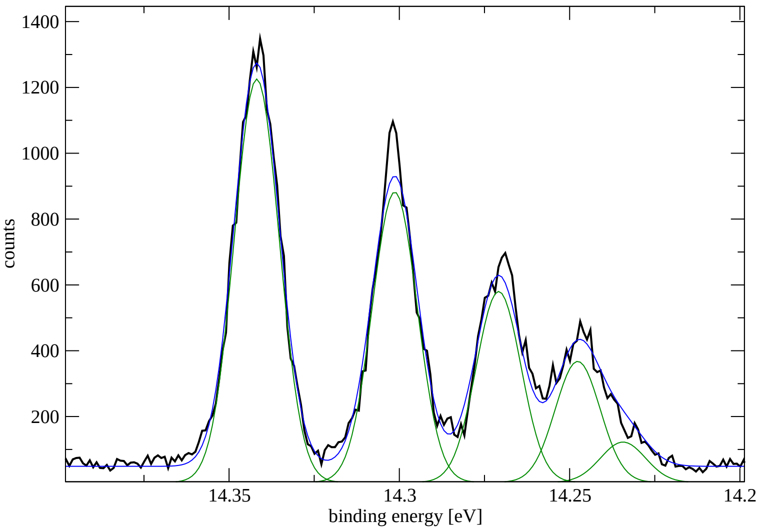

Figure 2: *fine structure resolved photoelectron spectrum for the main SCK line*

The photoline resulting from the main Super-Coster-Kronig (SCK) autoionization decay is depicted in figure 2. The spectrum has a overall experimental resolution of 15.5 meV at a photon energy of about 50.5 eV which is excellent for photoelectron spectra taken from a metal vapour. Its assignment of $3d^4 4s^2\ ^5D$ lets it split up into five fine structure states, which are quite well separated.

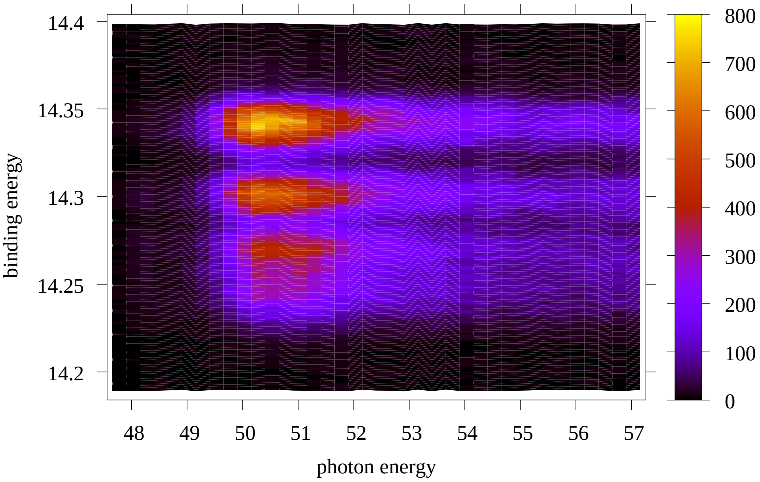

Figure 3: *2D CIS plot of the main photoelectron line*

The CIS spectrum of the main decay line is presented in Figure 3. To record this kind of spectrum the electron analyzer software was extended by a monochromator control module. In one of our previous experiments there was a indication for an energy dependency of the intensity of the five fine structure lines, which however could not be confirmed by closer analysis of this new data.

References

[1] S. Witfield, M. Krause, P. van der Meulen, and C. Caldwell. Phys. Rev. A, **50** 1269 (1994).

Photoionization experiments of atomic Fe and molecular $FeCl_2$ in the region of the L edge of Fe

T. Wolff, T. Richter, P. Zimmermann
Institut für Atomare Physik und Fachdidaktik, Technische Universität Berlin

K. Godehusen
Berliner Elektronenspeicherring-Gesellschaft für Synchrotronstrahlung mbH

M. Martins
Institut für Experimentalphysik, Universität Hamburg

Photoionization of 3d elements and their compounds in the region of the 2p excitation/ionization has become a powerful technique to study their magnetic and electronic properties (e.g. [1]). The analysis of the spectra relies on the correct interpretation of the interactions of the cole hole with the valence electrons. Gas phase experiments on Sc, Mn and Ni have shown [2, 3, 4, 5] that the spectra cannot satisfactory be described by the one-electron picture of the $2p_{3/2} - 2p_{1/2}$ spin-orbit splitting but a large amount of the multiplet structure is caused by multi-electron effects due to the electrostatic interaction of the 2p hole states with the unfilled 3d subshell.
We have studied the 2p photoabsorption and photoemission spectra of atomic Fe and molecular $FeCl_2$. The atomic or molecular beams were produced by thermal evaporation of the metal or compound using temperature of roughly 1750 K for Fe and 700 K for $FeCl_2$. The absorption experiments were performed at the beamline U49/1-SGM-1 in the energy region from 700 to 730 eV. The photoions where detected by a conventional time-of-flight spectrometer which was operated in pulsed voltage mode. The photoelectrons were produced by photons of 800 eV and analyzed by a Scienta SES 2002 spectrometer.

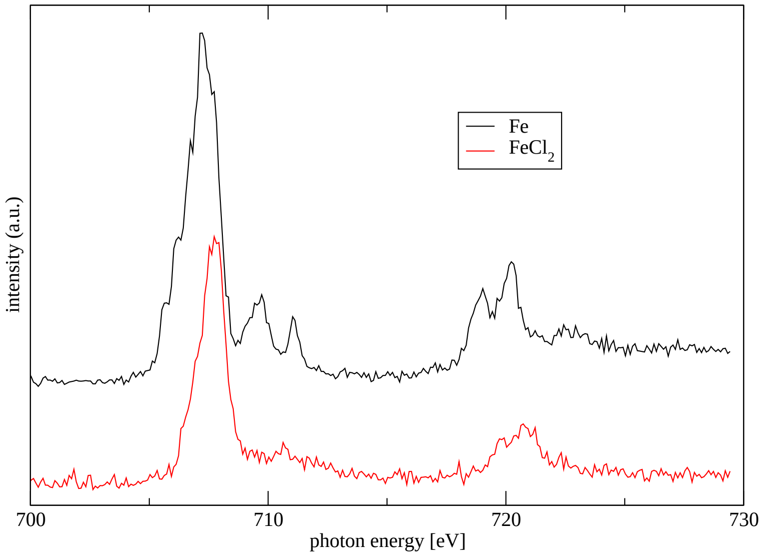

Figure 1: *Total ion yield spectra of Fe and $FeCl_2$*

Figure 1 shows the total ion yield spectra of Fe and $FeCl_2$. One observes that in the atomic case the spectrum is dominated by the spin-orbit splitting of $2p_{1/2} - 2p_{3/2}$ but also contains additional features originating from the Coulomb interaction of the 2p hole with the 3d valence electrons. Comparing this with the molecular spectrum this multi-electron effect nearly disappears, which suggests that the molecular influence effects the localization of the 3d electrons.
In figure 2 the 2p photoelectron spectra of the Fe and $FeCl_2$ are depicted. Also the photoemission spectra are dominated by the spin-orbit splitting. Here the comparison yields more pronounced differences. The atomic spectrum shows the multiplet splitting whereas in the molecular case a

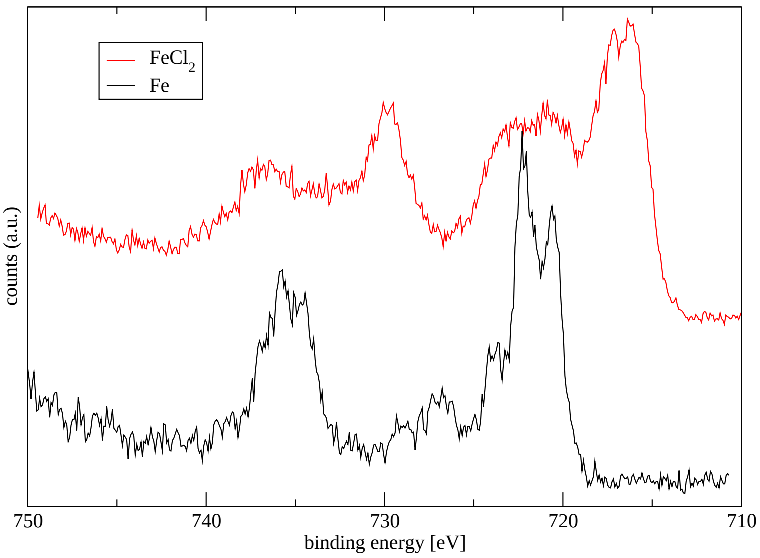

Figure 2: *2p photoelectron spectra of Fe and FeCl$_2$*

double-peak structure appears. According to [6], where solid-state FeCl$_2$ has been studied theoretically and experimentally, this is due to strong satellite transitions induced by the molecular structure.

References

[1] M. C. Richter, P. Bencok, R. Brodier, V. Jlakovac, et al. Phys. Rev. B, **63** 205416 (2001).

[2] B. Obst, T. Richter, . M. Martins, and P. Zimmermann. J. Phys. B, **34** L657 (2001).

[3] T. Richter, B. Obst, . M. Martins, and P. Zimmermann. J. Phys. B, **36** 155 (2003).

[4] P. Wernet, B. Sonntag, M. Martins, P. Glatzel, et al. Phys. Rev. A, **63** 050702 (2001).

[5] K. Godehusen, T. Richter, P. Zimmermann, and M. Martins. Phys. Rev. Lett., **88** 217601 (2002).

[6] K. Okada and A. Kotani. J. Phys. Soc. Japan, **61** 4619 (1992).

High resolution photoelectron spectroscopy of atomic Cs and Cs halide molecules

K. Godehusen[1], T. Richter[2], P. Zimmermann[2], M. Martins[3], R. Weber[4], B. Winter[4]

[1]*BESSY GmbH* [2]*Institut für Atomare Physik, TU Berlin*
[3]*Institut für Experimentalphysik, Universität Hamburg* [4]*Max-Born-Institut, Berlin*

Cs halides are regarded as molecules of pure ionic bonding. Photoelectron spectroscopy is an ideal tool to investigate the details of this bonding as a function of the halide counter part. Furthermore, we were interested to what extent the electron binding energies derived from the gas phase molecules correlate with the binding energies of the respective alkali halide salt dissolved in liquid water (see figure 2). In aqueous solution, at least for sufficiently low salt concentration, the respective anions and cations are individually solvated. Therefore it is expected that in the solution the binding energies of the Cs lines do not vary under the exchange of the halide part.

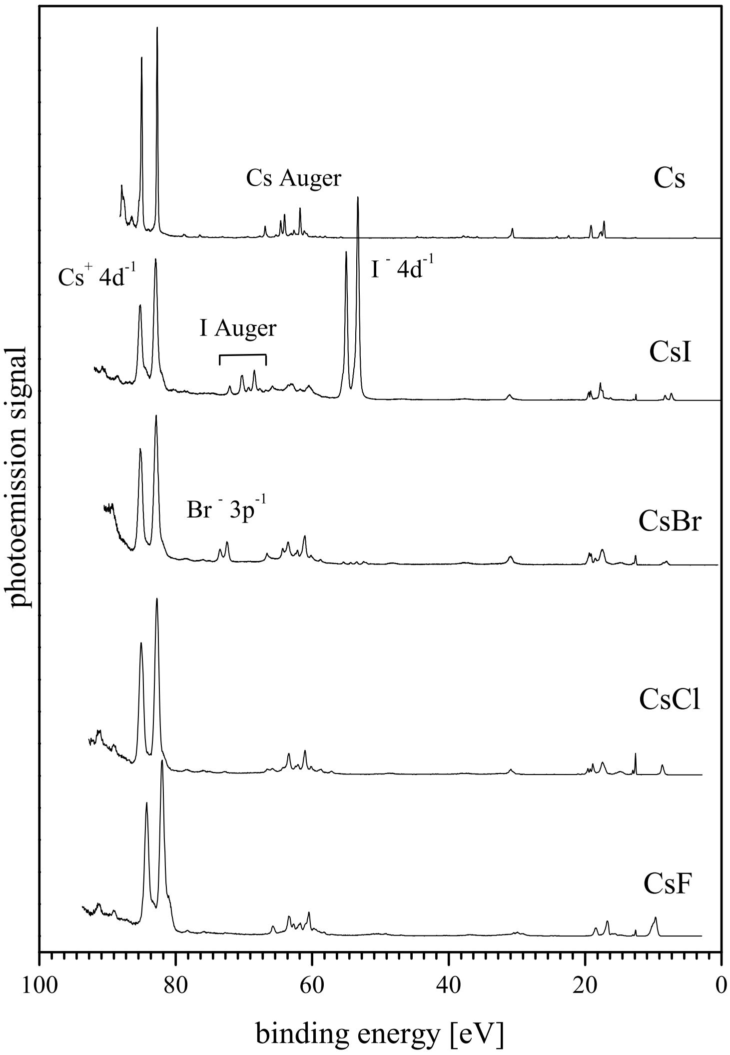

Figure 1: Photoelectron spectra of atomic Cs and the Cs halides at 100 eV photon energy.

The Cs metal and the Cs halide molecules have been evaporated from a resistively heated crucible. The resulting free atomic/molecular beam was crossed with the synchrotron radiation. The photoelectron spectra were recorded by a Scienta SES-2002 hemispherical electron analyzer mounted under the magic angle with respect to the polarization of the synchrotron radiation. In addition, the charge and mass distribution of the photofragments could be analyzed by a time-of-flight ion spectrometer. This TOF enabled us to analyze the molecular fragmentation and the portion of dimers in our molecular beam.

Figure 1 shows the photoelectron spectra of free Cs atoms and the Cs halides taken at a photon energy of 100 eV. The most prominent features are the Cs 4d photoelectron lines, also the I 4d and the Br 3p can be seen easily. The strong enhancement of the I 4d lines (compared to Br 3d) is due to the 4d →4f giant resonance.

The Cs 4d spectra of the Cs halides are, as expected, entirely core like. They consist of two features (see figure 1), $4d_{3/2}$ and $4d_{5/2}$. Additional features at the lower binding energy side of these lines can be attributed to photoemission from dimers. As for the Cs 5p photoemission, the binding energy increases with the decrease of the electronegativity of the halogen anion. Another important similarity to the 5p shell ionization is that the binding energy of the 4d shell from the Cs^+ cation is very close to that of the free atomic Cs (compare figure 1).

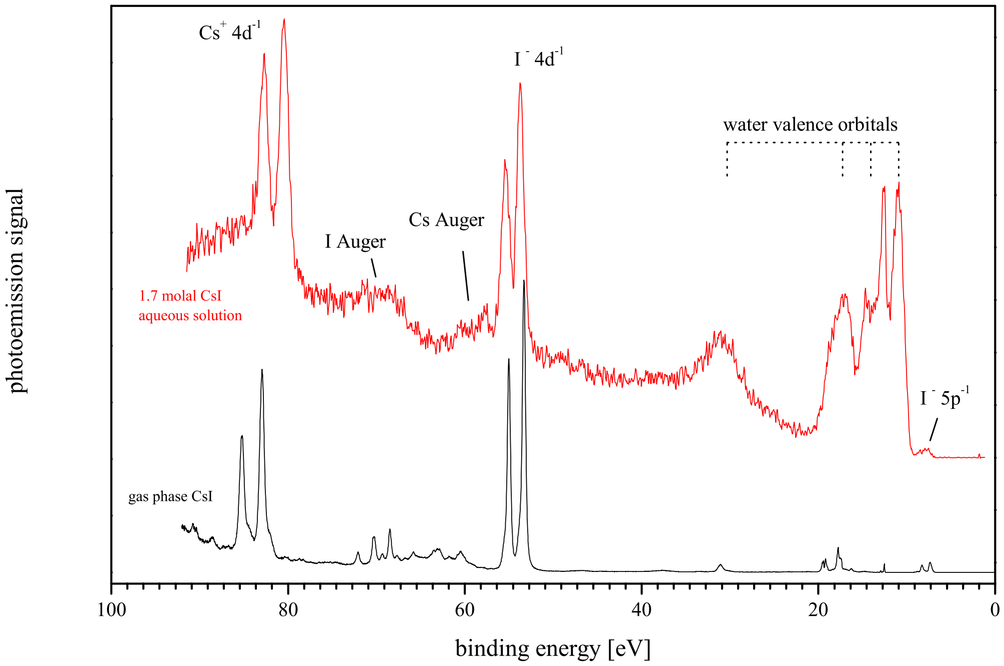

Figure 2: Comparison of the photoelectron spectra of gas phase CsI and CsI dissolved in liquid water.

The comparison of the photoelectron spectra of gas phase CsI and CsI dissolved in liquid water (figure 2) reveals distinct differences in the binding energies for the photolines and the Auger lines. A closer analysis of these shifts can give a deeper insight in how the solvation takes place and also into the mechanisms of ion bonding.

Photoelectron-Auger electron coincidence measurements of the N_2O *K*-shell photoionization

Oliver Kugeler, Simon Marburger and Uwe Hergenhahn

Fritz-Haber-Institut der Max-Planck-Gesellschaft, Faradayweg 4-6, 14195 Berlin and
Max-Planck-Institut für Plasmaphysik, Boltzmannstr. 2, 85748 Garching

Introduction: Molecular Auger spectra are complex due to the large number of doubly charged final states that can be populated. Moreover, in conventional Auger electron spectroscopy contributions of all intermediate states are overlapping in the final spectrum. These intermediate states can be different vibrational states of the core ionized molecule, but in molecules with several chemically inequivalent atoms with the same nuclear charge, contributions of these will overlap as well. A simple example of the latter case is the nitrogen *K*-shell photoionization of dinitrogenoxide, N_2O.

N_2O is a linear molecule. Its composition can be written as $N_T{=}N_C{=}O$, where N_T and N_C are called the terminal and the central nitrogen atom. Their N 1*s* photoionization thresholds are 408.5 and 412.5 eV, resp. In this project, we have used a new apparatus to separately record the *K-VV* Auger spectra of the two chemically shifted nitrogen core hole species. To this end, the Auger electrons were detected in coincidence with the pertaining photoelectrons.

Experimental: Electrons were detected by a combination of a Scienta 200 hemispherical electron spectrometer with two time-of-flight (TOF) detectors. The construction of the hemispherical analyser allows to detect an energy window of 0.1 times the pass energy in parallel. For the purpose of these experiments, it was equipped with a faster position sensitive electron detector based on the delay-line principle. This also allowed time and energy resolved detection of the electrons received in the hemispherical spectrometer on an event-by-event basis.

Due to its superior resolution for high energetic electrons, the Scienta was set to detect a portion of the N_2O N *K-VV* Auger spectrum. With 150 eV pass energy, an interval of the spectrum of 15 eV width could be recorded without scanning the analyser voltages. The pertaining N 1*s* photoelectrons were recorded by the time-of-flight spectrometers.

After initial set-up of the apparatus in single bunch mode, this arrangement was used for coincident spectroscopy of electron pairs in multi bunch as well. Arrival times of electrons in all analysers were recorded relative to the BESSY bunch clock, and were supplemented by a unique bunch number received from a counter which is incremented by the bunch clock. The event file resulting from these data can thus be searched for electron-electron coincidences in retrospect.

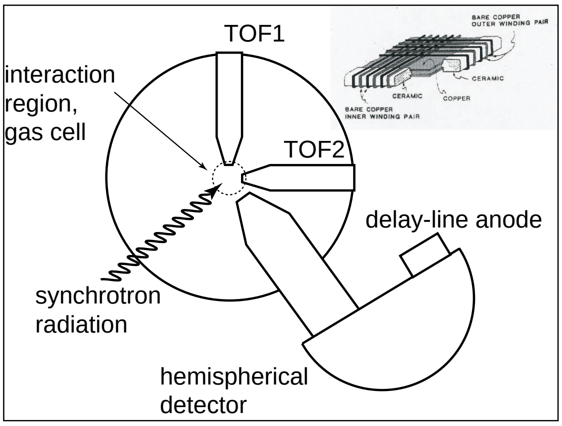

The discrimination of random coincidences from true events by this method is well possible even in multi bunch, since the true coincidences occur at a fixed time difference between the two electrons detected in the Scienta an in the TOF. The coincidence rate amounted to 1 Hz.

A sketch of the apparatus is shown beneath.

Results:

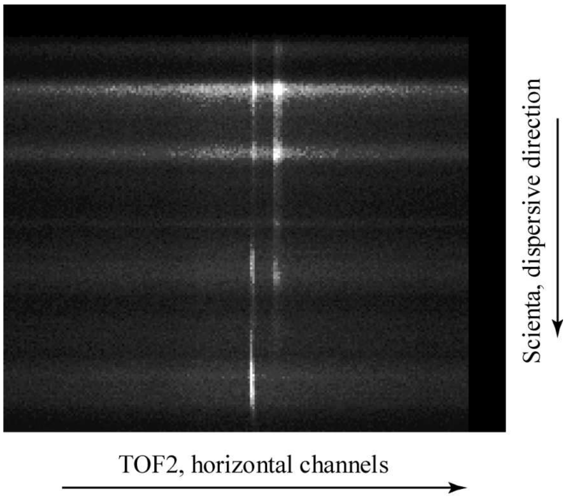

Fig. 1: Intensity plot of coincident events. The horizontal axis is proportional to the flight time of the photoelectron in the TOF spectrometer referred to the arrival time of the Auger electron, the vertical axis displays the kinetic energy of the Auger electron. The two light, vertical lines pertain to true coincidences, which occur at a fixed time difference of the two electrons, while the background of random coincidences may occur at any time difference. The energy spectrum of the true coincidences displayed in Fig. 3 is obtained from this plot by adding the channels of equal energy for each of the vertical lines, and subtracting a background of random coincidences.

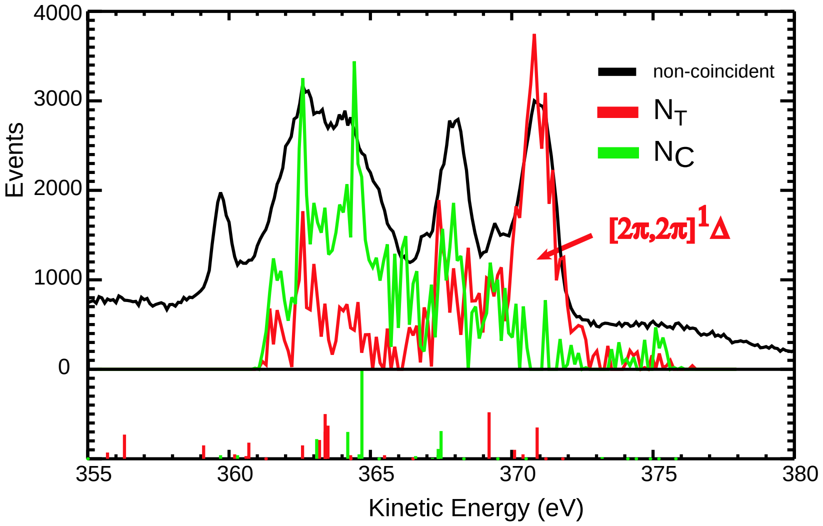

Fig. 2: N *K*-*VV* Auger spectrum of N_2O, separated into contributions from the terminal (N_T) and the central (N_C) nitrogen atom. The stick diagram below displays results of an *ab initio* calculation.[1]

For this project, in 2002 two weeks of single bunch and two weeks of multi bunch beamtime were allotted. We acknowledge funding by the DFG under contract no. He 3060/3-3 and by the EURATOM program.

References

[1] F. P. Larkins, J. Chem. Phys. **86**, 3239 (1987).

Double photoionisation of helium and argon double Auger decay

J. Viefhaus, S. Cvejanović, D. Rolles, T. Lischke, G. Prümper, and U. Becker

Fritz-Haber-Institut der Max-Planck-Gesellschaft,
Faradayweg 4-6, 14195 Berlin, Germany

Our studies in double electron emission concentrated on the double Auger decay as well as the higher energy regime of the helium double photoionisation.

Double Auger emission is an important manifestation of strong electron correlation in processes governed by the Coulomb interaction. Despite the difference in the interaction Hamiltonian they have much in common with double photoionisation phenomena. The major difference between these two types of double electron escape processes is the fact that the symmetry properties of the double Auger process are not influenced by a photon hence other symmetries of the two-electron continuum states can be investigated. Although double Auger decay is discussed in the literature for a long time now [1] it was not until last year when direct (i.e. coincident) energy and angle resolved measurements have become feasible [2]. On the experimental side the coincident investigation of the double Auger process involves the simultaneous detection of two electrons which can share the available kinetic energy in an - in principle - arbitrary way. As the energy in question is quite large the double Auger intensity is spread out over a wide range of kinetic energies in the electron spectrum. Coincident time-of-flight electron spectroscopy is therefore a very suitable technique for double Auger analysis because electrons of all kinetic energies can be detected simultaneously. The apparatus used for these studies consists of a multi-detectors coincident set-up based on 6 time-of-flight (TOF) analysers. Using the single bunch mode of BESSY at beamline UE56/2-PGM1 the relatively long time window of 800 ns allowed us to cover the kinetic energy range from less than 0.5 to more than 200 eV which is expected for electrons after ionization of the Ar 2p shell. A clear signature of double Auger processes are visible as diagonal lines in the twodimensional coincidence spectrum displayed in fig. 1.

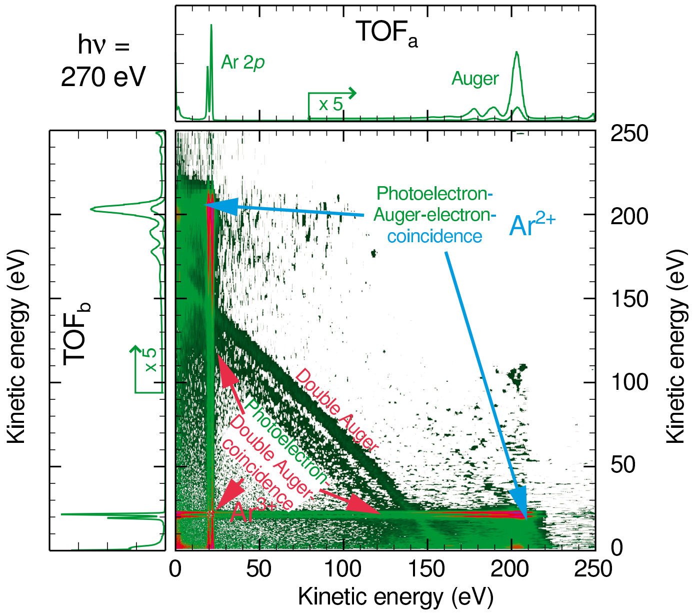

Figure 1: Two-dimensional electron-electron coincidence spectrum of Ar taken at $h\nu$ = 270 eV along with the two corresponding non-coincident spectra.

The circular polarization mode of the UE56 undulators has enabled us to use our multi-detector arrangement in a most effective way which allowed a measurement of the coincident angular distribution of the double Auger electron emission for the first time (fig. 2).

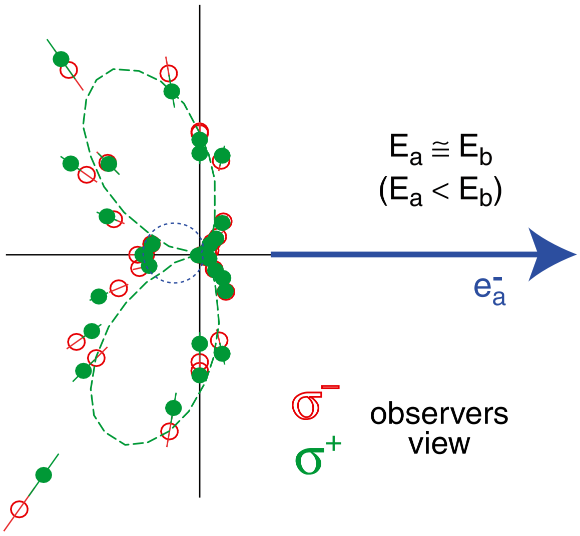

Figure 2: Coincident angular distribution of double Auger electrons taken at $h\nu$ = 270 eV. The energy sharing is close to equal energy sharing but the electron labelled 'a' is always the slow electron and emitted as indicated by the arrow.

The preliminary analysis shows that indeed different symmetries of the two-electron wavefunction are produced via the double Auger process. In particular the filling of the node in back-to-back emission of the two Auger electron is a clear signature of symmetries which are different to those after helium double photoionisation.

Furthermore we extend the studies of electron triple differential cross sections (TDCS) for Double photoionisation (DPI) of He using circularly polarised light to higher energies. The data measured at the beamline UE56/2-PGM2 complement our previous studies at lower excess energies. The data will be analysed using the global parametrisation of Cvejanovic and Reddish [3], to derive all amplitude parameters, including their relative phase shift, over a large range of excess energies.

In summary we have shown that rather different types of double electron emission processes can now be characterized experimentally on a rather high level of differentiation. This opens new perspectives for the investigations of strongly correlated electrons in particular with respect to their angular correlations. Further measurements also on more complex systems will allow us to obtain deeper insight into the generality of the three-body Coulomb problem properties [4].

This project has been supported by the Deutsche Forschungsgemeinschaft (Be 860/18-2) and the Bundesminister für Bildung und Forschung (BMBF-05KS1EB12).

References

[1] T. A. Carlson and M. O. Krause, Phys. Rev. Lett. 17, 1079 (1966)

[2] J. Viefhaus et al., Hasylab Annual Report 2001, 227 (2002)

[3] S. Cvejanovic and T. Reddish, J. Phys. B 33, 4691 (2000)

[4] I. Bray, Phys. Rev. Lett. 89, 273201 (2002)

Magnetic Circular Dichroism in the Ion Yield of Polarized Chromium Atoms at the 2p-edge

G. Prümper[1], S. Kröger[2], R. Müller[2], M. Martins[3], J. Viefhaus[1], P. Zimmermann[2], U. Becker[1]
[1] Fritz-Haber-Institut der Max-Planck-Gesellschaft,
Faradayweg 4-6, D-14195 Berlin, Germany
[2] Institut für Atomare Physik und Fachdidaktik, Technische Universität Berlin,
Hardenbergstr. 36 10623 Berlin, Germany
[3] Universität Hamburg, Institut für Experimentalphysik
Luruper Chaussee 149, D-22761 Hamburg, Germany

Magnetic Circular Dichroism (MCD) describes the different response of a magnetized sample to left- and right-handed circularly polarized light. For a direct comparison with solid state experiments, i.e. with absorption measurements of thin magnetic films an absorption or total ion yield measurement is needed. We measured the MCD for polarized chromium in the ground state ($1s^2\ 2s^2\ 2p^6\ 3s^2\ 3p^6\ 3d^5\ 4s^1\ \ {}^7S_3$) at the 2p-edge.

Independent of the complicated dynamics near the 2p-edge sum rules for the MCD asymmetry have been used to determine the expectation value of the orbital, spin, and magnetic dipole momentum of initial state for different transition metal samples [1]. These sum rules can be tested for the well known atomic ground state. The orbital momentum is proportional to A_{total}:

$$A_{total} = \frac{\sum_{560eV-590eV} (I_{\uparrow\uparrow} - I_{\downarrow\uparrow})}{\sum_{560eV-590eV} (I_{\uparrow\uparrow} + I_{\downarrow\uparrow})}$$

$I_{\uparrow\uparrow}$ and $I_{\downarrow\uparrow}$ are the ion count rates measured for the two different target polarizations.

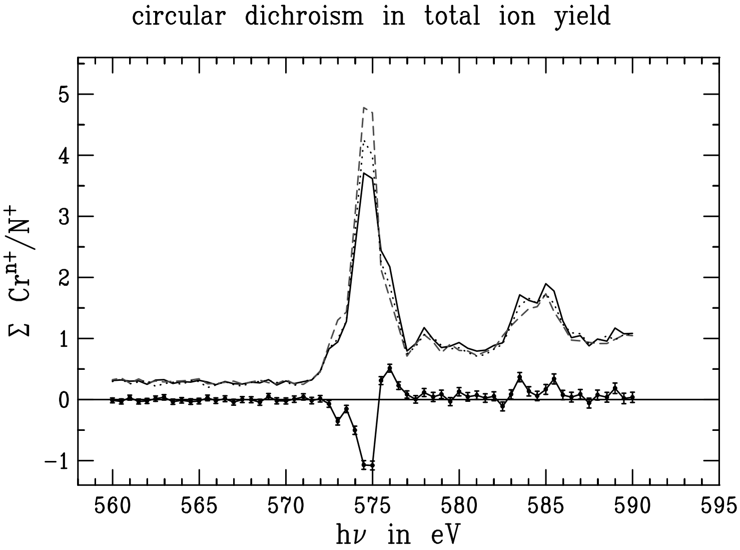

Figure 1: MCD in the total ion yield of chromium atoms. The dotted line belongs to the count rate for unpolarized atoms, the solid and the broken line belong to the ion count rate with opposite target polarization. The lower curve shows the difference of the two count rates i.e. the MCD.

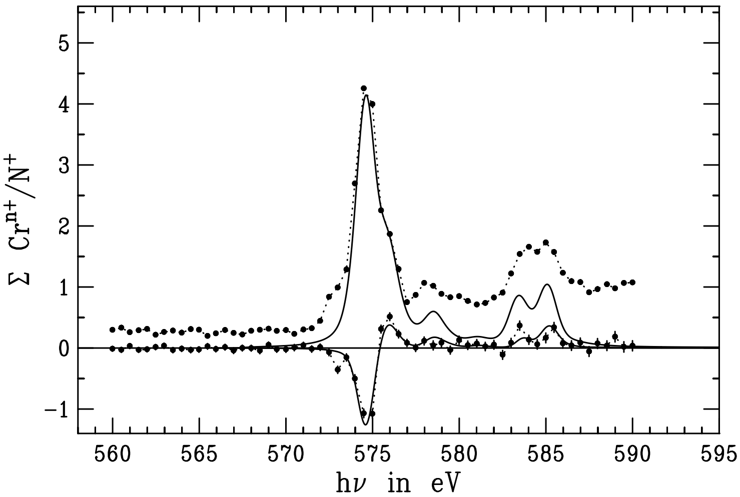

Figure 2: The solid curve represents the HF calculation results, while the dotted curves show the experimental results. (We convoluted the theoretical results with a gaussian of 0.6eV and shifted it 1.9 eV in photon energy). The main features of the data are described very well. The change in the MCD within the first peak is due to the coupling of the $2p_{3/2}$-hole with the other open shells. The states under the second peak have $2p_{1/2}$ and $2p_{3/2}$ contributions. Thus a separation of the 2p-edge in an L_3- and an L_2-interval is not possible for atomic chromium.

As the chromium ground state is an s-state, A_{total} has to be zero which is in reasonable agreement with our data A=-0.0074 ± 0.0048. For the calculation of the spin momentum the 2p-edge has to be split into L_3 and L_2 intervals. We performed a Hartree Fock calculation of the excitations at the 2p-edge, including the coupling of the 2p-hole with the 3d and 4s shell.

The difference curve in figure 1 changes sign at 575 eV. This can only be explained by a model that takes into account the coupling of the 2p-hole with the 3d and 4s shell. The excitations that contribute to the peak around 275 eV contain mostly contributions from the $p_{3/2}$-hole. The situation is more difficult for the peaks around 585 eV. This region contains significant contribution from $2p_{1/2}$- and $2p_{3/2}$-states. Therefore the ground state spin momentum cannot be determined from the dichroism at the 2p-edge for chromium. The contribution of $2p_{1/2}$- and $2p_{3/2}$-states can never be separated by an appropriate choice of the integration region. Despite some differences of our MCD results with solid state MCD curves for chromium layers [2] and compounds [3], we assume that a mixing of the $2p_{1/2}$- and $2p_{3/2}$-excitations is also possible in the solid state. Our results show that a double peak structure of the absorbtion signal is no clear indication for a separation of $2p_{1/2}$- and $2p_{3/2}$-excitations.

The experimental technique:
The beam of polarized chromium atoms crosses the beam of circularly polarized VUV synchrotron radiation from a Sasaki type undulator at the UE56-2 PGM1 beamline at BESSY II Synchrotron Light source. The ions are detected in a pulsed time-of-flight ion spectrometer. The time-of-flight spectrum contains Cr^+, Cr^{2+}, Cr^{3+}, Cr^{4+} and Cr^{5+}-ions and contributions from unpolarized gas molecules N^+, O^+, OH^+. N_2 was introduced into the vacuum chamber during the measurement for calibrating purpose. During the measurement the laser polarization, i.e. the direction of the target polarization, was switched with a frequency of 0.1 Hz. Depending on the state of the pumping laser beam (positive helicity, negative helicity or blocked), the time-of-flight signal of the ions is sent to one out of three input channels of a TDC-module. In this way the three measurements of the ion count rate were performed at almost the same time and the measured asymmetry is not influenced by the varying intensities of the synchrotron light source and the atomic beam.
The laser system consists of a 5 W UV Argon-ion pump laser and a tunable single-mode cw Stilbene 3 ring laser with internal frequency locking. The linearly polarized laser radiation is send through a fresnel rhombus. When the rhombus is rotated, the polarization plane of the light is tilted by 90 degrees. A $\lambda/4$-plate behind the rhombus transforms the linear polarization to circular polarization of positive or negative helicity. Chromium is evaporated in a 130 watt electron impact oven from an molybdenum crucible at 1800 K. The atoms become polarized by laser pumping when they pass the circularly polarized laser beam (40 mW, 1.5 mm diameter, 50 MHz bandwidth). A magnetic field of approximately 500 mT parallel to the propagation direction of the laser was applied to avoid any uncontrolled loss of target polarization by rotation of the magnetic moment around the magnetic field. The laser was 2 mm closer to the oven than the ionizing synchrotron radiation, to make sure that no excited atoms contribute to the target. The pumping process reached saturation, and the target polarization was higher than 80 %.

This work was supported by Deutsche Forschungsgemeinschafft Zi 183/12-1 and by the European Union for beam time at BESSY II.

References

[1] Chen C T, Idzerda Y U, Lin H J, Smith N V, Meigs G, Chaban E, Ho G H, Pellegrin E and Sette F, Experimental Confirmation of the X-Ray Magnetic Circular Dichroism Sum Rules for Iron and Cobalt, Phys. Rev. Lett. **75**, 152 (1995).

[2] Böske T, Clemens W, Schmitz D, Kojnok J, Schäfer M, Cros V, Guo G Y, Eberhardt W
The coupling of Cr to Fe studied by circular magnetic X-ray dichroism,
Appl. Phys. A, **61**, 119-122 (1995)

[3] Goering E, Justen M, Geissler J, Rüdiger U, Rabe M, Güntherodt G and Schütz G,
Magnetic anisotropy of textured CrO2 thin films investigated by X-ray magnetic circular dichroism,
Appl. Phys. A, **A74**, no.6, 747-53 (2002)

Partial cross sections of doubly excited helium up to the N=7 ionization threshold

Y. H. Jiang[1,3], R. Püttner[1], R. Hentges[2], J. Viefhaus[2], U. Becker[2], J. M. Rost[3]
and G. Kaindl[1]

[1] Institut für Experimentalphysik, Freie Universität Berlin, Arnimalle 14,
D-14195 Berlin-Dahlem
[2] Fritz-Haber Institut Berlin, Faradayweg 4-6, D-14195 Berlin-Dahlem
[3] Max Planck Institut für the Physik Komplexer Systeme, Nöthnitzer Str. 38,
D-0187 Dresden

Double excitations in helium offer an ideal possibility to investigate electron-electron correlations since their discovery by Madden and Codling in the early 1960's [1]. However, most of the high-resolution studies on doubly excited helium have focused on total absorption measurements [2]. Partial photoionization cross sections σ_n (n describes the principal quantum number of the electron in the He$^+$ ion subsequent to autoionization.) allow deeper inside into the decay dynamics of doubly excited resonances in helium. Third-generation synchrotron radiation in combination with Time-of-Flight (TOF) electron spectrometers can resolve the different decay channels and allow electron emission measurements with the resolving power and intensity necessary for these studies. Recently, Menzel et al. [3] completed measurements of the σ_n below the N=5 ionization threshold using spherical sector plate electrostatic analysers to detect the photoelectrons.

The resonant photoionization process can be described by

$$He(1s^2) + h\nu \rightarrow He^* N(K,T)^A_{n'} \rightarrow He^+(n) + e^- . \qquad (1)$$

Here $N(n')$ is the principal quantum numbers of the inner (outer) electron in the doubly excited state. K and T are the angular correlation quantum numbers. A is the radial correlation quantum numbers. The resonance series can also be described by $N, K_{n'}$ or $[N_1 N_2 m]^A_{n'}$ (parabolic quantum numbers); the different quantum numbers are related by $T = m$, $K = N_1 - N_2$ and $N = N_1 + N_2 + m + 1$ [4].

The measurements were completed at the undulator beamline U125/2-SGM (BUS-beamline) using a resolution of $\Delta E \approx$ 5-7 meV. A TOF spectrometer was used at the magic angle, i.e. $\vartheta = 55^0$ relative to the polarization direction of the light.

The helium atom can be described in a molecular picture analogous to H_2^+ by exchanging the electrons by nuclei and vice versa. From this picture the following propensity rules for the autoionzation process can be derived [4]:

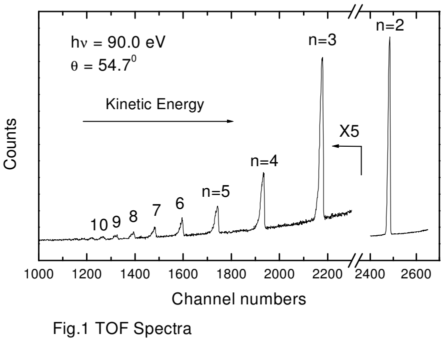

Fig.1 TOF Spectra

(A) **reduction of N_2 (radial transition)**
(B) **change of m (rotational coupling)**
(C) **reduction of N_1 (no explicit mechanism).**

The transition probability decrease strongly from A to C. The principal series in doubly excited helium, N,(N-2)$_{n'}$, decay via propensity rule A. From the molecular picture it is expected that autoionization processes with the same change in N_2, namely $\Delta N = -\Delta N_2 = N - n$, show similar lineshapes. For example, it is expected that the cross section for the decay of the principal series 6,4$_{n'}$ into the n=3 continuum (He$^+$(n=3)) shows a lineshape similar to that of the decay of the series 7,5$_{n'}$ into the n=4 continuum. In Fig. 1 we present a TOF spectrum of photonelectrons measured at $h\nu = 90.0$ eV, i.e. above the double ionization threshold with a recording time of 2000 s. In the spectrum the n=11 satellite for the photoionization process of helium can clearly be observed demonstrating the excellent experimental conditions.

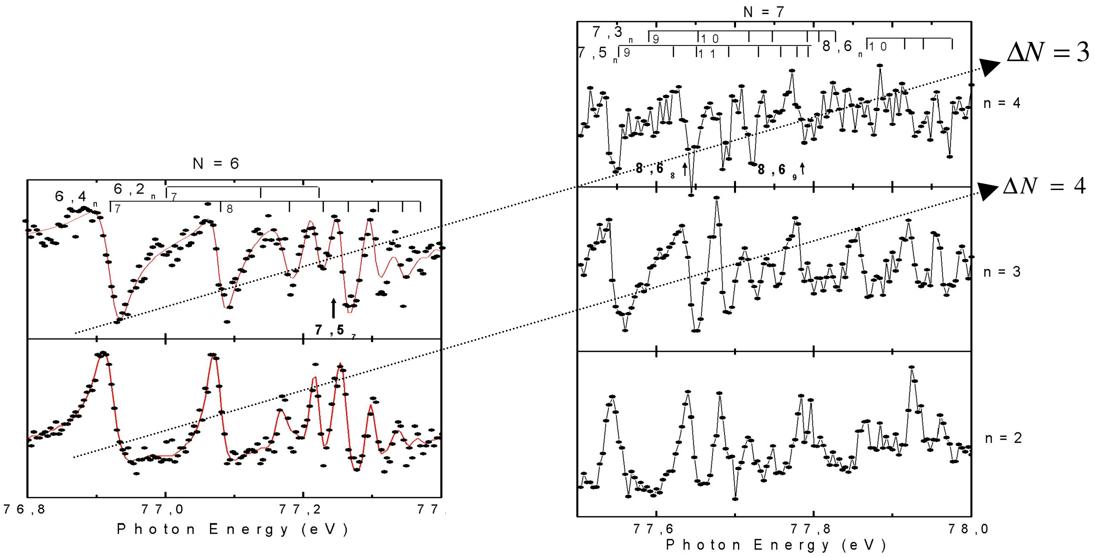

Fig. 2 Partial cross sections in the N=6 and N=7 thresholds as a function of photon energy. The dotted lines indicate spectra with the same change in ΔN

Similiar TOF spectra were measured between 76.8 and 78.0 eV using a step width of 5 meV. The normalized peak intensity of satellites are plotted as a function of photon energy and shown in Fig. 2. This figure shows first results for the partial photoionization cross sections in the region below the ionisation thresholds N = 6 and 7. In partial cross sections with the same ΔN (with ΔN=3 or 4) spectral similarities are seen, partially broken down in the vicinity of the perturbers, i.e. resonances which belong to higher ionisation threshold.
Present experiments in the cross section of ΔN=3 show reasonable agreement with advanced calculations [5], which are not shown here. No other data in literature are available. The solid lines in the spectra below the N=6 ionization threshold display the first fit results to the data.

References

[1] : R. P. Madden et al., Phy. Rev. Lett. 10, 516 (1963).
[2] : M. Domke et al., Phy. Rev. Lett. 69, 1171 (1992).
[3] : A. Menzel et al., Phy. Rev. Lett. 75, 1479 (1995); Phys. Rev. A 54, 2080(1996).
[4] : J. M. Rost et al., J. Phys. B 30, 4663 (1997).
[5] : H. W. van der Hart, and Ch. H. Creene, Phys. Rev. A 66, 022710 (2002).

High-Resolution ZEKE Photoelectron Spectroscopy of Free Van der Waals Clusters

R. Flesch [1], I. L. Bradeanu [1], A. A. Pavlychev [2], and E. Rühl [1,3]

[1] Fachbereich Physik, Universität Osnabrück, Barbarastr. 7, 49069 Osnabrück
[2] St. Petersburg State University, St. Petersburg 198904, Russian Federation
[3] Institut für Physikalische Chemie, Universität Würzburg, Am Hubland, 97074 Würzburg

Photoionization of free Van der Waals clusters is reported using zero kinetic energy (ZEKE) photoelectron spectroscopy. This experimental approach is suitable to detect cluster size dependent changes in electronic structure. Earlier work in this field has been reported, where both excitation with variable [1] and constant [2] photon energy was applied. Excitation far above the core ionization energy is often called '*ESCA spectroscopy*' [3] or '*X-ray photoelectron spectroscopy*' (XPS), where the kinetic energy of the photoelectrons is measured at constant photon energy. From earlier work on variable size clusters it became evident, that core ionization energies of surface and bulk sites in variable size argon clusters can be clearly distinguished in the Ar 2p-regime [2]. This is mostly due to the more substantial redshift, which is of the order of 0.26 eV, if the bulk core ionization energies are compared to the ionization energies of the surface sites, which is a result of polarization screening [4]. However, this approach does not give detailed information on the dynamics of the photoionization process including the energy exchange of the photoelectron with the Auger electron (post-collision interaction [5]), since the excitation energy is usually considerably higher than the core ionization threshold, which corresponds to a primary excitation deep in the core ionization continuum.

On the other hand, ZEKE photoelectron spectroscopy makes use of an excitation near the core ionization threshold. Earlier low resolution ZEKE work had the drawback that the energy resolution was not sufficient to derive any size effects in PCI-line shapes of surface and bulk sites [1]. It was only possible to determine a redshift of ~1 eV of the Ar 2p-ionization threshold of the bulk solid relative to the isolated atom [1]. This result is also in agreement with later non-resonant XPS work [2, 4]. Intense, narrow bandwidth, tunable soft X-rays are available at the UE52-SGM beam line. This allows us to study for the first time post-collision interaction (PCI) in variable size clusters.

The experimental setup is similar to that reported earlier [1], where variable size clusters are produced by supersaturation in a jet expansion. The expansion conditions allow us to estimate the average cluster site <N>. Zero kinetic energy photoelectrons are selected in the single bunch operation of BESSY by angular discrimination against energetic electrons and their time-of-flight, while scanning the photon energy in the regime of the core-ionization energies of the isolated and clustered species.

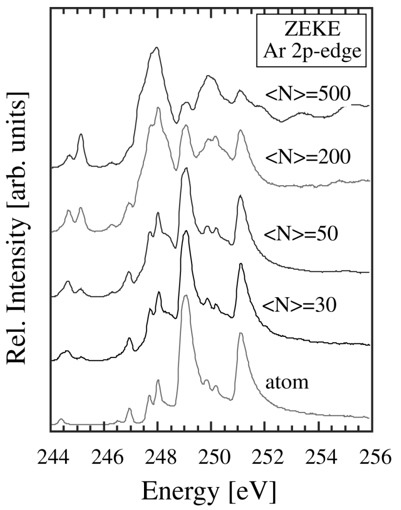

Fig. 1: Series of ZEKE photoelectron spectra of atomic argon (bottom) and argon clusters in the Ar 2p excitation regime.

Fig. 1 shows the evolution of ZEKE spectra of argon clusters in the Ar 2p regime. The ZEKE spectrum of the atom clearly shows the direct ionization energies (Ar $2p_{3/2}$ and Ar $2p_{1/2}$). These correspond to the dominant asymmetric peaks near 249 eV and 251 eV, respectively. Other weak features are due to symmetric lines that come from resonant excitation of Rydberg states. The lowest energy feature is the Ar $2p_{3/2}\rightarrow 4s$-transition at 244.39 eV.

As soon as there are clusters in the jet one observes the following changes in the ZEKE spectra: (i) the atomic features become weaker in intensity since the mixing ratio between clusters and atoms is increased with <N>; (ii) new features occur, which come primarily from direct Ar 2p photoionization of surface and bulk sites in clusters; (iii) the atomic Rydberg states are converted into the corresponding surface and bulk excitons (cf. [1, 2]). Fig. 1 clearly shows this evolution in the case of the lowest energy feature between 244.39 and 245.3 eV, so that at <N>=500 primarily bulk excitons are found. This is an independent indication for the occurrence of large clusters in the jet; (iv) oscillations are found in the Ar 2p continuum as a result of single and multiple scattering (cf. [6]).

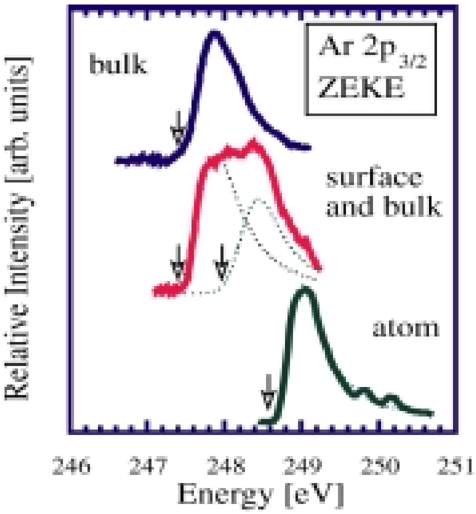

Fig. 2: Comparison of the direct Ar $2p_{3/2}$ photoionization of atomic, surface, and bulk sites. The vertical arrows correspond to the ionization energies. The dashed curves are obtained from a fit using PCI-profiles. See text for further details.

We focus our interest on the evolution of the direct photoionization process, which is not clearly visible in the raw cluster spectra shown in Fig. 1. Therefore, we have derived difference spectra, where the atomic contribution has been subtracted. The results are shown in Fig. 2, where only the Ar $2p_{3/2}$ regime is plotted. The atomic profile (bottom spectrum in Fig. 2) is clearly asymmetric in shape, where weak structures, occurring near 248.8 eV and 250.2 eV, are due to contributions from Rydberg-states that have not been subtracted. The direct ionization gives an entirely smooth signal in this regime. The vertical arrow corresponds to the Ar $2p_{3/2}$ ionization energy (E=248.66 eV), which is in full agreement with earlier ESCA work [7]. The line shape consists of two contributions: the PCI life time and a Gaussian width. Both are comparable in magnitude to the parameters that can be extracted from the Voigt profiles which are used to de-convolute the Rydberg states below the Ar 2p threshold.

The PCI profile of the bulk sites is obtained from the spectrum corresponding to <N>=500, where also contributions of high-lying exciton states, that occur with a high density of states right below the ionization threshold, are subtracted. This yields a single, asymmetric line profile, which is broadened compared to the atomic line. It turns out that this broadening is exclusively due to an increased Gaussian width, whereas the core-hole life time remains constant. This indicates that the PCI-dynamics is mostly dominated by the atomic core hole. In addition, inhomogeneous broadening effects, such as phonon broadening, give rise to the Gaussian contribution in the bulk. The core ionization energy is 247.5 eV. This is in agreement with earlier results [1, 2] (see vertical arrow in Fig. 2 (top spectrum)).

The de-convolution of a ZEKE-spectrum that contains both, surface and bulk sites, corresponding to small clusters, is shown in Fig. 2 (middle spectrum). The line shape of bulk sites is used as discussed above. The fit of the remaining spectrum requires only one other PCI profile using the same parameters as for the bulk. This is assigned to the surface Ar 2p ionization, where the ionization energy is 247.85 eV. This value is similar to previous ESCA work [2, 4], where a cluster size dependence of the surface Ar $2p_{3/2}$ binding energy was found. The parameters of the PCI profile indicate that there are no differences in core ionization dynamics and Gaussian broadening between surface and bulk sites.

We conclude that ZEKE photoelectron spectroscopy of variable size free clusters gives detailed insight into the dynamics of core photoionization processes. In the case of argon clusters one finds exclusively increased contributions from Gaussian broadening, if clusters are compared to the neat atom. We have also investigated molecular Van der Waals clusters, such as nitrogen clusters in the N 1s regime, where also broadening due to a shortened PCI life time is found. These results will be discussed elsewhere in greater detail [8].

References

1 A. Knop, H.-W. Jochims, A. L. D. Kilcoyne, A. P. Hitchcock, and E. Rühl, Chem. Phys. Lett. **223**, 553 (1994).
2 O. Björneholm, F. Federmann, and T. Möller, Phys. Rev. Lett. **74** (1995) 3017.
3 K. Siegbahn et al., ESCA Applied to Free Molecules, North Holland, Amsterdam, 1971.
4 O. Björneholm, Surf. Rev. Lett. **9**, 3 (2002).
5 A. Niehaus, J. Phys. B **10**, 1845 (1977).
6 E. Rühl, C. Heinzel, A. P. Hitchcock, and H. Baumgärtel, J. Chem. Phys. **98**, 2653 (1993).
7 L. Petersson, J. Nordgren, L. Selander, C. Nordling, and K. Siegbahn, J. El. Spectrosc. Relat. Phenom. **27**, 29 (1982).
8 I. L. Bradeanu, R. Flesch, A. A. Pavlychev, and E. Rühl, to be published (2003).

Financial support by the Deutsche Forschungsgemeinschaft and the Fonds der Chemischen Industrie is gratefully acknowledged.

Charging of single stored SiO_2 nanoparticles in the soft x-ray regime

M. Grimm[a], B. Langer[b], T. Lischke[c], E. Rühl[d,e], W. Widdra[b], D. Gerlich[a], U. Becker[c], S. Schlemmer[a]

[a]Institut für Physik, Technische Universität Chemnitz, 09107 Chemnitz

[b]Max-Born-Institut Berlin, Max-Born-Straße 2A, 12489 Berlin

[c]Fritz-Haber-Institut der MPG Berlin, Faradayweg 4-6, 14195 Berlin

[d]Fachbereich Physik, Universität Osnabrück, Barbarastr. 7, 49069 Osnabrück

[e]Institut für Physikalische Chemie, Universität Würzburg, Am Hubland, 97074 Würzburg

High-resolution Q/M measurements have been used to study the charging of single, isolated particles. A single 500 nm in diameter SiO_2 particle is stored in the centre of a three dimensional electrodynamical quadrupole trap over very long times, free from any contact to a substrate. The interaction with a laser beam as well as with synchrotron radiation can easily be studied due to the particle's good localisation. Scattered light detection from the laser (< 50 mW, □ = 532 nm) is used to determine the Q/M-ratio of the particle very precisely. This measurement is the basis of a non-destructive, high-resolution nanoparticle mass spectrometry (HRNPMS) which has been described in detail elsewhere [1,2].

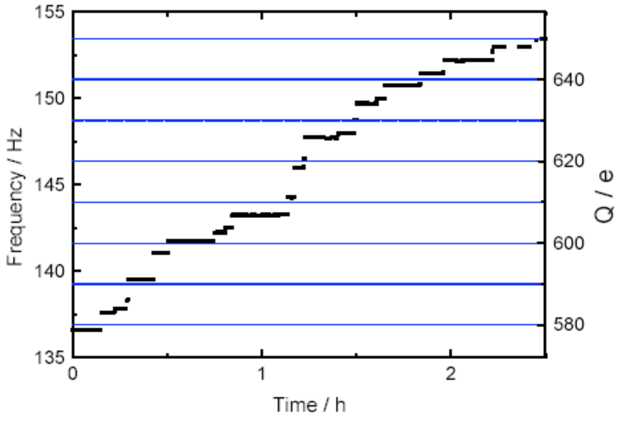

Fig. 1: Stepwise photo-induced charging of a trapped particle at $E_{□}$ = 500 eV.

Synchrotron radiation from BESSY has been used to charge the particle, where the photon energy is varied between 100 eV and 600 eV. At low fluences and low charge states (Q < 1000 e) charging of the particle has been detected as individual, temporally resolved events, occurring in steps of single or integer multiple of the elementary charge due secondary electron emission initiated by the photo- or Auger-electron, see Fig. 1. In the course of this process the particle charges positively. The absolute charge state of the particle, Q, has been determined from such measurements. In addition, probability distributions for the emission of secondary electrons have been obtained. The measured yields agree very well with values from standard tables [3] for a kinetic energy of the primary electron close to the respective photon energy. Moreover the distributions show an increased fraction of events where only the primary electron escapes from the particle. Investigations along these lines could be used to determine yields of secondary electron emission as a function of the charge state of the nanoparticle and the particle size.

From the temporal evolution of the charge state, Q(t), the charging current I = dQ/dt has been derived. I decreases as Q rises since electrons can only escape the electric field of the charged particle if their initial kinetic energy is larger than the potential energy at the place of their creation. The escape depth of the secondary electrons is of the order of several nm and therefore much smaller than the radius, a, of the particle. For this reason it is safe to assume that most of the charges contributing to Q are located near the surface such that the surface potential, U, can be correlated to the charge state, $E_{pot} = e\,U = e\,\frac{Q}{4\pi\varepsilon_0 a}$. Using this relation I(Q) can be transformed to $I(E_{pot})$, the integral current of all electrons faster than given by the limitation $E_{kin} > E_{pot}$. As a consequence the derivative $dI(E_{pot})/dE_{pot}$ is a measure of the probability of creating electron with a kinetic energy $E_{kin} = E_{pot}$. Evaluating I(Q) by this means leads to energy distributions which can be approximated by a Boltzmann-distribution, which is characterised by an electron temperature near 3 eV. This value is in good agreement with energy distributions obtained from bulk measurements using retarding field methods.

The charging current, I(Q), is a measure of the absorption cross section at a particular photon energy, $E_\gamma = h\nu$. For low charging states I(Q) can be considered as the total electron yield. This has been used in different measurements to obtain the charging current close to the O(1s) absorption edge. Fig. 2 shows such a measurement where the charge state Q(t) has been determined during a scan of the photon energy, $E_\gamma(t)$, at a constant scanning speed, dE_γ/dt. In the upper panel Q is plotted as a function of the photon energy. Below ~ 535 eV Q rises slowly while above this value the current increases significantly. In the lower panel $I(E_\gamma)$ is plotted. This spectrum shows almost no absorption at energies far from the absorption edge. Already below this edge the absorption increases significantly and some structured features can be identified between 535 eV and 542 eV. The main absorption is attributed to unoccupied states by photoabsorption. In conclusion, these are the first experiments on near-edge absorption spectra of a single nanoparticle.

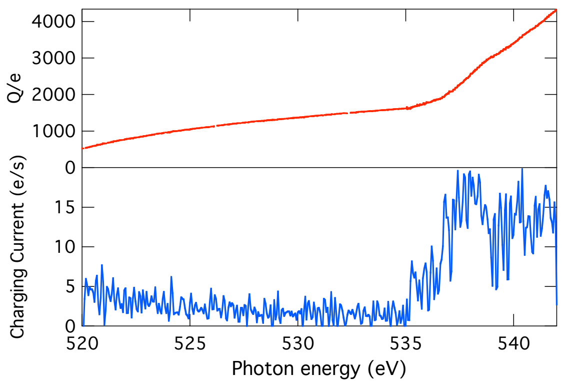

Fig. 2: Absorption spectrum of a single 500 nm SiO_2 particle detected via its charging (above Q, below I = dQ/dt). At $E_{\square} > 535$ eV an increase of the charging current is related to the excitation of bound electronic states leading to the emission of Auger-electrons.

Coulomb explosion and related phenomena [4] deal with the limits of charging. Most experiments in this respect have been conducted on liquids, especially micron-sized particles, whereas investigations on solids are rather sparse. At a photon energy of 250 eV, far from any absorption edge, the particle has been charged to its limit, which exceeds substantially the expected boundary given by the surface potential derived above. Moreover, the maximum charge state depends on the intensity of the synchrotron radiation. Apparently this is due to a combination of a charging and discharging current. Its ratio determines an equilibrium situation. Systematic studies on the kinetics of these two processes are under way.

The present experiments clearly demonstrate the potential of this novel experimental approach. It is anticipated that fundamental materials properties can be obtained from such experiments on photoemission, the production of Auger-electrons, near-edge absorption as well as from the limitations of particle charging. Future experiments will also deal with the scattering of synchrotron radiation from single, trapped particles.

This work has been supported by the BMBF (contract no 05KS1BMA/0). We gratefully acknowledge the help of the BESSY staff.

References

1 S. Schlemmer, J. Illemann, S. Wellert, and D. Gerlich, J. Appl. Phys. **90**, 5410 (2001)

2 S. Schlemmer, S. Wellert, F. Windisch, M. Grimm, S. Barth and D. Gerlich, Appl. Phys. A.. accepted.

3 CRC Handbook of Physics and Chemistry, CRC press, Boca Raton, 12-107 (1993**)**

4 D. Duft, T. Achtzehn, R. Müller, B. A. Huber, T. Leisner, *Nature*, **421** (2003) 128.

XMCD of small deposited Cr clusters

M. Reif, M. Martins, R. Nietubyc, L. Glaser, T. Lau, and W. Wurth
Universität Hamburg, Institut für Experimentalphysik
Luruper Chaussee 149, D-22761 Hamburg

For the understanding of the evolution of magnetic properties from atoms to bulk, the study of magnetism of small, deposited transition metal clusters is an ideal tool. Recent measurements on iron clusters [1, 2, 3] show a strong nonmonotonous behavior in the evolution of spin- and orbital momentum with cluster size in the range of 2 to 9 atoms per cluster. In particular, there exist pronounced minima and maxima of the magnetic momenta, which result from the size dependence of the geometric and electronic structure of the deposited clusters.

The observed evolution of the magnetic properties of iron clusters is a strong motivation for the investigation of different systems of transitions metal clusters. A particular interesting system to study are Chromium clusters. Chromium shows for the bulk and for thicker multilayers an antiferromagnetic behavior [4]. Compared to the ferromagnetic behavior of iron clusters, strongly different magnetic properties of small deposited Cr-clusters can be expected. Recent measurements and calculations on the Kondo effect for small deposited chromium clusters supported on Au(111) by Jamneala et al [5] and Kudasov et al [6], respectively, show that this is indeed the case. Scanning tunneling spectroscopy showed that the Chromium monomer and the dimer do not exhibit any Kondo resonance in contrast to the trimer. For the monomer this is explained by its very low Kondo temperature ($T_K < 6K$), which implies a very small exchange coupling constant between the Cr monomers and the conduction electrons of the Au substrate. In the case of the dimer the absence of the Kondo resonance is due to strong antiferromagnetic coupling of the Cr atoms and thus the formation of a net magnetic singlet between the two atoms. The magnetic properties of the trimer turn out to be strongly dependent on the geometric structure of the cluster with the symmetric triangle exhibiting the highest Kondo temperature.

X-ray magnetic circular dichroism (XMCD) measurements of Böske et al [4] on capped ultrathin 2D-Cr-layers deposited on iron in the range of 1 to 3 ML show a distinct thickness dependent magnetization. The Cr monolayer shows an antiferromagnetic coupling to the iron, and an asymmetry, which is in the range of what has been expected from theory. The signal of the dilayer shows a smaller asymmetry, referred to an antiferromagnetic coupling between the two Cr layers. The results for 3ML Cr are consistent with layerwise antiferromagnetic coupling of the Cr. These results show that Chromium is a very interesting magnetic system, especially when going from 3- to 2- to 1-dimensional systems.

In recent experiments at BESSY we studied small Chromium clusters deposited on Nickel. As a substrate ultrathin films of Ni epitaxially grown on Cu(100) have been used, which were remanently magnetized perpendicular to the surface [7]. To avoid cluster fragmentation, the clusters were deposited under soft landing conditions [8]. We used 10 monolayer of Argon, freezed upon the Ni-surface of our sample at 20K, to ensure these conditions. Before measuring the clusters on the Ni-surface, the Argon was desorbed by flash heating the sample to 100K; the XMCD experiments were performed at 20K. These samples were prepared in-situ under UHV-conditions at a base pressure of 2×10^{-10}mbar. A detailed overview of the cluster source

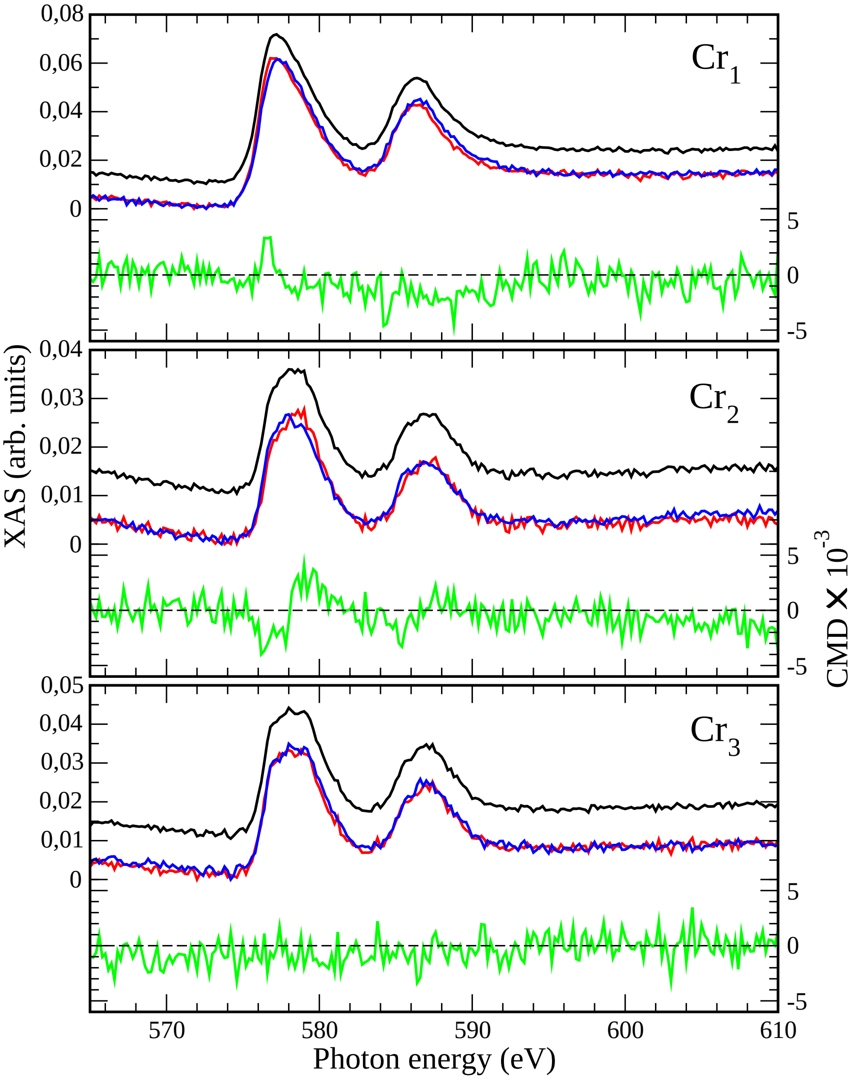

Figure 1: XAS and XMCD spectra of small deposited Cr atoms and small clusters. The red and blue curve show spectra obtained with circular polarized light. The black line is the spectra given by the addition of the two spectra taken with circular polarized light, whereas the green spectra is the difference spectra. For details see text.

and the spectroscopy chamber can be found in [1, 9]. The XMCD experiments have been performed at UE56/1 PGM. The absorption cross section has been determined by measuring the total electron yield from the sample.

The results of the experiments on monomers, dimers, and trimers are depicted in figure 1. The spectra in figure 1 show the raw data, taken with left- and right circular polarized light. The energy scale of one polarization had been shifted by 80meV before taking the difference. Surprisingly, the difference spectra show no (for the monomer and the trimer) or a very small (for the dimer) dichroic signal, depending on the cluster size. A possible reason for this behavior could be an arbitrary arrangement of the magnetic moments of the clusters, originating from a very weak exchange interaction between the clusters and the underlying magnetized Ni-layers which would give an asymmetry close to zero, as observed in these spectra. However, this appears not very likely. In the light of the recent results for small Cr Clusters on Au (see above) the observed behavior for the dimer and the trimer could be explained by an antiferromagnetic coupling of the Cr spins. However for the monomer the absence of a dichroic signal seems to imply that the net magnetic moment of the Cr atoms coupled to the Ni-substrate is close to zero. Whether this is also the case for the dimers and the trimers can not be decided on the basis of our experiments. In the near future we therefore plan to study Chromium clusters deposited on Fe, where a strong exchange coupling to the substrate appears well established and a ferromagnetic ground state of small clusters is predicted [10]. Since Fe/Ru shows Perpendicular Magnetic Anisotropy (PMA) for a small range of thickness [11], future investigations will focus on the system Cr-cluster/Fe/Ru.

We thank the BESSY staff for the great support during beamtime.
Financial support for the work was given by the BMBF under grant KS1 6UB/5.

References

[1] J. Lau, *Magnetische Eigenschaften kleiner massenselektierter Übergangsmetallcluster* (Desy-Thesis-2002-016, Notkestr. 85, 22607 Hamburg, 2002).

[2] J. Lau *et al.*, Phys. Rev. Lett. **89**, 57201 (2002).

[3] J. Lau *et al.*, New Journal of Physics **4**, 98.1 (2002).

[4] T. Böske *et al.*, Appl. Phys. **61**, 119 (1995).

[5] T. Jamneala, V.Madhavan, and M. Crommie, Phys. Rev. Lett. **87**, 256804 (2001).

[6] Y. Kudasov and V. Uzdin, Phys. Rev. Lett. **89**, 276802 (2002).

[7] W. O´Brien and B. Tonner, J. Appl. Phys. **79**, 5623 (1996).

[8] H. Cheng and U. Landman, Science **260**, 1304 (1993).

[9] J. Lau, A. Achleitner, and W. Wurth, Chem. Phys. Lett. **317**, 269 (2000).

[10] L. Pizzagalli, D. Stoeffler, and F. Gautier, Phys. Rev. B **54**, 12216 (1996).

[11] C. Liu and S. Bader, Phys. Rev. B **41**, 553 (1990).

Soft X-Ray Studies on Iron Nanoclusters Deposited in situ on Ultrathin Cobalt Films on W(110)

A. Kleibert, J. Bansmann, R.-P. Methling, M. Getzlaff*, and K.-H. Meiwes-Broer
Fachbereich Physik, Universität Rostock, D-18051 Rostock
**Institut für Angewandte Physik, Heinrich-Heine-Universität Düsseldorf, D-40225 Düsseldorf*
Supported by DFG ME835/14-3 and EU AMMARE GRD1-2000-25838.

Magnetic nanostructures possess unique properties that depend sensitively on their size and environment. In particular, the reduced atomic coordination at cluster surfaces and the interaction at interfaces is expected to cause altered magnetic orbital and spin moments. In this contribution, we report on element-specific soft X-ray studies on nanoscaled mass-filtered iron clusters deposited under UHV conditions onto epitaxialy grown Co(0001) films on W(110). X-ray circular magnetic dichroism (XMCD) investigations were carried out at the dipole beamline PM3 at BESSY II.

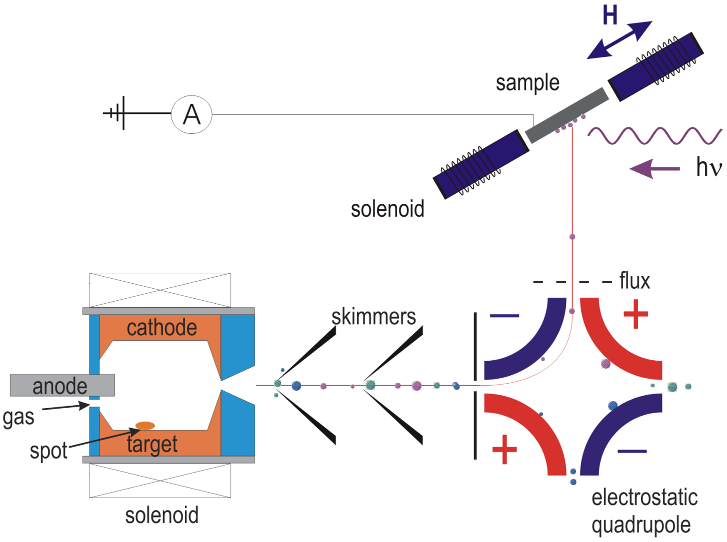

Figure 1: Schematic view of the experimental setup. In the lower part the continuously working arc cluster ion source (ACIS) and the electrostatic quadrupole is shown [1]. The upper part displays the XMCD geometry.

For the sample preparation we used an advanced and ultrahigh vacuum compatible version of the continuously working cluster source (ACIS) described in [1] for *in situ* cluster deposition. A schematic drawing is shown in the lower part of Fig. 1. The cluster apparatus mainly consists of a hollow cathode made from the target material (e.g. pure iron). At an argon pressure of several mbar the arc discharge vaporizes cathode material which is then carried by the Ar flux and condensates to clusters in the following adiabatic expansion. Charged clusters are subsequently mass-filtered by an electrostatic quadrupole deflector. As an example Fig. 2 shows a transmission electron microscopy (TEM) image and abundance spectra of iron clusters with a mean size of 12.0 nm ($\approx$ 100,000 atoms) deposited onto an amorphous carbon film on a commercial TEM grid. The image displays clusters with cubic shape and a small variation in their size. A detailed evaluation, cf. the histogram in Fig. 2, reveals a mass-resolution of about ±1 nm.

The W(110) substrate was prepared as described in e.g. [2]. Co films of about 15 ML were produced by means of molecular beam epitaxy at an evaporation rate of 0.6 ML/min. The base pressure did not exceed $5 \cdot 10^{-10}$ mbar during evaporation. The growth of hcp(0001) films was checked by LEED. Clusters were afterwards deposited *in situ* onto this well defined surfaces. During

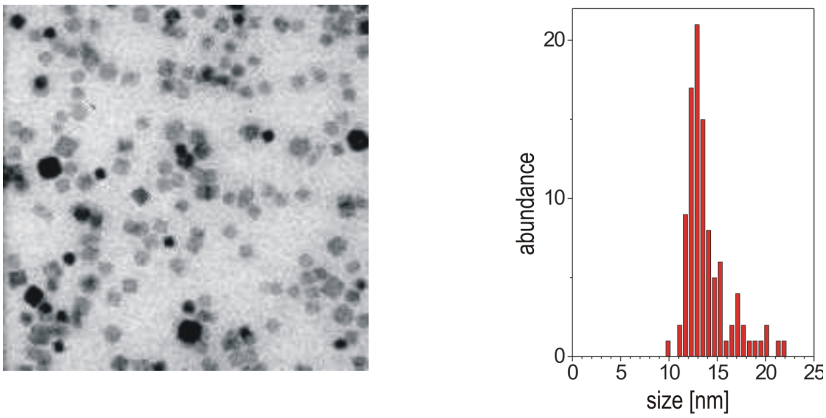

Figure 2: TEM image (left part) and its related abundance spectra (right part) for mass-filtered Fe clusters with a mean size of 12.0 nm.

deposition the pressure increased briefly up to $1 \cdot 10^{-6}$ mbar caused by the argon gas from the cluster source.

Ultrathin Co films on W(110) are known to exhibit a strong uniaxial in-plane magnetic anisotropy caused by magneto-elastic contributions due to a lattice mismatch between cobalt and tungsten. As a result the magnetic easy axis is oriented in-plane along $W[1\bar{1}0]$. In order to study the magnetic coupling between ensembles of deposited Fe clusters and these Co films we recently recorded element-specific hysteresis loops using the transverse magneto-optical Kerr-effect (T-MOKE) in the soft X-ray regime (not shown here). We observed a ferromagnetic coupling of the clusters to the film magnetization. This opens the possibility to alter the magnetization direction of the clusters simply by switching the film magnetization along the easy axis. The remanence of films and clusters thereby is nearly 100%.

XMCD experiments were performed at the PM3 beamline. The degree of circular polarization of the incident radiation is expected to be more than 90%. Data have been taken by means of total electron yield (TEY) via drain current. The experimental setup is shown in the upper part of Fig. 1. Photoabsorption spectra of Fe clusters (12.0 nm) deposited on Co/W(110) are shown in Fig. 3, where the photon energy range was chosen to cover the $2p_{3/2}$ and $2p_{1/2}$ Co and Fe edges, respectively. The upper left panel displays the Co film spectra while the Fe cluster data are shown in the upper right panel. Red and blue lines denotes spectra at opposite remanent magnetization states while leaving the photon helicity fixed.

From the corresponding difference spectra and integration over the energy (lower panels of Fig. 3) one can calculate element-specific spin and orbital moments, μ_s and μ_o, respectively. Here, we will only discuss the ratio of both contributions, which can be obtained using a ”sum rule” given by Chen et al. [3]:

$$\frac{\mu_o}{\mu_s} = \frac{2q}{9p - 6q}$$

The values of q and p can be extracted from the integrated difference spectra as displayed in Fig. 3. A comparison to reference data of thick iron and cobalt films is given in tab. 1. The data show that the value obtained for the Co film on W(110) is in reasonable good agreement to those found in literature. Contrary to this, we observe a slight increase in the orbital to spin ratio for the Fe clusters when compared to the reported thick iron film.

Increased values of μ_o/μ_s have already been found by several groups, but for deposited small iron clusters consisting of up to 600 atoms [4, 5]. The observed enhancement is mainly due to increased orbital moments related to surface and/or interface atoms of the clusters. The corresponding

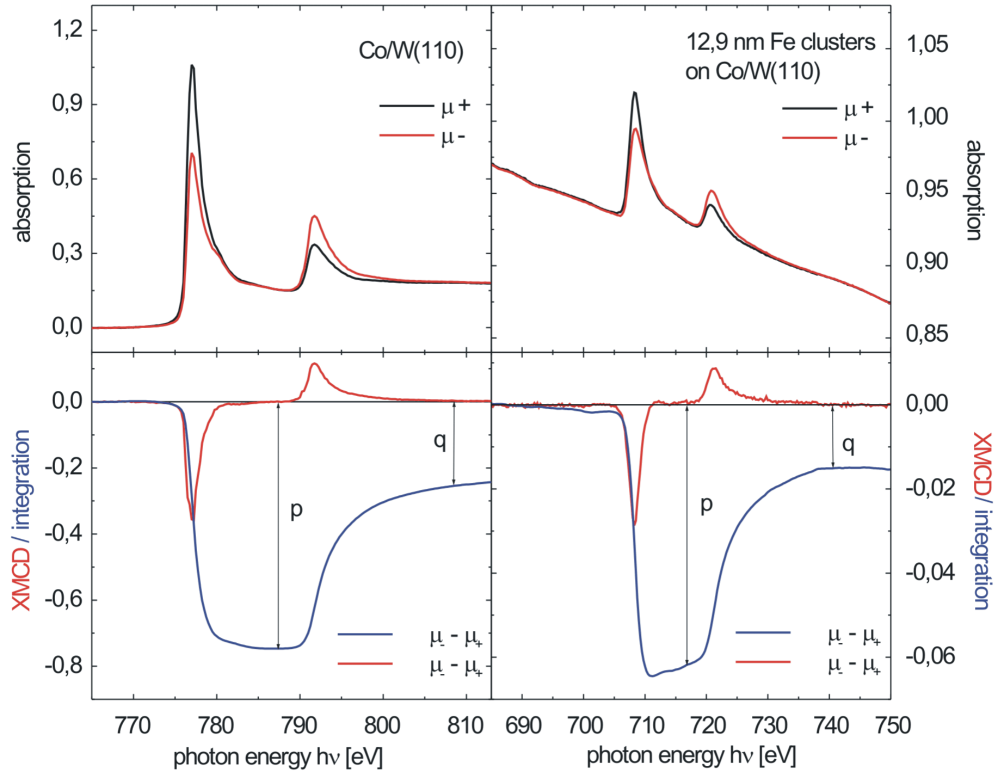

Figure 3: XMCD photoabsorption spectra (upper panels) and corresponding intensity differences (lower panel) from Fe clusters on hcp(0001) cobalt on W(110). The left column shows data from the cobalt film, the right one from the Fe clusters.

volume/bulk orbital moments are usually quenched. Thus, the enhancement is expected to be proportional to the ratio of surface to bulk atoms and μ_o/μ_s will recover the bulk value with increasing size. In comparison with above mentioned findings, our results surprisingly show that even Fe clusters consisting of about 100,000 atoms exhibit significantly altered properties compared to bulk iron. However, for a better understanding of these astonishing results a systematic study of the influence of the cluster-surface interaction on their magnetic properties is necessary.

μ_o/μ_s	our experiment	reference data from [3]
Co	0.10 ± 0.01	0.099
Fe	0.07 ± 0.02	0.043

Table 1: Comparison of the ratio between the orbital to spin moments for Fe and Co reported here and from reference data.

References:

[1] R.-P. Methling et al., Eur. Phys. J. D **16**, 173 (2001).
[2] A. Bettac et al., Surface Sci. **454-456**, 936 (2000).
[3] C. T. Chen et al., Phys. Rev. Lett.**75**, 152 (1995).
[4] K. W. Edmonds et al., Phys. Rev. B **60**, 472 (1999).
[5] J. T. Lau et al., Phys. Rev. Lett **89**, 057201 (2002).

Electron spectroscopy on Ar and Ne clusters

Simon Marburger, Oliver Kugeler and Uwe Hergenhahn

Fritz-Haber-Institut der Max-Planck-Gesellschaft, Faradayweg 4-6, 14195 Berlin and
Max-Planck-Institut für Plasmaphysik, Boltzmannstr. 2, 85748 Garching

Thomas Möller

Hasylab am DESY, Notkestr. 85, 22603 Hamburg

Introduction: Photoelectron spectroscopy of free van-der-Waals clusters can reveal important information on the electronic structure of these weakly bound systems and substantially benefits from the use of synchrotron radiation.[1,2] Obvious questions to be asked include the photon energy dependent dynamics of the photoionization cross section, as compared to the monomer, the amount of internal excitation created by the photoelectron before its release into the vacuum, and the energetics of multi-electron excited states.

A new process, which has recently been investigated theoretically, is the autoionization of singly ionized van-der-Waals clusters. Here, as compared to the monomer, the number of dicationic states is greatly increased since the two positive charges can be distributed among two different sites in the cluster. Calculations of the energies of these states, *e.g.* for $(\mathrm{Ne}_N)^{2+}$ clusters, have shown that these 'two-site' states have a significantly smaller binding energy than atomic Ne^{2+} states.[3] By that, autoionization of inner-valence vacancy states, like $(\mathrm{Ne}_N)^+$ $2s^{-1}$, is energetically possible, whereas this state would decay by flourescence in the atom. Other than conventional Auger decay, this process is only possible in the presence of the environment surrounding the vacancy, and therefore has been termed Internal Coulombic Decay (ICD).[4]

Experimental: The experimental setup consisted of two sections, an expansion chamber and the main experimental chamber. Gas was introduced into the expansion chamber through a nozzle of 200 µm diameter and 15° half opening angle, similar to the design introduced in Ref. 5. At stagnation pressures of 100-150 mbar the expansion chamber was pumped by two 240 l/s turbo pumps. To effectuate cluster formation, the nozzle was cooled to 40 K by liquid He. This temperature was stabilized by a control circuit including a heater element. After the central part of the beam passed through a conical skimmer, pressure in the main experimental chamber was better than $5\cdot10^{-6}$ mbar.

A Scienta 200 electron spectrometer was used to record the photoelectrons. For a pass energy of 5 eV, the transmission function of the analyser was checked by comparing the intensity of the Ne 2*s* photoline to literature data[6] and was found to substantially decrease for kinetic energies below 0.5 eV, with the lowest energy electrons detectable at 0.38 eV. However, no quantitative correction for that was attempted.

Results: To collect evidence for the ICD hypothesis, electron spectra of Ne clusters at photon energies below and above the 2*s* ionization threshold were collected. Representative spectra are shown in Fig. 1. The cluster bulk and surface components of the 2*s* line and the monomer component due to uncondensed atoms in the beam can well be distinguished. We interpret the presence of a peak-like feature with kinetic energies between 1.2 and 2 eV as strong evidence for the presence of the ICD process in these species. In Ar, the decay of 3*s* vacancy states by ICD is not possible. Consequently, in Ar photoelectron spectra recorded above the 3*s* photoionization edge for comparison, no comparable feature occurs (Fig. 2).

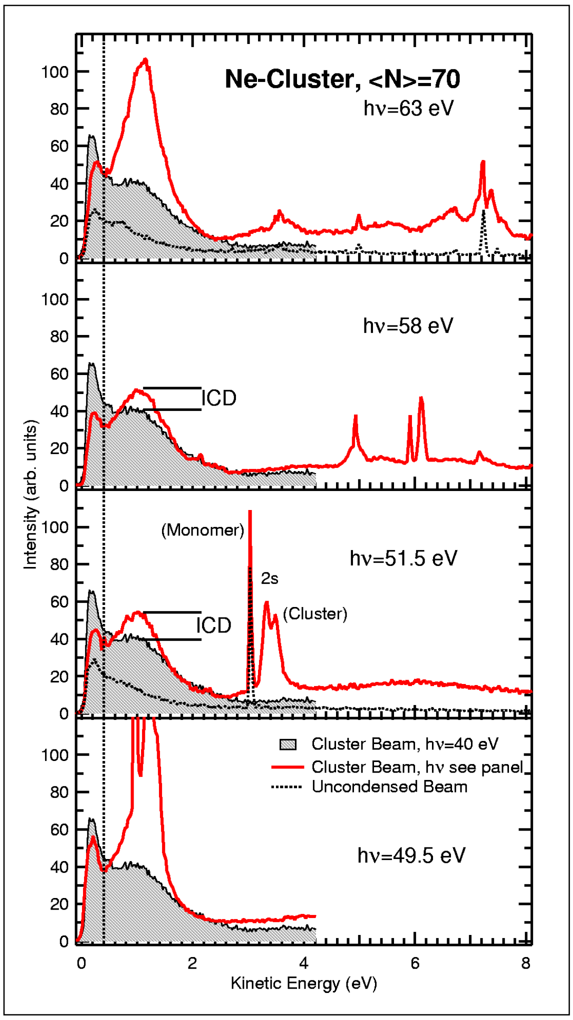

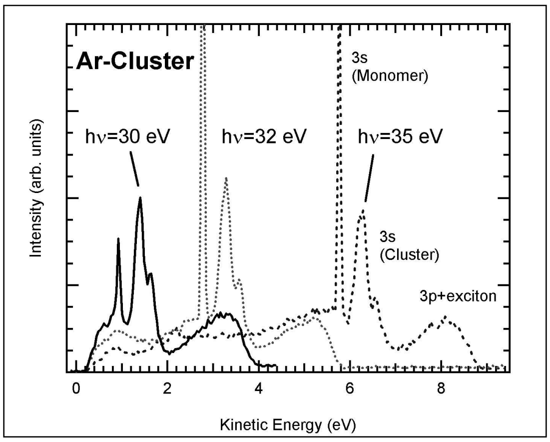

Fig. 1 (left): Photon excited electron spectra of Ne clusters with an average size of ⟨N⟩ = 70 atoms. The spectra depicted by red, solid lines are taken at varying photon energies above the Ne 2*s* threshold. For comparison, in every panel a spectrum recorded below the 2*s* threshold is shown (shaded region). At 51.5 eV and 63 eV, we also show the spectrum obtained with a Ne beam at temperatures slightly higher than the onset of condensation (thin, dotted lines). Units of the independent axis are arbitrary, but consistent for all panels. The signal at kinetic energies below 0.4 eV (vertical, dotted line) contains contributions of unphysical scattering electrons.

Fig. 2 (right): Photon excited electron spectra of Ar clusters with an average size of ⟨N⟩ = 35 atoms. Besides the 3*s* monomer and cluster photolines, a satellite line due to 3*p* photoionization followed by creation of a cluster exciton can be seen.[2]

For this project, in 2002 we have used two weeks of multi bunch beamtime at the U125/1-PGM beamline. We acknowledge funding by the EURATOM program.

References

[1] O. Björneholm, F. Federmann, F. Fössing, and T. Möller, Phys. Rev. Lett. **74**, 3017 (1995).

[2] U. Hergenhahn, A. Kolmakov, M. Riedler, A. R. B. de Castro, O. Löfken, and T. Möller, Chem. Phys. Lett. **351**, 235 (2002).

[3] R. Santra, J. Zobeley, L. S. Cederbaum, and N. Moiseyev, Phys. Rev. Lett. **85**, 4490 (2000).

[4] R. Santra and L. S. Cederbaum, Phys. Rep. **368**, 1 (2002).

[5] R. Karnbach, M. Joppien, J. Stapelfeldt, J. Wörmer, and T. Möller, Rev. Sci. Instrum. **64**, 2838 (1993).

[6] K.-H. Schartner, B. Magel, B. Möbus, H. Schmoranzer, and M. Wildberger, J. Phys. B **23**, L527 (1990).

High-resolution photoelectron spectroscopy for the investigation of CdS nanoparticles synthesized by wet chemistry

S. Joshi, R. Fink, C. Kumpf, T. Schmidt, C. Heske, and E. Umbach
Experimentelle Physik II, Universität Würzburg, Am Hubland, 97074 Würzburg
S. K. Kulkarni
Department of Physics, University of Pune, Pune 411 007, India

The study of semiconductor nanoparticles has been an interesting field of research for more than a decade. This is because it gives an opportunity to understand physical properties at low dimensions and to explore their vast potential for applications in optoelectronics. The latter is particularly based on the large variation of the band gap as a function of particle size [1]. Moreover, these particles allow a study of the important surface properties due to the high surface to bulk ratio.

In the present investigations our main object is to analyze the surface properties of wet-chemically synthesized CdS nanoparticles. The wet chemical synthesis offers low cost production and the ability to produce various sizes in large amounts. However, the size distribution is controlled by various parameters, which have to be optimized for a particular particle size. The particles are stabilized by organic capping agents. Our earlier studies on CdS nanoparticles (2.4 nm - 7 nm, stabilized by mercapto-propionic acid, MPA) show different atomic species of sulfur at the surface and reveal their contribution as a function of particle size [2]. We have taken efforts to improve the size distribution of the particles by using a different capping agent (Thioglycerol, TG), which also makes it possible to obtain smaller particle sizes. The particles are then deposited as films on a Au substrate, either by depositing a drop of the freshly synthesized nanoparticle solution or by electrophoresis. The CdS particles are first investigated by optical absorption to derive the size and the size distribution. From the absorption maximum, the size is determined by a tight binding approximation. The TG-capped particles are significantly smaller (1.5 nm – 4 nm) than the MPA-capped particles and hence give more direct access to the surface regime. Here we focus on highly monodisperse particles with a size of 1.5 (± 0.2) nm. High-resolution photoelectron spectroscopy with photons from an undulator source (U49-PGM at BESSY II) has been used to study chemical bonding at the surface of the particles. In the photoemission spectra in Fig. 1, we identify at least four different sulfur species. Not surprisingly, the intensities of the various components vary with photon energy, in particular when the photon energy is tuned o give maximal and minimal surface sensitivity. From our earlier investigations and from the observed intensities in the surface sensitive measurements (at a photon energy of 254 eV), it is possible to derive a tentative interpretation of the different chemical sulfur environments. These components are assigned to S atoms in the bulk, at the surface, in a thioglycerol molecule bound to the particle, and in a S-S bond. The contribution of these components also changes as a function of size (not shown here). The S-surface/S-bulk ratio decreases for increasing particle size.

We observe strong changes in the spectra when the particles are deposited by electrophoresis, which was done to obtain a homogeneous film as proven by AFM experiments. This finding, based on a detailed analysis of the number and intensity of the different sulfur species indicates that the drop deposition of the particles does not severely affect the individual particles, while during electrophoretic deposition the particles agglomerate. This can be seen in the spectra in fig. 1, (c) and (d), of a drop dried film and an electrophoretically deposited film, the latter of which exhibiting a substantially more "bulk like" spectrum.

Further detailed investigations, including sophisticated parallel fitting routines, are necessary to understand the detailed changes of all spectral components. Furthermore, a correlation with other spectroscopic techniques such as Raman spectroscopy is currently carried out to learn more about the role of the capping molecules. Preliminary results of the Raman investigations show that the particle solution does not contain any residual molecular thiol groups, i.e., that no free capping molecules contribute to the sulfur photoemission spectra. Further experiments with high-resolution photoemission are currently being conducted to increase the level of understanding of the size and preparation effects in these CdS nanoparticle films.

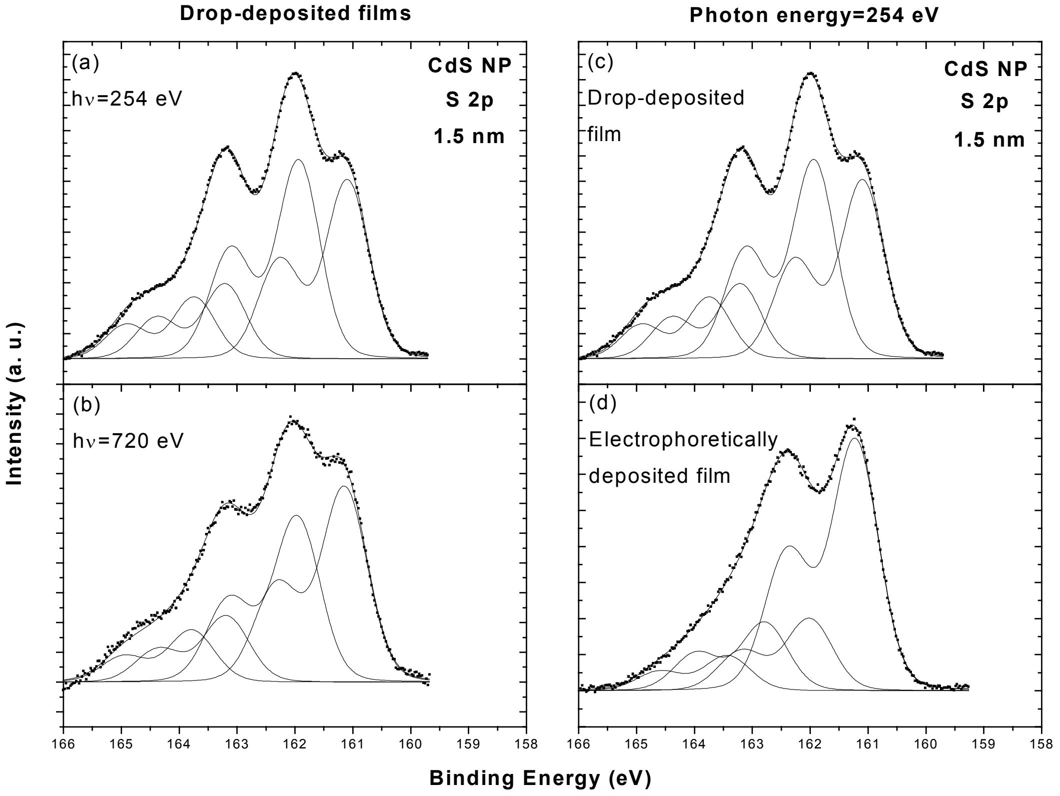

Fig. 1. High-resolution 2p photoemission spectra of 1.5 nm CdS particles. Figures 1 (a) and (b) demonstrate the spectral change when tuning the photon energy from 254 eV (surface sensitive) to 720 eV (bulk sensitive). Figures 1(c) and (d) indicate the effect of an electrophoretic film preparation (d), compared to drop deposition from the nanoparticle solution (c).

References

[1] *Y. Wang and N. Herron, J. Phys. Chem.1991, 95, 525-532.*

[2] *U. Winkler, D. Eich, Z. H. Chen, R. Fink, S. K. Kulkarni and E. Umbach, Chem. Phys. Letters, 1999, 306, 95-102.*

This work is supported by the DFG through SFB 410, TP C5.

Electronic structure of two-dimensional intercalation-like systems on Ni(111)/W(110)

A. Starodoubov, A. Loza, D. Popov, and V. K. Adamchuk
Institute of Physics, St. Petersburg State University, St. Petersburg 198904, Russia

E.Schierle[1], H.Ott[1], C.Schüssler-Langeheine[2], E.Weschke[1], and G.Kaindl[1]
[1]Institut für Experimentalphysik, Freie Universität Berlin, Arnimallee 14, D-14195 Berlin, Germany
[2] II.Physikalisches Institut der Universität zu Köln, ZulpicherStr.77, D-50937Köln, Germany

D.Vyalikh[1], S.Molodtsov[3]
[3]Institut für Oberflächenphysik und Mikrostrukturphysik, TU Dresden, D-01062 Dresden, Germany

Aim of the study: The aim of the study was to explore the possibilities of preparing graphite monolayers (GML) on epitaxial Ni(111) films grown on W(110). The preparation of GML's is usually carried out on the (111) surface of Ni single crystals [1-2], while our method opens interesting perspectives in modifying the Ni electronic structure by variation of the Ni film thickness down to a few monolayers.

Experiment:

The experiments were carried out at the Russian-German Beamline (RGBL) at BESSY II. This experimental station provides the facilities required to conduct the planned experiments, i.e. a preparation chamber including a LEED optics and quartz microbalance. The experimental chamber is equipped with a CLAM4 electron energy analyzer providing an experimental energy resolution of 30 meV, which is sufficient to resolve the expected features in the GML system.

The experiments were carried out good vacuum conditions with a base pressure of less than $2x10^{-10}$ mbar. Ni films with thicknesses of 120 and 10 Å were grown on a W(110) single-crystal surface by electron beam evaporation from a Ni rod. Subsequent annealing to lead to well-ordered Ni films which displayed sharp hexagonal LEED patterns as expected for an fcc(111) surface (Fig 1 a). It turned out that in fact GML's can be prepared with high quality on these Ni(111) films by the procedure already established in the case of Ni single crystal surfaces, i.e. by catalytic cracking of propylene at surface temperatures of 500°C (Fig. 1b).

Results:

The two Ni films of the present study have thicknesses of approximately 35 and 3 Ni monolayers, respectively.

Photoelectron spectra recorded from the GML's on these Ni films are found to be very similar to those obtained from GML prepared on (111) surfaces of a bulk Ni single crystal, as can be inferred from Figs. 2a and 2b. The dispersion of the π- and σ-derived bands can be nicely seen, with comparable band-edge

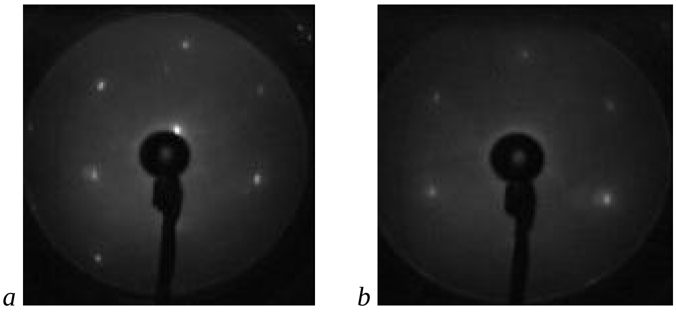

Fig.1

LEED patterns of (a) Ni(120Å)/W(110) and (b) GML/ Ni(120Å)/W(110) recorded at E_{kin}=147eV and E_{kin}=181eV accordingly.

energies as in the case of the GML's on bulk Ni. These results clearly show that the proposed method offers an interesting new way to prepare layer structures with GML.

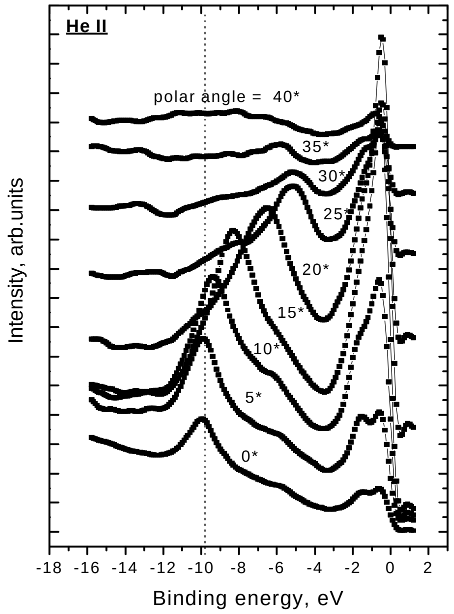

Fig.2 (a)
ARPES spectra of GML/Ni(111)

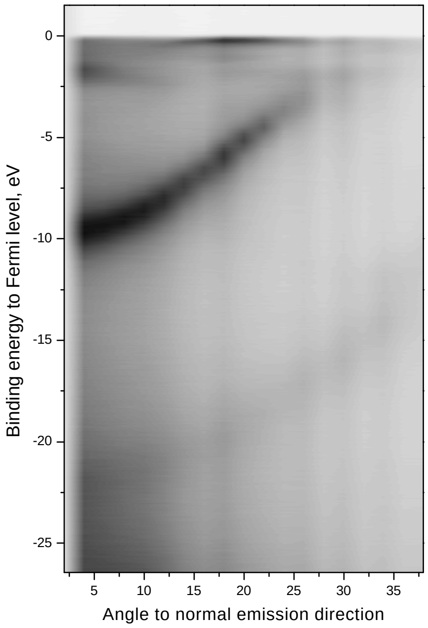

Fig.2 (b)
ARPES spectra of GML/Ni(120Å)/ W(110)

After characterization of the pure GML's, we focused on intercalation systems, starting with the well-characterized system Ag. For this purpose, silver was evaporated in several steps on GML/Ni(120Å)/W(110) with intermediate annealing to temperatures ranging from 250°C, 300°C, 400°C, 450°C and 475°C (see ARPES spectra in Fig. 3 for each of these steps). The final amount of evaporated silver was 50Å. During this procedure the form and position of the σ states peak changes substantially and as well as the relative amplitude of the σ-states peak of graphite, *d* states of silver and nickel. Such a behavior was also observed in the case of the GML system on bulk Ni and can be readily explained by the different stages of the intercalation process. For small amount of silver (10Å and 30Å) no intercalation was observed even after substantial annealing which only resulted in small changes in shape and amplitude of the silver 4*d* features. After additional deposition of 10Å of Ag, (cumulative

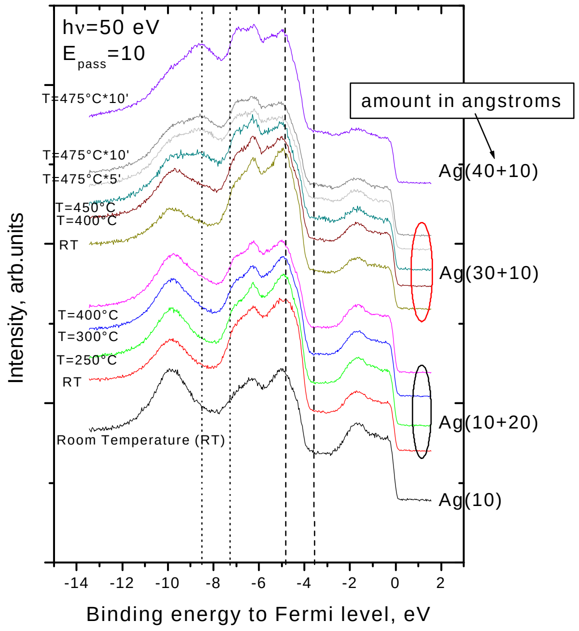

Fig.3
Spectra of Ag+GML/Ni(120Å)/ W(110)

amount 40Å) further annealing lead to the beginning of the intercalation process, which can be seen from the weakening of the silver and nickel peak height and in particular from the changed shape of the graphite σ-state emission around 10eV binding energy. A second component is observed at lower binding energy, which can be attributed to regions of the GML, where intercalation has taken place. The lower binding energy is due to the weaker interaction of silver with graphite. After a final deposition of additional 10Å of silver (cumulative amount 50Å) the position of the the σ-derived bands has shifted by 1.2 eV towards lower binding energy. A remaining shoulder at the of initial energy position, however, showed that not the whole GML took part in the intercalation process. Fig. 4 shows that the dispersion of the σ band of graphite exhibits essentially a rigid shift throughout the whole region of the Brillouin zone covered by the experiment.

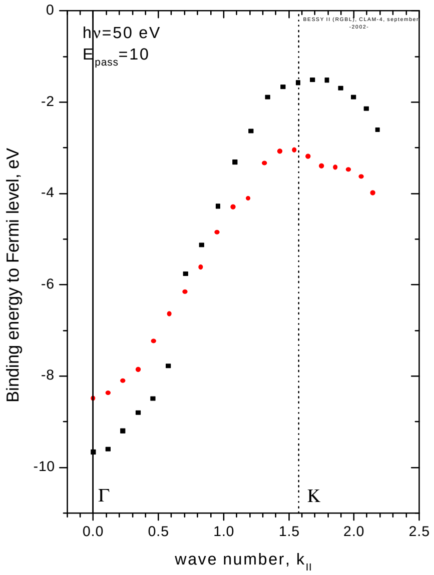

fig.4

Dispersion of graphite σ states
for GML/ Ag(50Å)/ Ni(120Å)/ W(110)

Conclusion: From these first experiments, we can conclude that high-quality GML's can be prepared on thin films of Ni(111), which permit intercalation studies as in the respective system using a bulk Ni crystal. The possibility of tuning the Ni-film thickness will be exploited in further studies.

Acknowledgments: We are very greatfull to Russian-German Committee, BESSYII and DFG (project Sfb 290/TPA6) for the opportunity to carry out our experiment and financial support.

References

1. A.M.Shikin, G.V.Prudnikova and V.K.Adamchuk, F.Moresco and K.-H.Rieder, Phys. Rev. B, 62, 13202 (2000).

2. Yu.S.Dedkov, A.M.Shikin, and V.K.Adamchuk, S.L.Molodtsov and C.Laubschat, A.Bauer and G.Kaindl, Phys. Rev. B, 64, 035405 (2001).

Electronic structure and magnetism of GdN thin layers: X-ray absorption and XMCD at the N-K edge

F. Leuenberger, A. Parge, and W. Felsch
Universität Göttingen, I. Physikalisches Institut, Bunsenstr. 9, D-37073 Göttingen

K. Fauth
Universität Würzburg, Physikalisches Institut, Experimentelle Physik IV, Am Hubland, D-9704 Würzburg

In contrast to most rare-earth pnictides that are semimetals, there is an uncertainty about the ferromagnet GdN (T_C ~ 60 K, rocksalt structure). Recent band-structure calculations [1] predict a transition from a *semiconductor* with an indirect narrow gap (~0.7 eV) in the paramagnetic phase to a *semimetal* in the ferromagnetic phase. The semimetallic overlap, concerning essentially Gd 5d t_{2g}-derived conduction band states and N 2p-derived valence band states, is quite small. It may even occur for one spin channel only. GdN then would be a *halfmetal* with complete spin polarization. Magnetism of GdN is a combination of local magnetic moments from the half-filled Gd-4f shell (ground state $^8S_{7/2}$) and exchange-induced itinerant magnetic moments of band electrons, signaling strong electron correlations. The magnetic moments induced on the Gd 5d-derived and N 2p-derived states are expected to oppose each other and to nearly cancel [1]. Most of these theoretical predictions remain to be verified experimentally. Little has been reported to determine the electronic structure of GdN using modern methods such as electron spectroscopy. There is no information, for example, on 4f-induced itinerant magnetism of conduction-band states derived from N-2p contributions.

Recently we succeeded in preparing high-quality thin films of GdN by N^+ plasma-assisted reactive sputtering. They show good stoichiometry, the Curie temperature T_C of the bulk material and the Hund's-rule value of the saturation moment (~7 μ_B/Gd ion) [2]. The electrical conduction is thermally activated down to T_C where a transition to metallic behavior occurs. The transition is considerably shifted in a sufficiently high magnetic field, as is evident in a giant magnetoresistance. Measurements of X-ray magnetic circular dichroism (XMCD) at the $M_{4,5}$(3d→4f) and $L_{2,3}$(2p→5d) edges performed at LURE in Orsay, France, reveal that the magnetic polarization of the Gd-4f and 5d moments mirror the behavior of the macroscopic magnetization.

In view of the predictions of the band structure calculations [1] the X-ray absorption (XA) and XMCD K-edge spectra (1s→2p transition) of nitrogen are of particular interest. The dichroic spectra will provide information on role of the electronic N 2p states in the mechanism of magnetic ordering in this system, which cannot be obtained by neutron scattering. We have tested the feasibility of this spectroscopy at BESSY in a preliminary experiment on beamline PM-3, using the experimental setup of the group of Prof. Schütz. Prior to the measurements, the protective AlN cap layer was removed from the GdN layer (100 nm thick, Si substrate) by ion etching. The UHV environment warranted a clean sample surface during data acquisition. The spectra were recorded in the total electron yield mode, in photon energy steps of 100 meV and with circular polarization of a degree of 90%; an external magnetic field of ±1 T was flipped at each data point. It is shown in the figure that spectra of very good quality are obtained. The beamline PM-3 is well suited to measure N spectra with good resolution, which may be of general interest. In particular, an XMCD signal at the N K edge can clearly be resolved below T_C. It amounts to about 0.5% and shows a characteristic structure that was well reproduced for different acquisitions. To our knowledge, this is the first observation of magnetic dichroism on nitrogen in a ferromagnet.

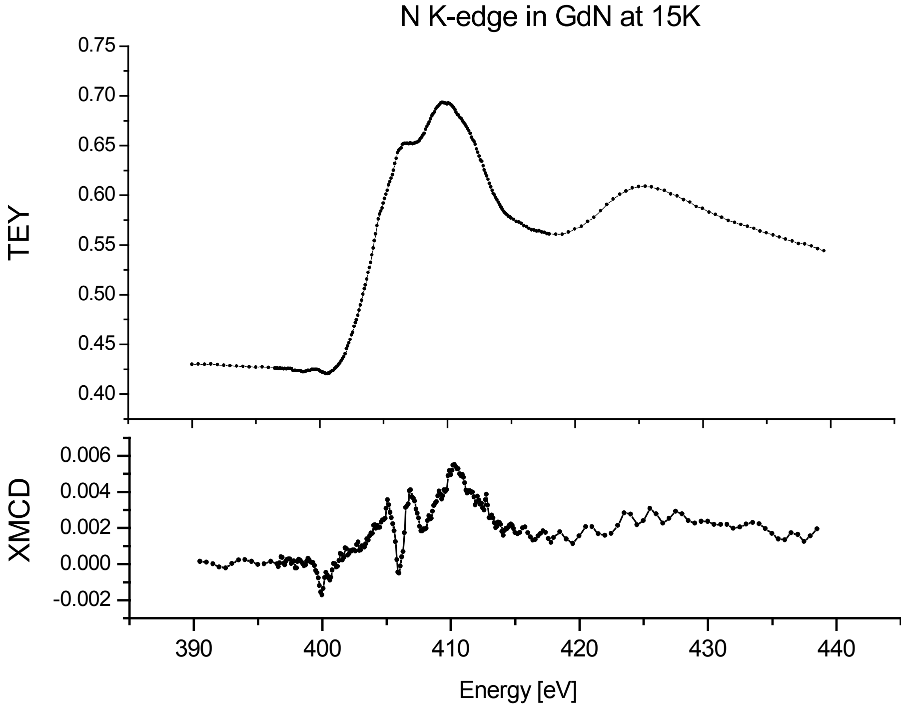

Figure: Total electron yield XA spectrum (upper panel) and XMCD signal (lower panel) at the N K-edge in a GdN layer at 15K.

The K-edge XMCD spectrum of N is of particular interest that goes beyond the actual system. It probes the projected orbital magnetization density of unoccupied p states of N [3]. No theoretical results for such spectra are available in the literature. We note that the rich information on K-edge XMCD in the soft x-ray range has recently been demonstrated for oxygen in CrO_2 [4] or in molecular CO adsorbates on ferromagnetic films [5]. It is clear that after this preliminary result we have to perform detailed measurements, for example of the temperature dependence of the dichroic spectra, before a comparison with the electronic band structure of GdN [1] can be made.

References

[1] A. G. Petukhov *et al.*, Phys. Rev. B **53**, 4324 (1996); W. R. L. Lambrecht, *ibid.* **62**, 13538 (2000).
[2] F. Leuenberger *et al.*, to be published.
[3] G.Y. Guo, J. Phys.: Condens. Matter **8**, L747 (1996); H. Ebert, Rep. Prog. Phys. **59**, 1665 (1996).
[4] E. Goering *et al.*, Europhys. Lett. **58**, 906 (2002).
[5] T. Yokoyama *et al.,* J. Electron Spectrosc. Relat. Phenom. **119**, 207 (2001).

Angular Dependence of 1T-$TiSe_2$ Photoemission in Γ-M Direction of Brillouin Zone

Yu.M.Yarmoshenko[1], M.V.Yablonskikh[1], A.N.Titov[1]
and
D.Vyalikh[2], S.Molodtsov[3]

[1] Institute of Metal Physics RAS, 18, Sofia Kovalevskaya St. GSP-170 Ekaterinburg 620219 Russia
[2] BESSY GmbH, Albert-Einstein-Str.15, 12489 Berlin, Germany
[3] Technische Universitaet Dresden D-01062 Dresden, Germany

Intercalation compounds of titanium dichalcogenides M_xTiX_2 (here M is an intercalated metal: Cr, Mn, Fe, Co, Ni; and X = S, Se, Te) are the layered structures where the layers of the host lattice alternate with the layers of intercalated component. These materials look quite the similar to the artificial layered system, which consists of magnetic metal layers alternated with nonmagnetic layers. In case of intercalation materials, the change of magnetic metal concentration leads to the change of the average distance between the magnetic atoms within the layer while the distance between the layers remains almost the same. Thus, intercalation materials are suitable for investigation of the influence of topochemical transformations on the bond structure and physical properties.

From the other hand, single crystals of TiX_2 and M_xTiX_2 are of strong anisotropy. So they are suitable for band structure investigation using ARPES technique, since it is easy to obtain a fresh flat surface for investigation by monocrystal chipping directly in chamber of spectrometer under the deep vacuum. The main problem is to obtain monocrystals with different concentrations of impurity. This problem has been solved using a technique of impurity deposition on the basal surface of crystal and annealing directly in the chamber of spectrometer till complete dissolving of evaporated layer. Such a technique has been developed first for compounds intercalated by alkaline metals [1]. Then it was applied for compounds intercalated by lanthanides [2]. An intercalation of metals leads, obviously, to modification of chemical bonds and, as a result, to rearrangement of the band structure in the wide energy range of valence band. To detect and explain these changes one should have pristine materials spectra in the same wide energy range with intensity high enough and admissible energy resolution. At the same time it was founded that for many interesting compound, like as $TiSe_2$, for example, such spectra are not reported at most. A lot of paper are devoted to investigation of pre-Fermi states for energy range from 0 to 2 eV (see for example [3-5]). The only article was devoted to the spectra of the more deep states, which were obtained in Γ-K direction, but it is known that intercalation is accompanied by high distortion of states in Γ-M direction [6]. For this direction dependencies E(k) were reported only [3], but spectra, which can be used as a reference, were not reported.

In present work an investigation of $TiSe_2$ is performed using ARPES technique in Γ-M direction for energy range from 0 to 7 eV. The results obtained may be used as a reference in investigation of the influence of intercalated metal on the band structure.

To obtain intensive spectra the energy of excitation was chosen 85 eV. Spectra were registered for polar angles from 16 to 40 degrees and energy range from 0 to 6 eV. Spectra presented in the picture give a sufficient information on the distribution of the electronic states. Line **“a”** is near the Fermi energy and corresponded to Ti3d states. This line is presented in spectra of all the titanium dichalcogenides [3,7,8]. Its origin is explained usually due to the presence of superstoichiometric titanium and its dispersionless shape characterizes localization of the impurity electrons. Lines **“b”**, **“c”**, **“d”** and **“e”** are below in energy scale and have a strong dispersive shape. These lines are corresponded to Se4p states.

An excitation energy was higher as usually, so dependence E(k) are not presented here, since the wave vector scans not only the first Brillouin zone but all the others too. That is why spectra are unsharpen.

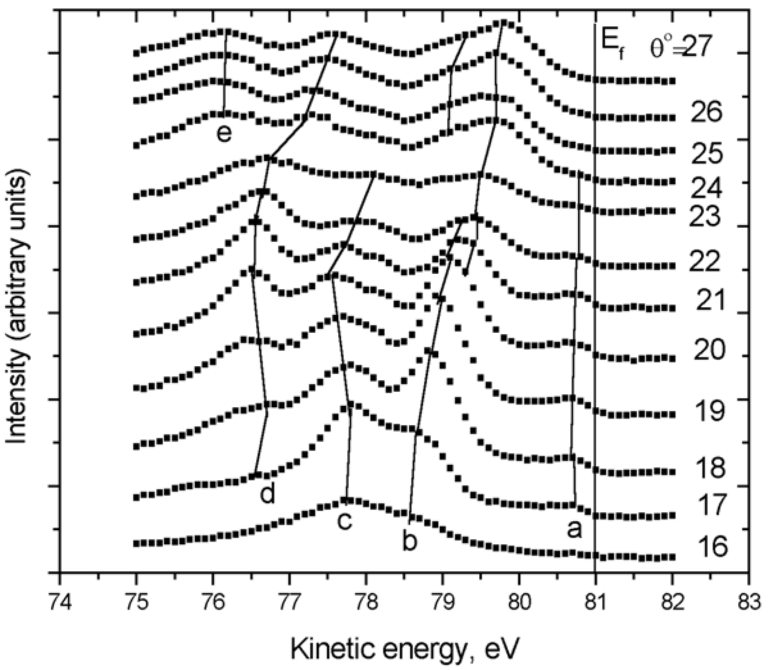

FIG.1. Photo-emission spectra for 1T-$TiSe_2$ at energy of exitation $\hbar\omega$ = 85 eV as a function of polar angle θ along Γ-M direction of Brillouin zone.

The spectra obtained are of high quality and will be used as a reference at investigation of the influence of $TiSe_2$ intercalation by transition and rare-earth metals on the band structure.

REFERENCES

1.H.E. Brauer H.E., H.I. Starnberg, L.J. Hollenboom, H.P. Huges,Surf. Sci. 333: 419, Part A JUL 1 (1995)

2. Danzenbacher S, Molodtsov SL, Koepernik K, Tomm Y, Laubschat C., Mol. Cryst. Liq. Cryst. 41: 849-854 (2000)

3. M. M. Traum, G. Margaritondo*, N. V. Smith, J. E. Rowe, and F. J. Di Salvo Phys. Rev. B 17, 1836–1838 (1978)

4. E. Pehlke, W. Schattke, O. Anderson, R. Manzke, and M. Skibowski, Phys. Rev. B **41**, 2982 (1990)
5. Th. Pillo, J. Hayoz, H.Berger, F. Lévy, L. Schlapbach, P. Aebi, Phys. Rev. B **61**, 16213 (2000).

6. T. Matsushita, S. Suga, A. Kimura, H. Negishi, and M. Inoue, Phys. Rev. B **60**, 1678 (1999).

7. M.Scharli, J.Brunner, H.P.Vaterlaus and F.Levy, J.Phys.C **16** 1527 (1983)

8. D. K. G. de Boer, C. F. van Bruggen, G. W. Bus. R. Coehoorn, C. Haas, G. A. Sawatzky H. W. Myron, D. Norman and H. Padmore, Phys. Rev. B 29, 6797 (1984).

Silicide formation upon Yb adsorption on Si(100)

M.V. Kuzmin[1], M.A. Mittsev[1], D.V. Vyalikh[2], and S.L. Molodtsov[3]

[1] *A.F. Ioffe Physico-Technical Institute, Russian Academy of Sciences, 194021 St. Petersburg, Russia*

[2] *Institut für Experimentalphysik, Freie Universität Berlin, 14195 Berlin, Germany*

[3] *Institut für Oberflächen- und Mikrostrukturphysik, TU Dresden, 01062 Dresden, Germany*

In this study, we have investigated the initial stages of Yb-Si(100)2×1 interface formation for the first time by photoelectron spectroscopy utilizing the synchrotron radiation. The measurements were performed at the Russian German beamline of the BESSY II synchrotron radiation facility. The end station of the beamline was equipped with an angle-resolved photoelectron spectrometer with a multichanneltron detector. The base pressure in the UHV chamber for measurements was better than 2×10^{-10} Torr. The angle of the incident photons was kept at 67° relative to the normal to the sample surface. A n-type Si(100) substrate was cleaned *in situ* by resistive heating up to ~ 920 K and flashing at ~ 1450 K. Yb was deposited onto the Si(100) surface from a well-degassed Knudsen cell. The pressure was less than 8×10^{-10} Torr during the Yb deposition. The evaporation rate was ~ 0.01 ML/s.

We recorded Si 2p and Yb 4f photoemission spectra for the systems grown by two different means. In the former one, Yb deposition onto Si(100)2×1 was done at room temperature (RT). The substrate was not annealed after the deposition. In the other one, Yb was also deposited at RT, however, the substrate was heated at 800 K for 3 min thereafter. According to the results of our measurements performed both at BESSY II and the Ioffe Institute [1], the processes of Yb-Si(100) interface formation are remarkably different for the cases described above and, for this reason, we will consider them separately.

(1) *Yb atoms are deposited onto Si(100) at RT and then Si 2p and Yb 4f spectra are recorded (Fig. 1).* In this case, the silicide formation does not occur at any thickness of metal film. Only a limited intermixing of Yb and Si atoms is found from the LEED experiments carried out at the Ioffe Institute. The Yb film is disordered, that is concluded from the fact that the LEED spots for clean Si(100)2×1 disappear gradually with increasing Yb coverage, whereas a new spots do not appear. In the following we will show that the conclusion about the disordered structure of such a film is well consistent with the results measured at BESSY II.

The analysis of Yb 4f spectra (Fig. 1(a)) shows that almost only the components caused by divalent Yb are found throughout the whole range of studied coverages (0 to 20 ML). The other observation from the above spectra is the broadening of peaks with Yb coverage. This behavior can be readily explained by the fact that the non-annealed Yb-Si(100) system is disordered and, therefore, Yb atoms have various coordinations, i.e. chemically different environment.

The Si 2p spectra shown in Fig. 1(b) can provide further information in this respect. In these spectra, the component S_U caused by Si dimers decreases after deposition of small content of Yb atoms (0.15 ML). However, with increasing of the Yb coverage the new components appears instead of S_U forming a very broad maximum at 0.7 – 1.0 ML. At 1.0 ML its intensity is higher than that of the main Si $2p_{3/2}$ peak (binding energy of 99.2 eV). The shape of this maximum suggests that several unresolved features contribute to that. Upon further increasing of the coverage, this broad maximum transforms into two well-resolved features, which in spite of the intensity decreasing can be found up to 20 ML. At the same time, the main maxima observed for clean Si(100) surface disappear at 3 ML. Preliminary analysis of the described data allows one to suggest that a limited intermixing occurs upon Yb deposition, with a fraction of Si atoms being dissolved in the metallic film. Beside that the Si 2p spectra should exhibit contributions resulting from a direct interaction at the interface of the Si crystal with the adsorbed disordered Yb film. It cannot be excluded that the topmost layer of Si substrate is amorphous too. Taking into account the above-mentioned consideration, one can assume that the broad maximum observed at 1.0 ML is due to the contributions of Si atoms in both states (i.e., at the interface and in the Yb bulk). Obviously, when increasing the Yb film thickness the signal from the Si substrate will be suppressed, whereas the signal from dissolved Si atoms will be constantly detected up to high coverages. Such a behavior is monitored at coverages > 1 ML in Fig. 1.

The position of maxima revealed in the Si 2p spectra upon Yb deposition implies the decrease of the binding energy of the 2p states for Si atoms interacting with Yb ones. Neglecting final-state effects in photoemission we explain this behavior by a charge transfer from Yb to Si. This can be supported by a variation of the work function observed in Ref. [1]. This variation reveals that, upon Yb deposition onto Si surface, the work function considerably decreases, e.g. by about 2.15 eV at 2 ML.

(2) *Yb atoms are deposited onto the Si(100) surface at RT, followed by the substrate annealing at 800 K for 3 min (Fig. 2).* The results of our structural investigations show that

the system is ordered in the sub-monolayer regime. That is verified also by looking at the Yb 4f spectra shown in Fig. 2(a). As follows from these spectra the broadening of maxima, as it was observed for the case of non-annealed system, does not occur with increasing Yb coverage. The other conclusion from the Yb 4f spectra analysis is that the Yb growth on Si at 800 K is accompanied by an increase of the density of states in the region of the Fermi level. Finally, the third observation is an appearing of the intense component corresponding to trivalent Yb atoms at ≥ 3 ML. Note that, according to our thermal desorption measurement, the silicide phase formation occurs at Yb coverages higher than 0.5 ML.

The transformation of Si 2p spectra (Fig. 2(b)) within 0 – 0.5 ML, i.e. prior to the silicide-formation stage, resembles the evolution of the spectra for non-annealed Yb layers. Similar to the latter case it can likely be explained by the charge-transfer arguments, that is supported by the work-function measurements as well. However, at Yb coverage higher than 0.5 ML (i.e. beyond the onset of silicide formation, the spectra for the annealed system are very different from those for the non-annealed one. The difference may be caused by two main reasons. First, it is unlikely that the ordered Yb silicide phase gives rise to amorphous topmost layer of Si substrate, as it can be the case of non-annealed layers. Second, the chemical surrounding of Si atoms in ordered silicide film is different from that in the amorphous film.

At ≥ 3 ML, the evolution of the Si 2p spectra is saturated. Four maxima are seen in these spectra. Two of them are characterized by the same binding energy as for the clean Si (99.2 eV and 99.8 eV), whereas the other two maxima correspond to the 2p states with lower binding energy. One may speculate on the origin of the two latter maxima. The Yb silicide is known to exhibit the graphite-like structure, in which Si layers alternate with Yb layers. It cannot be excluded that the essential charge transfer may occur from Yb layers to Si ones in such a structure formed by atoms having a large difference in electronegativity. Such a transfer can provide the substantial contribution to Si 2p components exhibiting lower binding energy.

[1] M. Kuzmin, R. E. Perälä, P. Laukkanen, R.-L. Vaara, *et al*. (to be published)

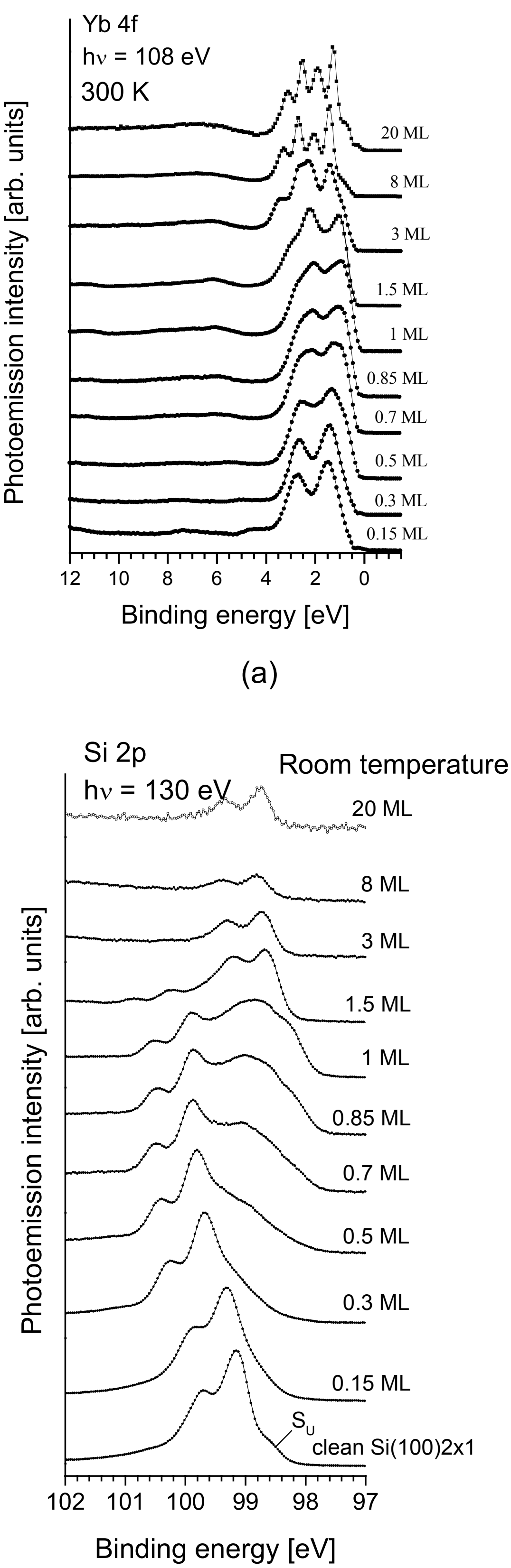

(a)

(b)

Fig. 1

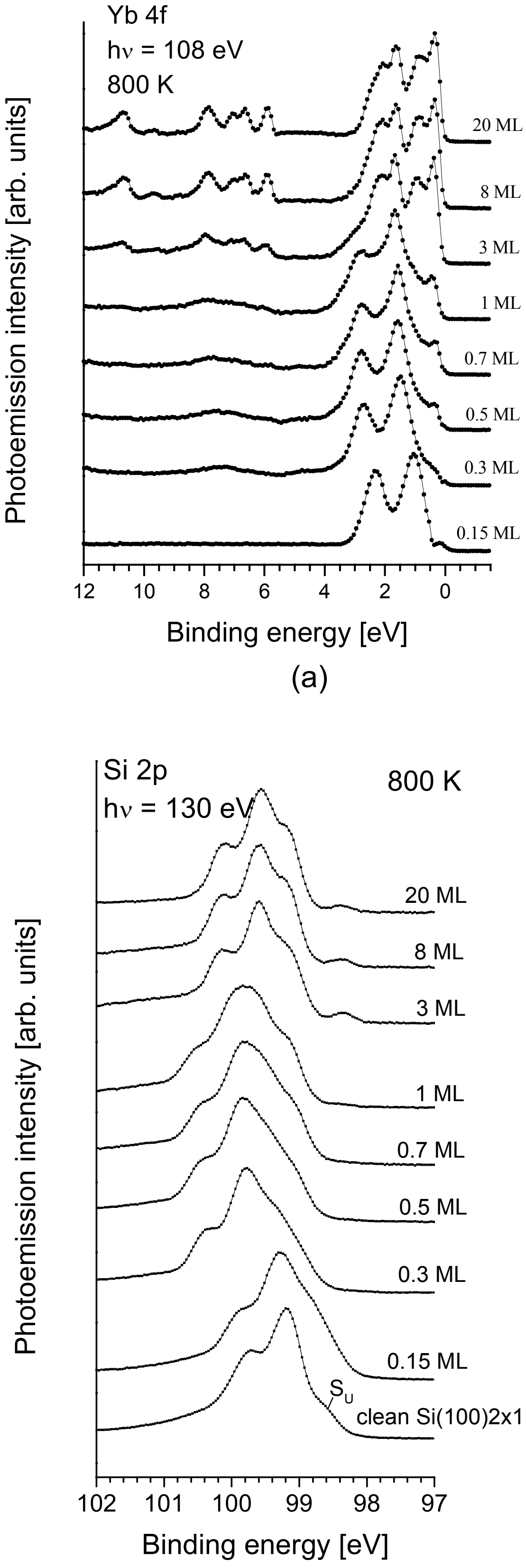

(a)

(b)

Fig. 2

Band mapping of the magnetite $Fe_3O_4(111)$ surface

Yu. S. Dedkov,[1] M. Fonin,[1] J. Hauch,[1] S. A. Kiryanov,[2] Yu. A. Babanov,[2] D. V. Vyalikh,[3]
S. L. Molodtsov,[3] U. Rüdiger,[1] and G. Güntherodt[1]
[1]*II. Physikalisches Institut, Rheinisch-Westfälische Technische Hochschule Aachen,*
D-52056 Aachen, Germany
[2]*Institute of Metal Physics Russian Academy of Sciences, S.Kovalevskaya str. 18,*
GSP-170 620219 Ekaterinburg, Russia
[3]*Institut für Oberflächen- und Mikrostrukturphysik, Technische Universität Dresden,*
D-01062 Dresden, Germany

Magnetite (Fe_3O_4) is an intensively studied strongly correlated 3*d* compound which is ferrimagnetically ordered below a relatively high transition temperature (T_C=851K) [1]. Magnetite crystallizes in the cubic inverse spinel structure with ***Fd3m*** space group, a lattice constant of a=8.396Å with 8 formulas per unit cell [2]. The oxygen anions (O^{2-}) form a close-packed *fcc* sublattice. The tetrahedral lattice sites in the inverse spinel structure are occupied by Fe^{2+} cations (Fe_{tet}) and octahedral lattice sites are occupied alternately by an equal number of Fe^{2+} and Fe^{3+} cations (Fe_{oct}).

The electronic band structure of Fe_3O_4 films was extensively investigated by means of X-ray magnetic circular dichroism (XMCD) [3,4], ultraviolet as well as X-ray photoelectron spectroscopy (UPS and XPS) [5,6], and spin-resolved photoelectron spectroscopy (SP-PES) [6,7]. However, the interpretation of the valence-band photoemission spectra of Fe_3O_4 has been a matter of debate since decades [8-10]. The recent investigations [5,7] showed that band structure calculations should be taken into account for the interpretation of PES spectra of Fe_3O_4.

In the present experiment the surface electronic band structure of *in situ* prepared epitaxial $Fe_3O_4(111)$ thin films was studied by means of angle-resolved photoelectron spectroscopy (ARPES) using synchrotron radiation. The dispersions of the O 2*p* and Fe 3*d* electronic states were measured along the $\overline{\Gamma}-\overline{M}$ direction of the $Fe_3O_4(111)$ surface Brillouin zone (SBZ). For the interpretation of these findings we propose a model which considers the magnetite $Fe_3O_4(111)$ thin film as an intercalation-like system, where Fe^{2+} and Fe^{3+} cations are incorporated into the tetrahedral and octahedral interstitial sites of a close-packed *fcc* oxygen sublattice [11]. Under this consideration the large dispersion of the O 2***p***-derived states was interpreted for the SBZ of the oxygen sublattice. Separately, the Fe 3***d***-derived states have a small periodic dispersion near the Fermi energy (E_F) across the SBZ given by the Fe_{tet} cations which form the (2×2) superstructure on the $Fe_3O_4(111)$ thin film surface.

The experiments were carried out in the Russian-German Laboratory at the BESSY II storage ring. The UHV system for ARPES at room temperature equipped with AES and LEED optics, a gas inlet, e-beam evaporation cells, and a CLAM4 analyzer for ARPES experiments with an energy resolution of 100 meV and angle resolution 1^o. The base pressure in the vacuum chamber was 1×10^{-10}mbar. Clean 100Å-thick Fe(110) films were prepared *in situ* by electron-beam evaporation on a W(110) substrate, while the thickness was simultaneously monitored by a quartz microbalance. The Fe(110) thin films were successfully oxidized into $Fe_3O_4(111)$ films by exposure to high-purity oxygen gas and subsequent annealing at 300^oC. The degree of crystalline order of the epitaxial $Fe_3O_4(111)$ films obtained in our experiments has been checked by LEED. In agreement with previous studies sharp (2×2)-reconstructed hexagonal LEED patterns have been observed. The surface cleanliness has been monitored by valence-band and core-level PES.

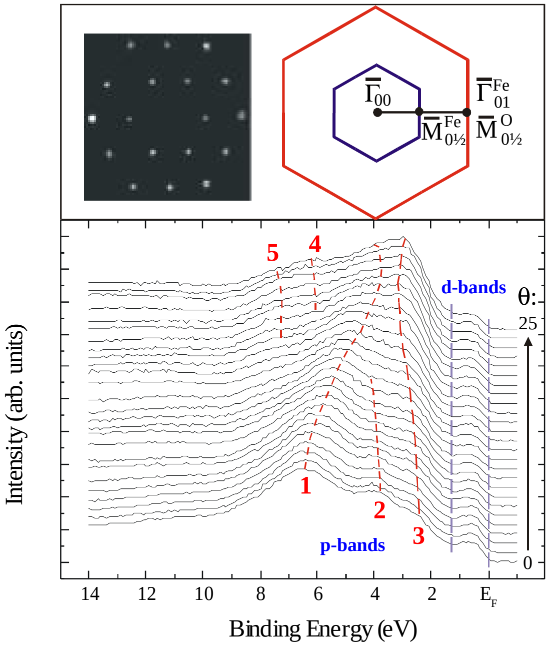

Fig.1. ARPES spectra of a Fe_3O_4(111) thin film surface recorded at *hn*=58eV for emission polar angles of 0-25° along the Γ-M direction of the Fe_3O_4(111) surface Brillouin zone; curves 1-5 mark the major O 2*p* electronic states dispersions; the upper panel shows a LEED image (E=121eV) of the Fe_3O_4(111) surface and the schematic representation of the oxygen-derived and the Fe_3O_4(111)-derived surface Brillouin zones.

The bottom panel of Fig.1 shows representative valence band spectra of an epitaxial Fe_3O_4(111) thin film as a function of the emission polar angle θ (0-25°) along the $\overline{\Gamma}-\overline{M}$ direction of the Fe_3O_4(111) SBZ. All spectra are normalized on the maximum intensity for each spectrum. A photon energy of *hn*=58eV, which corresponds to the Fe 3*p*-3*d* resonance [5,12], was used in all photoemission experiments which yelds an increased photoemission intensity from Fe 3*d* states near E_F. The ARPES spectra in Fig.1 show the Fe 3*d*-derived emission extended over 2eV below E_F and O 2*p*-derived emission between 2.5 and 9eV of binding energy. The major dispersions of the O 2*p* states in the Fe_3O_4(111) valence band are marked by dashed lines (1-5) in Fig.1.

The borders of the SBZs were calculated separately for the oxygen sublattice and the Fe_3O_4(111) sublattice SBZs (upper panel in Fig.1). Following the Fe_3O_4(111) surface structure the oxygen sublattice SBZ was considered with the wave vector corresponding to the border of the SBZ equal to $k_{\|Fe_3O_4}^{1\times1}=|\overline{\Gamma}-\overline{M}_{Fe_3O_4}|_{O-1\times1}$=1.22Å^{-1} giving the angle values of θ=19.04° and θ=22.32° for binding energies of E_F and 14 eV, respectively (line A in Fig.2). The Fe_3O_4(111) sublattice was considered in a similar way with $k_{\|Fe_3O_4}^{2\times2}=|\overline{\Gamma}-\overline{M}_{Fe_3O_4}|_{Fe-2\times2}$=0.61Å^{-1} giving the angle values of θ=9.39° and θ=10.95° for binding energies of E_F and 14eV, respectively (line B in Fig.2).

The obtained spectroscopic data was used to generate colored intensity maps of the Fe_3O_4(111) thin film valence band as shown in Fig.2 over a range of 14eV below E_F and over a range of 1.5eV below E_F (not shown here). The O 2*p* electronic states show a clear dispersion from about 9eV down to 2.5eV of binding energy within polar angle changes from 0 to 20° (lines 1-5 in Fig.2). At the same time the Fe 3*d* electronic states show an obviously symmetric dispersion with a half-period of 9° starting at the $\overline{\Gamma}_{00}$ point and running up to the $\overline{M}^{Fe}_{0\frac{1}{2}}$ point of the periodic SBZ of the (2×2) surface superstructure formed by the topmost Fe_{tet} atoms of the Fe_3O_4(111) film surface (not shown here) [12]. This $\overline{M}^{Fe}_{0\frac{1}{2}}$ point of the Fe_3O_4(111) SBZ at around θ=9° is in good coincidence with the calculated position of the Fe_3O_4(111) SBZ border. However, the dispersion symmetry of the O 2*p* electronic states can not be described in terms of the Fe_3O_4(111) SBZ as the symmetry point $\overline{M}^{O}_{0\frac{1}{2}}$ of the O 2*p* electronic states dispersion main branch (line 1 in Fig.2) lies at around θ=20° emission angle.

The $\overline{\mathrm{M}}^{O}_{0\frac{1}{2}}$ point also corresponds to the $\overline{\Gamma}^{Fe}_{01}$ point of the $Fe_3O_4(111)$ SBZ. This means that the full description of the surface electronic band structure of the $Fe_3O_4(111)$ film is only possible when two different SBZs are considered. The first one is the oxygen derived SBZ with the $\overline{\Gamma}_{00}$- $\overline{\mathrm{M}}^{O}_{0\frac{1}{2}}$ direction corresponding to the emission angles 0-20^{o} (line A in Fig.2) and the second one is the iron derived SBZ with the $\overline{\Gamma}_{00}$-$\overline{\mathrm{M}}^{Fe}_{0\frac{1}{2}}$ direction corresponding to the emission angles 0-9^{o} (line B in Fig.2). The small dispersion of the O 2*p* and Fe 3*d* states in the valence-band structures observed along the Γ-L direction [5,12] indicates an almost two-dimensional-like character of the crystalline arrangement and electronic structure of the $Fe_3O_4(111)$ surface.

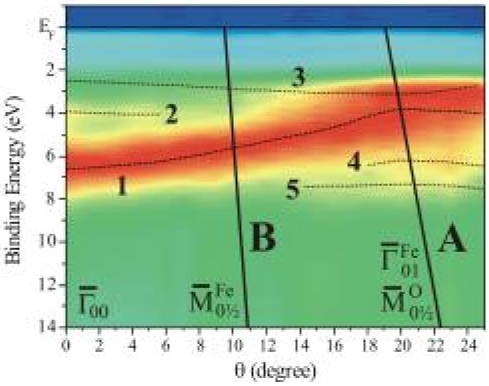

Fig.2. Contour plot of the ARPES intensity along the Γ-M direction: (a) for the emission between E_F and 14eV binding energy; and (b) extended over 1.5eV below the Fermi level.

The possibility to describe the $Fe_3O_4(111)$ surface electronic band structure as a product of two overlapping SBZs (the oxygen sublattice SBZ and the $Fe_3O_4(111)$ SBZ) is supported by the $Fe_3O_4(111)$ crystallographic structure which can be represented as multilayered system consisting of hexagonal close-packed oxygen (111) layers forming a cubic *ABCABC...* stacking sequence along the [111] direction with the periodicity of 14.6Å and 2.67Å between the oxygen close-packed layers. Between the oxygen (111) planes tetrahedrally and octahedrally coordinated Fe anions are located. The regular $Fe_3O_4(111)$ surface forms an unreconstructed bulk termination that exposes 1/4ML of Fe_{tet} atoms above the close-packed oxygen layer [12]. The $Fe_3O_4(111)$ surface can be described as an quasi-two-dimensional intercalate-like structure where Fe^{2+} and Fe^{3+} cations are incorporated into the tetrahedral and octahedral interstitial sites of the close-packed *fcc* oxygen [11].

This work was supported by the German Federal Ministry of Education and Research (BMBF) under grant No. FKZ 05KS1PAA/7.

References

1. L. Neel, Ann. Phys. (Leipzig) **3**, 137 (1948).
2. V. A. M. Brabers in *Handbook of Magnetic Materials*, edited by K. H. J. Buschow (Elsevier Science, Amsterdam, 1995), Vol. 8.
3. H. - J. Kim, J. - H. Park, and E. Vescovo, Phys. Rev.B **61**, 15284 (2000).
4. F. M. F. de Groot, J. C. Fuggle, B. T. Thole, and G. A. Sawatzky, Phys. Rev. B **42**, 5459 (1990).
5. Y. Q. Cai, M. Ritter, W. Weiss, and A. M. Bradshaw, Phys. Rev. B **58**, 5043 (1998).
6. H. - J. Kim, J. - H. Park, and E. Vescovo, Phys. Rev. B **61**, 152848 (2000).
7. Yu. S. Dedkov, U. Rüdiger, and G. Güntherodt, Phys. Rev. B **65**, 064417 (2002).
8. S. F. Alvarado, M. Erbudak, and P. Munz, Phys. Rev. B **14**, 2740 (1976).
9. A. Yanase and K. Siratori, J. Phys. Soc. Jap. **53**, 312 (1984).
10. Z. Zhang and S. Satpathy, Phys. Rev. B **44**, 13319 (1991).
11. C. N. Rao and B. Raveau in *Transitional Metal Oxides* (VCH, New York, 1995).
12. Yu. S. Dedkov, M. Fonine, J. O. Hauch, U. Rüdiger, and G. Güntherodt, to be submitted.

Electronic structure investigation of nanocomposite materials based on cage carbon

A.V.Okotrub, L.G.Bulusheva

Institute of Inorganic Chemistry, Siberian Branch of Russian Academy of Science – IIC SB RAS

During last ten years the cage carbon materials attract considerable interest owing their unique electronic, mechanical, and chemical properties, which can be utilized in different devices and technologies [1]. The aim of present project is investigation of the effects of morphology, dimensionality, defect structure and element composition of wide set of graphitic-like carbons on their electronic structure using a combination of X-ray absorption spectroscopy (BESSY II) and X-ray fluorescent spectroscopy and quantum chemistry (Institute of Inorganic Chemistry, Siberian Branch of Russian Academy of Science).

The samples of multiwall and single-wall carbon nanotubes, onion-like carbon particles, and graphites, produced by different synthetic conditions, were comparatively studied. Carbon nanotube can be thought as one (single-wall tube) or several (multiwall tube) graphite sheets rolled into cylinder, carbon onion consists of quasi-spherical graphitic shells. So, the investigated objects are graphite network based materials being different in dimensionality.

One of the most important problems in the carbon materials research is an evaluation of the defect dependence of electronic structure. The kind and portion of defects occurring in the graphite network are strongly governed by synthetic procedure, namely, the production temperature and following treatment for impurities removing.

We measured the angle dependence of X-ray absorption for crystallite graphite and highly oriented pyrolytic graphite. The weaker angle dependence of CK absorption edge for the latter sample indicated the significant imperfection of its structure caused by the low layer ordering and high defect portion. The alignment of multiwall carbon nanotubes vertically grown on a support (Fig.1(a)) was characterized by X-ray absorption and X-ray fluorescence. The angle dependence of these spectra is opposite to that measured for graphite (Fig. 1(b, c)) that is indicative of another orientation of graphite networks respective to the support.

Recently, we have investigated a change of X-ray fluorescent spectra of carbon nanoparticles, produced at the different temperatures of nanodiamonds annealing [2]. A strong increase of density of high-energy occupied states detected for onion-like carbon formed at the intermediate temperatures was assigned by the result of quantum-chemical calculation on various models to the holed structure of graphitic cages. The X-ray absorption spectra measured for these samples indicated the change in the density of unoccupied states that could help to more precise revealing of defect type in the onions.

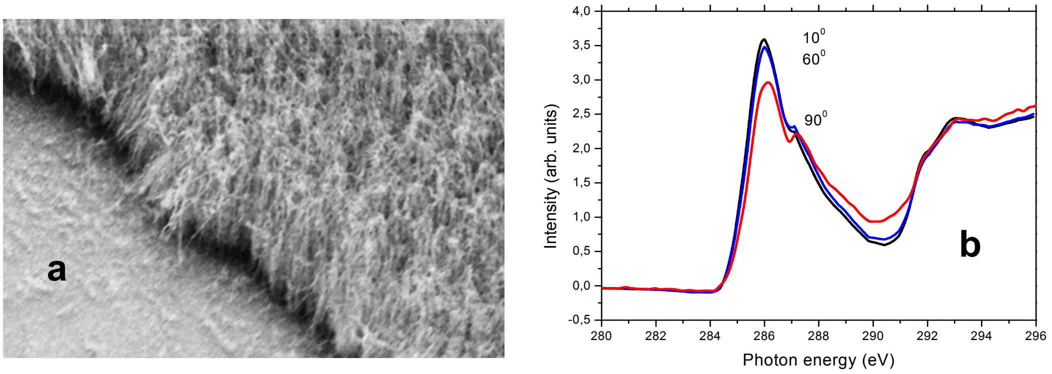

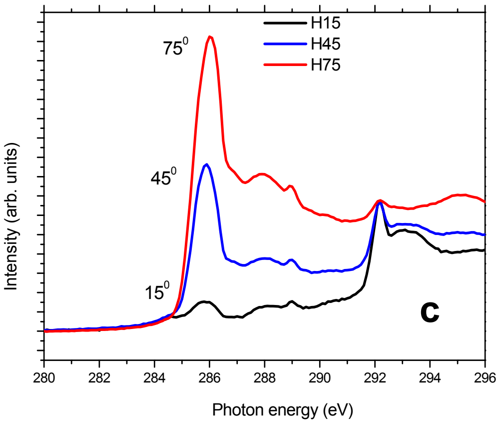

Fig. 1. Scanning tunneling microscopy image of carbon nanotubes vertically grown on the silicon support – (a). X-ray absorption spectra of aligned carbon nanotubes (b) and highly oriented graphite (c) measured at different take-off angles of radiation. The angle dependence of X-ray absorption for nanotubes has the opposite behavior compared to that for graphite.

The comparative study of the electronic structure of single-wall carbon nanotubes was performed for the samples produced using three different methods: electric arc, laser ablation, and high pressure CO decomposition technique. It is well known that the electronic structure of single-wall carbon nanotubes being one-dimensional objects is characterized by singularities appeared in the vicinity of the Fermi level [3]. The related peculiarities in the electronic structure of nanotubes were first observed in the X-ray absorption spectra (Fig. 2) that became possible due to the high resolution of X-ray monochromator. Effect of the sample purification with help of acid and/or air oxidation on the position and intensity of the singularities was revealed. Keeping the peculiarities in the electronic structure of treated nanotubes suggests slight acid action on the graphitic network arrangement. Further, we plane to determine the geometry of different type of single-wall carbon nanotubes from comparison of the results obtained with the quantum-chemical calculations.

Chemical treatment can be effective way for modification of the electronic structure of carbon materials. We comparatively investigated the pristine graphites and carbon nanotubes and fluorinated ones. The content of fluorine was determined by X-ray photoelectron spectroscopy to be no greater than 30% that assumes a keeping of π-system in the fluorinated materials. The X-ray absorption spectra were recorded for carbon and fluorine. In the case of multilayered structures the angle dependence of absorption and fluorescence was measured. The difference between spectra recorded at the different take-off angle of radiation provides the distribution of π-electrons in the valence and conduction bands of fluorinated graphites and carbon nanotubes. The quantum-chemical modeling of the data obtained will be used for revealing of fluorine distribution on the flat and cylindrical graphitic surfaces.

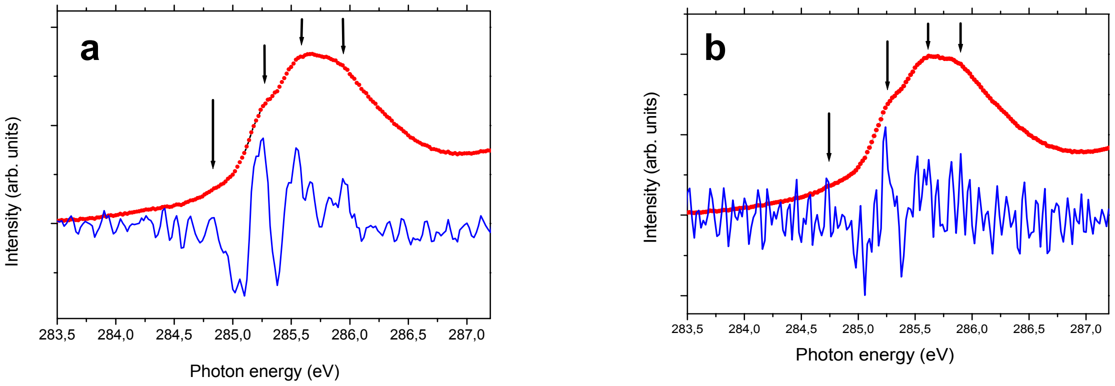

Fig. 2. Fist line (red color) of carbon X-ray absorption measured for pristine (a) and acid-oxidized (b) single-wall carbon nanotubes. Blue colored line corresponds to the second derivation of the spectrum. The arrows point to singularities, which are caused by one-dimensional tube structure.

Insertion of metal containing compounds into gas phase reactor for nanocarbon production can yield the metal nanoparticles coated by graphitic shells. Due to the small size of formed metallic particles and protection of their surface by graphite shells again oxidation, such type materials could find application in magnetic data storage, spin-dependant electronic devices, ferrofluides [4]. We studied the electronic state of graphitic shells covered the spherical cobalt nanoparticles or the iron nanowires. Comparison of X-ray absorption spectra of carbon measured for these composite structures and empty graphitic nanotubes and onions could provide the information about carbon-metal interactions.

We acknowledge Dr. Denis Vyalikh and Maxim Poyguin for technical assistance.

[1] Harris, P.J.F., *Carbon nanotubes and related structures: New materials for the 21st century,* Cambridge University Press, New York, 1999.

[2] Okotrub, A.V., Bulusheva, L.G., Kuznetsov, V.L., Butenko, Yu.V., Chuvilin, A.L., Heggie M.I. *X-ray emission studies of the valence band of nanodiamonds annealed at different temperatures* J. Phys. Chem. A 105 (2001) 9781-9787.

[3] White, C.T., Mintmire, J.W. *Density of states reflects diameter in nanotubes*, Nature 394 (1998) 29-30.

[4] Banhart, F., Grobert, N., Terrones, M., Charlier, J.-C., Ajayan, P.M. *Metal atoms in carbon nanotubes and related nanoparticles*, Int. J. Mod. Phys. B 15 (2001) 4037-4069.

A comparative study of photoemission and crossluminescence from BaF_2

M. Kirm [a], V.N. Makhov [b], S.L. Molodtsov [c], M.A. Terekhin [b], D.V. Vyalikh [d]

[a] Institut für Experimentalphysik der Universität Hamburg, 22761 Hamburg, Germany
[b] Lebedev Physical Institute, 119991 Moscow, Russia
[c] Institut für Oberflächen- und Mikrostrukturphysik, TU Dresden, 01062 Dresden, Germany
[d] Institut für Experimentalphysik, Freie Universität Berlin, 14195 Berlin, Germany

1. Introduction

Up to now no precise low-temperature photoemission data were reported for most insulating ionic crystals. Due to experimental difficulties of such measurements (surface charging) mainly room-temperature data obtained for a restricted number of crystals with quite a low resolution are available [1-7]. A special case of core hole relaxation is observed in some ionic crystals in which Auger-decay of the holes in the uppermost core band is energetically forbidden. Such crystals possess fast ($\tau < 3$ ns) intrinsic luminescence due to radiative transitions of the holes from the uppermost core band into the valence band [8]. This kind of luminescence is called either crossluminescence (CRL) or, alternatively, Auger-free luminescence, or core-valence radiative transitions, and is observed in a few ionic crystals after excitation by 14-21 eV photons causing ionization of the uppermost core band. The most well known CRL crystal is BaF_2. We have performed high-resolution photoemission study of this compound at different temperatures with the aim to compare obtained spectra with luminescence spectra taken before.

2. Experiment

The photoemission experiments have been carried out at the Russian-German beamline (bending magnet D16-1A) with excitation photon energies ranged between 85 and 130 eV. The photoelectron spectra were recorded with the CLAM4 electron energy analyzer. The BaF_2 films were prepared *in situ* by evaporation onto the stainless steel substrates. The substrates with evaporated BaF_2 films were installed onto the sample holder which can be cooled by liquid nitrogen. At the optimal film thicknesses less than 100 Å no disturbing influence of surface charging was observed .

Luminescence spectra from the BaF_2 single crystal samples were measured before under synchrotron radiation excitation from the DORIS storage ring [9,10].

3. Main results and discussion

The photoelectron spectra for the *in situ* evaporated thin films of BaF_2 were recorded at 300 K and, for the first time, at liquid nitrogen temperature (LNT, 80 K). The achieved energy resolution was much better ($\leq$50 meV, FWHM) than that used before by other authors for such specimens (usually 0.3-0.4 eV, FWHM). An example of such spectra for the BaF_2 film evaporated on the top of thin CsCl layer is shown in Fig.1 together with the decomposition of photoelectron spectra into the sum of Gaussian sub-spectra. In this case the photo-lines arising from both materials, BaF_2 and CsCl, are observed in the spectrum. The spin-orbit components of the Ba 5p band are clearly resolved, and the value of spin-orbit splitting is 2.0 eV. The FWHM for Ba $5p_{1/2}$ and Ba $5p_{3/2}$ bands resulting from the fits are 1.30 and 1.42 eV at 300 K, 1.28 and 1.20 eV at 80 K, respectively.

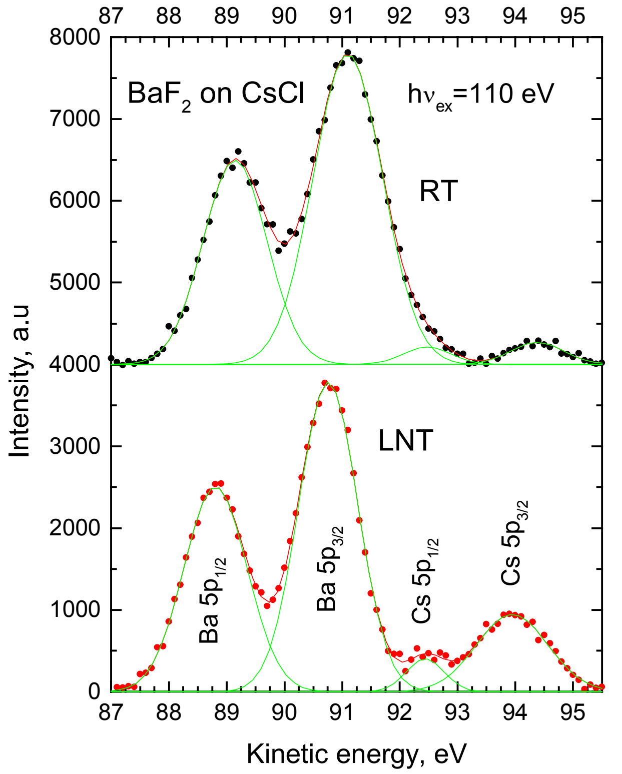

Fig.1. Decomposition into the sum of Gaussian functions of photoelectron spectra measured in the vicinity of the Ba 5p band at room and liquid nitrogen temperatures.

In crystals with CRL the lifetime of holes in the uppermost core bands is large ($\tau \sim 10^{-9}$ s) in comparison with typical core-hole lifetime ($\tau \sim 10^{-15}$ s) due to Auger-decay and the width of these bands possesses only phonon broadening. The temperature dependence of the bandwidth due to phonon broadening is given by: $\Gamma(T) = \Gamma_0\ [\coth\ (\hbar\omega/2k_BT)]^{1/2}$, where Γ_0 is the FWHM at zero temperature, ω is phonon frequency, k_B is Boltzman constant. If we assume that the widths of the bands at 80 K are practically the same as at T = 0 K we can make a crude estimation of energies for effective modes of lattice vibrations responsible for the phonon broadening. This gives the values of $\hbar\omega$ = 49 and 113 meV for the Ba $5p_{3/2}$ and Ba $5p_{1/2}$ bands, respectively. For the uppermost core Ba $5p_{3/2}$ band this phonon energy is close to the phonon cutoff energy in BaF_2 ($\hbar\omega_{LO}$ = 43 meV) and to phonon energies describing phonon broadening of the CRL bands in BaF_2 [9]. On the other hand the width of the Ba $5p_{1/2}$ band is almost independent of temperature, and such a behavior can be explained by lifetime contribution to the bandwidth because the hole in the Ba $5p_{1/2}$ band can energetically undergo Auger-decay.

The comparison of the photoelectron and CRL spectra for BaF_2 is shown in Fig.2 where the energy of photoelectrons was shifted along the x-axis in such a way that the main maxima in the CRL spectrum coincide with the positions of two main bands obtained after the decomposition of the photoelectron spectrum into the sum of Gaussian functions. In such a representation the zero-energy position, i.e. the energy position of the relaxed core hole, falls into the upper edge of the Ba $5p_{3/2}$ band in the photoelectron spectrum. However, this edge is due to the phonon tail of the corresponding electronic states in the Ba $5p_{3/2}$ band. Practically the energy of the uppermost electronic states in the Ba $5p_{3/2}$ band should lie near the maximum of the band, i.e. at about –1.3 eV in the scale of Fig.2. Assuming that the energy relaxation in photoemission from the Ba 5p states is negligible this value can be considered as an estimation of the relaxation energy for the core hole during its radiative lifetime.

Recently a new emission band peaking at 7.6 eV has been found when a BaF_2 sample was cooled down to 9 K [10]. In accordance with the simple energy band model of CRL the spectrum of CRL in BaF_2 covers the spectral region corresponding to the F 2p – Ba $5p_{3/2}$ electron transitions. Taking into account that the spin-orbit splitting of the Ba 5p band is 2 eV and that the main CRL band in BaF_2 is situated at 5.6 eV the new emission band at 7.6 eV was tentatively ascribed in [10] to the F 2p – Ba $5p_{1/2}$ electron transition. Since the widths of the bands in the photoelectron spectra are rather wide due to phonon broadening, we failed in our attempts to separate completely the spin-orbit components of the Ba $5p_{3/2,1/2}$ band in BaF_2 at LNT. However the gap between spin-orbit sub-bands of the Ba 5p band seems really to exist. It is possible that a narrow gap between the $5p_{1/2}$ and $5p_{3/2}$ sub-bands decreases strongly the probability of relaxation for core holes from the lower into the upper sub-band at low temperature.

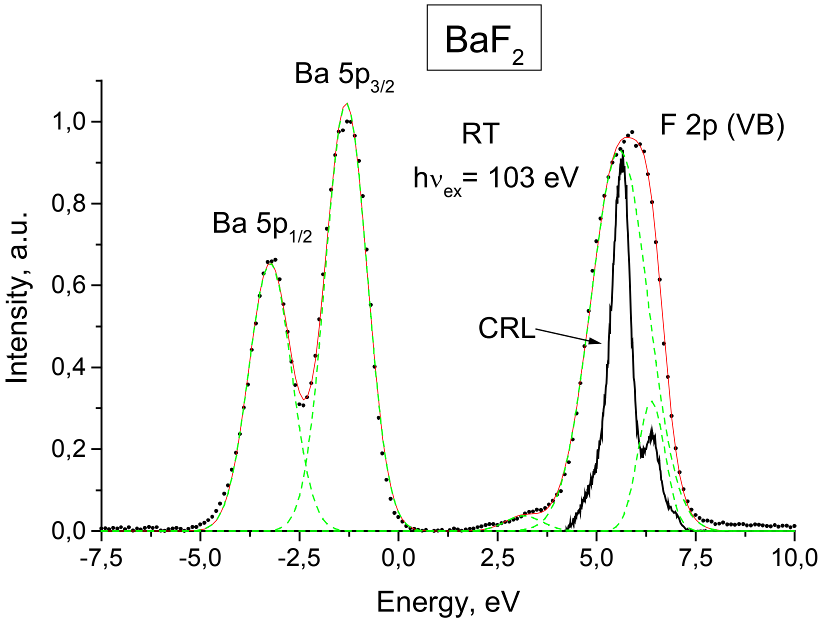

Fig.2. Comparison of photoelectron and crossluminescence spectra for BaF_2. T=300 K.

4. Conclusions

The photoelectron spectra for the *in situ* evaporated thin films of BaF_2 were recorded without remarkable influence of surface charging, for the first time at low temperature (80 K), with much better energy resolution (≤50 meV) than those obtained before by other authors. It was found that phonon broadening of Ba $5p_{1/2}$ and Ba $5p_{3/2}$ photoelectron bands differs from each other. The uppermost core (Ba $5p_{3/2}$) band shows a typical law of phonon broadening due to interaction with characteristic phonon frequencies of lattice vibrations. A comparison of crossluminescence and photoelectron spectra for BaF_2 has allowed to estimate the relaxation energy of the core (Ba $5p_{3/2}$) hole during its radiative lifetime with respect to crossluminescence transition. The photoelectron spectra obtained at low temperature favors the model of the F 2p – Ba $5p_{1/2}$ electron transition for the new emission band of BaF_2 at 7.6 eV.

5. Acknowledgements

The support of the Russian-German Laboratory at BESSY, INTAS Grant 99-01350 and Graduiertenkolleg "Fields and localized atoms – Atoms and localized fields: Spectroscopy of localized atomic systems“ is gratefully acknowledged.

References

[1] P.H. Citrin, P. Eisenberger, D.R. Hamann, Phys. Rev. Lett. 33 (1974) 965.

[2] J.A.D. Matthew, M.G. Devey, J. Phys.C: Solid State Phys. 7 (1974) L335.

[3] R.T.Poole, J.Szajman, R.C.G.Leckey, J.G.Jenkin, J.Liesegang, Phys. Rev. B12 (1975) 5872.

[4] V.K. Adamchuk, A.E. Kuchma, S.L. Molodtsov, Phys. stat. sol. (b) 155 (1989) 525.

[5] S.L. Molodtsov, A. Puschmann, C. Laubschat, G. Kaindl, V.K. Adamchuk, Phys. Rev. B44 (1991) 1333.

[6] G.K. Wertheim, J.E. Rowe, D.N.E. Buchanan, P.H. Citrin, Phys. Rev. B51 (1995) 13669.

[7] N.Yu. Kirikova, J.C. Krupa, V.N. Makhov, C. Severac, J. Electr. Spectr. Relat. Phenom. 122 (2002) 85.

[8] Yu.M. Aleksandrov, V.N. Makhov, P.A. Rodnyi, T.I. Syrejshchikova, M.N. Yakimenko, Sov. Phys. - Solid State 26 (1984) 1734.

[9] V.N. Makhov, I. Kuusmann, J. Becker, M. Runne, G. Zimmerer, J. Electr. Spectr. Relat. Phenom. 101-103 (1999) 817.

[10] M. Kirm, A. Lushchik, Ch. Lushchik, V. Makhov, E. Negodin, S. Vielhauer, G. Zimmerer, Nucl. Instr. and Meth. A 486 (2002) 422.

Electronic and atomic structure of cobalt silicides at initial stages of their formation

M.V.Gomoyunova [1], I.I.Pronin [1], N.R.Gall [1], S.L.Molodtsov [2], D.V.Vyalikh [3]

[1] Ioffe Physico-Technical Institute, 194021, St.Petersburg, Russia
[2] Institut für Oberflächenphysik und Mikrostrukturphysik Fachrichtung
Physik Technische Universität Dresden, D-01062 Dresden, Germany
[3] FU-Berlin 14195 Berlin-Dahlem, Germany

The Co/Si(100) system represents both scientific and technological interest due to a possibility of formation of the atomically abrupt $CoSi_2$/Si interface and the unique properties of cobalt disilicide films. The initial stages of $CoSi_2$ formation reveal rather complex behavior, so the problem is still under discussion. For example, there is no generally accepted point of view concerning the question, whether atomic Co reacts with the substrate to produce $CoSi_2$-like compound at the room temperature, or not [1-5]. The aim of the present work was to investigate the evolution of electronic and atomic structure of ultra thin cobalt silicide layers formed in UHV by means of solid phase epitaxy. To obtain such kind of information we have applied the photoelectron spectroscopy (PES) with a high energy resolution (140 meV) using beamline with the photon energy of 50 - 130 eV.

The experiments were carried out in a vacuum chamber with a base pressure $\sim 5\times10^{-11}$ Torr. The substrates used were Si(100) wafers with a misorientation of less than 0.1°. Before introduction into UHV they were prepared by wet chemical treatment according to the method of Shiraki. For final preparation, the samples were flashed up to 1200°C and cooled slowly, with the rate of less than 50°C/min, that ensured the 2×1 LEED pattern and the absence of C and O contaminations. Element composition of surfaces was monitored by PES. Co was deposited from an electron bombardment evaporator at a rate of ~ 1 ML/min (1ML = 6.8×10^{14} Co atoms/cm^2).

At the first stage of experiment ultra thin Co layers (≤10 ML) of increasing thickness were deposited on the clean silicon surface and the sets of Si2p, Co3p and valence-band spectra were taken after each deposition. The core lines were measured at photon energy of 130 eV to obtain the highest surface sensitivity. The valence-band photoelectron spectra were taken in a wide solid angle oriented along to the surface nornal. At the second step to investigate both the solid phase reaction between deposited Co and Si surface and the thermal stability of $CoSi_2$ films the similar data were obtained after stepwise sample heating until the temperature of 900°C.

The results obtained are illustrated in Fig. 1. Decomposition of the spectrum of Si(100)2×1 have revealed in accordance with Ref. [6] the presence of five surface components shifted relative to the bulk one. To minimize the complexity of the figure only two $2p_{3/2}$ surface modes (S_u and S_d) associated with upper and down atoms of asymmetric Si dimers are shown, the rest ones are combined with the bulk component into the B_1 mode. Adsorption of cobalt results in disappearance of the S_u and S_d modes, indicating the loss of initial reconstruction of the silicon surface. The effect can be explained by incorporation of chemisorbed Co into the top surface layer between four Si atoms, which saturates their dangling bonds. A new mode arising due to Co adsorption is shifted to lower binding energy relative to the bulk line that is evidence for the absence of nuclei of $CoSi_2$-like compound. Further Co deposition gives rise to intensive S mode of the spectra attributed to a solid solution Co-Si film, which turned out to be not continuous.

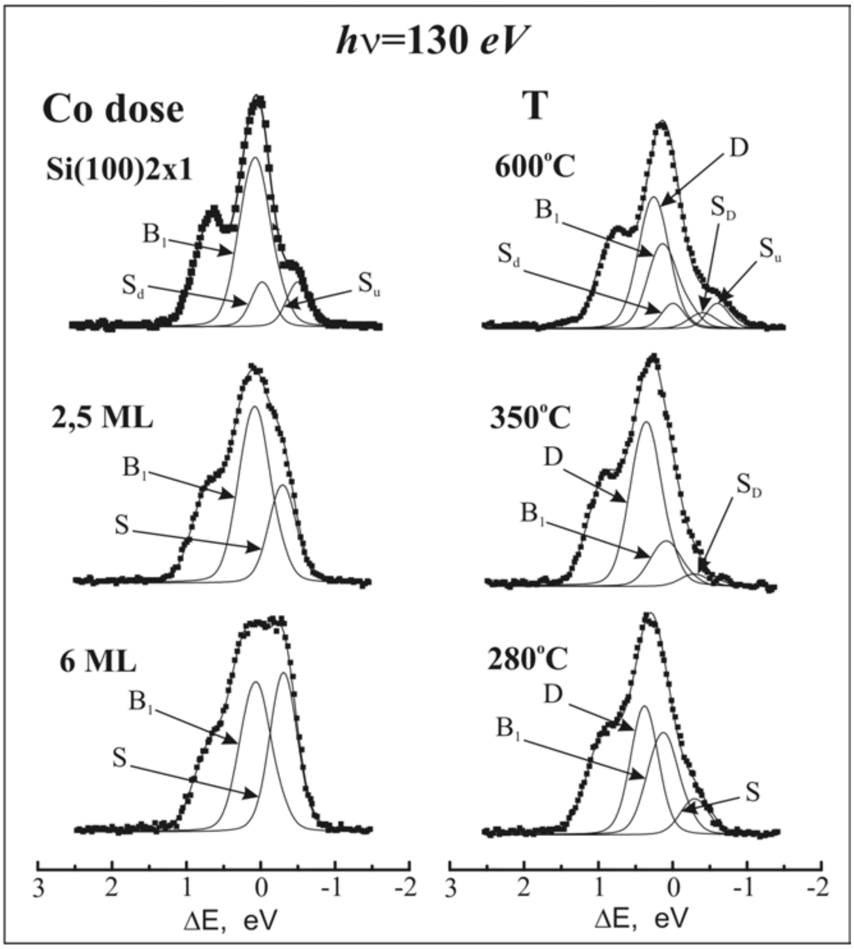

Fig.1. Background subtracted Si 2p spectra obtained for Co/Si(100) system and the results of their fitting. Left column illustrates the data related to room temperature Co deposition while the right one shows the spectra measured after annealing the sample covered with 6 ML of cobalt.

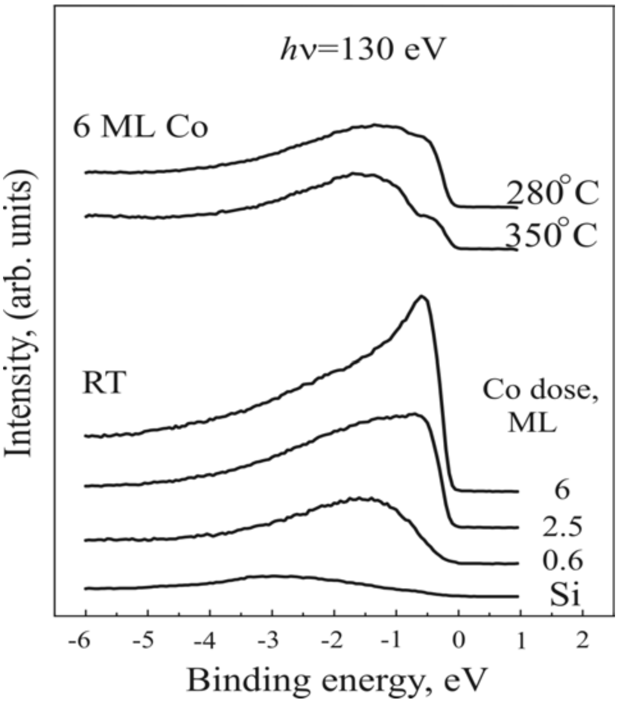

Fig. 2. Valence band spectra obtained for Co/Si(100) system during room temperature deposition of cobalt and subsequent heating the sample.

During sample annealing the changes in Si 2p spectra were found at the temperature of ~250°C. We observed both appearance of a new component (D) shifted to higher binding energy relative to the mode B_1 and decrease of the S component being an evidence for solid phase reaction between Co and Si. The energy shift of D mode is typical for the one of $CoSi_2$ with the stable CaF_2-structure. The reaction is completed at ~350°C when the S component is replaced by the S_D one, which can be attributed to the surface component of epitaxial film $CoSi_2(100)$. Further annealing at 600°C gives rise to both the increase of the B_1 component and a new observation of S_u and S_d modes typical for asymmetric dimers of the Si(100)2×1 surface, that is an evidence for pinholes formation.

Considerable changes observed in the valence band structure (see Fig. 2) during both the room temperature cobalt deposition and subsequent sample annealing confirm the foregoing conclusions.

The study was supported by Russian Foundation for Basic Research (grantt № 01-02-17288), Russian Ministry of Science (contract № 40.012.1.1.1152) and the Russian-German laborattory at BESSY II.

References

1. J.M. Gallego, R. Miranda, S.L. Molodtsov, C. Laubschat and G. Kaindl, Surf. Sci. 239 (1990) 203.
2. H.L. Meyerheim, U. Döbler and A. Puschmann, Phys. Rev. B44 (1991) 5738.
3. G. Rangelov, P. Augustin, J. Stober, and Th. Fauster, Phys. Rev. B49 (1994) 7535.
4. U. Starke, W. Weiss, G. Rangelov, Th. Fauster, G.R. Castro, K. Heinz, Surf. Sci. 352-354 (1996) 89.
5. W.S. Cho, J.Y. Kim, N.G. Park, I.W. Lyo, K. Jeong, S.S. Kim, D.S. Choi, S.N. Whang, K.H. Chae, Surf. Sci., 453 (2000) L309.
6. T.-W. Pi, C.-P. Ouyang, J.-F. Wen, L.-C. Tien, J. Hwang, C.-P. Cheng, G.K. Wertheim, Surf. Sci. 514 (2002) 327.

High-resolution near-edge fine structure in F 1s absorption spectra of 3d metal fluorides.

A.S. Vinogradov [1], S. I. Fedoseenko [1], S.A. Krasnikov [1,2], A.B. Preobrajenski [1,3],
V.N. Sivkov [1], D.V. Vyalikh [4,5], S. L. Molodtsov [1,4,6], V. K. Adamchuk [1],
C. Laubschat [6], and G. Kaindl [4]

[1] *V.A. Fock Institute of Physics, St. Petersburg State University, St. Petersburg, 198504 Russia*
[2] *W. Ostwald-Institut für Physikalische und Theoretische Chemie, Universität Leipzig, D-04103, Leipzig, Germany*
[3] *MAX-lab, Lund University, S-22100 Lund,Sweden*
[4] *Russian--German Laboratory at BESSY II, 12489 Berlin-Adleshof, Germany*
[5] *Institut für Experimentalphysik, Freie Universität Berlin, 14195 Berlin, Germany*
[6] *Institut für Oberflächen- und Mikrostrukturphysik, Technische Universität Dresden, 01062 Dresden, Germany*

In this paper we report high-resolution F 1s absorption spectra measured for the first time for a series of transition metal (TM) fluorides TiF_4, VF_4, VF_3, CrF_3, CrF_2, MnF_3, MnF_2, FeF_3, FeF_2, CoF_2, NiF_2, and ZnF_2. Fluorides were selected for the study because they are the most ionic, and among the simplest, of the 3d-metal compounds. Therefore, the understanding of their X-ray absorption (XA) spectra may help to explain the spectral features and electronic structure in more complicated covalent compounds. In the context of a simple ionic model it is natural to assume that the covalent TM 3d – F 2p bonding is virtually absent in TM fluorides. In this case the F^- $2p^6$ and M^{x+} $3d^n$ electrons make up two different subbands in the valence band, while the unoccupied 3d states of TM cation form the lower conduction band. Although X-ray absorption spectroscopy (XAS) has been widely used for several decades for obtaining information on unoccupied electronic states in TM compounds, systematic XAS studies of the role of the covalent mixing (hybridization) between the TM 3d electrons and ligand valence electrons in the formation of the electronic structure of these compounds are practically nonexistent. By a comparative analysis of the F 1s absorption spectra of TM fluorides we show that even in the case of such strongly ionic compounds of the 3d atoms as fluorides the covalent bonding plays an important role, causing a mixed TM 3d – F 2p character of vacant electronic states near the bottom of their conduction band.

The F 1s spectra in binary fluorides TiF_4, VF_4, VF_3, CrF_3, CrF_2, MnF_3, MnF_2, FeF_3, FeF_2, CoF_2, NiF_2, and ZnF_2, as well as in the gas-phase SF_6 molecule and in the PF_6^- and TiF_6^{2-} molecular anions of the solid compounds KPF_6 and K_2TiF_6 were measured at the Russian-German soft-X-ray beamline at BESSY II [1]. The spectra of solid and gaseous samples were taken by detecting the total electron yield from the sample and the photoionization yield, respectively. The energy resolution of the monochromator ΔE in the range of the F 1s absorption edge (~690 eV) was estimated to be approximately 115 meV. The other experimental details were given in our previous work [2], some of the spectra presented in this paper were briefly discussed at the same place.

Figure 1 shows high-resolution F 1s absorption spectra for binary fluorides of 3d atoms measured for the photon energy of 675-760 eV and normalized to the same absorption jump. Evidently, they differ very strongly both from the F 1s spectrum of the molecular anion TiF_6^{2-} in K_2TiF_6 and along the series of 3d-metal fluorides (with increasing number of TM 3d electrons: TiF_4 – VF_4 – VF_3 – CrF_3 – CrF_2 – MnF_3 – MnF_2 – FeF_3 – FeF_2 – CoF_2 – NiF_2 – ZnF_2). Nevertheless, one can distinguish three spectral ranges, whose structural features are similar for all the spectra, including that of covalent titanium hexafluoride. The first range, at about 2–7 eV, contains narrow resonances a, b, a', and b' located below the F 1s threshold (~690 eV), with their number varying between one and four. The second range is dominated by broader absorption bands c, d, and e that are located slightly above the absorption edge and significantly overlap with each other. It should be noted that despite the lower energy resolution of the F 1s absorption spectrum of ScF_3 taken for the photon energy range of 683-707 eV in Ref. [3], this spectrum also contains two similar ranges. The third energy range (above 700-705 eV) contains very broad and less intensive EXAFS-like oscillations.

Since for all fluorides under study an octahedral or nearly octahedral coordination of 3d atoms to fluorine is typical, these crystals are commonly considered as three-dimensional arrays of interlinked distorted MF_6 octahedra [4]. In this case, possible covalent bonding between the 3d atom M and surrounding fluorine atoms can, evidently, take place within the octahedron due to the mixing of the valence M 3d, 4s, and F 2p electronic states. To elucidate how this hybridization of the valence states can manifest itself in the F 1s absorption spectra of binary TM fluorides, we compared F 1s NEXAFS for the following isostructural covalent systems: the gas-phase SF_6 molecule and the solid-state molecular anions PF_6^- and TiF_6^{2-}, representing isolated regular octahedral [2]. Based on this comparative study, it was found that very narrow low-energy absorption peaks a and b in the spectrum of TiF_6^{2-} are associated with the F 1s electron transitions to lowest unoccupied MO's t_{2g} and e_g of the anion. These molecular states are mainly localized on the central (titanium) atom and are largely determined by its vacant 3d states, which are split in the anisotropic field of the fluorine octahedron into $3dt_{2g}$ and $3de_g$ components. They can be observed in the F 1s absorption spectrum of the TiF_6^{2-} anions due to the covalent bonding between the titanium and fluorine atoms causing a hybridized Ti 3d – F 2p character of these unoccupied electronic states.

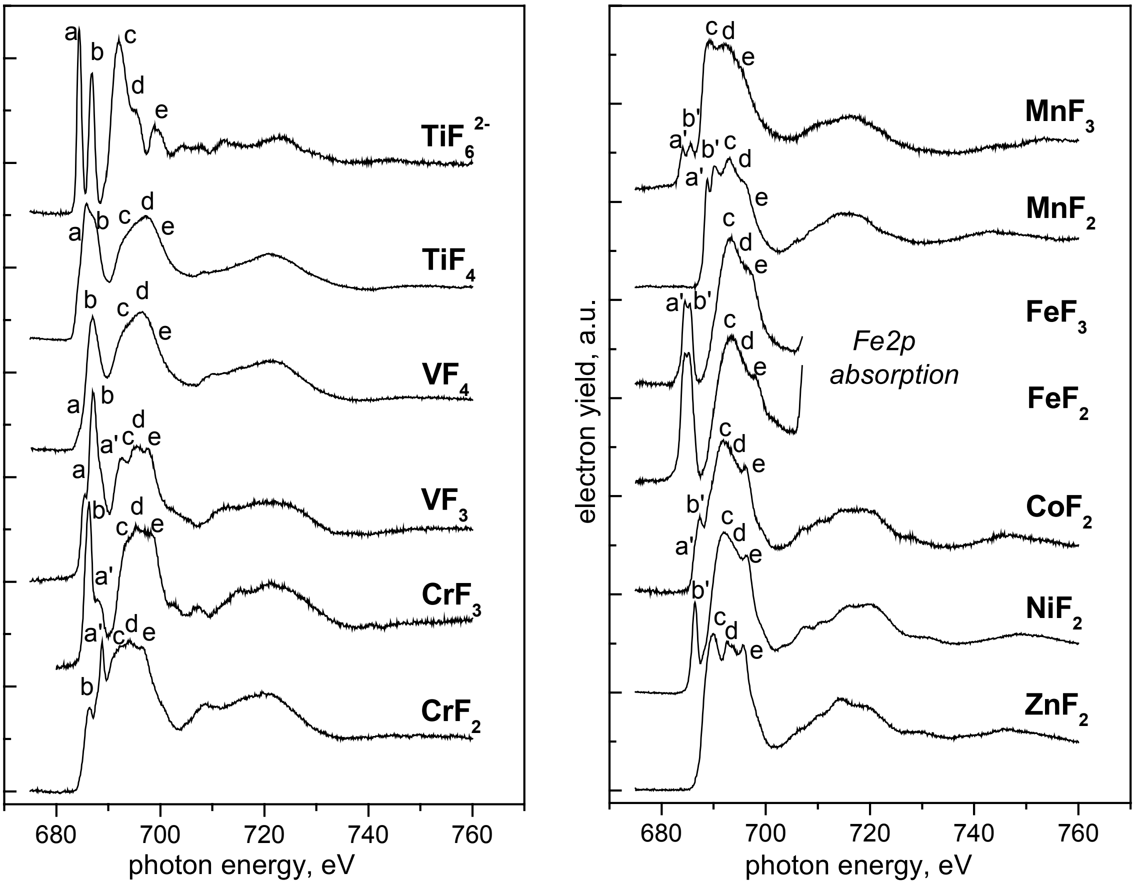

Fig. 1. *High-resolution F 1s absorption spectra of 3d atom fluorides. The spectra are normalized to the same continuum jump at the photon energy of 760 eV.*

By considering the low-energy structure in the F 1s absorption spectra in more detail (Fig. 2), one can see the similarity in general appearance and energy position for this structure in the spectra of ionic fluorides and the covalent molecular anion TiF_6^{2-}. This allows us to assign it in both cases to the free electron states with the mixed TM 3d – F 2p character resulting from the significant covalent bonding between the valence electrons of the metal and fluorine atoms. However, in going from the TiF_6^{2-} anion to the binary fluorides and further along the series TiF_4 - … - ZnF_2 the spectra of Fig. 2 exhibit marked changes in the number and relative intensity of the resonances, as well as in their energy positions with respect to each other and to the F 1s absorption edge. These changes are likely to be caused by (i) a decrease in number of unoccupied 3d states of the metal atom accompanied by a larger localization of these states along the series under study, (ii) a different exchange interaction between the 3d electrons in partially filled shells, (iii) a change in size of the fluorine octahedron and the character of its distortion, and (iv) a differing impact of the remaining part of the crystal on the quasi-molecule MF_6, which manifests itself particularly in a different coupling between these structural units in the crystal. Therefore, a complete understanding of all these changes is possible (if ever!) only on the basis of sophisticated theoretical calculations of the F 1s NEXAFS of binary fluorides, which unfortunately are not reported in the literature so far.

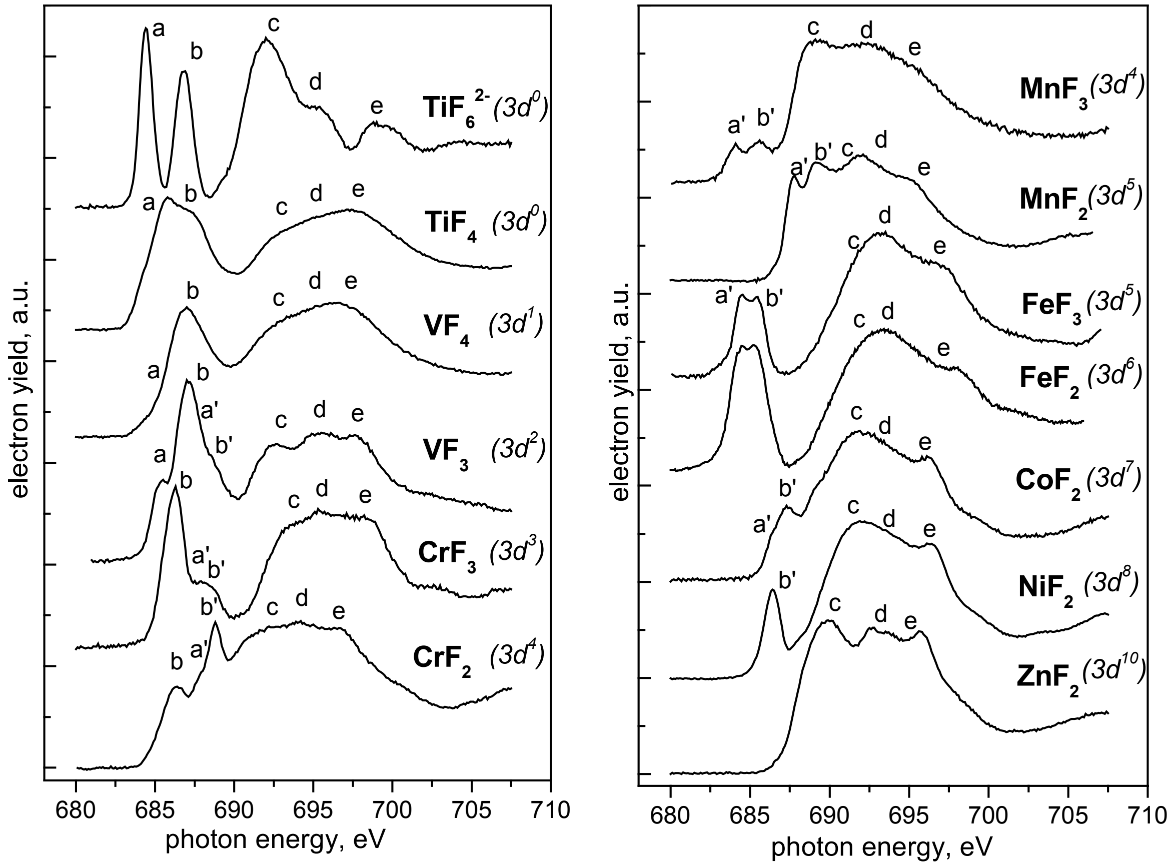

***Fig.2**. Low-energy fine structure of F 1s absorption spectra for 3d-atom fluorides.*

In conclusion, we emphasize that the basic results of our study provide a strong experimental evidence for importance of covalent mixing in the formation of unoccupied electronic states in crystalline 3d-TM fluorides. The F 1s absorption spectra are found to be of considerable promise in probing unoccupied 3d states of the central (TM) atoms in these compounds. On the whole, our results agree well with the conclusions of similar studies of compounds with less ionic character, 3d-TM oxides.

Acknowledgements

This work was supported by the Russian Foundation for Basic Research (project no. 01-03-32285), the Ministry of Industry and Science of the Russian Federation (project no. 40.030.1.1.11.17) and the Deutsche Forschungsgemeinschaft (SFB 463, TPB-4). We thank the staff of BESSY II for valuable technical assistance. A.S. Vinogradov, S.I. Fedoseenko and V.N. Sivkov gratefully acknowledge the financial support of BESSY and the Technische Universität Dresden. A.B. Preobrajenski warmly acknowledges the support of the Swedish Foundation for International Cooperation in Research and Higher Education (STINT).

References

1. S. A. Gorovikov, S. L. Molodtsov, and R. Follath, *Nucl. Instrum. Methods Phys. Res. A **411**, 506 (1998);* S. A. Gorovikov, R. Follath, S. L. Molodtsov, and G. Kaindl, *Nucl. Instrum. Methods Phys. Res. A **467-468**, 565 (2001);* S. I. Fedoseenko, I. E. Iossifov, S. A. Gorovikov, et al., *Nucl. Instrum. Methods Phys. Res. A **470**, 84 (2001).*
2. A.S. Vinogradov, S.I. Fedoseenko, D.V. Vyalikh, et al., *Annual Report BESSY 2001,162 (2002); Optika i Spektros.**93**, 935 (2002) [Optics and Spectrosc. **93**, 862 (2002)].*
3. M. Umeda, Y. Tezuka, S. Shin, and A. Yagishita, *Phys. Rev. B **53**, 1783 (1996).*
4. A. Wells, *Structural Inorganic Chemistry,(Clarendon, Oxford, UK, 1984).*

What the resonance peak does: anomalous enhancement of the coupling to the magnetic resonance mode in underdoped Pb-Bi2212.

Sergey Borisenko[1], Alexander Kordyuk[1,2], Timur Kim[1], Andreas Koitzsch[1], Martin Knupfer[1], Mark Golden[1,3], Jörg Fink[1], M. Eschrig[4], H. Berger[5], R. Follath[6]

[1]Institute for Solid State Research, IFW-Dresden, P.O.Box 270116, D-01171 Dresden, Germany
[2]Institute of Metal Physics of National Academy of Sciences of Ukraine, 03142 Kyiv, Ukraine
[3]Van der Waals-Zeeman Institute, University of Amsterdam, NL-1018 Amsterdam, The Netherlands
[4]Institut für Theoretische Festkörperphysik, Universität Karlsruhe, D-76128 Karlsruhe, Germany
[5]Institute of Physics of Complex Matter, EPFL, CH-1015 Lausanne, Switzerland
[6]BESSY GmbH, Albert-Einstein-Strasse 15, D-12489 Berlin, Germany

The sharp magnetic resonance peak observed in inelastic neutron scattering experiments [1] is unanimously considered to be one of the most striking features of the high temperature superconducting cuprates which suggests an important role of magnetism in the mechanism of the HTSC [2]. It has been argued that the emergence of the resonance below the superconducting transition has a strong feedback effect on the electronic properties of the cuprates, leading to the appearance of the peak-dip-hump (PDH) features in the angle-resolved photoemission (ARPES) spectra. Previous doping dependent ARPES studies [3] revealed a close connection between features in the spectral function and characteristics of the resonance mode, assuming that bilayer splitting effects were not relevant. Since this is clearly not the case -- we have shown recently [4] that such effects are dominant in PDH formation, at least in overdoped Pb-Bi2212 -- we apply high-resolution ARPES with variable excitation energies to disentangle bilayer splitting effects and intrinsic (self-energy) effects in the electronic spectral function near the $(\pi,0)$-point of differently doped Pb-Bi2212 [5]. In contrast to overdoped samples, where intrinsic effects at this point are virtually absent, we find in underdoped samples intrinsic effects in the superconducting-state $(\pi,0)$ spectra of the antibonding band (see panels a-c in Fig.). The collection of energy distribution maps shown in panels d-l of the Figure is an important and completely new dataset of ARPES data as they cover the $(\pi,0)$ region of both the overdoped *and* underdoped regimes for photon energies which differingly select the two bilayer-split bands. The coupling to the resonance mode makes itself felt as complete “wipe-out” of spectral weight at energies some 30-40 meV below the peak feature near (π,0).

This intrinsic effect is present only below the critical temperature T_C and weakens considerably with doping. Our results give strong support for models [6] which involve a strong coupling of electronic excitations with the resonance mode seen in inelastic neutron scattering experiments.

[1] e.g. J. M. Tranquada et al., Phys. Rev. B 46, 5561 (1992)
[2] e.g. Ar. Abanov and A. Chubukov, Phys. Rev. Lett. 83,1652 (1999)
[3] J. C. Campuzano et al., Phys. Rev. Lett. 83, 3709 (1999)
[4] A. A. Kordyuk et al., Phys. Rev. Lett. 89, 077003 (2002)
[5] S. V. Borisenko et al., cond-mat/0209435
[6] e.g. M. Eschrig and M. R. Norman, cond-mat/0206544

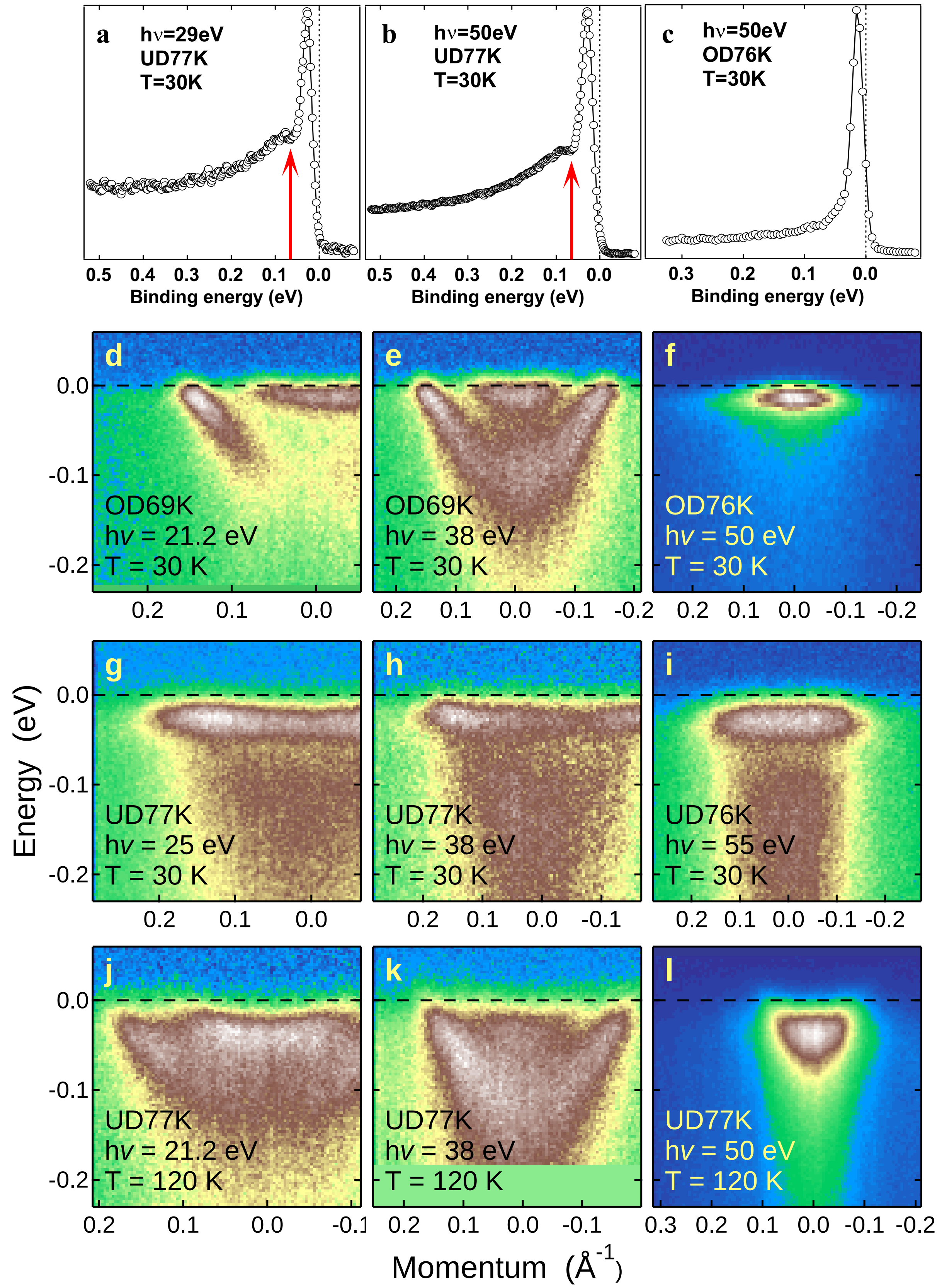

Figure caption:

(a)-(c) EDCs taken at (π, 0) using 29 and 50 eV excitation energies at which the contribution of the bonding states to the lineshape is negligible, thus unmasking the 'intrinsic' lineshape of the antibonding component. (d)-(l) Energy distribution maps taken straddling the (0,0)-(π,0) alongs cuts parallel to (π, π) — (π, 0) — (π, −π).

Superconducting gap in the presence of bilayer splitting in underdoped Pb-Bi2212.

Sergey Borisenko[1], Alexander Kordyuk[1,2], Timur Kim[1], Konstantin Nenkov[1], Martin Knupfer[1], Mark Golden[1,3], Jörg Fink[1], H. Berger[4], R. Follath[5]

[1]Institute for Solid State Research, IFW-Dresden, P.O.Box 270116, D-01171 Dresden, Germany
[2]Institute of Metal Physics of National Academy of Sciences of Ukraine, 03142 Kyiv, Ukraine
[3]Van der Waals-Zeeman Institute, University of Amsterdam, NL-1018 Amsterdam, The Netherlands
[4]Institute of Physics of Complex Matter, EPFL, CH-1015 Lausanne, Switzerland
[5]BESSY GmbH, Albert-Einstein-Strasse 15, D-12489 Berlin, Germany

The clearly resolved bilayer splitting in angle-resolved photoemission (ARPES) spectra of the underdoped high-temperature superconductor Pb-Bi2212 rises the question of how the bonding and antibonding sheets of the Fermi surface are gapped in the superconducting state (Fig. 1). Here we show that exploiting the relative variation of the photoionisation matrix elements for the bilayer split components, we are able to independently determine the leading edge gaps (LEG) corresponding to the different sheets of the Fermi surface in the superconducting state.

We have tuned the relative intensity of the bonding and antibonding bands using the different excitation conditions, i.e. varying the energy of the incident photons (Fig. 2). Looking at the “map of gaps” recorded using the photon energy of 25 eV (Fig.3, left panel) one can clearly see that both Fermi surface sheets are gapped. Our results suggest that within the experimental uncertainties both gaps are identical (Fig. 3, right panel).

As implied by the data presented on Fig. 2, choosing the excitation conditions in a way which results in the suppression of the photocurrent corresponding to the antibonding component we can determine the **k**-dependence of the LEG for its bonding counterpart for which emission then is favorable.

For the precise determination of **k**-dependence of the superconducting gap and thus its symmetry one needs to accurately locate a position on the (former) Fermi surface. For such precise navigation in **k**-space we recorded an intensity map (Fig. 4a), which facilitates identification of the **k**-vectors. Fig. 4b shows the greyscale "map of gaps" corresponding to the same area of the **k**-space. Visual inspection of the map of gaps already clearly points to the anisotropic character of the gap. The same dataset replotted in other coordinates, LEG value versus Fermi surface angle ϕ, gives the red symbols shown in Fig. 4c. The curve joining the low-gap extremity of these data points represents the true **k**-dependence of the superconducting LEG (Fig. 4c).

As is clear from the comparison shown in Fig. 4c, that the obtained **k**-dependence of the LEG for these underdoped crystals is quite different from that expected in the case of a simple d-wave gap function $\cos(k_x)-\cos(k_y)$ and could be explained invoking higher harmonics of the gap.

For details see Borisenko et al., Phys. Rev. B66, 140509(R) (2002).

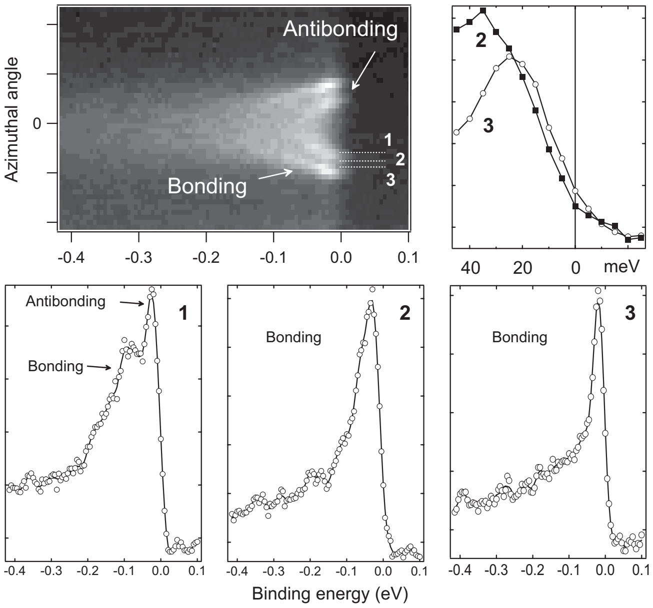

Fig.1 EDM showing the clearly resolved bilayer splitting and exemplary EDCs which illustrate how erroneous could be the determination of the superconducting gap if one does not take into account the bilayer splitting.

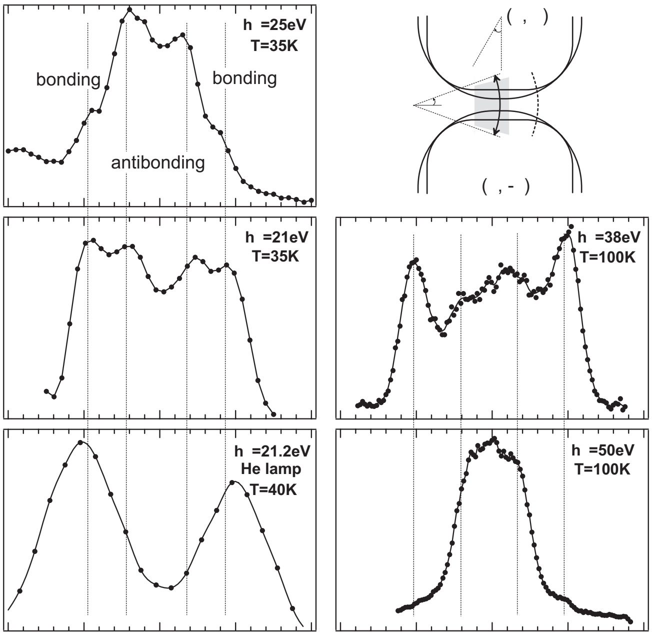

Fig.2 Azimuthal MDCs showing how relative intensity of the bonding and antibonding components could be tuned by choosing a suitable excitation energy. Inset illustrates which parts of **k** space were probed.

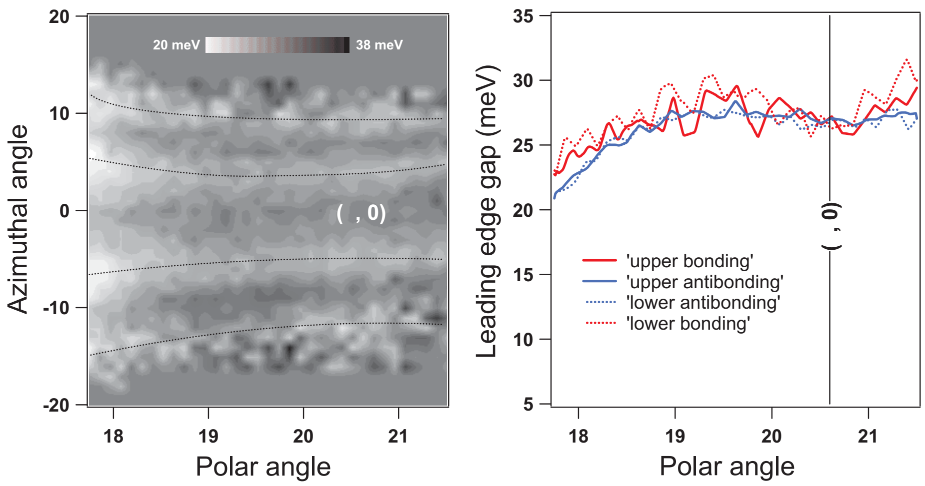

Fig.3 “Map of gaps” (color coded binding energies of the leading edges) taken in the part of the **k** space shown in the inset to Fig.2, and leading edge gaps (right panel) along the lines which correspond to both Fermi surfaces.

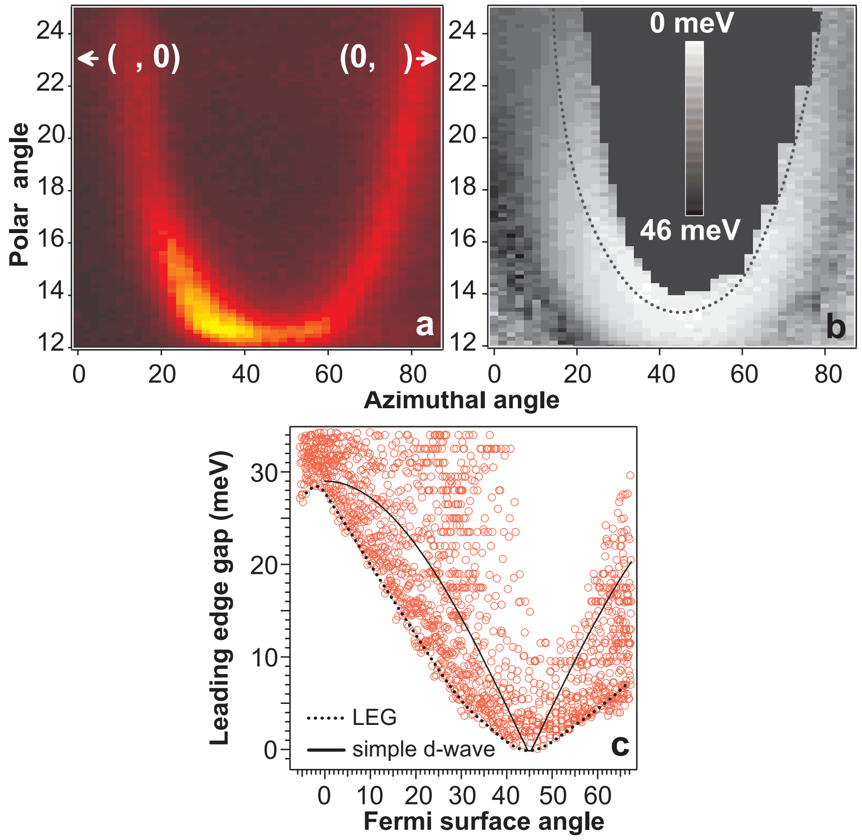

Fig.4 a) Angular distribution map of the photoemission intensity integrated showing the locus of $\mathbf{k}_F$-points. b) “Map of gaps” within the similar **k**-space area. c) Plot of the leading edge gaps as a function of the angle around the Fermi surface.

UPS study of oxidation process for yttrium surface

M.N.Mikheeva[1], V.G.Nazin[1], M.Y.Kuznetsov[1], S.L. Molodtsov[2],
D.V.Vyalikh[3], M.V.Poiguine[4]
[1] *Russian Research Centre "Kurchatov Institute" , Moscow, Russia*
[2]*Institut f. Oberflaechenphysik u. Mikrostrukturphysik Fachrichtung Physik Technische Universitaet, Dresden, Germany*
[3]*Free University of Berlin, Germany*
[4]*Saint-Petersburg State University, Saint-Petersburg, Russia*

The discovery of high temperature superconductivity (HTSC) of oxygen deficient complex copper-based oxides [1] had lead to great interest to study oxides of metals. During investigations of HTSC La2CuO4 single crystals we found large resonance of valence band states near La5p threshold [2]. Intensity of resonance depended on orientation of emission angle, crystal axes and polarization [3]. Recently we have studied oxidation process for lanthanum[4] and found similar resonance of valence band states occurs near La5p excitation threshold for metallic La surface with small oxidation level [5]. In spite of polycrystalline sample structure we observe ordered structure of lanthanum surface with ~0.5 L of oxygen. It is worth noticing that such resonance was not observed for pure metal surface and "heavy" oxidized surface (oxidized with high oxygen doses). It is interested to study of yttrium in order to make comparison of oxidation process and electronic structure of these two metals. Indeed this metals have the same symmetry of electron wave functions. The only difference is nuclear charge and therefore presence of empty La4f states some above Fermi level. The purpose of our work is to investigate oxidation process for yttrium surface and search resonances near Y4p excitation threshold for partly oxidized yttrium metal with low oxygen content at surface.

Our study of the electronic structure changes of yttrium surface during oxidation were made at the Russian German beamline of the BESSY II synchrotron radiation facility. Photoemission (PE) measurements were performed in UHV (base pressure 2×10^{-10} mbar), employing a PE spectrometer equipped with a VG CLAM-4 electron-energy analyzer. Polycrystalline sample of yttrium with 99.9% purity was used. Metal surface was cleaned mechanically *in situ* using tungsten brush by the same procedure as for lanthanum [4,5]. Oxidation was made by injecting pure oxygen into the spectrometer until the pressure achieved $(1\text{- }10)*10^{-8}$ Mbar for 30 – 200 seconds. The dose of D is expressed in Langmuirs L (1 L = 10^{-6} torr*s). All procedures with specimen and measurements were performed at room temperature. UPS measurements were made at photon energies from 24 to 580 eV. Energy scale is referred to Fermi level.

Some of UPS spectra of yttrium surface with different oxidation levels are presented at Fig.1. This measurements were made at photon energy 55 eV in one cycle without changing sample position. Different degrees of oxidation were obtained by subsequent addition of portions of oxygen. As can be seen from the figure, the distinguishing features of spectrum with low oxygen doze (curve 1) are the narrow triangular metal valence band with a sharp maximum near the Fermi level, complex structure of the Y4p states with sharp features at 26 eV and 27.1 eV binding energies. There is also pronounced narrow band of 5.7 eV binding energy with semi width 1.4 eV due to presence of oxygen (D~0.2 L).When increasing oxygen doze the form spectra changed dramatically (curves 2 – 5). For spectrum with high oxidation level (curve 5) metal spectra features disappeared, Y4p states looks like a peak with 28.9 eV binding energy and small shoulder at 30.5 eV binding energy, oxide valence band arises with 4.6 eV width. There is also intensity increasing of peak of O2s level at 21.5 eV binding energy. Oxide energy gap is about 4.5 eV. At oxygen doze above 3 L no pronounced changes of shapes and intensity of spectra were observed – only peak of 12 eV binding energy arises due to adsorption of molecular oxygen at sample surface. It means that oxide layer thickness exceeded photoelectron escape depth. All these results are very close to data for lanthanum [4].

From above data we tried to find resonance near Y4p threshold for partly oxidized yttrium surface (D ~ 0.5 L) at photon energies 24 - 35 eV. No significant increasing of valence band emission was found at any photon energy in this photon energy range. Opposite situation occurs. Some of valence band spectra for yttrium surface with 0.5 L oxygen doze at photon energy range 27.5 – 30.5 eV spectra are presented at Fig.2. As one can see from Fig.2 there is pronounced decreasing of oxide band at photon energies near 30 eV. This feature is more likely due to oxygen electron state structure above Fermi level. So photoemission features near Y4p threshold for yttrium is much more different then for features near La5p threshold for lanthanum.

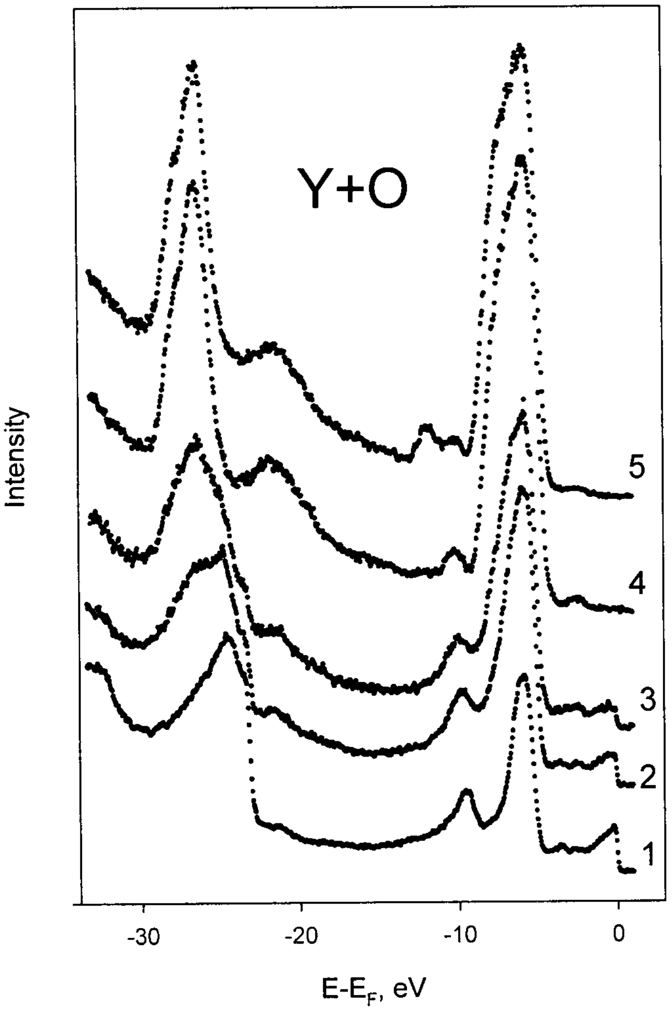

Fig.1. Spectra of yttrium surface with different oxygen dozes: curve 1- D=0.2 L, 2 – D=0.78 L, 3 – D= 1.4 L, 4 – D=3.2 L, 5 – D=30 L. Spectra were measured at photon energy 55 eV.

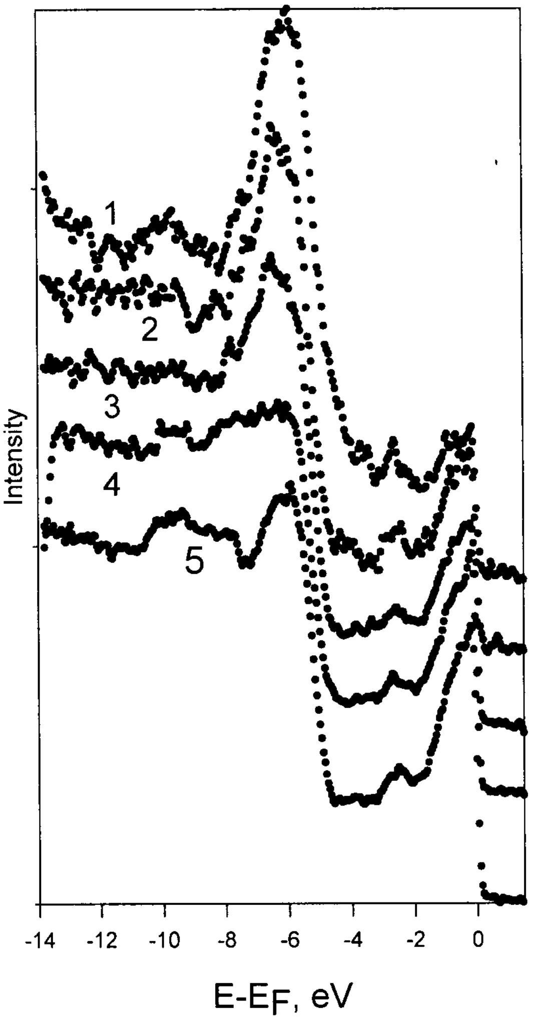

Fig.2. Spectra of yttrium surface with D ~0.5 L 1 – photon energy 27.5 eV, 2 – 29 eV, 3 – 29,5 eV 4 – 30 eV, 5 – 30.5 eV

This work was supported by Russian-German laborattory at BESSY II and RFBR (Russia), project 01-02-17307a .

1. J.G.Bednorz, K.A.Muller, Z.Phys..B, 1986, v.64, 189.

2. M.N.Mikheeva, V.G.Nazin, A.V.Svishchev, D.S.L.Law, T.S.Turner, P.Bailey, D.Teehan, N.Barilo and P.V.Gritskov, Surf.Sci., 287/288 (1993) 662.

3. D.S.-L.Law, M.N.Mikheeva, V.G.Nazin, A.V.Svishchev, M.B.Tsetlin, O.E.Parfionov, Nuclear Instruments and Methods in Physics Research B 97(1995) 148.

4. V.G.Nazin, M.B.Tsetlin, M.N.Mikheeva, L.L.Lev, D.S.-L.Law, N.Hayes, S.Downes, Surface investigation, (1997), v.12, 1113.

5. M.B.Tsetlin, V.G.Nazin, E.A.Shagarov, M.N.Mikheeva, D.S.-L.Law, N.Hayes, S.Downes, Poverhnost', 1998, v.7, 65. (in Russian)

Epitaxial Fe_3O_4 layers on MgO and $MgAl_2O_4$ substrates studied by x-ray fluorescence and absorption spectroscopy

S.A. Krasnikov [1], A.S. Vinogradov [2], K.-H. Hallmeier [1], R. Höhne [3], M. Ziese [3],
P. Esquinazi [3], T. Chassé [1], R. Szargan [1]

[1] Wilhelm-Ostwald-Institut für Physikalische und Theoretische Chemie, Universität Leipzig, Linnéstr. 2, D-04103 Leipzig, Germany; [2] V.A. Fock Institute of Physics, St. Petersburg State University, 198504 St. Petersburg, Russia; [3] Department of Superconductivity and Magnetism, Institut für Experimentelle Physik II, Universität Leipzig, Linnéstr. 5, D-04103 Leipzig, Germany.

Investigation of electronic structure of iron oxides has been an active field of research for several decades [1,2]. Iron oxides are materials of great importance in many technological applications such as catalysts and magnetic devices. Their interesting magnetic as well as electrical properties are attributed to the strong coupling between charge and spin of the electrons and the lattice degrees of freedom in transition metal oxides. Magnetite, Fe_3O_4, a ferrimagnetic material, has received much attention and has been considered as an important potential material for future spintronics. Fe_3O_4 forms in the cubic inverse spinel structure, in which one-third of the iron ions are tetrahedrally coordinated with four oxygen ions and two-thirds are octahedrally coordinated with six oxygen ions.

X-ray absorption spectroscopy (XAS) and x-ray fluorescence (XF) are important and commonly used tools in the study of the electronic structure of matter. The configuration of the empty Fe 3d states in iron oxides is best probed in x-ray absorption experiment by excitation of Fe 2p core electrons to unfilled electronic states. XF due to its elemental selectivity and dipole selection rules allows to study the occupied Fe 3d valence states of iron oxides separately from other states. Nowadays XF becomes more and more popular due to the advent of high-brilliance synchrotron radiation (SR) sources. With x-ray fluorescence and x-ray absorption spectroscopy we studied the electronic structure of epitaxial Fe_3O_4 layers and its dependence on film thickness and the influence of ambient environment.

The x-ray fluorescence measurements on epitaxial Fe_3O_4 layers were performed using the x-ray monochromator XES 300 (mounted on the end station ROSA) and synchrotron radiation at the U41-PGM beam-line at BESSY II. The estimated energy resolution of Fe L emission spectra was better than 1 eV. The axis of the x-ray monochromator was set perpendicular to the beam-line axis in the plane of polarization of incident radiation in order to avoid the elastically scattered peak. The angle between the sample normal and the monochromator axis was 30°. The x-ray absorption measurements on iron oxide layers were performed at the Russian-German beam-line at BESSY II in the total electron yield detection mode. The estimated photon-energy resolution at the Fe $2p_{3/2}$ edge (~710 eV) was better than 0.2 eV. The spectra were normalized monitoring the incident photon flux by means of the I_0-signal of a gold mesh. The Fe_3O_4 films with different thicknesses were prepared at the Department of Superconductivity and Magnetism, Institut für Experimentelle Physik II, Universität Leipzig by pulsed laser deposition (PLD) onto (001)-MgO and (001)-$MgAl_2O_4$ substrates from a ceramic stoichiometric magnetite target. A Lambda-Physik Excimer laser at a wavelength of 248 nm (KrF) operated at a repetition rate of 5 Hz and a pulse energy of 600 mJ was used. The deposition temperature was 550 °C and oxygen partial pressure was 1.0×10^{-5}

mbar. *In situ* prepared thin $BaTiO_3$ protecting layer covered some of the samples to study the influence of the environment.

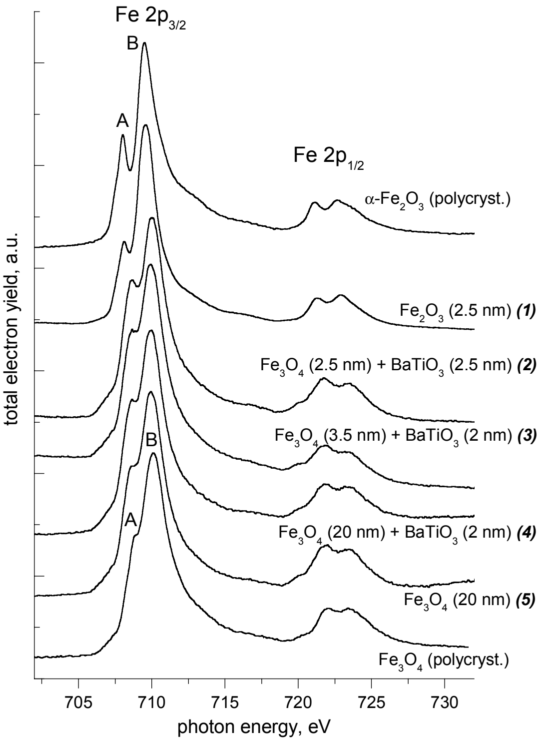

Fig. 1. *Fe 2p absorption spectra of iron oxide films on MgO (samples 1-3) and $MgAl_2O_4$ (samples 4,5) substrates.*

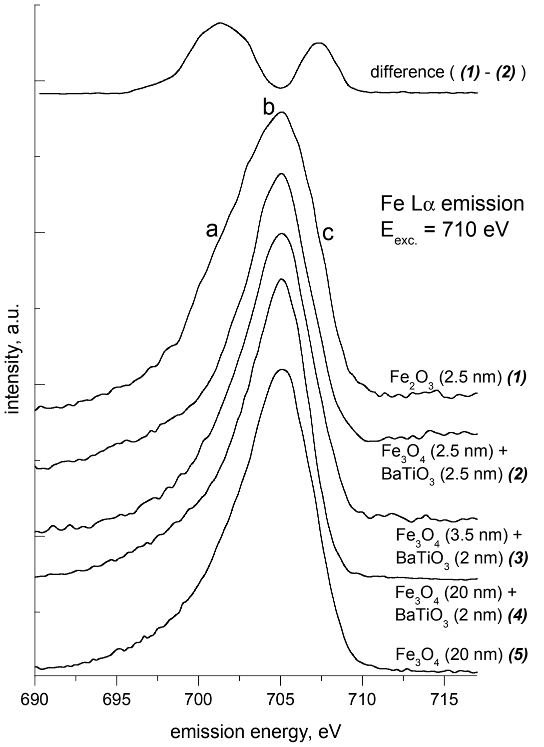

Fig. 2. *Fe Lα emission spectra of iron oxide films on MgO (samples 1-3) and $MgAl_2O_4$ (samples 4,5) substrates. The upper spectrum represents the difference between spectra of samples 1 and 2.*

Figure 1 shows the measured Fe 2p absorption spectra for the studied iron oxide films on MgO and $MgAl_2O_4$ substrates in comparison with previously measured polycrystalline Fe_3O_4 and α-Fe_2O_3 [3]. The relative intensities of the spectra have been normalized to the intensity of the band B. In this paper only the Fe $2p_{3/2}$ spectra will be discussed paying attention to the protection of the Fe_3O_4 films.

Examining the set of Fe $2p_{3/2}$ absorption spectra in Fig. 1 one can see that all spectra have the similar absorption band with the double-peaked structure A-B associated with the transitions of Fe 2p electrons to empty 3d electronic states. In the case of the thick Fe_3O_4 films (samples 4 and 5) the absorption spectra of the films, unprotected and protected by a thin $BaTiO_3$ layer, are identical to the absorption spectrum of the polycrystalline Fe_3O_4 powder. Exactly the same spectra one can see for the protected thin Fe_3O_4 films (samples 2 and 3). In the case of the thin unprotected film (sample 1) the shape of the Fe 2p absorption spectrum is similar to one taken from polycrystalline α-Fe_2O_3 powder. This finding in the shape of absorption spectra means that the thin (2.5 nm) unprotected Fe_3O_4 layer was further oxidized to the Fe_2O_3 stage during one-week oxygen exposure on air. But for the thick (20 nm) Fe_3O_4 films protection by thin $BaTiO_3$ layer plays no significant role on the same time scale. This fact can be originated from the crystal structure of magnetite films on MgO (or $MgAl_2O_4$) substrate. When the thickness of the Fe_3O_4 film is not large enough all layers are strained because of the lattice mismatch between film and substrate, leading to further oxidation. In the case of the thicker Fe_3O_4 films (>20 nm) the layers near the substrate are strained, while the layers on the surface are relaxed [4]. Moreover, the x-ray absorption spectrum of the Fe_2O_3 (2.5 nm) film is similar to the theoretical one for γ-Fe_2O_3 [2]. The XPS measurements for the studied iron oxide films confirm the oxidation state of iron for each sample.

Figure 2 shows the measured Fe Lα (3d→$2p_{3/2}$ transition) emission spectra for the studied iron oxide films on MgO and $MgAl_2O_4$ substrates taken at the excitation energy 710 eV which corresponds to the Fe $2p_{3/2}$ absorption maximum in iron oxides (709.56 eV and 710.05 eV for Fe_2O_3 and Fe_3O_4, respectively). The relative intensities of the spectra have been normalized to the intensity of the emission line b. All emission spectra have the similar shape which consists of main line b and shoulders a and c. In this set of spectra we will pay attention to the difference between the emission spectrum taken from the Fe_2O_3 film (sample 1) and emission spectra taken from Fe_3O_4 films. In order to visualize this shape difference the upper spectrum in Fig. 2 represents the result of subtraction of the emission spectrum measured for the Fe_3O_4 (2.5 nm) film covered with a $BaTiO_3$ (2.5 nm) layer from the emission spectrum measured for the Fe_2O_3 film. One can see that in the case of the Fe_2O_3 film the intensities of shoulders a and c are significantly higher. The increasing of intensities of the shoulders a and c going from Fe_3O_4 to Fe_2O_3 film can be explained by the different structure of these oxides. In the case of Fe_2O_3 iron ions are octahedrally (slightly distorted from perfect O_h symmetry) surrounded by oxygen ions. In Fe_3O_4 iron sites are distorted octahedra and tetrahedra.

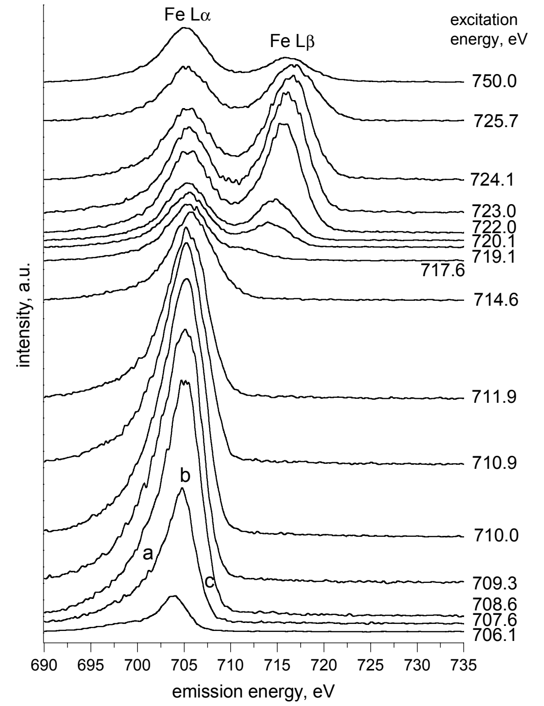

Fig. 3. *Resonant XF spectra of Fe_3O_4 (20 nm) on $MgAl_2O_4$ substrate.*

Figure 3 shows resonant XF spectra of Fe_3O_4 (20 nm) film on $MgAl_2O_4$ substrate across the Fe 2p absorption edge. One can see the enhancement of the Fe Lα and Lβ emission lines when the excitation energy is equal to Fe $2p_{3/2}$ (710 eV) and Fe $2p_{1/2}$ (723 eV) absorption maxima, respectively. To explain the relative changes of intensities of the a, b and c lines theoretical studies are needed.

In summary, it was shown by x-ray absorption and fluorescence measurements on Fe_3O_4 films with different thicknesses that protection of thin Fe_3O_4 (~2.5 nm) films plays a significant role. The structure of the Fe_2O_3 film obtained due to further oxidation of the Fe_3O_4 remains an open question.

Acknowledgements:

We wish to thank C. Jung and S.L. Molodtsov for continuous support at BESSY. This research is supported by the DFG grants GK 152/3 and FOR 404 and by the BMBF grant Nr. 05 SR8OL1-2.

References:

[1] P. Kuiper et al., *Phys. Rev. Lett.* **70** (1993) 1549; T. Fujii et al., *Phys. Rev. B* **59** (1999) 3195.

[2] J.P Crocombette et al., *Phys. Rev. B* **52** (1995) 3143.

[3] A.S. Vinogradov et al., *BESSY Annual Report 2000,* p.160; *Surf. Rev. Lett.* **9** (2002) 359.

[4] C.A. Kleint et al., *J. Appl. Phys.* **84** (1998) 5097; R. Höhne et al., *J. Magn. Magn. Mater.* **211** (2000) 271.

Resonant and nonresonant XES study of s – p, d mixing in the valence band of metal sulfides and complexes

K.H. Hallmeier[1], L. Zhang[1], D. Wett[1], D. Schulze[1], B. Flemmig[1], J. Reinhold[1],
T. Chassé[2], R. Szargan[1]

[1]Wilhelm-Ostwald-Institut für Physikalische und Theoretische Chemie, Universität Leipzig, Linnéstr. 2, D-04103 Leipzig, Germany, [2]Institut für Oberflächenmodifizierung e.V. Leipzig, Permoserstr. 15, D-04318 Leipzig, Germany

The sulfur-metal bonding in complex compounds and layered sulfid systems has attracted increasing interest in the past several years since such materials find many applications in photovoltaics, gas sensing, catalysis and other fields. In earlier investigations the deprotonation of organic molecules containing the atomic sequence (-CS-NH-CO-) during complexation with metal ions in aqueous solution as well as the bidentate bonding of the ligand have been proved by means of chemical shifts of the N 1s and S 2p electron binding energies respectively [1].

In order to obtain a direct evidence for the participation of the thionyl groups of compounds like N-Benzoyl-N'-diethyl-thiourea in sulfur to metal donor bonds of a chelate ring system (see inset, fig. 1), the X-ray emission bands were recorded using the X-ray monochromator XES 300 (mounted on the end station ROSA) and synchrotron radiation at the U41-PGM beam-line at BESSY II.

The intensity profiles of the S $L_{2,3}$ emission bands of the Zn and Cd complexes (fig. 1) are dominated by the local partial density of S 3s states. A clear indication for s-d mixing was found first time for the complexes from a doublet peak on the high energy side of the S $L_{2,3}$ emission band maximum positioned exactly in the region of the Zn 3d or Cd 4d density of states, respectively [2-5].

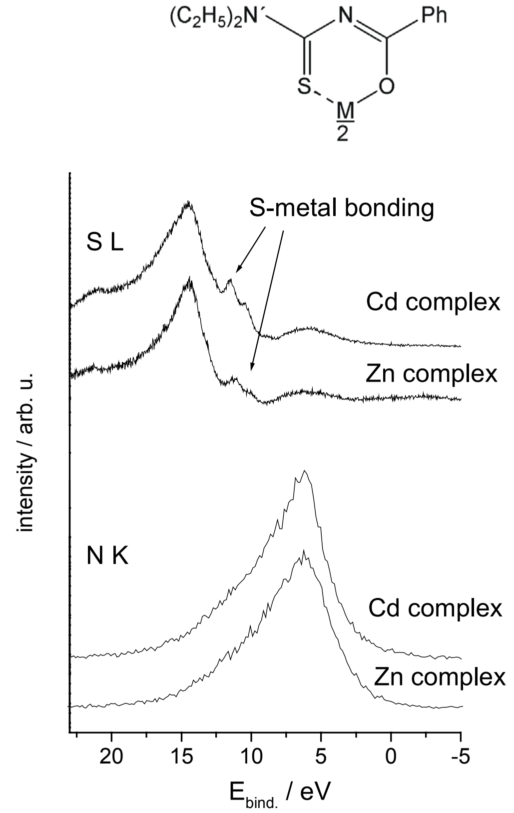

***Fig. 1**: S L and N K X-ray emission spectra of the Cd and Zn complex compounds. The binding energy scale is related to the S $2p_{3/2}$ and N 1s XPS data*

The S $L_{2,3}$ components below 10 eV point at some S 3s - X np (X=C, N,…) mixing in the upper part of the valence band. This region is dominated by p states contributing separately to the K X-ray fluorescence of the individual atoms. In order to elucidate the arrangement of these p components more in detail DFT calculations adopting B3LYP-functionals of the building molecular unit H_2N-C(S)-NH-C(O)H of the chelat ligand was performed. The calculated MO energies composed from N 2p contributions of both nitrogen atoms are spread over a range of about 10 eV (see lower part of fig. 2) filling the band widths of the overlapping N K twins (N', N $1s^{-1}$ → N', N $2p^{-1}$, VB). The twin components from the N and N' atoms have to be shifted on the binding energy scale considering the N 1s level difference of 1.5 eV (initial state of the X-ray fluorescence) but can not be separated in the normal excitation mode of the X-ray fluorescence. First measurements of N K fluorescence emission have been carried out, therefore, discriminating the excitation of the stronger bound N' 1s level of the (-NR_2) group by tuning the photon energy between 395 eV and 495 eV (fig. 3). The appearance of an additional N K component at photon energies close to 390 eV crossing the excitation edge between 397 and 398 eV nicely unfolds both contributions of the N K band.

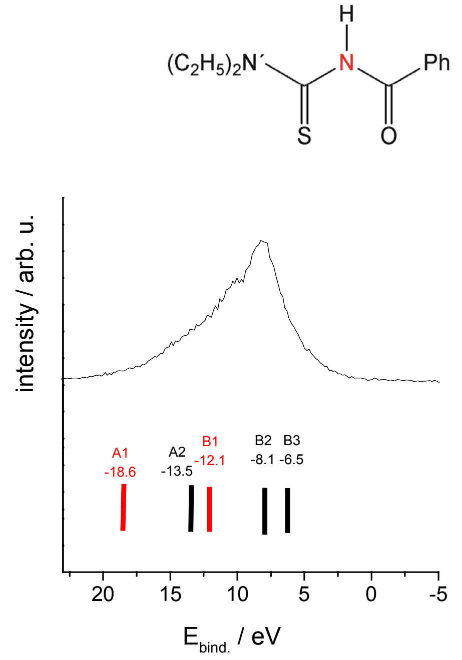

***Fig. 2**: Comparison between an experimental non-resonantly excited N K X-ray emission spectrum of the bidentate ligand and energies from a DFT calculation (A - σ states, B - π states). The black components originate from electron density of both nitrogen atoms, the red ones from the >N-H nitrogen only.*

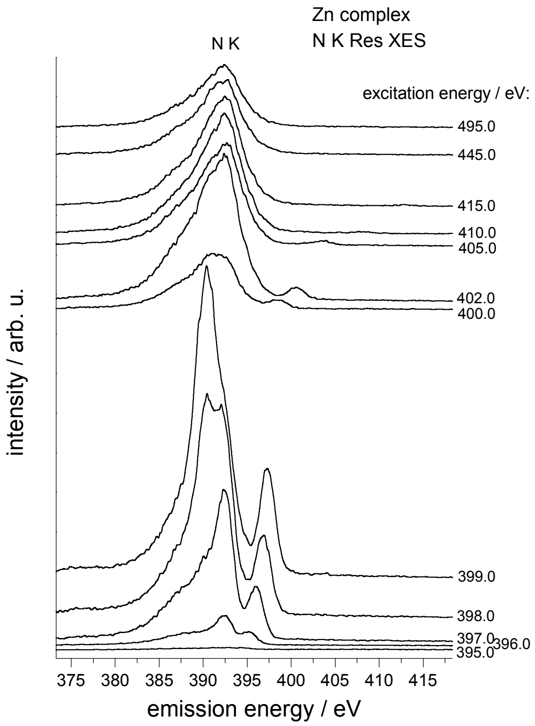

***Fig. 3**: Resonantly excited N K X-ray emission spectra of the Zn complex*

A further investigation of S $L_{2,3}$ emission on ZnS powders, ZnS epitaxial films (4 nm) grown on GaP(001) substrate at variable temperatures, and Cu/ZnS/GaP(001) heterostructures was focused on changes of the local partial density of states at the sulfur atoms. All spectra are dominated by the peaks of the S $2p^{-1}$ → S $3s^{-1}$, VB transitions from the lower and upper part of the valence band centred at 147 eV and 157 eV, respectively. The well resolved doublet structure centred at 152 eV exhibits the s – d mixing only in the cases of the ZnS powder and the ZnS/GaP film revealing the Zn – S bonding. However, with deposition of Cu (1 nm) onto ZnS/GaP(001), the S $L_{2,3}$ spectra exhibit some changes, as shown in Fig. 4.

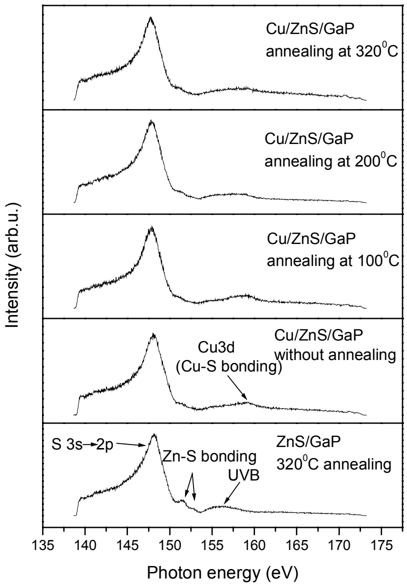

Fig. 4: *S $L_{2,3}$ spectra of ZnS/GaP(001) and Cu/ZnS/GaP(001) heterojunctions*

The features associated with Zn 3d orbitals were almost totally suppressed, on the other hand, a feature related to Cu 3d arises in the UVB region. In order to show the changes more clearly, a reference ZnS spectrum was subtracted from spectra of Cu/ZnS/GaP(001) both normalised and aligned at the peak maximum (see fig. 5). Minima and maxima of the differences above 150 eV give evidence for replacing of Zn – S bonding by Cu – S bonding, respectively, independent of annealing procedures.

Acknowledgements

The financial support by the BMBF 05KS1OL1/3 and the Deutsche Forschungsgemeinschaft GK152/3 as well as the support of the BESSY staff especially by C. Jung and M. Mast, and the disposal of organic compound by F. Dietze (Univ. Leipzig) are gratefully acknowledged.

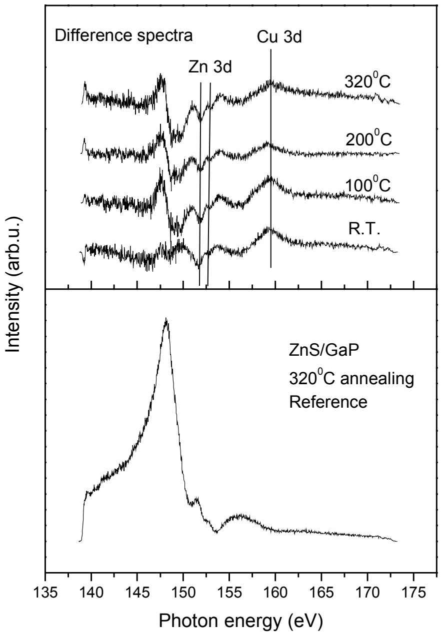

Fig. 5: *S $L_{2,3}$ difference spectra of Cu/ZnS/GaP(001), with ZnS/GaP(001) as a reference*

References:

[1] L. Beyer, F. Dietze, P. Scheibler, R. Szargan, E. Hoyer, Ya. V. Salyn, V. I. Nefedov, Z. anorg. allg. Chem. 434 (1977), 16-28

[2] A. Meisel, I. Steuer, R. Szargan, Spectrochimica Acta 23 B (1968), 527-533

[3] R. Szargan, A. Meisel, Wiss. Zeitschrift der KMU, math.-nat. R 20 (1971), 41-47

[4] C. Heske, U. Groh, O. Fuchs, E. Umbach, N. Franco, C. Bostedt, and L.J. Terminello, R.C.C. Perera, K.H. Hallmeier, A. Preobrajenski, R. Szargan, S. Zweigart, W.Riedl, F. Karg, phys. status sol. (a) 187 (2001) 13-24

[5] A. Meisel ,G. Leonhardt, R. Szargan, X-Ray Spectra and Chemical Binding, Spinger Verlag Berlin, Heidelberg, New York 1989

Electronic structure of fluorinated copper phthalocyanines

H. Peisert, M. Knupfer, T. Schwieger, G.G. Fuentes, D. Olligs, J. Fink
Institute for Solid State and Materials Research (IFW) Dresden, D-01069 Dresden, Germany
Th. Schmidt
Universität Würzburg, Am Hubland, D-97074 Würzburg, Germany

During the last years the interest in the field of thin organic films has grown dramatically due to their successful application in optical and electronic devices, such as light emitting diodes or field effect transistors. The family of the phthalocyanines (PC's) represents one of the most promising candidates for ordered organic thin films in organic electronics, as these systems possess advantageous attributes such as chemical stability, excellent film growth and electronic properties. Especially for the realization of complementary logic circuits it is advantageous that both p- and n-type conductivity can be attained within this substance class, and that the preferred type can be chosen by slight chemical modifications: for instance, copper PC (CuPC) is known as p-type material in air, whereas its perfluorinated relative $CuPCF_{16}$ is one of the few organic semiconductors, which have demonstrated high performance and stability in air for n-channel operation. A detailed knowledge of the electronic structure and the injection as well as the transport of charge carriers in the organic devices is essential for a microscopic understanding of the different properties of the device components.

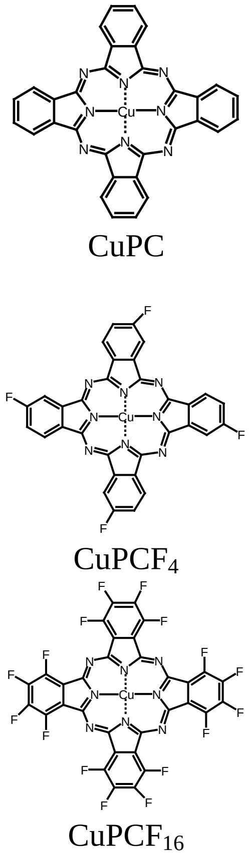

CuPC

$CuPCF_4$

$CuPCF_{16}$

Fig.1 Chemical structure of differently fluorinated PCs

The detailed study of the influence of the fluorination of CuPC on the electronic structure of the PC forms the subject of this paper. The x-ray photoemission spectroscopy measurements were performed at the UE-52 undulator beamline (SXPS) using a 200 mm hemispherical energy analyzer (Scienta SES200) and at a commercial PHI 5600 spectrometer (XPS).The introduction of fluorine atoms into CuPC occurs via the substitution of hydrogen atoms, in the case of $CuPCF_4$ four of the outermost atoms and for the perfluorinated $CuPCF_{16}$ all hydrogen atoms are substituted (see Fig. 1). In Fig. 2 we show N 1s and F 1s XP spectra for $CuPCF_{16}$ and $CuPCF_4$. The main components of both N 1s and F 1s appear as one single peak, i.e. the chemical environment of the two inequivalent types of N atoms is very similar and thus the related features are not resolved in both the corresponding XP-spectra in Fig. 2 and the additionally measured SXP-spectra (not shown). Besides the main lines, small peaks shifted to about 1.5 .. 1.8 eV higher BEs are visible in Fig. 2, denoted S_N and S_F. These peaks are ascribed to satellite features, caused by a (kinetic) energy loss of the photoelectrons due to simultaneously excited $\pi \rightarrow \pi^*$ transitions (shake up structures), e.g. from the highest occupied molecular orbital (HOMO) to the lowest unoccupied molecular orbital (LUMO). Although the typical satellite structures S_N and S_F for phthalocyanines such as $CuPCF_4$ and $CuPCF_{16}$ consist of mainly one peak, indeed the satellite structure is more complicated (see e.g. N 1s in Fig. 2), as discussed in more detail in Ref. 1 for $CuPCF_4$. The BEs are surprisingly very similar for $CuPCF_4$ and $CuPCF_{16}$, the same behavior as was found comparing CuPC and $CuPCF_4$ [1]. This indicates that the fluorination neither changes the position of Fermi level within the gap of the organic semiconductor significantly (which

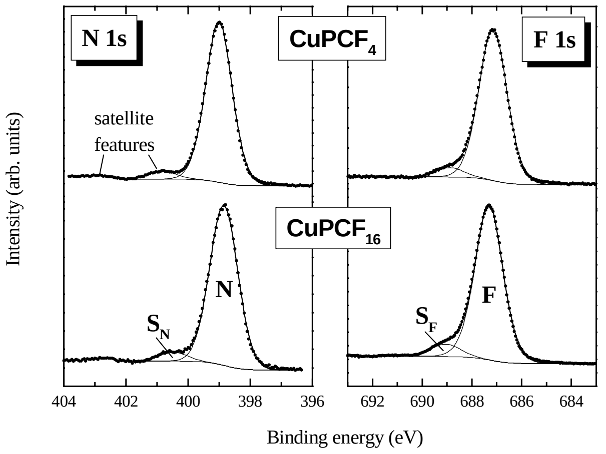

Fig. 2 N 1s and F 1s XP spectra of 9 nm thick films of $CuPCF_4$ and $CuPCF_{16}$ on Au. Although the satellite features (S) can be well described by single peaks, the structure is more complicated as can be seen from the N 1s spectra [3].

could be assumed in the case of a doping process), nor affects significantly the electron density at the corresponding atom sites.

The analysis of the shape of the C 1s spectra is more complicated since satellite features are partially overlapped by the C 1s main components. In this context, highly resolved spectra are advantageous for a more exact analysis of the peak shape, which can be achieved for instance using synchrotron radiation as excitation source. In Fig. 3 C 1s SXP- spectra of $CuPCF_4$ and $CuPCF_{16}$ are shown, relatively high excitation energies were chosen (800 and 900 eV) to probe the bulk properties. In comparison to XPS measurements [1], we observe more clearly resolved the main components C-2 and C-F and the distinct shoulder of the satellite feature at about 288.1 eV. This offers a new route to describe these features in more detail. Previously, the main components in the C 1s spectra of $CuPCF_4$ and $CuPCF_{16}$ have been attributed to the aromatic carbon of the benzene rings (C-1), pyrrole carbon linked to nitrogen (C-2) and to benzene carbon linked to fluorine. As we have shown for CuPC and $CuPCF_4$, π-π^* satellite features for *all* carbon sites have to be taken into consideration (S_{C-1}, S_{C-2}, S_{C-F}) [1]. In many cases (and especially for PCs) the assumption of simply *one* $\pi \rightarrow \pi^*$ transition works well, as can be seen above for S_N and S_F and for the C 1s satellites in CuPC and $CuPCF_4$ [1]. Therefore, also for the corresponding C 1s satellites of $CuPCF_{16}$ we have introduced *single* peaks S_{C-1}, S_{C-2} and S_{C-F} in the peak fit, neglecting a more complicated shake-up structure. Note, that the parameters for the satellites, such as relative intensity, energetic position and peak shape cannot be assumed to be constant and thus have to be extracted from the data. The determined intensity ratios for the different carbon features agree well with expected values for the molecules: counting the number of carbon atoms per ligand contributing to C-1, C-2 and C-F, the intensity ratios for $CuPCF_4$ and $CuPCF_{16}$ should be 5/2/1 and 2/2/4, respectively - the fitted SXPS peak areas $(C\text{-}1+S_{C-1})/(C\text{-}2+S_{C-2})/\ (C\text{-}F+S_{C-F})$ correspond to 5/1.9/0.9 ($CuPCF_4$) and 2/1.9/4.5 ($CuPCF_{16}$). Analyzing the intensity of the satellites more exactly, it is obvious from Figs. 2 and 3, that the relative intensity is not the same for each component. The corresponding values are summarized in Table I. For all PCs the highest satellite intensity relative to the corresponding main component is observed for S_{C-2} and the relative intensities of N 1s and F 1s satellites are generally low. Different values for the satellite intensities are explainable by the atomic orbital composition of the HOMO and the LUMO, as recently calculated for the metal-free PC molecule [2]. The predicted high contribution of the carbon directly bonded to nitrogen (C-2) to the HOMO *and* to the LUMO [2], is experimentally clearly expressed by the significantly higher intensity of S_{C-2}

Table I Intensity of the satellites in % in photoemission core level spectra of CuPC (Ref. 6), $CuPCF_4$ and $CuPCF_{16}$ (Figs. 2, 3) with respect to the corresponding main component. [3]

	S_{C-1}	S_{C-2}	S_{C-F}	S_N	S_F
CuPC	10	20	-	6	-
$CuPCF_4$	6	18	15	5	6
$CuPCF_{16}$	9	34	16	6	8

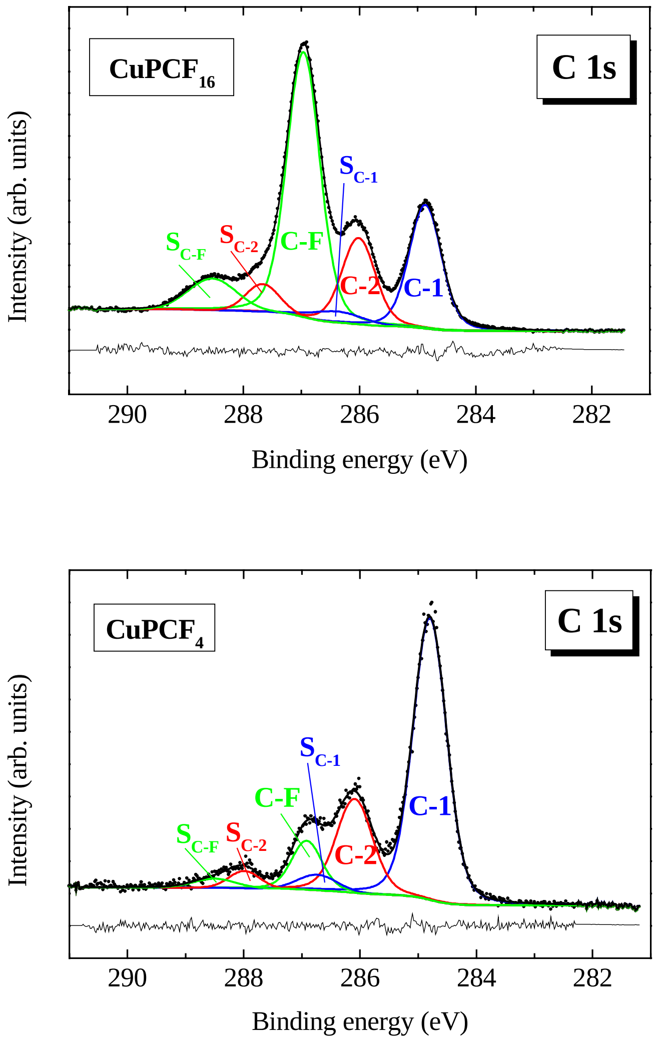

Fig. 3 C 1s spectra of bulk $CuPCF_4$ and $CuPCF_{16}$ measured using synchrotron radiation, the excitation energy is 800 and 900 eV, respectively. The clearly resolved main components C-2 and C-F and the distinct shoulder of the satellite feature at about 288. 1 eV allow a detailed analysis of the peak shape [3].

in PCs. The results of Ref. 2 also show, that the carbon atoms of the benzene rings (C-1 or C-F) contribute less (but not zero) than C-2 to the HOMO and to the LUMO, resulting in a lower relative satellite intensity of the S_{C-1s} components. Furthermore, from the relatively high intensity of S_{C-F} (compared to S_{C-1}) one can argue that the fluorination causes a slight increase of localization of the HOMO/LUMO at the corresponding atom sites (the benzene ring). The fact however, that for all core level peaks HOMO-LUMO shake-up features are present, shows that indeed the HOMO and LUMO wave functions are delocalized about the entire molecule, even though the probability for each atom site can be different. We note however, that further non-local shake-up channels may be taken into consideration, i.e. the nature of the excitation can be intrinsic and/or extrinsic. For instance, the low-intensity satellite S_F is probably mainly due to extrinsic processes, since F atoms are assumed to contribute not or very weakly to the HOMO/LUMO.

Nevertheless, the detailed analysis of the satellite intensity of each core level spectrum contains information about the probability amplitude of the HOMO and the LUMO. If both, the HOMO *and* the LUMO amplitude at the atom site under consideration is high, we expect a high relative intensity of the corresponding satellite. Thus, from the similar relative satellite intensities for each component in CuPC, $CuPCF_4$ and $CuPCF_{16}$ one can conclude, that the effect of the fluorination of the PC molecules on the HOMO and LUMO distribution is very small. This assumption can be verified by further experiments (see Ref. 3).

This work was supported by BMBF under grant no. 01BI 163. For valuable discussions and technical assistance we thank H. Kuhlenbeck and S. Pohl (FHI Berlin), Ch. Jung (BESSY), as well as R. Hübel and S. Leger (IFW Dresden).

[1] H. Peisert, M. Knupfer, J. Fink, Surf. Sci. **515,** 491 (2002).
[2] E. Ortí, R. Crespo, M.C. Piqueras and F. Thomás, J. Mater. Chem. **6,** 1751 (1996).
[3] H. Peisert, M. Knupfer, T. Schwieger, G.G. Fuentes, D. Olligs, J. Fink, Th. Schmidt, J. Appl. Phys. (submitted).

X-ray absorption studies of $Bi_{2-y}Pb_ySr_{2-x}La_xCuO_{6+\delta}$

M. Schneider, R. Mitdank, R.-St. Unger, R. Bartmann, T. Stemmler, A. Krapf,
C. Janowitz, R. Manzke
Humboldt-Universität zu Berlin, Institut für Physik, Invalidenstraße 110, 10115 Berlin

In the cuprates the electronic states near the Fermi energy E_F leading to superconductivity, are mainly due to holes in the CuO_2 planes. Soft X-ray-absorption spectroscopy (XAS) has been utilized to obtain information about these unoccupied states at both the O and Cu sites [1]. The aim of our investigations is to understand the details of hole-doping on the critical temperature T_C.

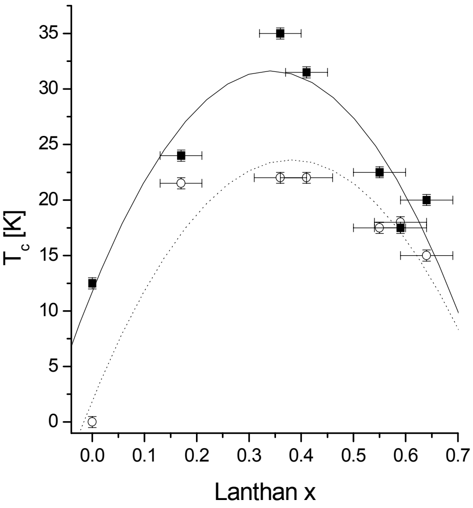

Fig. 1. Transition temperature T_c of $(BiPb)_2Sr_{2-x}La_xCuO_{6+\delta}$ ceramics as a function of La content x pre (○) and after (■) annealing. Increasing hole doping runs from right to left.

Here we present XAS data from $Bi_{2-y}Pb_ySr_{2-x}La_xCuO_{6+\delta}$ samples. All samples are sintered pellets prepared by standard powder metallurgical methods [2]. The Pb doping suppresses the superstructure and scales, dependent of La, from y = 0.2 to 0.4. In addition, Pb affects as oxidant [3]. The content of La and Pb was accurately determined by energy dispersive X-ray analysis (EDX).

To increase the transition temperature T_C it is necessary to vary the hole doping level. Here, we control the hole concentration by variation of the La-content x and the O-excess δ. Adding La, the hole doping level decreases with increasing x. Reducing the O-excess by annealing under low pressure ($<10^{-5}$ mbar, at T=500°C), the hole concentration decreases with decreasing δ. Starting with Lanthanum free samples, i.e. at high hole doping, the cuprate runs through different phases: From a Fermi-liquid through a strongly correlated metallic and superconducting phase into an insolating antiferromagnetic phase. The strongly correlated metallic phase reveals a relative maximum of T_C in the superconducting region (see Fig. 1).

The X-ray absorption measurements were performed at the BESSY II beamline U49/2-PGM2, with an energy resolution better than 100 meV. As total electron yield detector (TEY) a channeltron was used, arranged -45° with respect to the incident synchrotron radiation (SR). A retarding potential of –130 V was applied. The fluorescence yield was detected at an angle of 45° with respect to the photon beam using a Ge detector. For both methods a fresh surface has been prepared by rasping. The energy window for pulse counting at the oxygen and copper edge was adjusted to the detector resolution of about 100 eV. During the measurements the base pressure in the chamber was in the $1\cdot10^{-10}$ mbar range and the sample temperature was 77 K.

In Fig. 2-4 typical absorption spectra are shown taken near the O-K and Cu-L-edge on the same sample point. The O spectrum exhibits a prepeak at about 529 eV which is a measure for the concentration of hole states above the Fermi level.

For a quantitative comparison before and after annealing, the prepeak intensity was normalized on the Cu-intensity. The normalization on the copper intensity excludes random effects on the signal intensity. Thus we take the ratios $I_{PRE} = I_O/I_{Cu}$ before and after annealing.

From the spectra in Fig. 2 and Fig. 3 follows a decreased prepeak intensity upon annealing.

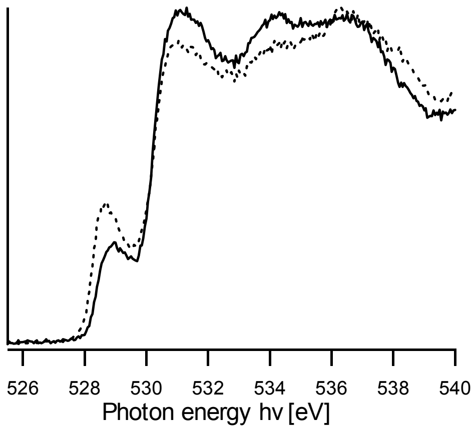

Fig. 2. Fluorescence yield detected XAS spectra of the O 1s prepeak of $Bi_{1.65}Pb_{0.35}Sr_{1.5}La_{0.5}CuO_{6+\delta}$. (dots - as grown, line - vacuum annealed)

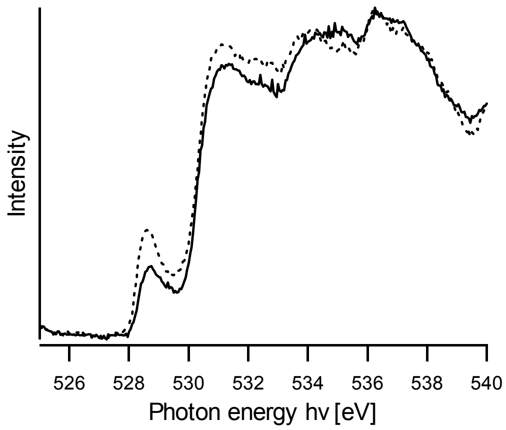

Fig. 3. Total electron yield detected (TEY) XAS spectra of the O 1s prepeak of $Bi_{1.65}Pb_{0.35}Sr_{1.5}La_{0.5}CuO_{6+\delta}$. Retarding potential -130 V. (dots - as grown, line - vacuum annealed)

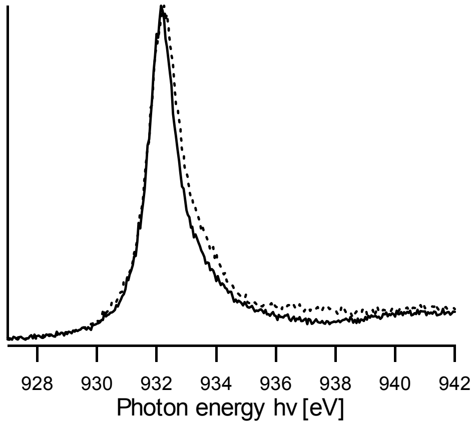

Fig. 4. Fluorescence yield detection of the Cu-L-edge of $Bi_{1.65}Pb_{0.35}Sr_{1.5}La_{0.5}CuO_{6+\delta}$. (dots - as grown, line - vacuum annealed)

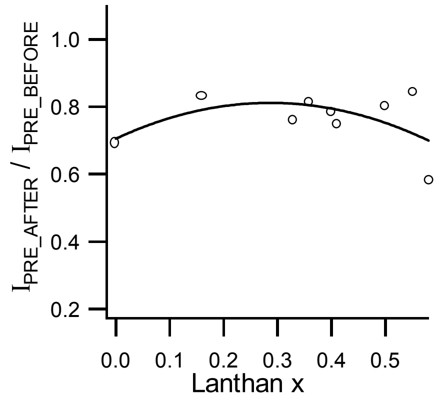

Fig. 5. Ratio of prepeak intensity of vacuum annealed to as grown samples as a function of La content x (from fluorescence yield).

The ratio $I_{PRE\_AFTER} / I_{PRE\_BEFORE}$ reveals a value of about 0.8 (Fig. 5) almost independent of x. The transition temperature increases (Fig. 1) upon annealing irrespective the decrease of hole concentration. Obviously, this corresponds to a redistribution of the oxygen and hole density to an optimal value. Outgassing oxygen upon vacuum annealing could be another reason to explain this result.

We acknowledge assistance by the staff of the synchrotron radiation facility BESSY, especially that of Dr. D. Bachelor. This work was supported by the BMBF, Project No. 05 KS1 KHA0.

REFERENCES

[1] J. Fink et al., J. Electron Spectroscopy Rel. Phen. **66** (1994) 395
[2] A. Krapf et al., to be published
[3] Z. Jianwu et al., Supercond. Sci. Technol. **14** (2001) 599-602

Optical Properties of Yttrium Hydrides

H. Schröter, A. Borgschulte, U. Barkow, M. Marutzky, M. Broschwitz, J. Schoenes, and C. Cobet[1]

Institut für Halbleiterphysik und Optik, T U Braunschweig, Mendelssohnstr. 3, 38106 Braunschweig, www.tu-bs.de/Institute/halbleiterphys
[1] Institut für Festkörperphysik, T U Berlin, Hardenbergstr 36, 10623 Berlin

In 1996, Huiberts et al. [1] reported that the optical and electronic properties of thin Y films change drastically when exposed to hydrogen. YH_x changes from a high reflecting hcp metal (α-$YH_{x<0.2}$) to a very weakly transparent fcc metal (β-YH_2) and finally, to a transparent hcp insulator. For an understanding of the mechanism driving this metal-insulator (MI) transition, the precise measurement of the optical properties is mandatory.

Previous investigations had to use yttrium films capped by a metallic Pd layer. The hydrogenation followed after preparation of the films by diffusion and dissociation of H_2 through the Pd cap layer. But this layer complicates the interpretation of the optical spectra. We present here, for the first time, optical measurements on in-situ grown epitaxial yttrium hydride films without a metallic cap layer.

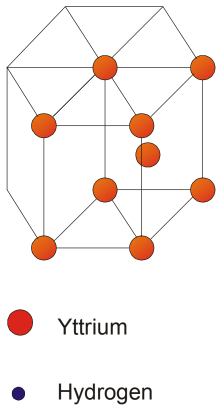

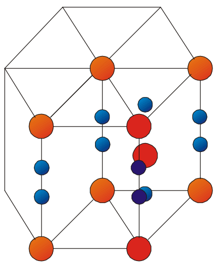
$YH_{0<x<0,2}$
α-Phase

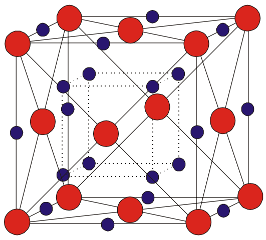
$YH_{2<x<2,1}$
β-Phase

Spectroscopic ellipsometry is a powerful tool to determine the real and the imaginary part of the complex refractive index or the dielectric function. Linear polarized light with oblique incidence is reflected from the surface under consideration. If the vector of polarisation is not parallel or pependicular to the plane of incidence then the linear polarized light is tranformed to elliptic polarized light. Analysing the reflected light, i.e. measuring the azimuth angle and the ellipticity the complex reflection ratio and from this the dielectric function or refractive index can be calculated. The analysis is done e.g. with a rotating analyzer ellipsometer, as used at the VUV-ellipsometer at the 3m-NIM-1 monochromator at BESSY II.

The YH_X films have been grown on quartz and $CaF_2(111)$ by molecular beam epitaxy (MBE). Pure yttrium films were prepared under UHV conditions ($R = 0.2$ nm/s, $p < 5*10^{-9}$ mbar).
Y evaporation under a H_2 partial pressure leads to the incorporation of hydrogen. By varying the H_2 pressure, YH_X films with $0<x<2$ can be obtained. The concentration of H depends on the temperature of the substrate, too. The optical properties of Y and YH_2 are known from literature [2,3,4]. Therefore, ellipsometry can be used to characterize the hydrogen concentration in the film.

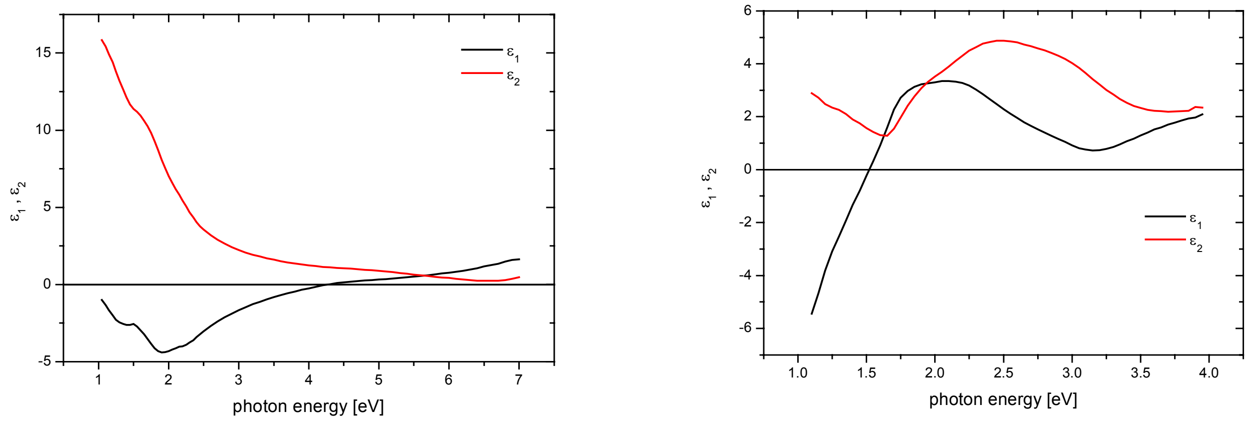

Fig. 1: Dielectric function of Y and YH_2, Ref [2], [3], [5]

Our measurements were performed using a home made ellipsometer for the energy range 1.1 eV to 4.3 eV and the VUV ellipsometer for the energy range 4 eV to 10 eV. As a first example of the change in the dielectric function due to the H-concentration the imaginary part for different growth pressures is depicted in fig. 2. The substrate was CaF_2 (111) with a growth temperature for the film of 200 °C.

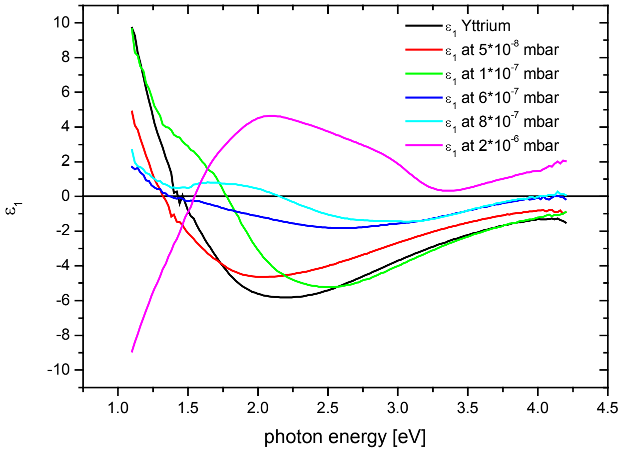

Fig. 2: real part of ε for different growth pressures

The transition to the β-Phase starts at a pressure of $6*10^{-6}$ mbar. The spectra for this sample in the range between 1.1.eV and 10 eV and for pure Y are shown in fig. 3.

The substrate for both films were CaF_2 (111). The Yttrium hcp films are (0001) and the $YH_{0<x<2}$ films are (111) oriented. From the spectra we conclude that at this pressure the films are in the α-phase

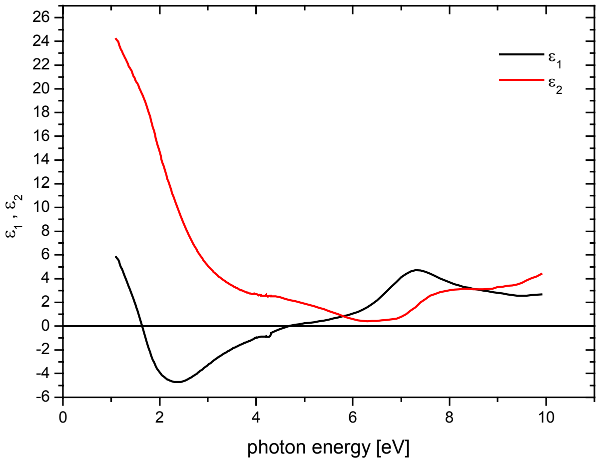

Fig. 3a: Dielectric functions for Y films

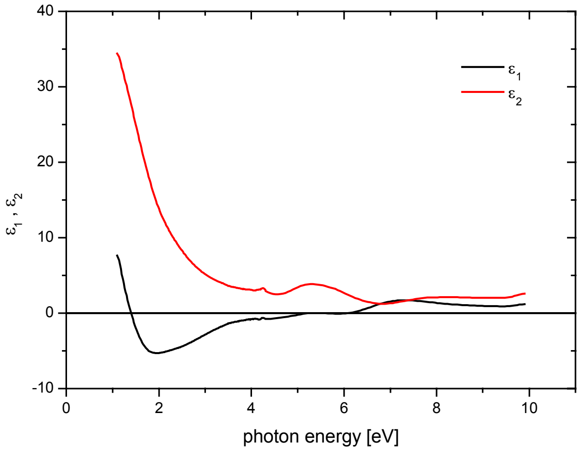

Fig. 3b: Dielectric functions for $YH_{0<x0}$ films

At a pressure of $4.5*10^{-6}$ mbar the transition to the β-phase is visible. In fig. 4 the dielectric functions for this sample are shown. By comparison with literature [4] we conclude that YH_2 films are grown under this pressure. This has also been proven by X-ray analysis. Structures in ε_2 originate from interband transitions. This can be interpreted in the framework of the band structure calculations shown in fig. 5 [5]. At about 10 eV a further structure is visible. So we will try toextend the measurements up to 20 eV.

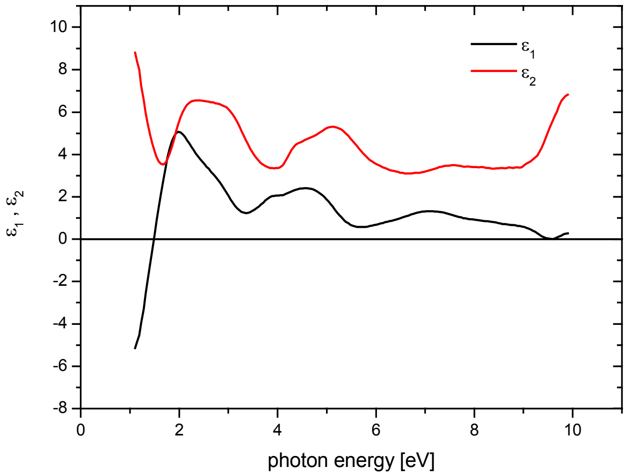

Fig. 4: Dielectric function of YH_2 in the visible and UV range

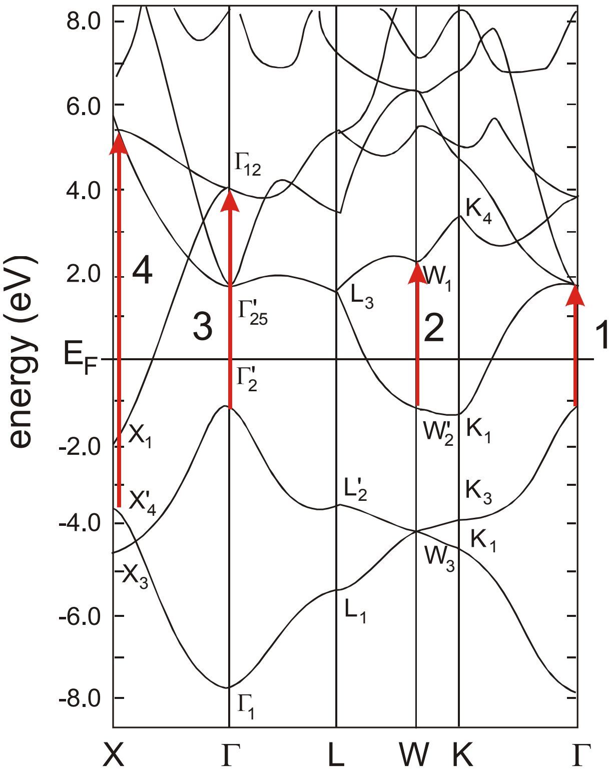

Fig. 5: Band structure of YH_2 and possible optical transitions

Acknowledgments

We acknowledge the research group of Dr. N. Esser for the possibility to use the VUV ellipsometer and the BESSY company for beam time and financial support.

References:
[1] Huibert et.al. Nature 380, 231 (1996)
[2] J.H. Weawer and C.G. Olson, Phys. Rev. B 15, 590 (1977)
[3] M. Broschwitz et.al., Verh. DPG 35, 447, (2000)
[4] van Gogh et.al., Phys. Rev. B, 63, 195105 (2001)
[5] D.D. Peterman et.al. Phys. Rev. B, 19, 4867 (1979)

NEXAFS investigation of ultrathin Ni films grown on oxygen induced reconstructed $(\sqrt{2}x2\sqrt{2})R45^o$ O/Cu(001)

T. Gleitsmann, A. Scherz, Ch. Litwinski, C. Sorg, Z. Li, H. Wende, and K. Baberschke
Freie Universität Berlin, Institut für Experimentalphysik, Arnimallee 14, D-14195 Berlin-Dahlem, Germany

Controllable ways of improving film quality and tuning film properties are an intense and active field of modern research. Recent experiments have shown that by pre-adsorption of oxygen on Cu(001) the layer-by-layer growth of ultrathin Ni films can be extended to larger thicknesses and the spin-reorientation transition from in-plane to out-of-plane can be shifted to lower coverages, i.e. the thickness range for perpendicular-magnetized Ni films is expanded [1,2]. However, the position and the chemical bonding of oxygen after Ni deposition cannot be determined unambiguously via low energy electron diffraction (LEED) and Auger electron spectroscopy (AES). Therefore, the electronic structure of the Ni films grown both on the clean Cu(001) and the reconstructed $(\sqrt{2}x2\sqrt{2})R45^o$ O/Cu(001) was investigated by virtue of the near-edge x-ray absorption fine structure spectroscopy (NEXAFS). It has been demonstrated that NEXAFS studies of an oxygen-exposed Ni(001) or Cu(001) surface provide a sensitive fingerprint for the nature of the chemical bonding of O and the local structure of the surface [3,4].

NEXAFS spectra were recorded at the Ni and Cu $L_{2,3}$ edges and the O-*K* edge at normal incidence of linear polarized light with respect to the surface (**E** in the surface plane) using the total electron yield (TEY) detection mode. The high photon flux over the near-edge energy range was provided by the gap-scan mode at the UE56/1-PGM beamline. For precise analysis the O-NEXAFS spectra with the surfactant were divided by those of the clean samples.

The NEXAFS spectra provide evidence that a floating oxygen layer is formed and, moreover, that no NiO is formed: In Fig. 1 the absorption fine structure at the O-*K* edge is shown for the $(\sqrt{2}x2\sqrt{2})R45^o$ O/Cu(001) surface before (dashed line), and after deposition of a 4.5 ML Ni film (solid line). The edge jump (which is a sensitive measure of the number of atoms) of O stayed constant (~4%) after deposition of 4.5 ML of Ni, i.e. there is no damping of the O-absorption. This observation supports the hypothesis that oxygen as a surfactant floats on top. The hybridized states of O and Ni are in principle comparable to the ones of O and Cu. This is reflected by the spectral features albeit at slightly different energies which, in turn, highlights the sensitivity of our experiment. Incorporation of oxygen in the Ni film and NiO formation would lead to profound modifications of the O-NEXAFS. For comparison we include the O-*K* edge spectrum from NiO in Fig. 1 (dotted line). In detail, the absorption fine structure in the extended energy-range above the *K* edge arise from single and multiple scattering of the photoelectron

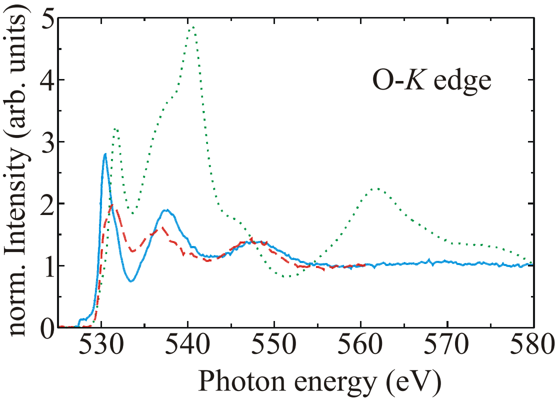

Fig.1: Successively measured NEXAFS spectra at the O-*K* edge: for the reconstructed O/Cu(001) surface before (dashed line) and after deposition of a 4.5 ML Ni film (solid line). For comparison the O-*K* edge spectrum from NiO is also included (dotted line).

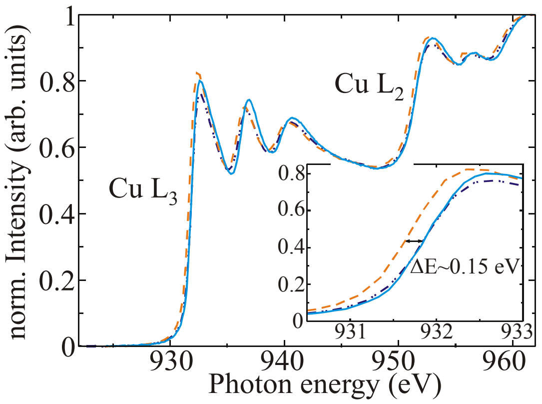

Fig.2 Successively measured NEXAFS spectra at the Cu $L_{2,3}$ edges: for the clean Cu(001) (dashed-2-dotted line), the reconstructed O/Cu(001) (dashed line) and after deposition of a 4.5 ML Ni film (solid line). A magnification of the L_3 edge reveals a chemical-shift for the reconstructed O/Cu(001) (inset).

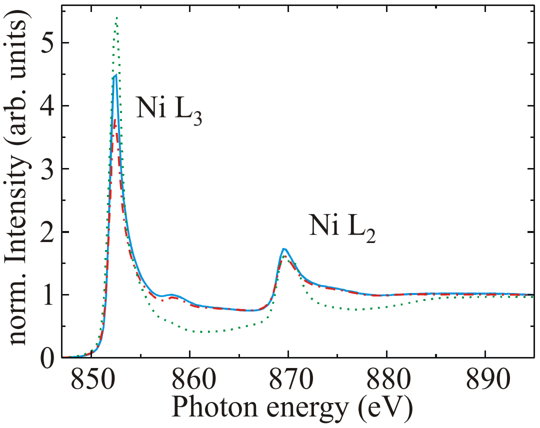

Fig.3: Normalized XAS spectrum at the Ni $L_{2,3}$ edges for a 4.5 ML Ni film deposited on O/Cu(001) (solid line). XAS spectra of 4.5 ML NiO/Cu(001) (dotted line) and 12 ML Ni/Cu(001) (dashed-dotted line) are exhibited for a direct comparison of the near-edge fine structure.

with the oxygen environment. The two peaks in the near-edge range at the *K* edge are associated with hybridized states of O(*2p*) with the surface(*3d,4sp*) [5,6]. The first structure at the threshold corresponds to antibonding *2p-3d* states just above the Fermi level. Whereas the stronger interaction of O-*2p* with Cu- or Ni-*4sp* states leads to a large splitting of the bonding-antibonding states resulting in the broad peak 5-6 eV above the Fermi level. The formation of NiO on top or in the film would drastically change the O-NEXAFS as has been demonstrated by progressive dosage of O [3,7]. By dosage of 1200 L at 450 K one is certain of transforming a Ni film to NiO. The direct comparison of the O fine structure in terms of relative intensity and energy for the 4.5 ML Ni O/Cu(001) and the 4.5 ML (NiO)/Cu(001) with [3,7] indicates that we have the two extreme cases, namely, a c(2x2) oxygen overlayer when Ni grows on preoxidized Cu(001) and a thin NiO film after dosing the clean Ni/Cu(001) film with oxygen, respectively.

Furthermore, the interpretation of a floating oxygen layer is supported by a reversible chemical-shift of the Cu $L_{2,3}$ edges shown in Fig. 2. Due to the surface-sensitivity of the TEY detection mode a small shift in energy is observed for the reconstructed O/Cu (dashed line). After evaporating the Ni film (solid line) the shift disappears with respect to the clean Cu surface (dashed-2dotted line). The reversibility of the oxygen-induced modifications indicates that the O-Cu bonding breaks upon deposition of Ni and a Ni/Cu interface is formed. Inspection of the O-*K* edge and the Cu $L_{2,3}$ edges testified on the position of oxygen.

Now we turn the discussion to the information coming from the Ni $L_{2,3}$ edges. The *2p-3d* hybridized states close to the Fermi level affect the electronic properties of Ni in terms of charge transfer, and hence, they affect the magnetic properties which are dominated by the *d*-states. In Fig. 3 the Ni $L_{2,3}$ edges are presented for the O/Ni film (solid line) and for the NiO (dotted line) film together with a clean 12 ML Ni film on Cu(001) (dashed-dotted line). Note that transitions occur primary into *d*-states at the thresholds, i.e. just above the Fermi level. The increased intensity at the $L_{2,3}$ edges evidence an enhancement of unoccupied *d*-states showing a sizable charge transfer from Ni to O. Furthermore, the increased intensity extends up to ~15 eV above the edges. Interestingly, progressive oxidation of Ni films show a systematic reduction of the intensities in this energy-range (dotted line, Fig. 3) [7] in agreement with theory [8]. Hence, direct comparison of the spectra of Fig. 3 yields the conclusion that it is most unlikely that the O-surfactant forms a bulk-like NiO at the surface. The number of unoccupied *d*-states n_h per atom averaged over the entire Ni film is approximately given by the area under the white-line intensity. Thus, n_h of the Ni film with oxygen on top is in between the one for a clean thick Ni film (n_h=1.45 holes per atom [9]) and the one for NiO (formally $3d^8$, that gives n_h=2.0 holes per atom). A quantitative analysis by integrating the spectra up to the L_3 maximum (transition into continuum states can be ignored) yields n_h=1.52(6) holes per Ni atom. Then, n_h is enhanced approximately by 12 % at the surface. That is, even though no NiO is formed, the Ni electronic structure changes moderately from the one of bulk Ni towards the atom-like Ni one, since the oxygen atoms are chemisorbed on the Ni surface.

In summary, ultrathin Ni films grown on reconstructed $(\sqrt{2}\mathrm{x}2\sqrt{2})\mathrm{R}45^{\circ}$ O/Cu(001) have been studied by means of NEXAFS measurements. When depositing Ni on the preoxidized substrate the O-Cu bonding breaks and the oxygen flows always on top of the Ni film. The inspection of the O-*K* edge and the Ni $L_{2,3}$ edges reveal that oxygen is chemisorbed on the Ni surface and no NiO is formed. A moderate charge transfer from the Ni *d*-states to the O-*2p* states is observed.

This work is supported by the BMBF (05 KS1 KEB 4) and the DFG (Sfb 290).

References:

[1] J. Lindner, P. Poulopoulos, R. Nünthel, E. Kosubek, H. Wende, and K. Baberschke, Surf. Sci. **523**, L65 (2003).

[2] R. Nünthel, T. Gleitsmann, P. Poulopoulos, A. Scherz, J. Lindner, E. Kosubek, Ch. Litwinski, Z. Li, H. Wende and K. Baberschke, submitted to Surf. Sci.

[3] D. Norman, J. Stöhr, R. Jaeger, P.J. Durham, and J.B. Pendry, Phys. Rev. Lett. **51**, 2052 (1983).

[4] D. D. Vvedensky, J. B. Pendry, U. Döbler, and K. Baberschke, Phys. Rev. B **35**, 7756 (1987).

[5] H. Tillborg, A. Nilsson, T. Wiell, N. Wassdahl, N. Mårtensson, and J. Nordgren, Phys. Rev. B **47**, 16464 (1993).

[6] R. W. Godby, G. A. Benesh, R. Haydock, and V. Heine, Phys. Rev. B **32**, 655 (1985).

[7] F. May, M. Tischer, D. Arvanitis, M. Russo, J. Hunter Dunn, H. Henneken, H. Wende, R. Chauvistré, N. Mårtensson, and K. Baberschke, Phys. Rev. B **53**, 1076 (1996).

[8] G. van der Laan, J. Zaanen, G. A. Sawatzky, R. Karnatak, and J.-M. Esteva, Phys. Rev. B **33**, 4253 (1986).

[9] P. Srivastava, N. Haack, H. Wende, R. Chauvistré, and K. Baberschke, Phys. Rev. B **56**, R4398 (1997).

Electronic properties of Si and FeSi interlayers in antiferromagnetically exchange coupled magnetic trilayers

D.E. Bürgler, L.L. Pohlmann, R.R. Gareev, S. Cramm, P. Grünberg
Institut für Festkörperforschung, Forschungszentrum Jülich GmbH, 52425 Jülich

A. Zimina, S. Eisebitt
BESSY GmbH, 12489 Berlin

Magnetic interlayer exchange coupling was discovered in 1986 and meanwhile its origin is well understood, although there is still quite some discrepancy between the theoretically predicted and experimentally measured coupling strengths. On the other hand, there is an increasing interest in interlayer coupling, in particular in systems with strong coupling, due to applications as artificial antiferromagnets or ferrimagnets in magnetic sensors or more recently in antiferromagnetically coupled (AFC) storage media for harddisk drives.

Fe/Si/Fe exchange coupled structures attract permanent interest due to an unusual coupling behaviour and strong coupling. However, the reason is still unclear. Interdiffusion at the Fe/Si interfaces possibly with the formation of different iron-silicides makes the behaviour of the interlayer coupling sensitive to deposition procedures. Iron-silicides tend to form in the spacer layers, especially at elevated temperatures. Recently, we have grown epitaxial Fe/$Fe_{1-x}Si_x$/Fe trilayers with varying nominal Si content x [1,2]. For x=0.5 epitaxially stabilised, non-magnetic, and metallic $Fe_{0.5}Si_{0.5}$ forms which shows oscillatory coupling with a coupling strength of the order of 1 mJ/m^2 [1] in accordance with the expectations for a metallic spacer [3]. For higher Si content x, the antiferromagnetic coupling strength increases and reaches for nominally pure Si spacers of only 8 Å thickness a maximum of about 6 mJ/m^2 [2]. The value is among the largest ever found for antiferromagnetic interlayer coupling. This increase of the coupling with x is theoretically not understood and might be the manifestation of a new coupling mechanism. The coupling strength can be further enhanced by adding ultrathin $Fe_{0.5}Si_{0.5}$ diffusion barriers at the Fe/Si interfaces [4]. Furthermore, Si-rich spacers show an exponential decay of the coupling with spacer thickness as predicted for insulating spacer layers [3]. Detailed information about the electronic and structural properties of the spacer layers is needed for a deeper understanding of the coupling mechanism and as input for theoretical modelling.

The Fe/$Fe_{1-x}Si_x$/Fe samples with varying nominal Si content x in the spacer layer ($0.4<x<1.0$) are prepared in an multichamber ultrahigh-vacuum system by molecular-beam epitaxy onto Ag-buffered GaAs(001) wafers. In particular, the $Fe_{1-x}Si_x$ spacer layers are grown by co-deposition of Fe and Si from two separate e-beam evaporators. The nominal Si content x is calculated from the atomic fluxes of Fe and Si measured by quartz monitors. Some spacer layers are wedge-shaped, i.e. the thickness of the spacer varies with lateral position on the sample. Typical spacer thicknesses are smaller than 30 Å. In some cases we intentionally add $Fe_{0.5}Si_{0.5}$ diffusion barriers at the Fe/Si interfaces. The Fe layers are always 50 Å thick, and a

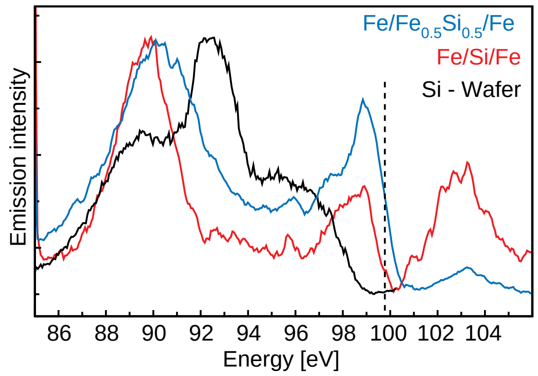

Fig. 1: SXE spectra of Fe/Fe$_{1-x}$Si$_x$/Fe trilayers with a 21 Å-thick Fe$_{0.5}$Si$_{0.5}$ spacer (x=0.5, blue) and a 16 Å-thick nominally pure Si spacer (x=1.0, red) compared with a reference spectrum (black) taken from an oxidised Si wafer. The spectra are normalised to the intensity maxima.

10 Å-thick Cr cap layer protects the Fe layers from oxidation. Details of the sample preparation can be found in Refs. [1,2,4].

We used the CRG-UE56-1/SGM beamline and the SXE spectrometer to measure soft x-ray emission (SXE) and near-edge x-ray absorption (NEXAFS) at the Si $L_{2,3}$ edge. Here, we present data showing the feasibility of the measurement, but we are not yet able to provide a full interpretation and the correlation to the magnetic properties for which further data analysis and magnetic characterisation are required. Examples of SXE spectra for two nominal Si contents are shown in Fig. 1. The spectrum from the Si wafer maps the occupied density of states (DOS) of *s* and *d* symmetry. For the spacer layers, we observe a different DOS. The spectral shape for the metallic Fe$_{0.5}$Si$_{0.5}$ spacer (x=0.5, blue) is in agreement with published spectra of bulk FeSi [5]. Compared to the semiconducting Si wafer we observe a clear shift of the valence band (VB) maximum to higher energies. For the nominally pure Si spacer (x=1.0, red) the spectral shape resembles that of FeSi, but the energy position of the VB maximum is between those of the Si wafer and the metallic Fe$_{0.5}$Si$_{0.5}$ spacer.

The detailed interpretation of the differences between the blue and red spectra, e.g. the different peak widths, in terms of different silicide contributions [5] and different structures needs further analysis. The broad structure at about 103 eV is most likely due to Ga VB → $3p_{3/2}$ emission in the substrate wafer.

Table I: Absorption edge positions (in eV) for the Cr and Fe in 6th and 7th order, respectively.

	Fe L_2	Fe L_3	Cr L_2	Cr L_3
1st order	719.9	706.8	583.8	574.4
6th order			97.3	95.7
7th order	102.8	101.0		

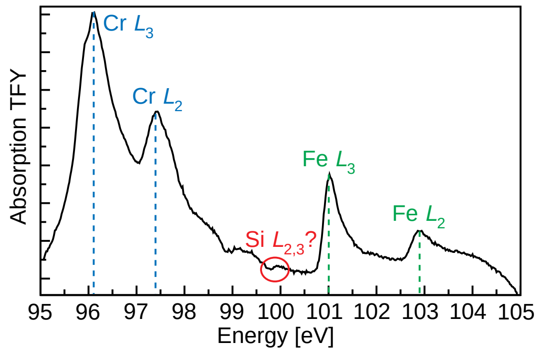

Fig. 2: TFY absorption spectrum of a trilayer with a 17 Å-thick Fe$_{0.5}$Si$_{0.5}$ (x=0.5) spacer layer. The spectrum is normalised to the Au mesh current.

The measurement of Si absorption spectra in the exchange coupled structures using either the total-electron-yield (TEY) signal measured via the sample current or the total-fluorescence-yield (TFY) signal measured by a photodiode turned out to be difficult. Figure 2 shows a TFY spectrum normalised to the incident beam intensity as measured by an Au mesh in the incident beam. The dominant peaks result from small contributions of higher order x-rays in the beamline, which give rise to absorption in the Fe layers and the Cr cap of the exchange coupled layers. Unfortunately, these higher order absorption structures appear close to the Si L_3 absorption edge at 99.8 eV (see labels in Fig. 2 and Table I).

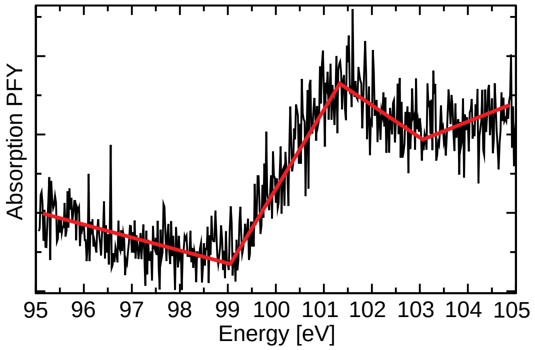

Fig. 3: PFY absorption spectrum of the same sample as in Fig. 2. The spectrum is normalised to the Au mesh current.

We can eliminate all these spurious contributions to the absorption spectrum by measuring the partial fluorescence yield (PFY) from the Si $L_{2,3}$ edge. To do so, the emitted light is energy analysed using the SXE spectrometer, and only photons in an energy window corresponding to the emission from Si are counted. This procedure reduces the count rate by about two orders of magnitude and leads to a much lower signal-to-noise level. An example of such a PFY spectrum is shown in Fig. 3. We observe an edge at about 100 eV that we attribute to Si absorption.

The data in Figs. 1 and 3 show that it is possible to measure SXE and NEXAFS from the Si $L_{2,3}$ edge even for a single, thin (about 20 Å) Si or $Fe_{1-x}Si_x$ layer buried in a $Fe/Fe_{1-x}Si_x/Fe$ trilayer structure with a Cr cap layer. The analysis in progress addresses the following questions: (i) Does the combination of PFY-NEXAFS and SXE allow a precise determination of the electronic gap of the $Fe_{1-x}Si_x$ spacers? (ii) How does the gap change as a function of Si content *x* and the spacer thickness? (iii) What types of silicides are present in various spacers? (iv) How do these results correlate with the coupling behaviour and transport measurements [6]?

This work was supported by the HGF-Strategiefondsprojekt "Magnetoelectronics".

References

[1] R.R. Gareev, D.E. Bürgler, M. Buchmeier, D. Olligs, R. Schreiber, P. Grünberg, Phys. Rev. Lett. **87**, 157202 (2001)

[2] R.R. Gareev, D.E. Bürgler, M. Buchmeier, R. Schreiber, P. Grünberg, J. Magn. Magn. Mater. **240**, 237 (2002)

[3] P. Bruno, Phys. Rev. B **52**, 411 (1995)

[4] R.R. Gareev, D.E. Bürgler, M. Buchmeier, R. Schreiber, P. Grünberg, Appl. Phys. Lett. **81**, 1264 (2002)

[5] J.J. Jia, T.A. Callcott, W.L. O´Brian, Q.Y. Dong, D.R. Mueller, D.L. Ederer, Z. Tan, and J.I. Budnick, Phys. Rev. B **46**, 9446 (1992)

[6] R.R. Gareev, L.L. Pohlmann, S. Stein, D.E. Bürgler, P.A. Grünberg, J. Appl. Phys. **in press** (2003)

Angle dependent transverse magneto-optical Kerr effect in the soft X-ray regime on thin iron films on W(110)

J. Bansmann, A. Kleibert, V. Senz, D. Abramsohn*, and H.-Ch. Mertins*
Fachbereich Physik, Universität Rostock, 18051 Rostock
* BESSY GmbH Berlin, 12489 Berlin
funded by BMBF 05 SC8HRA 6

The research program was focussed onto the reflection of linearly polarized soft X-ray radiation from thin magnetic films. Here, we will report on first results obtained from epitaxially grown Fe(110) films on W(110) capped with silver against oxidation. The fabrication of such films by thermal evaporation as well as their structural, electronic and magnetic properties are well known [1,2]. Due to a strong surface anisotropy the easy magnetization axis is lying in-plane along the W$[1\bar{1}0]$ axis [1].
The experiments have been carried out using BESSY equipment (polarimeter chamber) at the undulator beamline U49/2-PGM1 providing linearly polarized radiation from 80eV up to 1500eV. The set-up offers accurate angle resolved reflection measurements of the tuneable radiation using a X-ray sensitive photodiode together with a switching of the magnetization. In this case we have used the transverse geometry of the magneto-optical Kerr-effect (T-MOKE), where photon intensity differences can be recorded depending on the magnetization state of the sample. Such effects have first been observed by Kao et al. [3] at the Fe 2p core levels with a huge magnitude (asymmetries with more than 10%) compared to small values in the valence band. It should furthermore be mentioned that the results are element-specific due to resonant scattering close to the respective core levels and also not disturbed by external magnetic fields as in the case of photoabsorption and photoelectron spectroscopy.

Figure 1 shows two reflectivity spectra for opposite magnetization states obtained in the energy range near the Fe 2p core levels at an angle of 40° with respect to the surface.

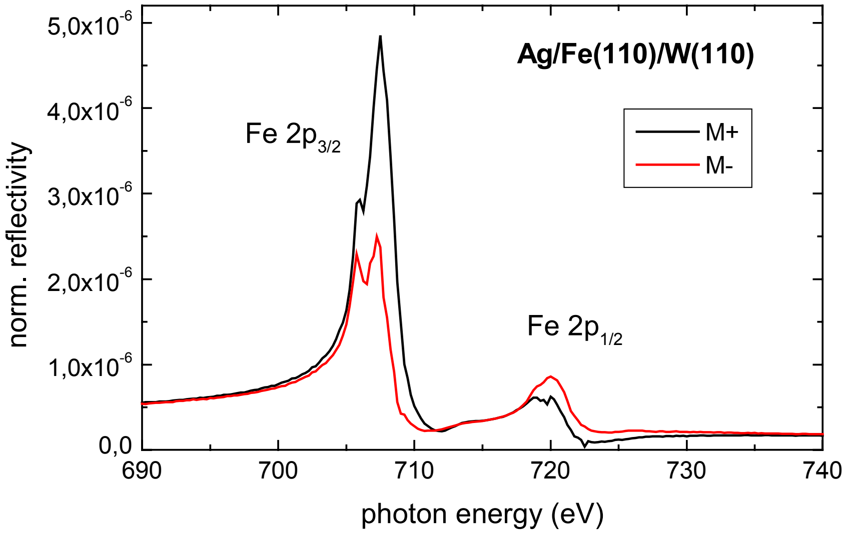

Fig. 1: X-ray reflectivity spectra (T-MOKE geometry) from a thin Fe(110) films on W(110) capped with silver for opposite magnetization states.

The measurements clearly show the enhanced resonant reflection close to the $2p_{3/2}$ and $2p_{1/2}$ levels superimposed by a large magnetic intensity difference. The intensity of the second peak (Fe $2p_{1/2}$) is quenched due to the onset of photoabsorption at the Fe $2p_{3/2}$ edge. Additionally to the huge T-MOKE visible here, one can recognize different peaks in each of the spin-orbit split Fe core levels. The magnetic interaction lifts the degeneracy of e.g., the four Fe $2p_{3/2}$ sublevels and thus leads to the fact that reflectivity of each sublevel is different according to the symmetry of initial state. However, the reflectivity spectra as well as magnetically-induced intensity differences for opposite magnetization directions strongly vary with the angle of the incident radiation.

We will furthermore present angular scans (θ-2θ scans) for several photon energies close to the Fe 2p core levels, cf. Fig. 2.

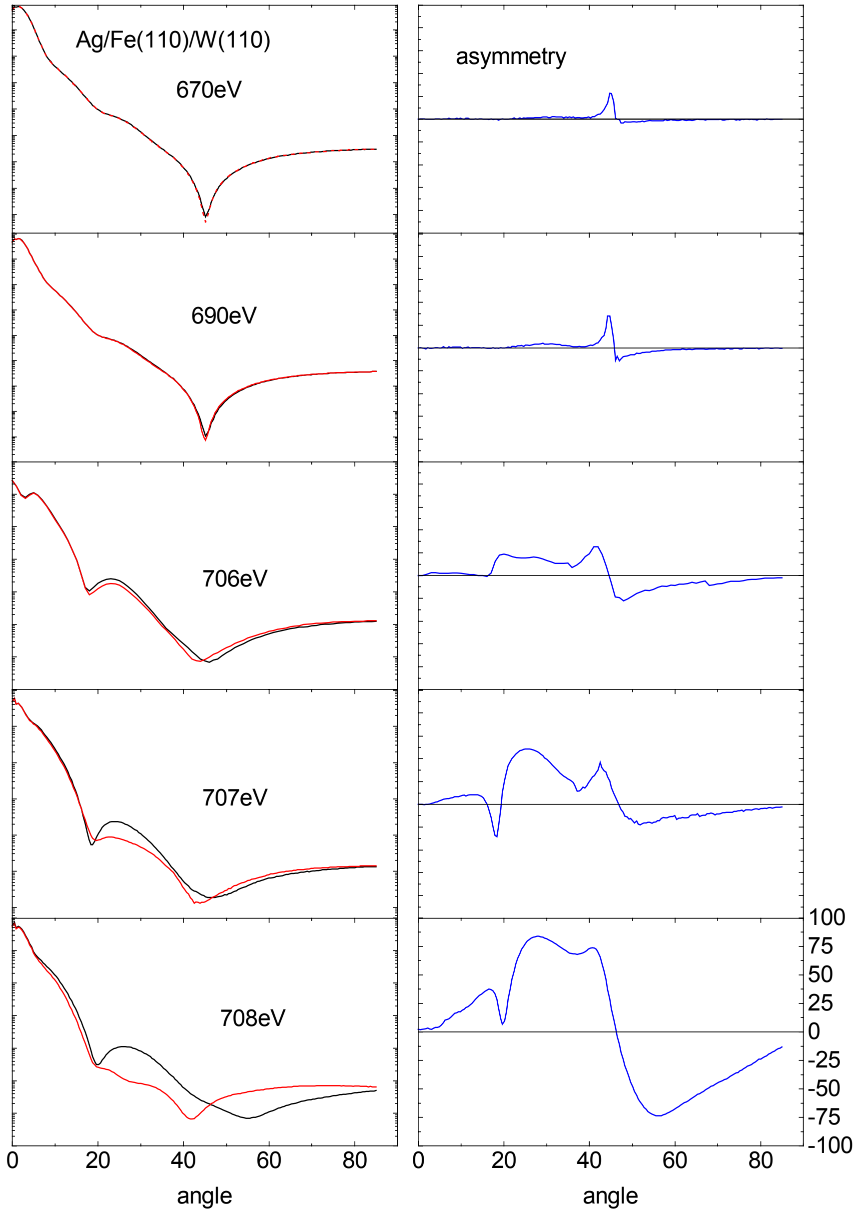

Fig. 2: Angular scans of the specularly reflected radiation for the sample described in Fig. 1. Left part: reflectivity spectra for opposite magnetization directions, right part: corresponding asymmetry values. Note that the scale in the asymmetry is always kept constant.

The spectra shown in Fig. 2 display the specularly reflected intensity of the incident, p-linearly polarized radiation when varying the angle of incidence for both magnetization states. The right part of figure 2 additionally shows the corresponding asymmetry values. The data in the two upper panels (670eV and 690eV) display the well known strong decrease of the reflected intensity in the soft X-ray regime from grazing incidence (small angles) to the Brewster angle close to 45°. Above this value, a smaller increase in the reflectivity towards normal incidence is found. Here, magnetic asymmetries are very small due to the off-resonantly chosen photon energy.

However, the situation drastically changes when the photon energy reaches the Fe $2p_{3/2}$ level (708eV). Here, we generally observe an increase in the reflectivity by several orders of magnitude due to resonant scattering. The enhanced intensity leads to the presence of oscillations in the reflectivity (Kiessig fringes). These oscillations depend on the thickness of the individual layers on the substrate (here: Fe and Ag) and result from interference of incoming and reflected radiation.

On top of these oscillations we find strong differences in the reflectivity for opposite magnetization directions, please note the logarithmic scale in all left panels. The asymmetry curves displayed in the right panel demonstrate the magnitude of the intensity difference; in the lowest panel (hν=708eV), the asymmetry reaches more than 80% at certain angles. Furthermore, the asymmetry clearly depends on the photon energy of the incident radiation, the largest effects were observed in the high energy shoulder of the Fe $2p_{3/2}$ level (708eV, cf. Fig. 1).

We would also like to focus the attention to the fact that the minimum in the reflectivity with p-polarized radiation (i.e., the Brewster angle) begins to split for the different magnetization states when entering the regime of resonant scattering. The process starts at approximately 706eV with a small splitting of $\approx 2°$ and already shows more than 10° at 708eV. This splitting of the minimum in reflection with p-linearly polarized radiation is directly related to the optical constants of Fe in the soft X-ray regime. For non-magnetic materials these optical values are known, cf. Henke et al. [4]. First attempts to determine the magneto-optical constants which enter the complex index of refraction have been carried out by Mertins et al. [5] using both Bragg scattering and Faraday rotation. On the basis of this knowledge we will try to analyse our results in detail.

References:

[1] U. Gradmann et al., Surf. Sci. 116 (1982) 539; Appl. Phys. A 39 (1986) 101
[2] V. Senz et al., Surf. Rev. Lett. 9 (2002) 913
[3] C.C. Kao et al., Phys. Rev. Lett.65 (1990) 373
[4] B.L. Henke et al., http:// www-crxo.lbl.gov/optical_constants/asf.html
[5] H.C. Mertins et al., J. Magn. Magn. Mat. 240 (2002) 451

SXPS studies of SiC surfaces and interfaces with oxides

Th. Seyller[1], N. Sieber[1], K.Y. Gao[1], R. Graupner[1], L. Ley[1],
A. Taddich[2], D. James[2], J. Riley[2], R. Leckey[2]

[1] Institut für Technische Physik, Universität Erlangen-Nürnberg
[2] School of Physics, La Trobe University, Bundoora, Vic 3083 Australia

Introduction

The wide band gap semiconductor silicon carbide is an interesting candidate for high power, high temperature and high frequency applications. As a consequence, the electronic and structural properties of SiC surfaces have been subject to a number of studies, most of them dealing with the hexagonal {0001} surfaces of 4H- and 6H-SiC, but also to some extend with the (111) and (001) surfaces of 3C-SiC. In the past, our group was particulary interested in the properties of wet-chemically prepared SiC{0001} surfaces [1-4], the silicate adlayer reconstruction on SiC{0001} [5-7], and especially hydrogen saturated SiC{0001} surfaces [8-13].

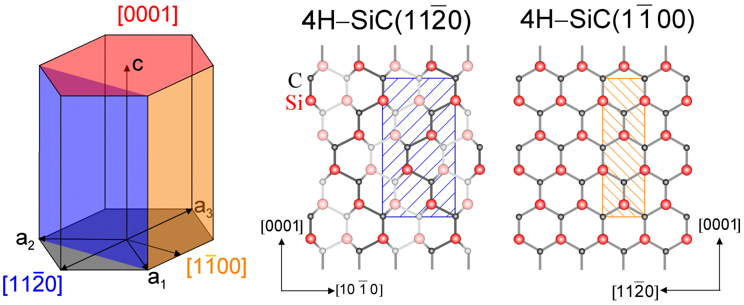

Fig. 1: Orientation of the a-planes of hexagonal SiC within the unit cell and their top view.

Very recently we have extended our studies towards the so-called a-planes of hexagonal SiC polytypes (see fig. 1). These surfaces show a number of interesting properties. Because of the fact that these surfaces contain the information about the polytype's stacking sequence they can act as a template in crystal growth and thus inhibit polytype fluctuations [14-16]. In contrast to 4H-SiC(0001), where step-bunching is sometimes observed during epitaxy, no such behavior is seen on 4H-SiC($11\bar{2}0$), and the occurrence of so-called triangular defects is suppressed [17, 18]. A-planes also have advantages for annealing out crystal defects after ion implantation (lower temperature) [19-21] and exhibit a lower density of interface states (D_{it}) at the SiC/SiO$_2$-interface than corresponding structures formed on the (0001) plane [22, 23]. Therefore it seems mandatory to study the yet unknown electronic and structural properties of these a-planes.

Today commercially available SiC devices are limited to Schottky diodes and the commercialization of a JFET is in sight. Ultimately it would be an advantage if SiC could be used for power MOSFET's. Unfortunately this is currently not feasible because of the high density of electrically active interface states which are present at the SiC/SiO$_2$ interface[24, 25]. Whereas some groups intend to improve this interface, we have started to investigate Al$_2$O$_3$ as an alternative gate oxide on SiC.

In the present activity report we will present first results of our current studies. XPS and FTIR measurements were carried out in our home laboratory. Using beam line UE56/2-PGM1 and 2 we have studied the surface core level shifts of hydrogen terminated 4H-SiC($1\bar{1}00$) and ($11\bar{2}0$) surfaces by SXPS. The initial stages of oxidation of 4H-SiC($11\bar{2}0$) and the interface between Al$_2$O$_3$ and 6H-SiC(0001) were investigated by SXPS as well.

The H-terminated ($1\bar{1}00$) plane of 4H-SiC

In order to start our investigations on the structural and electronic properties of the a-planes we have hydrogenated the surfaces with the same method used previously on the {0001} surfaces, i.e. annealing in ultra-pure hydrogen at 1100°C. For both, 4H-SiC($1\bar{1}00$) and ($11\bar{2}0$) we obtained a clean surface with (1×1) symmetry [26], as shown in fig. 2 for the case of 4H-SiC($1\bar{1}00$). Quantitative analysis of the XP spectra taken from these surfaces indicate that they are of mixed stoichiometry, i.e. that their Si to C ratio is 1:1 and no carbon or silicon overlayer is present [26].

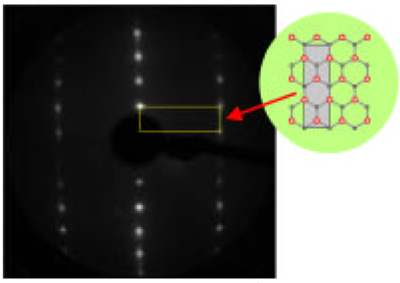

Fig. 2: LEED pattern of H-terminated 4H-SiC($1\bar{1}00$) showing (1´1) symmetry.

Considering the bulk crystal lattice of 4H-SiC it is possible to create three different (1×1) surfaces, which are shown in fig. 3 for the case of full dangling bond saturation by hydrogen. All these surfaces have a Si to C ratio of 1:1. As can also be seen from that figure, two of the three inequivalent surfaces possess Si-H and C-H monohydrides as well as dihydrides in a ratio of 1:1. Only one structure can be found which exhibits only monohydrides. Thus it should be possible to identify the correct structure by looking for the spectral signature of these hydrides.

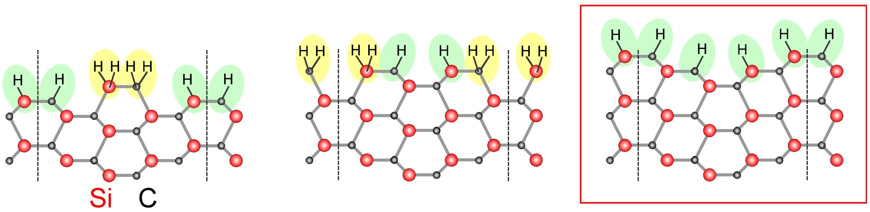

Fig. 3: *Possible (1´1) surfaces of 4H-SiC($1\bar{1}00$) with all dangling bonds saturated by hydrogen.*

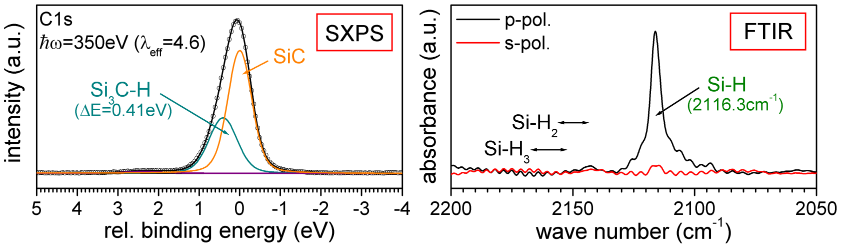

Fig. 4: SXPS spectrum of the C1s core level FTIR spectrum of the Si-H stretch mode of hydrogen terminated 4H-SiC($1\bar{1}00$).

C-H bonds can easily be identified in the C1s spectra of the hydrogenated 4H-SiC($1\bar{1}00$) as demonstrated in fig. 4, where a C1s spectrum is shown which is deconvoluted into a bulk line and a chemically shifted component. The surface nature of this component was checked by varying the surface sensitivity. The chemical shift of (0.41±0.05) eV is in good agreement with the shift observed on H-terminated 6H-SiC($000\bar{1}$) [12, 13]. Dihydrides would lead to a second surface component which would be equally large with a chemical shift twice as large. This is clearly not the case. Within a simple layer attenuation model, the relative intensity of the C-H monohydride component agrees well with what is expected for a complete saturation of all C dangling bonds. On the other hand, Si-H bonds can be readily identified using Fourier-transform infrared absorption spectroscopy (FTIR). In this way the presence of Si-H monohydrides can be established (see fig. 5) on the hydrogenated 4H-SiC($1\bar{1}00$) surface. No di- and trihydrides are detectable. Therefore, based on the spectroscopic data, we propose the structure model emphasized by the red box in fig. 4 as the correct one.

Initial stages of the oxidation of a-planes of 4H-SiC

We have investigated the early stages of oxidation of 4H-SiC($1\bar{1}00$) and ($11\bar{2}0$) and the resulting SiC/SiO_2 interface by measuring the core levels after exposing the surface to molecular oxygen at 800°C. In an attempt to simulate a technical process we have used wet-chemically cleaned surfaces. Here we will concentrate on the structural properties of the interface between the 4H-SiC($11\bar{2}0$) substrate and the SiO_2 formed by this thermal oxidation process.

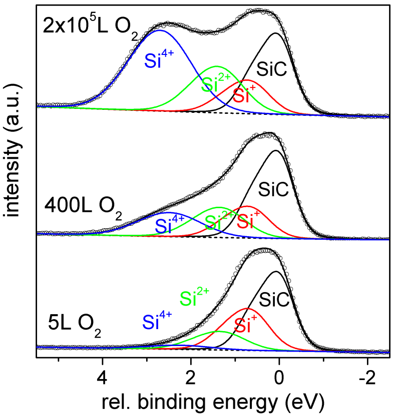

Fig. 5: Si2p core level spectra of 4H-SiC($11\bar{2}0$) after exposure to O_2 at 800°C.

Fig. 5 displays Si2p core level spectra obtained after exposing the surface to different amounts of oxygen. After exposure to 5 L of oxygen the formation of Si in oxidation state 1+ and also 2+ is observed. A component due to Si^{4+} is negligible. At 400 L O_2 exposure the formation of Si^{4+} becomes evident. No Si^{3+} is observed. Finally, at 2×10^5 L O_2 exposure Si^{4+} component is the dominant signal, indicating the formation of a SiO_2 layer. Again, no Si^{3+} is observed. From the variation of the relative intensities of the four different components with surface sensitivity (not shown) we can conclude that the Si^{4+} component is located at the surface and the Si^{+} and Si^{2+} are restricted to the interface. This behavior is in contrast to the (0001) surface which was studied intensively by the group of Johansson et al. [27-29], who observed consistently that at the SiO_2/SiC(0001) surface only Si^{+} is formed. As a consequence, we can state that apparently the structure of the interface between SiO_2 and SiC is different for the (0001) and ($11\bar{2}0$) surface. This is no surprise because the structure of the surfaces themselves are completely different. However, one may speculate whether or not the possibility of the ($11\bar{2}0$) surface to form Si^{2+} at the interface is the cause for the observed lower density of electrically active interface states. Building Si^{2+} into the interface may lower stress at the interface and the more relaxed SiO_2 network in close proximity of the SiC substrate may tend towards lower defect formation. Of course the presence of C on the SiC($11\bar{2}0$) surface raises the question about the role of carbon in the interface. Corresponding C1s spectra were also taken in the course of our studies. However, due to relatively large initial hydrocarbon contamination of the *ex-situ* prepared surfaces, little can be said about the local geometry of the carbon atoms at the interface. Additional work is required, especially using hydrogen terminated samples, which are free of any contamination with hydrocarbons.

Interfaces between SiC(0001) and Al_2O_3

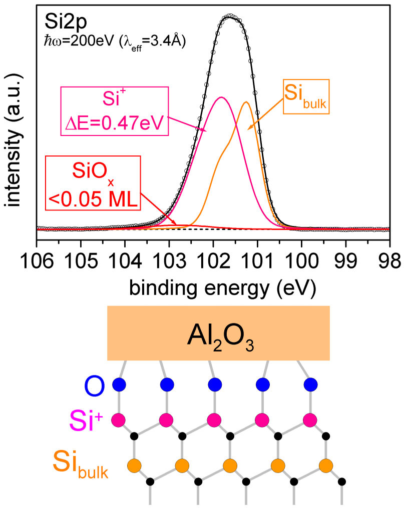

Fig. 6: Si2p spectrum of 3.5Å Al_2O_3 deposited on SiC(0001 -(1×1)-H and sketch of the interface.

We have also studied the interface between SiC(0001) and Al_2O_3 deposited by ALCVD. It is known that the deposition of dielectrics on Si can lead to the formation of a thin suboxide (SiO_x) interface layer. The thickness depends on the deposited material and may be a few Å [30, 31]. The interfacial oxide acts in two ways. First of all the deposited oxide and the interfacial oxide act as two capacitors in series affecting the electrical behavior of the MOS capacitor. Therefore an exact control over the thickness of the interfacial layer is required. Secondly, and more importantly, the density of electrically effective interface states is determined by any interfacial silicon oxide formed during deposition and not by the deposited dielectric. Consequently, in order to improve the situation an SiO_x interface layer has to be avoided and our first task is to check whether or not we can deposit Al_2O_3 by ALCVD on SiC(0001) without interfacial Si oxide. Fig. 6 shows a Si2p core level spectrum taken from an ultra-thin layer of Al_2O_3 deposited on H-terminated 6H-SiC(0001). The spectrum can be deconvoluted into two strong components. One component is due to emission from the bulk. The second component is due to Si atoms with oxidation state 1+, which is located at the interface as shown by changing the surface sensitivity. The relative intensity of the Si^+ component is in good agreement with what we would expect for a full monolayer of Si-O bonds [2] and is therefore consistent with the structural model also shown in fig. 6. A third, weak component is necessary in order to get a good agreement between the experimental data and the model curve. This component indicates a small amount of SiO_x at the interface. Quantitative evaluation shows that the amount of SiO_x is below 5% of a monolayer. Hence, the formation of a significant SiO_x layer at the interface can be excluded [32]. First electrical measurements show that the density of interface states at the Al_2O_3/SiC(0001) interface is about an order of magnitude lower than for thermal SiO_2 gate oxides [32].

Summary

The above described experimental results show that SXPS at BESSY II allows us to get detailed information about the surface and interface properties of SiC. The combination with other techniques such as LEED and FTIR is a powerful tool for gaining structural information about the surfaces. Additional electrical measurements on interfaces can provide an evaluation of these materials systems for there usefulness in technical applications.

References

1. N. Sieber, T. Seyller, R. Graupner, L. Ley, R. Mikalo, P. Hoffmann, D. Batchelor, and D. Schmeißer, Appl. Surf. Sci. 184 (2001) 280-284.
2. N. Sieber, T. Seyller, R. Graupner, L. Ley, R. Mikalo, P. Hoffmann, D. Batchelor, and D. Schmeißer, Mater. Sci. Forum 389-393 (2002) 717-720.
3. M. Hollering, B. Mattern, F. Maier, L. Ley, A.P.J. Stampfl, J. Xue, J.D. Riley, and R.C.G. Leckey, Mater. Sci. Forum 264-268 (1998) 331.
4. M. Hollering, J. Bernhardt, J. Schardt, A. Ziegler, R. Graupner, B. Mattern, A.P.J. Stampfl, U. Starke, K. Heinz, and L. Ley, Phys. Rev. B 58 (1998) 4992.
5. M. Hollering, F. Maier, N. Sieber, M. Stammler, J. Ristein, L. Ley, A.P.J. Stampfl, J.D. Riley, R.C.G. Leckey, F.P. Leisenberger, and F.P. Netzer, Surf. Sci. 442 (1999) 531-542.
6. M. Hollering, N. Sieber, J. Ristein, L. Ley, J.D. Riley, R.C.G. Leckey, F.P. Leisenberger, and F.P. Netzer, Mater. Sci. Forum 338-342 (2000) 387-390.
7. N. Sieber, M. Hollering, J. Ristein, and L. Ley, Mater. Sci. Forum 338-342 (2000) 391-294.
8. N. Sieber, T. Seyller, B.F. Mantel, J. Ristein, and L. Ley, Mater. Sci. Forum 353-356 (2001) 223-226.
9. N. Sieber, B.F. Mantel, T. Seyller, J. Ristein, and L. Ley, Diamond Relat. Mater. 10 (2001) 1291-1294.
10. N. Sieber, B.F. Mantel, T. Seyller, J. Ristein, L. Ley, T. Heller, D.R. Batchelor, and D. Schmeißer, Appl. Phys. Lett. 78 (2001) 1216-1218.
11. N. Sieber, T. Stark, T. Seyller, L. Ley, C. Zorman, and M. Mereghany, Appl. Phys. Lett. 80 (2002) 4726.
12. N. Sieber, T. Seyller, L. Ley, M. Polcik, D. James, J.D. Riley, and R.G.C. Leckey, Mater. Sci. Forum 389-393 (2002) 713-716.
13. N. Sieber, T. Seyller, L. Ley, D. James, J.D. Riley, R.G.C. Leckey, and M. Polcik, submitted to Phys. Rev. B.
14. J. Takahashi and N. Ohtani, Phys. Stat. Sol. (b) 202 (1997) 163-175.
15. J. Takahashi, N. Ohtani, M. Katsuno, and S. Shinoyama, J. Crystal Growth 181 (1997) 229-240.
16. T. Nishiguchi, T. Shimizu, M. Sasaki, S. Ohshima, and S. Nishino, Mater. Sci. Forum 353-356 (2000) 69-72.
17. T. Kimoto, T. Yamamoto, Z.Y. Chen, H. Yano, and H. Matsunami, Mater. Sci. Forum 338-342 (2000) 543-548.
18. T. Kimoto, H. Yano, S. Tamura, N. Miyamoto, K. Fujihira, Y. Negoro, and H. Matsunami, Mater. Sci. Forum 353-356 (2001) 543-548.
19. M. Satoh, K. Okamoto, Y. Nakaike, K. Kuriyama, M. Kanaya, and N. Ohtani, Nucl. Instrum. Meth. Phys. Res. B 148 (1999) 567-572.
20. M. Satoh, Y. Nakaike, K. Uchimura, and K. Kuriyama, Mater. Sci. Forum 338-342 (2000) 905-908.
21. M. Satoh, Y. Nakaike, and T. Nakamura, Journal of Applied Physics 89 (2001) 1986-1988.
22. H. Yano, T. Hirao, T. Kimoto, H. Matsunami, K. Asano, and Y. Sugawara, IEEE Electron Device Lett. 20 (1999) 611.
23. H. Yano, T. Hirao, T. Kimoto, and H. Matsunami, Appl. Phys. Lett. 78 (2001) 374.
24. G. Pensl, M. Bassler, F. Ciobanu, H. Avanasév, H. Yano, T. Kimoto, and H. Matsunami, Mat. Res. Soc. Symp. Proc. 640 (2001) H3.2.
25. V.V. Afanas'ev, M. Bassler, and G. Pensl, phys. stat. sol. (a) 162 (1997) 321-337.
26. T. Seyller, R. Graupner, L. Ley, A. Taddich, D. James, J.D. Riley, and R.G.C. Leckey, to be published.
27. C. Virojanadara and L.I. Johansson, Surface Science 472 (2001) L145-L149.
28. C. Virojanadara and L.I. Johansson, Mater. Sci. Forum 389-393 (2002) 701-704.
29. C. Virojanadara and L.I. Johansson, Surface Science 505 (2002) 358-366.
30. B.W. Busch, O. Pluchery, Y.J. Chabal, D.A. Muller, R.L. Opila, J.R. Kwo, and E. Garfunkel, MRS Bulletin 27 (2002) 206-211.
31. R.S. Johnson, G. Lucovsky, and I. Baumvol, J. Vac. Sci. Technol. A 19 (2001) 1353-1360.
32. K.Y. Gao, T. Seyller, L. Ley, A. Taddich, J.D. Riley, R.G.C. Leckey, F. Ciobanu, and G. Pensl, to be published.

Electronic structure of stoichiometric polycrystalline V_2O_5 thin films

Q. Wu, D. Ensling, J. Fernandez-Madrigal, R. Hunger, A. Thißen and W. Jaegermann
Fachbereich Materialwissenschaften, Fachgebiet Oberflächenforschung,
Technische Universität Darmstadt, Petersenstraße 23, D-64287 Darmstadt

Transition metal oxides with layered crystal structures like V_2O_5, $LiCoO_2$, $LiNiO_2$, $LiCo_xNi_{1-x}O_2$ and $LiMn_2O_4$ can be used as cathode materials in thin film Na- or Li-intercalation batteries. The cathode is connected via an electrolyte to the anode material. The battery can be charged by an external voltage, leading to deintercalation of the alkaline metals from the cathode, transport through the ionic conducting electrolyte and insertion into the anode. The discharge process leads to an intercalation of alkaline metal ions into the transition metal oxides. The electrochemical data of the cell are mostly determined by the change of the electronic structure of the cathode material during intercalation. For materials with complicated electronic structures like transition metal oxides these changes can not be described by the filling of rigid bands by electrons.

This study deals with vanadium pentoxide as a cathode material, because of the chance to grow thin films of the oxide on cleaved HOPG surfaces by a simple PVD process and the alkaline metal intercalation can be studied subsequently to simple adsorption experiments. All experiments have been carried out using the SoLiAS spectrometer at the TGM7 beamline.

In a first step the electronic structure of stoichiometric vanadium pentoxide had to be clarified, especially with respect to partial valence band density of states for Oxygen and Vanadium and the calculation of O2p- and V3d-occupation numbers. Therefore resonant photoemission in the photon energy range from 20eV to 120eV has been carried out. Valence bands and conduction bands of V_2O_5 are generated by the hybridisation of V3d- and O2p-states. Due to the different atomic orbital energies the V3d-admixture to the valence band and the O2p-admixture to the conduction band is thought to be small. Reduction of or charge transfer to V_2O_5 induces a band gap state at a binding energy of about 1.5eV. For photon energies higher than the V3p-3d excitation threshold (>42eV) there are three different emission processes, direct photoemission, autoionization and a Super-Coster-Kronig Auger transition (Figure 1, left). It has been shown [1] that the direct photoemission and the autoionization process are coherently superposed, because they have the same initial and final states. The resonant enhancement of the V3d-photoionization cross section can be described by a Fano-profile [2] (Figure 1, right). The left part of figure 2 shows an energy series of the valence band region of a nearly stoichiometric V_2O_5 film. Obviously the intensities of the valence band structures A-D are strongly influenced by the photon energy. The presence of the gap state G indicates a slight reduction (about 4%) of the film due to the deposition conditions. The intensity of G is also a function of the photon energy, that cannot only be explained by the variation of the non-resonant O2p and V3d photoionization cross sections [3]. This correlation is shown in the middle part of Figure 2. The gap state intensity can be described by a Fano-profile with a maximum around 50eV, indicating the V3d-like character of these states. The maximum is shifted from the V3p-3d excitation threshold by about 8eV. This fact is also known from other transition metal oxides and is caused by the phase shift between the direct photoemission and the autoionization process [1,4]. In the right part of figure 2 an off-resonance (41eV) and an in-resonance spectrum (50eV) is shown. In the latter one the intensity of the V3d-like part of the valence band emission is strongly enhanced. After different normalization the difference spectra reflect the pure O2p- and the V3d-like states in the valence band. A comparison to a recent full-potential-DFT-calculation [5] shows a good agreement between calculation and experiment. From these PVBDOS measurements and calculations, the V3d-admixture to the valence band has been calculated to be about 25%, indicating a quite covalent bonding character of $V^{+2.5}O^{-1}$, which is in good agreement with data taken from LCAO calculations [6] and Auger spectroscopy [7].

This work was supported by the Deutsche Forschungsgemeinschaft (DFG).

[1] L.C. Davis, L.A. Feldkamp, J. Appl. Phys. 59 (1986) R25
[2] U. Fano, Phys. Rev. 124 (1961) 1866
[3] J.J. Yeh, I. Lindau, Atomic Data and Nuclear Data Tables 32 (1985) 1
[4] R. Heise, R. Courths, S. Witzel, Solid State Comm. 84 (1992) 599
[5] M. Schütz, P.C. Schmidt, private communication
[6] D.W. Bullett, J. Phys. C 13 (1980) L595
[7] G.A. Sawatzki, D. Post, Phys. Rev. B 20 (1979) 1546

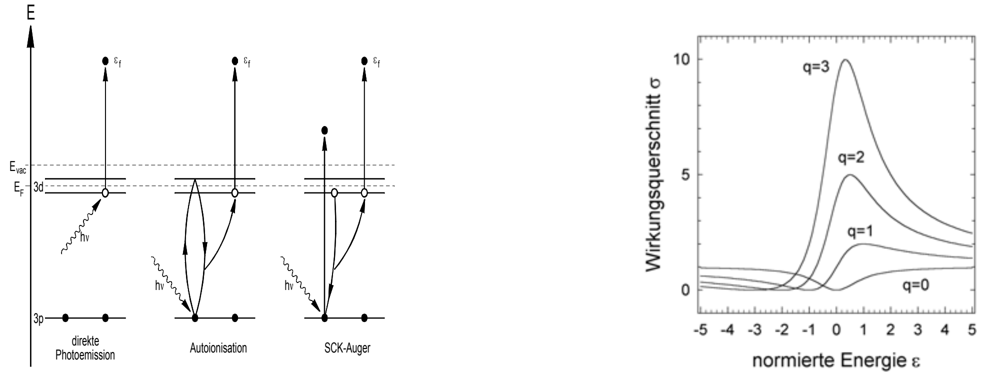

Figure 1: Resonant Photoemission process for V_2O_5 (left) and Fano-profile (right).

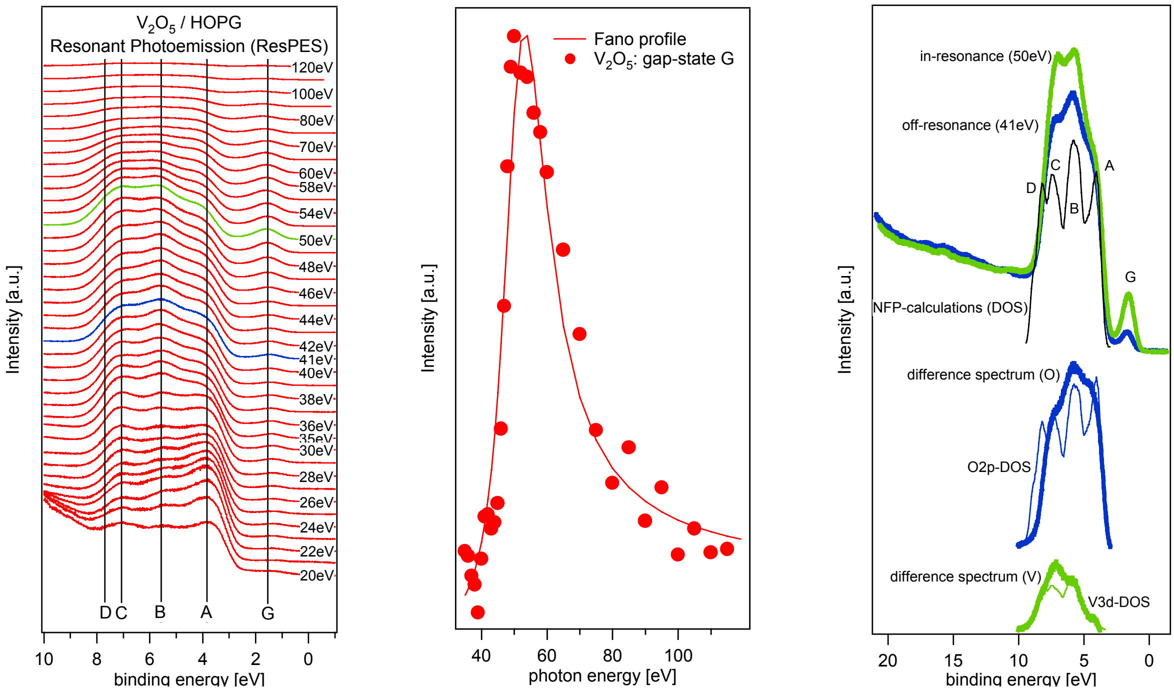

Figure 2: Resonant Photoemission series (left), gap-state intensity (middle) and the comparison of difference spectra with calculated partial valence band density of states (PVBDOS) [5] (right) of stoichiometric V_2O_5.

High-resolution photoelectron spectra of the Si(111):GaSe van der Waals surface termination prepared by a single step process

R. Fritsche, B. Jaeckel, T. Schulmeyer, A. Klein, W. Jaegermann
Darmstadt University of Technology, Inst. of Materials Science, D-64287 Darmstadt

The heterostructure of GaSe on Si(111), including the interface formation, the heteroepitaxial growth and the structure of the Si(111):GaSe system have been examined by several research groups (for more details see Ref. 1, 2 and references therein). For the preparation of a Si(111):GaSe surface termination it is possible to selenize a monolayer of Ga, which has been deposited at elevated temperatures. Applying this stepwise preparation it is possible to follow the evolution of surface chemical bonds leading to electronic passivation of the Si(111):GaSe surface [1, 2]. But it is also possible to deposit GaSe in a single step process onto either hydrogen terminated silicon surfaces or onto a Si(111)-7×7 surface at a temperature > 500°C [3, 4]. This is supposed to be a more promising way for the preparation the Si(111):GaSe surface termination, because no rearrangements of Si and Ga atoms on the surface might be necessary [2]. Therefore GaSe was deposited onto Si(111) (n^+- and p-doped) at different temperatures and for different times. The deposition chamber was directly attached to a photoelectron spectrometer system connected to the U49-2/PGM2 beamline of the BTU Cottbus/HMI/TU Darmstadt CRG.

Fig. 1 shows Si 2*p* core-level photoelectron spectra as obtained after deposition of GaSe on the n^+-Si(111)-7×7 surface. GaSe was deposited at 2Å/min for a constant time of 2 min at different substrate temperature. At lower temperature the shape of the Si 2*p* level is dominated by a two component emission structure attributed to an imperfect surface termination and GaSe layer growth. With increasing temperature the shape of the Si 2*p* emission line is getting sharper and the spectra shifts to higher binding energies. This indicates the increase in quality of surface passivation by the formation of a Si(111):GaSe half-sheet termination layer. The spectra obtained at a substrate temperature of 530°C shows the best surface passivation, almost flatband condition have been achieved for this preparation step, and only one component can be identified in the very sharp developed Si 2*p* emission line. This temperature has been reported before as the best for preparing the Si(111):GaSe termination layer [3]. A further increase in temperature leads to a reduction in surface passivation and again a two component emission structure appears in the Si 2*p* emission line. The Si(111):GaSe surface termination is not stable at temperatures above 550°C. Se desorbs from the termination layer and leaves behind an almost Ga covered Si surface. A shift to lower binding energies is observed, due to an increase in surface band bending induced by the metal, which remains on the surface and the shoulder at low binding energy site of the Si 2*p* emission line can be attributed to the formation of Si-Ga bonds.

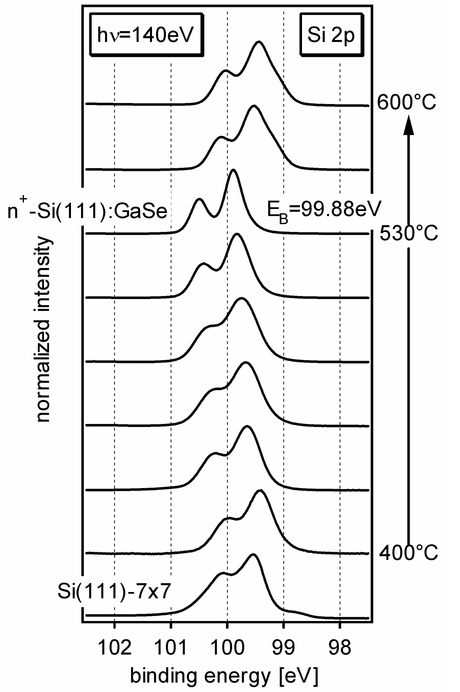

Fig. 1: *Si 2p core-level photo-electron spectra obtained after deposition of GaSe for 2min onto n^+-Si(111)-7×7 held at different temperatures.*

With the experiment shown in Fig. 1 we demonstrate, that it is possible to achieve a very high quality Si(111):GaSe half-sheet termination layer using a one step preparation process, if the temperature meets the very tight window of 520°C-540°C, which allows the best

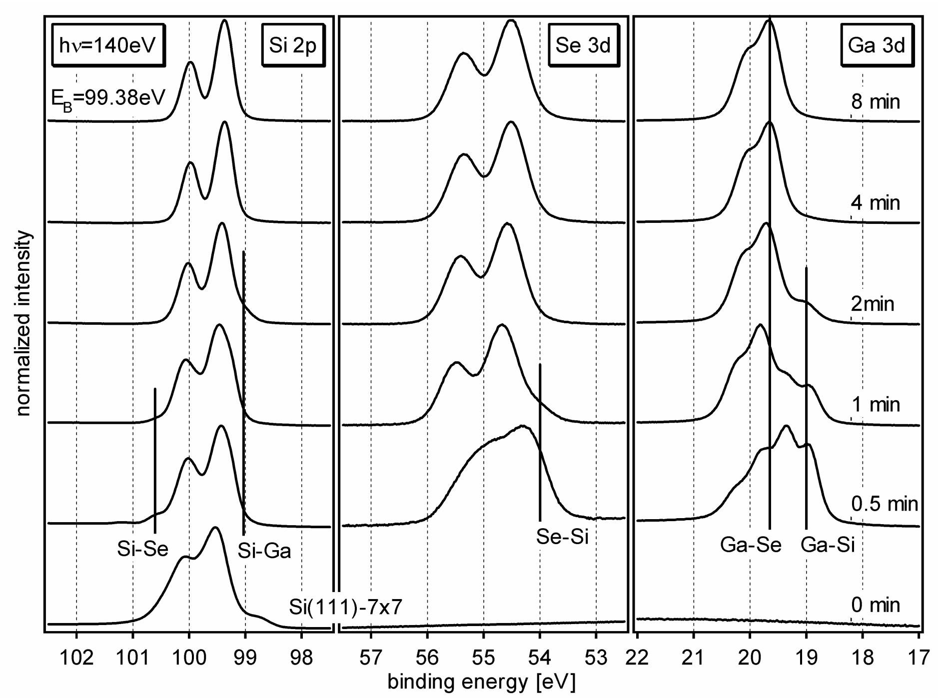

Fig. 2: *Si 2p, Ga 3d and Se 3d core-level photo-electron spectra obtained after deposition of GaSe onto p-Si(111)-7×7 held at 510°C for 0.5 min, 1 min, 2 min, 4 min and 8 min.*

quality in Si surface passivation. In a second set of experiments we clarified the evolution of the formation of the Si(111):GaSe termination layer by evaporation GaSe in very small deposition steps onto the Si(111)-7×7 held at 510°C.

Fig. 2 shows Si 2*p*, Ga 3d, Se 3d core-level photoelectron spectra as obtained after deposition of GaSe onto p-Si(111)-7×7 surface. GaSe was deposited at 1Å/min and the deposition time increases from 0.5 min up to 8 min. After the first deposition step of 0.5 min all emission lines shows several components with different intensities. The Si 2*p* emission is characterized by the appearance of three different components, which can be attributed to Si-Se bonds (on the high binding energy site and low in intensity), to Si-Ga bonds (on the low binding energy site and low in intensity) and to Si atoms passivated by a GaSe termination layer. The Se *3d* and the Ga *3d* emission lines show mainly two components, which can be attributed to the Se-Si bonds, respectively the Ga-Si bonds (in both cases on the low binding energy site, with an intensity which is approximately 80% of the intensity of the Ga-Se bonds) and to the Ga-Se bonds, forming the Si(111):GaSe surface passivation layer.

With increasing deposition time the intensity of the components, which are attributed to the Si-Ga and Si-Se bonds, reduces in intensity and after 4 min of GaSe deposition the spectra of all emission lines have developed a sharp well defined shape, which can be correlated to single component emis-sion. In all emission lines the components, which can be attributed to the Si(111):GaSe half-sheet termination layer, are shifting to lower binding energies, due to a decrease in surface band bending with increasing the quality and area of surface passivation.

This experiment shows that using a one step preparation process, the growth of the Si(111):GaSe half-sheet termination layer takes place in the same way as has been reported from the two step preparation process, which means that several intermediate steps of Si, Ga and Se surface atoms rearrangements are necessary before the surface passivation layer is build up over large areas, even if the temperature of the substrate was held at an optimal value. The passivation, which was achieved in this experiment, is not ideal for p-doped Si, but the spectra shown in Fig 2 after 8 min of GaSe deposition are all very sharp in shape and only one component can be attributed to this emissions. Therefore the not ideal passivation might be due to fact, that the substrate temperature, which have been used for this experiment, does not fit exactly in the very tight window of 520°C-540°C, where the best Si surface passivation can be achieved. Indeed, in another experiment (this is not shown here, because the deposition steps are not that small as in the experiment shown in Fig 2, therefore the evolution of the growth of the surface termination layer can not be seen that good), which was made at a substrate temperature of 540°C, the quality of the p-Si(111):GaSe surface passivation can be optimised (A spectra of the Si *2p* emission line obtained after deposition of GaSe onto a p-doped Si substrate held at 540°C was shown in Fig 3 as starting condition for an additional experiment.)

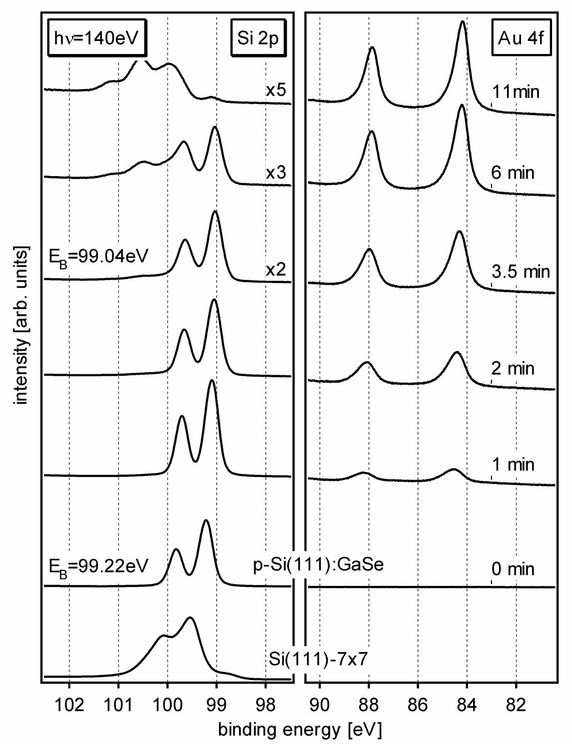

Fig. 3: *Si and Au 4f core-level photoelectron spectra of the Si(111):GaSe surface after deposition of Au for 0 min, 1 min, 2 min, 3.5 min, 6 min and 11 min.*

Finally we conclude, that the one step process take place almost in the same manner as the two step process, but due to the fact that the one step process is much simpler and leads to the same results, it is the superior for preparing a Si(111):GaSe half-sheet termination layer.

Fig 3 shows Si *2p* and Au *4f* core-level photoelectron spectra as obtained after deposition of Au onto p-Si(111):GaSe surface. The spectra show that with increasing amount of Au on the surface the emission of the Si *2p* was suppressed and finally (after 3.5 min of Au deposition) the Au starts to react with the Si surface and a second component appears on the high binding energy site of the Si *2p* emission line, but is still very low in intensity at this stage of interface reaction. The intensity of the new component, which can be attributed to the Au-Si interface reaction, increase with further increase in the amount of Au on the surface. The Ga *3d* and Se *3d* emission lines are not shown here. These emission lines are not changing in shape und intensity. With increasing amount of Au on the surface, the position of the Si *2p*, the Ga *3d* and the Se *3d* emission line shifts towards lower binding energy. The binding energy of the Si *2p* level changes with Au deposition, to $E_B = 99.04$ eV for p-type and to $E_B = 99.07$ eV for n-type Si substrates (spectra not shown here). This corresponds to a Fermi level position of $E_F - E_{VBM} \approx 0.05$eV at the Si(111):GaSe/Au interface. Although the Au/Si interface reaction is not fully suppressed, the GaSe surface termination modifies the Schottky barrier height by ≈ 0.3 eV.

This work was supported by the Deutsche Forschungsgemeinschaft.

[1] R. Fritsche, E. Wisotzki, A. B. M. O. Islam, A. Thißen, A. Klein, W. Jaegermann, R. Rudolph, D. Tonti and C. Pettenkofer, Appl. Phys. Lett. **80**, 1388 (2002).

[2] R. Fritsche, E. Wisotzki, A. B. M. O. Islam, A. Thißen, A. Klein, W. Jaegermann, R. Rudolph, D. Tonti and C. Pettenkofer, Surf. Sci. 515, 296 (2002).

[3] S. Meng, B. R. Schroeder, and M. A. Olmstead, Phys. Rev. B **61,** 7215 (2000)

[4] Köebel, Y. Zheng, J. F. Pétroff, J. C. Boulliard, B. Capelle and M. Eddrief, Phys. Rev. B **56**, 12296 (1997).

Resonant scattering from stepped $SrTiO_3$

C. Schüßler-Langeheine, M. Haverkort, Z. Hu, M. Braden, L. H. Tjeng
II. Physikalisches Institut der Universität zu Köln, Zülpicher Str. 77, 50937 Köln
E. Schierle, A. Starodubov, G. Kaindl, E. Weschke
Institut für Experimentalphysik. Freie Universität Berlin, Arnimallee 14, 14195 Berlin
G. Rijnders, M. Huijben, D. H. A. Blank
Faculty of Science and Technology. University of Twente, P.O. Box 217, 7500 AE Enschede, Netherlands

Many unusual properties of strongly correlated electron systems like metal-to-insulator transitions, colossal magnetoresistance and superconductivy in transition metal oxides are discussed in terms of long-range ordering phenomena like charge, spin and orbital ordering. Such ordering can be studied by diffraction techniques, but the standard techniques neutron scattering and hard x-ray scattering are essentially probing the crystalline and magnetic structure and may only indirectly allow to relate lattice modulations to a possible charge ordering. A particularly sensitive tool for the investigation of ordering phenomena involving certain electronic states is resonant x-ray scattering at the $L_{2,3}$-edges of the 3*d* metals. The multiplet structure of these resonances has been extensively studied experimentally and theoretically in the past, thus providing a sound background for the assignment of multiplet components to certain transitions. By appropriate choice of the photon energy, the resonant excitation can be restricted to constituents in a certain oxidation state or those in a certain chemical environment. By choice of the polarization of the incident light, the excitation can be additionally restricted to sites with the respective orbital orientation. Furthermore resonant scattering in the soft x-ray range takes advantage from the strong enhancement of the scattering cross section, which allowed, e.g., the investigation of antiferromagnetic films of only a few monolayer thickness [1]. Third-generation synchrotron radiation sources and state-of-the-art monochromators give a sufficiently high flux of monochromatic photons to make such experiments possible. There are two major limitations to the method: a) the photon wavelength of the order of 20 Å, which is much longer than inter-atomic distances and b) effects like the strong change of optical properties across the resonance render the interpretation of the results not straightforward. For particular cases like $La_{0.5}Sr_{1.5}MnO_3$ at the Bragg peak, a result is predicted, where the scattering cross section and the absorption signal have barely any similarity [2], therefore the method has to be carefully tested and requires a close cooperation between experiment and theoretical treatment.

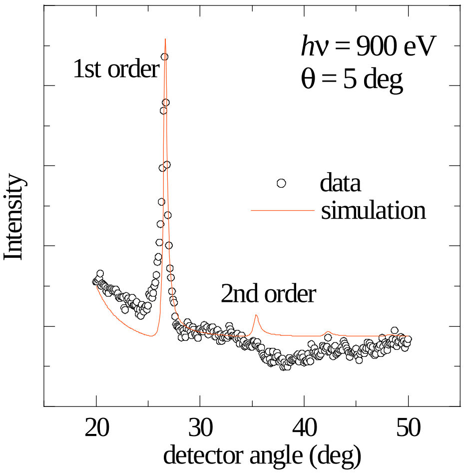

Fig. 1: Diffraction pattern (dots) from a stepped $SrTiO_3$ surface. The data were taken by scanning the detector and keeping the light-incidence angle fixed at 5 deg. The red solid line is the result of a kinematical simulation.

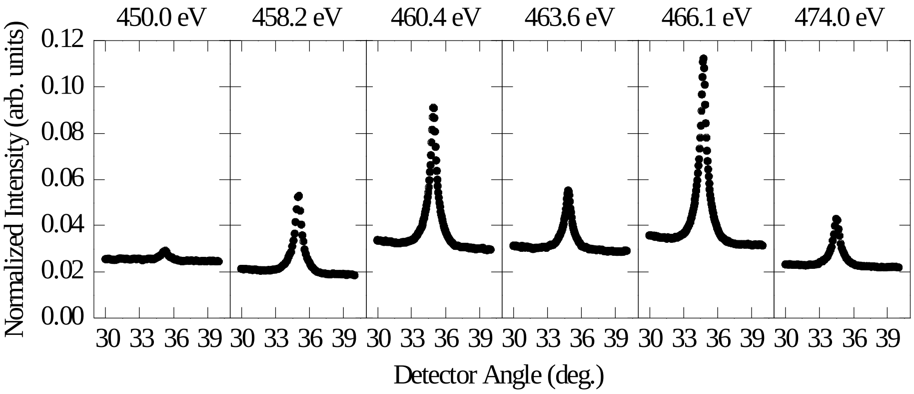

Fig. 2: First-order superstructure peak for different photon energies across the Ti $L_{2,3}$ resonance. The light-incidence angle was 5 deg.

Even though the wavelength is too long for crystalline unit cells, it is well suited to study the ordering phenomena in many systems. Our approach to develop the method and create a background for the interpretation of data obtained from complicated systems is to use simple model systems like the well understood reference systems $SrTiO_3$ [3]. In order to overcome the limitations imposed by the long wavelength on resonance, we look at samples with an artificial periodicity created by a surface miscut. We performed the experiment at the U49/2-PGM1 beamline of BESSY II using a home-built UHV diffractometer with a silicon-diode photon detector. For the first experiment, we used a $SrTiO_3$ single crystal with a vicinal surface cut 1.1 degree relative to the (001) planes. In order to achieve a single (TiO_2) termination, the sample was treated following the procedure as presented by G. Koster et al. [4]. The surface has an approximate 53-fold lateral superstructure given by the distance between two steps at the surface which leads to additional peaks in the reflected intensity. Fig. 1 shows the observed first-order reflection peak from this surface, recorded far from resonance at 900-eV photon energy together with a simulation (solid line). The simulation is based on a kinematical model, which should be appropriate far from resonance; the asymmetry of the simulated peaks comes from the finite absorption length of the photons included into the model. Interestingly, the second-order satellite is missing in the diffraction pattern, even though the simulation predicts an observable intensity for it. At the present stage we can only speculate that this observation may be related to a modulation of the terrace widths of the sample.

The first-order peak for different photon energies across the resonance is shown in Fig. 2. The modulation of the peak intensity is clearly visible as well as the intensity modulation of the strong background the peak is riding on. It can be seen, that the background and the peak have a different resonance behavior: at 460.4 eV and 463.6 eV photon energy, the background has the same intensity whereas the peak intensity is different. An analysis of the peak intensity across the $L_{3,2}$ resonance is shown in Fig. 3 together with the absorption signal as measured by total-electron yield under the same photon-incidence angle. The resonance is clearly reflected in the intensity variation of the diffraction-peak intensity, but we find relative intensities of the multiplet components different from the absorption signal. The most striking difference is in the relative intensity between the two strong crystal-field split lines of the two resonances. While both have about the same intensity in the absorption signal, the components at lower energy, which are due to excitations into the t_{2g} states, are much weaker in the scattering cross section. The two pre-peaks and the weak component at 458.9-eV photon energy are missing for the scattering cross section.

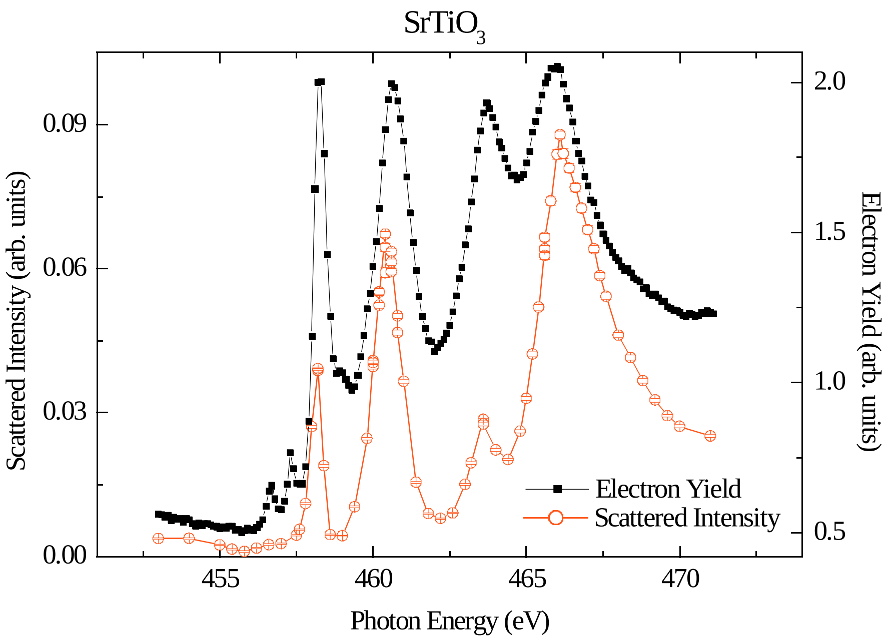

Fig. 3: Absorption cross section (filled symbols) and scattered intensity (red open symbols) across the Ti $L_{3,2}$ resonance. The light incidence angle was 5 degrees for both data sets.

From multiplet calculations of the absorption signal, we see, that the relative intensity of the crystal-field components as observed for the scattering cross section looks like that for Ti in a weaker crystal field of lower symmetry. Such situation one would find on the terraces or at step edges, where the oxygen coordination of the Ti is lower. This demonstrates the ability of the method to do spectroscopy selectively on sites with a certain periodicity. Even though the Ti-sites with reduced coordination form only a small fraction of the whole probed sample volume, the signal from the sample part with the proper spatial periodicity is focused in momentum space and therefore well observable. The origin of the background has to be further investigated. It can be due to inelastic processes, caused by the bulk part of the sample, or due to disorder in the system.

In conclusion, we have shown the potential of resonant soft x-ray scattering to perform spectroscopy selectively on sites with certain periodicity and that stepped surfaces like SrTiO$_3$ are suited samples to develop the method on well understood and controlled reference systems. By use of samples with different miscut angles the fraction of surface atoms at steps can be easily chosen and by growth of other materials on these stepped systems the surface properties can be changed in a controlled way.

This work was funded by the DFG in the SFB 608, TP C4 and by the BMBF (05KS1KEE/8). We gratefully acknowledge the experimental and administrative support from the BESSY staff and the excellent working conditions there.

[1] C. Schüßler-Langeheine, E. Weschke, A. Yu. Grigoriev, H. Ott, R. Meier, D. V. Vyalikh, Chandan Mazumdar, C. Sutter, D. Abernathy, G. Grübel, G. Kaindl, Journ. Electr. Spectroc. Relat. Phenom. 114116, 953 (2001).
[2] C. W. M. Castleton and M. Altarelli, Phys. Rev. B 62, 1033 (2000).
[3] F. M. F. de Groot, J. C. Fuggle, B. T. Thole, G. A. Sawatzwy, Phys. Rev. B 41, 928 (1990).
[4] G. Koster, B. L. Kropman, G. Rijnders, D. H. A. Blank, H. Rogalla, Appl. Phys. Lett. 73 2920 (1998).

Resonant photoemission at the Pr_2O_3 / Si(001) interface

Dieter Schmeißer
Angewandte Physik-Sensorik, Brandenburgische Technische Universität Cottbus, 03013 Cottbus, Postfach 10 13 44, Germany

In resonant photoemission studies photoelectron spectroscopy (PES) is done at photon energies that enable the excitation from a deep core hole to the empty conduction band states. At resonant condition only such states are selectively enhanced which allow an optical coupling of the core hole to the empty conduction band states. Information is to be gained from the shape of the particular resonance and by a comparison of the valence band data at excitation energies off and on resonance. Such studies provide information on the electronic structure, in particular how to separate individual contributions in the valence band and conduction band regime.

Pr_2O_3 is a high-k oxide which is considered as a novel gate oxide in Si based field effect devices /1, 2/ and is known to grow epitaxial on Si(001) /1/ via a silicate interface layer /2/. The electronic structure of Pr_2O_3 is well characterized /3, 4/. We focus on the valence band photoelectron spectra at the Pr4d resonance around 120eV which involves transitions from the Pr4d core levels to the empty conduction band states and study the changes induced by the silicate formation.

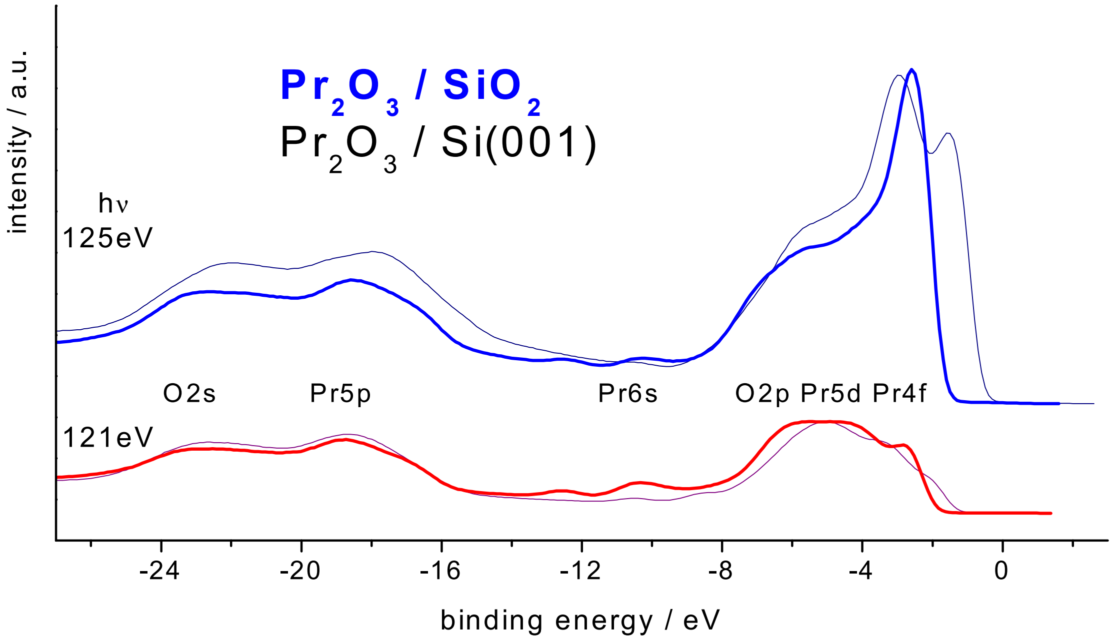

Fig.1: The valence band spectra of Pr_2O_3 in the silicate phase and of pure Pr_2O_3 (bold) taken on (hν = 125eV) and off (hν = 121eV) the Pr4d resonance, respectively.

In fig.1 we have displayed the valence band spectra taken at energies close to and right at the 4d resonance which is around 125eV. We have plotted these spectra for a Pr_2O_3 film deposited to the native SiO_2 layer (bold lines) to resemble bulk Pr_2O_3 properties. Another sample is characteristic of the silicate phase. It is prepared like an epitaxial oxide layer on Si(001), however with a thickness of about 1nm (thinner lines). In this comparison the binding energies of the Pr5p and O2s levels serve as a reference while the valence band states show significant variations.

The valence states have a significant contribution from the Pr5d electrons which shows up in the characteristic behavior at the Cooper minimum around 240eV /2/. Here, we focus on the interface properties and notice that there are significant variations occurring for the uppermost valence states close to the valence band maximum (VBM). Obviously, in the interface region the electronic structure is modified and the chemical bonding and valence band occupancy within the topmost states is influenced. The Pr6s states are shifted upwards while the Pr5d states move downwards. The Pr4f electron states can be identified by their enhancement at resonance (hν=125eV). Obviously, the band at -3eV is a Pr4f state which also becomes down shifted in the silicate phase. In addition we notice that this emission is split in the interface layer. There appears a new band in the silicate phase at -1.5eV. It is another Pr4f state because of its resonant enhancement. At this point, however, it re-mains open whether it is due to a ground state occupancy or is a consequence of the charge transfer processes (CT) caused by the interaction of the core hole to the Pr4f levels in the final state /3, 4/.

In Fig.2 we display XAS spectra recorded at photon energies between 90eV and 150eV. The spectrum of the silicate layer shows an onset at the Si2p edge near 100eV. The Pr4d resonance spectrum starts at 108eV with a clearly resolved edge. There is some weak fine structure with a characteristic triple peak structure. Next we identify the main Pr4d resonance which in the literature is often assigned as the giant resonance. It is a rather broad resonance which has two peaks at energies around 123eV and at around 130eV.

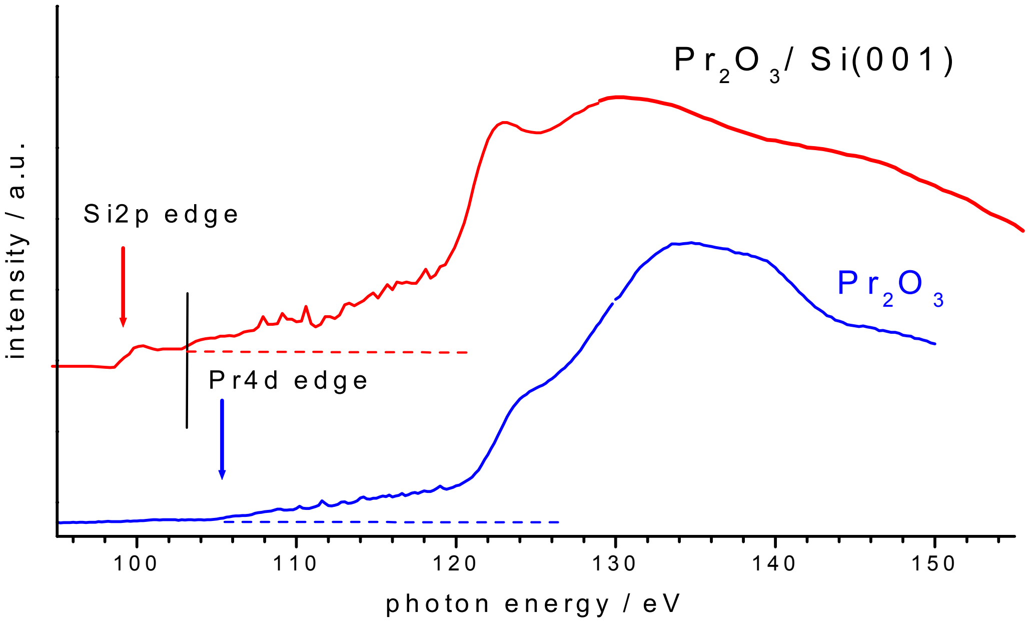

Fig.2: XAS spectra taken at the Pr4d resonance. The upper curve is that of the silicate phase, the lower curve is the spectrum taken for the pure Pr_2O_3 oxide.

We now compare the silicate phase data to those of bulk Pr_2O_3. The interface data show the Si2p edge at around 105eV, the weak fine structure signals as well as the first giant resonance at 123eV are more pronounced. Also, there is are shifts of towards lower excitation energies at the onset of the Pr4d edge (1eV) and in the broad maximum around 130eV (5eV). Within the giant resonance there are two final states for the excitation from the Pr4d levels. These structures are due to unoccupied Pr4f (123eV) and Pr5d (130eV) states in the empty conduction band (CB). This assignment is supported by corresponding constant initial state photoemission experiments in which the first reso-nance at 123eV shows a distinct Fano profile, in particular for the Pr4f initial states /2/. The second resonance at around 130eV shows no Fano

profile and is attributed to the empty covalent bonded Pr5d, O2p, and Pr4f states. The intensity gain in the giant resonance at 123eV indicates a change in the Pr4f occupancy while the Pr5d states just exhibit a significant shift and broadening.
The data can be rationalized as in the silicate phase the formation of Si-O-Pr networks causes an increase in the covalent bonding behavior, i.e. the interaction among the Si3p, O2p, and Pr5d / Pr4f states. The increased covalency changes the b.e. of the contributing states but also enables CT processes in the initial state. An empty Pr4f level becomes filled by a valence electron leaving a valence hole (L) as well as a more localized Pr4f ^{2}L state. The higher the covalency the more stable the valence hole will be. This mechanism explains both, the new state next to the VBM and the increase of the intensity in the 123eV resonance. The increase of the intensity in the fine structure close to the Pr4d edge can also be attributed to the increased covalency. These transitions gain more spectral weight as the selection rules for the individual excitations are less strictly applied.

In summary, the VB and the CB of Pr_2O_3 are built by covalent Pr6s, Pr5d, Pr4f, and O2p states. There is a significant contribution of Pr5d states in the valence band. The Pr4f states are the states next to the VBM / CBM while the Pr6s states appear at the bottom of the valence band. In the silicate phase there is an increased covalent bonding in the valence states caused by the Si-O-Pr bonds. Additional, localized Pr4f states are filled by CT processes. They appear above the covalent bonded valence states right at VBM and enhance the 4f contribution in the Pr4d-Pr4f giant resonance.

/1/ H.J.Osten, J.P.Liu, H.J.Müssig, Appl.Phys.Lett. 80 (2002) 297.
/2/ D.Schmeißer, Comp.Materials Science, in press.
/3/ O.Gunnarson, K.Schönhammer, Phys.Rev.B28 (1983) 4315.
/4/ A.Kotani, H.Ogasawara, J.Electron Spectr.Rel.Phen.86 (1997) 65.

Angle-dependent resonant x-ray emission spectroscopy of PTCDA molecules on Ag(111)

O. Fuchs, L. Weinhardt, C. Heske, and E. Umbach, *Experimentelle Physik II, Universität Würzburg, Am Hubland, 97074 Würzburg*
Y. Zubavichus and M. Grunze, *Angewandte Physikalische Chemie, Universität Heidelberg, Im Neuenheimer Feld 253, 69120 Heidelberg*

Resonant inelastic soft x-ray scattering (RIXS) is an element-specific photon-in-photon-out method and hence follows the dipole selection rules. Thus, this technique provides detailed information about the local partial density of states (LPDOS). Applied to ordered molecular systems, a polarization-dependent linear dichroism can be used to study the symmetry of the involved molecular orbitals. In order to fully exploit this possibility, an independent selection of both, the direction of the polarization vector of the exciting synchrotron beam as well as the emission angle relative to the sample surface, is necessary. At an undulator beamline providing linearly polarized light with a fixed direction, this can only be achieved by using an apparatus equipped with a rotatable analyzer chamber. The rotatable spectroscopy apparatus ROSA (Prof. R. Szargan, Universität Leipzig [1]) is uniquely suited for such angle-dependent investigations. Furthermore it is additionally equipped with an electron energy analyzer to independently study the core levels involved in the RIXS process.

The studied system, PTCDA (perylene-3,4,9,10-tetracarboxylic dianhydride) multilayers adsorbed on a Ag(111) surface, is known to be a highly ordered system in which the planar PTCDA molecules lie flat on the silver surface [2,3]. Thus, the molecular π orbitals of the

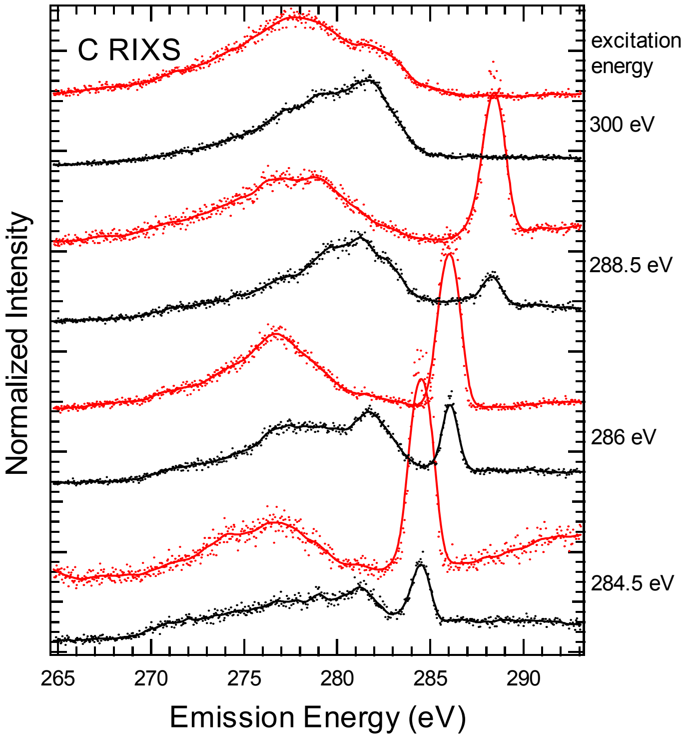

Fig. 1: Resonant series of C 1s XES spectra with excitation into π^* orbitals. Emission from σ orbitals is shown in red, combined emission from π and σ orbitals in black.

perylene ring system are oriented perpendicular to the surface, whereas the σ orbitals are parallel. This fact allows to exclusively excite electrons either into the π^* states with light polarized perpendicular to the surface, or into the σ^* states if the polarization is parallel to the surface. Furthermore, on the emission side, only σ states can contribute to the signal in normal emission, whereas in grazing emission, both σ and π states can emit in the direction of the soft x-ray spectrometer.

The substrate preparation, consisting of sputtering with Ar^+ ions and annealing at 800 K and subsequent evaporation of PTCDA was done *in situ* in ultra high vacuum (at a pressure of $1x10^{-9}$ mbar). The Ag substrate was held at room temperature during evaporation. In order to minimize beam damage effects due to the high excitation intensity of the U41-PGM beamline, the sample was moved to obtain a pristine excitation spot on the sample every 60 seconds.

Figure 1 shows a resonant series of C 1s RIXS spectra taken by exciting exclusively into the π^* resonances of the PTCDA absorption spectrum (i.e., the incoming light was polarized perpendicular to the sample surface). Red spectra were recorded in normal emission, with contribution only from σ states, whereas the black spectra show grazing emission spectra with contributions from both σ and π orbitals. The big spectral differences between the two orientations prove that the PTCDA multilayer is highly ordered.

Based on previous detailed studies of the PTCDA NEXAFS spectra [4], the different π* resonances correspond to excitations in selected functional groups of the PTCDA molecules. In detail, excitation at 284.5 eV and 286 eV excites carbon atoms within the perylene ring system, while an excitation energy of 288.5 eV creates core holes in carbon atoms in the anhydride groups of PTCDA. Apparently, the occupied molecular orbitals exhibit pronounced differences between these different subregions of the molecule.

In order to understand the taken spectra quantitatively, DFT (density functional theory) calculations yielding the energy levels and geometries of the molecular orbitals are currently being performed. Based on such calculations, theoretical RIXS spectra will be produced and compared to the experimental spectra. Applying the final state rule [5,6] for this system, ground state calculations should already prove very valuable to gain a detailed understanding of the observed RIXS spectra.

We gratefully acknowledge the technical support by C. Jung and the BESSY staff as well as funding by the BMBF (FKZ 05KS1WW1/6 and 05KS1VHA).

References:

[1] C. Heske, U. Groh, O. Fuchs, E. Umbach, N. Franco, C. Bostedt, L.J. Terminello, R.C.C. Perera, K.H. Hallmeier, A. Preobrajenski, R. Szargan, S. Zweigart, W. Riedl, and F. Karg, phys. stat. sol. (a) **187**, 13 (2001).

[2] E. Umbach, M. Sokolowski, and R. Fink, Appl. Phys. A **63** (1996) 565.

[3] E. Umbach, K. Glöckler, and M. Sokolowski, Surf. Sci. **402-404** (1998) 20.

[4] J. Taborski, P. Väterlein, H. Dietz, U. Zimmermann, and E. Umbach, J. Electr. Spectr. Relat. Phenom. **75** (1995) 129.

[5] V.I. Grebennikov, Y.A. Babanov, and O.B. Sokolov, phys. stat. sol. **79** (1977) 423.

[6] U. von Barth, and G. Grossmann, Phys. Rev. B **25** (1982) 5150.

Buried Antiferromagnetic Films Investigated by X-Ray Magneto-Optical Reflection Spectroscopy

P.M. Oppeneer*, H.-Ch. Mertins, D. Abramsohn, A. Gaupp, S. Valencia, W. Gudat,
J. Kunes*, C. M. Schneider*
BESSY GmbH, Albert-Einstein-Str. 15, D-12489 Berlin
*Leibniz- Institute of Solid State and Materials Research, P.O. Box 270016, D-01171 Dresden

Among the magnetic materials of current technological interest antiferromagnets (AFM's) have gained appreciable importance lately, because they find key applications in novel spintronic devices, such as magnetoresistive, tunnelmagnetoresistive, or other exchange-biased micro- and nanostructures [1]. In these devices, that often comprise embedded AFM layers coupled to ferromagnetic (FM) layers, the spin-polarized electronic structure of the AFM's plays an important role. Surprisingly, there exists only littly experimental knowledge of the AFM spin-resolved electronic structure. This is related to the inability of traditional techniques applied up to now to sensitively probe the AFM spin-electronic state. Magneto-optical (MO) spectroscopies that are sensitive to the square of the magnetization M would be applicable to investigate AFM's. To such spectroscopies belong the x-ray Voigt effect and the x-ray magnetic linear dichroism (XMLD), measured in transmission [2] or absorption [3], respectively.

Here we report a novel x-ray MO reflection spectroscopy [4] applicable to AFM’s. In this spectroscopy, we utilize the large penetration depth of soft x-rays of typically 20-100 nm to investigate buried AFM layers of ex-situ grown samples. The geometry which we employ to observe the MO spectrum is shown in Fig. 1a) for XMLD-transmission experiments and in Fig. 1b) for the new XMLD-type reflection experiments. The spin axis $\boldsymbol{a}$ of the material (not shown) is oriented in-plane, while linearly polarized synchrotron radiation is incident on the material at normal incidence for XMLD-transmission experiments and at an glancing angle θ for reflection experiments, respectively. At fixed angle θ the transmission T (reflectance R) of the material is measured twice, once with the spin axis parallel ($T_{||}$, $R_{||}$) and once with spin axis perpendicular ($T_{\perp}$, $R_{\perp}$) to the film-projected component of the polarization vector $\boldsymbol{E}$. The XMLD effect is defined by the difference, $\Delta T = T_{||} - T_{\perp}$ or $\Delta R = R_{||} - R_{\perp}$, respectively. Both measurements, transmission and reflection, probe the fundamental MO quantity $Im\,(\varepsilon_{\parallel} - \varepsilon_{\perp})$, which is the imaginary part of the difference of the components of the dielectric tensor, that are parallel or perpendicular to the spin axis [2]. The measurement of ΔR serves as a new x-ray spectroscopic access to the spin-polarized density of states of AFM's [4].

The room-temperature experiments were performed at the BESSY UE56/1 beamline, using the UHV-polarimeter [5], equipped with coils for magnetic scattering experiments [6]. The FM samples were sputter deposited Co (50 nm) on a Si_3N_4 membrane (100 nm) and 30 nm Co on Si, capped with 3 nm Al to prevent oxidation. The AFM sample was a NiO/Co/Ta/Cu (50/5/4/1 nm) layered structure with the AFM at the bottom. It was slowly cooled through the respective Néel temperature in an applied field. The exchange coupling between the FM and AFM spins is thereby exploited to predefine the direction of the spin axis in the AFM.

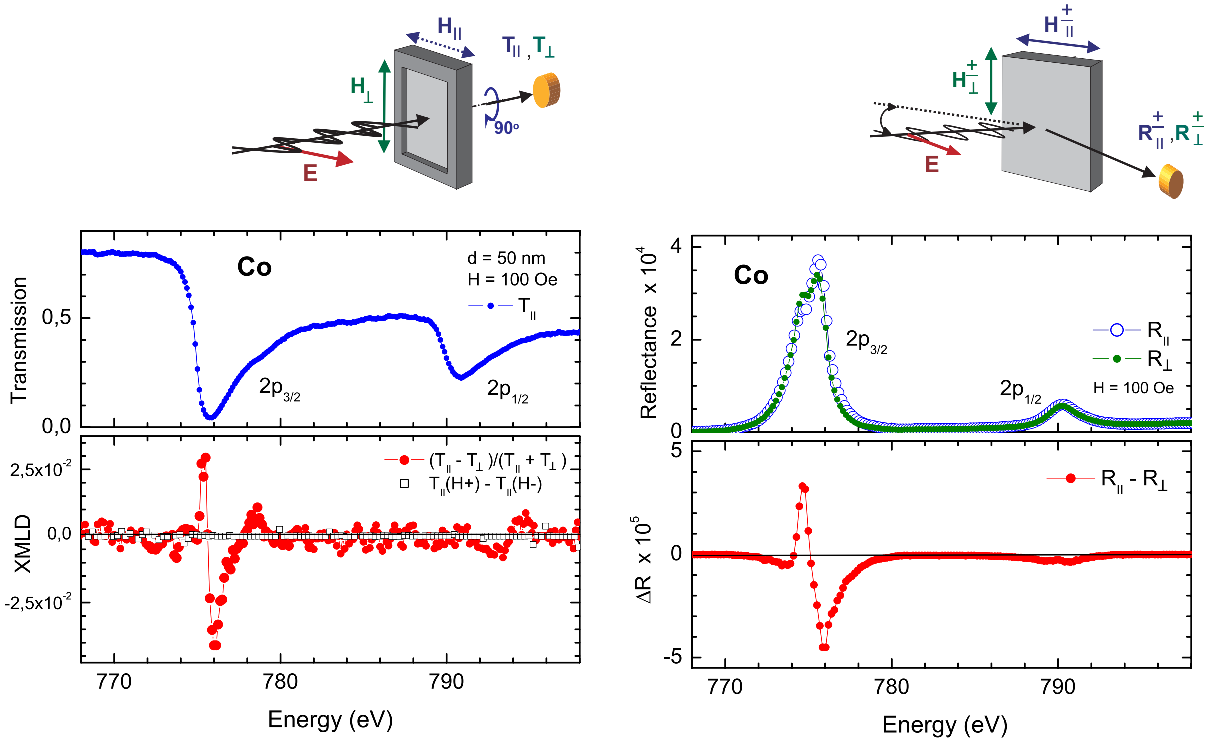

Fig1. Experimental set up for recording XMLD spectra of magnetic films in transmission (a) and in reflection (b). The spin axis ***a*** lies in the film plane and can be oriented for FM's by applying external fields H□□ or $H_{\perp}$. Transmission (a) and reflection spectra (b) across the Co 2p edges and the corresponding XMLD signals. The XMLD is even in the magnetization, shown by the vanishing difference signal for inverted magnetization direction ((a) open circles). The correspondence of XMLD spectra (a) and (b) shows that the reflectance signal ΔR is quadratic in the magnetization and serves as a new spectroscopic access to

To demonstrate that the novel XMLD-reflection effect can be observed indeed we first measured the spectrum of FM Co in reflection and compared it with results obtained in transmission. Fig. 1a shows the XMLD-transmission structure [2]. It displays a pronounced structure at the $2p_{3/2}$ edge due to the resonant excitations from 2*p* to 3*d* levels. As expected, it is even in *M*, as shown by the vanishing difference signal for inverted magnetization direction (open symbols). The XMLD-reflection spectrum is shown in Fig. 1b. For a FM material additional terms that are linear in *M* can be cancelled out by measuring the reflectance for two antiparallel magnetization directions, and, subsequently, by replacing $R_{||,\perp}$ by $R_{||,\perp} = ½\{R_{||,\perp}(H+) + R_{||,\perp}(H-)\}$. The reflection spectrum resembles the structure that has been observed by transmission spectroscopy (Fig. 1a), proving that we have observed the MO response in reflectance that is even in *M*. The reflection signal is effortlessly detectable and by a factor of 5 larger than that obtained in transmission. Moreover, a clear ΔR signal could be measured for a wide range of glancing angles of incidence up to 40^o so that depth profiling becomes feasible by tuning *θ*.

After successfully detecting the XMLD-reflection effect, we studied the exchange-biased micro-structure with buried AFM layer. The reflectance spectra were recorded by rotating the sample about the surface normal over 90° (Fig. 2). The spectrum ΔR measured across the Ni $2p$ edges of NiO/Co/Ta/Cu shows peak values larger than 20%. In addition multiplet structures appear in the spectrum, which are typical for $3d$-oxides [7]. The multiplet splitting at the $2p$ edge is particularly exploited for imaging of AFM domains in insulating $3d$-oxides by photo electron spectroscopy (PEEM) [7]. In PEEM the largest XMLD contrast is found at the $2p_{1/2}$ edge, whereas in reflection we find the largest contrast at the $2p_{3/2}$ edge, where also the intensity is largest. The PEEM technique is associated with the sensitivity of XMLD to the multiplet fine structure, while our approach is not restricted to insulating AFM oxides. This we could show for a metallic AFM system Ta/MnNi/Co/Ta/Cu [4].

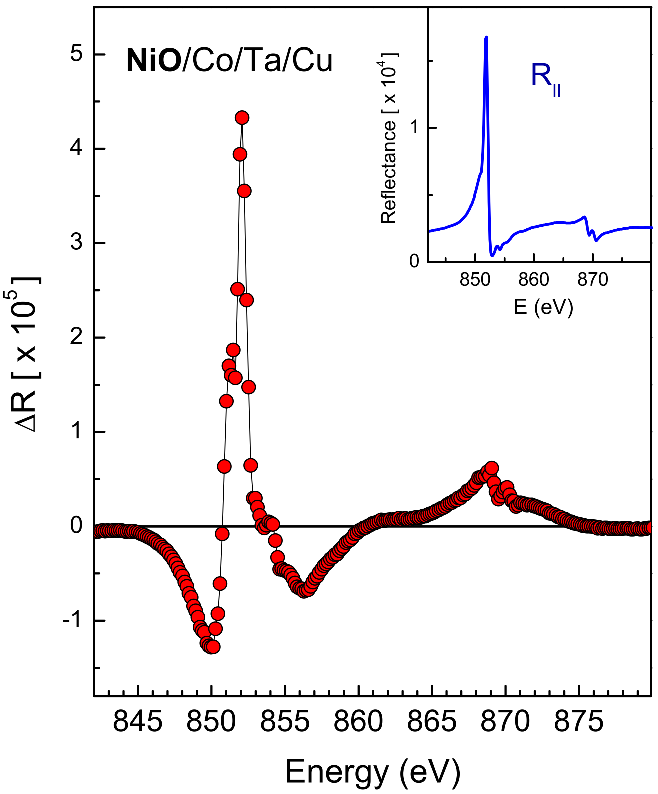

Fig. 2 XMLD reflection spectrum ΔR of buried AFM NiO in NiO/Co/Ta/Cu across the Ni $2p$ edge at $\theta = 18^{\circ}$. Signals larger than 20% are obtained, most pronounced at the $2p_{3/2}$ edge. The fine structure is due to the multiplet splitting, typical for 3d-oxides. Inset: reflectance R□□.

In conclusion, we developed a new XMLD-reflection spectroscopy that provides large signals and hat can be applied to arbitrary, e.g. industrial systems, including samples with buried AFM layers or even “dirty” surfaces. Such samples cannot be probed by photoelectron-based spectroscopy, due to the small escape depth of 2-4 nm of the secondary electrons.

1 S. A. Wolf et al., Science **294**, 1488 (2001).
2 H.-Ch. Mertins et al., Phys. Rev. Lett. **87**, 047401 (2001).
3 S. S. Dhesi et al., Phys. Rev. Lett. **87**, 067201 (2001).
4 P.M. Oppeneer et al., Phys. Rev. B, in press (2003)
5 F. Schäfers et al., Appl. Opt. **38**, 4074 (1999)
6 H.-Ch. Mertins et al., Phys. Rev. B **66**, 184404-1 (2002)
7 A. Scholl et al., Science **287**, 1014 (2000)

Supported by the BMBF 05KS1IPB/8

Near edge X-ray absorption fine structure of thin perylene films deposited on $Al_20_3/Ni_3Al(111)$

M. B. Casu, A. Schöll, D. Hübner, Y. Zou, K. R. Bauchspieß, Th. Schmidt, C. Heske, and E. Umbach

Experimentelle Physik II, Universität Würzburg, Am Hubland, D-97074 Würzburg, Germany

Organic field effect transistors (OFETs) are part of a rapidly developing field and a technological challenge of modern solid-state physics [1]. One of the main goals is to prepare organic thin films with physical properties comparable to those of organic single crystals [2]. Thus it would be possible to use low-cost deposition methods for optimised and efficient devices. Our aim is to develop a MISFET device with optimised performance, step by step, starting from choosing the most suitable substrate/insulator/organic system, improving the characteristics of the organic layer, developing suitable methods for contact formation, and performing electrical and electronic characterisation of the complete device. In this work we present the results of a near-edge x-ray absorption fine structure (NEXAFS) investigation of thin perylene films, one of the promising candidates as OFET material, deposited on $Al_20_3/Ni_3Al(111)$.

We prepared thin films of perylene [3, 4] by organic molecular deposition (OMBD) in-situ using strictly controlled evaporation conditions in order to obtain well ordered films. We were interested in the influence of the growth parameters on the molecular orientation, the possible consequential changes in the electronic fine structure, and the correlation between X-ray photoelectron spectroscopy (XPS) and NEXAFS. The measurements were performed at Beamline UE52-PGM at BESSY. The $Ni_3Al(111)$ single-crystal substrate was oriented with an accuracy better than 0.4° and mechanically polished on one side. It was cleaned in UHV by means of repeated cycles of Ar-sputtering and subsequent annealing. The preparation of the oxide was carried out by exposing the single crystal at 1000 K to oxygen (partial pressure $3x10^{-8}$ mbar). This method gives a thin oxide layer of 5 Å [5], suitable for investigation by standard electron spectroscopies without any charging phenomena. In addition, the thin oxide layer is intended to simulate the electronic and structural properties of thick oxide layers employed in industrially relevant OFETs. Each step of the substrate preparation was checked by using XPS and NEXAFS. Perylene was deposited on $Al_20_3/Ni_3Al(111)$ with different deposition parameters. The deposition was monitored with a quadrupole mass spectrometer and the nominal thickness was determined by using the attenuation of the XPS signal at well known spectral lines (Al_{2p} and Ni_{3p}). We carried out NEXAFS measurements in the partial yield mode (PY) in grazing incidence (70°). In order to investigate the molecular orientation on the surface we took advantage of the dependence of the NEXAFS spectra on the polarisation of the incident radiation [6]. Hence, we measured the spectra by using both horizontally and vertically linearly polarised synchrotron radiation tuning the polarisation by means of the undulator. Finally the spectra were normalised by taking the I_0 current and the clean substrate signal into account [7].

Figure 1 shows the C-K NEXAFS spectra obtained from 7 ML (a) and 5 ML (b) of perylene on $Al_20_3/Ni_3Al(111)$ deposited under different preparation conditions. The spectra were taken in grazing incidence for horizontal (black curves) and vertical (red curves) polarization. The main features due to the π*-resonances exhibit a strong polarisation dependence, indicating a high degree of orientational order in the films, and allowing us to determine the molecular orientation from the observed dichroic behaviour [6]. At a substrate temperature of 240 K and with an evaporation rate of 1 ML/min (Fig. 1 a), the molecules are close to the upright position with respect to the substrate plane (θ =74° between the molecular plane and the substrate surface), while the molecules appear to be lying almost flat (θ = 27°) when the film is grown at 0.4 ML/min and at a substrate temperature of 100 K (Fig. 1 b). Furthermore, the electronic structure of the two films is slightly different, as seen from the different dichroic behaviour of the peak at about 289 eV. These are only two examples among the recorded spectra. As a preliminary result we find that it is possible to tune the molecular orientation of perylene by using different sets of growth parameters. We observe that the perylene molecular plane is parallel to the substrate surface when the film deposition rate is low, while the molecules stand upright when a high-rate deposition is chosen.

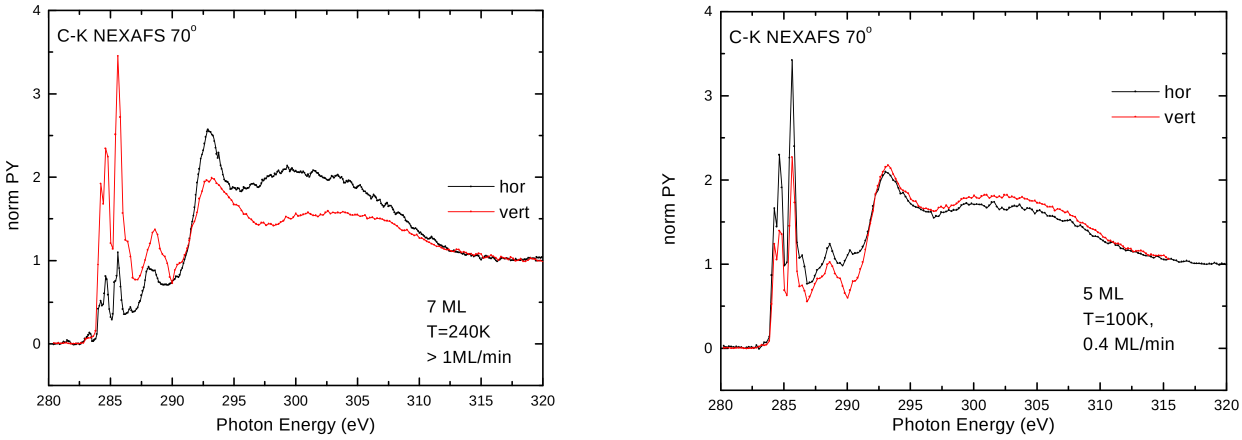

(a)

(b)

Fig. 1. C-K NEXAFS spectra obtained from 7 ML (a) and 5 ML (b) of perylene on $Al_20_3/Ni_3Al(111)$ deposited under different preparation conditions. The spectra were taken in grazing incidence for horizontal (black curve) and vertical (red curve) polarisation.

In conclusion, the results from NEXAFS investigations show that the growth parameters play a fundamental role in the molecular orientation and in the electronic structure of well ordered thin films of perylene deposited on $Al_20_3/Ni_3Al(111)$.

We found that for a high deposition rate with the substrate being at room temperature the molecules are standing upright. This is of strong technological relevance since perylene films:

a) can be prepared in an “easy” way,
b) are well oriented,
c) can have a molecular orientation that favours charge transport parallel to the substrate surface as needed for FETs in the conventional geometry (better overlap of the π orbitals).

We point out by NEXAFS that perylene/$Al_2O_3/Ni_3Al(111)$ is a suitable organic/insulator/substrate model system for developing an optimised MISFET.

Acknowledgements

The authors would like to thank the BESSY staff for technical support and Prof. M. Sokolowski, Universität Bonn, Germany, for supplying highly purified perylene. Financial support by the DFG through the OFET-Schwerpunktprogramm Um 6/8-1 and by the BMBF under contract 05KS1WWA/5 is gratefully acknowledged.

References

[1] H. E. Katz, A. J. Lovinger, J. Johnson, C. Kloc, T. Siegrist, W. Li, Y.-Y. Lin, and A. Dodabalapur, Nature 404 (2000) 478.
[2] H. E. Katz and Z. Bao, J. Phys. Chem. B 104 (2000) 671.
[3] A. Camerman and J. Trotter, Proc. Royal Soc. A279 (1963) 129.
[4] J. Tanaka, Bull. Chem. Soc. Jpn 36 (1963) 1237.
[5] A. Rosenhahn, J. Schneider, J. Kandler, C. Becker, and K. Wandelt, Surf. Sci. 433-435 (1999) 705.
[6] J. Stöhr and D. A. Outka, Phys. Rev. B 36 (1987) 7891.
[7] A. Schöll, Th. Schmidt, Y. Zou, R. Fink, and E. Umbach, J. Electron. Spectrosc. (2003) at press.

Photoemission with time-correlated Laser and Synchrotron radiation: Charge carrier dynamics at semiconductor surfaces

D. Bröcker[1], T. Gießel[1], D. Pop[1], P. Schmidt[1], B. Winter[1], W. Widdra[1,2]
[1]*Max-Born-Institut, D-12489 Berlin, Germany*
[2]*Institut für Atomare Physik und Fachdidaktik, TU Berlin, Germany*

The success in time-resolved laser spectroscopy using visible and near-IR radiation have inspired further demand for time-resolved X-ray and EUV spectroscopy techniques. In our experimental setup synchrotron radiation (SR) is combined with synchronized Laser pulses. Third generation synchrotron sources like BESSY provide SR pulse width sufficiently short to investigate dynamical processes in the ps time domain.

Here we present a study on the time-resolved charge carrier surface recombination at Si(100) surfaces. Charge carriers are generated by the laser pulse and the temporally excited sample, characterized by a dynamical surface photo voltage is probed with core level photoemission by SR.

For the single bunch experiments a specially designed Nd:YVO_4 laser system, operated at 25 MHz repetition rate, pulse picked to 1.25 MHz (pulse width 14 ps) has been synchronized to the BESSY single bunch frequency. The Laser/SR time delay can be controlled between 0 and 800 ns electronically. Additionally we use a optical delay in a 3 ns time range. Both, laser fundamental and second harmonic generated in a periodically poled crystal have been used, 1064 and 532 nm, respectively. The overall time resolution of the experiments is about 60 ps which is the SR pulse length.

Standard surface science techniques have been used for preparation and characterization of the clean Si(100)-(2x1) surface and the SiO_2/Si(100) interface. The latter was prepared by thermal oxidation of the clean surface at 850 K at 10^{-6} mbar O_2.

Although charge carrier recombination at surfaces and interfaces in semiconductors is of importance for many technological processes, details about carrier dynamics in the surface region are still under debate [1, 2]. Here we present photoemission data on the recombination dynamics at the thermally-grown SiO_2/Si(100) interface.

Fig. 1 shows high-resolution Si 2p core level spectra obtained for 130 eV photon energy for two different SiO_2 layers on Si(100). The dominating feature corresponds to the atomic Si 2p doublet at binding energies around 100 eV. Additionally three shifted components due to the different Si oxidation states can be identified[3, 4]. Upon laser excitation at 532 nm the core levels show a rigid shift of up to 300 meV to lower binding energy due to the surface photo voltage. The amount of the shift depends on the pump-probe delay and the laser intensity. Laser-generated electron hole-pairs are separated in the near-surface field. Their electric field partly compensates the field in the absence of light which causes the well-known band bending at semiconductor surfaces. After the laser pulse the charge carriers will recombine, primarily at the surface which leads to the reappearance of the band bending and a shift of the surface core level back to its initial value. The charge carrier surface recombination time strongly depends on the surface/interface structure and ranges from sub-ps up to μs.

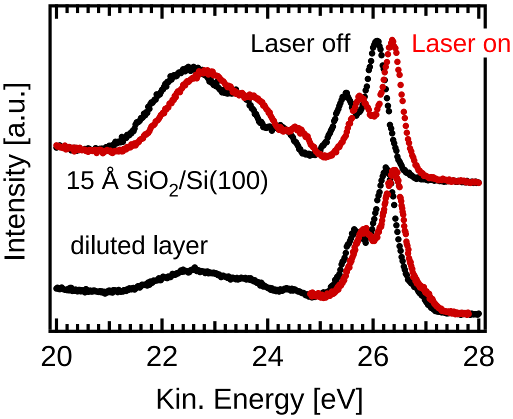

Fig. 1: High resolution Si 2p XPS spectra for a 15 Å SiO_2/Si(100) surface an a diluted layer at $h\nu = 130$eV, $P_{Laser} = 160$ mW @ 530 nm and $\Delta t = 200$ *ps*.

The recombination dynamics at the SiO_2/Si(100) interface after laser excitation at 1064 nm is summarized in Fig. 2. It shows the Si 2p core level shift as a function of the laser-pump SR-probe delay logarithmic time scale. The data show a non-exponential decay in time.

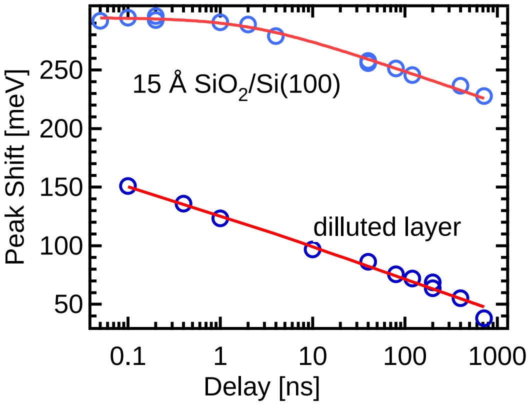

Fig. 2: Si 2p core level shift ΔV as function of Laser-pump SR-probe delay for two different SiO$_2$/Si layers.

Defining the decay rate by $\tau^{-1} \cdot V = -\partial V/\partial t$, its dependence on the surface field can be described by a thermally activated behavior:

$$\tau = \tau(\Delta V) = \tau_\infty \cdot e^{-\Delta V/ckT} \; .$$

For thinner oxide layers on Si(100) we observe smaller shifts and faster decays. However, in all cases the data show a decay rate depending exponentially on the peak shift (band bending) which corresponds to a linear range in Fig. 2.

The observed behavior is interpreted as charge carrier recombination controlled by transport over a dynamic barrier generated by the band bending [5]. Initially, after laser excitation carrier (hole) diffusion is fast due to the small surface voltage. With decreasing carrier densities the band bending in the near surface region partially reappears. For subsequent recombination the carriers have to overcome the increasing energy barrier given by the band bending. This leads to an approximately exponential dependence of the decay rate on the surface photovoltage shift. Numerical simulations of this model, as indicated by the solid line in Fig. 2 using only three parameters, can essentially describe the experimental data over more than three orders of magnitude in time.

The details of the onset of the surface photovoltage shift are shown in Fig. 3 for Laser excitation at 532 nm. The experimental time resolution (60 ps here) is sketched as Gaussian-like peak.

For positive delays we find only a weak decrease within the first 800 ps. The onset of the shift in the range from -800 ps to 0 can be fully understood as intrinsic property of the photoelectron spectroscopy method in the presence of a sudden potential change at the sample. A laser-induced instantaneous (sub ps) surface potential change at time $t = 0$ interacts via its electric field with the outgoing photoelectrons generated earlier. The peak shift reflects, as indicated by the solid line in Fig. 3, the long-range electric field of a surface dipole with radius R

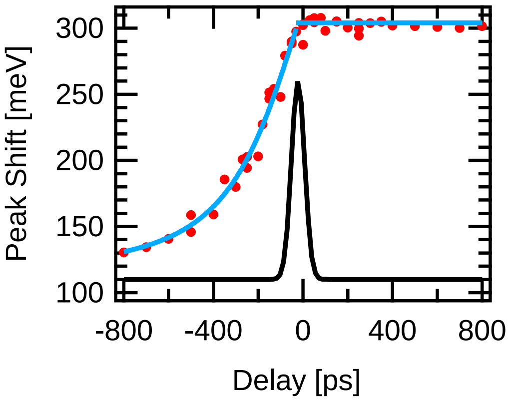

Fig. 3: Onset of the time resolved Si 2p core level shift ΔV. The gaussian indicates the time resolution of the experiment. The solid line is a fit based on the surface potential described in the text.

$$V(z) \propto 1 - z \cdot (R^2 + z^2)^{-1/2} \; .$$

The surface potential detected in time domain by a photoemission measurement is related to this potential function by

$$V(\tau) = V(-\frac{z}{v}) \quad \text{(for negativ delays } \tau) \; ,$$

for a photoelectron velocity v. This effect needs to be considered whenever the dynamics of small energy shifts are analyzed in the presence of a substantial surface photovoltage shift.

To summarize, the charge carrier recombination dynamics at the SiO$_2$/Si(100) surfaces have been studied in the 60 ps to 800 ns regime by Laser/ synchrotron radiation pump-probe photoemission. The observed core level shifts are due to a dynamic surface photovoltage and are well-understood within a simple modell. These studies demonstrate the potential of laser and synchrotron radiation pump-probe experiments.

References

[1] N. J. Halas and J. Bokor, *Phys. Rev. Lett.* **62**, 1679 (1989).

[2] N. P. Long et al., *Phys. Rev. Lett.* **64**, 1158 (1989).

[3] F. J. Himpsel et al., *Phys. Rev. B* **38**, 6084 (1988).

[4] T. W. Pi et al., *Surf. Sci.* **478**, L333-L8 (2001).

[5] R. J. Hamers and D. G. Cahill, *J. Vac. Sci. Technol.* **B9(2)**, 5148 (1991).

Relative partial photoionization cross section of liquid water

R. Weber[1], M. Faubel[2], P. Schmidt[1], W. Widdra[1,3], B. Winter[1]

[1] *Max-Born-Institut, Berlin, Germany*
[2] *Max-Planck-Institut für Strömungsforschung, Göttingen, Germany*
[3] *Institut für Atomare Physik und Fachdidaktik, TU Berlin, Germany*

Using a micron-sized liquid jet valence band photoemission spectra from liquid water have been measured in the 30-120 eV photon energy range at the MBI undulator beamline (U125 SGM). The spectra of liquid water exhibit differential energy shifts as well as peak broadening of the water orbital binding energies relative to the corresponding gaseous features. These differences are of multiple origin, including bond contraction, electronic polarization, and surface dipoles, as discussed elsewhere [1]. Representative photoemission spectra of water are shown in Fig. 1.

The central panel is the pure gas phase spectrum (which is obtained by suitable translation of the jet relative to the electron detection), the top panel displays the measured liquid spectrum characterized by maximum liquid to gas phase intensity ratio, and the center curve is the respective difference spectrum.

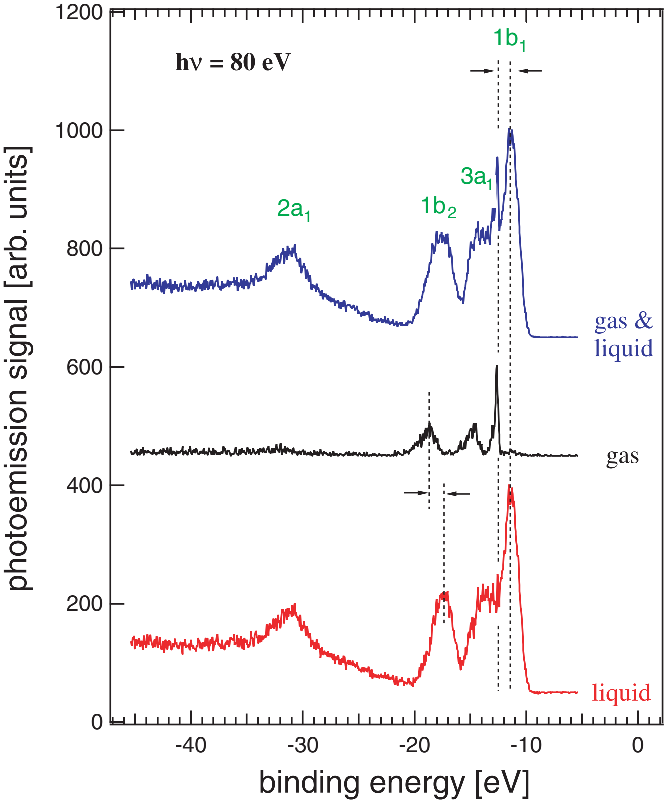

Fig. 1: Photoemission spectra from gas phase water sampled 0.5 μm aside the liquid jet (center), sampled for maximum liquid signal (top) and difference spectrum (bottom), obtained for 80 eV photon energy. The water orbital features, $2a_1$, $1b_2$, $3a_1$, $1b_1$, are assigned.

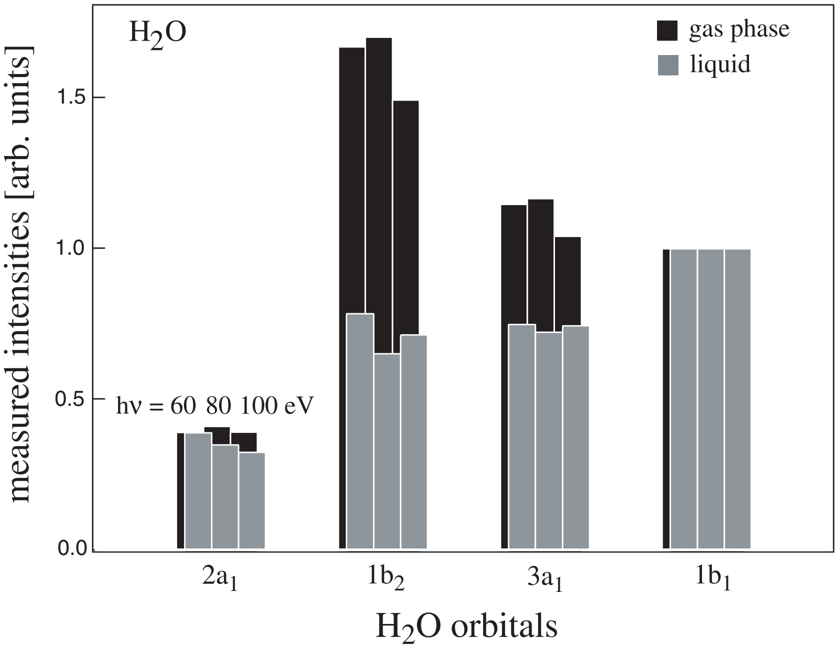

Fig. 2: Measured differential photoionization cross section of the four water valence orbitals for liquid and gaseous H_2O obtained for 60, 80, 100 eV photon energy.

Concerning the relative partial photoionization cross section, $d\sigma_i/d\Omega$, considerably lower values are obtained for the $1b_2$ and $3a_1$ orbitals for liquid as compared to gas phase water. This is shown in Fig. 2 where we display the corresponding measured integrated photoemission intensities, normalized to the $1b_1$ value, for three photon energies (60, 80, 100 eV). These differences can be associated with the decrease of the corresponding differential cross sections, which correlates with a decrease of the respective anisotropy parameters [2, 3], β_{1b_2} and β_{3a_1}. The β value for a given orbital and energy is the result of the interference between the respective partial waves and will change if the orbital structure changes. Notice that the geometry being used in the present study (electron detection normal to the light polarization) ideally suits the detection of *β changes*, for β being in the range of 1.0 to 1.5, which are the values relevant here. Specifically, the electron emission probability is about 50 % smaller for $\beta = 1.5$ than for 1.0.

Surface-specific contributions to the observed cross sectional behavior are ruled out, largely due to the curved surface of the microjet (the jet radius being much smaller than both the synchrotron focal size and the detector entrance of the spectrometer [1]), which leads to an averaging over a wide range of jet surface normal directions. In conclusion, different photoemission cross sections are found for liquid vs. gas phase water. The result is explained by molecular orbital changes due to H-bonding, and can be interpreted in terms of the relative increase of β_{1b_2} and β_{3a_1}, with respect to the gas phase values.

References

[1] B. Winter, R. Weber, W. Widdra, M. Dittmar, and M. Faubel, *J. Phys. Chem.*, (submitted).

[2] J. Cooper and R. N. Zare, J. Chem. Phys. **48**, 942 (1968).

[3] M. S. Banna, B. H. McQuaide, R. Malutzki, and V. Schmidt, J. Chem. Phys. **84**, 4739 (1986).

NanoESCA on polycrystalline $Al_{0.98}Sn_{0.02}$

S. Schmidt[1], P. Bernhard[2], M. Escher[3], F. Forster[1], D. Funnemann[4],
B. Krömker[4], M. Merkel[3], F. Reinert[1], G. Schönhense[2], C. Ziethen[2]
[1] *Universität des Saarlandes,*
FR 7.2 Experimentalphysik, Saarbrücken
[2] *Johannes Gutenberg Universität Mainz,*
Institut für Physik
[3] *Focus GmbH, Görsroth*
[4] *Omicron Nanotechnology GmbH, Taunusstein*

We present spatially resolved XPS data of polycrystalline $Al_{0.98}Sn_{0.02}$. Spectra of the Al 2p and O 1s core-level, taken on the grains and their boundary show that the main part of the oxygen is located in the grain boundaries and bound to Al (presumably as Al_2O_3). The Al 2p energy scan measured on neighboring Al-grains also reveals small differences in the peak position suggesting that the method is also sensitive to different crystallographic orientations of the grains.

For the investigation of the spatial and chemical structure of grains and grain-boundaries in polycrystalline $Al_{0.98}Sn_{0.02}$ there is the requirement of both a good XPS energy resolution and an adequate spatial resolution. The data presented here were measured using a new instrument design that is currently developed in collaboration between two universities and two companies[1]. This NanoESCA system consists of a PEEM in combination with a band-pass energy filter (double-hemispherical electron analyzer) which — at the current state — is capable of simultaneous energy and spatial resolution of 600 meV and 140 nm as documented in a separate contribution to this annual report. The data of this investigation were taken at beam-line UE-52/SGM1 of BESSY II using photon energies hν= 200 and 625 eV for the Al 2p and O 1s core-level, respectively. The photon spot of the beam-line nicely matched the field of view of $\approx 40\,\mu$m allowing optimum intensity and reduced integration time per picture. The polished sample was cleaned using Argon sputtering to remove contaminants from the surface. The measurements were taken at a base pressure of 8×10^{-10} mbar at room temperature using only ion getter pumps to reduce vibrations.

The line-graph in Fig. 1 shows three energy scans across the O 1s core-level energy taken on different sample areas (red, green and blue rectangles in picture a, b and c) corresponding to grain boundaries (red and blue rectangle) and on the surface of one particular grain (green rectangle). The three greyscale pictures show the energy-filtered data at the different kinetic energy indicated in the graph. The intensities in the spectra correspond to the integrated intensities enclosed by the rectangles normalized to the sampled rectangular area. We observe a strong accumulation of oxygen in the grain boundaries (white = high intensity) that spectroscopically has a higher binding energy (chemical shift) than the oxygen detected on the grain. Together with the following remarks, the latter is attributed to adsorbed oxygen. We find the above interpretation supported if we also take into account the Al 2p energy scans shown in Fig. 2 taken on areas corresponding to those in Fig. 1 (grains and boundaries). We clearly observe two different energy positions and conclude that the Al exists in two different chemical surroundings. Thus in Fig. 2 the red and green rectangles monitor grain-boundaries with a strong chemical shift to lower kinetic energies (higher binding energies), and the white structures in b) are therefore attributed to areas with oxidized aluminum (Al_2O_3). The two remaining (light and dark blue) areas are positioned in the center of two grains where Al is metallic. During the energy scan it is also noticeable that between the different metallic grains we observe an energy shift of several tens of meV which is much smaller than the boundary-grain differences (different grains "lighten up" at slightly different E_{kin}). These small differences could be the result of different crystallographic orientations of the grains which — due to the different surface termination — cause these energy-shifts.

This work was supported by the BMBF (FKZN 13N7865, 13N7863, 13N7864, 13N7847) and the DFG(SFB 277). We like to thank the BESSY II staff, esp. F. Senf for his help with the beam-line.

---

[1] D. Funnemann, P. Bernhard, M. Escher, F. Forster, B. Krömker, M. Merkel, F. Reinert, S. Schmidt, G. Schönhense, J. Westermann, et al., Bessy Annual Report 2002 (2003), to be published.

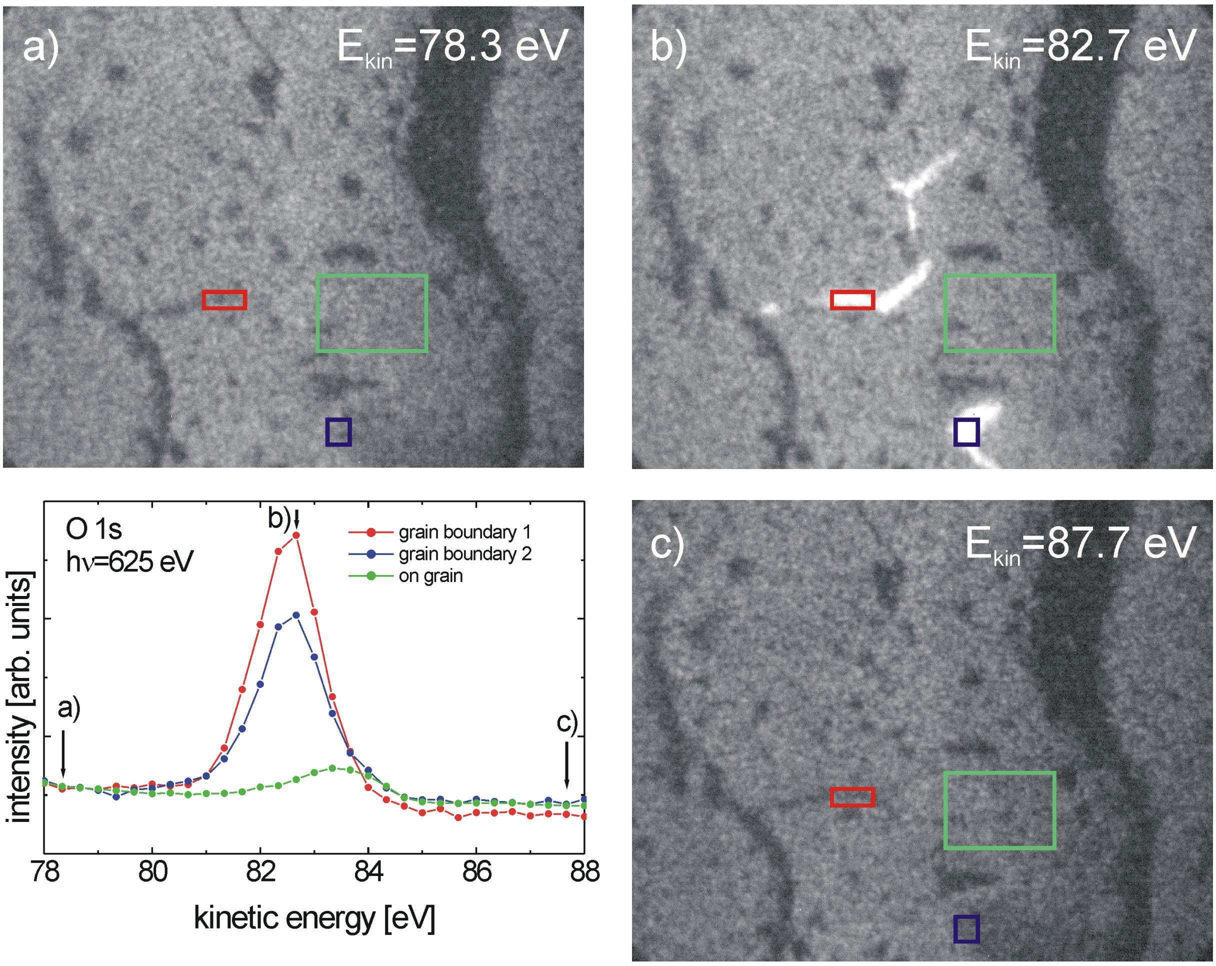

FIG. 1: Energy scans across the O 1s core-level on different sample positions taken at hν = 625 eV. The intensities in the line-scans are normalized to the corresponding areas.

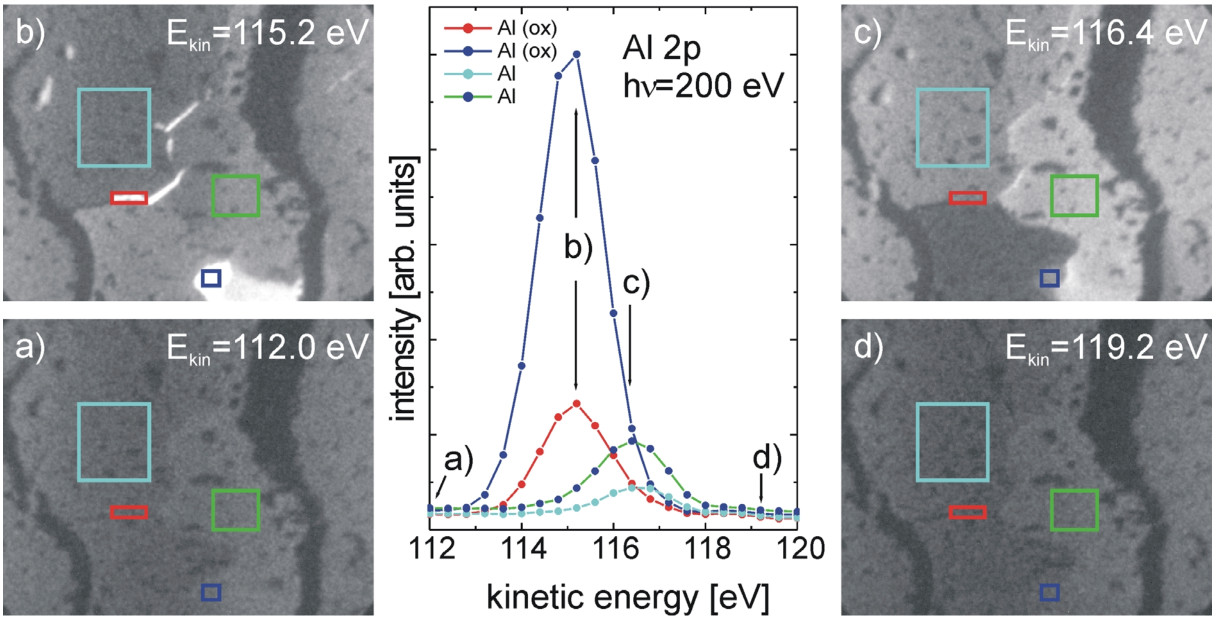

FIG. 2: Energy scans across the Al 2p core-level on sample positions that correspond to those in Fig. 1 (hν = 200 eV, intensities normalized to areas). The different grains are clearly distinguished due to small shifts in the peak energy.

Photoemission Experiments on Chiral Molecules on Si

M.Carbone[a], M.N.Piancastelli[a], A. Kumar[b], M. Tallarida[b] and K. Horn[b]

[a]Department of Chemical Sciences and Technologies and INFM, University “Tor Vergata”,
Rome, Italy
[b]Fritz-Haber-Institut der MPG, Berlin, Germany

We have performed experiments on both S,S and R,R 2,3-butandiol on Si(100)2×1 at the beam line UE56/2-PGM2. In order to reinforce the effect of using circularly polarized light we chose a system which has two chiral centres.

We have measured C1s photoemission spectra corresponding to a monolayer of butandiol on Si, at liquid-nitrogen temperature using both left and right circular polarization as well as horizontal and vertical polarization. We also used two geometries of the sample with respect to the incident beam, grazing and normal.

We can summarize the findings and drawbacks in three points.

1) C1s peaks intensity ratio

The C1s spectra show 2 peaks. On the basis of electronegativity arguments, the higher kinetic energy peak can be assigned to the external carbon atoms (-CH_3), the lower kinetic energy one to the and internal ones (-CHOH). Since there is an equal number of internal and external carbon atoms in the molecule, the ratio between the two peaks should in principle be 1:1. It can be seen in Fig. 1 this it is not the case.

The smaller intensity of the spectral feature deriving from the -CH_3 group can be related to a fragmentation process that occurs upon adsorption, similar to what we already observed for methanol and ethanol on Si(111)7×7[1],[2].

2) Dichroism

In Fig. 1 the C1s spectra of 2,3-S,S butandiol on Si(100)2×1, taken with 4 different polarizations at grazing incidence, are reported, roughly normalized for the smaller peak intensity. The higher kinetic energy peak intensity varies with the polarization. In particular the peaks taken with left polarized (green curve) and right polarized (blue curve) light are different. However, some care must be taken, because those two curves also show some different line-shape, which might indicate some sample modification that occurred during the data recording.

3) Cracking

The cracking of the adsorbate for long exposures to the beam is shown in Fig.2, where a monolayer of 2,3-R,R butandiol is monitored as a function of exposure to the synchrotron light, during 2h20’.

In the figure the first and the last spectrum are reported . The radiation effect results in a gradual change both of peaks ratio and position. The VB changes accordingly. The process is not spontaneous since the check of non-irradiated sample spots yields spectra not affected by the peak shift.

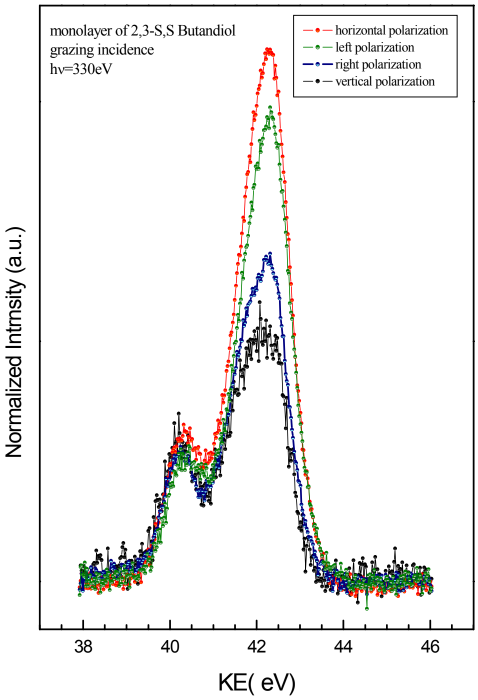

Fig.1 C1s photoemission spectra as a function of the beam polarization

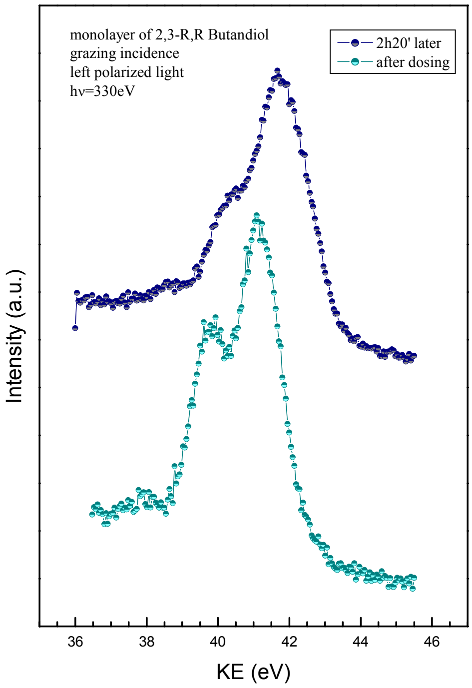

Fig.2 C1s peaks as a function of sample irradiation

References

---

[1] M. Carbone, M.N. Piancastelli, R. Zanoni, G.Comtet, G. Dujardin, L. Hellner, *Surf. Sci.* 370 **(1997)** L179.

[2] M. Carbone, M.N. Piancastelli, J.J. Paggel, Chr. Weindel, K. Horn, *Surf. Sci.* 412 **(1998)** 441.

Photon-induced processes in co-condensed glycine/water thin films

G. Tzvetkov[a], Y. Zubavichus[b], G. Koller[a], O. Fuchs[c], C. Heske[c], E. Umbach[c], M. Grunze[b], M. G. Ramsey[a], F. P. Netzer[a]

[a]*Institut für Experimentalphysik, Karl-Franzens-Univesität Graz, Universitätsplatz 5, A-8010 Graz, Austria*
[b]*Angewandte Physikalische Chemie, Universität Heidelberg, Im Neuenheimer Feld 253, 69120 Heidelberg, Germany*
[c]*Experimentelle Physik II, Universität Würzburg, Am Hubland, 97074 Würzburg, Germany*

The adsorption/co-adsorption of molecules on/with ice has attracted much attention because of its importance for understanding solvation, vaporization and surface reactions [1]. In particular, the adsorption studies of biologically active molecules (amino acids, peptides, etc.) may play a crucial role in the emerging field of bioengineered materials [2]. In such investigations the spectroscopic methods using synchrotron radiation for generating photoelectrons are frequently exploited. Sometimes, however, the high photon flux available at synchrotron beamlines may induce undesired chemical reactivity and sample degradation [3]. We have investigated therefore in this work the soft X-ray synchrotron radiation (160-610 eV) induced processes of desorption and decomposition in co-condesed *in vacuo* glycine (NH_2CH_2COOH)/water thin films as model systems for more complicated biological systems.

The experiments were performed on the UE52-PGM undulator beamline with a SCIENTA SES-200 analyser and on the PM-1 bending magnet beamline at BESSY 2. Vapour deposition of glycine was achieved from a specially designed Knudsen cell-type molecule evaporator [4]. Simultaneously the sample was exposed to H_2O by backfilling the preparation chamber with a water pressure up to ~10^{-7} mbar. Two condensed films at 85 K were investigated: 6 L (1 L = 1×10^{-6} Torr s) of water + 10 ML glycine (denoted as 6W10G) and 60 L of water + 10 ML glycine (denoted as 60W10G) on an Al_2O_3/NiAl(110) surface. Fig. 1 shows the consequence of the

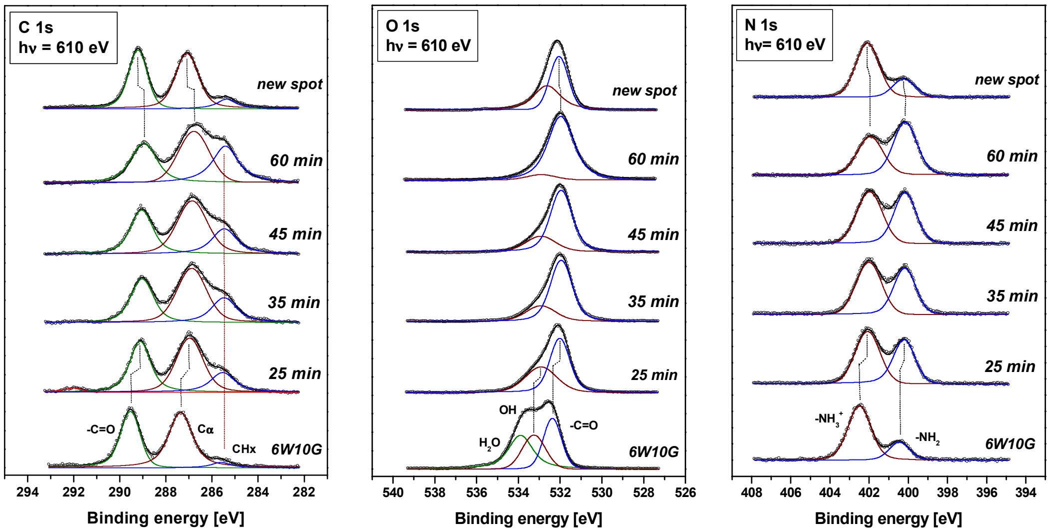

Fig. 1. Development of the C1s, O1s and N1s photoelectron spectra of the 6WG10 film with increasing periods of synchrotron irradiation.

photon-induced changes in the 6W10G film as probed by the C1s, O1s and N1s core level spectra. As one can see after 25 min of irradiation the spectra show significant changes, namely a shift of the glycine spectral components to the lower binding energies, an increase of the C1s signal at 285.5 eV (hydrocarbon decomposition products), the appearance of a new C1s component at 291.9 eV (probably due to the formation of CO_2), an increase of the N1s component at 400.5 eV (amino group), and the absence of the water O1s signal at 534 eV. The valence region PES spectrum of the 6W10G film (Fig. 2) after 60 min of irradiation still shows the three bands A, B and C characteristic of the zwitterionic glycine ($NH_3^+CH_2COO^-$), but the presence of the Ni 3d emission from the substrate indicates strong radiation-induced desorption from the film. After 60 min of irradiation a new spot on the film was probed by moving the crystal by ~1 mm. The spectra now show only small changes compared to the original 6W10G film indicating a lower degree of decomposition.

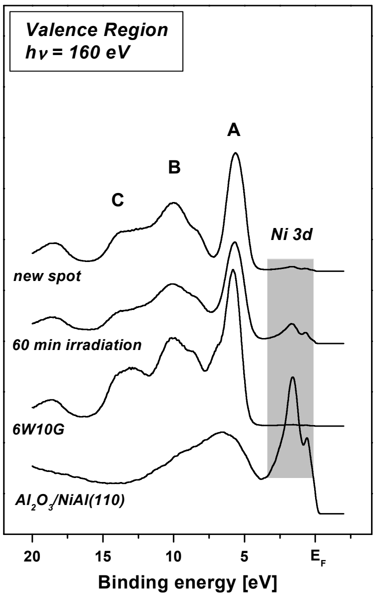

Fig. 2. Development of the valence region photoelectron spectrum of the 6WG10 film.

The changes in the C1s PES after 60 min of irradiation of the water-rich 60W10G film can be seen in Fig. 3 (bottom two spectra). Judging from the intensity of the C1s component at 285.5 eV, which is due to the emission from decomposition fragments of glycine, we can conclude that the 60W10G film is less influenced by irradiation than the 6W10G film. As it is shown in Fig. 4 almost no changes are detected in the valence band region spectrum of the 60 min irradiated film. Only the three highest occupied orbitals of water ($1b_1$, $3a_1$ and $1b_2$) are present in the spectrum, due to the relatively large amount of water on the surface.

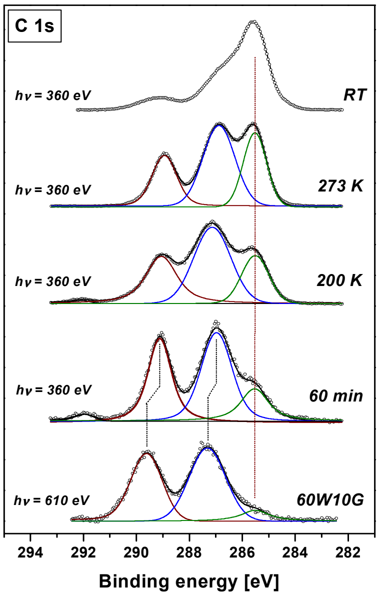

Fig. 3. Development of the C1s photoelectron spectrum of the 60WG10 film upon 60 min of irradiation and subsequent heating of the film to the temperatures indicated.

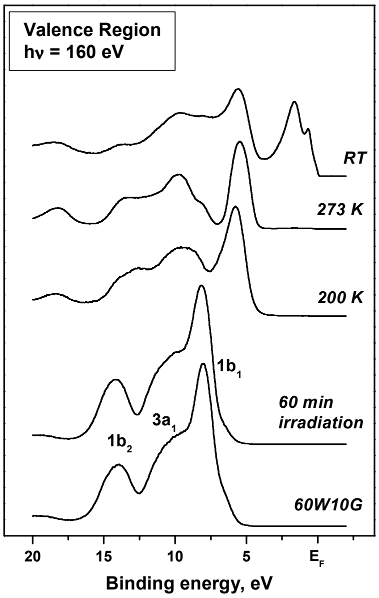

Fig. 4. Development of the valence region photoelrctron spectrum of the 60WG10 film.

The C1s spectrum of the 60W10G film heated to 200 K, i.e. a temperature above the desorption of water multilayers and below the desorption of glycine multilayers, indicates further degradation of the film (Fig. 3). The C1s spectrum of the 273 K heated film, i.e. a temperature still before desorption of glycine multilayers, shows further decomposition of the glycine. Indeed, the observed changes after heating the 60W10G film are due to the synchrotron irradiation of the ice-free surfaces, but some structural changes in the film upon heating also occur. The valence band spectra of the two heated surfaces show only minor differences: in both spectra the emission from glycine orbitals is present and it is difficult to detect the extent of decomposition of the glycine. The C1s and valence band PES spectra of the 60W10G film heated up to room temperature reveal severely damaged glycine molecules on the surface. Although the valence band spectrum still suggests the presence of glycine-like species, the component due to hydrocarbon fragments in the C1s spectrum is dominant.

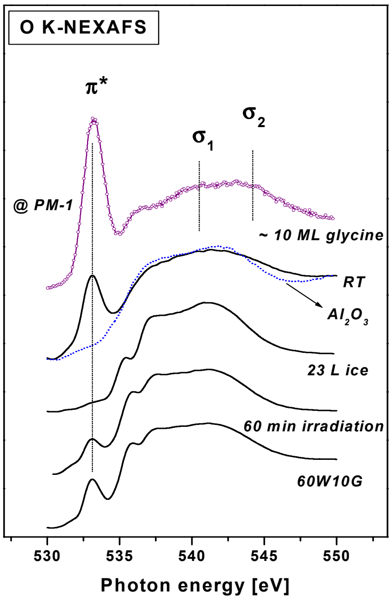

Fig. 5. Comparison of the NEXAFS spectrum of the 60W10G film with reference spectra of ice, the oxide substrate and a condensed glycine layer.

The 60W10G film was investigated with NEXAFS as well. In Fig. 5 the Auger-electron-yield O K-edge NEXAFS spectrum of the 60W10G film is compared with the spectrum of ice (23 L of water condensed at 85 K on the same substrate). In addition to the NEXAFS peaks of ice, the spectrum of 60W10G shows a C=O π*-resonance at ~533 eV due to the presence of glycine. In the NEXAFS spectrum of the 60 min irradiated film this peak appears less intense, which is probably due to the destruction of the carboxyl groups and formation of hydrocarbon species. The increase of the intensity of π*-resonance of glycine after heating the 60W10G film to room temperature might be explained with a particular orientation of the glycine molecules in the non-decomposed monolayer on Al_2O_3/NiAl(110).

The present results show that the influence of synchrotron irradiation on mixed ice/amino acid films is significant, leading to both desorption of the water and the decomposition of organic molecules. The former changes the environment of the amino acids and thereby possibly the chemical state of the molecules, whereas the latter leads to a destruction of the organic species. These effects are detrimental and should be considered in studies of biological systems with synchrotron radiation.

We would like to thank Dr. B. Casu, Dr. Th. Schmidt, A. Schöll, and D. Hübner (Uni Würzburg) for the valuable technical assistance. Furthermore, we are indebted to the BESSY staff for the support, in particular to Dr. W. Braun for his help and many discussions. This work was supported by the Austrian Science Foundation and BMBF (contracts No. 05 KS1VHA and 05 KS1WW1/6).

References

1. Y. Hara, N. T. Hashimoto, M Nagaoka, Chem. Phys. Lett. 348 (2001) 107.
2. B. Kasemo, Curr. Opinion Solid State Mater. Sci. 5 (1998) 3.
3. T Stunskus, C. Hahn, M. Grunze, J. Electr. Spectr. Relat. Phenom. 61 (1993) 193.
4. G. Tzvetkov, M. G. Ramsey, F. P. Netzer, Surf. Sci., *in press*.

VUV-SE spectra of guanine layers on H-Si(111) surfaces

S. D. Silaghi, H. Mendez, M. Friedrich, T. U. Kampen, and D. R. T. Zahn
Institut für Physik, TU Chemnitz, 09107 Chemnitz, Germany

C. Cobet, N. Esser, and W. Richter
Institut für Festkörperphysik, TU Berlin, 10623, Germany

W. Braun
BESSY GmbH, Albert-Einstein-Straße 15, 12489 Berlin-Adlerhof, Germany

Among DNA bases (adenine-A, thymine-T, guanine-G, cytosine-C), guanine (Figure 1) is important in the field of bioelectronic devices at molecular scale like biomolecular nanowires [1,2]. In order to identify the electronic transitions and determine the optical constants (**n**, **k**) of the guanine layers deposited on H-passivated Si(111), vacuum ultraviolet (VUV) spectroscopic ellipsometry (SE) technique is employed. A literature survey did not reveal any investigation concerning the optical constants of any DNA bases. Guanine layers with different thicknesses namely ~40 nm and ~100 nm were grown on H-Si(111) surfaces by organic molecular beam deposition (OMBD) under ultra-high vacuum (UHV) conditions (base pressure ~ $3{\cdot}10^{-9}$ mbar). Prior to guanine deposition, clean H-Si(111) surfaces were wet-chemically prepared as follows: first the substrates were degreased of organic contaminants by rinsing in isopropanol and de-ionized water; afterwards the native oxide was removed by etching for 2 min in hydrofluoric acid (HF 40%) resulting in H-terminated Si(111) surfaces showing a sharp 1x1 LEED pattern. Guanine was evaporated onto H-Si(111) surfaces with a rate of 2nm/min from a Knudsen cell at a temperature of about 510K. During the guanine deposition the substrates were kept at room temperature (RT).

The VUV-SE measurements were performed on the guanine layers with the VUV ellipsometer operating with the **3m**-**N**ormal-**I**ncidence-**M**onochromator **1** as light source and MgF_2 Rochon prisms as polarizer and analyzer. The SE spectra were recorded in the photon energy range from 3.0 to 9.5 eV at an angle of incidence of 68°. To our knowledge, these are the first SE measurements of guanine layers on H-Si(111) surfaces prepared under UHV conditions using synchrotron radiation. Unlike the aging processes of guanine layers on LiF substrates observed under high-vacuum conditions [3], no aging of the guanine layers was observed after 2 days in UHV at a pressure of 7×10^{-10} mbar. The exposure to the synchrotron radiation did not cause any deterioration of the samples.

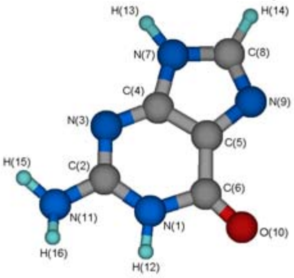

Figure 1. Chemical structure of a guanine molecule.

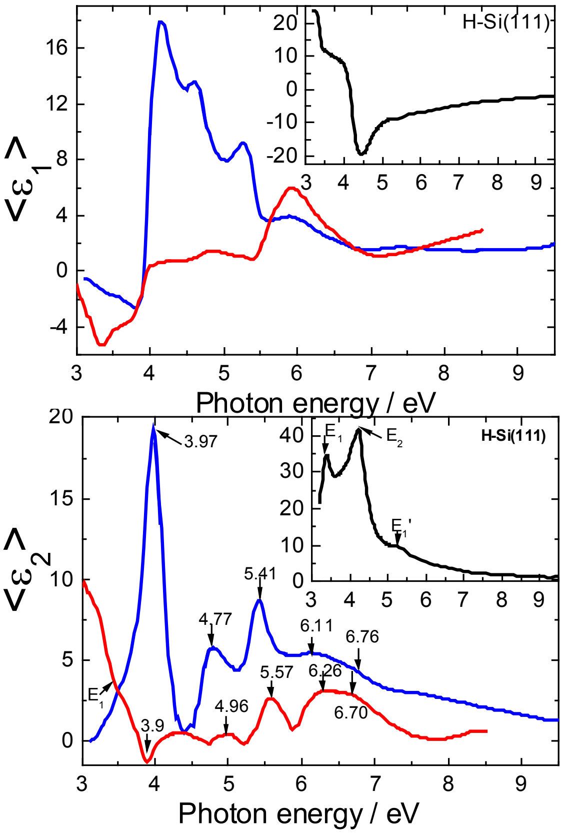

Figure 2. Measured effective dielectric functions $<\varepsilon_1>$, $<\varepsilon_2>$ of guanine layers (~ 40 nm – red lines; ~ 100 nm **– blue lines**) on H-Si(111). In the inset $<\varepsilon_1>$, $<\varepsilon_2>$ of the H-Si(111) substrate are shown.

Figure 2 shows the real $<\varepsilon_1>$ and imaginary part $<\varepsilon_2>$ of the measured effective dielectric functions of guanine layers on H-Si(111) surfaces. Measurements performed as a function of azimuthal angle showed that the guanine layers are optically isotropic. The spectra are dominated by strong interference features at 3.9 eV in the thin layer and 3.97 eV in the thicker one. Above 4 eV, the spectra are dominated by the features due to guanine involving electronic transitions with π-π^* character. Three features can be distinguished in the spectra of both guanine layers. The first peak corresponds to the HOMO-LUMO transition. The positions of the features for 100 nm layer thickness are at 4.77, 5.41, 6.11 eV and a shoulder at 6.76 eV. All features are shifted towards higher energy for a layer thickness of 40 nm. Absorption spectra of high-vacuum deposited guanine layers on LiF substrates exhibit features at lower energy values (4.31, 4.90, 6.20 and 6.70 eV) compared to the energy positions in SE spectra. The shifts in peak positions may be related to a difference in the thickness of guanine layers. However, further experimental and theoretical investigations are required. A theoretical study involving the calculations of electronic transitions of guanine molecule and dimers using DFT theory at different levels is in progress.

---

[1] A. Calzolari, R. Di Felice, E. Molinari and A. Garbesi, “Appl. Phys. Lett.” 80 (2002) 3331

[2] R. Di Felice, A. Calzolari, E. Molinari and A. Garbesi, “Phys. Rev. B”, 65 (2002) 045104

[3] T. Yamada and H. Fukutome, “Biopolymers”, 6 (1968) 43-54

NEXAFS study of a family of Copper Porphyrazines

D.R. Batchelor, D. Pop, B. Winters, W. Freyer, M. Sperling, B. Tepper, W. Widdra

BESSY, Albert Einstein Str. 15, 12489 Berlin
MBI for non linear optics, Max-Born-Straße 2 A, 12489 Berlin

The aim of this study was to investigate the charge transfer between the Copper atom and the Nitrogen ligand of a family Copper Porphyrazines [1] which differ principally in the degree of Benzolation. A combined approach using NEXAFS of both Nitrogen K and Copper $L_{2,3}$ edges together with Photoemission was employed. Only the NEXAFS results will be presented here.

Samples were prepared insitu by evaporation, except for P3 the largest molecule, at PM3 where Photoemission and Auger yield NEXAFS were measured. A cursory investigation of the Nitrogen NEXAFS with angle revealed only a weak dependence of the sigma and pi resonance regions. This weak dependence was attributed to the high deposition rate and polycrystalline gold substrate. The samples were subsequently transferred in air to the BTUC beamline where fluorescence NEXAFS was measured. Both Copper and Nitrogen NEXAFS showed minimal change between the two sets of measurements with the exception that the data from the undulator beamline are better resolved and that more care had to be taken due to radiation damage. Figure 1 shows the Nitrogen NEXAFS which compare well with published data [2]. Several trends can be observed. Firstly there is a steady progression of structure in the π resonance region to lower binding energies as the degree of benzolation is increased. Associated with this progression is an abrupt decrease in the main π resonance (399eV) for P3. The smallest molecule P0 shows a shift in this resonance to lower binding energy (-0.47eV) and a more resolved double peak structure. Finally for the two intermediate molecules this resonance shows a Fano like dip.

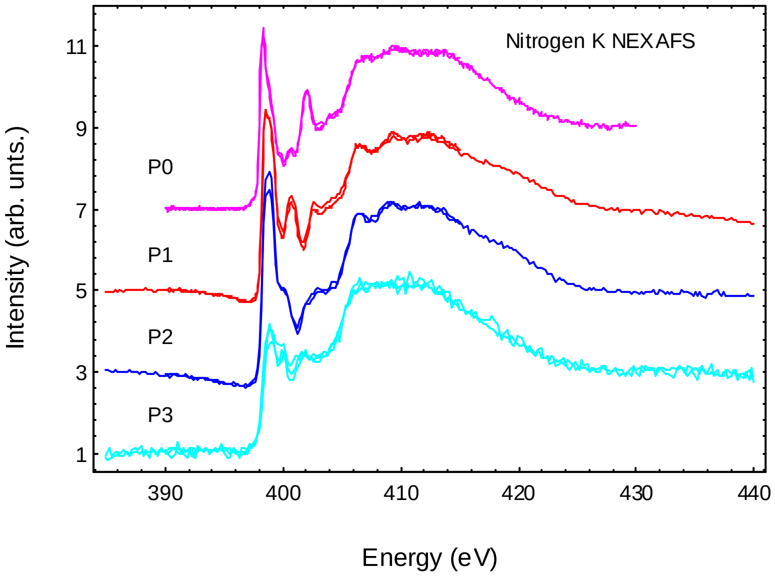

Figure 1. Nitrogen Fluorescence NEXAFS measurements from the Cottbusser beamline. The data have been normalised using the pre and post edge (385 and 430eV) and shifted for clariy. The number P*n* denotes the degree of benzolation.

The copper NEXAFS is shown in Figure 2. Again a shift to lower binding energy of the principal resonance, although smaller (-0.37eV), is seen for the smaller molecule, in addition it is weaker and broader than the others. The 2p3d resonance [3] is most intense and sharp for P1 and P2. For P3 it becomes broader and there is a large shift to lower binding energies of 1eV which is not seen for the Nitrogen NEXAFS.

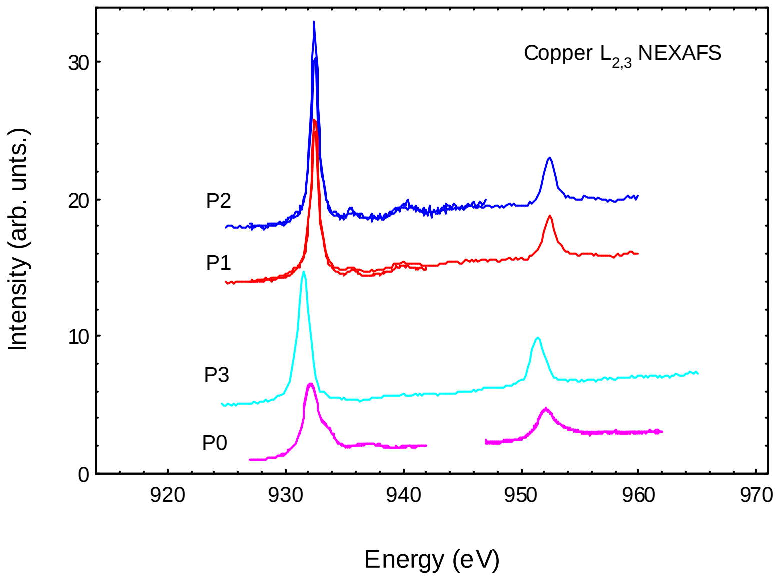

Figure 2. Copper $L_{2,3}$ Fluorescence NEXAFS measurements from the Cottbusser beamline. The data have been normalised using the pre and post edge (928 and 960eV) and shifted for clariy. The number P*n* denotes the degree of benzolation.

In an attempt to throw some additional light on the results some semi emperical calculations were made on both the Copper and the metal free compounds. The results for the unoccupied DOS of the metal free compunds are shown below in Figure 3 and are in reasonable agreement with other calculations [4]. The same trends are seen for the Copper calculations as for the metal free except there are additional DOS contributions from the Copper at intermediate energies; This is also seen in the experimental data of T. Okajima et al [1]. The energy scale both absolute and relative do not agree with the data, however a common trend is seen; there is an increase in the DOS to lower energy as the benzolation increases (peaks B) and the lowest unoccupied levels (peaks A) shifts to lower energy for P0. Further work involving more accurate ab-initio calculations together with NEXAFS simulations using FEFF 8.2 are underway. Additional experimental work on the P3 compound and in particular resonant Auger at the Copper $L_{2,3}$ edge on the four compounds is planned.

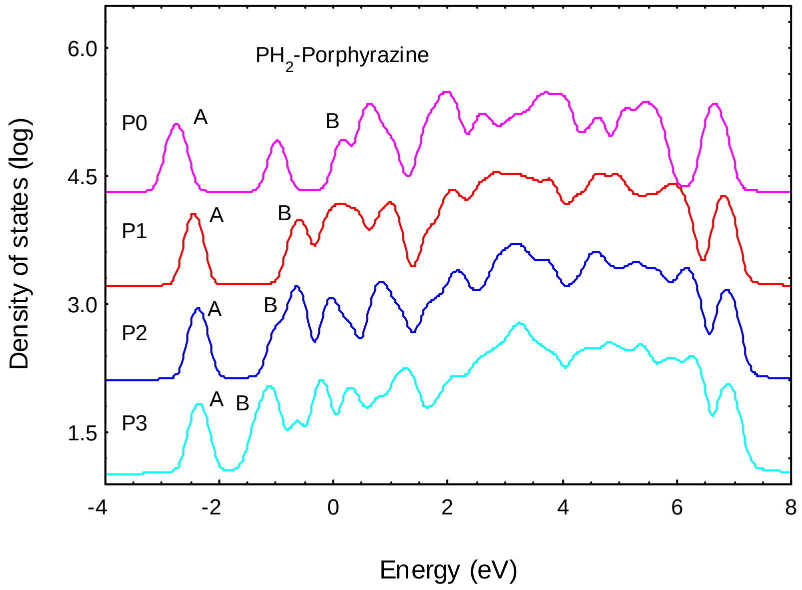

Figure 3. Density of states for the unoccupied levels of the metal free compound. The Logarthym has been plotted as a crude simulation of the overlap between the Nitrogen core and molecular orbital. i.e. the matrix elements are ignored.

Acknowledgments

R. Mitdank (Humboldt) Fluorescence chamber support, P. Hoffmann (BTUC) beamline support, T. Kachel (PM3) beamline support, and P. Bressler, D. Schmeißer and W. Braun for useful discussions.

References

[1] D. Pop, Ph.D. Thesis, MBI for non linear optic, Feb.. 2003

[2] T. Okajima, H. Fujimoto, M. Sumitomo, T. Araki, E. Ito, H. Ishi, Y. Ouchi, K. Seki, Surf. Rev. and Let., 9(2002)441-446

[3] M. Grioni, J.B. Goedkoop, R. Schoorl, F.M.F. de Groot, and J.C. Fuggle, F. Schäfers and E. E. Koch, G. Rossi, J.M. Esteva, and R. C. Karnatak Phys. Rev. B 39(1989)1541

[4] E. Orti, J.L. Bredas, J. Chem. Phys, 92(1990)1228

Electronic and structural properties of DiMePTCDI/ S- GaAs(100) interfaces

G.Gavrila[1], T.U.Kampen[1], H.Méndez[1], J. Wells[2] , D.V. Vyalikh[3], W. Braun[4], and D.R.T Zahn[1]

[1] Institut für Physik, Technische Universität Chemnitz, D-09107, Chemnitz, Germany.
[2] Trinity College, Dublin.
[3] Fachbereich Physik, Freie Universität Berlin, Arnimallee 14,14195 Berlin, Germany.
[4] BESSY GmbH, Albert-Einstein-Straße 15, D-12489 Berlin-Adlershof, Germany.

Introduction

Planar and highly symmetric molecules like N,N'-dimethyl-3,4,9,10-perylenetetracarboximide (DiMePTCDI) belong to a material class known as organic semiconductors. These molecules interact predominantly via van-der-Waals forces and can form ordered crystalline solids or thin films. The weak van-der-Waals bonding between organic molecules and substrates allows quasiepitaxial growth even in the presence of lattice mismatch. Our work is focused on the modification of semiconductor surfaces and interfaces using such organic semiconductors. The energy level alignment at the interfaces is investigated using Photoemission Spectroscopy (PES) while Near Edge X-ray Fine Structure spectroscopy (NEXAFS) is used to determine the orientation of the molecules.

Experimental

The GaAs(100) surfaces were passivated by etching in S_2Cl_2:CCl_4 (1:3) for ten seconds, followed by rinsing in CCl_4, acetone, ethanol and de-ionised water for 5 seconds each and finally dried in a N_2 flow. Annealing for 30 min at 470°C and a pressure below $5\cdot10^{-9}$ mbar results in sulphur passivated 2×1 reconstructed GaAs(100) surfaces, further on being denoted as S-GaAs. The organic layer is deposited by organic molecular beam deposition (OMBD) onto the S-GaAs substrates with the thickness monitored by a quartz microbalance. Photoemission and NEXAFS spectra were recorded at the Russian-German Beam Line at BESSY. The photoelectron spectra were detected with a CLAM 4 analyser and the NEXAFS studies were performed in the partial photoelectron yield mode. The C1s NEXAFS raw data were divided by the current of the incident X-ray beam and normalized with respect to the absorption at 325eV.

Energy level alignment

Figure. 1 presents an example of valence band structure for the clean S-GaAs(100) surface and after a deposition of a 15 nm DiMe-PTCDI film.

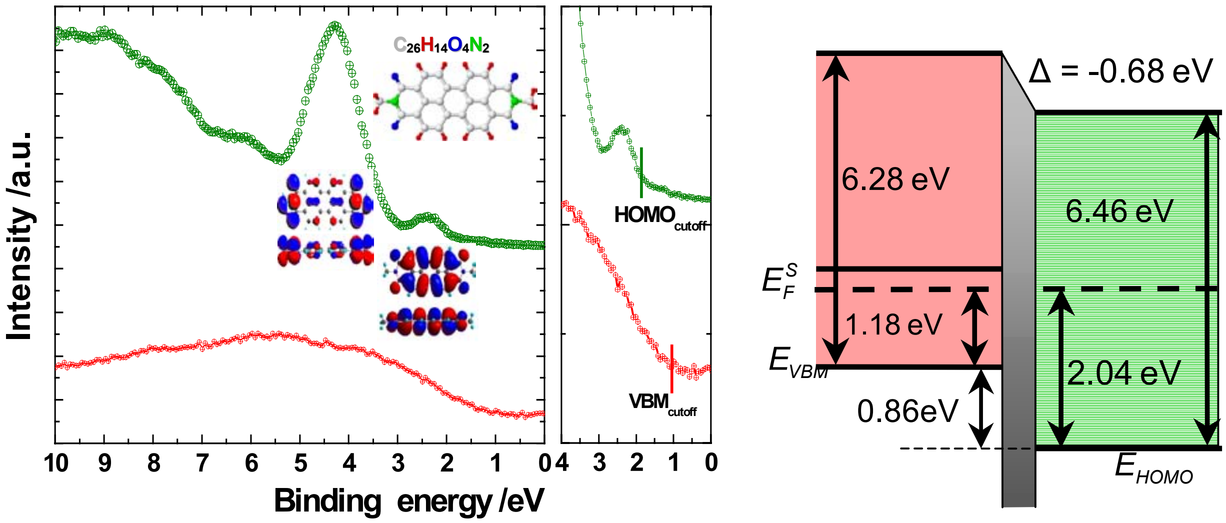

Fig.1: Photoemission spectra of a clean S-GaAs(100) and after evaporation of a 15 nm DiMe-PTCDI film and top view and side view of the calculated molecular orbitals. The energy band diagram for the DiMe-PTCDI/ S-GaAs(100) interface is also shown

The feature with the lowest binding energy in the DiMePTCDI spectrum originates from the highest occupied molecular orbital (HOMO). This molecular orbital has π-character as can be seen from the top and side view of the charge distribution on the molecule calculated using Gaussian 98 (B3LYP/3-21G)[1] . Six molecular orbitals contribute to the dominant feature at 4.2 eV binding energy. These orbitals show predominantly π-character and are located around the imide group. Here, E_{HOMO} and E_{VBM} represent the energy edge of the highest occupied molecular orbital of the DiMePTCDI and the valence band maximum of the substrate, respectively, relative to E_F. The E_{VBM}–E_{HOMO} offset is determined to be (0.86±0.10) eV. The ionization energies of (6.28±0.10) eV and (6.46±0.10) eV for S-GaAs(100) and DiMe-PTCDI the interface dipole is determined to be (–0.68±0.10) eV.

Orientation of molecules

In NEXAFS absorption of the incident synchrotron light takes place due to the excitation of an electron from a core shell into the lowest unoccupied states. In perylene derivatives the lowest unoccupied molecular orbitals are derived from the π-electron system with its orbitals oriented perpendicular to the molecular plane. Due to selection rules excitation between the core shell and the π-orbitals takes place if the electric field vector of the incident light has a component parallel to the π-orbitals. Figure. 2 presents selected C-K shell spectra of DiMe-PTCDI for different angles of incidence. The incident synchrotron light is linearly polarized with the electric field vector lying in the plane of incidence. Due to the orthogonal orientation of the π^* and σ^* orbitals any increase in π^*-resonance is accompanied by a decrease of the σ^*-resonance. The features above and below 288 eV are attributed to unoccupied π- and σ-states, respectively. With increasing angle of incidence the intensity in the π^*-resonance increases. This is a clear evidence that the molecular plane of the molecule is tilted with respect to the substrate surface.

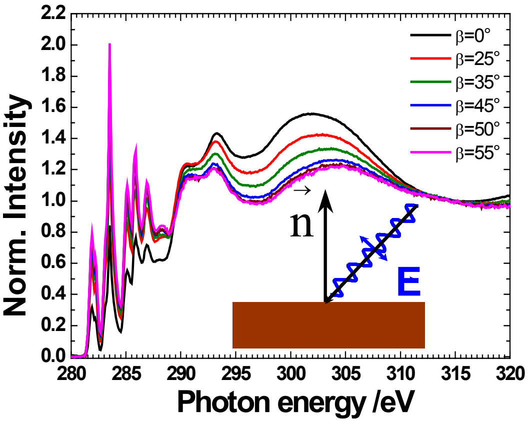

Fig.2: NEXAFS spectra of the C-K edge of DiMePTCDI as a function of the angle of incidence of synchrotron light

In combination with Raman spectroscopy the angle between the (102) plane of crystalline domains and the substrate plane is determined to be 56°±4°[2]. The long molecular axis of the 2 molecules in the unit cell are deviating from the [110] direction of the substrate by –9° and -48°, respectively.

Summary

The growth of DiMe-PTCDI on S-GaAs(100) surfaces has been investigated using PES and NEXAFS. The valence band maximum of S-GaAs(100) is found to be (0.86±0.1) eV above the HOMO of DiMe-PTCDI. The interface dipole amounts to –0.68 eV with the vacuum level of the DiMe-PTCDI below the vacuum level of S-GaAs(100). NEXAFS investigations show that the molecular planes are tilted with respect to the substrate surface.

Acknowledgements

Financial support by the *Bundesministerium für Bildung and Forschung* (BMBF contract No. 05 KS1OCA / 1) and the EU DIODE network is gratefully acknowledged. We thank the staff of BESSY for valuable technical assistance.

1. Gaussian 98 (Revision A.1), M. J. Frisch *et. al.,* Gaussian Inc., Pittsburgh PA, 1998.
2. T. U. Kampen, G. Salvan, A. Paraian, C. Himcinschi, A. Yu. Kobitski, M. Friedrich, and D. R. T. Zahn, Appl. Surf. Sci., to be published.

4f-derived electronic structure in the bulk and at the surface of α-Ce metal

Yu. Kucherenko[1)], S.L. Molodtsov[2)], M. Heber[2)], and C. Laubschat[2)]
[1)] Inst. of Metal Physics, National Academy of Sciences, UA-03142 Kiev, Ukraine
[2)] Inst. f. Oberflächen- u. Mikrostrukturphysik, TU Dresden, 01062 Dresden, Germany

At the surface of rare-earth (RE) solids 4f states are energetically lowered due to the decrease of cohesive energy [1]. This phenomenon may directly be observed in photoemission (PE) by a splitting of the 4f-derived emission into surface and bulk components separated by the well-known surface core-level shift. In Sm and Tm metal as well as in several trivalent Sm, Eu, Tm, and Yb compounds unoccupied $4f^{n+1}$ configurations are shifted below the Fermi energy by this mechanism leading to surface valence transitions that are reflected in the PE spectra by the appearance of both $4f^{n-1}$ and $4f^{n}$ final states. 4f PE spectra of Ce systems reveal always a splitting into $4f^0$ and $4f^1$ components that, however, is not due to a surface effect but due to hybridisation. The phenomenon may be described in the framework of the single-impurity Anderson model (SIAM) by a hopping interaction between the 4f states and the valence band [2]. The energy lowering of the 4f states together with the reduction of atomic coordination at the surface leads here to dehybridization reflected in the spectra by a decrease of the $4f^1$ signal in addition to an energy shift of the $4f^0$ emission. Both effects have to be considered for a proper interpretation of Ce PE spectra.

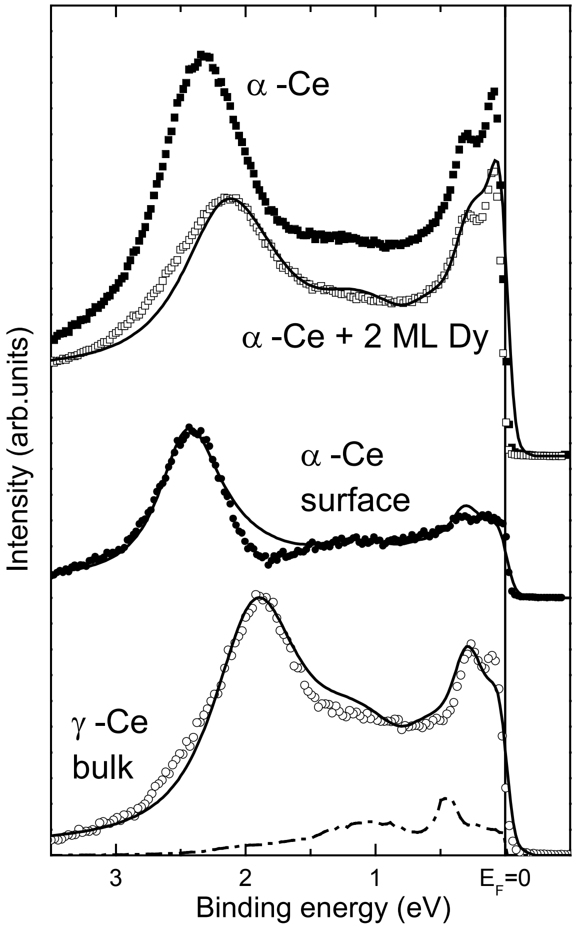

Fig. 1 Resonant 4f PE spectra of α- and γ-Ce taken at the 4d→4f absorption threshold at 121 eV photon energy. Surface and bulk contributions were separated by quenching the surface signal by a Dy overlayer.

For α-Ce metal a surface energy shift of the $4f^0$ component towards lower binding energy was predicted [3] in sharp contrast to observed surface core-level shifts of heavier RE´s that according to the surface energy lowering of the 4f states are always directed towards higher binding energy. This unusual behavior may be understood on the basis of SIAM where the energy position of the $4f^0$ emission is roughly given by $\sqrt{(\varepsilon^2 + 4\Delta^2)}$. Here, ε denotes the binding energy of the nonhybridized $4f^0$ state and Δ a hybridisation parameter that describes the hopping probability. If Δ decreases at the surface due to the reduced atomic coordination a decreasing binding energy may be obtained from this expression in spite of an increase of ε. In order to prove this prediction experimentally we performed resonant PE experiments at the

U-49/2-PGM1 undulator beamline of BESSY II. Thin films (about 100 Å) of α-Ce metal were prepared by thermal deposition of the pure metal onto a W(110) substrate held at a temperature of 50 K. In the PE spectra surface and bulk components of the 4f emission were separated by quenching the surface signal by thin overlayers of Dy metal. Fig. 1 shows a PE spectrum of α-Ce (top, black squares) taken on-resonance at the 4d→4f absorption threshold and separated into bulk (top, open symbols) and surface components (center). A bulk spectrum of γ-Ce is shown in the bottom. As compared to γ-Ce the bulk spectrum of the α-phase reveals a shift of the $4f^0$ peak at about 2 eV to higher binding energy and an increase of the $4f^1$ emission at the Fermi energy. Since ε should be almost the same in both phases these effects reflect the increase of hybridization in the α-phase. Solid curves through the data points reflect results of a numerical analysis on the basis of SIAM considering the effects of a realistic density of valence-band states [4]. While ε remains almost constant (1.3 - 1.4 eV) the hybridization parameter is found to increase from 0.72 eV to 0.87 eV in going from γ- to α-Ce leading to an decrease of the 4f occupation from 0.99 to 0.92. In contrast to the theoretical prediction the surface component reveals a $4f^0$ emission shifted to higher binding with respect to the bulk component. The $4f^1$ peak is even smaller than in γ-Ce. Our analysis in the light of SIAM shows that with respect to the bulk Δ decreases only slightly (0.83 eV) and that the observed changes of spectral shape are predominantly due to energetic lowering of ε by 0.5 eV. The unexpected small variation of Δ might be due to interactions with a d-like surface state observed for all trivalent RE metals.

Acknowledgement: This work was supported by the Deutsche Forschungsgemeinschaft, SFB 463, projects B4 and B11.

References:

1) C. Laubschat, J. Appl. Phys. A 65, 573 (1997), and references therein
2) O. Gunnarsson and K. Schönhammer, Phys. Rev. B 28, 4315 (1983)
3) L.Z. Liu et al., Phys. Rev. B 45, 8934 (1992)
4) R. Hayn et al., Phys. Rev. B 64, 115106 (2001)

Local Electronic Structure in NaCl / H_20 Electrolytes

M. Freiwald, S. Eisebitt, W. Eberhardt
BESSY GmbH, Albert-Einstein-Str. 15, 12489 Berlin
S. Cramm
IFF, Forschungszentrum Jülich, 52425 Jülich

As compared to solids or gases, little is known about the electronic structure of liquids or dissolved species, although the electronic structure in wet environments is crucial for many processes in biology, medicine and chemistry. On the theoretical side, *ab initio* molecular dynamics calculation for liquids have only recently become feasible [1]. Experimentally, standard techniques of soft x-ray spectroscopy were difficult to apply due to the high vacuum requirements. We have designed a wet sample cell in which a liquid can be circulated in a UHV chamber. Soft x-rays are coupled in and out of the sample volume by a SiN_x membrane of 150 nm thickness, allowing us to record fluorescence yield (FY) soft x-ray absorption (SXA) and soft x-ray emission (SXE) spectra. Here we report on FY-SXA experiments on NaCl / H_2O solutions as a function of the salt concentration. The spectra were recorded at the UE56/1-SGM beamline using a photodiode to detect the total fluorecence yield.

NaCl/H_2O is an often encountered electrolyte. Earth's oceans consist on average out of a 0.6 M NaCl solution. Bodily fluids and cells of *e.g.* mammals contain many ions, with Na^+ and Cl^- being the ions with by far the highest concentrations in plasma and interstitial liquid. A 0.15 M solution of NaCl is isotonic to human blood. Na^+ ions in aqueous solution are surrounded by water molecules with the O atoms directed towards the Na^+ ion. Calculations [2-4] indicate that the first solvation shell is made up out of 6 H_2O molecules, with an Na-O distance of 2.3 Å. Electrostatic effects in electrolyte solutions are described under certain simplifying approximations by Debye-Hückel theory, which predicts the existence of a cloud of oppositely charged counter ions around any given ion [5]. Mathematically, the counter ion charge can be envisioned as being concentrated in a shell of radius r_D, the Debye length. For 0.1 M, 0.5 M, 1.0 M, 5.0 M NaCl / H_2O, r_D = 9.6 Å, 4.3 Å, 3.0 Å, 1.4 Å, respectively. Due to its approximations – in particular treating ions as point charges – Debye-Hückel theory can not be expected to be quantitatively valid for concentrations above 0.1 M. The Na–Cl nearest neighbor distance in solid NaCl is 2.82 Å. The numbers calculated above nevertheless suggest that the counter ions and ions in concentrated solutions will come in into close proximity. At room temperature, 6.14 M NaCl is a saturated solution, *i.e.* for higher concentrations, NaCl will precipitate. A Monte Carlo calculation for 1M NaCl [4] exhibits a fist peak in the Na-Cl ion radial distribution at 23 Å. We are not aware of any calculation of the electrolyte structure for concentrated electrolytes such as 5 M NaCl at the present time. Apart form ionization potentials of $Na^+(H_20)_n$ clusters, there does not seem to be any theoretical modeling of the electronic structure at the Na^+ ions in solution at the present time.

In Fig. 1, we present Na 1s FY-SXA spectra of 0.1 M, 0.5 M, 1.0 M and 5.0 M NaCl / H_2O solutions at room temperature. In order to facilitate the comparison, the 5 M NaCl spectrum (line) is superimposed on the other measured spectra of NaCl/H_2O. A spectrum of solid NaCl and of Na gas with a calculation assigning transitions [6] has been included for reference. The spectrum of the solid is in good agreement with published spectra [7] but shows finer detail due to improved instrumental resolution. The features in the gas phase spectrum are well explained by modeling the 1s-np transitions [6]. The electrolyte spectra are characterized by two broad peaks at 1080.1 eV and 1075.9 eV. The latter peak has a shoulder at 1074.5 eV. Finally, we observe a small absorption peak at 1072.8 eV. A clear change of the spectral shape can be seen as a function of NaCl concentration. The SXA spectrum reflects the *local* electronic structure at the Na+ ion. At the present time we can only speculate that the observed change in spectral shape is due Cl^- ions being able to penetrate into the first solvation shell. The average relative lifetime of e.g $Na^+(H_20)_5Cl^-$ complexes should increase with increasing NaCl concentration. Counter ions in the first solvation shell would be at distances comparable to solid NaCl which is close enough to produce electronic overlap in the valence and conduction band states. Charge transfer and "ion softening" of the Na^+ [8] can be expected to be different if $H^{(\delta+)}{}_2O^{(\delta2-)}$ from the solvation shell is replaced by Cl^-. A detailed understanding of the changes in the electronic structure will require a theoretical analysis of the electronic structure, based on a molecular dynamics calculation. Experiments varying the type and concentration of the counter ions have been carried out and are currently being analyzed.

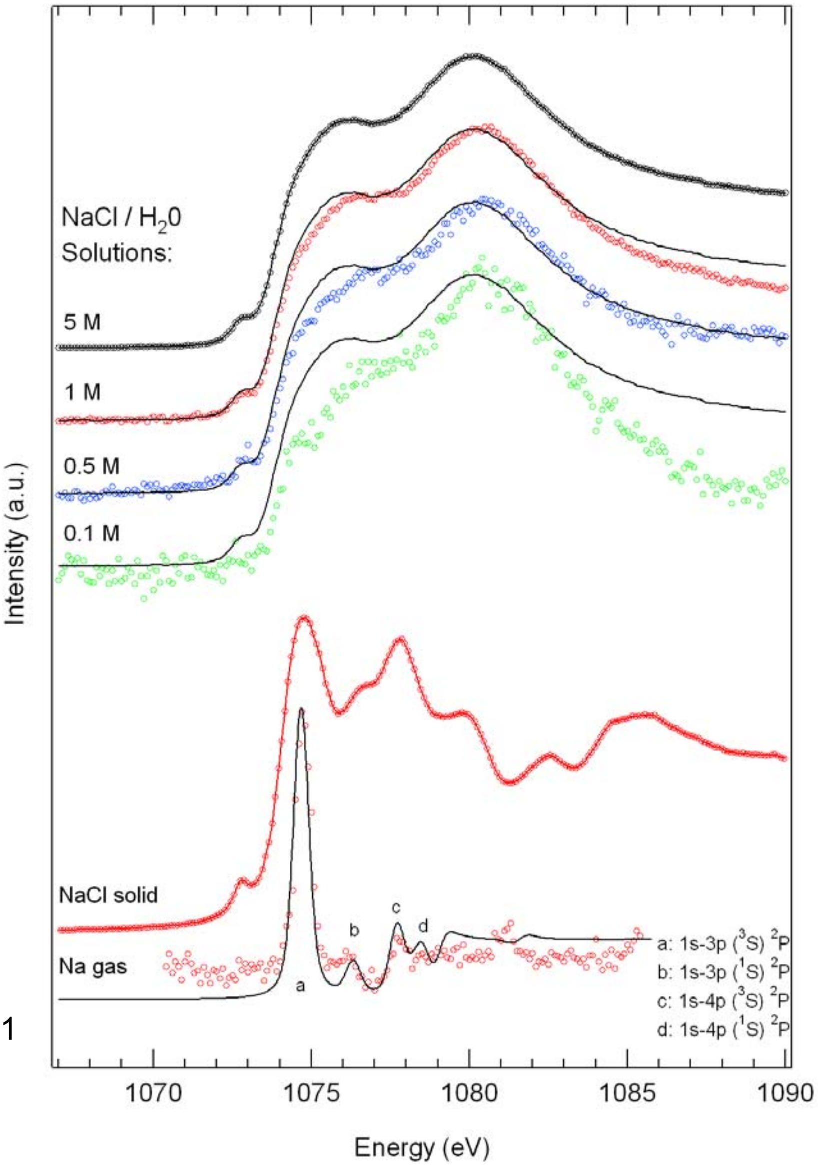

Fig.1

References

[1] K. Laasonen, M. Sprik, M. Parrinello, *et al.*, Journal of Chemical Physics **99**, 9080 (1993).

[2] K. Hashimoto and K. Morokuma, Journal of the American Chemical Society **116**, 11436 (1994).

[3] L. M. Ramaniah, M. Bernasconi, and M. Parrinello, Journal of Chemical Physics **109**, 6839 (1998).

[4] L. Degreve and F. L. B. da Silva, Journal of Chemical Physics **110**, 3070 (1999).

[5] P. W. Attkins, *Physical Chemistry* (Oxford Universtiy Press, Oxford, 1986).

[6] K. Godehusen, private communication (2003).

[7] M. Kasrai, M. E. Fleet, G. M. Bancroft, *et al.*, Physical Review B **43**, 1763 (1991).

[8] W. A. Harrison, *Electronic Structure and Properties of Solids* (Dover Publications Inc., New York, 1989).

Stepped epitaxial graphite by transformation of vicinal SiC(0001)

A.Varykhalov[a,b], A.M.Shikin[a,b], O.Rader[a], W.Gudat[a],
A.Loza[b], M.Poiguine[b],V.K.Adamchuk[b],
D.Vyalikh[c].
a) BESSY, Albert-Einstein-Str. 15, D-12489, Berlin, Germany
b) St.Petersburg State University, Institute of Physics, Uljanovskaja 1,
Petrodvoretz, St.Petersburg, 198904, Russia
c) Freie Universitaet Berlin, Fachbereich Physik, Arnimalle 14, D-14195, Berlin, Germany

In the past decades, the structuring of solids at a length scale comparable to interatomic distances became an object of great attention. The main way of fabrication of such structures is self-organization and step-decoration on surfaces. An ideal way to minimize electronic interaction with the substrate for this kind of systems is to use a substrate material where the atomic layers are only weakly bonded to each other by means of van-der-Waals interaction as is the case with graphite. However, graphite is too soft for producing stepped surfaces in the standard way of cutting a crystal at a certain angle followed by mechanical polishing. The solution to this problem is initial graphitization of a well-characterized stepped substrate.

We report here a novel technique for formation of stepped graphite, based on the application of the graphitization method[1-4] to stepped 6H-SiC surfaces. Graihitization takes place after prolonged heating up to relatively high temperatures due to Si-atom evaporation. The reported technique is studied through observation of distinct core-levels of carbon and silicon (C1s and Si2p, respectively) while increasing time and temperature of the heat treatment with 50K step each time. Also LEED techniques were involved to show that the stepped character of the vicinal SiC(0001) surface remains after the treatment. Eventually, we applied angle-resolved photoemission to map the resulting band structure and to compare it to the one of bulk graphite.

Experiments have been performed in an ultra-high vacuum chamber equipped with a LEED optics and a CLAM-4 hemispherical electron analyzer set to 50 meV energy and angular resolution. The Russian-German beamline used as a source of photons. Base pressure during experiment was in the low 10^{-10} mbar range.

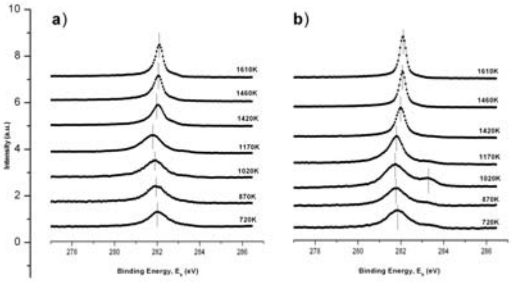

Fig. 1. Deviations in C1s core level peak energy and intensity along with annealing up to given temperatures. The two sets of spectra are given for (a) Flat 6H-SiC(0001) surface and (b) stepped 6H-SiC(0001) and measured with photon energy hν = 320 eV in normal emission.

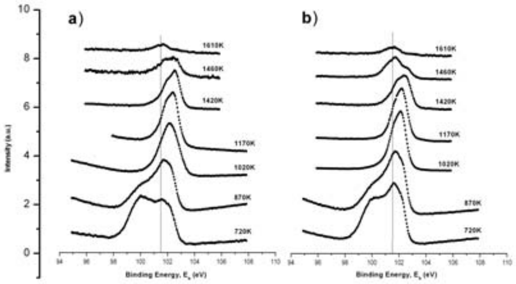

Fig. 2. Evolution of Si2p core level peak with increasing annealing temperature. hν = 130 eV and 160 eV. Spectra for a) Flat 6H-SiC(0001) surface and (b) stepped one show that the graphitization process is similar and in both cases the Si2p signal vanishes almost completely.

Fig. 1 and Fig.2 shows the evolution of the C1s and Si2p core level for different annealing temperatures. Two samples - flat (a) and stepped (b) SiC(0001) - are presented for comparison. The spectra reveal typical behavior for graphitization. C1s peak becomes more intense with increasing of annealing temperature while Si2p decreases due to Si-atom evaporation. Some minor shifts and variations in the shape of spectra can be explained by different surface reconstructions subsequently realized with increasing annealing temperature. Several works addressed this question for flat SiC[1,3,4]. The state of the sample when intensity of Si2p became comparable with background counts (after annealing at 1500K) was regarded as completely graphitized. For this state LEED observations as well as band structure mapping were done.

It is well known that the LEED images from a regularly stepped crystalline surface must lead to an observable splitting of diffraction spots, which is explained by the presence of a macro surface having different indices than the base plane (i. e., the terraces). Such splitting is in fact observed in our case. The LEED pattern from vicinal SiC(0001) after graphitization taken *in-situ* is reproduced in Fig. 3. The ratio of splitting-distance to the lattice constant derived from LEED pattern in reciprocal space allows us to evaluate terrace widths of the graphitized surface. It reveals that this value is about 20-22 lattice constants (35-40Å) of a graphite plane, which is in good agreement with the terrace size of the initial (non-graphitized) surface.

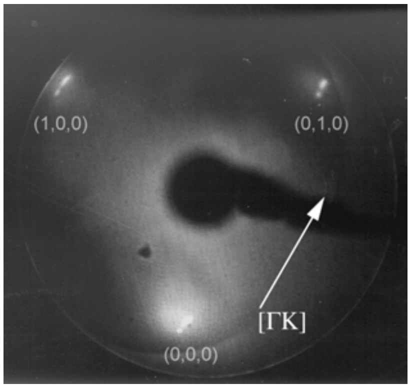

Fig. 3. LEED pattern from graphitized 6H-Si(0001) stepped surface. Primary electron beam energy $E_p = 61$ eV. Because of big distance from the sample to the screen only three spots fit onto the screen. The obvious splitting of the spots proves the assumption that the graphitized surface kept its initial stepped character.

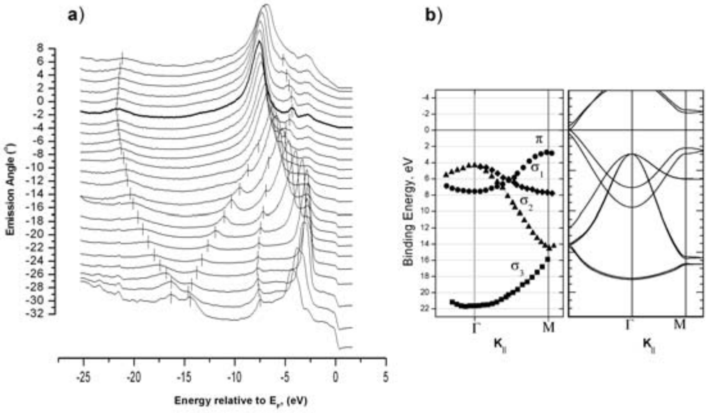

Fig. 4. Mapping of the band structure of stepped 6H-Si(0001); (a) valence band spectra sets with dispersing peaks in ΓM direction. Measured in the range from –32° up to +8° degrees relatively to normal emission in angle-resolved mode of analyzer. hν = 65 eV was employed for the measuring, (b) The band structure extracted from measured data compared to band structure of flat graphite.

The last criterion for the characterization of the newly produced structure is whether it shows the typical in-plane band dispersion of graphite in angle-resolved photoemission. Energy dispersion was measured in ΓM direction (perpendicular to terraces) for stepped graphitized SiC(0001) surface. The data, given in Fig. 4a, shows a set of spectra with peak positions marked and Fig. 4b the dispersion derived from the spectra compared to the calculation[5,6]. One can see that the band structure is nearly the same as the theoretical one.

All these points allow us to conclude that fabrication of stepped graphite surface through the effect of 6H-SiC(0001) surface graphitization has been achieved for the first time.

References

[1] A. J. Van Bommel, J. E. Crombeen, and A. Van Tooren, Surf. Sci. **48**, 463 (1975).
[2] I. Forbeaux, J.-M. Themlin, and J.-M. Debever, Phys. Rev. B **58**, 16396 (1998).
[3] K. Heinz, U. Starke, J. Bernhardt, and J. Schardt, Appl. Surf. Sci. **162-163**, 9 (2000).
[4] I. Forbeaux, J.-M. Themlin, A.Charrier, F. Thibaudau, and J.-M. Debever, Appl. Surf. Sci. **162-163**, 406 (2000).
[5] R. Saito, M. Fujita, G. Dresselhaus, and M. S. Dresselhaus, Phys. Rev. B, **46**, 1804 (1992).
[6] P. Carra and M. van Veenendaal, ESRF Newsletter, July issue (1997)

Au stripes on W(145) showing quantum-well states of sp- and d-character

A. Shikin[1,2]*, O. Rader*[1]*, S. Bozhko*[3]*, A. Ionov*[3]*, W. Gudat*[1]*, V. Adamchuk*[2]
1. *BESSY, Albert-Einstein-Str. 15, D-12489, Germany*
2. *St.-Petersburg State University, St.-Petersburg, 198904 Russia*
3. *Institute of Solid State Physics,142432 Moscow-Chernogolovka, Russia*

Following earlier theoretical predictions the observation of the formation of quantized electronic states has in recent years become a common phenomenon in atomically thin two-dimensional metal films.(see e.g. Ref.1), Confining electrons to even lower dimensionality and controlling the effect of the finite size on the electronic structure along two directions at the same time then is a challenge within reach. So-called quantum stripes are an example for such structures and they can in principle be formed by metal deposition on a regularly stepped substrate crystal, the so-called step decoration technique. Thickness and width of the stripes should be determined by cutoff angle of the substrate, the crystallographic orientation of the terrasses and the deposited atomic adlayers. The aim of the current work is to explore whether it is possible at all to form Au quantum stripes on top of a stepped W crystal, whether stripes of different thicknesses can be grown, and to investigate by photoemission techniques whether sp- and d-derived quantum-well states (QWS's) develop in such a system.

As a substrate we used the stepped W(145) surface with a (110) terrace structure exposed by the cutoff angle of 10.9°. It is well known that the shape of steps and their crystallographic direction play an important role in the step-decoration process. We used the [111] step direction in order to provide close-packed step edges. Important for the current investigation is the comparison to our recent work on QWS's of sp- and d-character in ultrathin Au films on flat W(110) [1].

Figure 1 presents a series of angle-resolved photoemission spectra for Au deposition on W(145) measured under the same conditions as in Ref. [1], i. e., emission normal to the (110)-terraces with 1° angle resolution at the UE56/1-PGM beamline with 62.5 eV photon energy. The angle of light incidence was 30° relative to the terrace normal with the electric vector along < 111> directions. The bottom spectrum corresponds to the clean W(145) surface. Under deposition of Au, the W-derived features are attenuated and new Au-derived features appear in the region of binding energies (BE's) between 2 and 8 eV. By analogy with the Au/W(110) system [1], the features observed here can be ascribed to QWS's of sp- and d-character which we label 1sp, $1d_4$, 2sp, $2d_4$, for thicknesses of 1 and 2 monolayers (ML). In Fig. 1 the spectra corresponding to formation of 1.0 and 2.0 ML Au are marked by red lines. The changes with Au- coverage of the BE's of the main features are traced in Fig. 2a. Open circles are related to the W-derived features. Au-derived features are shown by solid circles. Here, the corresponding energies expected from the 'extended phase accumulation' model for 1 and 2 ML of Au have been reproduced from Ref. [1] (crosses) along with the identification according to the notation introduced there. Evidently the energy of each QWS changes as abruptly as expected. The corresponding development of the QWS intensities are presented in Fig. 2b. Maxima in this graph correspond to formation of first, second, ... monolayer of Au. Note how well intensity maxima for QWS's of different character (1sp and $1d_4$) coincide showing the precision of the thickness calibration reached in this way and that QWS's of 2 ML form at the expense of those of 1 ML showing true layer-by-layer growth.

The materials Au and W have been chosen among other aspects because Au does not interdiffuse when grown on W. Thus a change of the step structure during Au deposition on the W(145) substrate is therefore excluded. This means that the present results showing predominantly 1-ML QWS's in the thickness range 0 - 1 ML and 2-ML QWS's in the thickness range 1 - 2 ML directly prove that quantum stripes of 1- and 2-ML thickness are formed. Annealing of the 2-ML system (see the upper spectrum in Fig. 1) does not lead to significant modification of the spectrum. The quantum stripes are therefore considered thermodynamically stable in this range. As the electronic structure of the present system develops in an analogous way to the one for Au/W(110) [1], it is suggested that QWS's will be a good indicator of the formation of well defined quantum stripes also for other systems. A comparative analysis of lateral quantum-size effects for electron wave vectors perpendicular and parallel to the stripes will be published elsewhere later.

1. A. M. Shikin, O. Rader, G. V. Prudnikova, V. K. Adamchuk, W. Gudat, Phys. Rev. B 65, 075403 (2002).
2. A. M. Shikin et al., to be published.

Au/W(145) Normal Emission

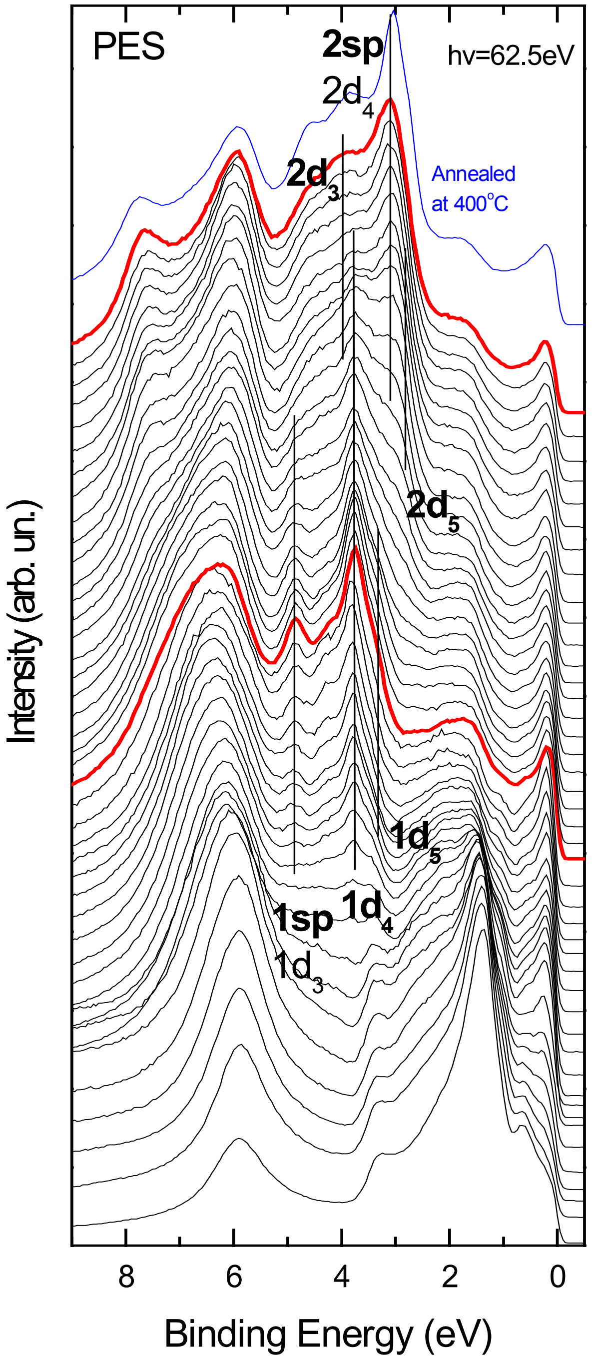

Fig.1. Series of normal emission valence band photoemission spectra obtained while 2 monolayer Au are deposited on W(145).

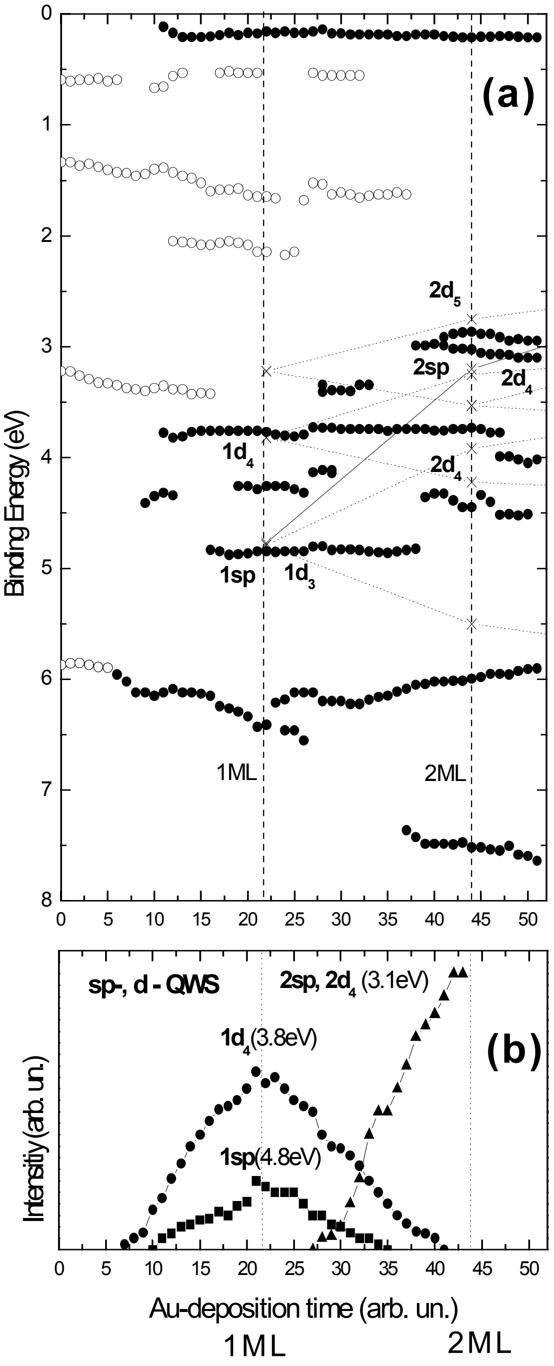

Fig.2. Binding energies (a) and intensities (b) of sp- and d- derived QWS's developed under deposition of Au on W(145).

Valence band umklapp at the step superlattice of W(331)

A.M. Shikin[1,2], A.Varykhalov[1,2], G.V. Prudnikova[1,2], V. Mozhaiskii[1,2], W.Gudat[1], O. Rader[1]
1) BESSY, Albert-Einstein-Str.15, D-12489, Germany
2) St.-Petersburg State University, St.-Petersburg, 198904 Russia

Many aspects of angle-resolved valence-band photoemission can be explained based on the ground state electronic structure. Among the processes inherent of the photoexcitation process, umklapp transitions lead to modifications of photoemission spectra that cannot easily be separated from contributions assigned to ground-state properties of the electronic structure.

The present work aims at understanding to what extent umkapp processes are important in angle-resolved photoemission from superlattices formed by stepped crystal surfaces. To this end, we compare angle-resolved photoemission spectra of flat W(110) to those from W(331). The W(331) surface is characterized by a 13^o cutoff angle relative to the (110) basis plane leading to (110) terraces of six-atomic-row width and a regular arrangement of steps running along the [1-10] direction. In terms of the bulk Brillouin zone, this corresponds to the ΓN-direction of W. The experiments were carried out at U125/1-PGM and UE56/1-PGM beamlines under vacuum better than 2×10^{-10} mbar. Samples were cleaned using standard procedures, i. e., oxygen treatment followed by high-temperature flashing, so that both W(110) and W(331) surfaces did not show any C or O 1s peaks.

Figure 1a shows measured band dispersions from the W(110) surface as reference. Data are plotted versus the surface projection of the electron wave vector along [1-10], i. e., the ΓH-direction in the (110) surface plane. The data distinguishes between photon energies of 62.5 eV, 81 eV, and 110 eV. The photon-energy-dependent data in normal emission (electron wave vector along [110] or ΓN) given in Fig. 1b clarifies that the dispersion in Fig. 1 measured at 110 eV which reaches 9 eV binding energy starts at the Γ-point and stays near the ΓH-direction for parallel wave vectors not too far from zero. The dispersions measured at 62.5 and 81 eV reaching 6 eV binding energy occur close to the N-point. For comparison, calculated dispersions [1] are given in Fig. 1a for both high-symmetry bulk directions. The calculated dispersions shall help us to identify features derived from bulk states knowing that W surfaces are characterized also by a wealth of surface states and surface resonances (see, for instance, Refs. 2 and 3).

As far as bulk states are considered, the electronic structure measured from W(331) is expected to be very close to the one identified above since W(331) consists of (110)-oriented terraces. In order to test this assumption we investigated the corresponding valence band dispersions for the stepped W(331) surface. Like above, we focus on the [1-10]-azimuth, i. e. near the ΓH-direction which is the one perpendicular to the step edges. Data for 62.5 eV photon energy are presented in Fig. 2 for two positions of the sample rotated by 180^o. Solid lines indicate the branches measured from the flat W(110). The identification of $k_{||}=0$ with the macrosurface normal (vertical line) is arbitrary and without consequences as we will consider only differences in the parallel wave vector. Another vertical line marks the terrace normal. It is readily seen that dispersions very similar to the ones from flat W(110) appear centered around the terrace normal and no dispersion is related to the macrosurface normal. This is in agreement with expectations based on the comparatively large terrace width of three lattice constants. Note, however, that some features, in particular the strongly dispersing bands between 4 and 6 eV binding energy discussed above, are shifted away from the terrace normal. We marked this shift by vertical dotted lines and the vector G. The value of G corresponds to the superlattice period of the terraces. The photoemission intensities (not shown) of the branches between 4 and 6 eV behave in an interesting way: The terrace-centered branches lead to significantly less intensity than those shifted away from the terrace normal by the wave vector G. In order to verify that this is not due to any geometrical reasons of the experiment like light incidence, we analyzed this also for Position 2, rotated by 180°. Again, the branch shifted away from the macrosurface normal has higher intensity.

We conclude from our analysis that introducing a new periodicity by a regular step arrangement at the surface strongly modifies the electronic structure as measured in angle-resolved photoemission. Extra branches appear away from the macrosurface normal, i. e., in the upstairs direction of the step lattice. If the observed dispersion were interpreted as first and second Brillouin-zone emission of the superlattice, the intensity behavior, i. e., higher intensity for the shifted branches, would be difficult to explain. In this case, i. e., ground-state properties of the superlattice as the reason for the observed behavior, also some features related to

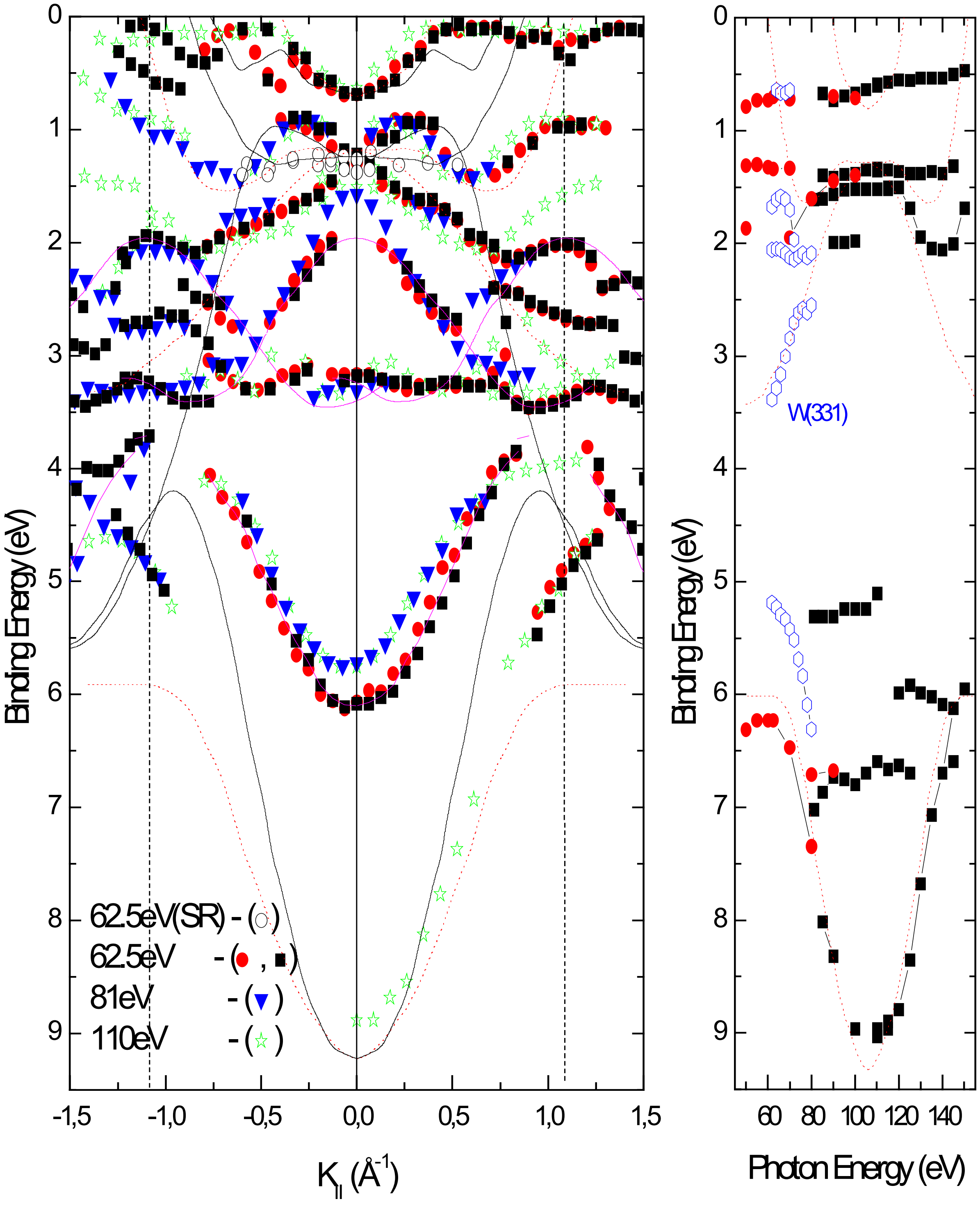

Fig.1. (a) Angle-dispersion of the valence band electron states for W(110) near the ΓH direction. Solid and dotted lines correspond to theoretical dispersions in the ΓH and ΓN directions taken from Ref. 1. (b) Experimental photon energy dependence of the main valence band states in comparison with the theoretical one in the ΓN direction taken from Ref. 1.

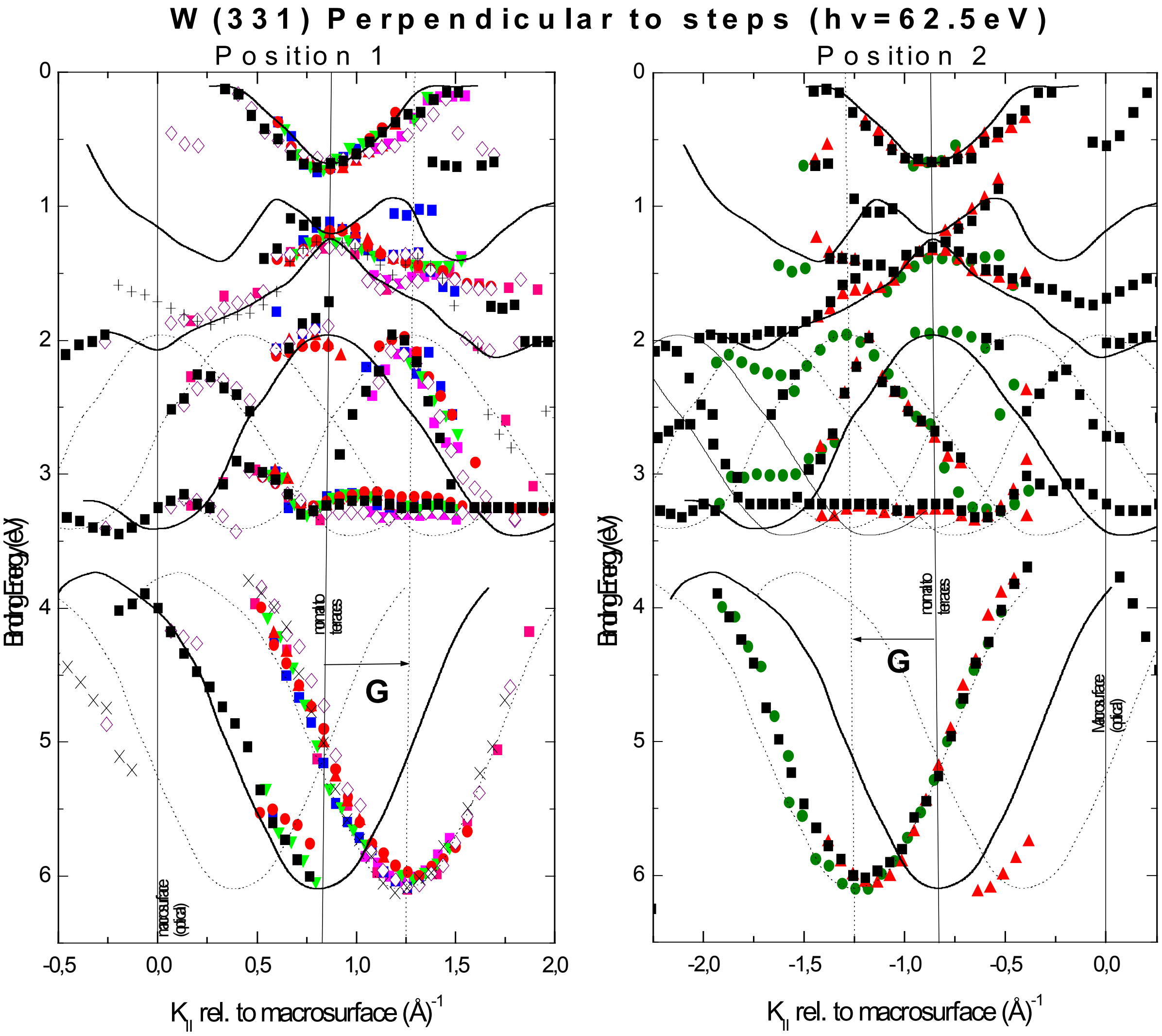

Fig. 2. Experimental valence band dispersions for W(331) along the direction perpendicular to steps (i. e., the same azimuth as in Fig. 1) measured at the photon energy of 62.5eV for two positions of the sample rotated by 180°.

the macrosurface normal might be expected but do not appear in our data. Strong intensity for hydrogen-induced umklapp has been reported for the W(100) surface [4], and we believe that the present results which, in contrast to previous studies, enable a direct comparison between direct photoemission and the umklapp process in terms of intensity shows that there are cases where umklapp leads to stronger intensity than direct photoemission. The consequences for experimental band-structure determination are grave: The photon-energy dependence from W(331) for emission along [110] leads to the behavior given by the blue open symbols in Fig. 1b, a dispersion which deviates by 1 eV in the determination of the N-point of the bulk Brillouin zone. From Fig. 2 and our analysis it is understood now that this measurement is actually the photon energy dependence of the umkapp-scattered band structure.

1. T.L. Loucks, Phys. Rev. Lett.14, 693 (1965); R.F. Willis, N.E. Christensen, Phys. Rev.B18, 5140 (1978).
2. K. Jeong, R.H. Gaylord, S.D. Kevan, Phys. Rev. B38, 10302 (1988); R.H. Gaylord, S.D. Kevan, Phys. Rev B36, 9337 (1987).
3. J. Feydt, A. Elbe, H. Engelhard, G. Meister, Ch. Jung, A. Goldmann, Phys. Rev. B58, 14007 (1998).
4. J. Anderson, G.J. Lapeyre, Phys. Rev. Lett. 36, 376 (1976).

4f hybridization in heavy rare-earth compounds

S.L. Molodtsov(1), Yu. Kucherenko(2), D.V. Vyalikh(3), G. Behr(4),
A. Starodubov(3), and C. Laubschat(1)
(1)Institut f. Oberflächen- u. Mikrostrukturphysik, TU Dresden, D-01219 Dresden, Germany
(2)Institute of Metal Physics, National Academy of Sciences, UA-03142 Kiev, Ukraine
(3)Institut f. Experimentalphysik, FU Berlin, D-14195 Berlin, Germany
(4)IFW Dresden, Postfach 270016, D-01171 Dresden, Germany

The localized character of the 4f states is mainly responsible for the magnetic properties of rare-earth (RE) compounds. In photoemission (PE) experiments this localized character is reflected by the appearance of broad $4f^{n-1}$ final-state multiplets. Recently, additional splittings of the 4f emission have been reported for Pr and Nd transition-metal compounds that are even larger than the multiplet splitting and are caused by hybridization. The phenomenon could be quantitatively described in the framework of a single-impurity Anderson model (SIAM) by formation of symmetric and antisymmetric fd hybrids that lifts the energy degeneracy between $4f^{n-1}$ and valence-band states in the final state [1]. For the $4f^{n}$ ground states this hybridization leads to admixtures of $4f^{n+1}$ configurations in the order 5% and may have consequences for the magnetic properties of these systems.

For the heavy RE elements Tb and Dy the relative energy separation between adjacent $4f^{n}$ configurations are similar to that for Pr and Nd, respectively. Hence, extrapolating the experimentally determined hybridization strength in Ce, Pr, and Nd compounds as a function of atomic number Z one might expect finite configuration mixing in the respective Tb and Dy compounds as well. In order to prove this conjecture resonant PE experiments on TbRh, TbPd, and DyRh have been performed at the 4d→4f absorption threshold using synchrotron radiation from the Russian-German beamline of BESSY II. Single-phase polycrystalline compounds were prepared by arc-melting and were cleaned in-situ by scraping with a diamond file. Fig. 1 shows on-resonance (thin line through solid circles) and anti-resonance (dashed line) 4f PE spectra of TbRh taken at hν=155 eV and hν=142 eV, respectively, and normalized to the photon flux. The on-resonance spectrum reflects almost exclusively emissions from the 4f states and may be compared directly with the expected Tb $4f^7$ final-state multiplet given below as a bar diagram. Here, the $^8S_{7/2}$ term is well separated from the other terms of the multiplet and corresponds to the 4f final state with the lowest binding energy (BE). In the

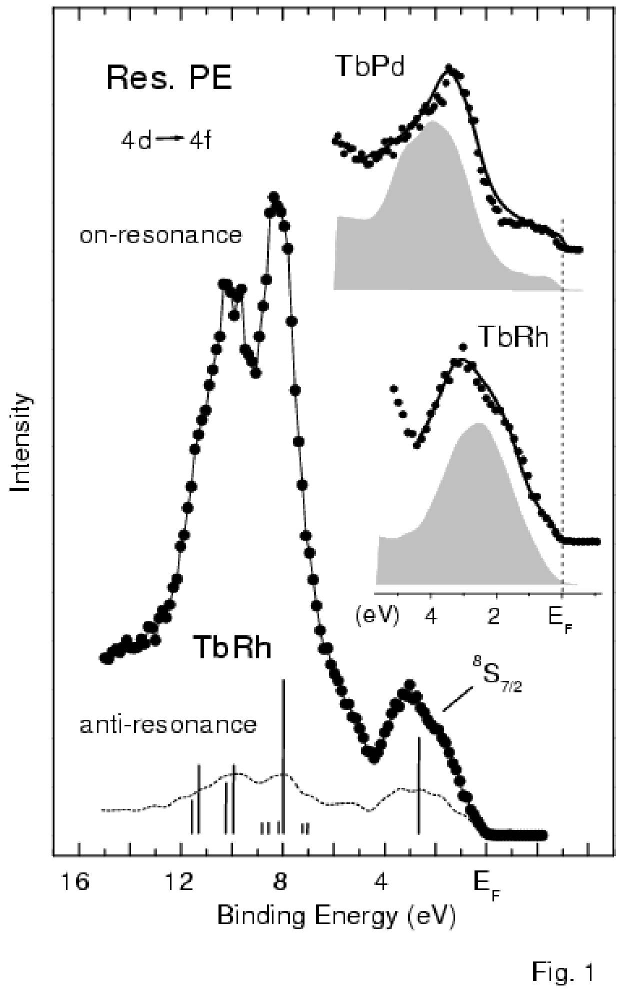

Fig. 1

experiment this term appears to be broadened and seems to consist of two components at about 2 eV and 3 eV BE, respectively. In the insert the spectral shape in the region of the $^8S_{7/2}$ state is shown in more detail for TbRh (bottom) and TbPd (top). For comparison, valence-band spectra of the same region taken at hν=70 eV are shown below as shadowed areas. These spectra reflect predominantly emissions from the almost filled 4d bands of the transition elements that reveal much larger PE cross sections than the 4f states at this low photon energy. On resonance respective spectral contributions are negligible small due to a Cooper minimum of the 4d cross section. As is evident from these spectra, the energy position of the 4d band coincides in TbRh with the expected position of the $^8S_{7/2}$ term and corresponds to a dip in the shape of the observed PE peak while in case of TbPd the 4d band is shifted to higher energy and the 4f emission is narrower and consists of only one peak at about 3 eV with a weak shoulder at higher BE. In the inset, solid lines through the data points reflect results of a numerical analysis in the light of SIAM [2]. This model, that is usually only applied to Ce systems, may be extended to Tb assuming that in the Hund´s rule Tb $4f^8$ ground state only the electron with antiparallel spin interacts with valence-band states, while the seven 4f electrons with parallel spin remain unaffected by hybridization due to the high stability of a half-filled shell. In the analysis also a (non-resolved) splitting of the 4f emission due to the surface core-level shift (0.5 eV towards higher BE) and a reduction of fd hybridization (66%) due to the reduced coordination at the surface were considered. As a result, bulk hybridization parameters of 0.9 eV and 0.6 eV are obtained for TbRh and TbPd, respectively, leading in case of TbRh to about 2% $4f^9$ admixture to the $4f^8$ ground state (1% for TbPd). The hybridization parameters of PrRh and DyRh are 1.3 eV and 1.15 eV, respectively, while the corresponding values of the Pd compounds are 0.85 eV and 0.75 eV, respectively. Similar effects as in TbRh are observed in DyPd that could be described with a hybridization parameter of 0.6 eV and lead to about 1% admixture of the $4f^{10}$ configuration to the $4f^9$ ground state.

Acknowledgement: This work was supported by the DFG, SFB 463, projects A1 and B4, and the BMBF, project 05 SR8KE11.

References:
1) Yu. Kucherenko et al., Phys Rev B 65, 165119 (2002), and Phys Rev. B 66, 165438 (2002)
2) R. Hayn et al., Phys. Rev. B 64, 115106 (2001), and references therein

Spectroscopy of $V_2O_3(0001)$ thin films on W(110)

M. Abu Haija, A.-C. Dupuis, B. Richter⋆, H. Kuhlenbeck, H.-J. Freund
Fritz Haber Institute of the Max Planck Society, Chemical Physics Department
Faradayweg 4-6, 14195 Berlin
⋆present address: Specs GmbH, Voltastraße 5, 13355 Berlin

Vanadium oxides exhibit catalytic activity for several reactions, most of them involving transfer of oxygen atoms. In the context of an extended project dealing with the chemical properties of the surfaces of different vanadium oxides also the chemical properties of $V_2O_3(0001)$ were investigated. Thin films were epitaxially grown on W(110) and studied with synchrotron radiation with respect to their surface electronic structure and the surface termination. Typical film thicknesses were between 30 and 100 Å.

Using vibrational spectroscopy it could be shown that the surface is terminated by vanadyl groups which lead to the loss at 127 meV in Fig. 1. A similar results was obtained before for the (0001) surface of Cr_2O_3 which exhibits corundum structure like V_2O_3. The vanadyl groups are thermally stable up to $T \geq 1000$ K and may be removed by exposing the surface to electron irradiation, leaving a surface behind which is possibly terminated by vanadium atoms. Tentative models for the two differently terminated surfaces are displayed in Fig. 2. For the vanadium terminated surface it was assumed that its structure is similar to that of the metal terminated $Cr_2O_3(0001)$ surface which was previously studied with I/V LEED [1, 2]. We note that the atomic arrangements at the two differently terminated $V_2O_3(0001)$ surfaces are not exactly known since structural studies do not yet exist.

The two $V_2O_3(0001)$ surfaces have been studied with high-resolution photoelectron spectroscopy of the O1s and V2p levels and the valence band. Fig. 3 displays O1s and V2p core level spectra recorded with 630 eV photons which means that the kinetic energy of the photoelectrons is

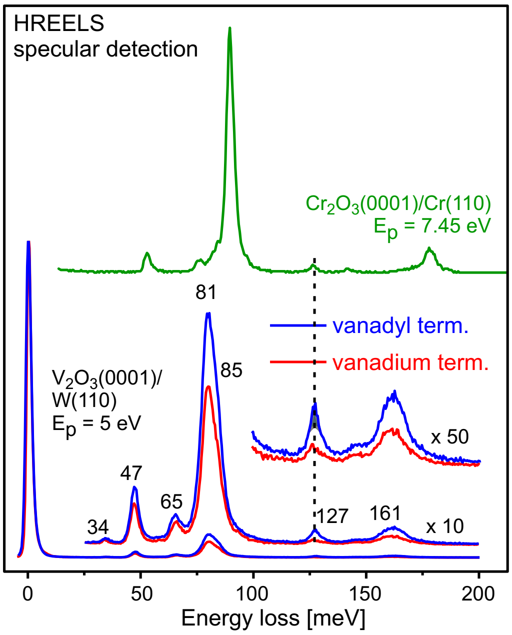

Figure 1: HREELS data of the vanadium terminated and the vanadyl terminated $V_2O_3(0001)$ surface in comparison with a spectrum of $Cr_2O_3(0001)$.

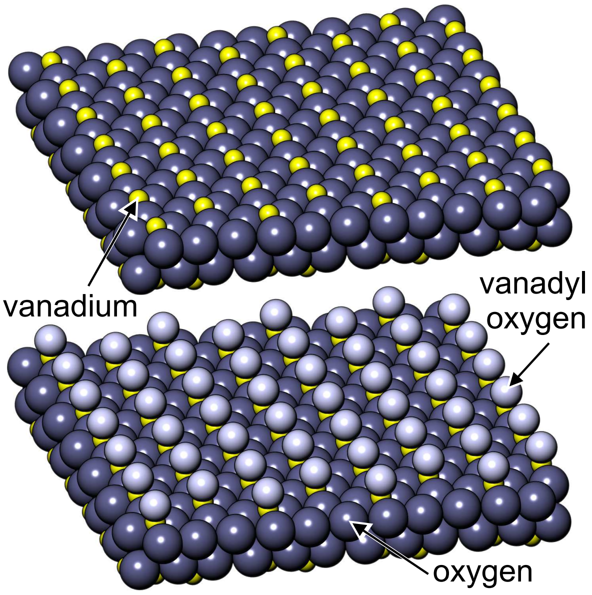

Figure 2: Drawings of the vanadium terminated (top) and the vanadyl terminated $V_2O_3(0001)$ surface (bottom).

near to 100 eV where the surface sensitivity is high. The main message of this figure is that the $2p_{1/2}$ and $2p_{3/2}$ bulk levels of the vanadyl terminated surface are accompanied by surface states at higher binding energy which gain intensity at grazing electron emission angle (second spectrum from top). For the vanadium terminated surface the intensity of the surface state is significantly smaller (third spectrum from top). In view of the structural differences of the two surfaces (see Fig. 2) we assign the surface state to emission from the vanadium atoms of the vanadyl groups. As shown by Sawatzky and Post the binding energy of the V2p levels increases with increasing oxidation state [3]. Therefore the higher binding energy of the surface states may be viewed as an indication that the oxidation state of the surface vanadium atoms is higher than that of the bulk vanadium atoms which is also indicated by a comparison with the spectrum of $V_2O_5(001)$ (bottom). This result is not unreasonable since the vanadium atoms of the vanadyl groups have two bonds to the oxygen atoms of the vanadyl groups and three bonds to the underlying oxygen atoms which means that their formal oxidation state is 5+. Some hints on the origin of the other features in the V2p and O1s spectra of $V_2O_3(0001)$ may be found in reference [4].

Surface sensitive valence band spectra of the two different surfaces are compared in Fig. 4. The vanadyl terminated surface is characterized by a peak at about 5 eV binding energy which shows up at nearly all detection angles. Another characteristic is the smaller intensity of the V3d levels which is due to the higher oxidation state of the vanadium atoms of the vanadyl groups. The higher binding energy of the O2p+V3d levels for the case of the vanadyl terminated surface is

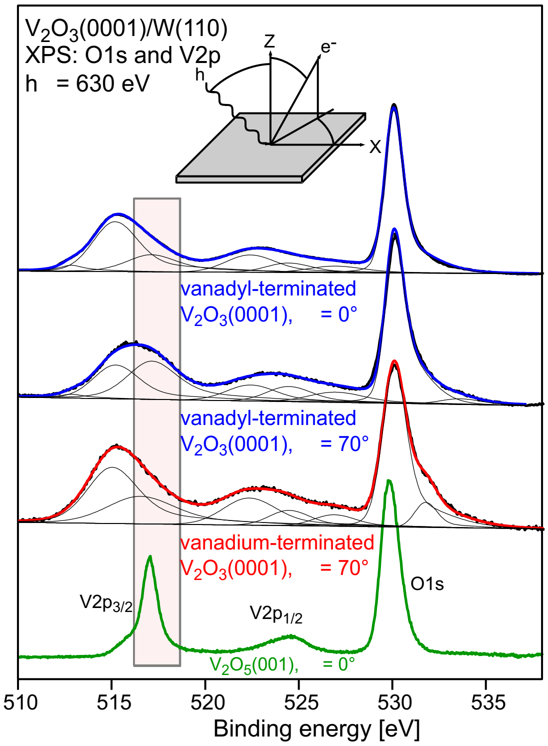

Figure 3: XPS spectra of the V2p and O1s core levels of $V_2O_3(0001)/W(110)$ in comparison with a spectrum of the $V_2O_5(0001)$ surface. The spectra of the $V_2O_3(0001)$ surface have been fitted by asymmetrically broadened products of Gaussians and Lorentzians. A Tougard-type background has been subtracted from all spectra.

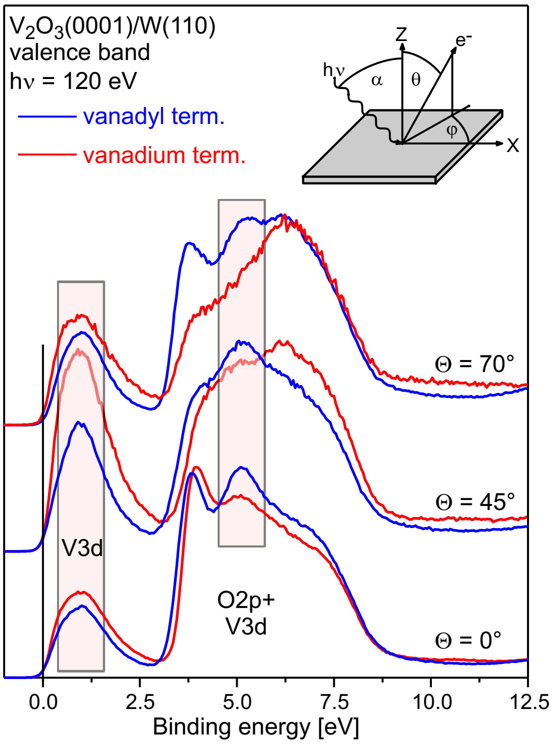

Figure 4: Valence band photoelectron spectra of vanadyl terminated and vanadium terminated $V_2O_3(0001)/W(110)$ recorded at different electron emission angles.

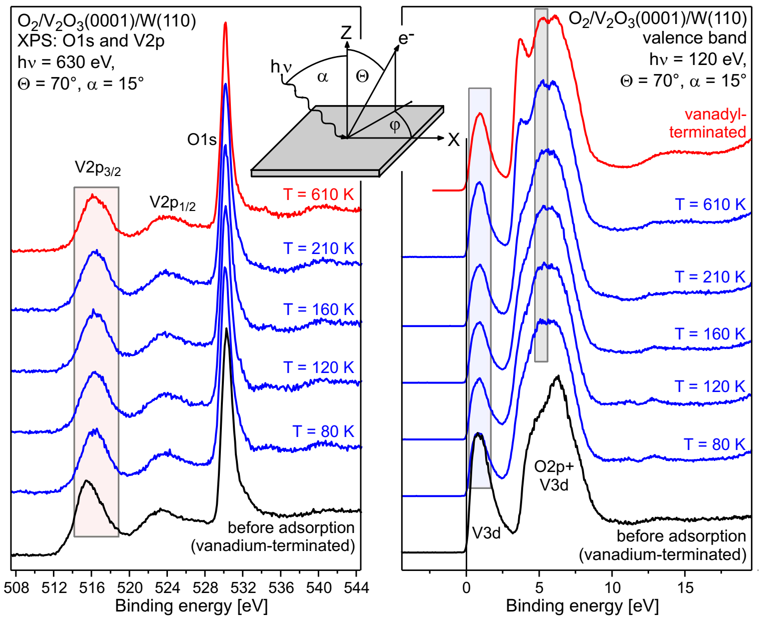

Figure 5: Photoelectron spectra obtained after annealing a vanadium terminated $V_2O_3(0001)/W(110)$ surface at different temperatures after exposure to 10 L of O_2 at T = 80 K.

also due to the higher oxidation state of the vanadium atoms as revealed by a comparison with calculated densities of states of different vanadium oxides [5].

Interaction with oxygen transforms the vanadium terminated surface into the vanadyl terminated one as demonstrated by the spectra displayed in Fig. 5. At T = 80 K exposure to O_2 leads to immediate reduction of the V3d intensity, indicating an increase of the oxidation state of the surface vanadium atoms. After annealing at 610 K the spectrum of the vanadyl terminated surface is recovered. Below this temperature the oxygen on the surface is in a somewhat different electronic/geometric state. Comparison with results obtained previously for $Cr_2O_3(0001)$ suggests that this species may be negatively charged molecular oxygen [6].

References

[1] F. Rohr, M. Bäumer, H.-J. Freund, J. A. Mejias, V. Staemmler, S. Müller, L. Hammer, and K. Heinz, Surf. Sci. **372**, L291 (1997).

[2] F. Rohr, M. Bäumer, H.-J. Freund, J. A. Mejias, V. Staemmler, S. Müller, L. Hammer, and K. Heinz, Surf. Sci. **389**, 391 (1997).

[3] G. A. Sawatzky and D. Post, Physical Review B **20**, 1546 (1979).

[4] R. Zimmermann, R. Claessen, F. Reinert, P. Steiner, and S. Hüfner, J. Phys. - Cond. Mat. **10**, 5697 (1998).

[5] K. Hermann and M. Witko, *Theory of physical and chemical behaviour of transition metal oxides: Vanadium and molybdenum oxides*, in *Oxide Surfaces*, editors D. A. King and D. P. Woodruff, volume 9 of *The Chemical Physics of Solid Surfaces*, pages 136–191, Elsevier (2001).

[6] B. Dillmann, F. Rohr, O. Seiferth, G. Klivenyi, M. Bender, K. Homann, I. N. Yakovkin, D. Ehrlich, M. Bäumer, H. Kuhlenbeck, and H.-J. Freund, Faraday Disc. **105**, 295 (1996).

Investigation of the interface between SiO_2 and 4H-SiC(0001) by angle-scanned photoelectron diffraction

Mark Schürmann, Stefan Dreiner, Ulf Berges, Carsten Westphal

Universität Dortmund, Fachbereich Physik,
Otto-Hahn-Straße 4, 44221 Dortmund, Germany

Silicon carbide (SiC) has received significant attention in recent years due to its properties which make it suitable for applications in high temperature, high voltage, high power, and high frequency devices and sensors. It is a wide bandgap IV-IV compound semiconductor with high thermal conductivity which is supposed to replace silicon in metal-oxide-semiconductor field-effect transistors for special applications where high temperatures, voltages or frequencys are involved or in chemically harsh environments. Unfortunately, the properties of the SiC/SiO_2 interface are not as convenient as these of the Si/SiO_2 interface. The inertness of the material to chemical reactions makes it difficult to achieve high quality ohmic and Schottky contacts or high quality SiC/SiO_2 interfaces for MOS device applications. For this reason, the interest in improving the quality of the interface between SiC and its native oxide has been growing constantly in the recent years.

In this project we use the method of angle-scanned x-ray photoelectron diffraction (XPD) to investigate the interface between SiO_2 and 4H-SiC(0001). XPD is a surface sensitive technique, which is, because of its susceptibility to short range order, ideally suited to investigate interfaces between crystalline materials and thin amourphous films (see for example [1]). In XPD measurements angle-resolved XPS-spectra are recorded over the full half sphere above the sample. The individual spectra can be decomposed into their chemically shifted components if the experimental energy-resolution is sufficient. In this way, intensity distributions can be obtained, which contain information on the local atomic environments of the different emitters. Simulation calculations are required in order to extract structural information from these intensity distribution patterns.

In this work, 4H-SiC(0001) samples were thermally oxidized in-situ. The oxidation started at the clean silicon-terminated $\sqrt{3} \times \sqrt{3}R30^\circ$ surface. During the oxidation process, the sample was held at a temperature of about 800°C for about 10 minutes at an O_2 pressure of about 1×10^{-5} mbar. This procedure resulted in a thin SiO_2 film covering the surface. An XPS spectrum of this sample, recorded at normal emission (Si2p, $h\nu = 179$eV) at the U41-PGM beamline, is shown in Fig. 1. It can be decomposed into three components: a SiC bulk

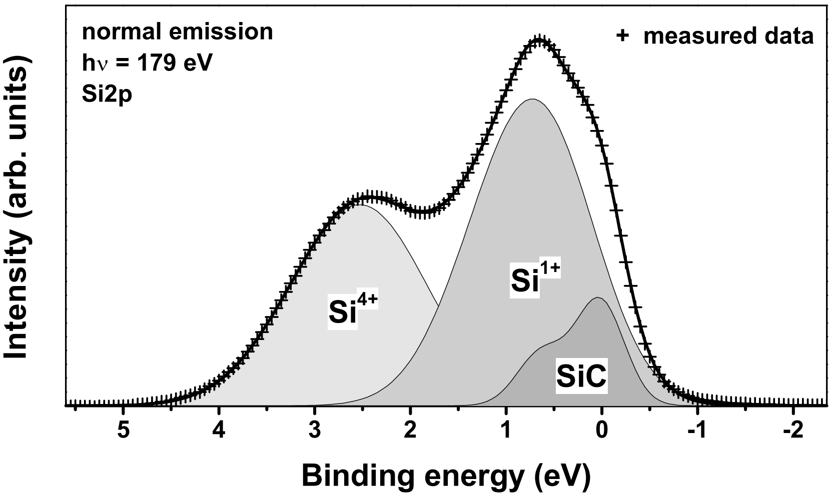

Figure 1: Si2p spectrum of the oxidized 4H-SiC(0001) sample recorded at a photon energy of $h\nu = 179 eV$

component, a SiO_2 component shifted by about 2.3 eV to higher binding energy and a third component, termed Si^+, shifted by about 0.5 eV to higher binding energy. Similar spectra have also been observed by other authors (e. g. [2], [3]). This third component is supposed to result from emitting atoms located in the interface region. The analysis of the whole photoelectron diffraction data-set will give more detailed information about the origin of these species and shall show, if their bonding configuration is similar to that of the top silicon atoms in an ordered silicate adlayer reconstruction, which has been found by Sieber et. al. [4] some years ago.

This Work was supported by the Deutsche Forschungsgemeinschaft (No. We 1649/3). We wish to thank the BESSY team, especially Ch. Jung, for the kind support during the measurements.

References

[1] S. Dreiner, M. Schürmann, C. Westphal, H. Zacharias, Phys. Rev. Lett. **86(18)**, 4068 (2001).

[2] N. Sieber, Th. Seyller, R. Graupner, L. Ley, R. Mikalo, P. Hoffmann, D. R. Batchelor, D. Schmeisser Appl. Surf. Sci. **184**, 278 (2001).

[3] C. Virojanadara, L. I. Johansson, Surf. Sci. **472**, L145 (2001).

[4] N. Sieber, M. Hollering, J. Ristein, L. Ley, Mat. Sci. Forum **338-342**, 391 (2000).

In-situ high-resolution XPS Study of NO adsorption on Pt(111)

J.F. Zhu, M. Kinne, T. Fuhrmann, B. Tränkenschuh, R. Denecke, H.-P. Steinrück
Physikalische Chemie II, Universität Erlangen-Nürnberg

The adsorption of NO on Pt(111) has received significant attention during the past years, due to its importance in many technical processes, e.g., the performance of automotive catalytic converters. However, there are a number of inconsistencies between the results achieved by the different methods, in particular concerning the number and the occupation of different adsorption sites (see, for example, Ref. [1-3]). High-resolution X-ray photoelectron spectroscopy (HRXPS), particularly combined with high energy resolution and high photon flux third generation synchrotron radiation sources, is a rather unique and competitive method to monitor the adsorption kinetics due to the facts that it can not only qualitatively identify the surface species and their adsorption sites but also quantitatively determine their individual coverages. The aim of this work is to gain further insight in the NO adsorption on Pt(111) concerning structure, adsorption site occupation and saturation coverage by HRXPS in combination with molecular beam methods, LEED and TPD. Through the measurements performed at BESSY II beamlines U49/1-SGM in December 2001 and U49/2-PGM2 in May 2002, a real time in-situ observation of the coverage-dependent site occupations has been achieved by measuring O 1s, N 1s, and Pt 4f core levels in a few seconds. In addition, the site occupation during desorption has been determined from temperature-programmed XPS (TPXPS). All experiments were carried out in a transportable UHV system specially designed for HRXPS at synchrotron sources, which has been described in detail elsewhere [4].

Figure 1 presents sets of O 1s and N 1s spectra recorded during NO uptake on Pt(111) at 110 K. Only molecular adsorption occurs under these conditions as is evidenced by the absence of peaks due to atomic O and N, which have binding energies of 529.9 and 397.7 eV, respectively, as observed in separate experiments. For low NO exposures (< 0.7 L) only one peak at a binding energy of 530.3 eV, which is assigned to NO adsorption on three-fold fcc hollow sites, is observed in the O 1s region [5]. With increasing exposure a second peak due to NO adsorbed on on-top sites appears at 532.0 eV and gradually grows in intensity. Upon further increasing the NO exposure, a third O 1s component, located at 530.6 eV, develops on the expense of the 530.3 eV feature. This peak can be assigned to fcc- and hcp-hollow sites being both occupied in one unit cell due to the similar environments for the NO species in fcc- and hcp-hollow sites. After ~2.6 L NO exposure the surface is saturated. In contrast to the O 1s spectra, the shape of the N 1s spectra shows no significant changes with exposure. Only a single asymmetric peak at 400.4

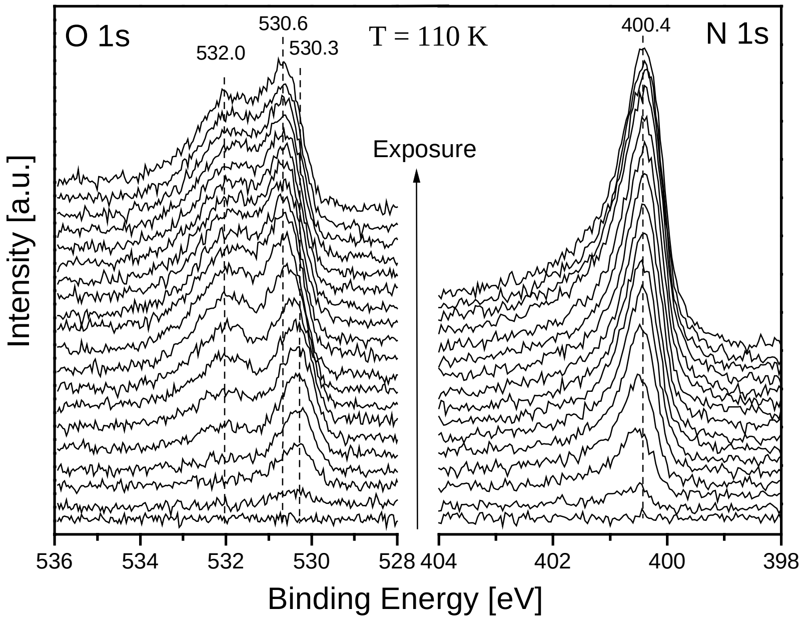

Fig. 1 : O 1s and N 1s spectra (raw data after background subtraction) measured during NO uptake on Pt (111) at 110 K with p_{NO} = 5.3x10^{-8} mbar. The photon energies are 650 and 500 eV for O 1s and N 1s spectra, respectively.

eV can be seen during NO uptake; this behavior indicates that the N 1s binding energy is not sensitive to different adsorption sites and was already observed by Kiskinova *et al.* using low-resolution XPS [6].

For quantitative analysis, the O 1s spectra can be decomposed into three components. The saturation coverage at different temperatures has been calculated by comparison of the O 1s intensity to that for an ordered c(4x2)-CO layer on Pt(111) with a coverage of 0.5 ML [5]. The saturation coverage below 150 K is around 0.77 ML; between 225 and 300 K, it is approximately 0.57 ML. With the help of LEED observations, which show a very clear (2x2) LEED pattern above 0.7 L until saturation at 110 K and also at saturation coverage at 250 K, we are able to confirm the structure model proposed by Matsumoto *et al.* [1,2] through the intensity changes in the O 1s and Pt 4f spectra as a function of NO coverage and substrate temperature. In the unit cell of (2x2)-NO at 0.25 ML, NO only absorbs on threefold fcc-hollow sites. The (2x2)-2NO structure at 0.5 ML contains one on-top NO molecule and one fcc-hollow NO molecule per unit cell. Finally, for the (2x2)-3NO structure one on-top NO and two hollow (fcc+hcp) NO species make up the unit cell. An alternative model for the (2x2)-3NO structure proposed by Metka et al. [3] can definitely be ruled out by our measurements. The small deviations of the calculated saturation coverages from the nominal coverages of the (2x2) unit cell can be explained by photoelectron diffraction effects.

We have also investigated the evolution of the adsorbate layer by measuring the O 1s, N 1s, and Pt 4f spectra in situ while a linear temperature ramp of 0.2 K/s was applied to the Pt(111) sample saturated with NO at 110 K. It demonstrates that no dissociation is taking place upon heating of the NO layer. The decrease of the O 1s intensity of the fcc+hcp-hollow site related peak at 530.6 eV and the increase of the exclusively fcc-hollow peak at 530.3 eV above 150 K suggests that the weakly bonded hcp-hollow NO species starts to desorb, consistent with TPD results [7]. At ~220 K, the O 1s peak at 530.6 eV disappears indicating that the hcp-hollow NO species has completely desorbed. In the temperature range from 220 K to 275 K the (2x2)-2NO structure exists on the surface and no desorption occurs, the intensities of all components stay nearly constant. Starting at 275 K, the O 1s peak at 532.0 eV begins to decrease, indicating the desorption of on-top NO. Upon further heating to 320 K this desorption continues and the O 1s spectra show that the fcc-hollow NO species also starts to desorb. Above 325 K the on-top NO species is completely desorbed from the surface. Finally, above 375 K, NO is completely removed from the surface. The TPXPS results coincide with TPD results very well [7].

In order to further explore the surface chemistry of NO on Pt(111), coadsorption of NO with oxygen has been studied. A detailed quantitative analysis of these data is still in progress. The pre-adsorbed (2x2)-O occupies three-fold fcc hollow sites [8] and blocks the NO adsorption on these sites. As a consequence, NO initially populates on-top sites, which is the only species at 250 K. For higher coverages at 110 K, NO can sequentially adsorb at hcp hollow sites, thereby inducing a shift of the O 1s binding energy of atomic oxygen towards lower energies by about 0.3 eV. Furthermore, the bond strength of the hcp hollow NO species to the substrate is weakened by the presence of atomic oxygen. The total saturation coverage of NO on (2x2)-O/Pt(111) is smaller compared to the clean Pt surface, while the initial sticking coefficient of NO remains the same.

This work is supported by DFG through Ste 620/4-1.

[1] M. Matsumoto, K. Fukutani, T. Okano, K. Miyake, H. Shigekawa, H. Kato, H. Okuyama and M. Kawai, Surf. Sci. 454-456 (2000) 101.

[2] M. Matsumoto, N. Tatsumi, K. Fukutani and T. Okano, Surf. Sci. 513 (2002) 485.

[3] U. Metka, M.G. Schweitzer, H.–R. Volpp, J. Wolfrum and J. Warnatz, Z. Phys. Chem. 214 (2000) 865.

[4] R. Denecke, M. Kinne, C.M. Whelan and H.-P. Steinrück, Surf. Rev. Lett. 9 (2002) 797.

[5] J.F. Zhu, M. Kinne, T. Fuhrmann, R. Denecke and H.-P. Steinrück, Surf. Sci., submitted.

[6] M. Kiskinova, G. Pirug and H.P. Bonzel, Surf. Sci. 136 (1984) 285.

[7] R.J. Gorte, L.D. Schmidt and J.L. Gland, Surf. Sci. 109 (1981) 367; C. Xu and B.E. Koel, Surf. Sci. 310 (1994) 198.

[8] N. Materer, U. Starke, A. Barbieri, R. Doll, K. Heinz, M. A. Van Hove, and G. A. Somorjai, Surf. Sci. **325**, (1995), 207

In-situ XPS study of the coadsorption of CO and D_2O on a Pt(111) surface

M. Kinne, T. Fuhrmann, J. F. Zhu, B. Tränkenschuh, R. Denecke, H.-P. Steinrück
Physikalische Chemie II, Universität Erlangen-Nürnberg

Core level photoelectron spectroscopy utilising synchrotron radiation from third generation sources has been proven to be a powerful method to examine the kinetic behavior of small molecules on surfaces in a time-resolved and adsorption site specific manner. Recently, the ad- and desorption kinetics of CO on Pt(111)[1] and the kinetics of the catalytic oxidation reaction of CO on this surface[2] were subject to measurements performed at BESSY II undulator beamlines. In order to complete our understanding of the properties of CO on the Pt(111) surface and the interaction with other molecules, the coadsorption with water (D_2O) has been studied in this project. Technologically, this system is of particular interest because in real Pt catalysts for CO oxidation water is likely to act as a contaminant; relevance for basic research stems from the possible comparison of the UHV experiments with CO adsorption processes in electrochemical cells.

The transportable UHV setup used has been described in more detail elsewhere[1,3]; its main parts are an electron energy analyser (Omicron EA125 HR) and a three-stage supersonic molecular beam device, which has been used for CO dosing. Besides that, a capillary array doser connected to the system allows for D_2O dosing. For temperature programmed XPS (TPXPS) measurements, a linear temperature ramp can be applied to the sample by a programmable temperature controller. Synchrotron light from the beamlines U49/2-PGM1 and U49/2-PGM2 with an energy of 380 eV for the C1s region and 650 eV for the O1s region has been used. Collection times used in this project were 6 s/spectrum for the C1s region and 11 s/spectrum for the O1s region. Water adsorbs on Pt(111) in multilayers at temperatures below 140 K; TPD shows two distinct peaks, which can be related to multilayer desorption at 150 K and desorption of a bilayer (1 BL consists of 0.66 D_2O molecules per surface atom) at ~170 K[4,5]. In our experiments a bilayer of water was prepared by dosing D_2O at a temperature of 152 K until equilibrium is reached, and subsequently cooling down to 125 K.

O1s XP spectra during uptake of D_2O on clean Pt(111) at 110 K show two main features: at low coverages a peak at a binding energy (BE) of 532.2 eV appears, which for higher coverages saturates in intensity, while another feature at 532.9 eV begins to grow (Fig. 1a). Subsequent heating with a linear temperature ramp of 0.1 K/s causes the high binding energy peak to decrease (T ~ 149 K); the low BE peak also looses intensity at a temperature of about 165 K. From this result and by comparison with TPD[5] (taking different heating

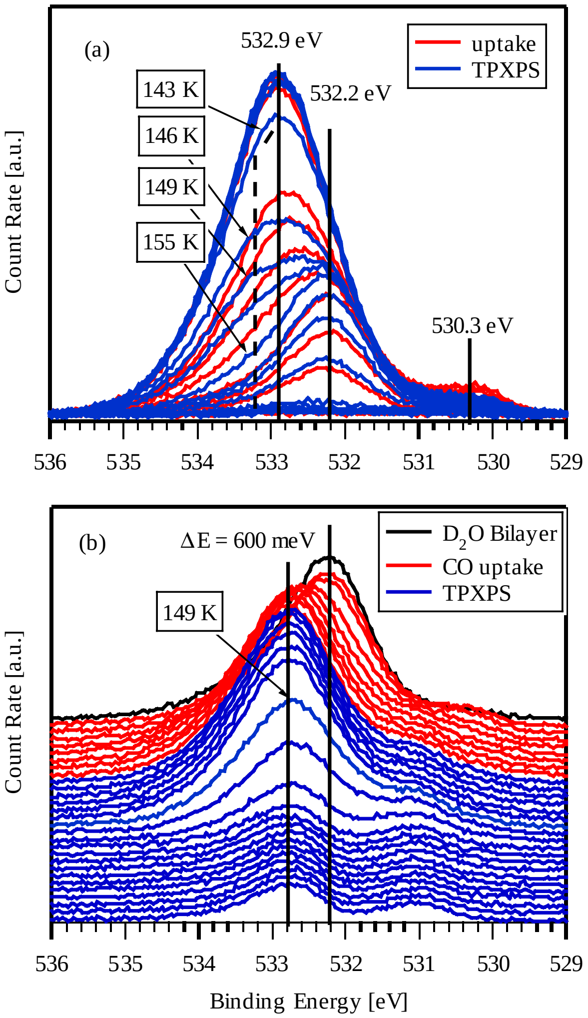

Figure 1: *O1s spectra measured at $h\nu = 650$ eV.*
(a) *D_2O uptake ($1.5\cdot10^{-9}$ mbar, 125 K, time between spectra:60s) and TPXPS (125 – 200 K, 0.1 K/s);*
(b) *CO uptake on D_2O bilayer (125 K, $5\cdot10^{-8}$ mbar, time between spectra: 30s) and TPXPS (125 – 200 K, 0.1 K/s).*

rates and different coverages into account, which can influence desorption temperatures), the low BE peak is identified with the water bilayer and the other one with the multilayer. Note that during desorption the multilayer peak shifts by about 300 meV towards higher binding energies; the reason for this behaviour is presently unclear. Fitting symmetric line profiles to the spectra allows for a quantitative determination of coverages (not shown here), which are calibrated with respect to the saturated bilayer peak. In accord with literature, no decomposition of D_2O is encountered; a small feature at E_B = 530.3 eV, which can be associated with OD is due to beam damage caused by prolonged X-ray irradiation.

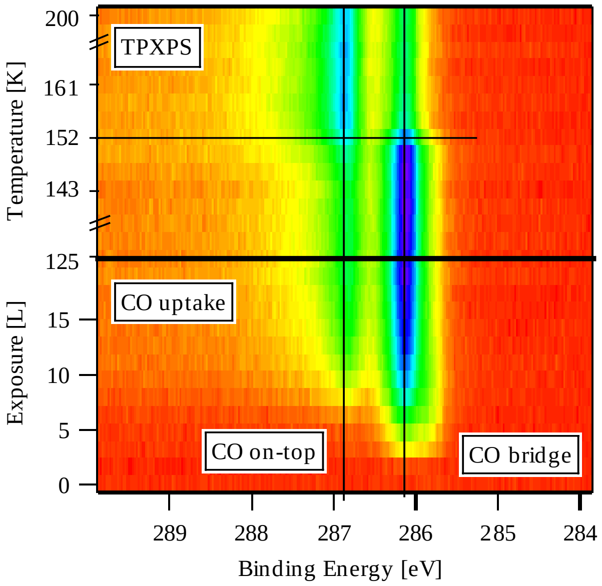

Figure 2: *C1s spectra obtained at $h\nu$ = 380 eV. Lower part: CO uptake on 1BL D_2O / Pt(111) (125 K, $5\cdot10^{-8}$ mbar). Upper part: TPXPS (0.1 K/s) after uptake (red / blue: low / high intensity)*

The effect of CO postdosing on a bilayer of D_2O is shown in Fig. 1b. The bilayer peak is shifted by 0.6 eV towards higher binding energies; during TPXPS D_2O is found to desorb at a temperature of ~149 K, which is a significantly lower value than for the pure D_2O case. At a temperature of 200 K only CO is left on the surface; the two peaks at 531.1 eV and 532.8 eV correspond to CO located on bridge and on-top sites, respectively[1]. As the CO- and the D_2O- related parts of the spectrum overlap, the behaviour of CO in the presence of D_2O can only be observed in spectra of the C1s region, which are shown in Fig. 2. As for pure CO adsorption, the spectra show two peaks at 286.1 eV (CO on bridge sites) and 286.8 eV (CO on-top) but with the difference that in the presence of D_2O the order of occupation is permuted: now bridge sites are occupied first and later on-top sites. This effect has been described qualitatively in literature[6]. TPXPS following the adsorption leads to a change in relative intensities; the temperature where this change occurs coincides with the desorption temperature of D_2O. Quantitative analysis shows that the total coverage of CO stays constant during TPXPS (the coverage in this case was 0.3 ML) proofing that no reaction occurs, in agreement with literature[7]. Our experiments show that the process of site exchange also takes place if the dosing order is reversed: Postdosing of D_2O on a surface precovered with ~0.3 ML of CO leads to an increase in bridge site occupation at constant total coverage. Concerning the kinetics of the CO adsorption process we finally compared the initial sticking coefficient S_0 (calculated from the slope of the coverage vs. time curve) for the case of a clean and a D_2O precovered (1 BL D_2O) sample at 125 K. As a result we found a reduction of S_0 by a factor of approx. 10 by the presence of D_2O; an effect, which qualitatively agrees with the results reported by Löfgren et al.[8].

This work was supported by DFG through Ste620/4-1.

[1] M. Kinne, T. Fuhrmann, C. M. Whelan, J. F. Zhu, J. Pantförder, M. Probst, G. Held, R. Denecke, and H. P. Steinrück, J. Chem. Phys. **117** (23), 10852 (2002).
[2] M. Kinne, R. Denecke, T. Fuhrmann, J. F. Zhu, C. Whelan, and H. P. Steinrück, in *BESSY Annual Report* (2001), pp. 210.
[3] R. Denecke, M. Kinne, C. M. Whelan, and H. P. Steinrück, Surf. Rev. Lett. **9** (2), 797 (2002).
[4] G. B. Fisher and J. L. Gland, Surf. Sci. **94**, 446 (1980).
[5] S. Haq, J. Harnett, and A. Hodgson, Surf. Sci. **505**, 171 (2002).
[6] N. Kizhakevariam, X. Jiang, and J. Weaver, J. Chem. Phys. **100**, 6750 (1994).
[7] F. T. Wagner, T. E. Moylan, and S. J. Schmieg, Surf. Sci. **195**, 403 (1988).
[8] P. Löfgren and B. Kasemo, Catal. Lett. **53**, 33 (1998).

XAS measurements on vanadium based compounds at the BAMline

L. Wilde[a], M. Schneider[a], D. Herein[a], H. Riesemeier[b] and M. Radtke[b]

[a] Institut für Angewandte Chemie Berlin-Adlershof, Richard-Willstätter-Str. 12, 12489 Berlin
[b] Bundesanstalt für Materialforschung und –prüfung, Unter den Eichen 87, 12205 Berlin

Introduction

The BAM together with the PTB operates a hard X-ray beamline at a 7T wave length shifter. The beamline is equipped with a Si(111) or Si(311) double crystal monochromator for the energy selection and a W/Si multilayer monochromator for the elimination of higher harmonics. Together with the ACA a setup was installed to do XAS spectroscopy measurements in transmission as well as in fluorescence mode.
A first series of measurements was taken at the VK-edge (E_K= 5.465 keV) on vanadium containing compounds in order to demonstrate the suitability of the BAMline and its components for XAS spectroscopy.

Experimental

Homemade ionisation chambers were used as detectors within the transmission measurements. For the fluorescence measurements a commercial Si/Li detector came into operation. The controlling software was developed by the PTB for the transmission measurements and by the BAM for the fluorescence measurements respectively. The samples was adjusted by a special positioning unit.
We used well known compounds such as vanadium metal foil, several vanadium oxides for comparative reasons as well as real catalysts. These catalysts basing on $(VO)_2P_2O_7$ are used for the selective oxidation of butane. They were prepared by two different means (organic preparation: reduction agent isobutanol versus inorganic preparation: reduction agent HCl). These samples were measured in transmission mode. Additionally, a highly diluted vanadium oxide (1.8%) catalyst on a SiO_2 support was studied in fluorescence mode. The vanadium fluorescence signal was normalized against the silicon fluorescence signal instead of the signal from the first ionisation chamber because of different integration times.

Results

The XAS measurement of a vanadium metal foil compares well to a similar measurement taken at Hasylab E4 beamline with respect to signal/noise ratio and energy resolution as can be seen from fig. 1.

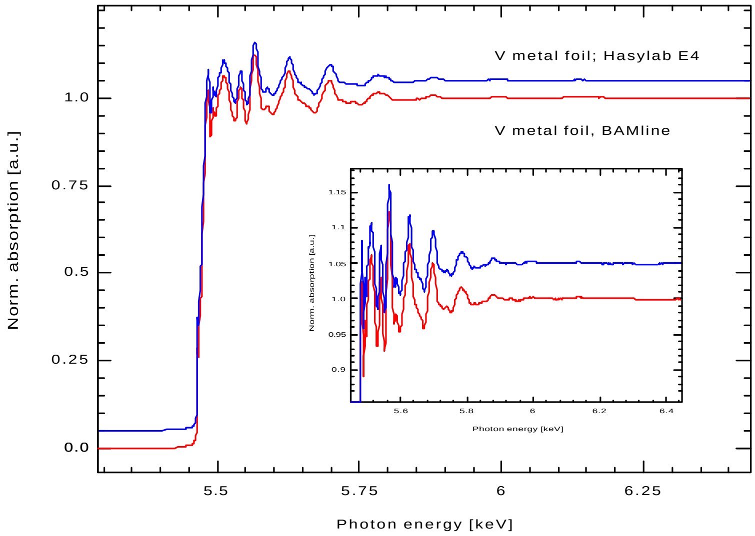

Fig. 1 Comparison of XAS measurements on vanadium metal foil taken on BAMline or Hasylab E4

To further study a potential influence of higher harmonics a fit of the first four shells was carried out in q-space, that very well reproduced the bcc vanadium structure (fig. 2). Therefore we conclude, that a negative impact of higher harmonics is not existent.

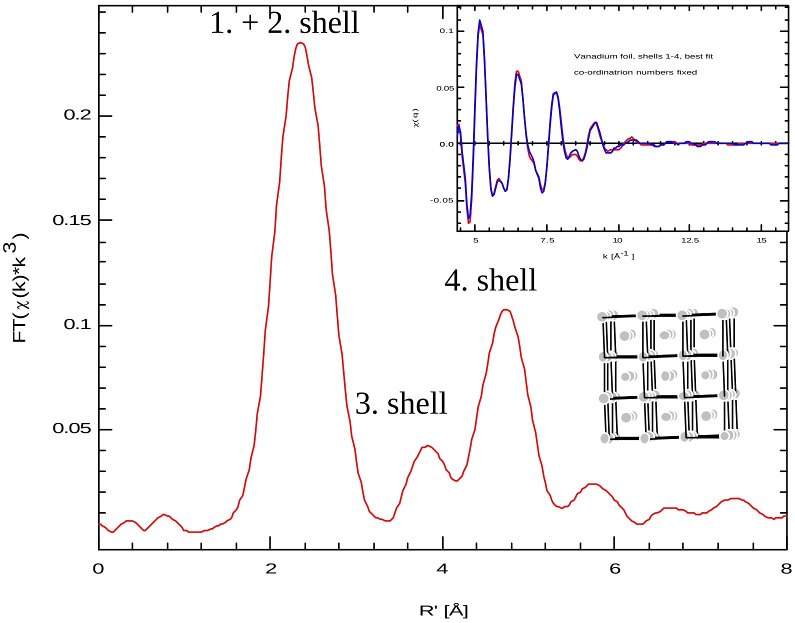

Fig. 2 Fit of the XAS data with the first four shells of the bcc structure model of vanadium metal

An example for the investigation of a real catalyst is shown in fig. 3. From that picture can be seen, that the pre-edge peak of an organically prepared $(VO)_2P_2O_7$ (red curve) is split and that the edge is shifted towards higher energies. This leads to the assumption, that a second phase is present within this catalyst, with a vanadium valence state of +5 and the vanadium atom being co-ordinated by a water molecule. A model substance for such a phase is $VOPO_4 \times 2\ H_2O$. In the insert of fig. 3 it is shown, that a linear combination of about 2/3 $(VO)_2P_2O_7$ and 1/3 $VOPO_4 \times 2\ H_2O$ fits very well to the observed XANES spectrum.

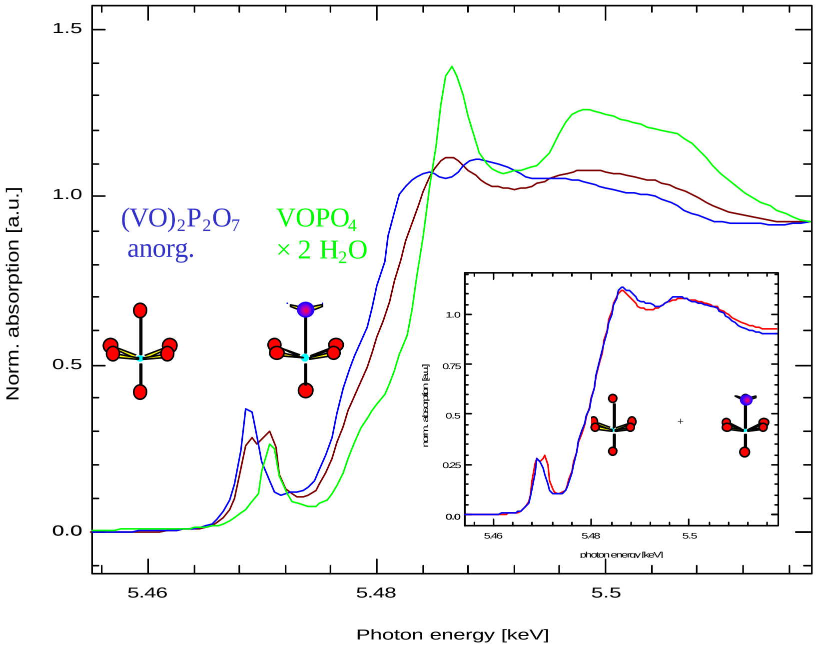

Fig. 3 Fit of the XAS data with the first four shells of the bcc structure model of vanadium metal

In order to demonstrate the suitability of the BAMline for XAS measurements in fluorescence mode, a diluted 1.8% VO_x/SiO_2 catalyst was investigated. The XANES spectrum of this catalyst compares very well to that of a (bulk) vanadium oxide (81% V^V, 19% V^{IV}) that was measured in transmission mode (see fig. 4).

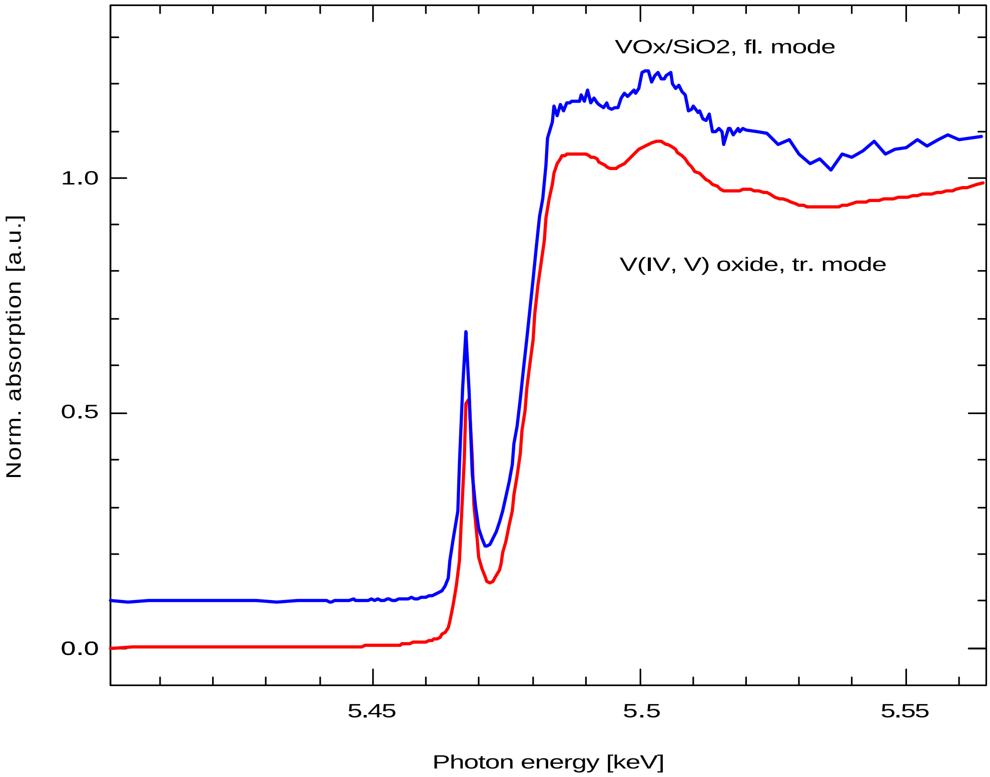

Fig. 4 Comparison of a VO_x/SiO_2 fluorescence spectrum and that of a V(IV, V) oxide

Acknowledgements
The authors gratefully acknowledge the financial assistance of the Senatsverwaltung für Wissenschaft, Forschung und Kultur and from the BMBF (03C3013).

Quantitative determination of the adsorption structure of carbonate on Ag(110)

M. Kittel, D.I. Sayago, J.T. Hoeft, M. Polcik,
Fritz-Haber-Institut der Max-Planck-Gesellschaft, Berlin, Germany

R.L.Toomes, D.P.Woodruff
Physics Department, University of Warwick, UK

M. Pascal, C.L.A. Lamont,
University of Huddersfield,UK

Although reaction intermediates at surfaces are potentially of great importance in understanding specific processes in heterogeneous catalysis, there have been very few quantitative structural studies of such species, notable exceptions including studies of the formate (HCOO-), acetate (CH_3COO-), methoxy (CH_3O-) and ethylidyne (CH_3C-) species [1]. Here we present the results of a study of the surface carbonate species, CO_3, on Ag(110) by means of scanned-energy mode photoelectron diffraction (PhD). The carbonate species seems to have been first identified on Ag surfaces in infrared absorption experiments following the reaction of CO_2 with oxygen-precovered silver catalysts by Force and Bell [2] in the course of investigations of these catalysts in the partial oxidation of ethylene to ethylene oxide. The adsorption geometry of CO_3 on Ag(110) has been studied by several methods but there is still controversy about it.

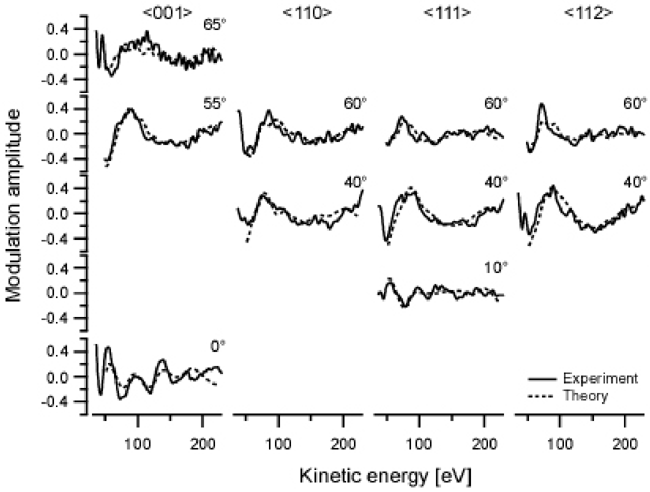

Fig. 1 Experimental (full) and theoretical (dotted) PhD modulation curves for the best-fit model

The experiments were conducted taking the incident radiation from the UE56/2-PGM-2 beamline of BESSY II using a 56 mm period undulator, followed by a plane grating monochromator. The resulting C 1s PhD modulation curves are shown in Fig. 1. The corresponding structural model is shown in Fig. 2.

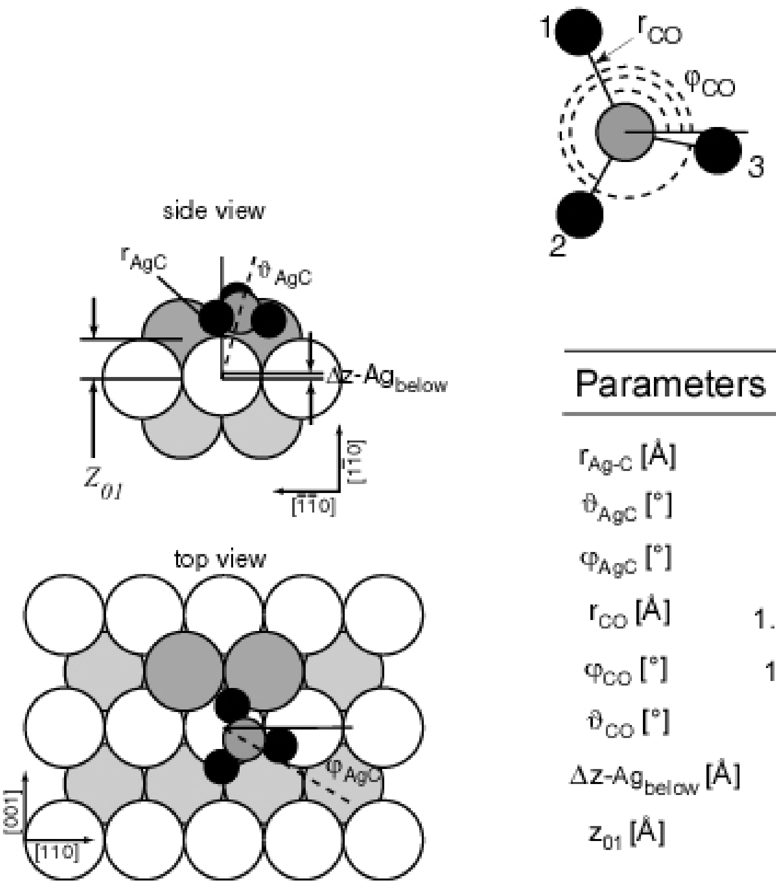

Parameters	Values		
$r_{Ag\text{-}C}$ [Å]		2.64 ± 0.09	
ϑ_{AgC} [°]		14 ± 7	
φ_{AgC} [°]		-27±33	
r_{CO} [Å]	$1.26^{+0.04}_{-0.08}$	1.30±0.04	1.30±0.07
φ_{CO} [°]	102±4	224±12	349±25
ϑ_{CO} [°]	89±9	87±9	100±5
Δz-Ag$_{below}$ [Å]		0.0±0.3	
z_{01} [Å]		1.5±0.4	

Fig 2. Structural model of CO3 adsorption on Ag(110)

The carbonate species is essentially planar and adsorbs almost parallel to the surface in an off-atop site relative to an outermost layer Ag atom, at a C-Ag layer spacing of 2.64±0.09 Å, with a well-defined azimuthal orientation. This geometry is best understood in terms of the added-row model proposed by Guo and Madix [3] in which additional Ag atoms lie adjacent to the carbonate, such that bonding can occur through at least one of the oxygen atoms. The distance between this oxygen and its nearest neighbour Ag adatom is 1.90±0.42Å. The C-O distances are in the range 1.26-1.30 Å. While the symmetry of the carbonate in the optimum structure is reduced, the D_{3h} symmetry of the isolated species lies within the limits of precision.

References:

[1] P.R.Watson, M.A. Van Hove and K.Hermann, *NIST Surface Structure Database Ver. 4.*0, NIST Standard Reference Data Program, Gaithersburg, MD.(2002)

[2] E.L.Force and A.T.Bell, J.Catal. 38 (1975) 440

[3] X.-C.Guo and R.J.Madix, Surf.Sci. 489 (2001) 37

Structural investigation of glycine on Cu(100)

R.L.Toomes, J.-H. Kang, D.P.Woodruff
Physics Department, University of Warwick, UK

M. Kittel, J.T.Hoeft, M.Polcik
Fritz-Haber-Institut der Max-Planck-Gesellschaft, Berlin, Germany

There is growing interest in the interaction of chiral molecules with surfaces, especially because of the great potential importance of new enantiomer-specific heterogeneous catalytic processes. One important group of chiral molecules are the amino acids, NH_2HRC^*OOH, where R is a side chain and the asterisk denotes the atom which defines the chiral centre. In the simplest amino acid, glycine, R is simply a hydrogen atom, so the presence of two H atoms bonded to the atom means that the free molecule is not truly chiral. One question which has recently been debated, however, is whether the individual ordered structural domains of glycinate on the surface contain both enantiomers (i.e. the domains are heterochiral), or whether the individual domains may be of a single enantiomer (i.e. are homochiral as indicated in Fig. 1). In this contribution we applied photoelectron diffraction in scanned-energy mode (PhD) to study the structure of glycinate adsorbed on Cu(100).

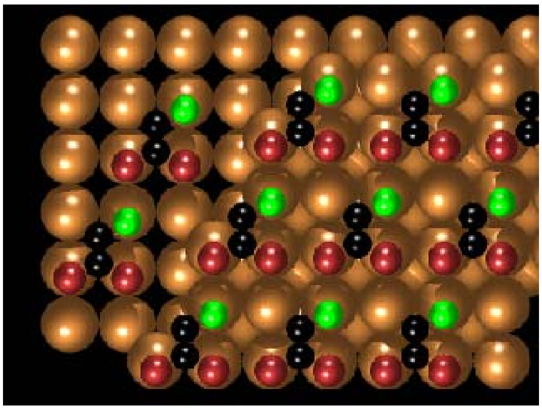

Fig. 1 Homochiral structure of glycine on Cu(100) proposed in [1]

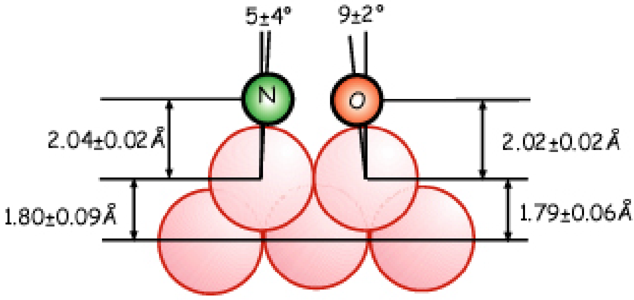

Fig. 2 Structural model for glycine on Cu(100)

The experiments were performed in a purpose-built UHV system installed on the high-energy toroidal grating monochromator beamline (HE-TGM 1) at the BESSY I synchrotron radiation facility in Berlin. The glycine powder was contained in a glass tube which could be heated via a surrounding copper coil and its temperature was measured by a thermocouple attached to a wire mesh within the tube. The doser was held within a small, separately pumped armature separated from the upper chamber by a gate valve. During dosing the glycine was heated to about 390 K and the Cu(100) crystal, at room temperature, was positioned facing the open gate valve to the doser.

The best agreement between the experimental and simulated data has been achieved for a structural model shown in Fig. 2 in which both O and N atoms adopt near-atop positions. The N 1s PhD modulation curves are presented in Fig. 3. Combining our results with the LEED observations which show the (2x4)-glide plane structure, we believe that hydrogen bonded chains of molecules are formed in heterochiral domains, although it is possible that homochiral domains of c(2x4) symmetry co-exist with the heterochiral domains.

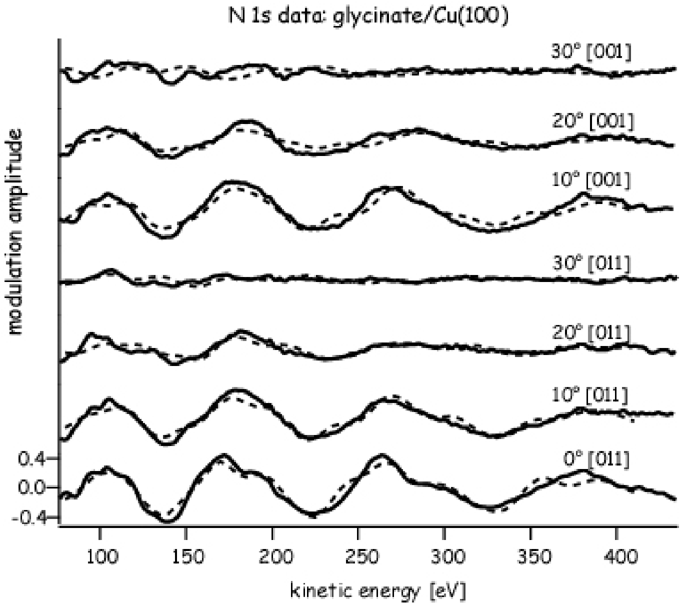

Fig 3. N 1s PhD modulation curves – experimental (full) and best fit simulated curves (dashed).

References

[1] X. Zhao, Z. Gai, R.G. Zhao, W.S. Yang, T. Sakurai, Suf.Sci. 424 (1999) L347

Structure of methanethiolate on unreconstructed Cu(111)

R.L.Toomes, J. Robinson, D.P.Woodruff
Physics Department, University of Warwick, UK

M. Kittel, D.I. Sayago, J.T.Hoeft, M.Polcik
Fritz-Haber-Institut der Max-Planck-Gesellschaft, Berlin, Germany

M. Pascal, C.L.A. Lamont
University of Huddersfield, UK

Quantitative structural information on the local registry of adsorbed thiols is rather sparse, despite the considerable interest in the self-assembled monolayers formed by alkane thiols on many surfaces. In the case of Cu(111), high-resolution soft X-ray photoelectron spectroscopy (SXPS) of the sulphur 2p core levels [1] revealed two states of the adsorbed methanethiolate species with different photoelectron binding energies. One of the states was dominant at low temperature (<173 K) and was attributed to adsorption on unreconstructed areas of the Cu(111) surface. As the temperature was raised this thiolate state was replaced by a second state associated with a reconstruction. These two species were referred to as the low temperature and room temperature (LT and RT) thiolates. An investigation of the adsorption geometries of the two thiolate states was carried out using chemical shift NIXSW (CS-NISXW) in which the 'chemical shifts' of the S 1s photoelectron binding energies were used to separate the NIXSW from the two species [2]. For the LT thiolate the results were somewhat inconclusive; they could be suggested that additional occupation of mixed hollow sites in the interstices between the hexagons (or even atop sites in the centres of the hexagons) might occur, although these were not imaged in the STM, see Fig. 1. In this paper we report a quantitative determination of the adsorption geometry of methanethiolate on unreconstructed Cu(111) (i.e. the LT thiolate)using energy-scanned photoelectron diffraction (PhD)with chemical-state resolution.

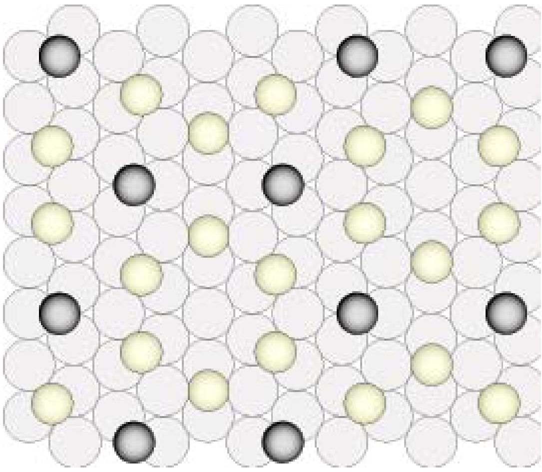

Fig.1.Structural model proposed in the earlier STM study [3]for the metastable honeycomb phase,identifed with the LT thiolate of the present study,which was observed in the middle of the Cu(1 1 1) terraces while dosing dimethyl disulphide at RT.

The experiments were performed in a purpose-built UHV system installed on the undulator beamline U49-1 at the BESSY II synchrotron radiation facility in Berlin. The clean surface was exposed to dimethyl disulphide $(CH_3S)_2$ at 135K to form adsorbed methanethiolate by S-S bond scission.

The best agreement between the experimental and simulated photoelectron diffraction modulation curves is shown in Fig. 2. In the overlayer which we prepared there was 71(+ 14 –16) % occupation of the bridge sites, 29±14% occupation of the fcc hollow sites and 0 ± 19% occupation of the hcp hollow sites. The methanethiolate adsorbed in the bridge site has a layer spacing of the sulphur atom to the outermost substrate layer of 1.87± 0.03Å giving a Cu–S bondlength of 2.27± 0.03Å. The methanethiolate adsorbed in the fcc hollow site has a layer spacing of the sulphur atom to the outermost substrate layer of 1.73± 0.04Å, corresponding to the same Cu –S bondlength of 2.27± 0.04 Å. The S–C bondlength was found to be 1.92± 0.10Å, which is somewhat longer than the gas phase value. The S–C bond axis of the bridge-bound thiolate is tilted strongly away from the surface normal and the data suggest it is preferentially tilted by 45 ±12° to the surface normal in the azimuth directed towards the fcc hollow site.

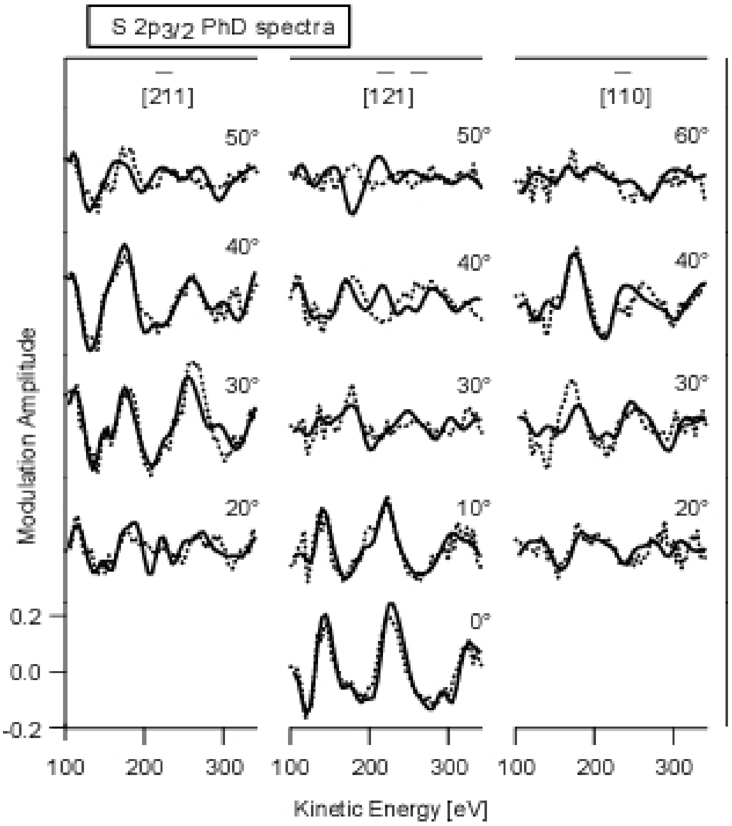

Fig. 2 Best agreement between the experimental (dotted) and simulated (full lines) PhD spectra

References

[1] M.S.Kariapper, G.F.Grom, G.J.Jackson, C.F.McConville,D.P.Woodruff, J.Phys.:Condens.Matter 10 (1998) 8661

[2] G.J.Jackson, D.P.Woodruff ,R.G.Jones, N.K.Singh A.S.Y.Chan, B.C.C.Cowie, V.Formoso, Phys.Rev.Lett. 84 (2000)119

[3] S.M.Driver,D.P.Woodruff , Surf.Sci.457 (2000)11

Study of activated adsorption of methane on Ni(111) using in situ high resolution XPS and molecular beam techniques

T. Fuhrmann, M. Kinne, J.F. Zhu, B. Tränkenschuh, R. Denecke and H.-P. Steinrück
Physikalische Chemie II, Universität Erlangen-Nürnberg

Ni is used as an industrial catalyst for methane steam reforming. Using molecular beam techniques, dissociative adsorption of methane, which should be an important step in this reaction, can be studied under UHV conditions. By heating the nozzle and seeding CH_4 into He, both the kinetic energy and the vibrational state of the molecules can be varied. Combining a supersonic molecular beam set-up with high resolution photoelectron spectroscopy using synchrotron radiation as an excitation source, we are able to observe the influence of these parameters on the adsorption process in situ. C1s XP-spectra are recorded in a time-resolved manner with an acquisition time of about 6 s. We are also able to perform TPXPS experiments by heating the sample while measuring XP-spectra. Observing the thermal evolution of the adsorbate allows to monitor temperature induced reactions and to identify intermediate species. In order to help identifying adsorbed species, separate experiments with other hydrocarbons, e.g. C_2H_2, were performed.

The complete apparatus used has been described elsewhere.[1] While the CH_4 beam was impinging on the surface, C1s spectra using an excitation energy of 380 eV and choosing a combined resolution of about 200 meV have been recorded. A seeded beam of 5 % CH_4 in Helium with a nozzle temperature of 700°C was used, impinging on Ni(111) with normal incidence. The surface temperature of the sample was 110 K.

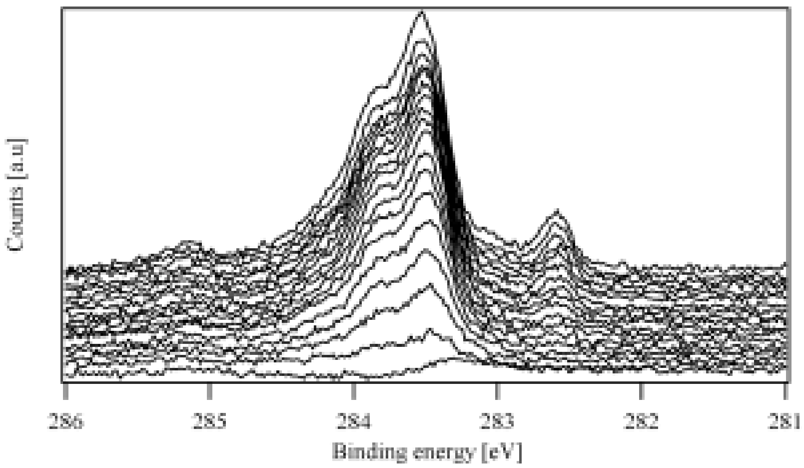

Fig. 1: Typical set of C1s uptake spectra, T_{nozzle}=700°C, 5% CH_4 in He, E_{kin}=0,58 eV, T_{sample}=110 K.

A typical adsorption experiment, called uptake is shown in Fig 1. Deconvoluting the spectra into separate components shows the major peak at a binding energy of 283.53 eV. Two smaller peaks at 283.87 and 284.21 eV are also observed. Since they show the same rate of intensity increase as the main peak and since all three peaks exhibit constant binding energy differences of approximately 340 meV, they can be assigned to the vibrational progression caused by excitation of the C-H stretching mode. To confirm this assumption, comparable adsorption experiments using CD_4 were performed, leading to a similar shape of the spectra, but with a smaller peak separation between the adiabatic main peak and the peaks caused by excitation of higher vibrational levels. This is consistent with the mass increase. Varying the molecular beam parameters, such as the kinetic energy or the degree on internal excitation of the methane molecules, always leads to the same surface species, identified as CH_3 or CD_3, respectively. The small peak, growing at 282.6 eV is caused by synchrotron radiation damage.

Concerning the thermal evolution of the adsorbed CH_3, it is known from literature [2] that in a first step CH is formed, followed by a C-C coupling process yielding C_2H_2 at around 250 K. For higher coverages C_6H_6 formation is also observed. Results of a TPXPS experiment monitoring these surface reactions between 110 and 440 K are shown as a density plot in Fig. 2. The first intermediate, giving rise to the peak at around 282.6 eV for a temperature of about 210 K is assigned to CH, in agreement with literature.[2] The possibility to populate this species also by radiation damage confirms this assignment. The presence of C_2H_2 at temperatures above 250 K is indicated by the peak at 283.3 eV. This peak position was confirmed by separate C_2H_2 adsorption experiments. A quantitative analysis of the data using peak fitting is in progress.

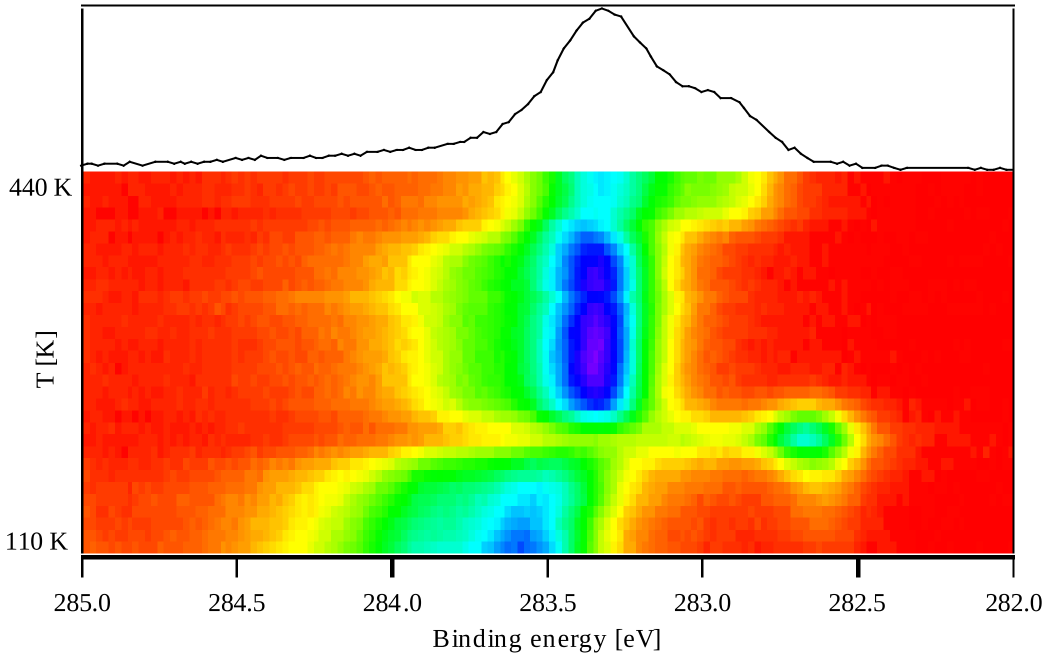

Fig. 2: TPXPS density plot of CH_3/Ni(111) for the C 1s region, heating rate 0.4 Ks^{-1}. Blue=high intensity, red=low intensity. Spectrum for 440 K shown on top.

This work was supported by DFG (Ste620/4-1).

[1] R. Denecke, M. Kinne, C. M. Whelan, H.-P. Steinrück, *Surface Review and Letters* **2002**, *9*, 797.

[2] Q. Y. Yang, K. J. Maynard, A. D. Johnson, S. T. Ceyer, *Journal of Chemical Physics* **1995**, *102*, 7734.

Adsorption geometry and electronic structure of simple molecules adsorbed on the chiral Pt{531} surface

S. J. Pratt, E.A. Hawkins, G. Held

University of Cambridge, Department of Chemistry, Lensfield Rd Cambridge CB2 1EW, UK

Asymmetry or stereochemical specificity permeates throughout nature since different enantiomers of chiral molecules often exhibit drastically different reactivity in living matter. Thus the manufacture of single enantiomer products is essential in drug design, and new technologies for enantioselective catalysis are currently sought. The further development of heterogeneous methods by introducing enantioselective catalyst surface geometries would, to this end, harness the distinct advantages of heterogeneous processes over the homogeneous methods predominantly in use [1].

One of the principal strategies for enantioselective heterogeneous catalysis is to use a chiral substrate to 'stereodirect' a surface reaction. Certain high Miller-index surfaces of symmetric bulk crystal structures are intrinsically chiral because they have no mirror planes. There are some examples in the literature of enantioselective reactions on such surfaces of Pt and Cu [2,3,4,5]. However, it is rather difficult to discriminate between enantiomers with most conventional Surface Science techniques because they probe only scalar quantities (e.g. mass, vibrational frequency, electronic binding energy). Only crystallographic methods and polarisation-dependent optical methods are able to discriminate directly between enantiomers.

This preliminary study of CO on Pt{531} is the first of a series, eventually aiming for the observation of enantioselective surface reactions of chiral molecules on this surface. We have chosen Pt{531} because it has the smallest surface unit cell of all chiral Pt surfaces for which enatioselective reactions have been reported, allowing a theoretical treatment with DFT methods alongside the experiments [6].

The experiments were performed at the beamline UE52-PGM (CRG) at BESSY II using a Scienta 200 mm electron energy analyser with pass energies of 75eV and 20eV. Circularly polarised light was not available at the beamline when these experiments were performed, however, the orientation of the linear polarisation vector, **E**, could be switched from horizontal to vertical with respect to the ring plane; for most experiments horizontal polarisation was used at photon energies between 162eV (for valence and Pt 4f levels) and 400eV (for C 1s). The polar angle of incidence with respect to the surface normal was 15° and the emission angle 40°. We were able to optimise the overall energy resolution of beamline and electron energy analyser to 40 – 50 meV (for photon energy 162eV, measured at the Fermi edge). With this resolution it is now possible to observe temperature effects at the Fermi level and vibrational excitations at this beamline. The binding energies of all spectra were calibrated with corresponding measurements at the Fermi energy for the same photon energy and pass energy. The intensities were normalized with respect to the background at the low binding energy side of each spectrum.

The base pressure of the uhv system was $2x10^{-10}$ mbar. CO was dosed by backfilling the chamber to a pressure of $3x10^{-9}$ mbar at either 100K or 430K. All PES measurements were carried out at a sample temperature of 100K.

The first set of data, depicted in Figure 1, shows the Pt 4f lines for clean Pt{531} (black curve) and the same surface saturated with CO at 430 K (red curve). It is surprising that no peak showing a surface core level shift (SCLS) is resolved in the clean surface spectrum, independent of the emission angle. Instead the 4f doublet consists of two rather narrow lines at the bulk binding energies (BE = 71.0 eV, FWHM = 0.8 eV for $4f_{7/2}$). This is in contrast to the spectra of Pt{111}. There a distinct difference of -0.3 eV in BE between the $4f_{7/2}$ signals arising from surface atoms and those from bulk was observed [7,8]. It is commonly assumed that the SCLS increases with surface energy and should therefore be larger for the highly corrugated {531} than for the close packed {111} surface [9].

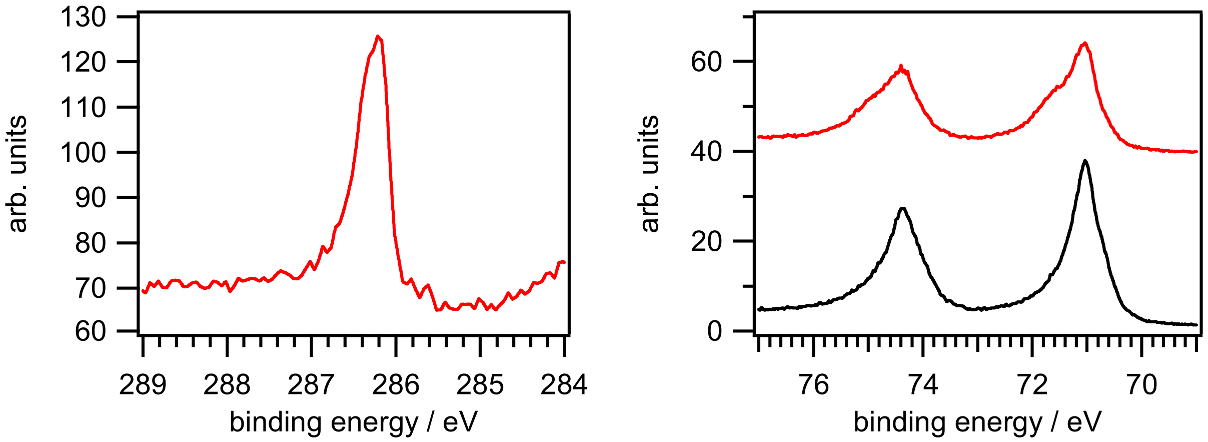

Figure 1: left: C 1s spectrum for CO adsorbed at 430K; right: Pt 4f spectra from the clean Pt{531} surface (black) and the CO covered surface (red).

After CO adsorption at 430 K, a shoulder appears in the Pt $4f_{7/2}$ spectrum at 71.6eV. A similar feature at 71.4 eV has been attributed to surface Pt atoms involved in CO adsorption on a bridge site based on earlier LEED and PhD work [7,8]. The BE of the C 1s peak (286.2 eV), also shown in figure 1, is consistent with this site assignment; a very similar BE of 286.1 eV has been assigned to bridge adsorption on Pt{111} (BE 286.1) [7,8]. Further support for this site assignment comes from recent DFT calculations carried out in our group, which have identified one of the two available bridge sites on this surface as the preferred adsorption site for CO [6].

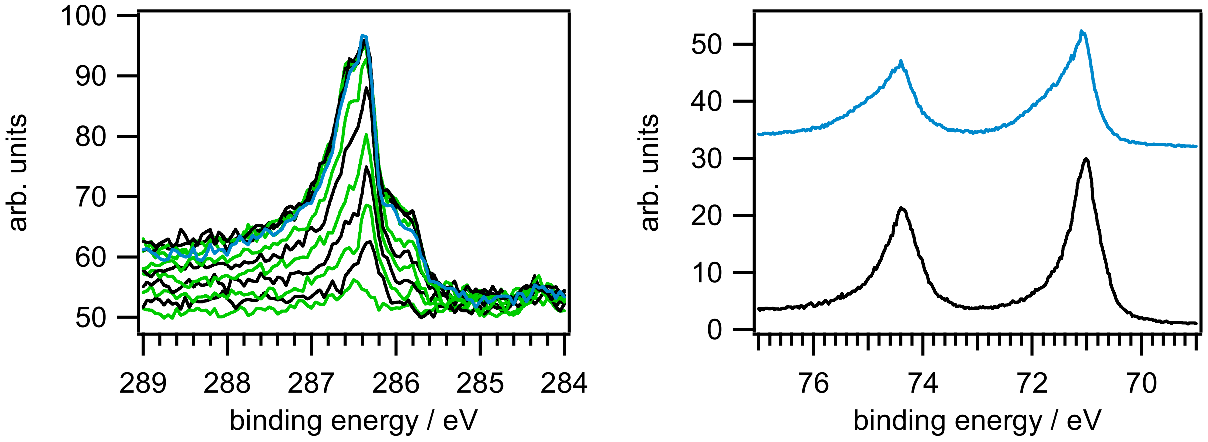

Figure 2: left: Series of C 1s spectra for CO adsorbed at 100K (exposure 0 – 2L); right: Pt 4f spectra from the clean Pt{531} surface (black) and the CO covered surface (red).

After adsorption at 100 K (see figure 2), two additional features appear in the C 1s spectra at BE 286.5 and 285.8 eV in addition to the dominant peak at 286.3 eV. These features indicate that CO adsorbs at two further sites, which are most probably a second bridge site and a hollow site, respectively, according to the rule that the BE decreases for increasing coordination of CO.

By changing the linear polarisation of the synchrotron radiation from p (horizontal) to s (vertical), dramatic changes are observed in the valence band region for CO adsorbed at 430K (see figure 3). We assign the pronounced features observed with p-polarised light at 11.4eV and 8.9eV to the 4σ and 5σ molecular states of adsorbed CO, respectively. The 4σ peak is almost entirely attenuated when s polarised light is used which indicates that the molecule is adsorbed in a very near-upright geometry. With the support of valence band spectra calculated for CO adsorbed in the most favourable bridge site, we conclude that half of the 1π-related states are forming part of the signal at 8.9eV, overlapping with the 5σ state. The orthogonal 1π states give rise to the pronounced signal at 7.8eV, observed with s-polarised light. This polarisation dependence and splitting of the 1π levels is typical for upright CO adsorption in bridge positions and, therefore, supports again, the site assignment made before. The valence electronic structure is currently the subject of a detailed theoretical investigation, carried out in our group [6].

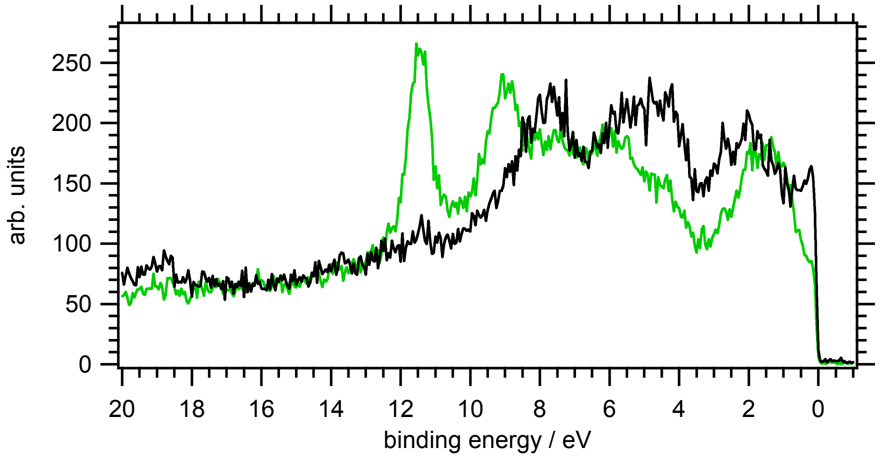

Figure 3: Valence spectra (162 eV) from Pt{531} predosed with CO at 430 K with p (green) and s (black) polarised radiation.

This work has been supported by the European Commission under the "Human Potential Programme, Transnational Access to Major Research Infrastructures", Contract No HPRI-1999-00028 and by EPSRC. We also gratefully acknowledge scientific and financial support by Prof. Sir D.A. King and many helpful discussions with S.J. Jenkins.

References:

[1] R. Raval, CATTECH (2001) 5 12.

[2] G. A. Attard, A. Ahmadi, J. Feliu, A. Rodes, E. Herrero, S. Blaise and G. Jerkiewicz, J. Phys. Chem. B (1999) 103 1381.

[3] A. Ahmadi, G. A. Attard, J. Feliu and A. Rodes, Langmuir (1999) 15 2420

[4] G. A. Attard, J. Phys. Chem. B (2001) 105 3158.

[5] J. D. Horvath and A. J. Gellman, J. Am. Chem. Soc. (2001) 123 7953.

[6] S.J. Pratt, V. Ranea, E. A. Hawkins, G. Held, S. J. Jenkins, E. E. Mola and D. A. King, to be published.

[7] O. Björneholm, A. Nilsson, H. Tillborg, P. Bennich, A. Sandell, B. Hennas, C. Puglia, N. Martensson, Surf. Sci. Lett. 315 (1994) L983.

[8] M. Kinne, T. Fuhrmann, C. M. Wheelan, J. F. Zhu, J. Pantförder, M. Probst, G. Held, R. Denecke, H.-P. Steinrück , J. Chem. Phys. 117 (2002) 10852.

[9] N. Martensson, H.B. Saalfeld, H. Kuhlenbeck, M. Neumann, Phys. Rev. B 39 (1989) 8181.

In situ X-ray photoelectron spectroscopy of the methanol oxidation on copper

H. Bluhm[1], M. Hävecker[1], A. Knop-Gericke[1], D. Teschner[1], E. Kleimenov[1], V.I. Bukhtiyarov[2],
D.F. Ogletree[3], M. Salmeron[3], R. Schlögl[1]

[1]*Fritz-Haber-Institut der Max-Planck-Gesellschaft, Faradayweg 4-6, D-14195 Berlin, Germany*
[2]*Boreskov Institute of Catalyis, 6300090 Novosibirsk, Russia*
[3]*Lawrence Berkeley National Laboratory, Materials Sciences Division, Berkeley, CA 94720, USA*

Introduction

We have used *in situ* X-ray photoelectron spectroscopy (XPS) to investigate the catalytic oxidation of methanol over a polycrystalline copper foil. There are two main reaction paths for the oxidation of methanol: a partial oxidation to formaldehyde and a total oxidation, which would be thermodynamically favored under equilibrium conditions:

(1) $CH_3OH + 1/2O_2 \rightarrow CH_2O + H_2O$ (partial oxidation) $\Delta H = -159$ kJ/mol

(2) $CH_3OH + 3/2O_2 \rightarrow CO_2 + 2H_2O$ (total oxidation) $\Delta H = -674$ kJ/mol

In situ near-edge X-ray absorption spectroscopy results at the O *K*-edge revealed that the formaldehyde yield is correlated to the presence of a suboxide species at the sample surface that could only be detected under *in situ* conditions. [1] The goal of our experiments was to use *in situ* XPS [2] to determine the nature of the active species during the catalytic reaction, and to measure their abundance as a function of reaction conditions. By varying the incident photon energy we have also performed depth-profiling of the active species at the copper surface under reaction conditions.

Experimental

A polycrystalline Cu foil was mounted onto a temperature-controlled sample stage in the experimental cell. The maximum pressure in the cell is ~10 mbar. X-rays are admitted to the experimental cell trough a 100 nm thick SiN_x window. The electrons that are emitted by the sample or the gas phase enter a differentially pumped electrostatic lens system through a 1 mm diameter aperture. The electrons are focussed onto two additional apertures before being focussed into the focal plane of a standard electron energy analyzer situated downstream, in the high vacuum region. The methanol vapor and oxygen flow into the experimental cell were regulated using calibrated mass flow controllers. The combined methanol and oxygen pressure in the experimental cell was 0.6 mbar at a methanol-to-oxygen flow ratio of 3:1. The sample temperature was varied in the range from 25 ºC...450 ºC. The experiments were performed at the undulator beam line U49/2-PGM1.

Results

Fig. 1 shows the O1s region of photoemission spectra (hν = 720 eV) taken at 25 °C and 400 °C in the reaction mixture. Since the incident X-ray beam irradiates part of the gas phase in front of the sample in addition to the sample surface, the spectra in Fig. 1 contain gas phase peaks alongside the surface peaks. Peaks with a binding energy (BE) higher than 534 eV are due to gas phase species, those with a BE smaller than 534 eV are due to oxygen species at the surface.

Both gas phase and surface peaks in the spectra in Fig. 1 show a strong dependence on the sample temperature. At 25 °C, only gas phase peaks of the two reactants (O_2 and CH_3OH) are present in the spectrum, indicating that there is no catalytic conversion. The presence of gas phase peaks of the reaction products (CH_2O, H_2O, and CO_2) in the spectrum taken at 400 °C shows that the Cu foil is catalytically active at this temperature.

In the spectra in Fig. 1 we can distinguish three different species at the surface or in the near-surface region (apart from some residual hydrocarbon-related contamination at 25 °C). At 25 °C the Cu_2O peak (BE 530.4 eV) dominates the spectrum. Two smaller peaks at 529.9 eV and 531.5 eV are also present at room temperature. These peaks dominate the O1*s* spectra of the catalytically active Cu surface at 400 °C, while the oxide peak is not present, i.e. the surface has now a metallic character. This is confirmed by the valence band spectrum taken at 400 °C, which shows the characteristic spectrum for metallic copper.

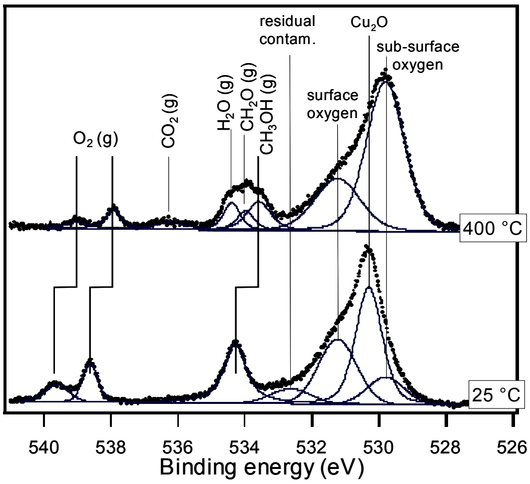

Fig. 1: *In situ XPS O 1s spectra of copper foil in 0.15 mbar* O_2 *+ 0.45 mbar* CH_3OH*. At 25 °C the sample is oxidic and catalytically inactive. At 400 °C the surface is metallic and shows a strong sub-surface oxygen peak. There are also peaks from the gaseous reaction products at 400 °C. The BE scale is referenced to the surface peaks. The BE difference of the gas phase peaks at 25 °C and 400 °C is due to a change in the work function of the sample surface.*

The nature of the peaks at BE 529.9 eV and 531.5 eV was investigated using depth-profiling. To this end O1*s* spectra were recorded at different incident photon beam energies These measurements revealed that the 531.5 eV peak intensity decreased with increasing mean free path length, whereas the 529.9 eV peak intensity increased with increasing mean free path length. This implies that the 531.5 eV species is located at the surface, while the 529.9 eV species is distributed in the sub-surface region. We can rule out that either of these species is a carbon-oxygen compound, since the C1*s* region of the photoemission spectrum does not show surface peaks that correlate to the O1*s* peaks under our reaction conditions. The 529.9 eV peak due to sub-surface oxygen was only observed in *in situ* measurements.

Fig. 2 shows the dependence of the CH_2O yield on the abundance of sub-surface oxygen in the sample (expressed in terms of its peak area) for different temperatures between 25 °C and 450 °C. There is a clear correlation between the abundance of sub-surface oxygen and the yield of CH_2O. Sub-surface oxygen could increase the catalytic activity by inducing stress in the Cu lattice, which could lead to an upward shift of the *d*-states and thereby to a stronger surface-adsorbate interaction. [3] The role of the sub-surface oxygen in the catalytic oxidation of methanol is subject of further investigations in our laboratory.

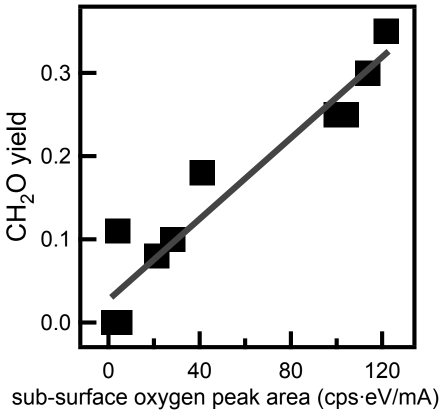

***Fig 2**: Formaldehyde yield as a function of subsurface oxygen peak area*

Acknowledgements

The BESSY staff is acknowledged for its continuing support of our experiments.

References

[1] A. Knop-Gericke, M. Hävecker, T. Schedel-Niedrig, R. Schlögl. Top. Catal. 15 (2001) 27-34.
[2] D.F. Ogletree, H. Bluhm, G. Lebedev, C.S. Fadley, Z. Hussain, M. Salmeron, Rev. Sci. Instrum. 73 (2002) 3872-3877.
[3] M. Mavrikakis, B. Hammer, J.K. Nørskov, Phys. Rev. Lett. 81 (1998) 2819-2822.

Characterization of VPO catalysts for n-butane oxidation using in- situ XPS

E. Kleimenov, I. Ayub, H. Bluhm, M. Hävecker, K. Ihmann,
A. Knop-Gericke, D. Teschner, R. Schlögl
Fritz-Haber-Institut der Max-Planck-Gesellschaft,
Department of Inorganic Chemistry, Faradayweg 4-6,
D-14195 Berlin, Germany.

A.Kharlamov, B.L. Ushkalov
Institute for Problems of Materials Science, Kiev, Ukraine

A.V. Zazhigalov
Ukrainian-Polish Laboratory of Catalyst, Institute for Sorption and Problems of Endoecology, National Academy of Sciences of Ukraine, Kiev, Ukraine

D.F. Ogletree, M. Salmeron
Lawrence Berkeley National Laboratory, Materials Sciences Division, Berkeley, CA 94720.

Introduction

Vanadium phosphorous oxides (VPO) are well-known as industrial catalysts for the selective oxidation of n-butane to maleic anhydride in the reaction

$$C_4H_{10} + 7/2\ O_2 \rightarrow C_4H_2O_3 + 4H_2O.$$

Usual industrial conditions for this reaction are p=1 atm. and T=375-480°C. It is known from measurements using a variety of different methods that VPO catalysts undergo significant structural changes during the activation process [1].

X-ray photoelectron spectroscopy (XPS) has been a powerful tool in catalytic research for decades. [2] This technique was used by numerous authors to investigate the properties of the VPO surface, in particular the P/V ratio and the vanadium oxidation state at the surface. [3-6]

Due to the short mean free path of electrons in a gas electron spectroscopies generally must operate in high vacuum conditions. Traditional XPS is therefore not suited for the characterization of catalytic surfaces under reaction conditions. To overcome this limitation, we have developed a new high-pressure electron spectrometer.

Experiment

The in-situ XPS spectrometer is a modified standard XPS spectrometer. The electrostatic lenes of the spectrometer were combined with a 3-stage differential pumping system. The pressure in the analyzer was in the 10^{-8} mbar range when the reaction cell pressure was several mbar. The reaction cell was separated from the synchrotron beamline by a 100 nm thick SiN_x window.

The VPO catalyst was activated ex- situ by heating vanadyl hydrogen phosphate hemihydrate $VOHPO_4 \cdot 0.5\ H_2O$ precursors at 400°C in vacuum. The conversion and the selectivity of the material were measured at standard conditions (1 bar, 400°C) prior to the spectroscopic investigations.

The samples were investigated in a constant reactant flow of 0.4 mbar of O_2 + 1.6 mbar of a He+butane(1.5%) gas mixture (total pressure 2 mbar). The sample temperature was cycled several times from 250°C (far below the reaction temperature) to 400°C (the reaction temperature). The goal of the experiment was to detect changes in the surface stoichiometry between the working and non-working catalyst. Two sets of incident photon energies were used in the in situ XPS experiments to provide different information depths (about 3 and 7 monolayers).

Results and discussion

XPS spectra of the catalyst showed changes of shape both with temperature and information depth (Fig. 1). The V oxidation state was estimated by fitting the O1s and V2p3/2 peaks using Gaussian profiles after Shirley background subtraction. Because of the inhomogenity of the VPO catalyst's surface numerous types of phosphor, vanadium and carbon oxides can occur. The O1s peak was fitted by four peaks (O_I, O_{II}, O_{III}, O_{IV}). The O_I peak was assigned to oxygen bound to vanadium. Thus, only the O_I peak area was used in O/V ratio calculations. The O_{II} O_{III} and O_{IV} peaks nature was not clearly identified. The phosphorous/vanadium and oxygen/vanadium atomic ratios were calculated using photoionisation cross-sections from [7]. The oxygen/vanadium ratio increased at the surface under reaction conditions. The phosphorous/vanadium ratio decreased with increasing information depth. This indicates an enrichment of phosphorous at the surface. Additionally, the P/V ratio decreased with time on stream. This effect is in agreement with the observation of phosphor depletion in industrial catalysts [1]. The atomic ratios of V, P and O for the different measurement conditions are summarized in table 1.

Table 1

	O/V		P/V	
T, °C	1 nm depth	3 nm depth	1 nm depth	3 nm depth
250	5.7	5.5	3.2	2.4
400	7.8	6.2	3.1	2.7
250	6.1	5.7	3.1	2.5
400	8.5	6.2	2.8	2.6

The difference in BE between the O1s peak and the $V2p_{3/2}$ peak for different V oxidation states was used to deconvolute the $V2p_{3/2}$ peak into its V^{5+},V^{4+} and V^{3+} contributions. The BE values for the different V oxidation states are known from XPS investigations of single-crystal vanadium oxides ([8], [9]). The fitting parameters that were used can be found in table 2. After peak fitting the BE scale was calibrated to 530 eV for the O_I peak position ([9]).

Table 2

	O_I	O_{II}	O_{III}	O_{IV}	V^{5+}	V^{4+}	V^{3+}
BE relative O_I, eV	0	2.1	1.1	-1.3	-12.9	-14.0	-15.1
FWHM, eV	1.5	1.8	2.2	1.5	1.8	1.8	1.8

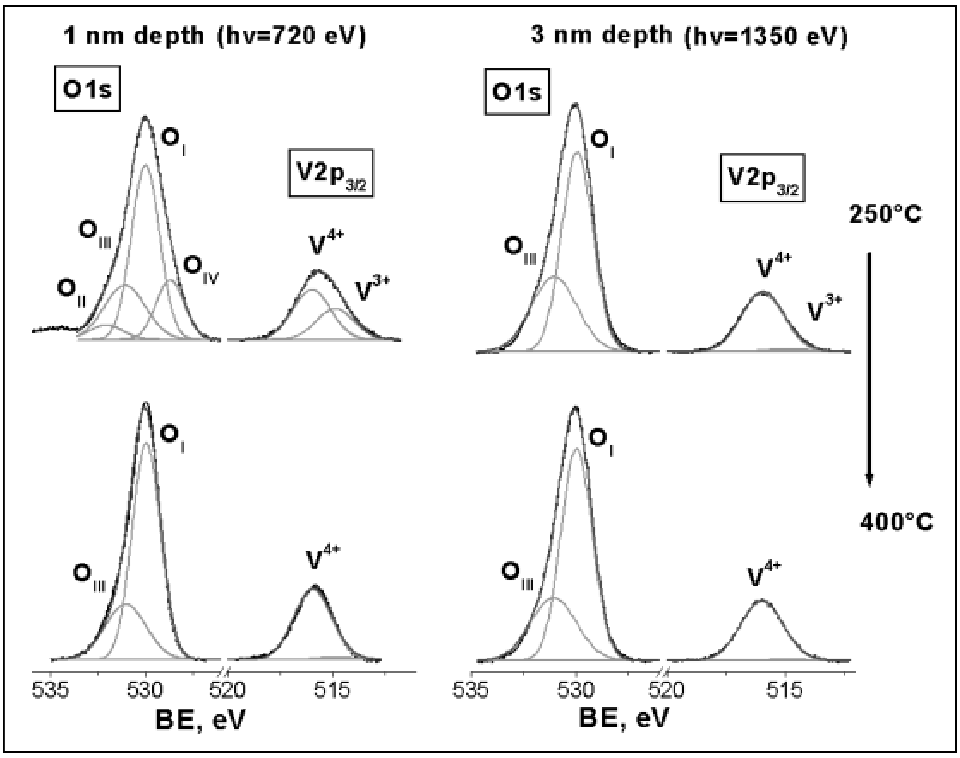

Fig. 1 Changes in O1s and V2p$_{3/2}$ XPS peaks with temperature and depth (Shirley background subtracted, the BE scale calibrated to BE(O_I)=530eV)

It was found that the oxidation state of the catalyst surface was V^{4+} under reaction conditions and a mixture of V^{4+} and V^{3+} for the non-active material at 250°C. The oxidation state of deeper layers did not show significant changes and remained V^{4+} at both temperatures.

References

1. J.-C. Volta, Chemistry, 3 (2000), pp. 717-723
2. ed. D. Briggs, M.P. Seah, Practical surface analysis (second ed.), vol. 1 (Auger and X-ray photoelectron spectroscopy), 1990
3. G.W. Coulston et al., J. of Catal., 163 (1996), 122-129
4. L.M. Cornaglia, E.A. Lombardo, Appl. Catal. A, 127 (1995), 125-138
5. M. Lopez Granados et al., Catal. Today, 40 (1998), 251-261
6. M. Abon et. al., J. of Catal., 156 (1995), 28-36
7. D.A.Verner, D.G.Yakovlev, Astr. Astroph. Suppl. Ser., 109 (1995), p. 125
8. Demeter et. al., Surface Science, 454-456 (2000), 41-44
9. J. Mendialdua et. al., J. Electr. Spectr., 71 (1995), 249-261

Growth of H_2O layers on an ultra-thin Al_2O_3 film: from monomeric species to ice

G. Tzvetkov[a], Y. Zubavichus[b], Th. Schmidt[c], O. Fuchs[c], C. Heske[c], E. Umbach[c], M. Grunze[b], M. G. Ramsey[a], F. P. Netzer[a]

[a]*Institut für Experimentalphysik, Karl-Franzens-Universität Graz, Universitätsplatz 5, A-8010 Graz, Austria*
[b]*Angewandte Physikalische Chemie, Universität Heidelberg, Im Neuenheimer Feld 253, 69120 Heidelberg, Germany*
[c]*Experimentelle Physik II, Universität Würzburg, Am Hubland 97074, Würzburg, Germany*

The molecular-level interaction of water with metal-oxide surfaces has been extensively studied during the last three decades. This adsorption system is of fundamental importance in fields such as heterogeneous catalysis, geochemistry, atmospheric chemistry, electrochemistry and corrosion [1]. Though H_2O/metal-oxide systems have been the focus of many investigations, there is only one oxygen-terminated oxide surface, FeO(111), which has been thoroughly investigated upon H_2O adsorption. Ranke and co-workers [2] have found that on the FeO(111) surface physisorbed H_2O monomers and a hydrogen-bonded bilayer with an ice-like structure exist.

In the present work, the adsorption of water on Al_2O_3/NiAl(110) has been investigated by means of high-resolution photoelectron spectroscopy (PES) and Auger-electron-yield O K-NEXAFS. The motivation was to extend the quite limited knowledge of the interaction of water with oxygen-terminated oxide surfaces. In addition, this study represents new insights into the surface properties of Al_2O_3/NiAl(110) films, which recently became an important substrate for studying model catalytic reactions.

The experiments were performed on the UE52-PGM undulator beamline of BESSY 2 with a SCIENTA SES-200 analyser. The water exposures were carried out by background dosing in the preparation chamber of the UHV system. All the exposures are quoted in Langmuirs (1 L = 1×10^{-6} Torr s).

Complementary TPD measurements of water on the Al_2O_3/NiAl(110) surface (performed in Graz) are shown in Fig. 1 for a series of different water doses at 100 K. The TPD spectra reveal two desorption events: peak α, which we attribute to desorption from clusters and ice multilayers, and peak β, which is due to the desorption of the weakly bound H_2O monomers on the surface. The change of the work function (φ) of Al_2O_3/NiAl(110) as a function of water exposure at 100 K is shown as an insert of Fig. 1. As one can see a rapid drop of the φ (Δφ=-0.7 eV) after adsorption of ~1 L H_2O is observed, followed by an increase of the φ (Δφ = +0.2 eV) above 1 L H_2O dose. On the basis of our UPS measurements in Graz we believe that at low coverages isolated water monomers exist on the Al_2O_3/NiAl(110) surface, which form hydrogen-bonded aggregates at >1 L H_2O dose. A re-orientation of the water dipoles in the aggregates with the oxygen atoms pointing toward the vacuum could explain the increase of the φ. At exposures >6 L the φ remains constant indicating the growth of 3D amorphous ice.

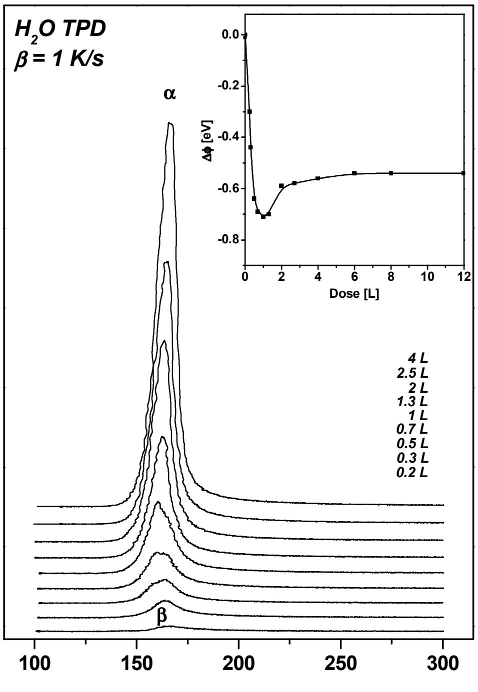

Fig. 1. H_2O TPD spectra from various H_2O exposures adsorbed on Al_2O_3/NiAl (110) at 100 K. The insert shows the change of the work function, Δφ, induced by the adsorbed H_2O.

The O 1s HR-XPS spectra as a function of water exposure at 100 K are presented in Fig. 2. The spectrum of the clean substrate shows an asymmetric peak centered at 531.3 eV. The tail at the high-binding energy side has been observed in previous studies of the Al_2O_3/NiAl (110) system [3] and is most probably due to the O^{2-}-surface species. After 0.3 L water exposure an additional feature appears at 533.7 eV which is due to the presence of molecular water. No evidence for the existence of OH-groups can be derived from the spectra. Up to ~1.5 L H_2O dose there is no shift of the O 1s water component. After 2 L H_2O dose this component is shifted by 0.2 eV to higher binding energy and after 4 L it shifts further by 0.1 eV. The shift of the water O 1s feature towards high binding energy has been ascribed to final-state screening effects [1]. It is worth noting that the first shift to higher B. E. occurs at this exposures where the reorganization of the H_2O species on the surface is indicated by Δφ data. Furthermore, the O1s B.E. of 534.0 eV is characteristic of an amorphous ice-like layer at the surface [4].

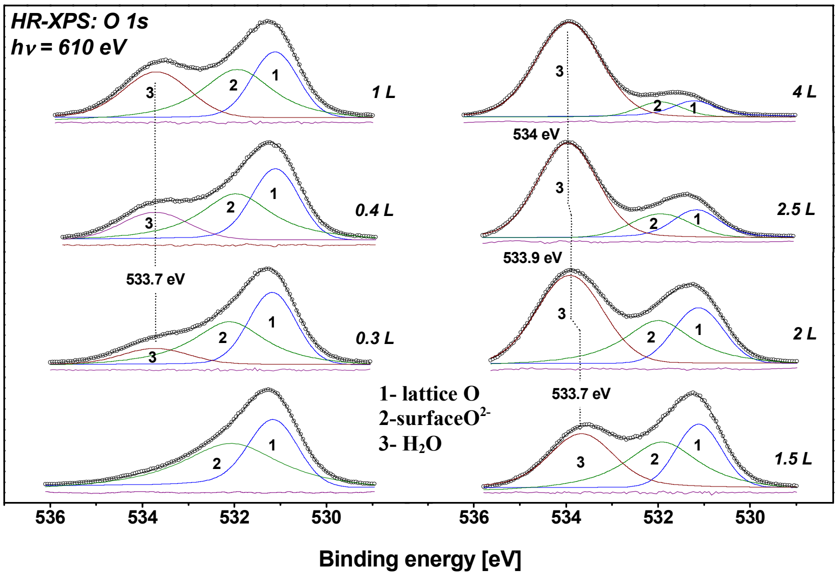

Fig. 3. O1s photoelectron spectra of the clean and water-exposed Al_2O_3/NiAl (110) surface at hv=610 eV. The fitting of the spectra was performed by using Doniach-Sunjic line-shapes convoluted with a major Gausian contribution as model functions for the individual components.

O K-edge NEXAFS spectra were taken for several H_2O-exposed Al_2O_3/NiAl(110) surfaces in order to determine the sensitivity of these spectra to water adsorption on this substrate. The observed changes in the O K-edge structure up to 4 L H_2O dose are small. First, there is a broadening of the spectrum after 4 L H_2O dose around 535 eV. A peak at 535 eV in the spectrum of gas phase water corresponds to an O 1s→4a$_1$ transition [4]. Other small differences are visible in the energy range of 536-543 eV and also the dip in the intensity around 547 eV is less pronounced in the H_2O-exposed spectra. Only after H_2O dose of 23 L the NEXAFS spectrum represents all features typical for ice [5]. Our NEXAFS results show that in contrast to the UPS (not shown) and XPS measurements, which suggest the existence of ice-like aggregates on the surface, NEXAFS spectra cannot give detailed information for the water layers at doses up to 4 L. Since the Auger-electron-yield NEXAFS spectroscopy is more bulk sensitive than the PES, the contribution of the oxide substrate to the O K-edge of low water coverages makes the separation of the features in the spectra difficult.

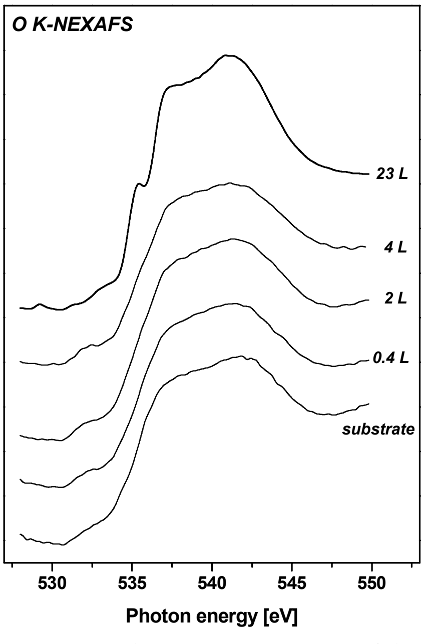

Fig. 3. O K-edge NEXAFS spectra of the clean and water-exposed Al_2O_3/NiAl(110) surfaces taken at glancing incidence and normal emission geometry.

We would like to thank Dr. B. Casu and A. Schöll (Uni Würzburg) for the valuable technical assistance. Furthermore, we are indebted to the BESSY staff for the support, in particular to Dr. W. Braun for his help and many discussions. This work was supported by the Austrian Science Foundation and BMBF (contracts No. 05 KS1VHA and 05 KS1WW1/6).

References

1.M. Henderson, Surf. Sci. Rep. 46 (2002) 1.
2.Y. Joseph, W. Ranke, W. Weiss, J. Phys. Chem. B, 104 (2000) 3224.
3. J. Libuda, M. Frank, A. Sandell, S. Andersson, P.A. Brühwiler, M. Bäumer, N. Martensson, H.-J. Freund, Surf. Sci. 384 (1997) 106.
4. G. R. Right, C. E. Brion, J. Electron Spectrosc. 4 (1974) 25.
5. H. Bluhm, D. F. Ogletree, C. S. Fadley, Z. Hussain, M. Salmeron, J. Phys.: Condens. Matter 14 (2002) L227.

Energy and Polarization Dependence of Coherent Resonant Small Angle Scattering from magnetic domains

M. Lörgen, S. Eisebitt, W. Eberhardt

BESSY GmbH, Albert−Einstein−Str. 15, D−12489 Berlin, Germany

J. Lüning, J. Stöhr

Stanford Synchrotron Radiation Laboratory, Menlo Park, CA 94025, USA

Abstract

We investigated the coherent small angle scattering process of a *Co/Pt* magnetic domain pattern with regard to energy and polarization variation and its influence on the contrast of the resulting speckle pattern. We observed polarization dependent interference of the incoming x−ray wave with the scattered signal. An understanding of this effect is essential for e.g. soft−x−ray holography on magnetic materials, reconstruction of magnetic structures in the spatial domain and photon correlation spectroscopy in the time domain. The energy dependence of the scattering process revealed an influence of the $Co\ L_3$ absorption edge on the speckle contrast.

Introduction

The resonant scattering of x−rays from synchrotron insertion devices has become an important technique during the last years. As a third generation synchrotron, BESSY offers highly brilliant soft−x−rays from its undulator IDs. The high brilliance causes a large coherent photon flux, and it is thus possible to perform coherent resonant scattering experiments.

Coherent scattering patterns show strong intensity variation due to constructive and destructive interference of the coherent waves, known as speckle. As a result, the scattering pattern is sensitive to the individual spatial arrangement of the sample under investigation. Under suitable conditions, the sample real space structure can be reconstructed from static coherent scattering images by exploiting an oversampling phasing method [1]. If the individual arrangement of the sample changes with time the speckle pattern does so, too. This is the basis of photon correlation spectroscopy for investigation of sample dynamics.

For the exploitation of coherent scattering for static or dynamic investigations an understanding of the scattering image formation is helpful. In this report we summarize the influences of energy variation and different polarization states on the scattering image formation process for resonant magnetic scattering.

Experimental Setup

We used a transmission geometry, aligning a spatial coherence filter (a pinhole of $2.5\ \mu m$ in diameter [2]), the sample on a $20 \times 30\ \mu m$ *SiN*−mebrane window and the multichannel detector for spatial resolved single x−ray photon counting. The sample contains 50 layers of 30 Å *Co* and 7 Å *Pt* with a 200 Å *Pt* bufferlayer and a 20 Å *Pt* caplayer [3]. The magnetic anisotropy is perpendicular to the sample plane, resulting in a worm−like domain structure with opposite magnetization directions (Fig. 1). The sample normal and thus the magnetization directions are (anti)parallel to the incident photon beam.

The experiments were performed in a UHV scattering chamber at the PGM and SGM beamlines of the UE56/1 undulator, allowing to change the polarization from linear to left and right circular at each beamline.

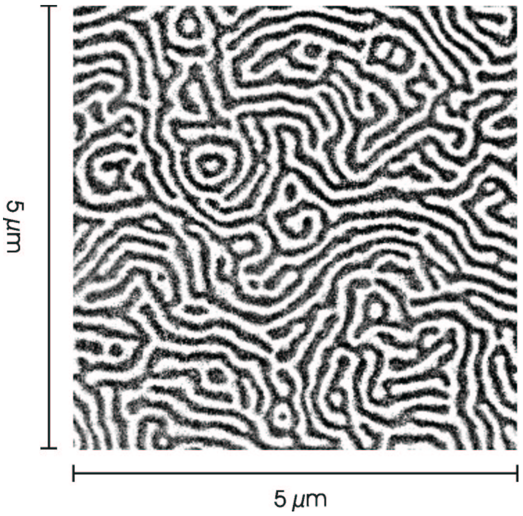

Fig. 1: Magnetic domain structure of Co/Pt multilayers [4]

Results and Discussion

Polarization

Resonant coherent small angle scattering was recorded in the vicinity of the $Co\ L_3$ resonance. In Fig. 2 we present the intensity distributions for resonant scattering with incident radiation of linear and circular polarization. At approximately $q = 30\ \mu m^{-1}$ the magnetic domain structure causes a strong circular speckle pattern. The q−value corresponds well to the magnetic in−plane correlation length of approximately $200\ nm$.

With circular polarization we observe interference of the diffraction pattern from the pinhole (Fraunhofer rings) and the scattering pattern from the magnetic domains. As a result the speckle pattern shows discontinuities of the Fraunhofer rings and weak circular streaks in the magnetic scattering ring. With linear polarized light these features disappear.

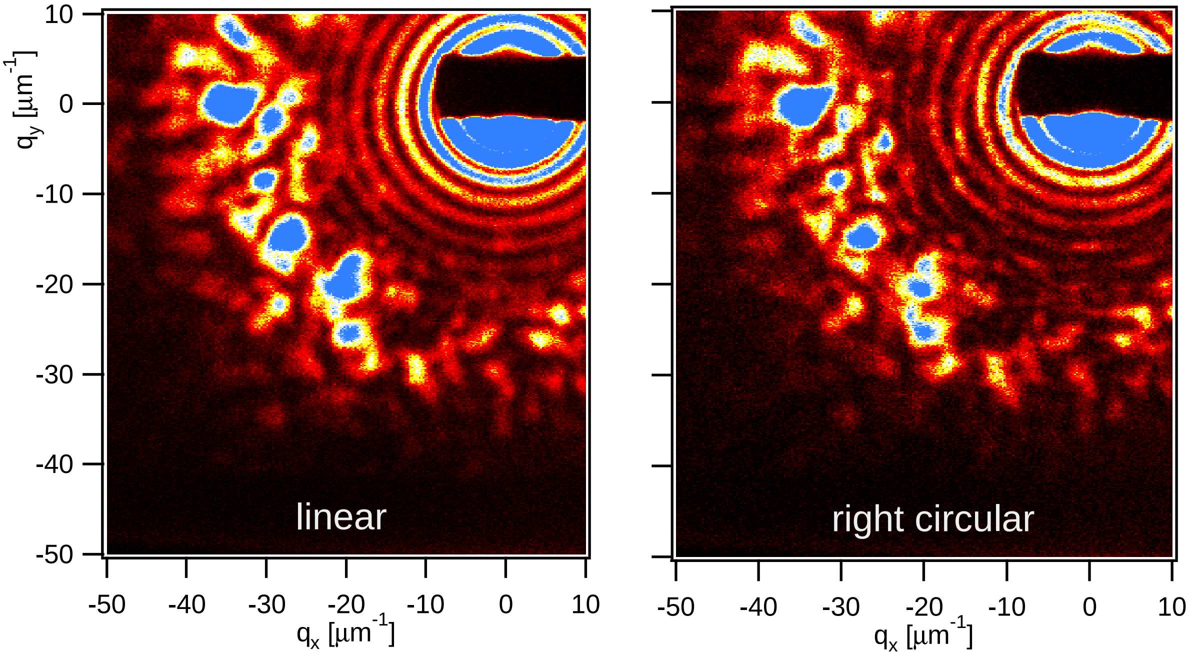

Fig. 2: Speckle pattern of Co/Pt domain structure. Energy: 778 eV. The Fraunhofer diffraction rings of the pinhole are clearly visible in the center. At approx. 30 µm^{-1} appears the magnetic scattering ring with the speckle structure; For circular polarized light the Fraunhofer rings are interrupted due to interference with the magnetic scattering.

This can be understood as follows: The diffraction process at the pinhole does not change the plane of linear polarization. In contrast to that the scattering process at the magnetic domain flips the polarization by $\pi/2$, as the polarization dependence of the relevant resonant scattering cross section is $(\mathbf{e}'\times\mathbf{e})\mathbf{M}$, where $\mathbf{e}$ and $\mathbf{e}'$ are the polarization vectors of the incident and scattered waves, respectively, and $\mathbf{M}$ is the unit vector of the magnetization direction [5,6]. As a consequence, the diffracted wave from the pinhole and the magnetically scattered wave from the sample cannot interfere at the detector. In case of circular polarized light neither the pinhole nor the magnetic domains change the state of polarization. Thus, the diffracted and the scattered waves can interfere. The existence of this interference is crucial for holographic experiments where the reference wave is typically generated by a diffracting object such as a pinhole.

Interference between charge and magnetic scattering from an antiferromagnetic sample has been observed in the past [7]. Due to the transmission geometry and the small layer roughness we observed no charge scattering in the present experiment (up to $q_{max}=80\ \mu m^{-1}$).

Contrast

We recorded the scattering pattern a function of energy of the incident soft x−rays. With fixed polarization the photon energy was tuned from $760\ eV$ to $783\ eV$, i.e. across the $Co\ L_3$ edge (Fig. 3). The total detected magnetic scattering intensity at $q=30\ \mu m^{-1}$ rises at the resonance and then decreases strongly at the onset of the L_3 absorption. This behaviour can be simulated quantatively using known optical constants for Co [8]. In spite of the fast changes in the optical constants at the resonance, the location of the individual speckle in the pattern is independent of the incident energy apart from the trivial variation due to the wavelength change, which can be neglected over the narrow energy interval of interest.

In Fig. 3 we show the contrast in the coherent speckle pattern as function of energy for linear polarized light (blue line) and right circular polarized radiation (black line). In a region of interest containing several speckle, the contrast is calculated by the standard deviation of intensities divided by the mean intensity [9].

Contrary to the total magnetic scattering intensity the contrast still increases above the $Co\ L_3$ absorption edge. The overall contrast for circular polarized light is slightly higher than in the linear case. As described above, with linear polarization the diffracted source wave and the magnetically scattered wave do not interfere, resulting in a reduced contrast.

A contrast variation is not predicted by standard speckle theory [9,10]. A speckle contrast decrease at

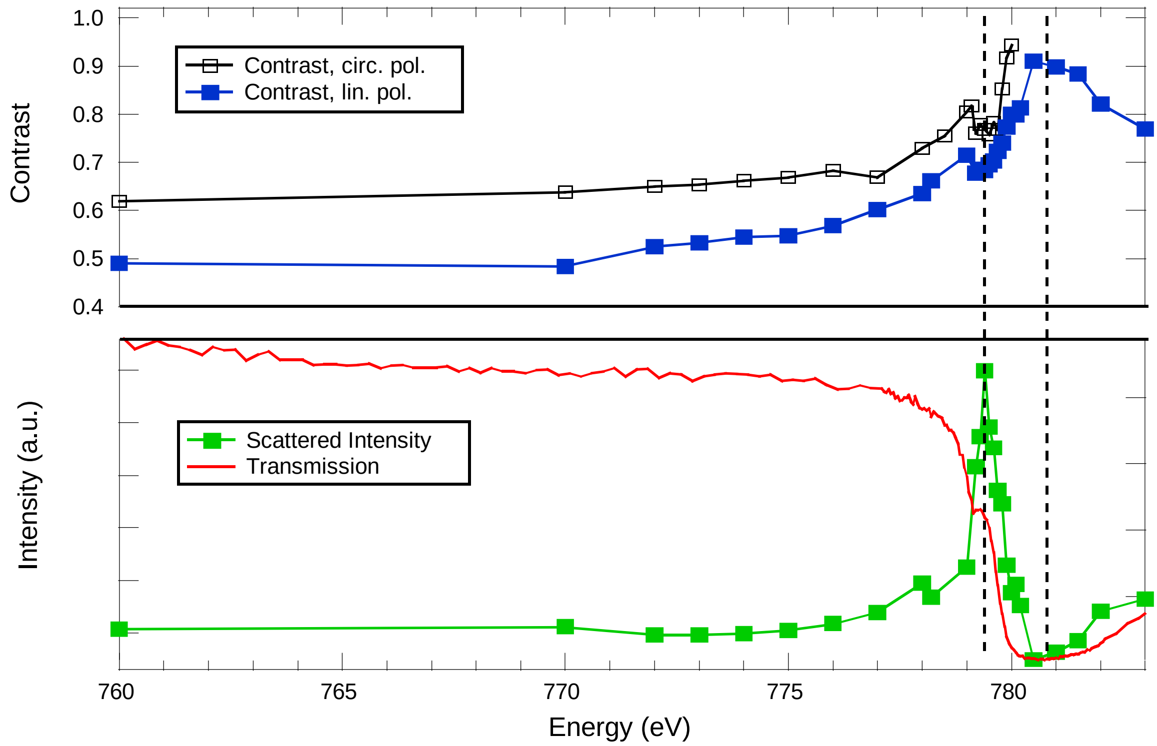

Fig. 3: Contrast and intensity variied by energy of linear polarized photons. The two vertical lines show the maximum of the scattered intensity and the minimum of the transmitted intensity, i.e. the maximum of absorption.

absorption edges has been observed for hard x−ray charge scattering in the past [11]. We are currently trying to model the magnetic speckle contrast variation taking the optical constants, source−magnetic interference effects and the overall signal to noise ratio into account.

Dynamics

With the current setup we recorded a q−space movie of domain motion with $30\ s$ time resolution. The time resolution is limited by the scattering intensity, which is in turn limited by the coherent photon flux through our spatial coherence filter. With suitable focussing on the pinhole (e.g. by a zone plate) it should be possible to increase the coherent flux accepted in our experiment by a factor of 10^4.

Acknowledgements

We thank E. E. Fullerton for the worm domain sample preparation, C. Rettner for the production of perfect pinholes and G. Denbeaux for the x−ray microscopy of the sample.

References

[1] J. W. Miao et al., NATURE, Vol. 400 No. 6742, p. 342, 1999

[2] Pinhole produced by C. Rettner, IBM Almaden Research Center, San Jose, CA 95120, USA

[3] Samples prepared by E. E. Fullerton et al.,IBM Almaden Research Center, San Jose, CA 95120, USA

[4] X−Ray Microscope image, G. Denbeaux, Advanced Light Source, Berkeley, CA 94720, USA

[5] J. P. Hannon et al., Physical Review Letters, Vol. 61 No. 10, 1988

[6] J. B. Kortright et al., Physical Review B, Vol. 64, 2001

[7] A. Rahmim et al., Physical Review B, Vol. 65, 2002

[8] J. B. Kortright, private communication

[9] J. W. Goodman, *Laser speckle and related phenomena*, ed. J. C. Dainty, Springer, 1984

[10] D. L. Abernathy et al., J. of Synchrotron Radiation, Vol. 5, p. 37−47, 1998

[11] C. C. Retsch et al., Physical Review Letters, Vol. 87, No. 7, 2001

Application of Regularization Method to the overlapping L-spectra of 3d metals

Yu. Babanov [1,2], S. Kiryanov [1], A. Sidorenko[1], L. Romashev[1], D. Vyalikh[3,4], S. Molodtsov[3,5,6], G. Guentherodt[7], U. Ruediger[7], Yu. Dedkov[7], M. Fonine[7]

[1] *Institute of MetalPhysics, RAN, 620219 Ekaterinburg,*
[2] *Udmurt State University, Izhevsk, Russia*
[3] *Russian--German Laboratory at BESSY II, 12489 Berlin-Adleshof, Germany*
[4] *Institut für Experimentalphysik, Freie Universität Berlin, 14195 Berlin, Germany*
[5] *Institut für Oberflächen- und Mikrostrukturphysik, Technische Universität Dresden, 01062 Dresden, Germany*
[6] *V.A. Fock Institute of Physics, St. Petersburg State University, St. Petersburg, 198504 Russia*
[7]*Physikalisches Institut RWTH Aachen D-52056, Germany*

Introduction

We propose a new method of obtaining the local structure information from the overlapping *L* EXAFS spectra for 3d matals using the Tikhonov's method of solving ill-posed problem [1]. In contrast of the conventional methods (Fourier transformation and fitting procedures) this method does not demand any assumption about model. Up to now this method was applyed to *K* EXAFS spectra [2, 3, 4]. Recently a special procedure of deconvolution L_2-, L_3- contributions [5] was used for obtaining local structure information.

Mathematical algorithm

For one component system the atomic distribution is described by the pair correlation function (PCF) $g(r)$ which may be written as

$$g(r) = \frac{1}{4\pi\rho_0}\sum_l \frac{N_l}{r_l^2\sigma_l\sqrt{2\pi}}\exp\left(-\frac{(r-r_l)^2}{2\sigma_l^{\,2}}\right). \qquad (1)$$

Here ρ_0 is an atomic density, N_l – a coordination number for *l* shell, r_l – a position of l^{th} shell, σ_l – a factor Debye–Waller for *l* shell. The normalized oscillating part of EXAFS signal $\chi(k)$ for the *K* – spectrum is described as

$$\chi(k) = 4\pi\rho_0 R(k)\int_0^\infty g(r)\times\frac{f(k,r)}{k}\times\exp\left(\frac{-2r}{\lambda(k)}\right)\times\sin\left(2kr+2\delta(k)+\varphi(k,r)\right). \qquad (2)$$

Here $R(k)$ – a reduction factor, $f(k,r)$– a backscattering amplitude module, $\lambda(k)$– a mean free path of photoelectron, $\delta(k)$– a central atom phase shift, $\varphi(k,r)$– a backscattering phase. All values are calculated by the program FEFF8 [6].

Using the dispersion laws for L_3, L_2, L_1 edges one may conclude – *L* edges have the same *E* space but different *k* spaces (namely k_1, k_2, k_3). It is very simple to find the laws for connection of k_1, k_2, k_3 spaces:

$$k_2 = f(k_3) = \sqrt{k_3^2 - \tfrac{E_2-E_3}{a}} \qquad\qquad k_1 = g(k_3) = \sqrt{k_3^2 - \tfrac{E_1-E_3}{a}}\,, \qquad (3)$$

where E_3, E_2, E_1 are energies of L_3, L_2, L_1 edges, $a = (\hbar^2k^2/(2m)) = 3.81$. Now the equation for sum of L_1, L_2, L_3 EXAFS spectra in unified k_3 space may be written as

$$\chi_{sum}(k_3) = W_{L3}\,\chi_{L3}(k_3) + W_{L2}\,\chi_{L2}(k_2 = f(k_3)) + W_{L1}\,\chi_{L1}(k_1 = g(k_3)), \tag{4}$$

where W_{L3}, W_{L2}, W_{L1} – weight coefficients used to account the contribution of each edge.

For L spectra the radial matrix elements are given by M_{01} for $l = 1 \rightarrow l = 0$ transitions and M_{21} for $l = 1 \rightarrow l = 2$ transitions. As shown in [7] for elements with $Z \geq 20$ M_{21} and M_{01} fulfil the relation:

$$\frac{\frac{1}{2}\left|\mathrm{M}_{01}\right|^2}{\left|\mathrm{M}_{21}\right|^2} \approx \frac{1}{50}, \tag{5}$$

i.e. the ratio is nearly independent of k, and the $p \rightarrow s$ contributions are practically unobservable, as $p \rightarrow d$ transitions are favored by a factor of 50. This means that all M_{01} contributions in integral equation can be neglected and hence the L spectra can be analyzed in the same way as is done for the K edges. As it was shown in FEFF calculation.

The integral equation for overlapping L spectra has a form:

$$\chi(k_3) = 4\pi\rho_0 \int_0^\infty dr\, g(r) \left\{ \begin{array}{l} W_{L1}\dfrac{f_1(k_1,r)}{k_1} \times \exp\left[\dfrac{-2r}{\lambda_1(k_1)}\right] \times \sin\left(2k_1 r + 2\delta_1(k_1) + \varphi_1(k_1,r)\right) \\ + W_{L2}\dfrac{f_2(k_2,r)}{k_2} \times \exp\left[\dfrac{-2r}{\lambda_2(k_2)}\right] \times \sin\left(2k_2 r + 2\delta_2(k_2) + \varphi_2(k_2,r)\right) \\ + W_{L3}\dfrac{f_3(k_3,r)}{k_3} \times \exp\left[\dfrac{-2r}{\lambda_3(k_3)}\right] \times \sin\left(2k_3 r + 2\delta_3(k_3) + \varphi_3(k_3,r)\right) \end{array} \right\} \tag{6}$$

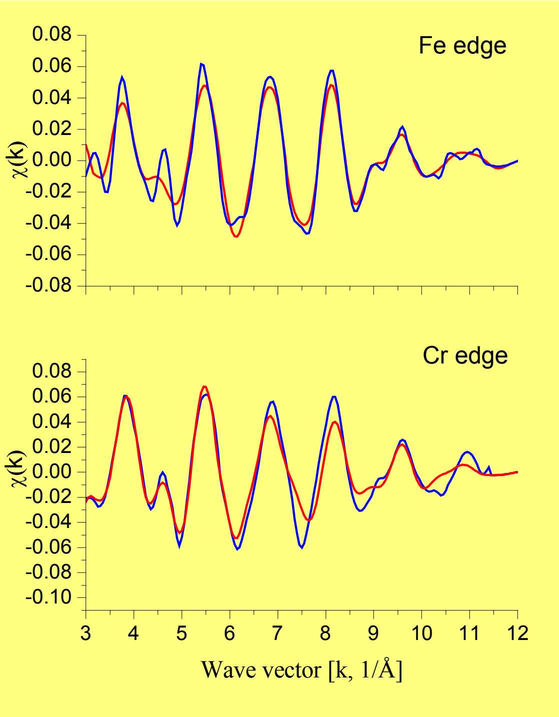

Fig. 1. Experimental (blue) and model (red) $\chi(k)$ functions.

Details of solution the EXAFS ill-posed problem may be found in [1–4]. For multicomponent system the theory is easy generalized. We apply this approach not only for overlapping L spectra but also for the overlapping K-L spectra (for example, in the oxides Fe_3O_4, Cr_2O_3).

Experimental

The samples used are policrystalline Fe and Cr films. Fe film of thickness ~ 300 Å was evaporated under UHV conditions onto W(110) substrate in the chamber for the sample preparation *in situ*. Cr film ot thickness ~ 300-400 Å was evaporated under UHV conditions onto MgO(100) substrate at the Institute of Metal Physics RAS. The measurements of Total Electron Yield were carried out at room temperature using facility of the RGBL beamline of BESSY II.

Fig. 1 shows the experimental $\chi(k)$ functions for Fe and Cr films in comparison with the model functions calculated by FEFF8 [6]. Applying the method described above, one can find the solutions that are shown on Fig. 2. We compare our results with model PCF functions calculated on the basis of the well known crystallographic data.

The following main characteristics of the peaks for the function $g(r)$ have been selected: interatomic distance r, the nearest neighbors coordination number N and Debye-Waller (DW) factor σ^2. We estimated these values according to the Gauss functions describing the peaks of the solution and presented in Table 1.

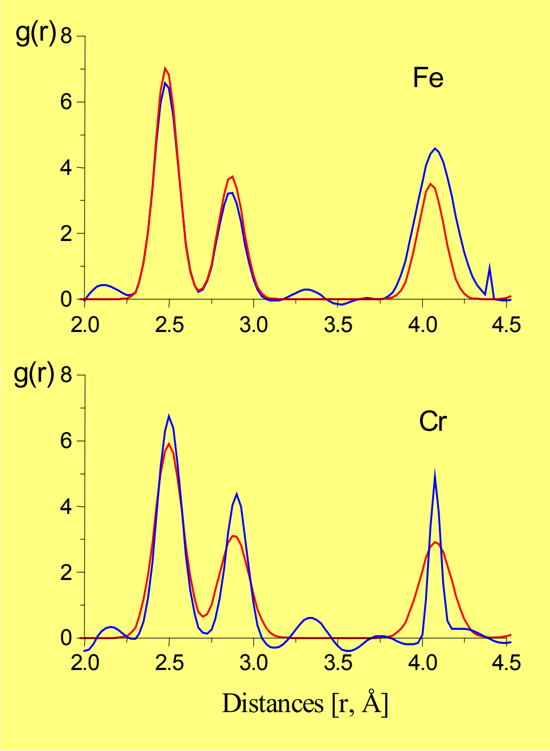

Fig. 2. Model PCF (red) and obtained (blue) solution.

Table 1. Comparison of the model and obtained results.

Fe film			
Number of coordination shell		1st	2nd
Model	r, Å	2.483	2.867
	N, at.	8.00	6.00
	σ^2	$0.472\cdot10^{-2}$	$0.534\cdot10^{-2}$
Experiment	r, Å	2.482	2.865
	N, at.	7.87	5.38
	σ^2	$0.524\cdot10^{-2}$	$0.567\cdot10^{-2}$
Cr film			
Number of coordination shell		1st	2nd
Model	r, Å	2.499	2.885
	N, at.	8.00	6.00
	σ^2	$0.681\cdot10^{-2}$	$0.771\cdot10^{-2}$
Experiment	r, Å	2.501	2.899
	N, at.	7.85	5.90
	σ^2	$0.501\cdot10^{-2}$	$0.376\cdot10^{-2}$

Discussion

It is necessary to note that during the solution the inverse problem (6) we do not account the contribution of photoelectron multiple scattering on the nearest neighbors. Another feature: we have a very high resolution in real space r with comparing Fourier transformation. On the curve of Fourier transformation it is impossible to distinguish the first and the second shells for BCC lattice. The main characteristics of the first and the second shells for crystalline Fe and Cr correspond to the table values.

References

[1] A.N.Tikhonov, V.Ya.Arsenin, Solution of Ill-Posed Problems, John Willey and Sons, Inc., New York, (1981)
[2] Yu.A. Babanov, V.V. Vasin, Phys. Stat. Sol. B 105, 747 (1981)
[3] N.V. Ershov, A.L. Ageev, V.V. Vasin, Yu.A. Babanov, Phys. Stat. Sol. B 108, 103 (1981)
[4] Yu.A. Babanov, N.V. Ershov,V.R. Shvetsov, A.V.Serikov, A.L. Ageev, V.V. Vasin, J. Non-Cryst. Sol. 79, 1 (1986)
[5] H. Wende, J.W. Freeland, V. Chakarian Y.U. Idzerda, L. Lemke, K. Babershke, J. Applied Phys. 83, 7028 (1998)
[6] Ankudinov A.,Ravel B., Rehr J.J., Conradson S. (1998), *Phys. Rev.* B58, 7565.
[7] B.K.Teo, EXAFS: Basic Principles and Data Analysis, Springer-Verlag, Berlin (1986)

X-ray standing wave studies of liquid crystal monolayer at the beamline KMC-2

S.I.Zheludeva[1*], N.N.Novikova[1], V.V.Lider[1], N.D.Stepina[1], N.N.Salaschenko[2], W.Haase[3], A.I.Erko[4], M.Fieber- Erdmann[4]

[1]*A.V.Shubnikov Institute of Crystallography RAS, Leninsky prosp. 59, 117333 Moscow, Russia.*
[2]*Institute of Physics of Microstructures Russian Academy of Sciences,GSP-105, 603600 Nizhny Novgorod, Russia.*
[3]*Institute of Physical Chemistry, Darmstadt University of Technology, Petersenstrasse 20, D-Darmstadt 64287, Germany.*
[4]*Berliner Electronenspeicherring-Gesellschaft fur Synchrotronstrahlung, Albert- Einstein- Strasse 15, 12489 Berlin, Germany.*
[*]*e-mail: zheludeva@ns.crys.ras.ru*

The X-ray standing wave (XRSW) technique is based on simultaneous measurements of angular dependencies of X-ray reflection and fluorescence yield excited by the primary X-ray beam as the incident angle is scanned through the Bragg diffraction peak or the total external reflection region. This high-resolution nondestructive X-ray method combines the advantages of precision X-ray diffraction experiments with spectroscopic selectivity.

Herein we present XRSW studies of monolayers of liquid crystal deposited on solid substrates by Langmuir-Blodgett technique performed at the beamline KMC-2.

Experimental details

In XRSW experiments the fluorescent spectrum is recorded at each point of the reflectivity curve (in contrast to X-ray fluorescence analysis, where the angle of the incident beam is held constant). The integrated intensity under each specific peak from individual elements is plotted as a function of the incident X-ray beam angle and the positional information is obtained from the analysis of angular dependencies of the fluorescence intensity.

To use KMC-2 beamline for XRSW experiments the angular divergence of the monochromatic beam has to be reduced to values less than the Bragg reflection width (a few tens of arc sec for the studied multilayers). Such a reduction was performed by cutting off peripheral regions of the convergent focused beam in the scattering (horizontal) plane. At the same time this reduction should not be too drastic as the beam intensity has to be high enough to excite a reasonable amount of secondary radiation yield from the studied ultra-thin films. The preliminary X-ray diffraction measurements on a Si (111) crystal allow to estimate the beam divergence to be 14 arc sec at horizontal slit setting of 100 μm. Finally, the slit widths of 100 μm (horizontal) and 620μm (vertical) were found to provide the optimum conditions for our measurements.

All the measurements were carried out at an X-ray beam energy of 13 500 eV. The reflected X-ray beam was detected by a scintillation detector. The fluorescence signal was measured by the ROENTEC X-Flash detector.

Results and discussion

We studied monolayer of mesogenic compound (dysprosium complexes of the Schiff base ligand) deposited on solid substrates by Langmuir-Blodgett technique. Metal-containing liquid crystals (metallomesogens) represent an important class of mesomorphic materials that combine the interesting magnetic properties with the advantages of the supramolecular organization in the mesophases. The samples under investigation were monolayers of $DyL_3\{CHF_2(CF_2)_5CH_2SO_4\}_3$ deposited on periodic multilayers consisting of 250 W/B_4C layers pairs (multilayer period *d=12,25 Å*). The multilayers were prepared using magnetron sputtering at the Institute of Physics of

Microstructures Russian Academy of Sciences (Nizhny Novgorod). The Dy^{III} compound was synthesised at the Kazan Physical-Technical Institute, Russian Academy of Sciences (Kazan).

The great potential of the XRSW technique for determining the position of atoms in ultra-thin surface layers have been demonstrated elsewhere. The general approach is as follows. X-ray standing wave is formed as a result of interference between the incident and reflected beams during Bragg diffraction from the periodic substrate. The period of the standing wave is equal to the d-spacing of the substrate. The position of XRSW antinodes with respect to the substrate surface depends on the incident angle: as the incident angle θ is scanned through the Bragg reflection the standing wave antinodes shift inward by one half of a d-spacing of the periodic substrate. Since the photoelectric effect is proportional to the local electric field intensity such dramatic changes of the XRSW field result in the large modulations on the angular dependence of fluorescence yield. This modulations are clearly seen in fig.1 where the angular dependence of Dy L_α fluorescence yields in the Bragg diffraction region is presented. Referring to fig.1, if the antinodes of XRSW coincide with the atom layer (on the low angle side of the Bragg peak) the fluorescence yield will be a maximum. For higher angles the nodes of XRSW (the minimum of electric field intensity) coincide with atomic layer and therefore at this angle the fluorescence yield should be minimum. The shape of fluorescence curve is strongly dependent on the mean position of the investigated atoms (the coherent position) and the distribution about this position (the coherent fraction).

It is evident that the main characteristics of XRSW generated by the multilayer: the amplitude and the position of the XRSW antinodes, are determined by multilayer parameters. Therefore the shape of angular dependencies of the fluorescence yield emitted from the organic film is determined not only by the mean position of the investigated atoms but depends strongly on the multilayer parameters and correct interpretation of XRSW data for deposited film requires preliminary information about the multilayer itself. In contrast to perfect single-crystals, the structural parameters of multilayer systems (atomic density and thickness of the component layers, the height of interfacial roughness) are not accurately known, for this reason the ambiguity in determining the atom position is the typical problem if the multilayer structures are used as a XRSW generator.Analytical calculations (to be published elsewhere) predict that at kinematical diffraction the phase of XRSW, i.e. the position of the XRSW antinodes, depends only on the thickness ratio of layers comprising the period of multilayer, while the XRSW amplitude is determined by peak reflectivity. Furthermore it was shown that under kinematical diffraction the thickness of component layers can be unambiguously determined from complimentary analysis of reflectivity curve and angular dependence of fluorescence yield from the multiplayer.

The above analytical results have been used for analysis of our experimental data. In order to obtain information about the multilayer substrate the analysis of the angular dependence of W L_α fluorescence (fig.2) excited from the W/B_4C was carried out. The fluorescence yield from the multilayer substrate has been measured simultaneously with the fluorescence yield from the monolayer becuase the full fluorescent spectrum was recorded at each angle of incidence. The shape of W fluorescence curve is typical for XRSW measurements at kinematical diffraction from thin multilayer where the extinction does not mask the effect of the XRSW movement with respect to the layers comprising multilayer structure and from the other hand the total thickness of W layers is less then the absorption length of W L_α fluorescence. In such a case the well-defined modulations are clearly visible. The thickness of the component layers has been determined by the fitting the theoretical x-ray reflectivity and W-fluorescence curve to the experimental data.

The theoretical Dy fluorescence curve was fitted by varying the mean position and a width of the Dy layer while holding the multilayer parameters fixed. Based on the best fit the Dy layer is at the mean position of *22Å* and has a width of *3Å*. The lengths of the Schiff's base complex was calculated by molecular modelling to be *47Å*, metal ion is positioned in the centre of the complex. The measured Dy layer position of *22Å* is shorter than the expected value *23,5Å* for fully extended molecule. This difference could be attributed to the conformational changes in the molecules of a mesogenic compound or/and a slight tilting of the alkyl chains relative to the substrate surface.

The presented experimental results demonstrate that such a precision X-ray diffraction method as the X-ray standing wave technique can be successfully performed at the KMC-2 beamline.

We would like to emphasize that the X-ray standing wave experiments were carried out at BESSY II for the first time and the contribution of KMC-2 staff to their success is invaluable and is greatly appreciated.

This work was supported by the Russian-German Laboratory, by Russian Foundation of Basic Research (grant № 01-02-16730) and by BMBF/DLR (grants RUS OO/202 and RUS OO/203), DFG (grant 436 RUS/113/401/0-3).

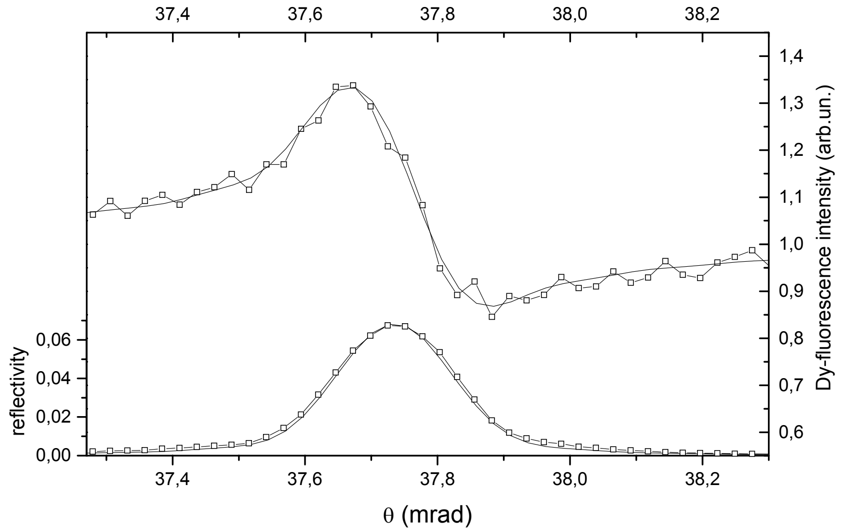

Figure 1
The experimental angular dependence of Dy L_{α} fluorescence from metallomesogenic monolayer deposited on the W/B_4C multilayer. Solid line – the best fit Solid line – the best fit corresponds to $D_{Dy}=22$ *Å*. Bottom curve – Bragg reflectivity. The incident X-ray energy was E=13,5 keV.

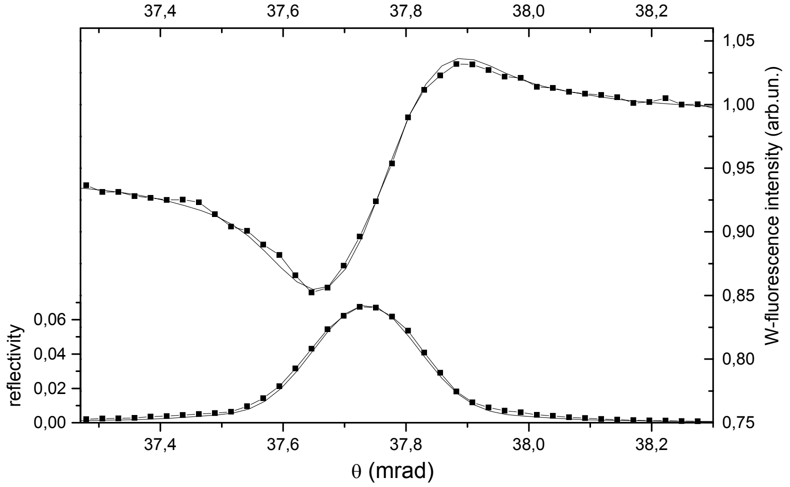

Figure 2
The experimental angular dependence of W L_{α} fluorescence from W/B_4C multilayer. Solid line – the best fit corresponds to $d_W=7,5$ *Å*. Bottom curve – Bragg reflectivity. The incident X-ray energy was E=13,5 keV.

Fe *K* and Pb L_3 edge NEXAFS characterization of glasses containing industrial wastes.

F. Pinakidou, M. Katsikini, E. C. Paloura*, P. Kavouras, Ph. Komninou, Th. Karakostas
Aristotle Univ. of Thessaloniki, Dept. of Physics, GR54124 Thessaloniki, Greece
A. Erko
BESSY GmbH, Albert Einstein Str. 15, 12489 Berlin, Germany.

The solidification and stabilization of toxic industrial waste (lead oxide-contaminated ash), is a process that allows for its safe disposal. The toxic ash (that mainly consists of Fe_2O_3 and $PbO{\cdot}PbBr_2$) is co-melted with SiO_2 and Na_2O at high temperatures (1300-1400°C) and it is then cooled down in air to form an opaque glass. The main advantage of this vitrification process is that it produces a chemically stable vitreous material, which can homogeneously incorporate into its matrix numerous toxic elements (such as heavy metals), and can be freely disposed or used as construction material[1].

The under study samples are the vitrified products of lead-rich ashes, produced by incineration of sludges that contain large quantities of toxic organic compounds. The incineration process involves co-melting of lead contaminated ash with the appropriate quantities of vitrifying and flux agents (SiO_2 and Na_2O, respectively) at high temperatures (1400°C), followed by quenching in order to form vitrified materials. The under study as-grown sample consists of 60% ash, 25% SiO_2 and 15% Na_2O. The sample was studied in the as-grown state as well as after isochronal annealing, for 2 hrs, at 440, 600 and 800 °C [1]. Additionally, two crystalline (powder) iron oxides, hematite α-Fe_2O_3 and magnetite Fe_3O_4, a crystalline lead oxide (PbO) and a Fe foil-sample were also studied as reference samples.

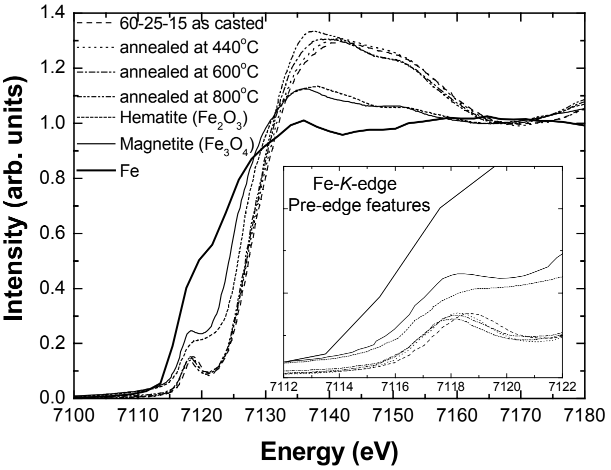

Figure 1: *Fe-K NEXAFS spectra of the under study samples*

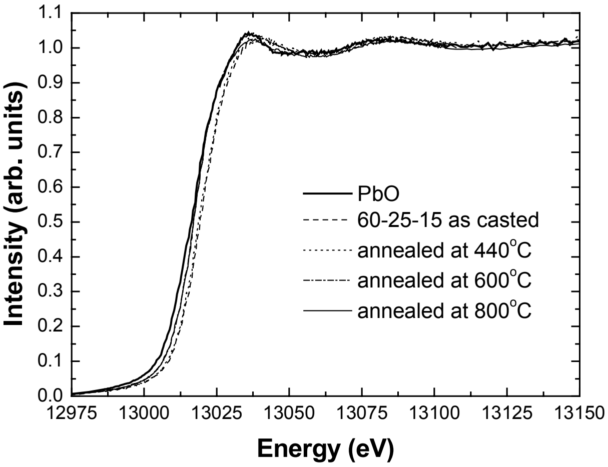

Figure 2: *Pb-L_3 NEXAFS spectra of the under study samples*

The NEXAFS measurements were conducted at room temperature, using the KMC2 double-crystal monochromator at BESSY-II, at the Fe-*K*-edge (7035-7100eV) and the Pb-L_3-edge (12775-12890eV), using a fluorescence yield detector (Si-PIN photodiode), at an angle of incidence θ=45°. The characteristics of the NEXAFS spectra were determined via fitting using a sigmoidal (Boltzman function), to simulate transitions to the continuum[2], and Lorentzians to fit the pre-edge peaks. Prior to fitting, the spectra were normalized for the transmission function of the monochromator and were subjected to background subtraction and normalization to the atomic limit. In octahedrally coordinated hematite, two peaks are observed in the pre-edge region

---

[*] *e-mail: paloura@auth.gr*

of the Fe-*K* NEXAFS spectrum, in agreement with theoretical predictions[3]. These pre-edge peaks (observed at about 7118 and 7120eV, respectively) are related to quadripolar electronic transitions to the t_{2g} levels[4]. The NEXAFS spectra measured at the Fe-*K*-edge and Pb-L_3-edge of the under study sample and reference compounds are shown in Figures 1 and 2 respectively.

The results of the fitting of the NEXAFS spectra are listed in Table I. As shown in the Table, the intensity and the total area under the pre-edge peaks decrease with increasing annealing temperature. It has been reported that the intensity of the pre-edge peak is inversely proportional to the coordination number of the absorbing atom[5]. Furthermore, the pre-edge intensity is greater in non-centrosymmetric complexes (such as magnetite) due to the large electric allowed dipole component from 3d-4p mixing, while in centrosymmetric complexes (such as hematite) the 1s→3d transition has an electric quadripole nature. Therefore, the observed decrease in the intensity of the pre-edge peaks in the annealed samples indicates that, upon annealing, the local environment around the Fe ion is becoming more ordered, i.e. the Fe atom tends to occupy octahedral sites into the matrix. It has also been reported that in a mixed valence sample the position of the pre-edge peaks is a measure of the portion of various oxidation states of Fe, i.e. the $Fe^{+3}/\Sigma Fe$ ratio, and depends on the bonding environment of the Fe atom[6]. Therefore, the red shift of the pre-edge peak, as the annealing temperature increases, indicates the decrease of the $Fe^{+3}/\Sigma Fe$ ratio.

Table I: *Characteristics of the NEXAFS spectra at the Fe-K-and Pb-L_3-edge*

Sample name	**Fe-*K*-edge**			**Pb-L_3-edge**
	Abs. Edge (eV)	**Pre-edge Position (eV)**	**Pre-edge Intensity (a.u.)**	**Abs. Edge (eV)**
PbO	-	-	-	13015.95±0.058
Fe	7121.64±0.32	7118.42±0.32	0.282±0.005	-
Hematite (α-Fe_2O_3)	7126.15±0.02	7118.07±0.06	0.075±0.001	-
		7120.72±0.15	0.168±0.001	-
Magnetite (Fe_3O_4)	7124.55±0.01	7118.33±0.03	0.200±0.002	-
60-25-15 as casted	7127.48±0.01	7118.70±0.02	0.141±0.002	13019.66±0.034
Annealed at 440°	7127.22±0.01	7118.33±0.03	0.141±0.002	13018.66±0.040
Annealed at 600°	7127.09±0.01	7118.29±0.03	0.145±0.002	13016.69±0.041
Annealed at 800°	7126.95±0.01	7118.14±0.03	0.133±0.002	13016.75±0.051

The energy position of the absorption edge at the Fe-*K*-edge, in all the under study samples, appears at energies higher than in hematite. However, as the annealing temperature increases, the absorption edge gradually approaches the value corresponding to hematite. The fact that the absorption edge appears at energies higher than expected is attributed to structural differences (distortion) in the Fe-O polyhedrons. This argument is supported by the decrease in the intensity of the pre-edge peaks. On the other hand at the Pb-L_3-edge, the energy position of the absorption edge is shifted towards lower energies with increasing annealing temperature and approaches the respective value in the reference PbO sample, i.e. the annealing process promotes the formation of the PbO phase into the glass matrix.

Acknowledgements: *F. Pinakidou acknowledges financial support from the Greek State's Scholarship Foundation.*

References

[1] *P. Kavouras et al., Waste Manag. (in print).*
[2] *J. Stöhr, NEXAFS Spectroscopy, Springer - Verlag, Berlin 1992, p. 114.*
[3] *Tami E Westre at al., J Am. Chem. Soc., 119, 6297- 6314 (1997).*
[4] *G. Drager, R. Frahm, G. Materlik and O. Bruhammer, Physics Status Solidi B, 146, 287-293 (1988).*
[5] *C. R. Randll et al, 34, 1036 (1995).*
[6] *S. Bajt, S. R. Ruton and J. S. Delabey, Geochimica et Cosmochimica Acta, 58, 23, 5209-5217 (1994).*

Identification of implantation-induced defects in GaN: A NEXAFS study.

M. Katsikini (a), F. Pinakidou (a), E. C. Paloura (a), W. Wesch(b).
(a) Aristotle Univ. of Thessaloniki, Dept. of Physics, GR54006 Thessaloniki, Greece
(b) Institüt fur Festkörperphysik, Friedrich-Schiller Univ. Jena, Max-Wien-Platz 1, D-07743, Germany.

GaN is a direct wide band-gap semiconductor, which finds applications in opto- and micro-electronics. Doping via ion implantation is used extensively because it permits precise control of the dopant profile. However, recovery of the implantation induced defects and activation of the dopants require annealing. Here we apply NEXAFS spectroscopy in order to study the effect of O, Si and Mg implantation on the density of empty states of GaN.

The GaN sample was grown by ECR-MBE, at 700^{o}C, on a (0001) Al_2O_3 substrate.[1] The as-grown GaN sample was diced and subjected to ion implantation using $^{16}O^+$, $^{28}Si^+$ (n-type dopants) and $^{24}Mg^+$ (p-type dopant) with fluencies and energies listed in Table I. The N*K* - NEXAFS spectra were recorded at the VLS-PGM beamline using a high purity Ge detector. The information depth of the fluorescence photons was 40nm, i.e. we probe only the implanted region of the sample, which extends about 200nm below the sample surface.

The NEXAFS spectra of the under study samples, after normalization to the primary beam current, linear background subtraction and normalization to the atomic limit, are shown in Fig. 1. The spectrum of the as-grown sample, which is shown at the bottom of Fig. 1, is characterized by a number of resonances, which correspond to maxima of the N p partial density of states in the conduction band. As the implantation dose increases those peaks become broader due to the increase of the static disorder. In addition to the broadening of the NEXAFS resonances, implantation generates two new resonance lines, hereafter denoted as RL1 and RL2.

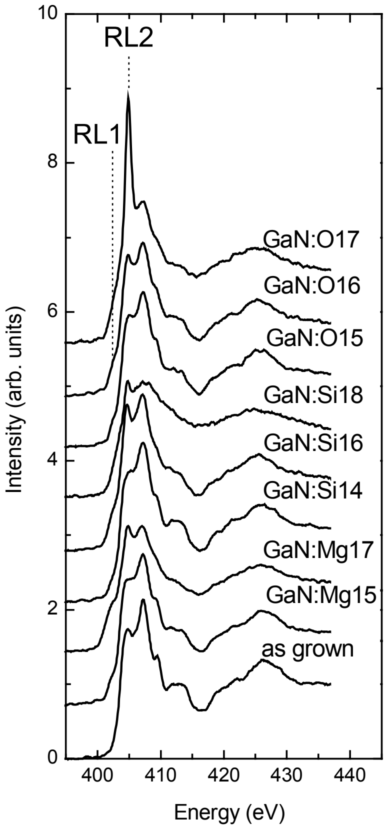

Fig. 1: *NK NEXAFS spectra of the as grown and implanted GaN samples. RL1 and RL2 are the resonances induced by the implantation.*

In order to derive quantitative information on the two resonances, the spectra were fitted in the energy range 395-410eV using a sigmoidal to simulate the transitions to the continuum and a number of Gaussians to simulate transitions to bound final states. The results of the fitting (FWHM and area under RL1 and RL2) are listed in Table I. The RL1 appears in all the implanted samples at 1.7eV below the absorption edge, i.e. its formation and energy position are independent of the projectile and the dose. RL1 is not detected only in the sample GaN:Si18, which has turned amorphous. RL2 appears at about 1.0eV above the absorption edge in the spectra of implanted samples, when the dose exceeds 1×10^{16} cm^{-2}.

More specifically RL1, whose formation and energy position do not depend on the projectile, corresponds to transitions to unfilled final N-p states of an implantation-induced defect. According to theoretical calculations, the point defects which induce empty states in the midgap are the nitrogen interstitial (N_i)[2,3,4], the nitrogen antisite (N_{Ga})[4] and the gallium antisite (Ga_N).[3] Ga_N is the native defect with the highest formation energy[2] and cannot be detected at the N *K* edge since substitution of N with Ga leads to the formation of Ga-Ga bonds. Between N_{Ga} and N_i the interstitial would be more easily formed via implantation.[5] N_i gives empty states at about 1.4-1.9eV above the valence band maximum[2,4], i.e. close to the energy position of RL1. Therefore, it is proposed that RL1 is the signature of the N_i defect.

Table I: *Sample names, implantation conditions and NEXAFS fitting results. The implantation with O was performed with 70keV ions while the energy of the Mg and Si ions was 100keV. The implantation-induced resonances RL1 and RL2 appear at 1.7 eV below and 1.0eV above the absorption edge, respectively.*

			Fitting results			
Sample			RL1		RL2	
Name	Ion	Dose (cm^{-2})	FWHM (eV)	Area (arb. un.)	FWHM (eV)	Area (arb. un.)
GaN	-	-	-	-	-	-
GaN:O15	$^{16}O^+$	$1\cdot10^{15}$	1.37	0.34	-	-
GaN:O16	$^{16}O^+$	$1\cdot10^{16}$	1.41	0.35	0.79	0.10
GaN:O17	$^{16}O^+$	$1\cdot10^{17}$	1.50	0.31	0.84	1.41
GaN:Mg15	$^{24}Mg^+$	$1\cdot10^{15}$	1.42	0.41	-	-
GaN:Mg17	$^{24}Mg^+$	$1\cdot10^{17}$	2.58	1.41	0.79	0.12
GaN:Si14	$^{28}Si^+$	$1\cdot10^{14}$	1.46	0.25	-	-
GaN:Si16	$^{28}Si^+$	$1\cdot10^{16}$	1.50	0.44	0.79	0.25
GaN:Si18	$^{28}Si^+$	$1\cdot10^{18}$	-	-	0.79	0.27

Contrary to RL1, the resonance line RL2 appears when the dose exceeds $1\times10^{16}cm^{-2}$. The fact that RL2 is still present in the spectrum of the amorphous GaN:Si18 sample is an indication that it is not affected by the short- or long-range periodicity and therefore it corresponds to a defect that is strongly localized on the absorbing atom. Such a defect that exists in large concentrations in ion implanted GaN and can be detected by N*K* edge NEXAFS, is the N dangling bond. More specifically, N dangling bonds exist in the neighborhood of a V_{Ga} and/or in three fold coordinated N, significant amount of which exists in amorphous and ion implanted GaN.[6] Our proposal that RL2 is related to the N dangling bond defect is further supported by the study by Y. Xin [7] who observed a similar resonance line in the N*K* EELS spectra recorded at the core of a pure edge threading dislocation with V_{Ga} vacancy core. It should be mentioned that a similar to RL2 resonance line has been observed in the N*K* NEXAFS spectra of N-rich Si_xN_y [8,9] and $Si_xN_yO_z$ [10] samples subjected to or grown by ion implantation, where it has been attributed to transitions to final Np states of the N dangling bond defect. The significantly larger area under RL2 in the spectra of GaN:O17, relative to that in the Mg and Si implanted samples, indicates that oxygen promotes the formation of RL2. In GaN the oxygen atom substitutes for N [11] while Mg and Si occupy Ga sites. Therefore partial substitution of V_{Ga} by Mg or Si would cause a reduction in the concentration of N dangling bonds and would act as a mechanism competitive to the formation of RL2. Furthermore, the formation of V_{Ga} in oxygen implanted GaN is enhanced since in the presence of O_N the formation of defect complexes V_{Ga}-O_N, whose formation energy is lower than that of isolated V_{Ga}, is promoted.[16]

In conclusion, we have applied NEXAFS spectroscopy in order to identify the signature of implantation-induced defects in the Np density of states in the conduction band of implanted GaN samples. It is found that the implantation increases the static disorder while in the case of implantation with 10^{18} Si ions / cm^2 the sample turns amorphous. Implantation introduces states at about 1.7 eV below the absorption edge (i.e. close to the mid-gap), which are attributed to nitrogen interstitials. At relatively high doses ($\geq10^{16}cm^{-2}$) implantation induces additional states at about 1 eV above the absorption edge that are strongly localized and are attributed to N dangling bonds.

Acknowledgements: *M. Katsikini acknowledges financial support from the Greek State's Scholarship Foundation.*

---

[1] *T. D. Moustakas, R. J. Molnar, Mat. Res. Soc. Symp. Proc.* ***281****, 753 (1993).*

[2] *J. Neugebauer, C. G. van de Walle, Phys. Rev . B,* ***50****, 8067 (1994).*

[3] *P. Boguslawski, E. L. Briggs, J. Bernholc, Phys. Rev. B.,* ***51****, 17255 (1995)*

[4] *I. Gorczyca, A. Svane, N. E. Christensen, Solid State Commun.* ***101****, 747 (1997)*

[5] *A. F. Wright, J. Appl. Phys.,* ***90****, 6526 (2001)*

[6] *P. Stumm and D. A. Drabold, Phys. Rev. Lett.,* ***79****, 677 (1997)*

[7] *Y. Xin, E. M. James et al., Appl. Phys. Lett.,* ***76****, 466 (2000)*

[8] *E. C. Paloura, A. Knop et al., J. Appl. Phys.,* ***73****, 2995 (1993).*

[9] *E. C. Paloura, Appl. Phys. Lett.,* ***71****, 3209 (1997).*

[10] *E. C. Paloura, M. Katsikini et al., Electrochemical Society Proceedings,* ***98-22****, 327 (1999).*

[11] *T. Mattila, R. M. Nieminen, Phys. Rev. B,* ***55****, 9571 (1997)*

Investigation of ultrathin MnAs epitaxial films on GaAs(001) during and immediately after the growth

B. Jenichen, W. Braun, V. M. Kaganer, M. Kästner, D. Satapathy, L. Däweritz, and K. H. Ploog
Paul-Drude-Institut für Festkörperelektronik,
Hausvogteiplatz 5–7, D-10117 Berlin, Germany

(Dated: January 15, 2003)

The molecular beam epitaxy (MBE) growth of MnAs on GaAs attracts considerable interest as a way to integrate materials with ferromagnetic and semiconducting properties in epitaxially grown heterostructures [1–4] with the aim to obtain spin injection. The bulk structure of MnAs is well known [5, 6]. Bulk MnAs crystals are ferromagnetic at room temperature. Slightly above room temperature, at about 40 °C, they experience a first-order transition from the ferromagnetic to the paramagnetic phase. This transition is accompanied by a large (∼1%) change of the lattice parameter a in the hexagonal plane. The c parameter changes continuously at the transition. At 125 °C there is another structural transition to the hexagonal phase.

Recently we have found [7–11] that the transition at 40 °C in epitaxial MnAs layers on GaAs(001) proceeds in a way qualitatively different from the bulk phase transition, with a wide temperature range where the two phases coexist in the layer.

In this report, we investigate the growth of a thin MnAs epitaxial layer on GaAs(001) and obtain additional information about the strain in such a layer immediately after growth.

Figure 1 shows a schematic view of the epitaxial relationship between GaAs(001) and the hexagonal MnAs lattice. The orthorhombic βMnAs unit cell is also indicated. The measurements were performed at the wiggler beamline U125/2 KMC using a double crystal Si(111) monochromator. The energy of the radiation was 12 keV. A six-circle x-ray diffractometer coupled with an MBE-system was used [12]. For the investigation of the ultrathin film during the growth the X-ray grazing incidence diffraction technique [13] was applied.

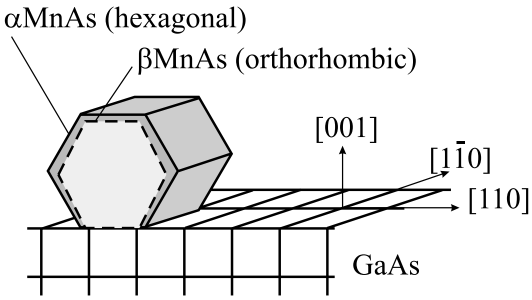

FIG. 1: Schematic view of the epitaxial relationship of MnAs on GaAs(001). The unit cells of the hexagonal α-MnAs phase and the orthorhombic β-MnAs phase are shown.

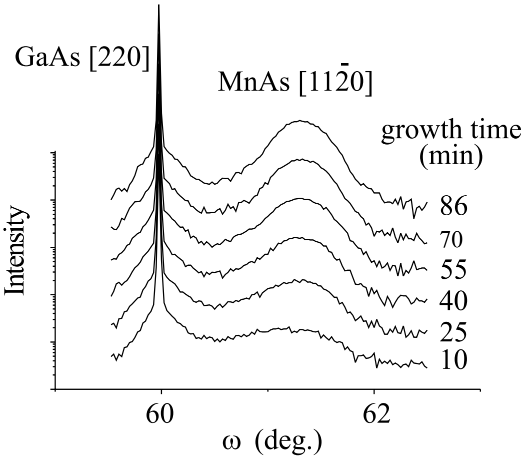

FIG. 2: Grazing incidence diffraction measurements of the epitaxial MnAs film growth at 250 °C. The diffraction vector is parallel to the surface and the a axis of the hexagonal MnAs cell. The approximate growth times are given.

The MnAs layers were grown by standard solid source molecular beam epitaxy (MBE). Commercially available GaAs(001) epi-ready substrates were used. As common in MBE, the oxide desorption temperature is taken as 580 °C, serving as a temperature reference [14]. A 100 nm thick GaAs buffer layer was grown first at 560°C under RHEED control at a growth rate of 250 nm h^{-1}. MnAs growth on GaAs(001) is initiated at a substrate temperature of 250 °C on an As-rich c(4×4) reconstructed surface. Under these growth conditions, the c axis of the hexagonal MnAs unit cell is parallel to the GaAs [1$\bar{1}$0] direction (cf. Figure 1).

Figure 2 shows the development of the MnAs 11$\bar{2}$0 reflection during heteroepitaxial growth. The first curve corresponds to a thickness below 10 nm. This ultrathin layer immediately forms a coincidence lattice as indicated by the peak position in Figure 2. The principle of a coincidence lattice is described in [15]. The peak shift between the curves for 10 and 25 min of growth indicates a further plastic relaxation of the MnAs lattice.

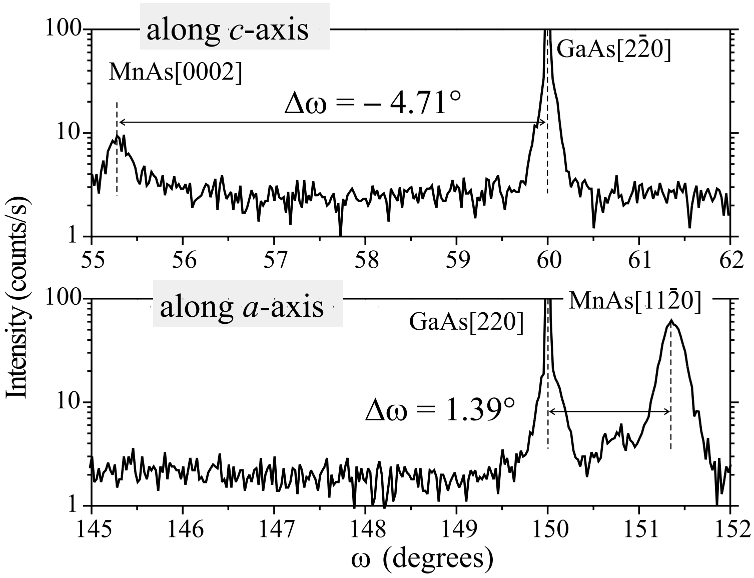

FIG. 3: Grazing incidence diffraction measurements of the epitaxial MnAs film at 200 °C. The diffraction vectors are parallel to the surface and either the c or the a axes of the hexagonal MnAs cell. The film thickness estimated from x-ray reflectivity measurements is below 10 nm.

Since the MnAs layer undergoes two structural phase transitions when being cooled down to room temperature, the strain state of the film during deposition cannot be determined in an *ex-situ* experiment. Figure 3 shows *in-situ* measurements (immediately after the growth) of the MnAs net plane spacings along the surface together with the corresponding substrate reflections in the GaAs [1$\bar{1}$0] and [110] directions. Despite the small film thickness, highly accurate measurements of lattice spacings can be performed. Combining the data from the MnAs 11$\bar{2}$0, 22$\bar{4}$0, 0002 and 0004 reflections, we obtain net plane distances $d_{\mathrm{MnAs}}(11\bar{2}0) = 1.8347\,\text{Å}$ and $d_{\mathrm{MnAs}}(0002) = 2.8978\,\text{Å}$ of the single phase epitaxial film. This corresponds to an expansion of 0.4 % along c and a compression of 0.8 % along the a axis parallel to the sample surface compared to the literature data for bulk MnAs. From the MnAs peak widths, using the Scherrer formula we obtain domain sizes of around 30 nm.

---

[1] G. A. Prinz, Science **250**, 1092 (1990).

[2] M. Tanaka, J. Cryst. Growth **201/202**, 660 (1999).

[3] H. Ohno, Physica E **6**, 702 (2000).

[4] M. Ramsteiner,H. Zhu,A. Kawaharazuka, H.-Y. Hao, and K. H. Ploog, Advances in Solid State Physics **42**, 95 (2002).

[5] B. T. Willis, and H. P. Rooksby, Proc. Phys. Soc. London B **67**, 290(1954).

[6] R. H. Wilson and J. S. Kasper, Acta Cryst. **17**, 95 (1964).

[7] V. M. Kaganer, B. Jenichen, F. Schippan, W. Braun, L. Däweritz, and K. H. Ploog, Phys. Rev. Lett. **85**, 341 (2000).

[8] V. M. Kaganer, B. Jenichen, F. Schippan, W. Braun, L. Däweritz, and K. H. Ploog, Phys. Rev. B **66**, 045305 (2002).

[9] L. Däweritz, F. Schippan, M. Kästner, B. Jenichen, V. M. Kaganer, K. H. Ploog, B. Dennis, K.-U. Neumann, and K. R. A. Ziebeck, Inst. Phys. Conf. Ser. **170**, 269 (2002).

[10] B. Jenichen, V. M. Kaganer, F. Schippan, W. Braun, L. Däweritz, and K. H. Ploog, Materials Science and Engineering B **91-92**, 433(2002).

[11] T. Plake, M. Ramsteiner, V. M. Kaganer, B. Jenichen, M. Kästner, L. Däweritz, and K. H. Ploog, Appl. Phys. Lett. **80**, 2523(2002).

[12] B. Jenichen, W. Braun, V. M. Kaganer, A. G. Shtukenberg, L. Däweritz, C. G. Schulz, and K. H. Ploog, Review of scientific instruments, in press

[13] W. C. Marra, P. Eisenberger, and A. J. Cho, J. Appl. Phys. **50**, 6927(1979).

[14] A. J. Springthorpe, S. J. Ingrey, B. Emmerstorfer, P. Mandeville, and W. T. Moore, J. Vac. Sci. Technol. B **5**, 739 (1987).

[15] A. Trampert, F. Schippan, L. Däweritz, K. H. Ploog, Inst. Phys. Conf. Ser. **164**, 305 (1999).

Constrained phase coexistence near the Curie temperature in MnAs(0001)/GaAs(111) epitaxial films

B. Jenichen, V. M. Kaganer, M. Kästner, C. Herrmann, L. Däweritz, and K. H. Ploog
Paul-Drude-Institut für Festkörperelektronik,
Hausvogteiplatz 5–7, D-10117 Berlin, Germany

N. Darowski and I. Zizak
Hahn-Meitner-Institut Berlin GmbH, Glienicker Strasse 100, D-14109 Berlin, Germany

(Dated: January 15, 2003)

The combination of magnetic and semiconducting materials leads to new pathways in the development of semiconductor devices utilizing the spin of the carriers [1–4]. Reliable operation of the devices demands high Curie temperatures of the ferromagnetic materials. A combination of ferromagnetic MnAs and semiconducting GaAs is promising for spin injection devices [4]. MnAs possesses, at the Curie temperature of approximately 40 °C, a first order ferromagnetic—paramagnetic phase transition accompanied by a lattice parameter discontinuity in the hexagonal plane as large as 1.2% [5, 6].

We have observed recently [7–10] the phase coexistence between the hexagonal ferromagnetic αMnAs phase and the orthorhombic paramagnetic βMnAs phase in MnAs layers grown on GaAs(001) substrates. The phase coexistence is caused by the epitaxial constraint on the mean lateral lattice parameter of the film: a discontinuous lattice parameter variation at the first order transition costs elastic energy and favors the coexistence of elastic domains of the two phases in a large temperature interval. In that former study, the c-axis of the hexagonal MnAs was parallel to the GaAs(001) surface, resulting in a high degree of in-plane anisotropy of the film: the elastic domains form a striped structure [8–11]. In contrast, the c-axis of MnAs layers grown on GaAs(111)B substrates is perpendicular to the surface, so that the film is elastically isotropic in the surface plane. As a consequence of the different epitaxial orientations of the MnAs films grown on GaAs(001) and on GaAs(111)B, differences in the magnetic anisotropies as well as in the strain related properties are observed [8–15].

In this report, we investigate the phase coexistence in a thin MnAs epitaxial layer grown on exactly oriented GaAs(111)B near the ferromagnetic phase transition αMnAs–βMnAs. Figure 1 shows a schematic view of the epitaxial relationship between GaAs(111) and the hexagonal MnAs lattice. The orthorhombic βMnAs unit cell is also indicated. The unit cell of GaAs can also be considered as pseudohexagonal [15] with the c-axis along [111].

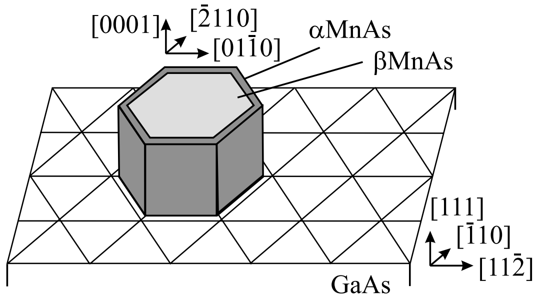

FIG. 1: Schematic view of the epitaxial relationship of MnAs on GaAs(111). The hexagonal plane after the phase transition to orthorhombic β-MnAs is also indicated. A pseudohexagonal unit cell can be defined [15] for GaAs with the c-axis along [111].

The structural change at the αMnAs–βMnAs transition consists of a large (≈1.2%) lattice parameter discontinuity in the hexagonal plane and a small (<0.2%) orthorhombic distortion [5, 6]. The c-parameter is continuous at the transition. Therefore, the most appropriate reflections to be measured lie in the hexagonal plane. We have chosen the reflections αMnAs($\bar{1}$100) and βMnAs(020). For the given film orientation, the X-ray grazing incidence diffraction technique had to be applied in order to access these reflections. The measurements were performed at the bending magnet beamline KMC2 using a double crystal Si(111) monochromator. The energy of the radiation was 8.09 keV. A six-circle x-ray diffractometer with a temperature controlled sample stage was used. The sample temperature was regulated by a standard temperature controller with resistive heating and thermocouple temperature measurement at the sample holder plate. The estimated systematic uncertainty in temperature determination was at most 1 °C. The incidence angle was 0.3 °, and the angular acceptance of the detector was 0.1 °.

The MnAs layers were grown by standard solid source molecular beam epitaxy (MBE). Commercially available GaAs(111)B epi-ready substrates without intentional miscut were used. The substrates were first degassed at 100 °C and then baked for 20 min at 300 °C in the preparation chamber before being introduced into the growth chamber. The oxide was desorbed inside the growth chamber under reflection high energy electron diffraction (RHEED) control. As common in MBE, the oxide desorption temperature is taken as 580 °C, serving as a temperature reference [17]. The temperature was measured by a thermocouple near the plate of the sample holder. The cell fluxes were calibrated by RHEED intensity oscillations [18, 19]. A 100 nm thick GaAs buffer layer was grown first at 600°C under RHEED control [15] and at a growth rate of 250 nm h^{-1}. Then, a 2 nm thick MnAs nucleation layer was grown at 225°C with a growth rate of 19.8 nm h^{-1} and a V/III ratio of 236. The main MnAs layer was grown at 300°C with a growth rate of 200 nm h^{-1} and a V/III ratio of 22. The thicknesses of the MnAs film is 430 nm as determined by subsequent scanning electron microscopy.

The surface morphology of this film characterised by atomic force microscopy shows a roughness near 10 nm, probably due to a facet formation during homoepitaxial growth on the exactly oriented GaAs(111)B surface [14]. Nevertheless the sample is suitable for a structural investigation of the ferromagnetic—paramagnetic phase transition in the MnAs epitaxial layer. We intend to perform analogous measurements with smoother layers in the future.

Figure 2 presents the temperature variations of the diffraction curves near the phase transition temperature. A single peak observed below the transition temperature is attributed to the αMnAs($\bar{1}100$) reflection, and the one above the transition temperature to the βMnAs(020) reflection. The βMnAs (020) peak has a higher peak intensity and a larger integrated intensity than the αMnAs($\bar{1}100$) reflection, which is slightly broadened. Near the transition, a continuous transformation from one peak to the other is observed. All peaks are well fitted to sums of two Gaussians, corresponding to peaks of the two phases. The full widths at half maxima (FWHMs) of the Gaussians were fixed at the values obtained from the peaks measured far away from the transition temperature. The peak positions and the integrated intensities were fitted. The phase fractions were assumed to be proportional to the integrated intensities scaled by the ones measured in the single-phase regions well above and well below the transition temperature.

The temperature dependence of the fraction of the αMnAs phase, calculated from the fits shown in Fig. 2, is presented in Fig. 3(a). Heating and cooling are marked by upward and downward triangles, respectively. The phase coexistence is observed between 40 °C and 50 °C. No temperature hysteresis is observed.

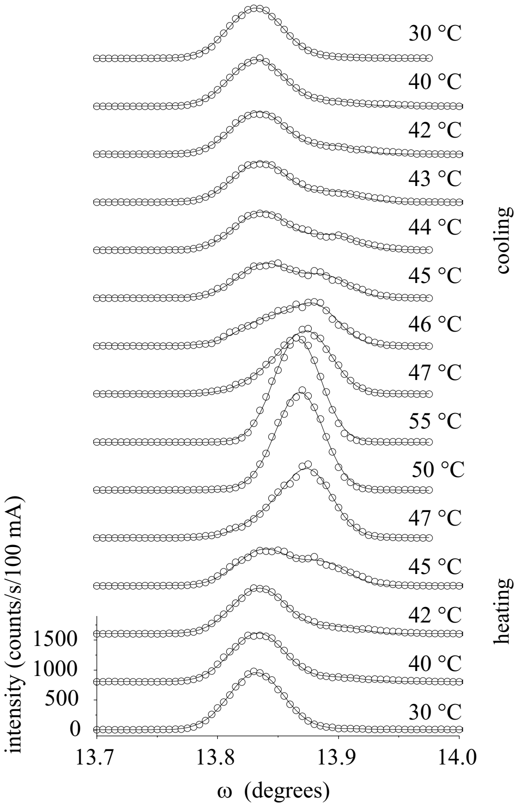

FIG. 2: Grazing incidence diffraction curves ($\omega - 2\theta$-scans) near the αMnAs($\bar{1}100$) and the βMnAs (020) reflections measured at different temperatures using grazing incidence synchrotron x-ray diffraction at an energy of 8.09KeV. The circles are the results of the measurements and the lines are the results of the fits to a sum of two Gaussians. The sample temperature is given for each curve.

Figure 3(b) presents the lattice spacings of both MnAs phases obtained from the peak positions in Fig. 2 and the mean in-plane spacing obtained from the lattice spacings and fractions of the two phases at a given temperature. The mean spacing decreases by approximately 0.24% on heating from the αMnAs to the βMnAs phase. This lattice spacing variation in the epitaxial film is small compared to the lattice spacing discontinuity in a bulk MnAs crystal at the phase transition of 1.2% [5]. The lattice spacing variation by plastic deformation can be excluded because of its reversible variation in heating and cooling cycles.

It is instructive to compare the two-phase coexistence in MnAs($1\bar{1}00$)/GaAs(001) films studied in Refs. [7–11] with that in MnAs(0001)/GaAs(111) films studied in the present work. The present work does not reveal any temperature hysteresis. In contrast, a temperature hysteresis up to 7 °C was observed in MnAs films on GaAs(001). The phase coexistence in MnAs($1\bar{1}00$)/GaAs(001) films was observed at lower temperatures, from 20 °C to

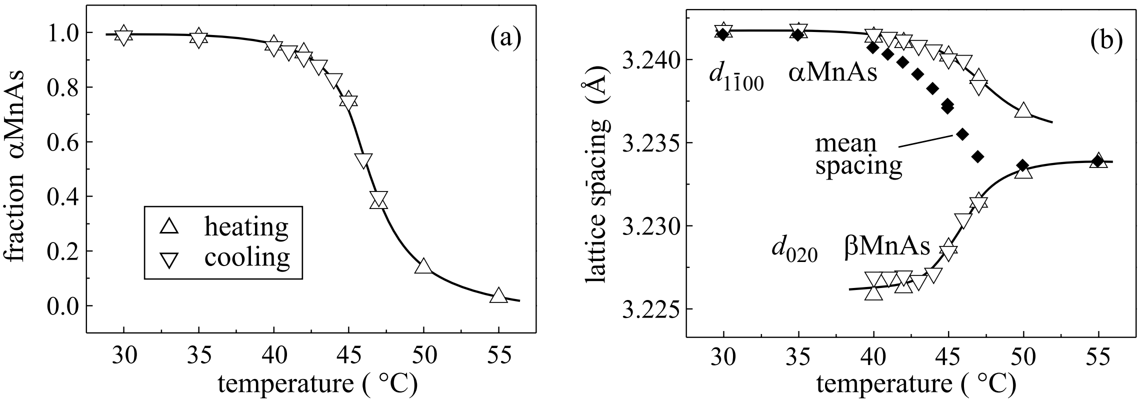

FIG. 3: (a) Temperature dependence of the αMnAs phase fraction near the first order ferromagnetic-paramagnetic phase transition. Heating and cooling are marked by upward and downward pointing triangles, respectively. (b) Temperature dependencies of the in-plane lattice spacings of the αMnAs and βMnAs phases (empty triangles) and the mean in-plane lattice spacing (full diamonds). The lines are guides for the eye.

40 °C, as compared to the present study (40 to 50 °C). The origin of this difference is not clear for us. We note that the phase transition in bulk MnAs crystals is commonly attributed to ≈40 °C but the temperature hysteresis as large as 15 °C does not allow an accurate Curie temperature determination.

Thus, we have found that the ferromagnetic phase transition in MnAs(0001) epitaxial films on GaAs(111)B proceeds via an equilibrium phase coexistence in a temperature interval of 10 °C. The phase coexistence is governed by the elastic strain at the first order phase transition, with the in-plane lattice expansion limited by the epitaxy of the film.

The authors would like to thank A. Erko for the beamline support and A. Bluhm for the SEM measurement of the layer morphology.

[1] G. A. Prinz, Science **250**, 1092 (1990).
[2] M. Tanaka, J. Cryst. Growth **201/202**, 660 (1999).
[3] H. Ohno, Physica E **6**, 702 (2000).
[4] M. Ramsteiner,H. Zhu,A. Kawaharazuka, H.-Y. Hao, and K. H. Ploog, Advances in Solid State Physics **42**, 95 (2002).
[5] B. T. Willis, and H. P. Rooksby, Proc. Phys. Soc. London B **67**, 290(1954).
[6] R. H. Wilson and J. S. Kasper, Acta Cryst. **17**, 95 (1964).
[7] V. M. Kaganer, B. Jenichen, F. Schippan, W. Braun, L. Däweritz, and K. H. Ploog, Phys. Rev. Lett. **85**, 341 (2000).
[8] V. M. Kaganer, B. Jenichen, F. Schippan, W. Braun, L. Däweritz, and K. H. Ploog, Phys. Rev. B **66**, 045305 (2002).
[9] L. Däweritz, F. Schippan, M. Kästner, B. Jenichen, V. M. Kaganer, K. H. Ploog, B. Dennis, K.-U. Neumann, and K. R. A. Ziebeck, Inst. Phys. Conf. Ser. **170**, 269 (2002).
[10] B. Jenichen, V. M. Kaganer, F. Schippan, W. Braun, L. Däweritz, and K. H. Ploog, Materials Science and Engineering B **91-92**, 433(2002).
[11] T. Plake, M. Ramsteiner, V. M. Kaganer, B. Jenichen, M. Kästner, L. Däweritz, and K. H. Ploog, Appl. Phys. Lett. **80**, 2523(2002).
[12] Y. Morishita, K. Iida, J. Abe, K. Sato, Jpn. J. Appl. Phys.**36**(2), L1100(1997).
[13] M. Tanaka, K. Saito, T. Nishinaga, Appl. Phys. Lett. **74**, 64(1999).
[14] S. Sugahara, M. Tanaka, J. Appl. Phys. **89**, 6677(2001).
[15] M. Kästner, L. Däweritz, and K. H. Ploog, Surface Science **511**, 323(2002).
[16] M. Tanaka, J. P. Harbison, M. C. Park, Y. S. Park, T. Shin, and G. M. Rothberg, Appl. Phys. Lett. **65**, 1964(1994).
[17] A. J. Springthorpe, S. J. Ingrey, B. Emmerstorfer, P. Mandeville, and W. T. Moore, J. Vac. Sci. Technol. B **5**, 739 (1987).
[18] J. H. Neave, B. A. Joyce, P. J. Dobson, Appl. Phys. A **34**, 179(1984).
[19] F. Schippan, M. Kästner, L. Däweritz, and K. H. Ploog, Appl. Phys. Lett. **76**, 834(2000).

Functionalization of GaAs surfaces with aromatic self-assembled monolayers

A. Shaporenko[1], K. Adlkofer[2], L. S. O. Johansson[3], M. Tanaka[2], M. Grunze[1],
and M. Zharnikov[1]

[1] *Angewandte Physikalische Chemie, Universität Heidelberg, Im Neuenheimer Feld 253,
D-69120 Heidelberg, Germany*

[2] *Lehrstuhl für Biophysik E22, Technische Universität München, James-Franck-Strasse,
D-85748, Garching b. München, Germany*

[3] *Department of Physics, Karlstad University, Universitetsgatan 1, S-65188 Karlstad, Sweden*

The design of functional interfaces and links between semiconductor materials and biological objects is of great scientific and practical interest. One of the most promising semiconductors in view of flexible band-gap engineering is GaAs, which exhibits high electron mobility in nanostructures and low-dimensional arrangements. Regretfully, the above-mentioned applications are difficult to realize due to chemical instability of GaAs surface, especially in physiological electrolytes, and lack of a strategy for reliable surface passivation with functional interlayers. However, these problems could be partly avoided through the functionalization of GaAs surfaces with self-assembled monolayers (SAMs).

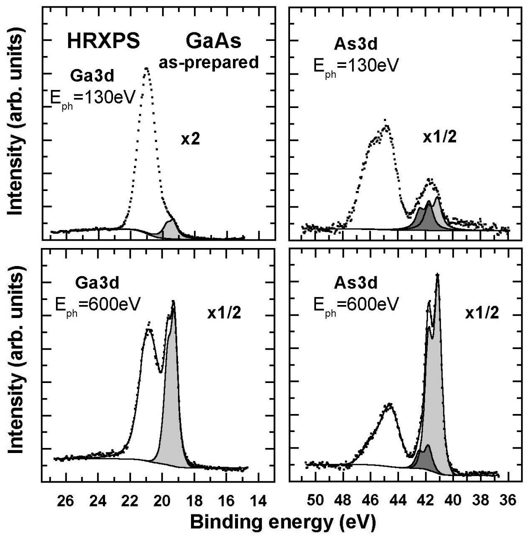

Fig. 1. Ga 3d and As 3d HRXPS spectra of an as-prepared GaAs sample.

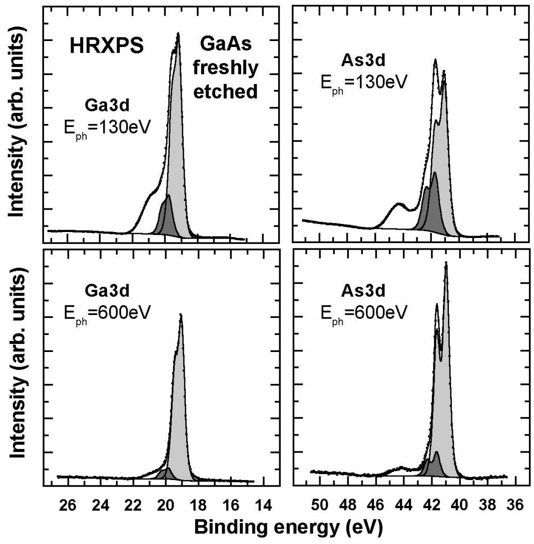

Fig. 2. Ga 3d and As 3d HRXPS spectra of freshly etched GaAs.

In this study, stochiometric GaAs (100) surfaces were functionalized with monolayers of an aromatic compound, 1,1'-biphenyl-4-thiol (BPT), and the engineered surfaces were characterized by synchrotron-based high resolution x-ray photoelectron spectroscopy (D1011 & I311, MAX-lab, Lund, Sweden) and near edge x-ray absorption fine structure (NEXAFS) spectroscopy (HE SGM, BESSY II). The functionalization of GaAs with BPT was found to prevent an oxidation and contamination of the surface, keeping the BPT/GaAs interface in a similar state as the freshly etched GaAs surface. The corresponding HRXPS spectra are shown in Figs. 1-3, the spectra acquired at photon energies of 130 eV (upper panels) and 600 eV (bottom panels) being dominated by contributions from the sample surface and bulk. The decomposition of the spectra by doublets related to individual chemical species is shown: **Ga 3d spectra:** light gray - GaAs, gray - a Ga oxide or the surface Ga 3d component; **As 3d spectra:** light gray - GaAs, gray - elementary

As, black - S-As. The shoulders at the high binding energy side of the shadowed doublets correspond to Ga and As oxides.

The observation of the "S-As"-related As 3d emission in the spectra in Figure 3 as well as the S 2p doublet at a characteristic[1] binding energy of 162.6 eV in the respective S 2p HRXPS spectra suggest that the attachment of the BPT molecules to the substrate occurs over the thiolate headgroup. The complementary NEXAFS spectroscopy measurements (Fig. 4) imply that BPT SAMs on GaAs are well ordered and densely packed: The NEXAFS spectra exhibit characteristic absorption resonances and a pronounced linear dichroism with x-ray incidence angle variation.

The quantitative analysis of the NEXAFS data gives an upright orientation of the BPT molecules in the BPT film with an average tilt angle of 31.4°±5°. The obtained value seems to be slightly larger than the corresponding values for the aromatic SAMs on noble metal substrates, such as (111) Au and Ag.[2] This can be explained by several reasons or their combination: (i) the larger As-As spacing between the anchor sites (As atoms) on (100) GaAs as compared to (111) Au and Ag, (ii) a different character of the thiolate-As bond as compared to the case of Au and Ag, and (iii) a lesser degree of the orientational order in the films on GaAs, which is presumably related to residual contaminants and oxides on the surface of freshly etched GaAs substrate.

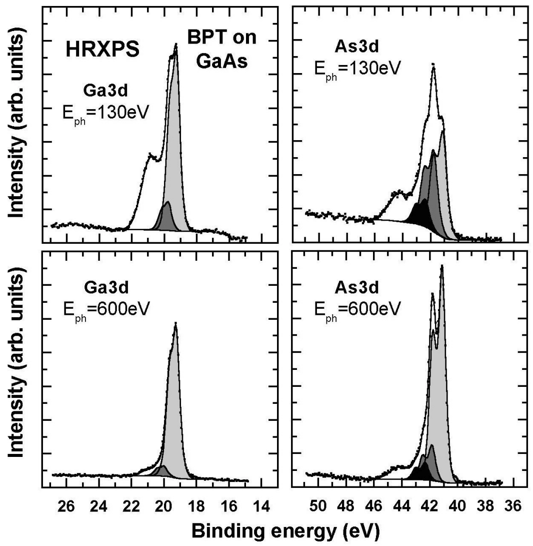

Fig. 3. Ga3d and As3d HRXPS spectra of GaAs functionalized with BPT.

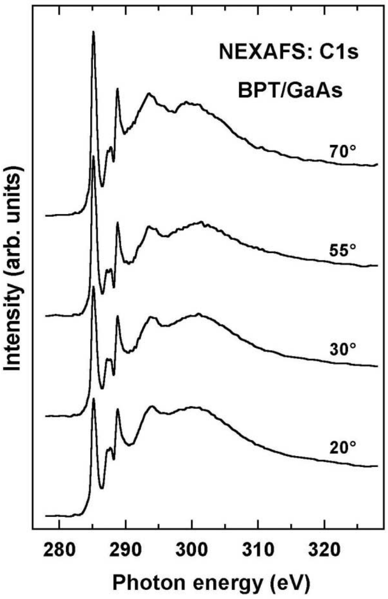

Fig. 4. Normalized C 1s NEXAFS spectra of a BPT-coated GaAs sample acquired at angles of X-ray incidence of 70°, 55°, 30°, and 20°.

Densely packed, chemically stable, and hydrophobic biphenyl monolayers on GaAs can be used for the protection of GaAs in air and in water, as well as for the further functionalization with polymer films and model biomembranes. In addition, applications within the SAM-based chemical lithography framework[3,4] enable the fabrication of multi-functional surfaces. Such a functionalization protocol can also be directly transferred onto various semiconductor heterostructures in the proximity of the GaAs surface, such as near-surface quantum dots, which can be effectively used for sensitive detection of specific recognition and selective transport in biological membranes.

This work has been supported by BMBF through grant GRE1HD.

References:

(1) K. Heister, M. Zharnikov, M. Grunze, L. S. O. Johansson, J. Phys. Chem. B. **105** (2001) 4058.

(2) S. Frey, V. Stadler, K. Heister, M. Zharnikov, M. Grunze, B. Zeysing, A. Terfort, Langmuir **17** (2001) 2408.

(3) W. Eck, V. Stadler, W. Geyer, M. Zharnikov, A. Gölzhäuser, M. Grunze, Adv. Mater. **12** (2000) 805.

(4) M. Zharnikov and M. Grunze, J. Vac. Sci. Tech. B **20** (2002) 1793.

Self-assembled monolayers of nitrile-functionalized alkanethiols on gold and silver substrates

S. Frey,[1] A. Shaporenko[1], P. Harder[2], D. L. Allara[2], M. Grunze[1], and M. Zharnikov[1]

[1] *Angewandte Physikalische Chemie, Universität Heidelberg, Im Neuenheimer Feld 253, D-69120 Heidelberg, Germany*

[2] *Departments of Chemistry and Materials Science, Pennsylvania State University, University Park, PA 16802, USA*

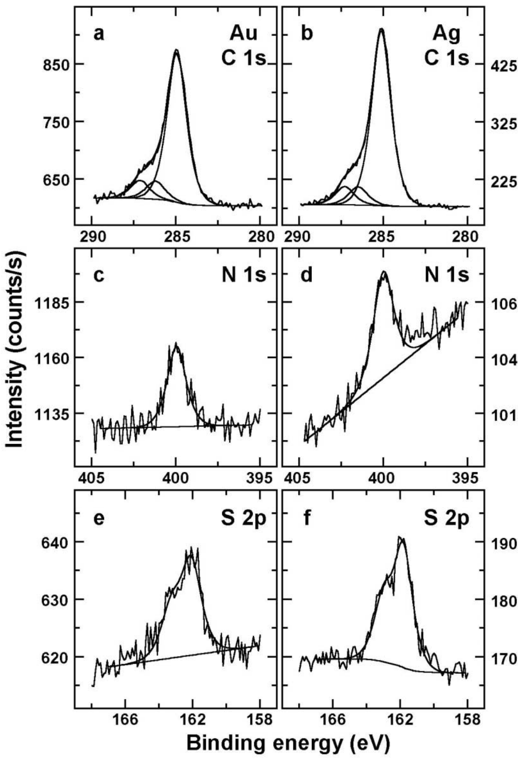

Fig. 1. XPS spectra of NC-C16 on Au and Ag.

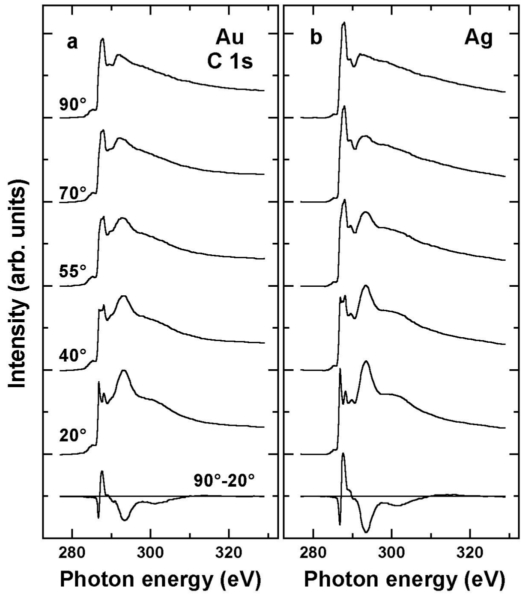

Fig. 2. C1s NEXAFS spectra of NC-C16 SAMs on Au and Ag.

In this paper we studied self-assembled monolayers (SAMs) formed from nitrile-functionalized alkanethiols (AT) $NC(CH_2)_{16}SH$ (NC-C16, 17-Mercapto-heptadecanenitrile) on (111) gold and silver substrates. These systems are interesting from both scientific and practical standpoints. From the practical point of view, the nitrile-functionalized SAMs are perspective candidates for SAM-based lithography[1] and the fabrication of non-hydrogen bond donor surfaces with low protein affinity. From the scientific standpoint, the polar nitrile group with a relatively large dipole moment is well-suitable to explore to what extent the structure of a non-substituted AT SAM can be affected by strongly interacting tailgroups. A theory predicts a strong influence of the electrostatic interactions between the nitrile tailgroups on the entire system.[2]

We used several complementary experimental techniques, such as X-ray photoelectron spectroscopy (XPS), near-edge X-ray absorption fine structure (NEXAFS) spectroscopy (HE SGM, BESSY II), and contact angle measurements to gain information on the chemical identity, packing density, and orientational and conformational order in the NC-C16 SAMs on Au and Ag. The C 1s, N 1s, and S 2p XPS spectra in Fig. 1 suggests intact NC-C16 films for both Au and Ag substrates. The bonding to the substrate occurs over the thiolate headgroup while the CN functionalities comprise the SAM/ambience interface. The packing density of NC-C16/Ag was found to be slightly higher than that for NC-C16/Au.

C1s and N1s NEXAFS spectra in Fig. 2 and 3 imply well-ordered, densely packed films for both NC-C16/Au and NC-C16/Ag. The characteristic absorption resonances for an intact alkyl chain (e.g. the R* and σ*(C-C) resonances) and a CN functionality (the π*(C*≡N) and π*(C≡N*) resonances) are clearly observed. These resonances exhibit pronounced linear dichroism at the variation of the incidence angle of x-ray light. The quantitative analysis of the NEXAFS data (Fig. 4) resulted in an average tilt angle of the alkyl chains of 42.5° and 37° for NC-C16/Au and NC-C16/Ag, respectively. An alternative "difference spectra" analysis of the NEXAFS data led to the same value for NC-C16/Au and a lower value of 29° for NC-C16/Ag. The latter value was considered to be more realistic than 37° in view of the complementary infrared spectroscopy data. Most important, the derived tilt angles for the NC-functionalized SAMs are noticeably higher than the respective values for the non-substituted AT SAMs, 35° for Au and 12° for Ag.[3] Along with other results, this difference suggests that the strongly-interacting nitrile entities have a strong influence on the molecular orientation, packing, and the structure of AT films on both Au and Ag substrates.

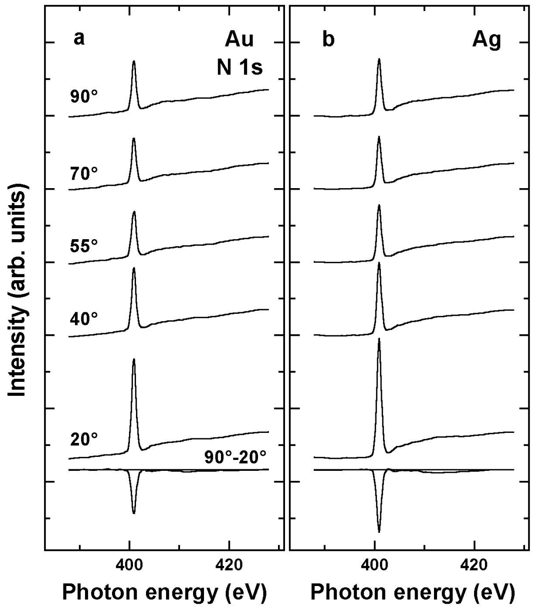

Fig. 3. N1s NEXAFS spectra of NC-C16 SAMs on Au and Ag.

As to the CN functionality, it has an in-plane orientation with the tilt angle of ≈65° for both NC-C16/Au and NC-C16/Ag (Fig. 4). This value agrees rather well with the theoretical estimate for NC-C16/Au (72.5°)[2], but differs significantly from the orientation, which could be expected for "non-disturbed" NC-C16 chains (53°[4] and 58°[5] in AT/Au and 27°[4] or 38.1°[5] for AT/Ag). The reorientation of the CN functionalities occurs due to a strong electrostatic interaction between these polar moieties, which additionally distorts the underlying 2D-lattice formed by AT chains. These types of effects are very important because they offer a means to control and understand the detailed structure of a SAM and its ambient surface for applications such as tailored wetting and biologically active surfaces. This work has been supported by BMBF through grant GRE1HD.

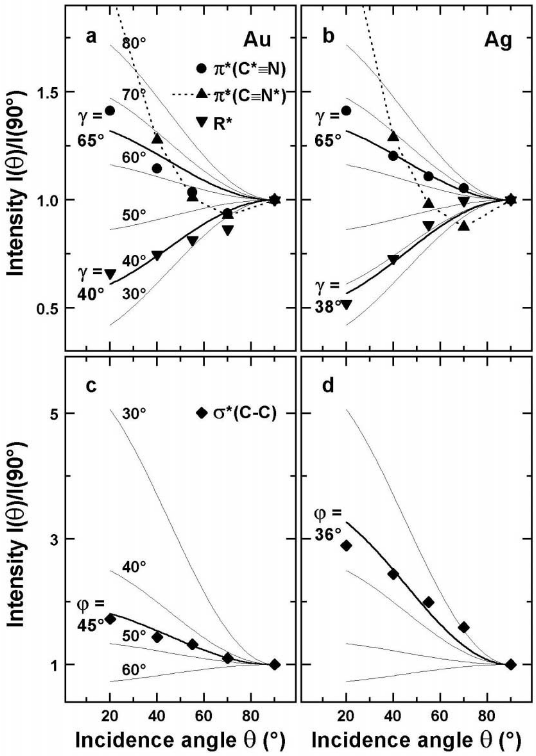

Fig. 4. The intensity of the π*(C*≡N) (a,b), σ*(C-C) (c, d), R* (a,b), and π*(C≡N*) (a,b) resonances for NC-C16/Au (a,c) and NC-C16/Ag (b,d) as a function of the incidence angle of the x-rays. For comparison, the theoretical dependencies for different tilt angles of the alkyl chains and C≡N moiety are added as thin solid lines.

References:

(1) M. Zharnikov and M. Grunze, J. Vac. Sci. Tech. B **20** (2002) 1793.

(2) J. Hautman, J. P. Bareman, W. Mar, M. L. Klein, J. Chem. Soc. Faraday Trans. **87** (1991) 2031.

(3) M. Zharnikov and M. Grunze, J. Phys. Condens. Matter. **13** (2001) 11333.

(4) M. M. Walczak, C. Chung, S. M. Stole, C. A. Widrig, M. D. Porter, J. Am. Chem. Soc. **113** (1991) 2370.

(5) A. Lampert, *PhD Thesis*, Universität Heidelberg, Heidelberg, Germany, 1997.

Synchrotron Radiation Photoelectron Spectroscopy and AFM Investigation on the Electrochemical Nanoroughening of Float Zone n-Si(111)

H. J. Lewerenz, H. Jungblut, M. Aggour, E. Gonçalves, E. Rüther, M. Kanis, C. Murrell,
M. Gaul, M. Winkelnkemper, J. Jakubowicz and P. A. Cox[1]
Division of Solar Energy, Interface Engineering Group, Hahn-Meitner-Institut, 14109 Berlin, Germany
[1]School of Pharmacy and Medical Sciences, Portsmouth University, Portsmouth, U.K.

In the quest for preparation of surfaces for advanced light-coupling into solar cell absorbers, photonic active material and immobolisation of biological molecules at surfaces, the control of topographic features in the nanometer scale becomes increasingly relevant (1). Among the various structuring possibilities, we focuss here on the self-organised structure formation induced by photoelectrochemical processing in weak acidic fluoride containing electrolytes which allows particularly accurate modification in the potentiostatic conditioning mode (2). The approach followed here combines the photoelectrochemical conditioning with AFM for structural analysis and SRPES for chemical analysis of dissolution reaction species (if combined with partial charge calculations). Fig. 1 shows the conditioning procedure: an H-terminated float zone silicon sample is anodised by scanning the potential in positive direction from the rest potential (labelled ocp for open circuit potential) under illumination. The light intensity is high enough to provide mass transport limited photocurrents. In the potential region below the first current maximum, the dissolution reaction is divalent, i.e. only two charges are needed to dissolve one Si atom (3) and porous Si can be formed for increased anodisation (4). The situations labelled (b) and (A) have been investigated by AFM and SRPES, respectively. The charge passed amounts to 0.5 bilayers and ~ 1 bilayer dissolution of the (111) oriented surface. The corresponding AFM image is shown in Fig.2 including a line scan across the surface. The former zig-zag structure of the H-terminated surface is still partly visible but also formation of pits with nanoscopic dimensions is observed.

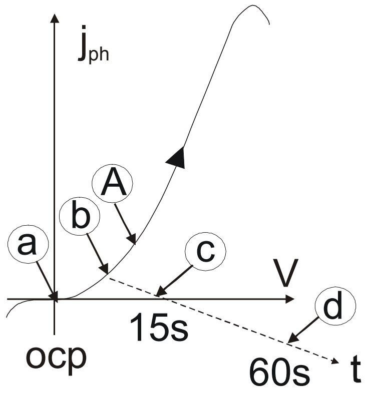

Fig.1 Schematic photocurrent-voltage characteristic of n-Si(111) in 0.1 M NH_4F at pH 4; labels (a – d) refer to the conditioning for AFM measurements, label (A) denotes the emersion potential for the SRPES experiment.

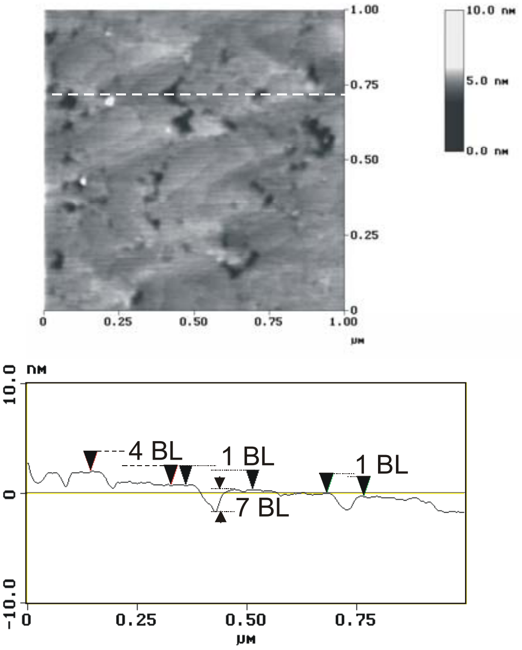

Fig.2 AFM image (contact mode) of the n-Si(111) surface after anodisation according to (b) in Fig.1; charge passed 0.28 $mCcm^{-2}$; right: line scan across indicated region in the left image.

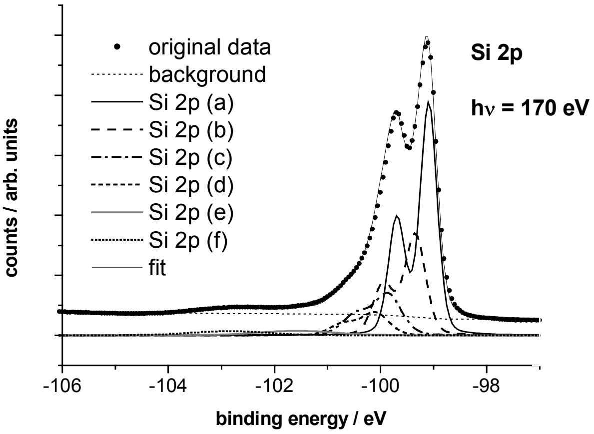

Fig.3 Photoelectron spectrum of the Si 2p core level after anodisation according to label (A) in Fig.1.

These pits form initially along the edges of terrace steps, one bilayer deep and the overall dissolution appears to produce step edges with a <-1-1 2> directed normal. The line scan shows terraces of considerable width and multiple bilayer deep pits which are in height asymmetrically bordered by the surrounding terraces. A photoelectron spectrum of the Si 2p core level recorded upon excitation with synchrotron radiation is shown in Fig.3 for a similar dissolution situation (point A in Fig.1). The envelope curve obtained from the measurement is shown together with deconvoluted signals. The bulk curve, attributed to Si° (full line) is positioned at –99.2 eV. In addition, we find signals shifted by ΔE_b = 0.3 eV, 0.8 eV, 1.0 eV, 2.3 eV and 3.6 eV. To infer surface chemical changes from these data, one needs to know which surface species would be expected from the dissolution reaction. We follow largely the predictions of the hitherto most established model (3) and have performed density functional theory (DFT) calculations on most of the expected intermediates. Assuming a linear relationship between the change in Si partial charge and in binding energy implies the validity of the so-called initial state model. Since on semiconductors, the Helmholtz layer is much more weakly bound to the surface and we apply very moderate external potentials, the action of an electrical field which might influence the final states in the photoemission process differently for different species can be neglected. In addition, effects from the band structure as found on Si(100) on the final states do not apply for (111) oriented samples (5). From the combination of the species postulated in the dissolution model and the DFT calculations, published earlier (6), we assign the species shifted by 0.3 eV to a surface core level shift (scls) due to remnant H-termination of the surface (coverage Θ = 0.55 monolayers), the signal shifted by 0.8 eV is attributed to a Si species with two backbonds to the lattice and an H and OH termination towards the solution with Θ = 0.3 ML; for ΔE_b = 1 eV, a species = Si –H-F is postulated with a coverage of 0.15 ML. The small signals with higher oxidation state could be attributed to a precipitate from the dissolution reaction, $SiOHF_3$, but the species with ΔE_b = 3.6 eV could not yet be identified. The corresponding calculated partial charges for the surface molecules were ρ = 0.1 (scls), 0.45, 0.54 and 1.29, respectively.

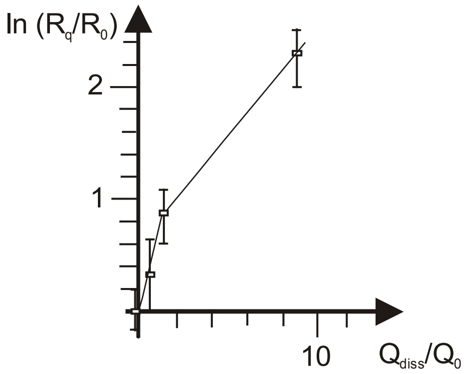

Fig.4 Correlation between AFM-determined roughness R_q vs normalised dissolution charge Q_{diss} (see text).

The corresponding O 1s line shows signals from OH and molecular water (data not shown here) in an intensity ratio of 1.5. This indicates the hydrophilicity of those parts of the surface which are no longer hydrogen terminated at which Si is terminated partly by OH. The F 1s line, located at – 687.1 eV is indicative of Si-F_x species, such as, for instance, $HSiF_3$ or $SiOHF_3$ thus supporting the identification of one of the higher oxidised species as a precipitate.

In a further chronoamperometric experiment, the electrochemical conditioning was extended from the potential labelled (b) in Fig.1 to 15s and 60s. The logarithm of the rms roughness, R_q, of the resulting AFM images, determined for these surfaces, shows an almost linear relationship with the dissolution charge, Q_{diss} (see Fig. 4). If one assumes that the terrace removal according to the dissolution mechanism leaves the roughness unaffected, it is the relative charge Q_{pit}/Q consumed in the pit formation which leads to the roughening. For normalisation, we take for R_0 the roughness of the H-terminated surface without miscut and Q_0 denotes the charge necessary to dissolve one bilayer in the divalent dissolution region. If one plots for simplification $\ln(R_q/R_0) = \text{const} + a\ Q_{diss}/Q_0$, one finds that for $Q_{diss}/Q_0 < 2$, about 60% of the charge is consumed for pit formation. This reaction branching between terrace removal and pit formation changes to 20% for pit formation for higher dissolution charge and indicates the sensitivity of this self-organised pitting with electrochemical parameters.

E. Gonçalves gratefully acknowledges financial support by the DFG in the priority program "Fundamentals of Electrochemical Nanotechnology".

References

1. U. Grüning and V. Lehmann, Thin Solid Films **276** (1996) 151
2. H. J. Lewerenz, Chem. Soc. Rev. **26** (1997) 239
3. H. Gerischer, P. Allongue and V. Costa Kieling, Ber. Bunsenges. Phys. Chem. **97** (1993) 753
4. J. Rappich and H. J. Lewerenz, Thin Solid Films **276** (1996) 25
5. E. Pehlke and M. Scheffler, Phys. Rev. Lett. **71** (1993) 2338
6. H. J. Lewerenz, M. Aggour, C. Murrell, M. Kanis, P. Hoffmann, H. Jungblut and D. Schmeißer, J. Non – Cryst. Solids **303** (2002) 1

Investigation of Oxidation and Migration Processes of Inorganic Compounds in Ink Corroded Manuscripts

Oliver Hahn[1], Wolfgang Malzer[2], Birgit Kanngießer[2], and Alexej Erko[3]
[1] *Federal Institute for Materials Research and Testing (BAM) Berlin*
[2] *Institute for Atomic Physics and Teacher Training, Technical University of Berlin*
[3] *Bessy GmbH, Berlin*

Motivation

The aim of this study is the investigation of the iron gall ink corrosion process. By means of µ-XANES and µ-XRF the Fe^{2+}/Fe^{3+} ratio and the major and minor constituents of the ink are determined in order to clarify oxidation and migration processes. Two manuscripts with different conservation states were investigated.

Iron gall ink and ink corrosion

Iron gall ink is produced from four basic ingredients: galls, vitriol, gum arabic as a binding media and an aqueous medium such as wine, beer or vinegar. By mixing gallic acid with iron sulfate, first a water soluble ferrous gallate complex is formed. Due to its solubility, the ink penetrates the paper surface, making it difficult to erase. When exposed to oxygen, a ferric pyrogallate pigment is formed. This complex is not water soluble, which contributes to its indelibility as a writing ink. Normally, the presence of oxygen leads directly to a formation of the ferric gallate pigment when mixing gallic acid and iron sulfate. To decrease the precipitation of this insoluble complex, a binder, such as gum arabic, is added to the mixture. Due to the variety of different recipes and the natural origin of these different materials, there is a wide range of different organic and inorganic components (Al, Zn, Cu, Mn) and impurities in historical iron gall inks that may cause a diversity of distinguishable degradation mechanisms containing changes in color, occasionally resulting in iron gall ink corrosion (see fig. 1).

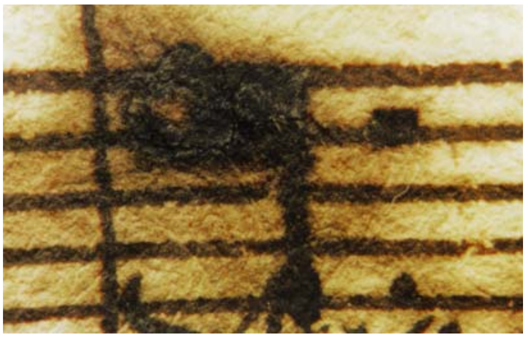

fig.1: J.S. Bach, Serenata für Leopold von Sachsen-Köthen, detail. showing an advanced ink corrosion

The reactions between iron gall ink [Iron(III)gallate] and carrier materials (e.g. paper, parchment) producing the ink corrosion are influenced by environmental and storage conditions especially by a change of temperature and humidity. There are two main reasons that cause the ink degradation of paper. The first one is the acidity of some inks that lead to the hydrolytic splitting of the cellulose. The second reason is the presence of soluble transition metal ions (such as Cu^{2+} and Fe^{2+}) which act as catalysts for the oxidative decomposition of the cellulose.

Experimental

XANES spectra at the Fe K-edge were collected on the microfocus beamline KMC-2 at BESSY, using a SiGe(111) double-crystal monochromator. The XANES-measurements were carried out from 7080eV to 7180eV, with 0.5eV steps for the edge region (7100-7140eV). The data were collected in fluorescence mode. In order to determine concentration profiles of other metals (e.g. Cu) that may influence the ink corrosion µ-XRF-mapping were done (see fig. 2). To decrease the effects of inhomogeneities, the data were collected with a spot size of 30 µm in 50 µm steps.

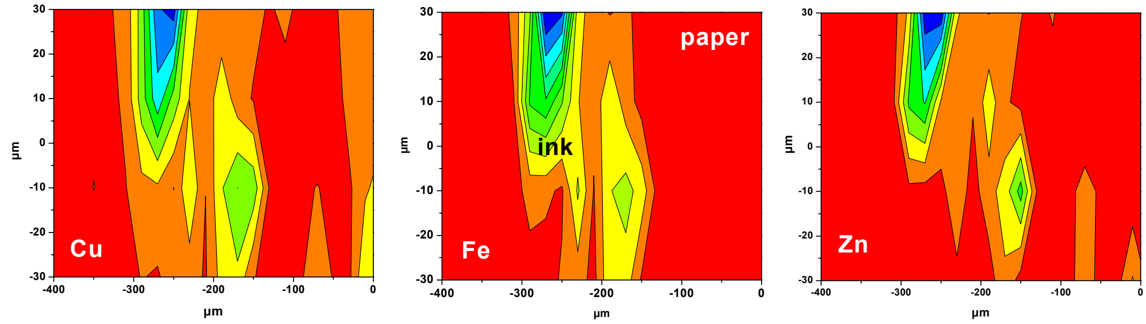

Fig.2: Elemental mapping with µ-XRF experiments, left: Cu, middle: Fe, right: Zn. The three plots show different scalings

Results

µ-XRF: Two manuscripts with different conservation states were investigated. The first sample shows a little amount of ink corrosion, the second one reveals an advanced state of decomposition. The experimental results of the µ-XRF-mapping indicate that both iron gall inks show a good correlation between major and minor components (see fig.3) in the area of the ink.

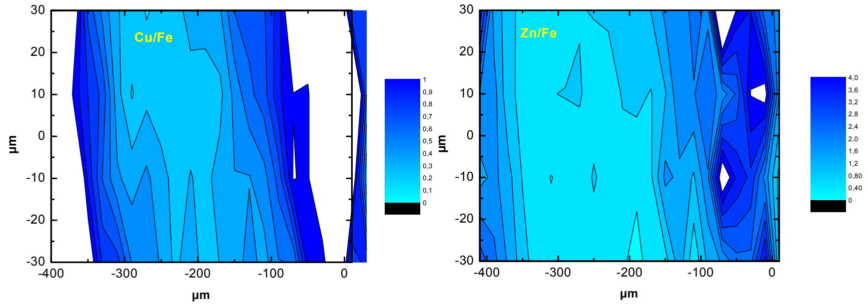

Fig.3: [Cu]/[Fe] and [Zn]/[Fe] ratios, calculated from the signal intensities. In the area of the ink spot the [Cu]/[Fe] and [Zn]/[Fe] ratio is quite constant.

Based on the present results taking into account a homogeneous distribution of major and minor components in the ink we might conclude that no independent migration of elements takes place.

µ-XANES: Both samples show characteristic Fe^{2+}/Fe^{3+} ratios (see fig.4). The first manuscript with the little amount of ink corrosion shows a constant Fe^{2+}/Fe^{3+} ratio, whereas the second sample with the advanced ink corrosion shows a characteristic local dependence between the iron content and the

Fe^{2+}/Fe^{3+} ratio. The inflection points of the various XANES-spectra are taken as a figure of merit for the different Fe^{2+}/Fe^{3+} ratios. A linescan shows the increase of this ratio for a decrease of the iron content (see fig. 4).

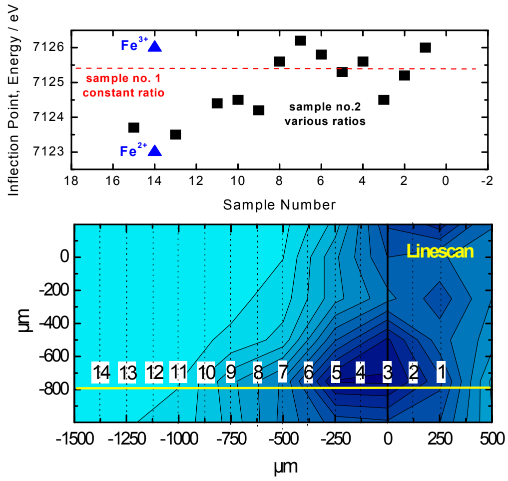

Fig.4: A linescan shows the increase of the Fe^{2+}/Fe^{3+} ratio for a decrease of the iron content

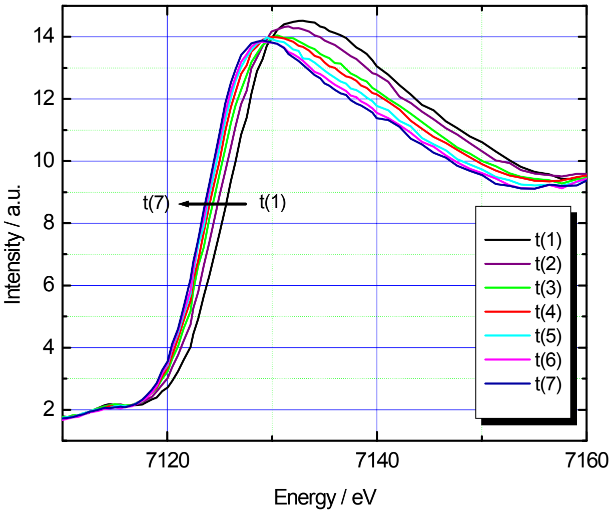

Fig.5: XANES-spectra, collected one after another, on the same spot. The absorption edges approach to the Fe^{2+}- absorption edge

Furthermore the experiments show a remarkable dependence between dose of radiation and position of the absorption edge. Series of XANES-spectra, collected one after another, reveal that the absorption edges approach to the Fe^{2+}- absorption edge (see fig.5).

Conclusions and perspectives

The experiment confirms in agreement with former investigations that the Fe^{2+} content is a chemical indicator for the degree of iron gall ink corrosion. Starting from the XANES-spectra collected from the standards it is not possible to determine the Fe^{2+}/Fe^{3+}-ratio by means of linear combination of data. For the correct determination of the Fe^{2+}/Fe^{3+} ratios in iron gall inks and the evaluation of the method in general further abinitio-calculations are necessary.

The investigations show a dramatic displacement of the redox equilibrium from a higher to a lower oxidation state of iron depending on the radiation dose. This phenomenon has already been observed in solid matters. Further investigations should clarify which parameters (e.g. humidity, matrix) influence this characteristic change.

After all subsequent investigations should verify the correlation between ink corrosion and other transition elements, such as Cu and Zn as possible catalysts for decomposition processes.

Acknowledgements

The authors are grateful to the Staatsbibliothek Berlin, Stiftung Preußischer Kulturbesitz.

Layer-by-layer growth of GaAs(001) studied by in situ synchrotron x-ray diffraction

Wolfgang Braun, Bernd Jenichen, Vladimir M. Kaganer,
Alexander G. Shtukenberg, Lutz Däweritz, and Klaus H. Ploog
Paul-Drude-Institut für Festkörperelektronik,
Hausvogteiplatz 5–7, D-10117 Berlin, Germany

Molecular beam epitaxy (MBE) is a versatile method to grow single crystals and heteroepitaxial structures with atomic layer precision. Layer-by-layer growth in MBE is commonly monitored by reflection high-energy electron diffraction (RHEED) through periodic modulations of the scattered intensity. Although RHEED intensity oscillations are widely used to control growth and measure growth rates, a quantitative interpretation of the measured intensities remains difficult due to the strong interaction of electrons with the surface, leading to strong multiple (dynamical) scattering. Due to the weak x-ray–matter interaction, surface x-ray scattering can be quantitatively interpreted using kinematical theory, thus providing information on the structure and morphology of the surface.

Here we report on surface x-ray scattering studies of GaAs(001) MBE growth [1]. The experiments were performed at the PHARAO surface diffraction beamline U125/2-KMC, dedicated to the *in situ* analysis of MBE growth of III-V-based structures [2]. The beamline is designed to perform diffraction experiments on surfaces and interfaces in an ultrahigh vacuum (UHV) environment during crystal growth by MBE.

We characterize the surface morphology first. Figure 1 presents ω scans (rotation of the sample about its normal) obtained on the same sample on two subsequent days of the x-ray measurements. The splitting of the peaks in Fig. 1(a) is the result of an ordered staircase of steps. From the angular peak separation $\Delta\omega = 0.029°$, one can determine the average terrace width $l_T = 366$ nm, smaller than the result of the AFM measurements on that sample (500 nm). The peak in Fig. 1(b) is not split, indicating stronger disorder in the terrace widths. The integrated intensities of the peaks in Figs. 1(a) and 1(b) differ by less than 3 %, which directly confirms the consistency of our treatment and the validity of the kinematical theory used.

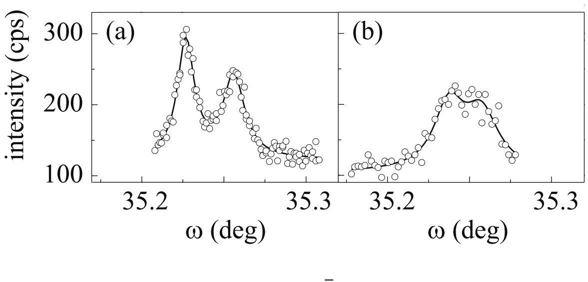

FIG. 1: Omega scans of the $\bar{3}\,1\,0.05$ reflection. Measurement (b) was carried out one day after measurement (a). The growth experiments were performed in between. Solid lines are fits to a sum of two Lorentzians. The substrate temperature is 560 °C and the V/III ratio is 9 based on hypothetical growth with a period of 7 s.

We performed time-resolved x-ray intensity measurements at different points L along the crystal truncation rods (CTRs) $\bar{1}1L$, $13L$, and $\bar{3}1L$. Figure 2 shows the time dependence of x-ray intensities recorded at different L along the CTR $13L$ (open circles). The background intensity is obtained from sufficiently wide ω scans of the sample prior to growth and subtracted from the measured intensity. The period of the intensity oscillations $\tau = 7\,\mathrm{s}$ is the time required to complete one bilayer of the GaAs crystal. From the measured time-dependent intensities, we obtain the layer coverages during growth. The solid lines in the intensity plots of Fig. 2 are calculated with the layer coverages $\theta_n(t)$ presented in the top panel. The fit of the intensity curves is obtained simultaneously, i.e. with one and the same layer coverages $\theta_n(t)$, for all values of L. At small L, the intensity decreases to zero at the minimum of the first oscillation, indicating that only one layer is partially covered at that moment. However, the following maxima do not reach the initial intensity, which means that the next layer starts to grow somewhat before the previous one is completed. The growth is rather close to the ideal, with the next layer containing less than 10 % when the previous one is filled to about 90%.

We conclude from the simultaneous fit of all curves that the structure amplitudes do not change during growth. The structure amplitude includes contributions from the bulk crystal and the reconstructed layer on top of it. A constant structure amplitude during growth means that the structure of the reconstructed cell is preserved during growth. On integer-order rods, the domain size of the reconstruction or any disorder in the relative positions of the surface unit cells is irrelevant, since all surface unit cells add up in phase. The simultaneous fit of the intensity curves for different L

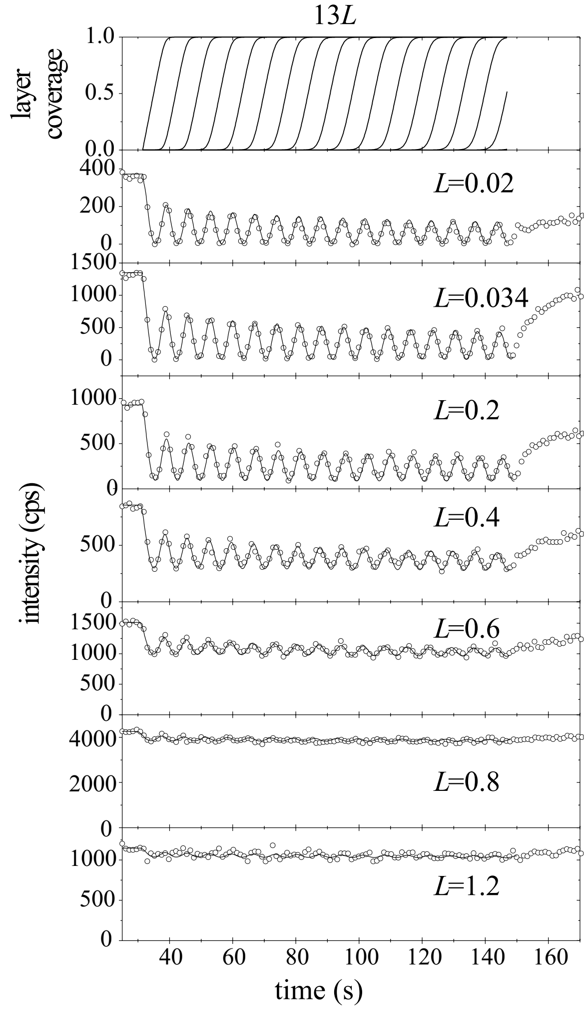

FIG. 2: X-ray intensity oscillations measured during the MBE of GaAs(001) at different points along the crystal truncation rod 13L (open circles). The fit (solid curves) is obtained simultaneously for all curves with the layer coverage shown in the top panel of the figure. The substrate temperature was 570 °C and the V/III ratio 13 at the start of the growth interval, 8 at the end of it.

also proves that the reconstruction is established on top of a nucleated layer in a time much smaller than the growth period.

Figure 3 compares the intensities along the CTR obtained prior to a growth run (completely covered surface layer) and at the first intensity minimum during growth (half-covered surface layers). The full symbols are the initial intensities obtained before growth by integrating over the ω scan. This is the quantity commonly measured and analyzed in surface structure analysis. The solid line is the CTR calculated by using the atomic coordinates of the GaAs(001) $\beta(2\times4)$ unit cell determined by room-temperature x-ray surface structure analysis [3], and assuming a flat surface without steps.

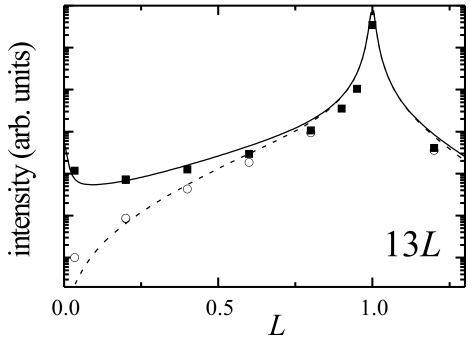

FIG. 3: Measured and calculated intensities along crystal truncation rods prior to growth (full symbols and solid lines) and at the first minimum of the growth intensity oscillations (open symbols and dashed lines).

From the good agreement between the measured and calculated CTRs, we conclude that the positions of the atoms in the reconstructed unit cell do not change noticeably between room temperature and the growth temperature.

The open symbols in Fig. 3 represent the intensity at the minimum of the first oscillation during growth, scaled to the pre-growth intensity. The first intensity minimum corresponds to the deposition of half a monolayer. The dashed curves in Fig. 3 are calculated with the same assumptions regarding surface flatness and atomic positions in the reconstructed cell as above, but with a 50% covered second layer. The agreement between the measurements and the calculations confirms that the structure of the $\beta(2\times4)$ surface reconstruction cell does not change during growth.

Thus, the results obtained at our combined synchrotron x-ray diffraction / MBE beamline show submonolayer sensitivity of surface diffraction experiments, which allows us to perform a detailed time-resolved analysis of GaAs(001) homoepitaxial growth.

---

[1] W. Braun, B. Jenichen, V. M. Kaganer, A. G. Shtukenberg, L. Däweritz, and K. H. Ploog, Surf. Sci. (2003), in press.

[2] B. Jenichen, W. Braun, V. M. Kaganer, A. G. Shtukenberg, L. Däweritz, C.-G. Schulz, K. H. Ploog, and A. Erko, Rev. Sci. Instrum. **74**, (2003), in press.

[3] Y. Garreau, M. Sauvage-Simkin, N. Jedrecy, R. Pinchaux, and M. B. Veron, Phys. Rev. B **54**, 17638 (1996).

Two-dimensional coarsening kinetics of reconstruction domains: GaAs(001)$\beta(2\times4)$

Vladimir M. Kaganer, Wolfgang Braun, Bernd Jenichen, Lutz Däweritz, and Klaus H.Ploog
Paul-Drude-Institut für Festkörperelektronik,
Hausvogteiplatz 5–7, D-10117 Berlin, Germany

A system quenched into a non-equilibrium polydomain state tries to reduce the total energy of the domain interfaces by increasing the sizes of individual domains. Lifshitz [1] and Allen and Cahn [2] showed that, if the domain coarsening is not restricted by a conservation law, the average domain size l increases in time as $l(t) \propto t^n$, with an exponent $n = 1/2$ in both two- and three-dimensional systems. Numerous computer simulations on the standard (Ising, Potts, XY, planar-rotor) models have shown the universality of the exponent 1/2 in two- and multistate systems. Although most of the numerical simulations were performed on two-dimensional models, the domain coarsening kinetics in two-dimensional systems with nonconserved order parameter was the subject of only very few experimental works. We are aware of studies on just one system, a chemisorbed oxygen monolayer on a tungsten surface, by low energy electron diffraction [3–5].

In the present work, we perform time-resolved x-ray diffraction studies of the coarsening kinetics of the $\beta(2\times4)$ reconstruction domains on the GaAs(001) surface. If a weak ordering along the short axis of the unit cell is neglected, the system possesses $m = 4$ equivalent translational domains (90° rotational domains are absent since the surface is polar) with two non-equivalent types of boundaries between the domains [6].

The measurements were performed at the PHARAO surface diffraction beamline U125/2-KMC in a combined molecular beam epitaxy (MBE) / 6-circle diffractometer system dedicated to the *in situ* x-ray scattering analysis of III-V semiconductors [7]. Standard MBE sample preparation procedures were used. From the rocking curve of the integer-order surface reflection 1 3 0.05, we obtain a mean terrace width $l = 2/\Delta q$ [where Δq is the full width at half maximum (FWHM) deconvolved with the instrumental resolution] of approximately 450 nm, which agrees with atomic force microscopy measurements of one of the samples.

X-ray diffraction allows for a separate study of the reconstruction domains in fractional-order reflections and the surface morphology in integer-order reflections, since the reconstruction domains differ by translations being multiples of the bulk lattice spacing and are not seen in the integer-order reflections.

For a quantitative study of reconstruction domain coarsening, we deposit one layer of GaAs. During the deposition, two-dimensional islands nucleate, grow in size by incorporating further adatoms, and coalesce. We can expect that the reconstruction develops independently on each island. The deposition of one layer results in a flat surface with as many reconstruction domains as two-dimensional islands were nucleated during the deposition. The inset in Fig. 1(c) shows the kinetics of the surface morphology. Intensity variations during the recovery in Fig. 1(c) are the result of interference between different reconstruction domains. The intensity increases due to domain coarsening and finally reaches a maximum when the domain sizes exceed the resolution of the x-ray diffraction experiment. Then, the different domains add incoherently to the total signal. This interpretation is verified in Figs. 1(d,e), which present ω-scans during recovery and the integrated intensities of the reflections, respectively. The ω-scans were obtained by stepwise rotation of the sample about its normal. One scan takes approximately 75 s.

The integrated intensity of each reflection changes only during the initial 300 s, Fig. 1(e), which can be explained by contributions from the domain boundaries covering a noticeable part of the surface when the domains are small. At later times, the integrated intensity does not change in time, as expected: this is the quantity used in structure analysis since it does not depend on the domain size. We conclude that, during recovery, the atomic structure of the reconstructed unit cell and the area of the reconstructed surface do not change.

Figure 1(f) presents the correlation lengths $l(t) = 2/\Delta q(t)$ obtained from the FWHMs $\Delta q(t)$ of the Lorentzian components of the Voigt fits shown in Fig. 1(b). The correlation lengths follow a power law, $l(t) \propto t^n$, with notably different exponents of half- and quarter-order reflections, given in Fig. 1(f).

Thus, we find that two-dimensional multidomain systems with energetically non-equivalent domain boundaries show a slower coarsening compared to the standard Lifshitz–Allen–Cahn theory. The system under investigation, $\beta(2\times4)$-reconstructed GaAs(001) surface, possesses four equivalent translational domains with two non-equivalent types of

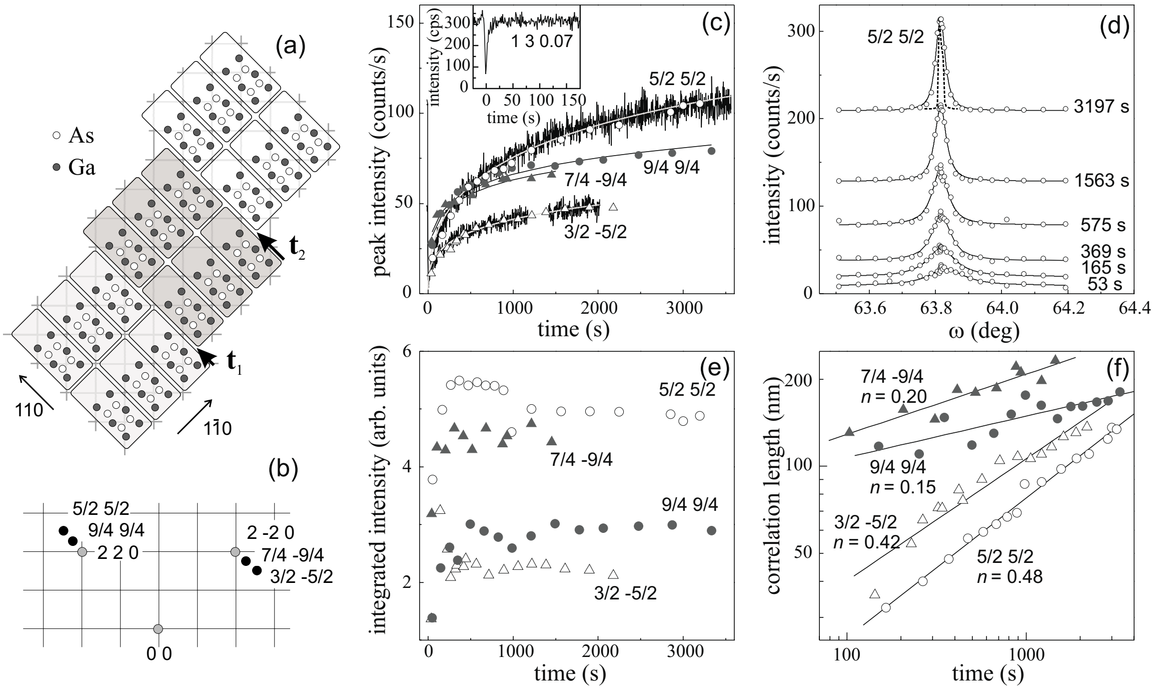

FIG. 1: (a) Unit cells and domains of the $\beta(2\times 4)$ reconstruction. Only the top As and Ga layers are shown. The characteristic feature of this reconstruction are the rows of missing As dimers, commonly seen as grooves on scanning tunneling microscope (STM) images. The boundaries between reconstruction domains are two non-equivalent stacking faults, $\mathbf{t}_1 = \pm\frac{1}{2}[110]$ and $\mathbf{t}_2 = [110]$, seen as kinks of the grooves in STM. The square mesh represents the termination of the bulk GaAs(001) surface. (b) Fractional order reflections chosen for the present study (black dots) and the nearest bulk reflections (gray dots). (c) Time dependence of the peak intensities after the deposition of one layer of GaAs. Black lines represent the measured peak intensities of the half-order reflections. Symbols are the peak intensities obtained from ω-scans during the recovery. The inset shows the kinetics of two-dimensional islands measured in an integer-order reflection. (d) ω-scans performed during the recovery. The time at each curve shows the moment of the measurement of the center of the curve. The broken line at the top curve is an ω-scan of the bulk reflection 220 used as the resolution. The solid lines are the Voigt function fits to the experimental data. The curves are shifted vertically for clarity. (e) Time dependence of the integrated intensities obtained from the Voigt fits shown in the ω-scans. The integrated intensity of the $\frac{7}{4}\frac{\bar{9}}{4}$ reflection is increased by a factor of 2. (f) Time dependence of the correlation lengths $l = 2/\Delta q$ obtained from the FWHMs Δq of the Lorentzian components of the Voigt function. The exponents n of the power law $l \propto t^n$ are shown for each reflection. The measurements were performed in the reciprocal space points $\frac{5}{2}\frac{5}{2}0.1$, $\frac{9}{4}\frac{9}{4}0.1$, $\frac{3}{2}\frac{\bar{5}}{2}0.2$, and $\frac{7}{4}\frac{\bar{9}}{4}0.2$. The in-plane Miller indices of the reflections are given in the Figure, the third index is omitted for simplicity. The substrate temperature is 530 °C, the V/III flux ratio during deposition is 2, the growth rate is 0.2 ML/s.

boundaries between the domains. Using *in situ* x-ray diffraction, we find that the growth of the reconstruction domains is described by two different time exponents: the correlation length increases as $l \propto t^{0.42\pm0.05}$ in the half-order reflections and $l \propto t^{0.22\pm0.05}$ in the quarter-order reflections.

---

[1] I. M. Lifshitz, Zh. Eksp. Teor. Fiz. **42**, 1354 (1962), [Sov. Phys. JETP **15**, 939 (1962)].

[2] S. M. Allen and J. W. Cahn, Acta Metall. **27**, 1085 (1979).

[3] G.-C. Wang and T.-M. Lu, Phys. Rev. Lett. **50**, 2014 (1983).

[4] P. K. Wu, J. H. Perepezko, J. T. McKinney, and M. G. Lagally, Phys. Rev. Lett. **51**, 1577 (1983).

[5] M. C. Tringides, P. K. Wu, and M. G. Lagally, Phys. Rev. Lett. **59**, 315 (1987).

[6] Y. Garreau, M. Sauvage-Simkin, N. Jedrecy, R. Pinchaux, and M. B. Veron, Phys. Rev. B **54**, 17638 (1996).

[7] B. Jenichen, W. Braun, V. M. Kaganer, A. G. Shtukenberg, L. Däweritz, C.-G. Schulz, K. H. Ploog, and A. Erko, Rev. Sci. Instrum. **74**, (2003), in press.

Island and hole kinetics on the growing GaAs(001) surface studied by synchrotron x-ray diffraction

Wolfgang Braun, Bernd Jenichen, Vladimir M. Kaganer,
Alexander S. Shtukenberg, Lutz Däweritz, and Klaus H. Ploog
Paul-Drude-Institut für Festkörperelektronik,
Hausvogteiplatz 5–7, D-10117 Berlin, Germany

Layer-by-layer growth is one of the basic growth modes in molecular beam epitaxy (MBE). The atoms arriving from the incoming flux diffuse on the surface until they nucleate monolayer-high islands. The islands grow by attaching further adatoms, coalesce and form a complete crystal layer. When one layer is almost completed, the atomic steps at the island edges no longer are sufficiently strong sinks for adatoms, and the next layer starts to nucleate and grow on top of the islands. The number of incompletely covered layers increases during growth. When the deposition is interrupted, the system tries to reduce its energy by smoothing the surface. This process is called recovery. Two processes, a fast and a slow one, have been identified in the recovery by reflection high energy electron diffraction (RHEED) [1–3]. The RHEED signal was fitted by a sum of two exponentials and explained either as short-range and long-range ordering [1], surface reconstruction changes and rearrangement of islands [2], or group III element migration and restoration of long-range order [3], respectively.

In the present work, we demonstrate that a reliable quantitative analysis of the recovery process can be performed using in situ synchrotron x-ray diffraction. We identify the two processes during recovery as island–hole annihilation and island or hole coarsening.

The experiments were performed at the PHARAO surface diffraction beamline U125/2-KMC, dedicated to the *in situ* analysis of MBE growth of III-V-based structures [4]. The beamline is designed to perform diffraction experiments on surfaces and interfaces in an ultrahigh vacuum (UHV) environment during crystal growth by MBE. GaAs homoepitaxy was performed in the center of the $\beta(2\times4)$ reconstruction temperature range, which corresponds to a substrate temperature of 520 °C. The V/III ratio, determined from As-limited growth oscillations, was around 2 during deposition.

To keep the thermal diffuse scattering background sufficiently low, either a grazing incidence or grazing exit geometry needs to be used in x-ray surface diffraction. It turns out that for GaAs(001), grazing incidence *and* grazing exit can be combined. This is due to the fact that the thickness of the growing layers is only half the period of the bulk cubic unit cell. Successive layers are therefore shifted laterally with respect to each other. From a diffraction point of view, the crystal grows in an ABAB stacking sequence. By placing the detector at a position of destructive interference of A and B layers, one can therefore measure growth oscillations in an in-plane geometry [5, 6].

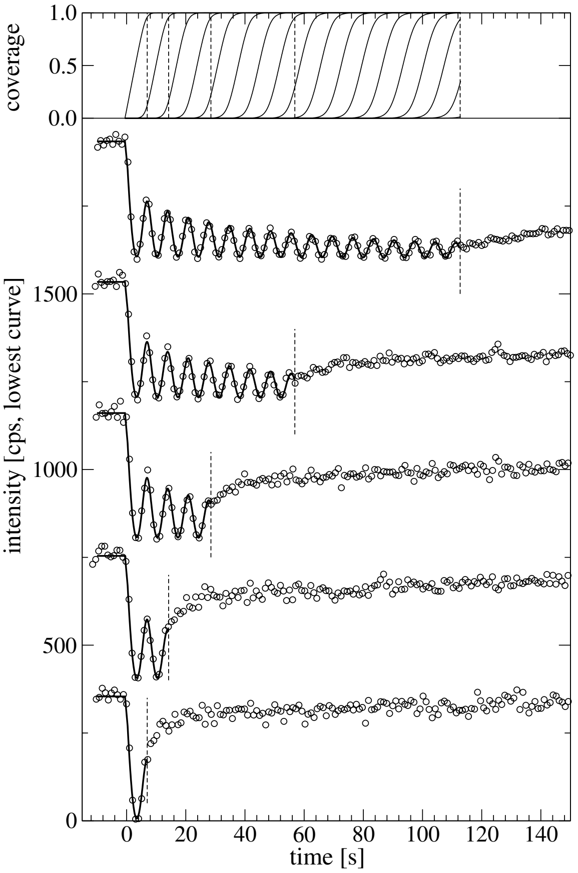

FIG. 1: X-ray intensity oscillations and fits to the curves yielding the layer coverages as a function of time. The growth terminations marked by dashed lines are determined from the starting points of the fits in Fig. 2 assuming annihilation of islands and holes during the fast recovery phase.

To study the recovery of a multi-layer surface morphology, we have measured complete growth and recovery sequences with close to 1, 2, 4, 8 and 16 ML deposition. The corresponding peak intensity curves are shown in Fig. 1. The layer coverages

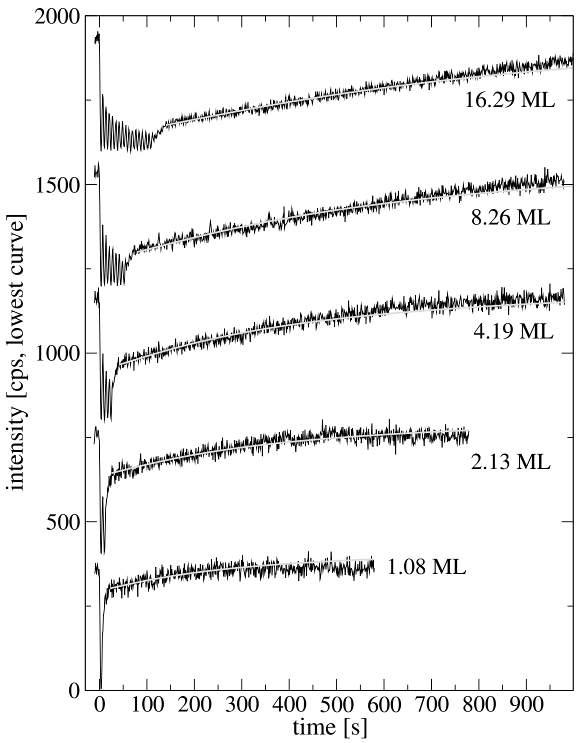

FIG. 2: Time dependence of the peak intensities after deposition of different near-integer numbers of layers.

shown in the top part of the figure were obtained from a model-independent fit [6] describing each layer by a smoothed Heaviside function. From the fits to the recovery curves, a certain coverage at the starting point of recovery results in a given intensity, since a difference between the total coverages of A and B layers results in a nonzero interference. To link the coverages from the oscillation fit to the recovery fit, Fig. 2, we sum up the layer coverages at the end of growth, counting coverages between 0 and 0.5 as positive, and subtracting the coverages between 0.5 and 1.0 for the almost completed layers. This corresponds to filling 2D holes with material from the islands, until a net coverage remains. If we take this net coverage as the starting point for the recovery fit, we can determine the time at which growth was terminated during the last growth oscillation. The fits to the recovery curves done in this way are shown in Fig. 2, the numbers at the curves giving the layer coverages determined from the starting points of the fits.

The positions along the time axis where growth was interrrupted are marked with dashed lines in Fig. 1. These positions should correspond to the shutter opening times that were used during growth, if the model is correct. The shutter times are compared to the deposition times obtained from the fits in Table I. The deviations are well below 1 % for all but the 1.08 ML growth. The good agreement indicates that our interpretation is indeed valid. We therefore associate the fast, short recovery process directly following the termination of growth with the mutual annihilation of holes and islands on the surface. The slower subsequent recovery is due to Ostwald ripening with island or hole coarsening. Both small islands and holes reduce their energy by shrinking in size, and therefore the annihilation process is faster. In Ostwald ripening, the large islands take up the material released from the small ones by increasing their energy, although at a slower rate than the one at which the small islands reduce their energy. The Ostwald ripening process is therefore slower.

Thus, the connection of quantitative fits for the layer coverages during layer-by-layer growth and during recovery leads us to explain the intermediate fast recovery process by the mutual annihilation of islands and holes.

coverage	shutter time	fit	deviation
1.08 ML	7.1 s	6.97 s	-1.5 %
2.13 ML	14.2 s	14.20 s	+0.3 %
4.19 ML	28.3 s	28.50 s	+0.7 %
8.26 ML	56.6 s	56.86 s	+0.4 %
16.29 ML	113.2 s	112.72 s	-0.5 %

TABLE I: Coverages and deposition times used for growth of the GaAs layers compared to the times obtained from the recovery fits.

[1] B. F. Lewis, F. J. Grunthaner, A. Madhukar, T. C. Lee, and R. Fernandez, J. Vac. Sci. Technol. B **3**, 1317 (1985).

[2] B. A. Joyce, T. Shitara, A. Yoshinaga, D. D. Vvedensky, J. H. Neave, and J. Zhang, Appl. Surf. Sci. **60/61**, 200 (1992).

[3] J. Hopkins, M. R. Leys, J. Brübach, W. C. van der Vleuten, and J. H. Wolter, Appl. Surf. Sci. **84** 299 (1995).

[4] B. Jenichen, W. Braun, V. M. Kaganer, A. G. Shtukenberg, L. Däweritz, C.-G. Schulz, K. H. Ploog, and A. Erko, Rev. Sci. Instrum. **74**, no. 3 (2003), in press.

[5] E. Vlieg, J. F. van der Veen, S. J. Gurman, C. Norris, and J. E. MacDonald, Surf. Sci. **210**, 301 (1989).

[6] W. Braun, B. Jenichen, V. M. Kaganer, A. S. Shtukenberg, L. Däweritz, and K. H. Ploog, Surf. Sci. (2003), in press.

Coarsening kinetics of 2D islands on GaAs(001) surface

Wolfgang Braun, Vladimir M. Kaganer, Bernd Jenichen, Lutz Däweritz, and Klaus H.Ploog
Paul-Drude-Institut für Festkörperelektronik,
Hausvogteiplatz 5–7, D-10117 Berlin, Germany

Epitaxial growth on large terraces proceeds by nucleation of two-dimensional (2D) islands, their growth by incorporation of further adatoms, and coalescence. When the deposition is interrupted, the 2D islands coarsen by Ostwald ripening: larger islands grow at the expense of smaller ones, which dissolve because they possess larger specific step energy. The kinetics of Ostwald ripening is well established in both 2D and 3D systems (for reviews see Refs. [1, 2]). The mean island size $l(t)$ follows a power law, $l(t) \propto t^n$, with the exponent $n = 1/3$ for diffusion-limited kinetics [3] and $n = 1/2$ for attachment-limited kinetics [4]. Numerous experiments and simulations [1, 2] show that these exponents are universal, independent of other features of the system. Diffusion-limited kinetics is the common mechanism during the late stages of spinodal decomposition in 3D solid solutions and is also observed in various 2D systems. Attachment-limited kinetics was proven to be the mechanism of coarsening of 2D islands on the Si(001) surface [5, 6], a system fairly close to the subject of the present study.

In the present work, we show that the coarsening of 2D islands on the reconstructed GaAs(001)$\beta(2\times 4)$ surface proceeds in a qualitatively different way: the coarsening exponent is $n = 1$, i.e., the mean island size increases *linearly* in time. The experimental verification of this result is based on the direct determination of the mean island size $l(t)$ from the widths of the x-ray diffraction peaks with a simultaneous check of mass conservation. We also determine the coverage, temperature, and orientation dependence of the coarsening rate.

The measurements, Fig. 1, were performed at the PHARAO surface diffraction beamline U125/2-KMC, dedicated to the *in situ* analysis of MBE growth of III-V-based structures in a combined molecular beam epitaxy (MBE) / 6-circle diffractometer system [7]. Standard MBE sample preparation procedures were used.

The bulk GaAs structure provides a possibility to obtain the highest sensitivity to surface steps while maintaining grazing incidence and grazing exit diffraction conditions. GaAs(001) grows by incorporating Ga-As bilayers. The bulk GaAs unit cell is formed by two such bilayers, being shifted by a relative translation $\mathbf{t} = a[0\frac{1}{2}\frac{1}{2}]$, where a is the bulk lattice period. A single surface step is one bilayer high and hence involves an in-plane translation of half the in-plane lattice period. When two columns (normal to the surface) of bulk unit cells are terminated at adjacent terraces separated by a single step, they are related by the translation $\mathbf{t}$. The same translation applies to the reconstructed cells on these terraces. Then, for a reflection $\mathbf{Q} = (2\pi/a)[hkL]$, the structure amplitudes of the two terraces differ by a phase factor $\exp(i\Phi)$, where $\Phi = \mathbf{Q}\cdot\mathbf{t} = \pi(k + L)$. In a reflection with odd h and k, the phase factor $\Phi = \pi$ is reached at $L = 0$ and causes destructive interference of waves diffracted from two adjacent terraces, resulting in the highest sensitivity to surface steps. In other words, the steps are detected due to a lateral displacement of the atoms by half the lattice period, rather than due to their vertical displacement.

Figure 1(b) shows the recovery of the diffracted intensity in the 1 3 0.05 reflection after the deposition of 0.5 monolayer (ML) of GaAs. The intensity drops to zero directly after the deposition, as a result of the destructive interference on the half-covered surface. The subsequent intensity increase is due to the growth of 2D islands: the number of 2D islands which coherently contribute to the diffracted intensity within the resolution of the diffraction experiment decreases. On a late stage, the island size exceeds the resolution limit and each island contributes incoherently.

More insight into the island growth is obtained from the ω-scans (rocking curves) performed during the recovery, Fig. 1(a). The ω-scans were obtained by stepwise rotation of the sample about its normal. Each scan took approximately 75 s. The ω steps were chosen non-uniformly, with a smaller spacing near the peak position, which allowed to accurately determine the shape both of wide peaks at the beginning of recovery and of narrow peaks at its end. The ω-scans were fitted to Voigt functions with the width of the Gaussian component fixed by the resolution and a variable width of the Lorentzian component. The resolution was obtained by interpolating between the peak widths of the 200, 220, and 400 in-plane bulk reflections. As an example, the ω-scan of the 220 reflection is shown in Fig. 1(a) by a broken line. We find that the Voigt function fit gives smaller χ^2 values than a Lorentzian or a Gaussian fit with the same number of fit parameters. Hence, the intrinsic peak profile is Lorentzian, which indicates an exponential correlation function. Repeatability of the intensity measurements is shown in Fig. 1(b) where the intensity maxima obtained in the ω-scans (circles)

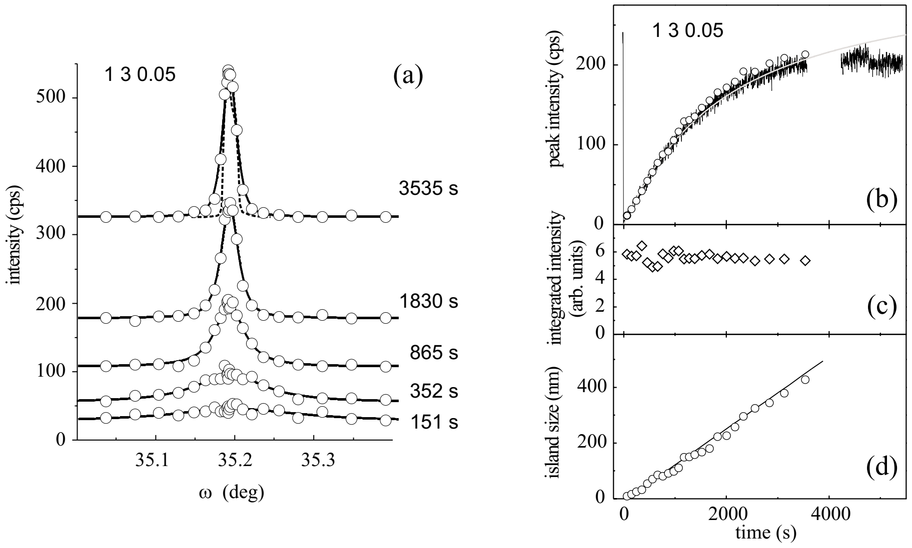

FIG. 1: (a) ω-scans performed during the recovery at the 1 3 0.05 reflection after deposition of 0.5 ML of GaAs. The time at each curve shows the moment of the measurement of the center of the curve. The broken line at the top curve is an ω-scan of the bulk reflection 220 used as the resolution. The curves are Voigt function fits to the experimental data. The curves are shifted vertically for clarity. (b) Time dependence of the peak intensity. The black line is the measured peak intensity. Circles are the peak intensities obtained from the ω-scans during recovery. The smooth gray line is a fit. (c) Time dependence of the integrated intensity obtained from the Voigt fits. (d) Time dependence of the correlation length $l = 2/\Delta q$ obtained from the FWHMs Δq of the Lorentzian components of the Voigt functions. Here, as in all subsequent figures, the measured intensity is normalized to a storage ring current of 100 mA and the background is subtracted. The substrate temperature is 530 °C, the V/III flux ratio during deposition is 2, the growth rate is 0.2 ML/s.

are overlapped with the peak intensity measured in an independent growth run (black curve).

The integrated intensities obtained from the ω-scans, Fig. 1(c), do not depend on time. In the kinematical theory of scattering, the integrated intensity is proportional to the total number of scatterers. Hence, the constant integrated intensity verifies the conserved coarsening of the 2D islands. Figure 1(d) presents the correlation length $l(t) = 2/\Delta q(t)$ obtained from the full width at half maximum (FWHM) $\Delta q(t)$ of the Lorentzian component of the Voigt fits shown in Fig. 1(a). The linear time dependence of the correlation length $l(t)$ on time t is evident from the plot. This is the main result of the present paper. The mean size of 2D islands increases with a constant rate of $dl/dt = 0.11$ nm/s.

Thus, the coarsening kinetics of 2D islands on the GaAs(001)$\beta(2 \times 4)$ reconstructed surface does not fall into one of the universality classes of conserved coarsening kinetics. The exponent $n = 1$, obtained in our x-ray diffraction experiment, is unexpectedly large and probably establishes a new universality class. The origin of this fast coarsening is not clear at present. It may be related to the large density of adatoms on the GaAs(001) surface [8], specific to the binary compound [9].

---

[1] O. G. Mouritsen, in *Kinetics of Ordering and Growth at Surfaces*, edited by M. G. Lagally (Plenum Press, N. Y., 1990), p. 1.
[2] A. J. Bray, Adv. Phys. **43**, 357 (1994).
[3] I. M. Lifshitz and V. V. Slyozov, J. Phys. Chem. Solids **19**, 35 (1961).
[4] C. Wagner, Z. Elektrochem. **65**, 581 (1961).
[5] W. Theis, N. C. Bartelt, and R. M. Tromp, Phys. Rev. Lett. **75**, 3328 (1995).
[6] N. C. Bartelt, W. Theis, and R. M. Tromp, Phys. Rev. B **54**, 11741 (1996).
[7] B. Jenichen, W. Braun, V. M. Kaganer, A. G. Shtukenberg, L. Däweritz, C.-G. Schulz, K. H. Ploog, and A. Erko, Rev. Sci. Instrum. **74**, (2003), in press.
[8] M. D. Johnson, K. T. Leung, A. Birch, B. G. Orr, and J. Tersoff, Surf. Sci. **350**, 254 (1996).
[9] J. Tersoff, M. D. Johnson, and B. G. Orr, Phys. Rev. Lett. **78**, 282 (1997).

NEXAFS study of nanocomposite Co-C films

A.N. Maratkanova[1], A.N. Deev[1], Yu.V. Ruts[1], N.I. Polushkin[2], A.L. Ankudinov[3],
D.V. Vyalikh[4], Y. Liu[5], and D.J. Sellmyer[5]

[1] Physical-Technical Institute, UB RAS, 426001 Izhevsk, Russia
[2] Institute for Physics of Microstructures of RAS, 603950 Nizhni Novgorod, Russia
[3] University of Washington, Seatle, WA 98195-1560, USA
[4] Institut für Experimentalphysik, Freie Universität Berlin,14195 Berlin, Germany
[5] CMRA, University of Nebraska, Lincoln, Nebraska 68588-0113, USA

Recently, nanostructured Fe(Co)-X (X=C,Cr,Pt,Pd,…) films have attracted a lot of research interest and they have been proposed for use as high-density magnetic recording media [1-3]. These films usually are prepared by sputtering multilayers or co-sputtering followed by thermal annealing. The latter procedure facilitates the growth of ferromagnetic grains (dots), which is essential in the context of possible applications. In our work we study a new approach to nanostructuring such films using local heat treatment [4,5]. Earlier the results have been reported (i) on laser-induced ferromagnetic ordering of Fe-C [4] and Co-C [6] films and (ii) on the properties of magnetic nanodot arrays produced by their interferometric laser annealing [6]. The aim of this study is to elucidate the structural changes, which can be responsible for the observed onset of ferromagnetism at short-pulsed (~10^{-8} s) laser irradiation with fluencies of ~0.1 J/cm^2. The peculiarities of such treatments are high annealing temperatures (above melting point) and accordingly short cooling time (~10^{-7} s).

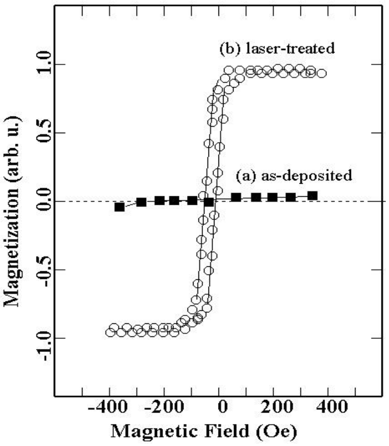

Fig.1. Magnetization curves of an as-deposited (a) and treated (b) Co(50at.%)-C layer

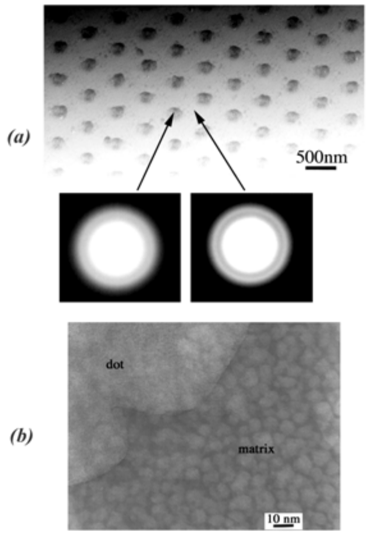

Fig.2. (a) TEM image with diffraction patterns inside the dots and out of them; (b) HRTEM image

In Fig. 1 magnetization curves at room temperatures obtained by SQUID magnetometry are shown (a) for an as-deposited Co(50 at.%)-C layer with a thickness of 30 nm and (b) for this sample after its treatment by interfering beams of an excimer laser. It should be noted that the trend of magnetization curve for the treated Co(50 at.%)-C layer is close to that of pure polycrystalline Co film but with higher saturation magnetization value. It is seen that the treated sample exhibits the hysteresis features which are typical of ferromagnets, while the as-deposited sample did not have a detectable magnetic response at moderate fields (< 500 Oe).

Using transmission electron microscopy (TEM), we have previously examined the nanostructure of as-deposited and treated Co-C samples. Fig. 2 shows TEM images and diffraction patterns of the sample inside the maxima of light intensity [dark contrast in (a)], and out of dots. The diffraction patterns indicate that the differences in the structure of the dots (annealed locations) and surrounding matrix (as-deposited sample) are subtle. Some additional information can be extracted from high resolution images (HRTEM) [Fig. 2(b)]. One can see a well-defined boundary that separates a region of solidified alloy (dot) from the matrix. It is striking that the matrix is essentially inhomogeneous at the scale of 10 nm, whereas the contrast inside the dots is rather uniform.

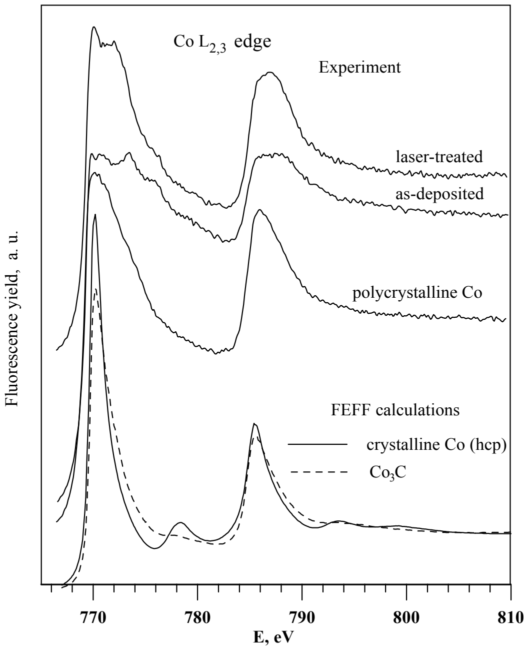

Fig. 3. NEXAFS spectra of as-deposited and laser-treated Co-C thin films in comparison with that of polycrystalline Co and theoretical calculations for crystalline Co and cobalt carbide Co_3C

The Near-Edge X-ray Absorption Fine Structure (NEXAFS) spectra at the Co $L_{2,3}$ edge were measured at the Russian-German Beamline of BESSY-II. The spectra were recorded in the fluorescence mode for as-deposited and laser-treated samples and presented in Fig.3 in comparison with that for pure Co polycrystalline film with a thickness of 20 nm. The experimental NEXAFS spectra are compared also with the spectra calculated by FEFF8 code [7] for crystalline cobalt and cobalt carbide Co_3C. It can be seen that the spectrum for the laser-treated sample is closer to that of a pure polycrystalline Co film. The obtained NEXAFS data allow us to suppose that in average the number of Co-Co pairs increases in treated samples in comparison with as-deposited ones. Such an increase can result in the observed modification in the magnetic properties (Fig.1).

Additional measurements and calculations are planned to verify this supposition.

We gratefully acknowledge technical and financial support provided by Russian-German Laboratory and BESSY II staff.

References

1. T. Hayashi, S. Hirono, M. Tomita, and S. Umemura, Nature (London) **381**, 772 (1996).
2. M. Yu, Y. Liu, and D.J. Sellmyer, J. Appl. Phys., **85**, 4319 (1999);
3. D. Babonneau, J. Briatico, F.Petroff, T. Cabioc'h, and A. Naudon, J.Appl.Phys, **87**, 3432 (2000);
4. N.I. Polushkin, S.A. Gusev, and M.N. Drozdov, Yu.K. Verevkin, and V.N. Petryakov, J.Appl. Phys. **81**, 5478 (1997);
5. A.M. Alekseev, Yu.K. Verevkin, N.V. Vostokov, V.N. Petryakov, N.I. Polushkin, A.F. Popkov, and N.N. Salashchenko, JETP Letters (RAS) **73**, 192 (2001);
6. M. Zheng, M. Yu, Y. Liu, R. Skomski, S.H. Liou, D.J. Sellmyer, V.N. Petryakov. Yu.K. Verevkin, N.I. Polushkin, and N.N. Salashchenko, Appl. Phys. Lett. 79, 2606 (2001);
7. A. L. Ankudinov, B. Ravel, J.J. Rehr, S.D. Conradson, Phys. Rev. B, **58**, 7565 (1998).

$\theta/2\theta$-x-ray reflection and XMLD investigations of NiO/NiFe exchange-bias bilayers modified by He-ion bombardment

D. Engel, I. Krug, A. Ehresmann, H. Schmoranzer
Fachbereich Physik, Technische Universität Kaiserslautern, D-67663 Kaiserslautern

H.C. Mertins, D. Abramsohn, W. Gudat
BESSY GmbH, D-14195 Berlin

He-ion bombardment at defined ion doses in an external magnetic field enables designing exchange-biased bilayer systems both in magnitude and in direction of the exchange bias field [1,2]. Defect creation in the antiferromagnet and at the ferromagnet-antiferromagnet interface due to the ion bombardment is regarded as a possible mechanism for the observed enhancement and reduction of the exchange bias field H_{eb}. In the present work, the ion bombardment induced changes in exchange biased polycristalline Ta(2nm)/NiFe(5nm)/NiO(50nm)/Si bilayer systems were investigated element selectively by $\theta/2\theta$-x-ray reflection and XMLD measurements. Experiments were carried out with the BESSY polarimeter [4] at the beamline UE56/1-PGM at BESSYII. The layer system has been sputter deposited and annealed [3]. After preparation the samples were bombarded with different ion doses in an applied magnetic field and the resulting exchange bias field was determined by L-MOKE.

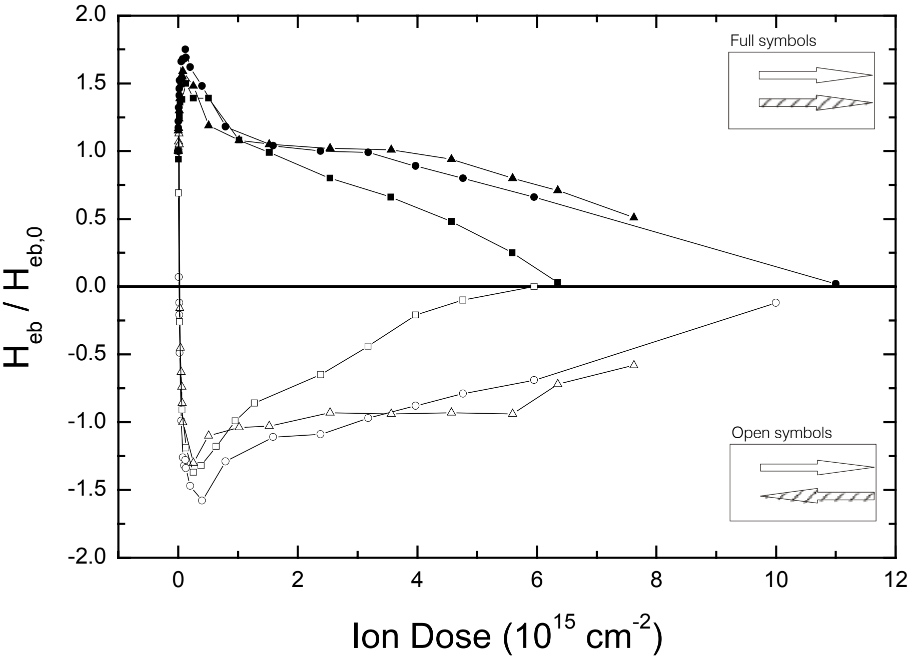

Fig. 1: Normalized exchange bias field $H_{eb}/H_{eb,0}$ as function of the He-ion dose for three different acceleration voltages: 5kV (squares), 10kV (circles) and 20kV (triangles), for a magnetic field applied during ion bombardment parallel (full symbols) and antiparallel (open symbols) to the growth field [3].

In Fig.1 the ion dose dependence of $H_{eb}/H_{eb,0}$ for He-ion bombardment at different acceleration voltages is shown. For bombardment in an applied magnetic field parallel to the field direction during preparation (H_{bom} ↑↑ H_{gro}) H_{eb} was enhanced for low ion doses (<1x10^{14} ions/cm^2). With further increase of the He-ion dose, H_{eb} is reduced up to complete suppression. For bombardment in a field H_{bom} ↓↑ H_{gro}, the exchange bias field is reversed in sign, but shows qualitatively the same dependence on the ion dose as for H_{bom} ↑↑ H_{gro}.

To investigate element specific hysteresis loops, samples were bombarded with an ion dose of 1x10^{14} ions/cm^2 to achieve a maximum enhancement or reversal of H_{eb}.

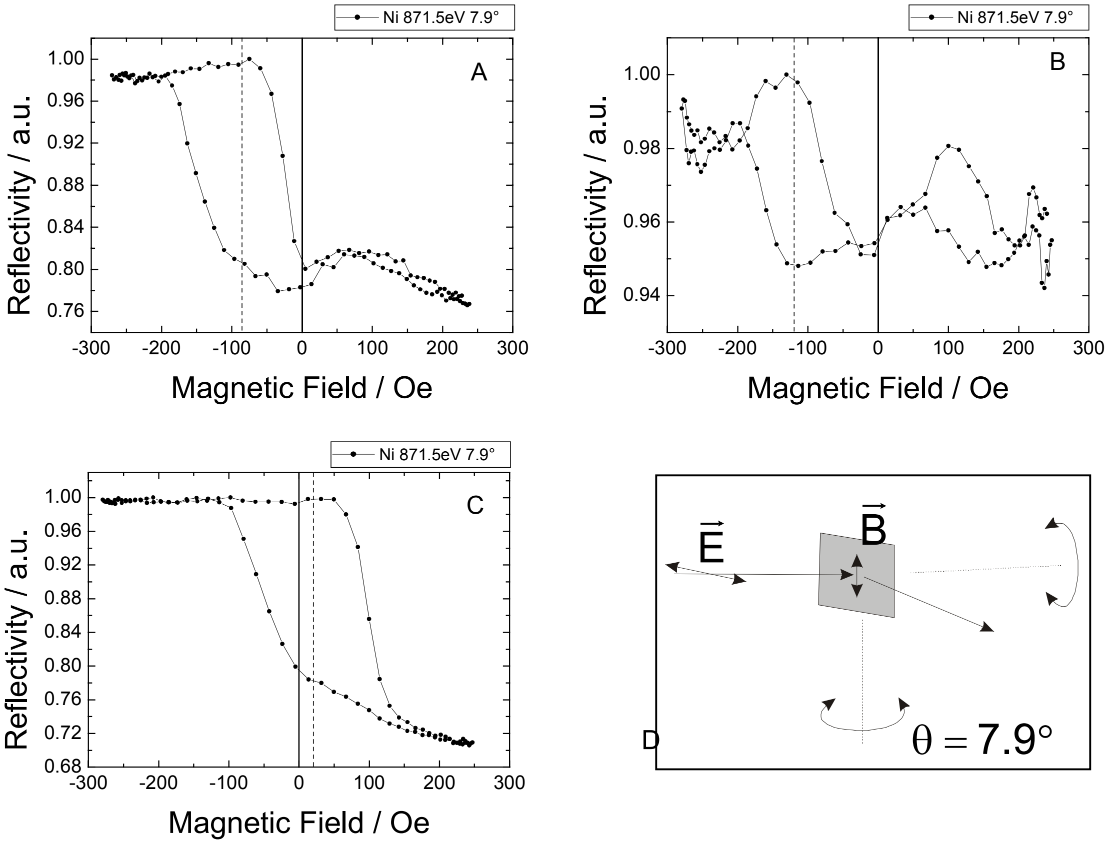

Fig.2: Reflectivity as a function of a transversely applied magnetic field for linearly polarized photons of 871.5 eV (p-geometry).Panel A: as prepared, Panel B: 1x10^{14} ions/cm^2 with H_{bom} ↑↑ H_{gro}, Panel C: 1x10^{14} ions/cm^2 with H_{bom} ↓↑ H_{gro}, Panel D: measurement geometry.

Fig.2 shows element specific hysteresis loops determined with linearly polarized synchrotron radiation in the geometry shown in Fig.2D at an energy of 871.5eV (Ni L_2 edge) and an angle of incidence of 7.9°. In Panel A a hysteresis loop for an "as prepared" sample is shown. The hysteresis loop is shifted by the amount of H_{eb} = 86 Oe to the left. Panel B shows the loop for a sample bombarded with 10 keV He ions in a parallel applied magnetic field with an ion dose of 1x10^{14} ions/cm^2. H_{eb} is clearly enhanced up to 118 Oe. For bombardment with H_{bom} ↓↑ H_{gro}, the sign of H_{eb} is changed as shown in Panel C. The observed changes in the hysteresis loops for Ni at the L_2 edge shown above reflect the modification of the exchange coupling at the ferromagnet-antiferromagnet interface due to ion bombardment.

In Fig.3 the reflectivity and the asymmetry for Fe is shown of an "as prepared" sample . At angles of incidence between 7° and 10° the asymmetry changes sign which can also be seen in the hysteresis loops. In this angle of incidence range constructive interference of x-rays reflected at the two interfaces of the NiFe layer occurs, enhancing the reflected intensity from the lower interface. At 5° and 11° destructive interference occurs, therefore the reflected intensity stems mainly from the bulk of the NiFe layer. The opposite hysteresis loop measured at 9° can thus be explained by formation of iron oxide at the lowermost interface due to oxygen diffusion from the NiO layer, similar to findings in [5].

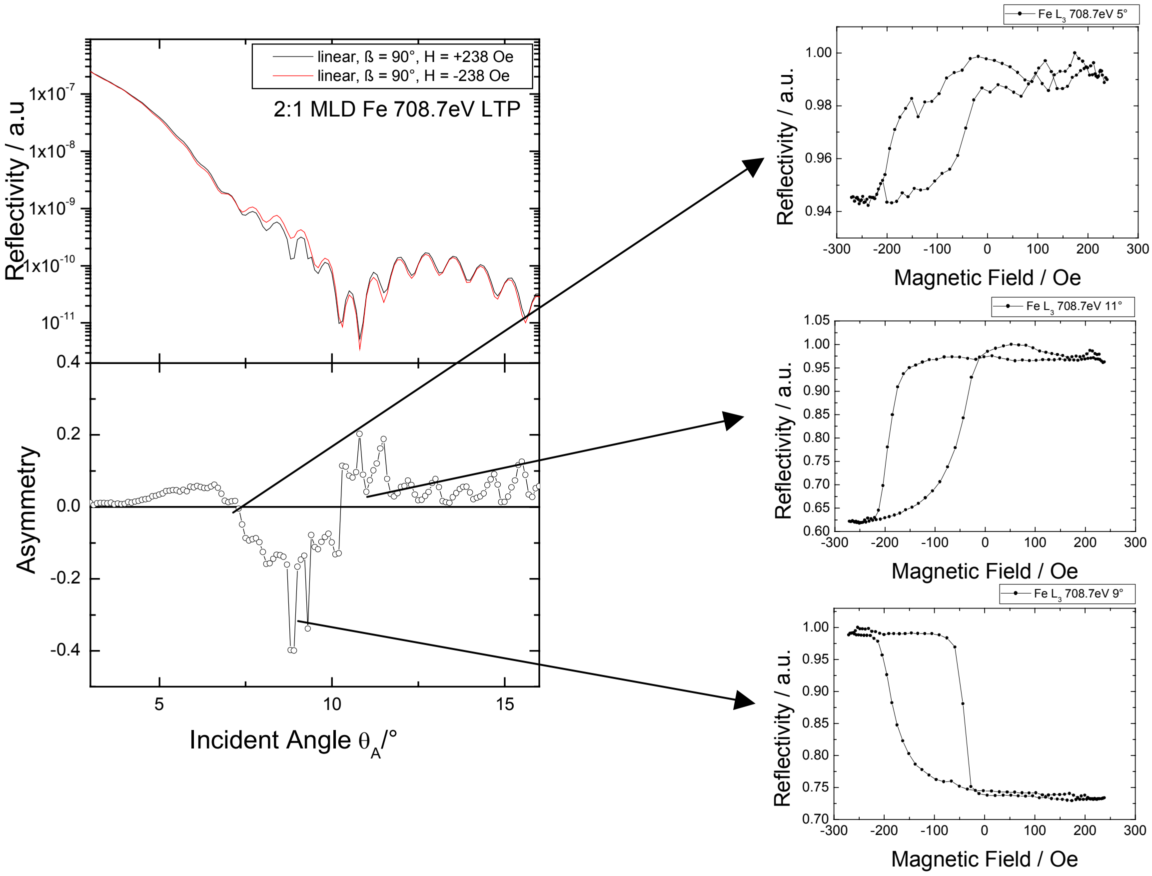

Fig.3: Reflectivity and asymmetry as a function of the angle of incidence for Fe at a photon energy of 708.7eV. On the right hand side the reflectivity as a function of the applied magnetic field at this energy for selected angles is shown.

[1] T. Mewes, R. Lopusnik, J. Fassbender, B. Hillebrands, M. Jung, D. Engel, A. Ehresmann, H. Schmoranzer, Appl. Phys. Lett. **76**, 1057 (2000).

[2] A. Mougin, T. Mewes, M. Jung, D. Engel, A. Ehresmann, H. Schmoranzer, J. Fassbender, B. Hillebrands, Phys. Rev. B **63**, 060409 (2001).

[3] D. Engel, A. Kronenberger, M. Jung, H. Schmoranzer, A. Ehresmann, A. Paetzold, K. Röll, J. Magn. Magn. Mater. in press (2003).

[4] F. Schäfers, H.-Ch. Mertins, A. Gaupp, W. Gudat, M. Mertin, I. Packe, F. Schmolla, S. Di Fonzo, G. Soullié, W. Jark, R. Walker, X. Le Cann, M. Eriksson, R. Nyholm, Appl. Opt. **38**, 4074 (1999).

[5] O. Zaharko, P.M. Oppeneer, H. Grimmer, M. Horisberger, H.-Ch. Mertins, D. Abramsohn, F. Schäfers, A. Bill, H.-B. Braun, Phys.Rev. B **66**, 134406 (2002)

Spectroscopic analysis of buried interfaces in Cu(In,Ga)(S,Se)$_2$ thin film solar cells by combining x-ray emission and photoelectron spectroscopy in the CISSY apparatus

Ch.-H. Fischer, M. Bär, A. Grimm, I. Kötschau, I. Lauermann, J. Reichardt, S. Sokoll, and M.C. Lux-Steiner, *Hahn-Meitner-Institut Berlin, GmbH*
L. Weinhardt , O. Fuchs, and C. Heske, *Experimentelle Physik II,Universität Würzburg*
C. Jung and W. Gudat, *BESSY GmbH, Berlin*
T. P. Niesen and F. Karg, *Shell Solar GmbH, München*

The general aim of the CISSY project is the investigation of buried interfaces and surfaces in Cu(In,Ga)(S,Se)$_2$ ("CIGSSe") thin film solar devices. The CISSY endstation (Fig.1), completed in 2002, combines several relevant in-system preparation tools for thin layer deposition (sputter chamber, glove box for wet chemical processes) and the spectroscopic equipment for x-ray emission (XES, Scienta Gammadata) and photoelectron spectroscopy (PES, VG CLAM 4) and a variety of laboratory techniques. The analytical concept of CISSY is based on information from XES and PES on the electronic properties and the chemical composition from different information depths (XES: several 100 nm; PES: surface) for the study of buried interfaces in layer systems.

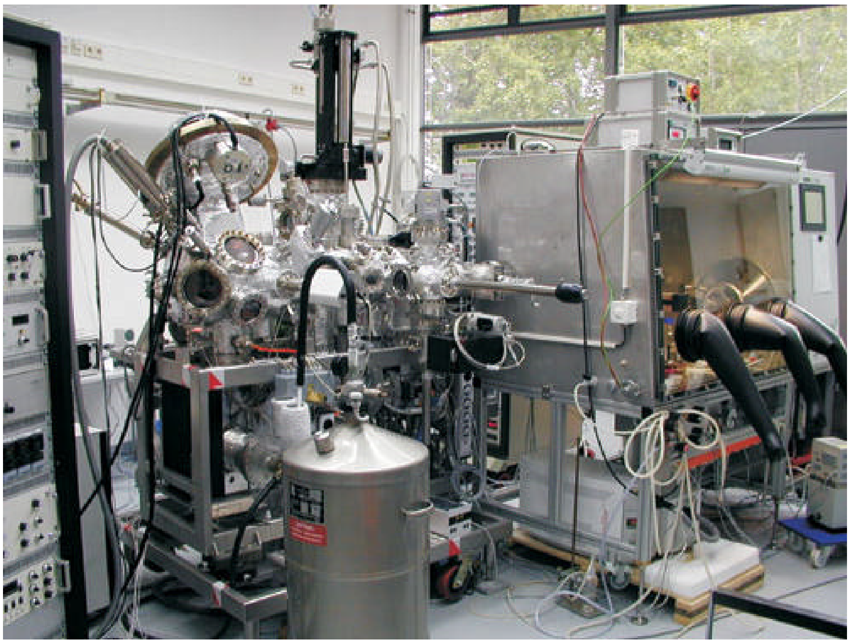

Fig.1 CISSY endstation with attached glovebox.

All CIGSSe absorbers stem from the pilot line of Shell Solar, and subsequent depositions of buffer layers (CdS, ZnS, ZnSe, ZnO) were performed either in the attached glovebox of the CISSY apparatus or in several labs at the HMI. Several preparation procedures were employed, including chemical bath deposition, absorber surface pre-treatments, and, in particular, the sequential cyclic ILGAR process (Ion Layer Gas Reaction) consisting of dipping and solid/gas reaction steps.

A broad study was dedicated to the stability of the CIGSSe solar cells during so-called "damp-heat tests" ("DH", 85°C/85% rel. humidity, 100 h for unencapsulated samples), a fundamental issue for the photovoltaic industry. We started with the systems ILGAR-ZnO/CIGSSe [1] and sputtered-i-ZnO/CIGSSe, each with Cd^{2+}/NH$_3$ treatment of the CIGSSe absorber [2]. In order to localize and understand the observed effects, variations of preparation conditions as well as measurements before and after damp-heat exposure were performed.

From the S L$_{2,3}$ XES spectra [3] in Fig. 2 we learn that ILGAR-ZnO deposited on CIGSSe under air contains sulfate, the signal of which disappears after damp-heat treatment (Fig.2, left), whereas in sputter-i-ZnO on CIGSSe sulfate is observed only after damp-heat exposure (Fig.2, right, and [4]). Apparently, the chemical composition and hence the electronic behavior of ZnO depends on the preparation method. One has to keep in mind that the sulfate represents only a small fraction of the volume analyzed by XES, i.e., that the sulfate contribution to the resulting spectrum is very small. For a better visualization of the sulfate signals, the spectra of the absorber *before* damp-heat treatment and *before* i-ZnO deposition, respectively, are subtracted from those taken *after* the respective treatments, in order to account for the large number of S atoms within a CIGSSe environment. For comparison a sulfate reference spectrum is also shown.

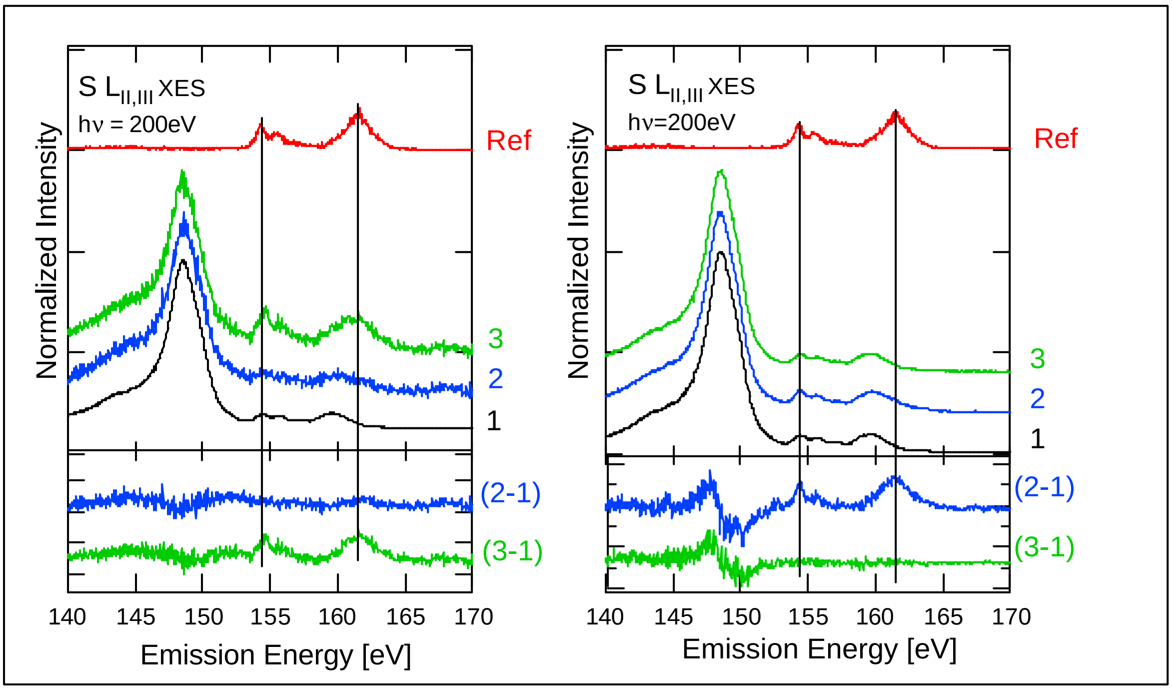

***Fig.2** . S L_{23} XES spectra of 25 nm ILGAR ZnO (left) and of 30 nm sputter i-ZnO (right), both on Cd^{2+}-treated CIGSSe, as well as difference spectra and a spectrum of a sulfate reference. 1. Cd-treated Absorber, 2. before DH, 3. after DH, Ref. $CdSO_4$.*

Complementarily, the PES spectra of the as deposited ILGAR sample give no evidence of sulfate at the ZnO surface. Therefore, the sulfate must be localized at (or near) the ZnO/CIGSSe interface. PES spectra of the same sample after DH show peaks corresponding to the absorber elements, indicating that the ZnO coverage is no longer complete, in agreement with scanning electron micrographs.

The unique CISSY feature of in-system preparation allows a preparation by wet chemical processes in the attached glovebox under N_2 atmosphere and therefore a direct comparison to products of standard preparation in air. When ILGAR-ZnO is deposited on CIGSSe in the glovebox, S $L_{2,3}$ XES spectra clearly show a reduced sulfate signal indicating that oxygen and/or humidity from the ambient environment is involved in the sulfate formation process. These results can be very important for better solar cell efficiency and stability and will be fed back directly into the solar cell production process.

Alternative ZnS buffer layers prepared by chemical bath deposition (“CBD”, A. Ennaoui, HMI) have resulted in high cell efficiencies. The presence of S-Zn bonds could be confirmed by XES (Fig. 3), in spite of the small amount of material (thickness of no more than a few nm). The difference of the spectra “after minus before deposition” obtained with an excitation energy of 200 eV points to the presence of ZnS and $ZnSO_4$. However, ZnS becomes more evident by XES with deliberate excitation below the sulfate absorption edge (165 eV). Therefore, in addition to the advantage of high flux

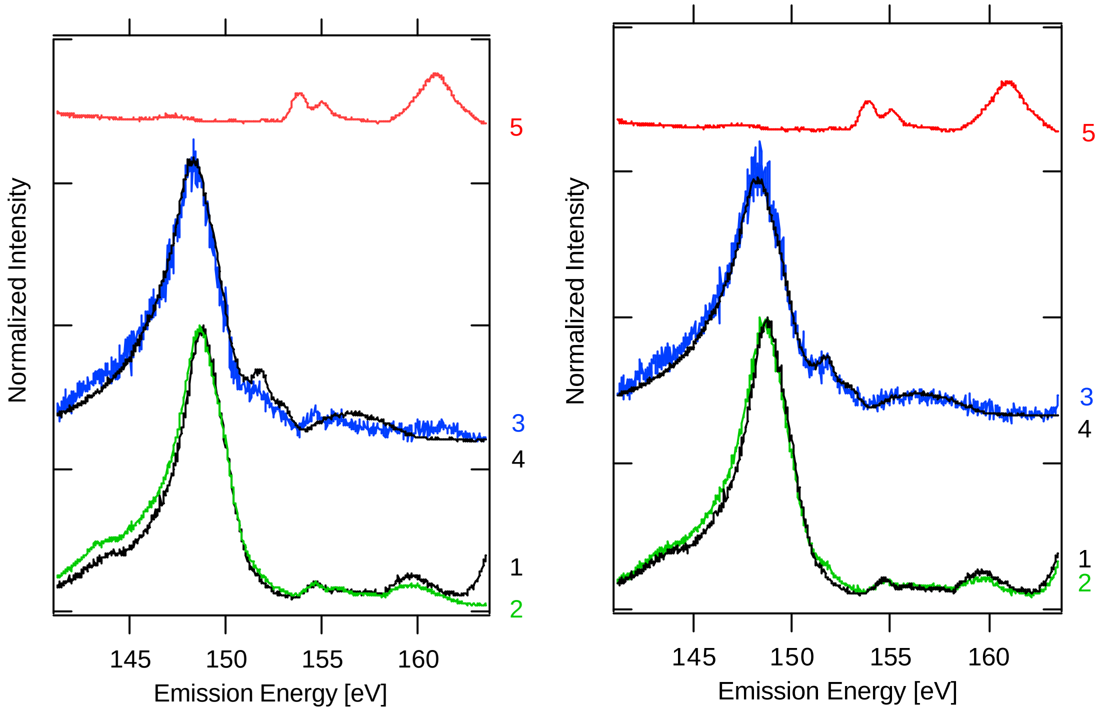

Fig. 3 S $L_{2,3}$ XES spectra of CBD-ZnS/CIGSSe, CIGSSe, and difference spectra for excitation energies of 200 eV (left) and 165 eV (right), showing the effect of deliberate excitation below the sulfate absorption edge. 1. bare CIGSSe-absorber, 2. CBD-ZnS on CIGSSe, 3. difference spectrum (2-1), 4. ZnS-reference, 5. sulfate-reference.

excitation, undulator-based synchrotron radiation also offers the possibility to “switch-off” a certain chemical core hole species, allowing a significantly enhanced spectral interpretation.

The present results, taken during the two inaugural beamtimes of the CISSY apparatus at the U41-PGM and the UE46-PGM beamline, give a first perspective of the multitude of information which can be obtained when combining different spectroscopic methods with in-system and, in a later stage, in-situ thin film preparation.

Funded by BMWi (03N8605/8) and BMBF (01SF0007, 0329218C).

References

[1] „High Efficiency Chalcopyrite Solar Cells with ILGAR-ZnO WEL – Device Characteristics Subject to the WEL Composition“, M. Bär, Ch.-H. Fischer, H.-J- Muffler, B. Leupolt, Th. P. Niesen, F. Karg, and M. Ch. Lux-Steiner, Proc. 29th IEEE PVSC, New Orleans, USA, 636 (2002).

[2] „CdS- and Cd(OH)$_2$-formation during Cd-treatments of Cu(In,Ga)(S,Se)$_2$ thin film solar cell absorbers”, L. Weinhardt, Th. Gleim, O. Fuchs, C. Heske, E. Umbach, M. Bär, H.-J. Muffler, Ch-H. Fischer, M. C. Lux-Steiner, Y. Zubavichus, T.P. Niesen, and F. Karg, Appl. Phys. Lett. 82 (2002), in press.

[3] „X-Ray Emission Spectroscopy of Cu(In,Ga)(S,Se)$_2$-Based Thin Film Solar Cells : Electronic Structure, Surface Oxidation, and Buried Interfaces”, C. Heske, U. Groh, O. Fuchs, E. Umbach, N. Franco, C. Bostedt, L.J. Terminello, R. C. C. Perera, K. H. Hallmeier, , A. Preobrajenski, R. Szargan, S. Zweigart, W. Riedl and F. Karg, phys. stat. sol. (a) 187, 13 (2001).

[4]„Damp -heat induced sulfate formation in Cu(In,Ga)(S,Se)$_2$-based thin film solar cells“, C. Heske, U. Groh, L. Weinhardt, O. Fuchs, B. Holder, E. Umbach, C. Bostedt, L.J. Terminello, S. Zweigart, T.P. Niesen and F. Karg, Appl. Phys. Lett. 81, 4550 (2002).

Synchrotron-μ–Tomography on Aluminium and Zinc Foams

A. Haibel[1], A. Rack[1], G. Weidemann[2], H. Riesemeier[2], J. Goebbels[2], J. Banhart[1]

[1]Hahn-Meitner-Institut Berlin, 14109 Berlin, Germany
[2]Bundesanstalt für Materialforschung und -prüfung (BAM), 12200 Berlin, Germany

Metallic foams are highly porous materials. They consist of aluminium or zinc alloys mixed with titanium or zirconium hydride particles as blowing agent. By heating–up the pressed and preformed materials to temperatures above the melting point of the blowing agent, the hydrogen is released and a pore structure arises.

Due to the low density, the high specific stiffness, and the high energy absorption capability, metallic foams become more and more popular for industrial applications, e.g. in the automobile or aircraft construction.

Our investigations aim at the understanding of the physical processes during the foaming and the optimization of the production by varying the preparation parameters. The 3D–μ–tomography represents an appropriate measurement method for non–destructively analyzing the complex inner and outer structure of such materials. In the following we present some results of our investigations.

As a first example Figure 1 shows an unfoamed powder compact (left) containing three different materials: an aliminium alloy, silicon carbide particles, and titanium hydride as the blowing agent. The SiC–particles (cyan) are embedded into the aluminium alloy matrix Al Si10 Mg (blue) in order to increase the viscosity of the material during the foaming process. The average diameter of the particles is about 70 μm. The titanium hydride particles (red) are also easily discernible. The silicon carbide particles have nearly the same X–ray absorption coefficient as the surrounding matrix (see Fig. 2). Nevertheless, the X–ray radiation monochromatized to 25 keV with $\Delta E/E = 10^{-2}$ (using a double multilayer monochromator) allows us to separate these two phases, which is hardly possible using conventional tomography. The center and the right part of Figure 1 shows the silicon carbide– and titanium hydride particle distribution, the rest of the matrix is transparently depictured.

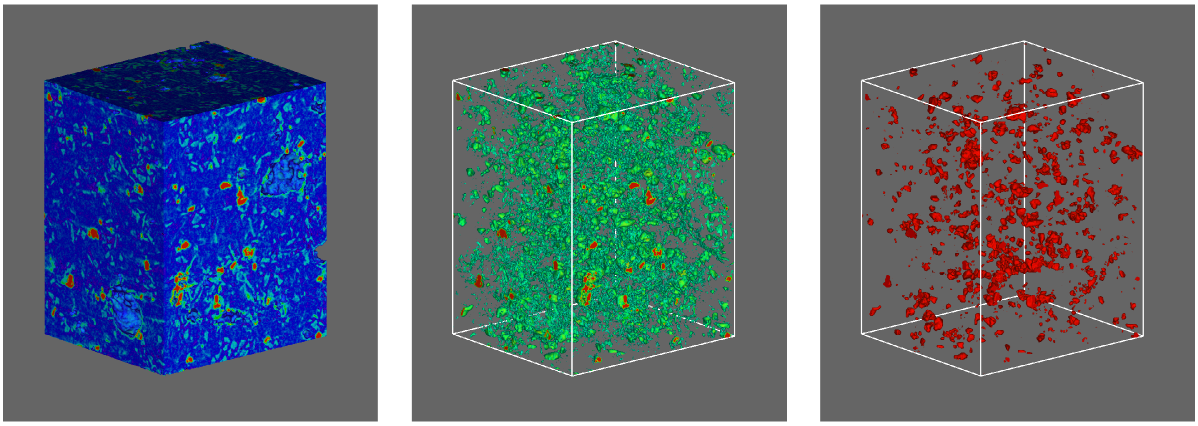

Figure 1: a) Al Si 10 Mg alloy containing 10 vol% SiC with a diameter of $d \approx 70\,\mu$m, b) distribution of SiC and blowing agent, c) the extracted blowing agent.

These preliminary studies on the material in the unfoamed state were necessary for further measurements of this alloy in the liquid foamed state. The goal is to clarify where and how the SiC–particle are located during the foaming process. First measurements in the liquid state have been performed and the analysis is currently under progress.

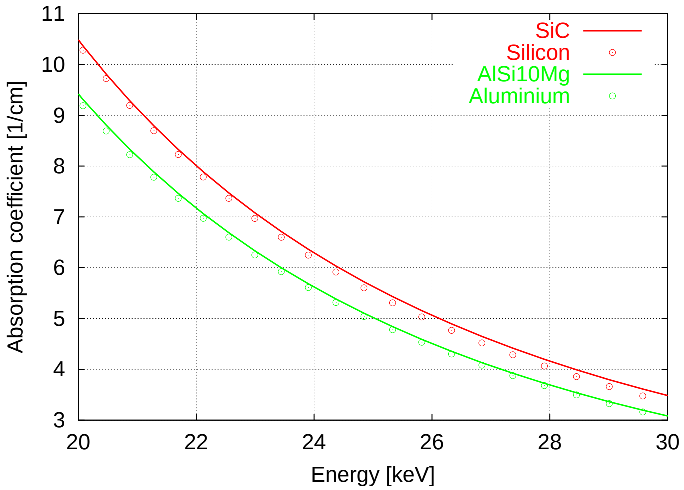

Figure 2: Absorption coefficients vs. X–ray energy for silicon carbide and the aluminium alloy Al Si10 Mg.

An other field of the investigations is full foamed zinc. Here the interesting parameter are the particle sizes of the blowing agents and their influence on the pore size distribution. During the preparation titan hydride with two different particle sizes, greater and less than 28 μm were admixed. The two zinc foams are depicted in Figure 3. For this tomography the foams were irradiated with an energy of 60 keV. In the left tomogram a blowing agent larger than 28 μm were used. In the right picture the size distribution was less than 28 μm. As a first result it is obvious that the pore sizes of both of the foams are correlated with the size of the blowing agents. We are now working on the quantitative analysis to find a statistic of the 3D pore size distribution.

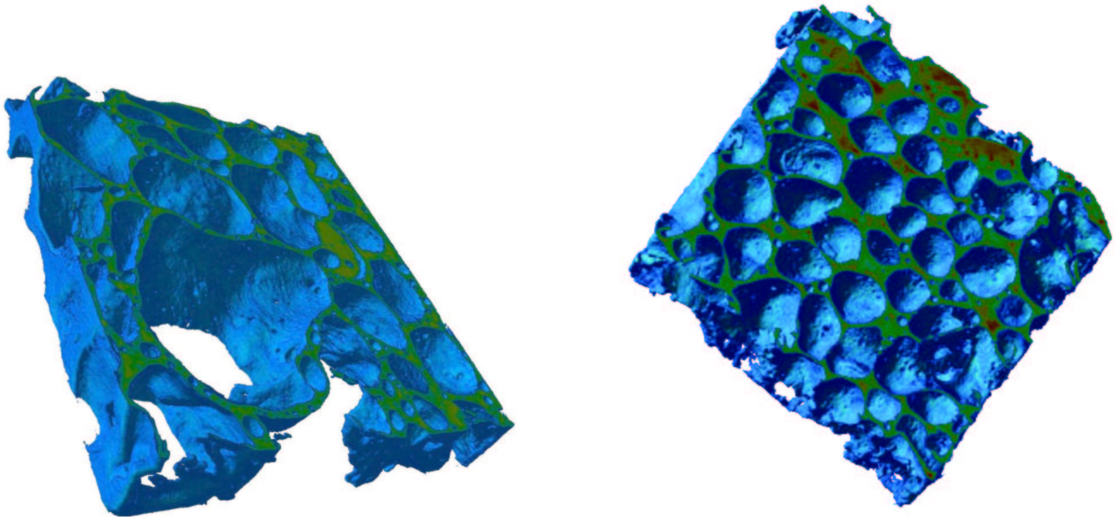

Figure 3: Zinc foam made of a) Zn and TiH_2-particles $> 28\,\mu$m, b) Zn and TiH_2-particles $< 28\,\mu$m.

References

[1] G. Weidemann, J. Goebbels, Th. Wolk, H. Riesemeier, *“First computed tomography experiments at BAMline”*, BESSY Annual Report 2001

[2] M. F. Ashby et al., *“Metal Foams: A Design Guide”*, Butterworth–Heinemann, Boston, 2000

[3] J. Banhart et al., Proc. of the International Conference on *Cellular Metals and Metal Foaming Technology*, 18. – 20. June 2001, Bremen (Germany), Verlag Metall Innovation Technologie MIT

Lattice Mismatch in Creep-Deformed Single Crystal Superalloy SC16

N. Darowski[a], I. Zizak[a], G. Schumacher[a], N. Wanderka[a],
H. Klingelhöffer[b], W. Chen[c], and W. Neumann[c]

[a] Hahn-Meitner-Institut, Glienicker Strasse 100, D-14109 Berlin
[b] Bundesanstalt für Materialforschung und –prüfung,
Unter den Eichen 87, 12205 Berlin
[c] Institut für Physik, HU Berlin, Invalidenstrasse 110, D-10115 Berlin

The superior high temperature strength of nickel base superalloys is attributed to the existence of γ' precipitates of $L1_2$ ordered intermetallic phase embedded coherently in a fcc γ matrix. In the last decades the volume fraction of γ' precipitates in superalloys has been increased from 20 – 30 % in Nimonic 80-type alloys to 40 – 70 % in modern single crystal superalloys for applications as high pressure turbine blade materials. The investigations on pure γ' phase materials showed, however, that the monolithic γ' materials do not provide further advantages in high temperature creep strength compared to that of superalloys [see e.g. 1]. The creep rate of monolithic γ' materials is even faster than that of most modern single crystal superalloys under comparable creep loading conditions. Microscopic investigations revealed that the inelastic deformation under creep loading at elevated temperatures essentially takes place in the γ matrix. The γ' precipitates are not sheared by mobile dislocations. The γ/γ' interfaces and the internal stresses induced by *lattice mismatch* between the γ' precipitates and the γ matrix are therefore considered to be the major reason for the superior high temperature creep strength of superalloys.

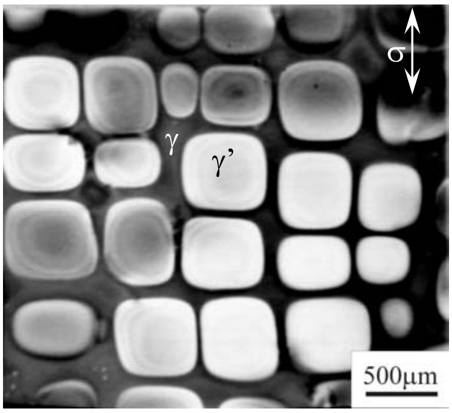

Fig. 1 Micrograph of initial microstructure of SC16 after full heat treatments

To understand the high temperature mechanical behaviour of superalloys, the γ'/γ lattice mismatch and its evolution at high temperature are of importance. In the present study, the γ'/γ lattice mismatch of a single crystal superalloy SC16 (3.5Al-16Cr-2.8Mo-3.5Ta-3.5Ti-Ni) with a γ' volume fraction of about 40 % (Fig. 1) has been measured as a function of temperatures up to 1173 K using high resolution synchrotron X ray diffraction technique. The measurements were conducted on both the undeformed specimen and the specimen with a creep strain of 0.5 % deformed at 1223 K using an x-ray energy of 8 keV at the beam line KMC2 at BESSY. A 6-circle diffractometer and a Si detector were used for the precise spectrum recording. The specimens were mounted directly on the heating plate in the furnace equipped with a semi-spherical Be dome (Fig. 2) and were measured under high vacuum at elevated temperatures.

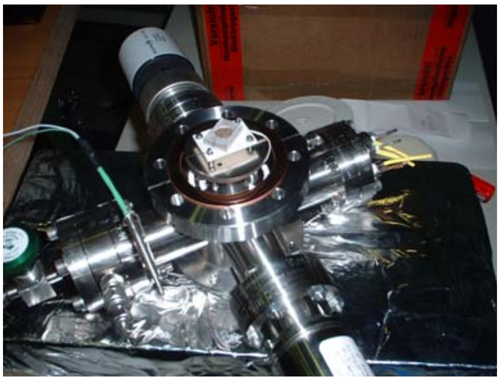

Fig. 2 SC16 specimen mounted on the heating plate in the furnace

Several definitions of lattice mismatch to describe the difference in lattice parameters between the precipitates and the matrix are reported in literature [2]. In the present paper the γ'/γ lattice mismatch is defined as follows

$$\delta = 2\cdot\frac{a_{\gamma'}-a_{\gamma}}{\left(a_{\gamma'}+a_{\gamma}\right)},$$

where $a_{\gamma'}$ and a_{γ} are lattice parameter of γ' and γ phases along their γ/γ' interface, respectively. Two kinds of lattice mismatch along the γ/γ' interfaces parallel and perpendicular to the load axis σ (see Fig. 1) were measured since under creep loading the inelastic deformation in the γ matrix channels related to the above γ/γ' interfaces is different and, therefore, leads to different evolution of lattice mismatch at these two kinds of γ'/γ interfaces.

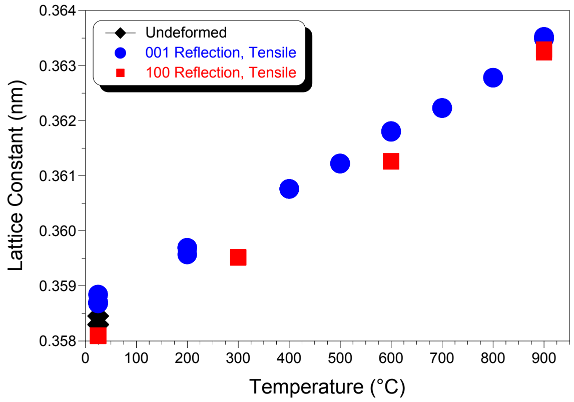

Fig. 3 Lattice parameter of γ' precipitates measured using (001) superlattice reflection

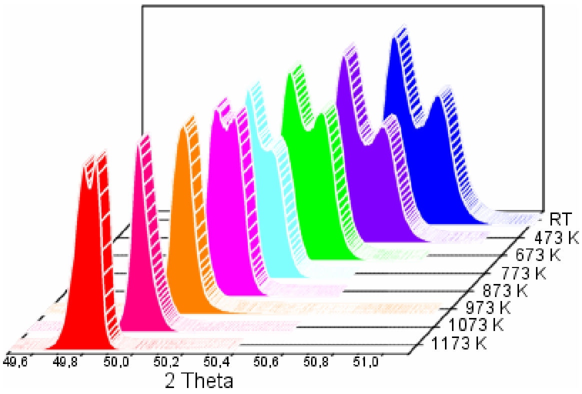

Fig. 4 Spectra of (002) reflection at various temperatures

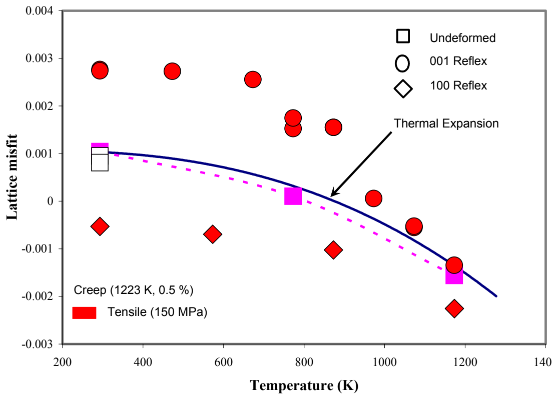

Fig. 5 Lattice mismatch of SC16 at various temperatures

The lattice parameters $a_{\gamma'}$ of γ' precipitates at the γ/γ' interfaces parallel and perpendicular to the load axis σ were determined using the spectra of (001) and (100) superlattice reflections of the γ' precipitates, see Fig. 3. Fig. 4 shows a series of θ-2θ scans for the (002) reflection conducted at various temperatures on the tensile creep-deformed specimen. With increasing temperature the spectrum shifts, as expected due to thermal expansion, towards the direction with smaller 2θ angles. At the same time, the γ' peak within the spectrum shifts from the left hand side at room temperature to the right hand side at high temperature because of different thermal expansion coefficients of both the γ' precipitates and the γ matrix and because of the difference in temperature-dependence of elastic constants of both the phases. To determine the lattice parameters a_{γ} of the γ matrix, the spectra of the (002) reflection were deconvoluted in the following way:

(i) The peak positions and the FWHM of the (002) reflection of the γ' phase were obtained using the data of the measurements on (001) superlattice reflection of the γ' phase;
(ii) the structure factors of both the γ and the γ' phases were calculated for various temperatures used in the present study;
(iii) the spectra of the (002) reflections were fitted using the above data and taking into account the peak intensity ratios of the γ- and γ'-phase corresponding to the γ'volume fraction of 40 % for the superalloy SC16.

Using the lattice parameters of γ’ precipitates and γ matrix measured by (001) superlattice reflection and (002) reflection, respectively, the lattice mismatch of SC16 is calculated and presented in Fig. 5.

In the undeformed state the superalloy shows a positive lattice mismatch of about 0.001 at ambient temperature. The lattice mismatch vanishes in the temperature range around 900 K due to the larger thermal expansion coefficient of γ matrix in comparison to that of γ’ precipitates [3]. At the service temperature of about 1173 K the lattice mismatch is negative. The negative sign of γ/γ’ lattice mismatch is believed to be beneficial for high temperature creep behaviour [4]. During creep deformation the lattice mismatch at the γ/γ’ interfaces parallel and perpendicular to the load axis **σ** developed differently. At the γ/γ’ interface perpendicular to the load axis **σ** the lattice mismatch shifts towards the negative direction, whereas an opposite trend is observed at the γ/γ’ interface parallel to the load axis **σ**. The effect becomes very pronounced for the measurements conducted at ambient temperature.

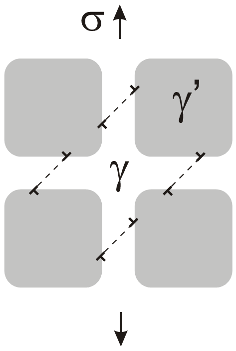

Fig. 6 Schematic presentation of configuration of mobile dislocations during tensile creep deformation in superalloys

A qualitative interpretation of the effect of creep deformation on lattice mismatch observed in the present study is schematically presented in Fig. 6. Under creep loading σ dislocation loops are emitted from a dislocation source on the (111) plane in the γ matrix channels between the γ’ precipitates. Since the γ’ precipitates are not sheared under the present creep loading condition the movement of the dislocation segments is stopped by the γ’ precipitates, see Fig. 6. At the γ/γ’ interface *perpendicular to the load axis* the edge component of the dislocations lies within the γ’ precipitates. The γ matrix channel related to the above γ/γ’ interface must be expanded in order to match the corresponding γ’ precipitate with the additional edge component of the dislocations. This leads to a lattice expansion in the γ matrix channel and a compression in the γ’ precipitate. In the undeformed state the superalloy has a positive lattice mismatch ($a_{\gamma'} > a_{\gamma}$), Fig. 5. The additional lattice expansion in the γ matrix channel and the compression in the γ’ precipitate caused by introduction of the edge component of the dislocation during creep deformation results in an increase in lattice parameter of γ phase and a decrease in γ’ lattice parameter, and consequently in a reduction of the γ/γ’ lattice mismatch at the above interface (rhombi in Fig. 5). In the case of the γ/γ’ interface *parallel to the load axis* the edge component of the mobile dislocations lies in the γ matrix channel, see Fig. 6. After creep deformation an additional tensile distortion exists in the side of the γ’ precipitate and a compressive distortion in the γ matrix. Therefore, an increase in lattice mismatch is measured (circles in Fig. 5).

* *Financial Support of the DFG (NE6465-3 & WA1378/1-2) is gratefully acknowledged.*

[1] M.V. Nathal, J.O. Diaz and R.V. Miner, High-Temperature Ordered Intermetallic Alloys III, Eds. C.T. Liu, et al., Vol. 133, MRS, Pittsburgh, USA, 269 (1988).
[2] A.E. Romanov and T. Wagner, Scr. Mater., **45**, 325 (2001).
[3] G. Schumacher, G. Frohberg, R.P. Wahi and H. Wever, Expreimentelle Bestimmung der Fehlpassung zwischen Matrix und γ’-Ausscheidung im unverspannten Zustand an SC16, SFB 339 final report, (DFG), TU Berlin, (1996).
[4] H. Harada, K. Ohno, T. Yamagata, T. Yokokawa and M. Yamazaki, Superalloys 1988, Eds. D.N. Duhl, et al., AIME, Pennsylvania, USA, 733 (1988).

Soft X-ray L-MOKE and magneto-optical constants for Co/Cu multilayers measured at the Co $L_{2,3}$ edges

M. Hecker[1], H.-C. Mertins[2], D. Abramsohn[2], C.M. Schneider[1]

[1]Institut f. Festkörper- u. Werkstofforschung Dresden, Helmholtzstraße 20, 01069 Dresden, Germany
[2]Berliner Elektronenspeicherring-Gesellschaft für Synchrotronstrahlung m.b.H. (BESSY), Albert-Einstein-Straße 15, 12489 Berlin, Germany

Nanoscale Co/Cu multilayers are of great fundamental and technological importance due to their unique magnetotransport properties as, for example, the giant magnetoresistance (GMR). A *simultaneous* access to both structural and magnetic features in such systems becomes feasible via the magneto-optical Kerr effect in resonant magnetic scattering of polarized soft X-rays (X-MOKE) [1].

We investigated Co/Cu multilayers with a nominal structure corresponding to the second antiferromagnetic (afm) coupling maximum (40×[Co(1nm)/Cu(2nm)]/Co(1nm)). They were prepared by dc magnetron sputtering onto thermally oxidized (100)-Si and showed a typical GMR value of 27%. The scattering experiments were performed at the BESSY II UE56-PGM undulator beamline utilizing the polarimeter set-up [2] in L-MOKE geometry.

In X-ray reflectometry with a photon energy close to the Co $L_{2,3}$ edges, in addition to the structural Bragg peaks a half-integer order magnetic peak can be observed, the presence of which has been first noticed by Sève et al. [1]. In subsequent studies the details of this magnetic peak were correlated to the magnetic and transport properties of the multilayers [3,4]. In our present investigation, we report on improved X-MOKE studies of the Co/Cu system at the Co $L_{2,3}$ absorption edges using circularly polarized light (p_{circ}=0.9). In contrast to previous investigations showing only the first order magnetic peak, we were able to resolve higher orders which are more sensitive to magnetic effects. The chosen L-MOKE geometry also enabled us to correlate the shift of multilayer Bragg peaks to the dispersive part of the optical constants. This quantity is an important ingredient for model calculations of the magnetic scattering from multilayers.

Reflectometry curves were measured both with circularly polarized radiation at the Co L_3 edge (Fig. 1a, bottom curves) and with Cu-K_α radiation (top curve) over a large range of angles. Several characteristic differences between both results can be noticed.

Firstly, at the L_3 edge higher order Bragg peaks appear which are not visible with Cu $K\alpha$ radiation. This behavior relates to the resonant intensity enhancement and to the enlarged contrast between Co and Cu for the anomalous scattering at the absorption edge.

Secondly and even more striking, in between the structural Bragg peaks (bottom curves) measured at 778eV a series of half-integer order peaks shows up. These are of purely magnetic origin and correspond to the magnetic periodicity length of the multilayer. By an applied magnetic field B the antiferromagnetic alignment of the Co layers can be broken up, causing an intensity reduction of the magnetic peaks.

Furthermore, the higher absorption cross section close to the L_3 edge lowers the penetration depth which leads to a dramatic suppression of the Kiessig fringes.

And finally, the plateau regions close to the critical angle of total reflection differ significantly, since the dispersion correction of the refractive index changes drastically at the L-edges. The latter feature was investigated in more detail by studying the shift of the Bragg peaks close to the L-edges.

Fig. 2 illustrates measurements of the 1st order Bragg peak for different photon energies. Apart from the resonant intensity enhancement and the increased asymmetry ratio (comparing the intensity for both signs of B) close to the absorption edge, also a difference in the peak position for both signs of B can be noticed. After a precise determination of the bilayer thickness d from a fit of all the Bragg peaks shown in Fig. 1 according to the modified Bragg equation

$$m\,\lambda = 2\,d\,(1 - \frac{\delta}{\sin^2\theta})\,\sin\theta, \tag{1}$$

where m is the order of the Bragg peak and δ is the dispersive contribution to the refractive index $n = 1 - \delta + i\beta$, we calculated in a second step δ from the energy-dependent peak shift of the first-order Bragg peak, with eq. (1) for m=1. Using a mixture rule for the refractive index composed of contributions from the Cu and Co layers, we finally extracted δ of the Co layers. The results are represented in Fig. 3. Far from the L edges, the data match to the bulk data from the tables of Henke et al. [5], whereas close to the edges δ shows a strong resonant structure. In particular, the difference in δ for both directions of the magnetic field corresponding to a dichroic contribution cannot be inferred from the nonmagnetic measurements [5]. The inset in Fig. 3 shows this difference corresponding to the magnetic contribution Δδ. Its inclusion in the modelling of the multilayer reflectivity allows one to better understand the measured reflectometry curves and, in particular, the reduction of the magnetic peak intensity with an applied magnetic field. One must consider, however, that the magnetic saturation state of the multilayer was still not reached at the maximum field applied, leading to remnants of the magnetic peaks and to an underestimation of the saturation values of Δδ by the method used. Also the nonmagnetic resonant variation of δ has a significant impact on the shape of the reflectometry curves. For example, in the energy range of negative δ values the refractive index becomes larger than 1. In this range, the total reflection plateau of the reflectometry curve disappears completely.

In conclusion, the data obtained at the Co L edges show a strong resonant enhancement of the magnetic scattering giving the possibility to investigate structural and magnetic features of Co/Cu multilayers simultaneously. The near-edge dispersive contribution to the refraction index of the multilayer including its magnetic contribution was determined from the scattering data as a precondition for a detailed modelling of polarized X-ray scattering in Co/Cu multilayer model systems.

We thank D. Tietjen for sample preparation and P. Oppeneer for helpful discussions. Financial support from BMBF through grant No. 05/KS1BD1/0 is gratefully acknowledged.

References

[1] L. Sève, J.M. Tonnerre, D. Raoux, J.F. Bobo, M. Piecuch, M. De Santis, P. Troussel, J.M. Brot, V. Chakarian, C.C. Kao, and C.T.Chen, J. Magn. Magn. Mater. **148**, 68 (1995).

[2] H.-Ch. Mertins, D. Abramsohn, A. Gaupp, F. Schäfers, W. Gudat, O. Zaharko, H. Grimmer, P.M. Oppeneer, Phys. Rev. **B66**, 184404 (2002).

[3] T.P.A. Hase, I. Pape, D.E. Read, B.K. Tanner, H. Dürr, E. Dudzik, G. van der Laan, C.H. Marrows, and B.J. Hickey, Phys. Rev. **B61**, 15331 (2000).

[4] M. Hecker, U. Muschiol, C.M. Schneider, H.-Ch. Mertins, D. Abramsohn, and F. Schäfers, J. Magn. Magn. Mat. **240**, 520 (2002).

[5] B.L. Henke, E.M. Gullikson, and J.C. Davis, At. Data Nucl. Data Tables **54**, 181 (1993).

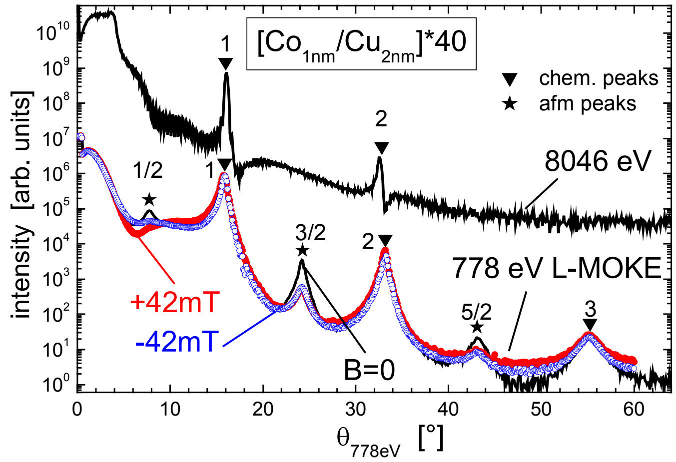

Fig. 1: Reflectometry curve measured with Cu-Kα radiation (θ recalculated for 778eV; upper black line), and at the Co-L3 edge with circularly polarized radiation (lower curves). The latter measurement was also performed with applied magnetic field of two different signs(blue and red line).

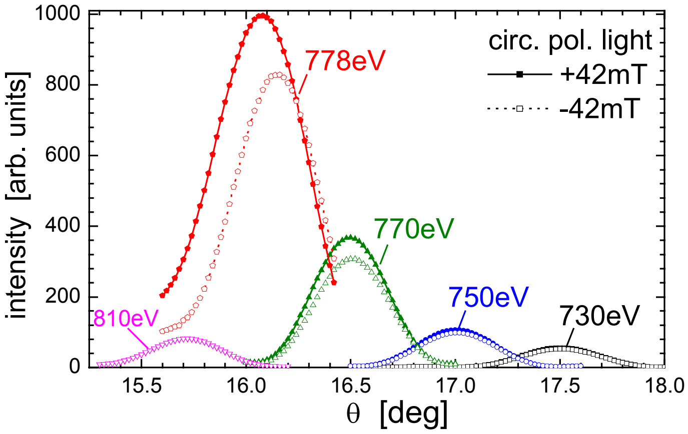

Fig. 2: 1st order Bragg peak of the Co/Cu multilayer for different photon energies and for the two opposite directions of the magnetic field (open and closed symbols corresponding to positive and negative sign of B, respectively).

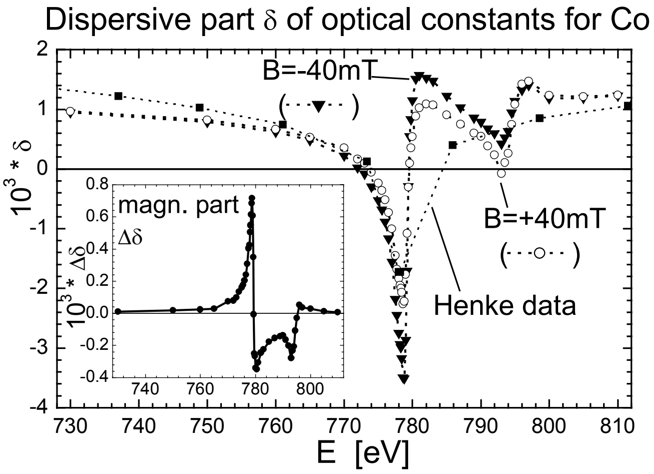

Fig. 3: Dispersive part of the refraction index of the Co layers in the multilayer as derived from the peak shift of the structural Bragg peak, and data for Co tabulated in [5].

Examinations of hard disc corrosion by combined XAS- and XPS- spectroscopy using X-PEEM and the 'Nano-ESCA'

P. Bernhard, Ch. Ziethen, F. Wegelin, R. Ohr, G. Schönhense
Institut für Physik – Johannes Gutenberg- Universität Mainz

H. Hilgers
IBM Speichersysteme Deutschland GmbH, Mainz

B. Krömker
OMICRON NanoTechnology, Taunusstein

F. Senf
Berliner Elektronenspeicherringgesellschaft für Synchrotronstrahlung mbH (BESSY II)

X-ray Absorption Spectroscopy (XAS) is an established method in today's materials research, which can be also used for chemical analysis of buried layers. Measurements of its fine structure, the so called XANES spectra (X-ray Absorption Near Edge Structure) even allow, in comparison with literature spectra, a determination of the bonding surroundings of the analysed elements. Using X-PEEM (X-ray Photo-Emission Electron Microscopy) as a measuring technique combines the advantage of the chemical analysis of XANES with the parallel imaging properties of a PEEM.

We used a FOCUS IS PEEM with a X-PEEM resolution up to 21 nm [1]for the analysis of the bonding surroundings of buried magnetic layers in the project "Innovative Reaktoren und in-situ Analytik für ultradünne Nanoschutzschichten" (funded by the BMBF, FKZ 13N7759) to investigate the corrosion protection of ultra-thin carbon layers that mechanically protect and in addition prevents the magnetic film from corrosion. In order to check the results, we used the 'Nano-ESCA' system (see the article of D. Funneman et al. in this issue; project funded by BMBF FKZ 13N7863) that combines *XPS and XAS of the same sample area* and provides a lateral resolution better than 200 nm in the XPS images.

Carbon layers are used in the hard discs production as protecting layers for corrosion and mechanical wear. The decrease of the layer thickness from 10 nm down to 2 nm or even below is one aim in today's development of hard disc coatings and in particular of the project mentioned above, as it can lead to a further increase of the storage density by about one order of magnitude. As the functional properties of the protecting layers have to remain unchanged when decreasing the thickness, the investigation of the corrosion protection in interrelation of the layer thickness is an essential task of applied research.

Answering these questions was one of our main tasks as partner in the project. Using an X-PEEM at the synchrotron radiation facility in Berlin (BESSY II), we measured micro-XANES spectra of the absorption edges of cobalt (see [2], [3] for the method) on series of samples with different thickness and different materials of the protecting layer. Co is the main (>60 %) constituent of the magnetic film. The determination of the layer thickness was done at IBM (Mainz) using ellipsometry.

Figure 1a shows results of the Co L_2/L_3 edge that were taken by photocurrent measurements on a series of samples with an amorphous carbon (a-C) layer. The films were produced by using a high current pulsed arc plasma source. Figure 1b shows the Co L_2/L_3 edge of Co metal and of CoO, as published by Regan et al. [4]. In comparison with figure 1b, the spectrum 1 of figure 1a clearly shows that the unprotected sample (layer thickness 0 nm) is oxidized, contrary to the other five measured spectra. Closer investigation also shows that

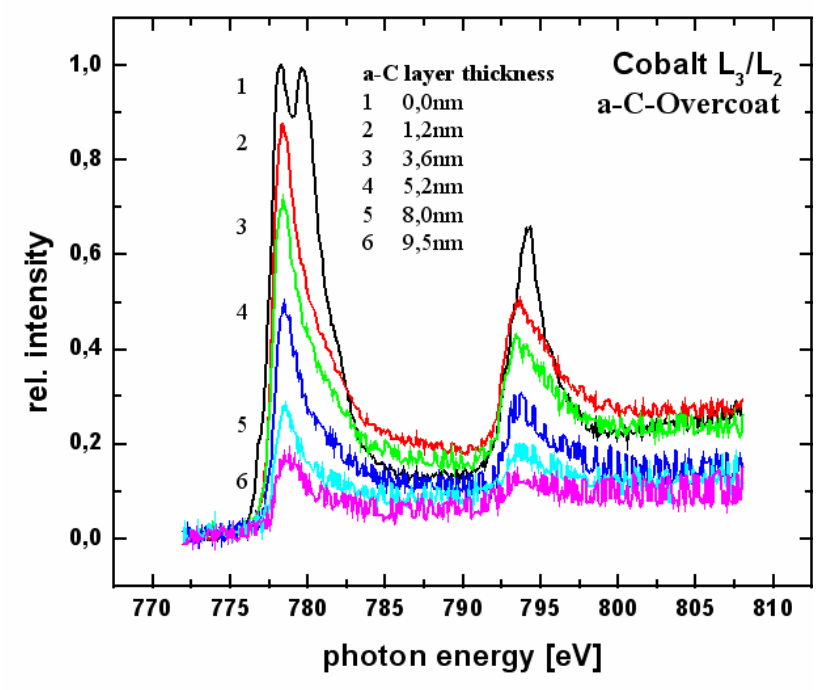

a)

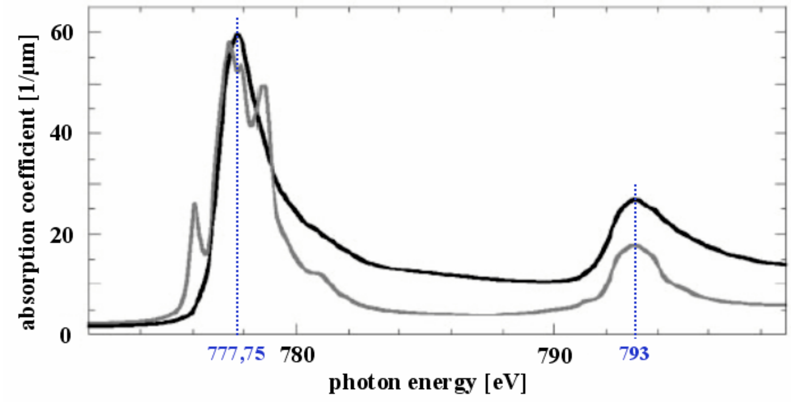

b)

Figure 1 : a) XANES spectra of Co L_2/L_3 edge measured on samples with different protecting layer thicknesses (photocurrent of the sample). The absolute layer thickness was measured using ellipsometry.
b) XANES spectra of Co (black) and CoO (grey) L_2/L_3 edge measured and published by Regan at al. [4]. In an oxidic bonding surrounding the L_3 edge splits up into 5 separate peaks.

even spectrum 2 (taken on a sample with layer thickness of 1.2 nm) shows none or just a negligible fraction of Co in bonding with oxygen.

Due to the fact that in the future major decisions might be drawn concerning the use of these coatings in production, we cross-checked these results by examining the hard-discs by two independent spectroscopies using the ‘Nano-ESCA’ System. No images are shown here, because at the surface of the magnetic storage media, no debris or defects are detected.

Figure 2 shows the XAS, Figure 3 the XPS results of buried layer spectroscopy only for the critical layer thickness below 2 nm. The XAS and XPS results were obtained at the same sample area (diameter of the imaged area was 30µm) of uncoated (black line) and coated (1.2 nm a-C, red line) hard disc. We used a SensiCam CCD- camera (PCO) for image acquisition. For every excitation energy (XAS) or kinetic energy (XPS) an image is taken. Spectra are calculated by recording the energy dependent intensity of regions-of-interest in the electron optical image. The XAS- result shows a highly resolved five-fold Co L_3- peak for the media without carbon overcoat, but a clear metallic like L_3- peak in the case of an overcoat thickness of 1.2 nm. Monochromator step-width was 0.1 eV. The XPS spectra are obtained using a photon energy of hν= 1000 eV, analyser step-width of 0.2 eV and a pass energy of the imaging energy filter of 100 eV. For the uncoated magnetic film, we get a peak at a binding energy of 779.5 eV. This is very close to the typical value of 780 eV known from XPS- spectra of pure CoO. The coated film shows a peak-shift to a lower binding energy of 777.8 eV, just in the range of pure metallic Co.

We can conclude from our measurements that for a-C layers with a thickness of $\geq$1.2 nm, a corrosion of the magnetic storage media is avoided. This result is additionally confirmed by

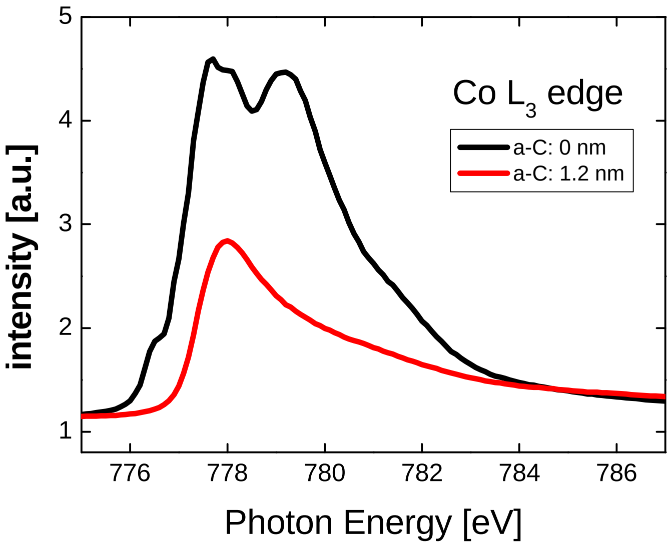

Figure 2: XAS of the Co L_3- edge at a 30µm sample area for uncoated (black curve) and coated (1.2 nm a-C, red curve) magnetic storage media.

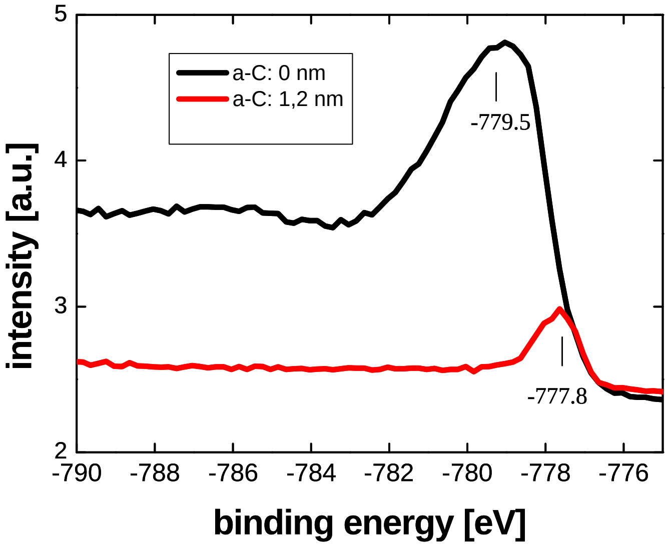

Figure 3: XPS of the Co 2p3/2 state at the same area (diam.= 30µm) as examined for figure 2. Excitation energy was 1000 eV. Uncoated (black curve) and coated (1.2 nm a-C, red curve) magnetic storage media.

non- laterally resolved XPS done at IBM [5]. Further functional tests will be needed to quantify this. Finally, we report the result for a-C:N films, which are candidates for future coatings, too. We applied the same measurement procedure as used for the a-C coatings (combined XPS + XAS analysis). The measurements lead to the result that for a-C:N films a thickness of 2.5 nm or more is needed to get a corrosion protection comparable to the thinner a-C films.

References

[1] Ch. Ziethen et al, BESSY annual report (2001) 324
[2] C.M. Schneider, G. Schönhense, Rep. Prog. Phys. 65 (2002) R1785
[3] Ch. Ziethen et al., J. Electron Spectr. Relat. Phenom., Vol. 88-91, (1998), 983; J. Electron_Spectr. Relat. Phenom., Vol. 107, (2000), 261; Diam. Rel. Mat., Vol. 11 , (2002), 1068
[4] T.J. Regan et al., Phys. Rev. B, Vol. 64, (2001) 214422s
[5] R. Ohr, PhD- thesis, in preparation

Funding : BMBF FKZ 13N7759, FKZ 13N7863

Antiferromagnetic coupling at the interface of the Fe/CoO exchange bias bilayer

F. Radu, J. Grabis, A. Nefedov, S. Erdt-Böhm, K. Westerholt and H. Zabel

Experimentalphysik IV, Ruhr-Universität Bochum, Universitätstrasse 150, 44780 Bochum Germany

After many years of intensive investigations, the exchange bias (EB) effect remains a fascinating interfacial effect between a ferromagnet and antiferromagnet with many problems being still unsolved [1]. Among the macroscopic characteristics of the EB systems one distinguishes: the shift of the hysteresis loop when the system is cooled in an applied magnetic field through the Neél temperature (T$_N$) of the antiferromagnet; the increase of the coercive field with the decrease of the temperature; the exchange bias effect appears when the system is cooled below a critical temperature called blocking temperature (T$_B$), which is lower that the T$_N$. A key question to the EB phenomenon is related to the microscopic behaviour of the FM/AFM interface. The most simple one to ask is whether the coupling between the FM and AFM spins is ferromagnetic (direct exchange) or antiferromagnetic (super-exchange). Such question is crucial in understanding the origin of the positive exchange bias [2], which is believed to be directly connected with a super-exchange interaction at the FM/AFM interface. Recently the positive exchange bias was observed in CoO/Co system [3], which is unexpected as long as it was shown experimentally that the interfacial coupling is ferromagnetic. Thus, we start reconsidering the question of the type of interfacial coupling in the FM/CoO systems [4]. In the present report we show data from Fe/CoO EB system measured by Soft X-Ray Resonance Magnetic Scattering (Soft-XRMS).

The sample was prepared by rf-sputtering. The Fe layer was deposited on a Si substrate and on top of it Co was sputtered in an oxygen atmosphere, leading to CoO. The interface was engineered to be Co terminated on the side of Fe. The measurements have been performed at the beamline PM3 of BESSY II using the ALICE diffractometer [5]. The sample was cooled down in an applied magnetic field of 100 Oe through the T$_N$=291 K of the CoO to the measuring temperature T=25 K. In Fig. 1 is shown the reflectivity taken close to CoL_3 absorption edge using circularly polarized light. By setting a fixed incoming angle ($2\theta = 8.4°$, arrow at Fig. 1) and sweeping the magnetic field we recorded the

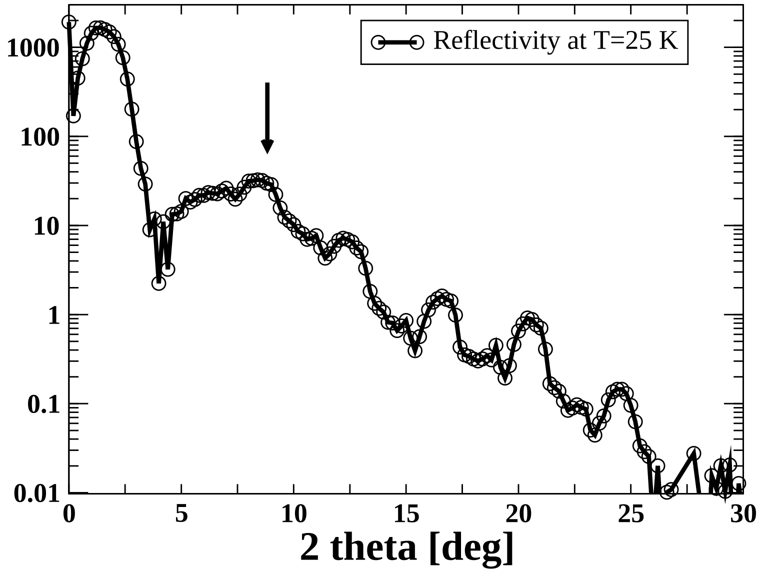

Figure 1: Reflectivity curve from CoO(40Å)/Fe(800 Å)/Si sample taken at T=25 K at an energy close to CoL_3 absorption edge.

hysteresis loops, which are shown in Fig. 2. One was taken for an energy corresponding to the FeL_3 absorption edge (Fig. 2 (a)) and another one at the CoL_3 absorption edge (Fig. 2 (b)).

The striking result is that the two hysteresis loops show different sign. That allows us to conclude that the interfacial coupling between the Co spins and Fe spins is antiferromagnetic. This result is opposite to the experimental findings in Ref. [4] were the interfacial coupling was shown to be direct-exchange.

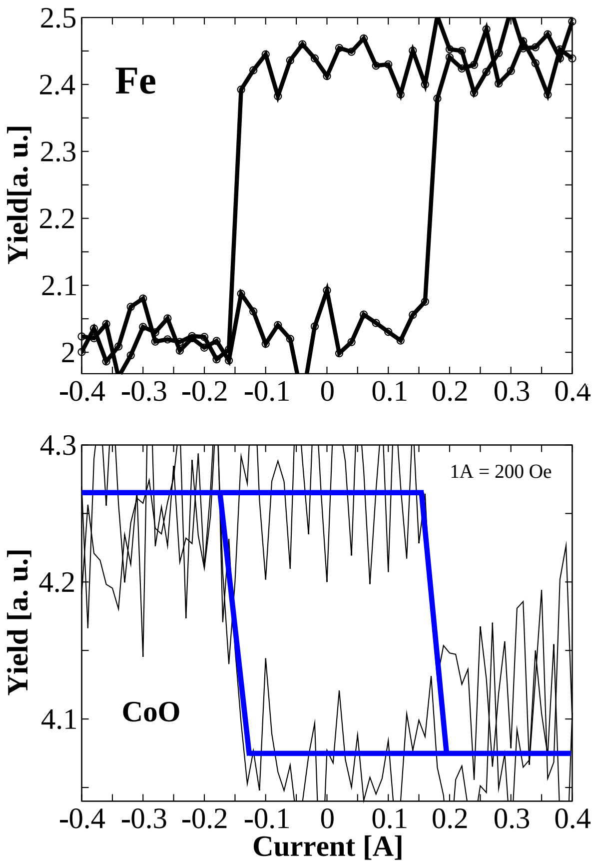

Figure 2: a) Hysteresis loop measured at the FeL_3 absorption edge by setting a fixed angle for the incoming radiation and sweeping the applied magnetic field; b) The hysteresis loop for CoO. The data suggest a super-exchange type of interaction at the interface between Fe and CoO.

This work is supported by DFG (SFB 491). We would like to thank T. Kachel (BESSY) for technical assistance during our experiments at BESSY.

References

[1] M. Kiwi, J. Magn. Magn. Mater. **234**, 584 (2001).

[2] J. Nogues, D. Lederman, T. J. Moran, and Ivan K. Schuller, Phys. Rev. Lett. **76**, 4624 (1996).

[3] F. Radu, M. Etzkorn, R. Siebrecht, T. Schmitte, K. Westerholt, H. Zabel, arXiv:cond-mat/0204607.

[4] F. T. Parker, Kentaro Takano, A. E. Berkowitz, Phys. Rev. B **61**, R866 (2000).

[5] J. Grabis, A. Nefedov, H. Zabel, *BESSY annual report* (2002).

Soft x-ray resonant magnetic scattering studies with new ALICE diffractometer

A. Nefedov, J. Grabis, A. Bergmann, F. Radu and H. Zabel

Experimentalphysik IV, Ruhr-Universität Bochum, Universitätstrasse 150, 44780 Bochum
Germany

A growing number of experiments using atom and shell selectivity of synchrotron radiation techniques are carried out to study magnetic properties. X-ray resonant magnetic scattering (XRMS) uses the energy dependence of corrective terms to the atomic scattering factor which is sensitive to the magnetization of the sample [1]. The resonant enhancement of the magnetic scattering cross section has been firstly observed at the L and M absorption edges of rare earths and actinides in hard x-ray range [2, 3]. In order to study XRMS in 3d transition metals experiments must be carried out over their L absorption edges (electronic transitions from 2p levels toward unoccupied 3d band states). Because of their L edge, energies in the soft x-ray range UHV diffractometer must be employed. Within the scope of the BMBF project ”Untersuchung magnetischer Grenzflächen mittels resonanter magnetischer Röntgenstreuung” we designed and built a new diffractometer ALICE for XRMS experiments based on a UHV compatible 2-circle goniometer (a horizontal scattering geometry) [4]. This diffractometer has been intensively tested and the first experiments have been carried out at the bending magnet beamline PM3 at BESSY II in Berlin in December 2002. The beamline optics allows to tune the energies in the range from 20 eV to 1900 eV with the possibility of tuning the polarization from linear to fully circular.

Firstly we used linear polarized light, which is sensitive to antiferromagnetically (AF) coupled multilayers, because for them the superlattice period is magnetically doubled and one can observe a magnetic half-order Bragg peak by tuning the photon energy to the corresponding absorption edge. As a first sample for testing purposes of the experimental setup we measured a Fe/Cr multilayer, which was before characterized at Daresbury together with T. Hase, Durham. The obtained data are

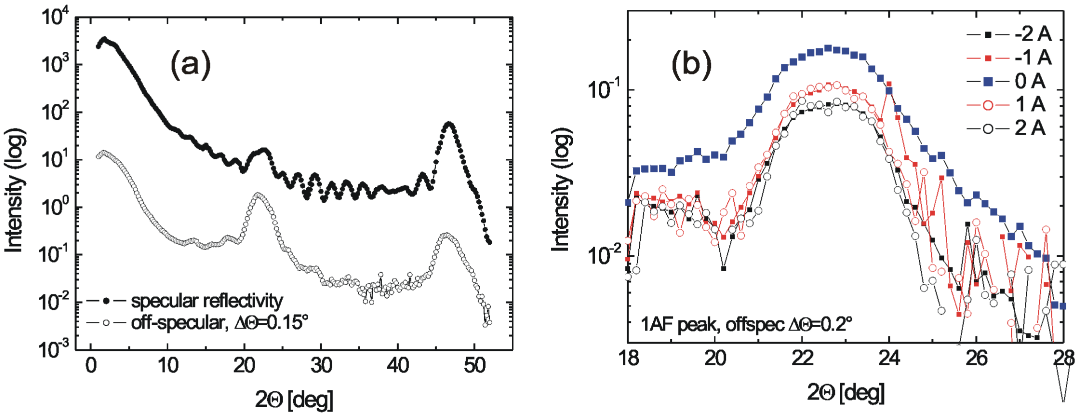

Figure 1: XRMS signal of a [Co(1 nm)/Cu(0.8 nm)]$_{25}$ multilayer on a Si substrate. The energy E=773.4 eV of the linearly polarized photons is slightly below the CoL_3 edge. (a) Specular and off-specular reflectivity in remanence. The half-order peak at $2\Theta = 22°$ and the diffuse scattering around it have a pure magnetic origin. (b) Magnetic field dependence of the diffuse scattering at the half-order Bragg peak.

coincident with the Daresbury results. Then we investigated an AF-coupled [Co/Cu]$_{25}$ multilayer, including its behaviour in a magnetic field. Reflectivity curves (specular and off-specular) are presented in Fig. 1 (a). The magnetic half-order Bragg peak is clearly seen for both curves. Similar results have been obtained by other groups before [5]. In Fig. 1 (b) the magnetic field dependence of the diffuse scattering at the half-order Bragg peak is presented. The peak intensity decreases with increasing absolute value of the field and independent on its direction. Such behavior corresponds to AF-coupled systems.

Then we tried to test a multielement system. For [Co$_2$MnGe/V]$_{50}$ Heusler superlattice the magnetic half-order Bragg peak has been observed with polarized neutron scattering, but this effect was not observed with soft x-rays at the Co$L_{3,2}$ as well as at MnL_3 absorption edges. Circular polarized light was used to study element-specific XRMS hysteresis loops at the structural Bragg peak $(2\theta = 17.2°)$ (Fig. 2), which is sensitive to ferromagnetism. The temperature dependent hysteresis loops at the CoL_3 edge (Fig. 2 (b)) coincide with SQUID measurements, whereas no magnetic signal has been observed at the MnL_3 edge (Fig.2 (a)).

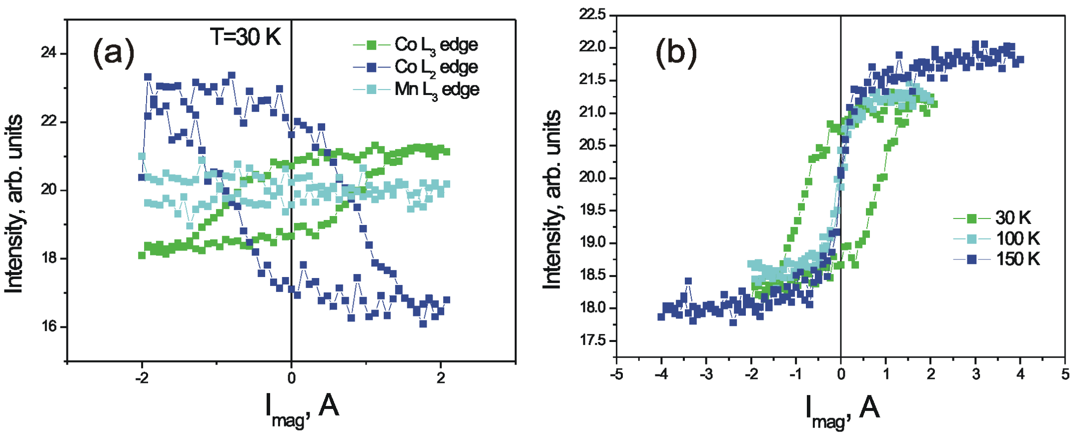

Figure 2: XRMS of a Heusler superlattice [Co$_2$MnGe/V]$_{50}$. Hysteresis loops are plotted for different photon energies (a) and at different temperatures (b). A current of 2 A through the coils corresponds to a magnetic field about 400 Oe.

This project is funded by BMBF (Contract No.O3ZAE7BO). We are grateful Tom Hase (Durham) for Co/Cu multilayer sample and T. Kachel (BESSY) for technical assistance during our experiments at BESSY.

References

[1] J. P. Hannon, G. T. Trammell, M. Blume, and D. Gibbs, *Phys. Rev. Lett.* **61**, 1245 (1988)

[2] D. B. McWhan et. al., *Phys. Rev. B* **42**, 6007 (1990)

[3] D. Gibbs et. al., *Phys. Rev. B* **43**, 5663 (1991)

[4] J. Grabis, A. Nefedov, H. Zabel, *BESSY annual report* (2002)

[5] T. P. A. Hase et. al., *Phys. Rev. B* **61**, R3792 (2000)

Domain structure in antiferromagnetic NiO(001) and exchange coupling to ferromagnetic Fe-adlayers

U. Mick, N.B. Weber, V. Bocatius, H. Meinert, E. Kisker

Institut für Angewandte Physik, Heinrich-Heine-Universität Düsseldorf

The interaction between antiferromagnetic (AF) and ferromagnetic (FM) materials is of interest for both technical applications and basic understanding of magnetic phenomena. Element-specific Photoemission Electron Microscopy (PEEM) utilizing x-ray magnetic linear dichroism (XMLD) was used to investigate the AF-domain-structure of in-situ cleaved NiO(001) surfaces. Thin ferromagnetic iron-layers have been deposited on the NiO-substrate to study its influence on the AF-domains. The FM-domain structure in the iron layer has also been examined by x-ray-magnetic circular dichroism (XMCD). Our experiment has been performed at the Bessy-Beamlines UE56/2-PGM2 and UE52-SGM, which provide x-rays with arbitrary polarization, namely linear S- and P-polarized light for XMLD and circular polarized light for the MCD experiments.

NiO has a bcc rocksalt structure with antiferromagnetic ordering between nearest neighbour Ni-Atoms. This allows the formation of 12 possible domain structures. The Ni-Moments form alternating (111) planes of ferromagnetically coupled Ni-Atoms in the NiO crystal (see fig. 1a) that can be stacked in 4 different ways. For each of these domain families there are three possible spin orientations inside the (111)-plane (fig. 1b), thus setting up 12 different types of AF-domains in the NiO. Two of these domains have identical in-plane moments with respect to the NiO(001) surface forming a set of 6 Twin-domains. These Twin-domains can be identified by the angular dependence of their absorption intensities at the Ni 2p1/2 edge, when the sample is illuminated with S-polarized light and rotated azimuthally around the [001] sample normal

The branching ratio between the absorption intensities of the magnetically split Ni-$2p_{-1/2}$ and the Ni-$2p_{+1/2}$-peaks should follow a cosine squared dependence between the light-polarization and the atoms magnetic Moment [1,2]. Hence the absorption intensities should show a periodicity of 180° degrees with respect to sample rotation when illuminated with S-polarized Light, resulting in a contrast reversal between the AF-twin-domains every 90°-rotation.

Figure 2 shows PEEM-images in different angles around the sample normal. The PEEM pictures are calculated from the difference of intensities between pictures taken at the Ni-$2p_{-1/2}$- and the Ni-$2p_{+1/2}$-peak normalized to the sum of both pictures $((I_{-1/2}-I_{+1/2}) / (I_{-1/2}+I_{+1/2}))$. The upper row shows pictures taken with S-polarized light and differ in the angle of rotation by 90°. The crystals [100] direction is not aligned with the incident beam but tilted about 15 degrees to uncover the variety of domains present in this area.

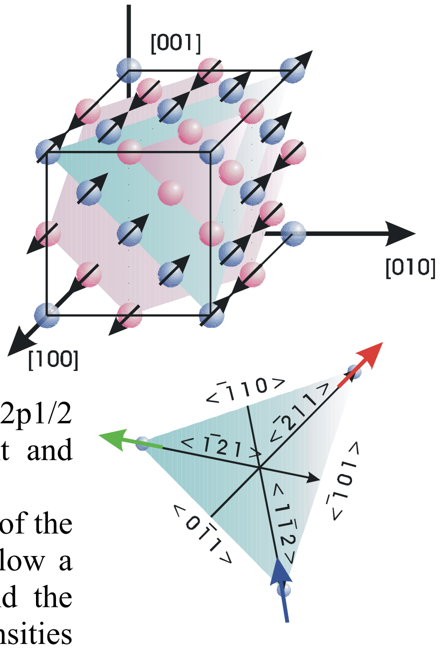

Fig. 1: (a. top) alternating ferromagnetic (111)-planes in NiO with three possible spin orientations within each plane (b. bottom)

The twin-domains have the same magnetic moments in in-plane direction but they differ in their moments normal to the NiO surface. Using P-polarized light adds sensitivity to the magnetic out-of-plane component and the angular dependence upon sample rotation allows to unambiguously identify the exact type of magnetic domain.

On azimuthally rotating the sample the angular dependence of the branching ratio in P-polarized light should show a periodicity of 360° with a contrast reversal by rotating of 180°. The lower row in figure 2 show the same area in the same orientation as in the upper row but illuminated with P-polarized light. These PEEM-pictures show the expected periodicity in the contrast behaviour and especially exhibit distinct areas that show contrast in P-polarized light but no contrast during rotation when observed with S-polarized light (see the area marked by circle). Thus the unambiguous identification of exact domain-types, which have not been distinguished until now, is possible using both S- and P-polarized light.

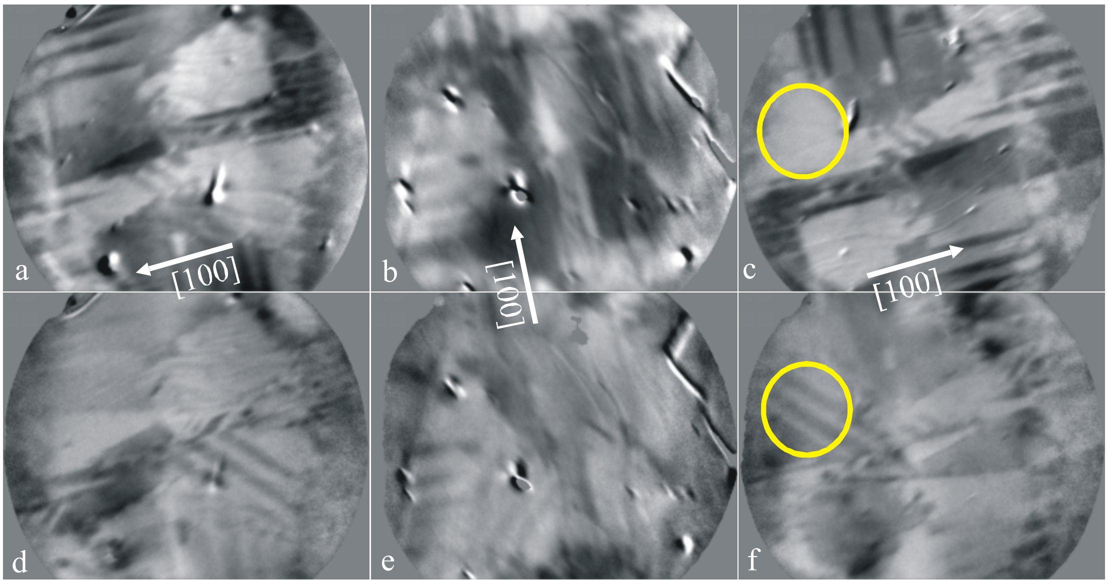

Fig. 2: Contrast images of the NiO(001) surface taken for different angles of azimuthal rotation. (a-c) (S-polarized X-Rays) show contrast reversal every 90° rotation and (d-f) (P-polarized X-Rays) exhibit contrast reversal upon 180° rotation. The field of view is 40µm. The area in the circle shows no contrast difference with S-light but domains distinguishable in P-light

Figure 3 shows the angular distribution of the branching ratio for one selected domain. It shows the expected 180° periodicity quite well, when measured with S-polarized light. For P-polarized light the actual quantitative data are strongly distorted and do not follow the expected sinusoidal characteristics although their trend is in agreement with the theory. The deviation might be caused by a crosstalk of a S-component of the P-polarized light that is due to the incident angle of the synchroton radiation. To improve the data-quality, more care on normalization and background correction has to be conducted in future experiments

Concerning our investigations on the influence of ferromagnetic adlayers, we observed a collinear orientation of the ferromagnetic Fe-Moments to the in-plane components of the AF-substrate, which is in agreement with recent work by Ohldag et al. [4]. From our data it looks like that some domains change their type while others remain unchanged. This would indicate a domain reorientation for some domains rather than an in-plane alignment of the Ni moments due to an adjacent ferromagnetic layer. The influence of sample treatment and sample preparation on these results will be subject to ongoing research.

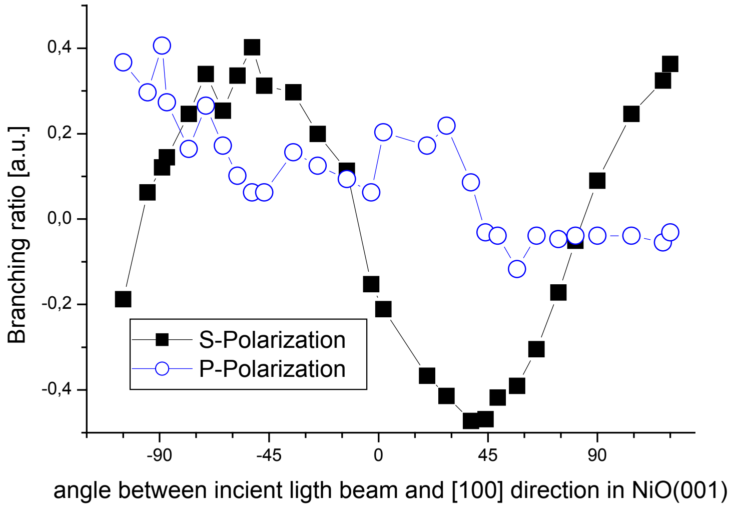

Fig. 3: angular distribution of the branching ratio in the Ni 2p$_{1/2}$-peak of a selected domain under illumination with S-polarized (squares) and P-polarized (circles) X-rays

Acknowledgements: Our work was supported by BMBF under project No. 05KSIPFB/1. We also gratefully acknowledge the financial aid by Bessy travel fund and the helpful support by the BESSY crew, notedly Dr. G. Reichardt and Mr. H. Pfau .

[1] D. Alders, J. Vogel et al., Euro Phy Lett. 32, 259 (1995)
[2] B. T. Thole, G. van der Laan, G. A. Sawatzky, Phys. Rev. Lett. 55, 2086 (1985)
[3] F.U. Hillebrecht, H. Ohldag, N. B. Weber et al. Phys. Rev. Lett. 86, 3419 (2001)
[4] H. Ohldag, A. Scholl, F. Nolting et al. Phys. Rev. Lett. 86, 2878 (2001)

Computed tomography experiments at BAM*line*

G. Weidemann, J. Goebbels, Th. Wolk, H. Riesemeier
Federal Institute for Materials Research and Testing (BAM)
Unter den Eichen 87, 12205 Berlin, Germany

After the first experiments at BAMline in 2001 several improvements on synchrotron computed tomography could be performed. At the beginning of the year the second monochromator was installed, a Double Multilayer Monochromator (DMM) consisting of 150 double layers of W/Si (1.2nm W and 1.56nm Si). The energy resolution of about 1 % compared to the energy resolution of 0.01 % of the Double Crystal Monochromator (DCM) is sufficient for computed tomography experiments. This rather low energy resolution is accompanied by a much higher photon flux density (about 100 times higher) as compared to the photon flux density of the DCM. This reduces the measuring time, improves the Signal to Noise ratio and reduces the image distortions resulting from instabilities of the whole system. To our knowledge for the first time a multilayer monochromator is used for CT-experiments at a synchrotron. The useful energies are in the range from about 5 keV up to 65 keV.

Using a combination of different optical lenses of the detector system the spatial resolution may be varied over a large range. Now voxel sizes of about 10 and 5 µm are routinely in use. The well-known problem of ring artefacts in CT caused by differences in the properties of the detector elements (CCD camera pixel sensitivity and scintillator properties) was partially solved by an appropriate scanning procedure.

Computed tomography offers excellent possibilities to analyse volume properties like pores in foam materials (cf. contribution of Banhart, Haibel et al.), density variations in green state ceramics, fibre distribution in composites or material distributions in geological samples. The monochromatic radiation at synchrotron sources improves in addition the characterization of interfaces, e.g. sharp transitions between different kinds of material. This advantage can be shown especially in very complex structures like biological samples. In collaboration with TU Dresden (TUD) and UKBF of FU Berlin implants and bone samples were investigated. As an example the right image in fig. 1 shows a Ti implant in a bone sample. The photon energy was 50 keV. The image voxel size of 10.8 x 10.8 x 10.8 µm^3 is determined by the area detector. The transitions between resin, bone and implant are very sharp. For the pure bone sample (left image) an energy of 25 keV was selected. Key words in connection with the investigations are bone structure and density, age-related bone loss, bone formation and surface modifications.

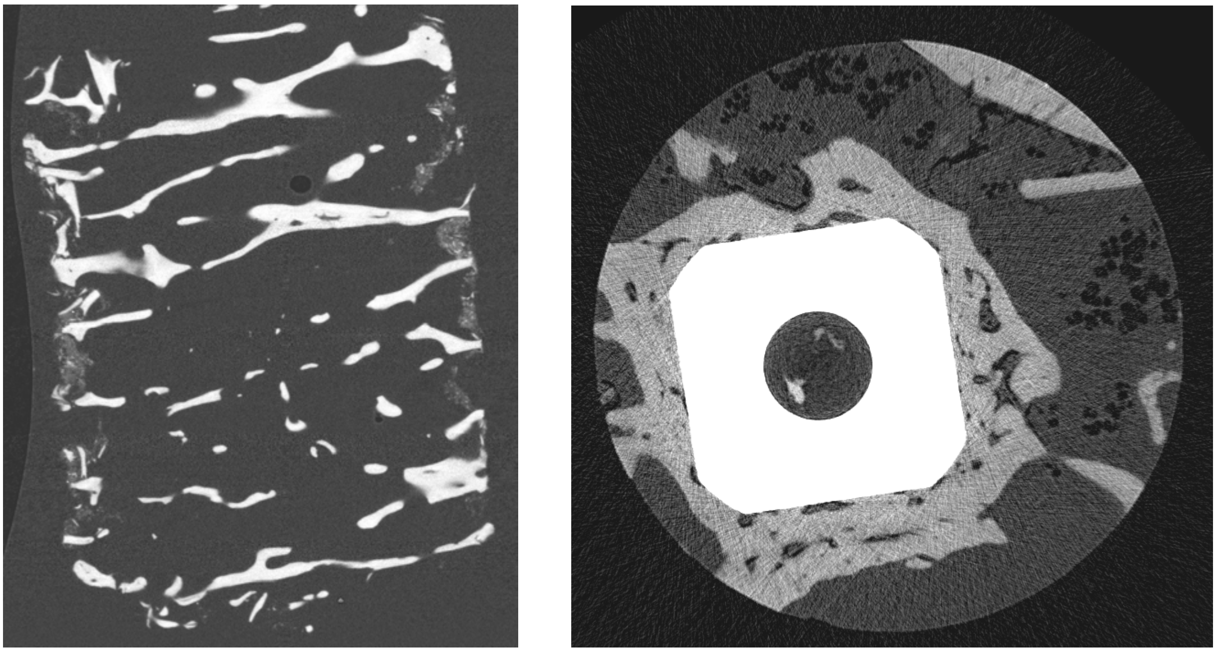

Fig. 1: Vertical slice of a bone sample without (left image) and horizontal slice with a Ti implant (right image). The scan conditions are 25 keV respective 50 keV; the voxel size was (10.8 µm)^3.

References

J. Goebbels, G. Weidemann, H. Riesemeier, A. Nitschke
Charakterisierung keramischer Mikrobauteile mittels Computertomographie-Vergleich von Laboranlagen und Synchrotronstrahlung
Jahrestagung der DGZfP, 6.-8. Mai 2002, Weimar,
Berichtsband 80-CD, ISBN 3-931381-39-0

H. Riesemeier, B. R. Müller, W. Görner, M. Radtke, M. Krumrey
Layout and first applications of the BAMline at BESSY II
EDXRS 2002 - European Conference on Energy Dispersive X-Ray Spectrometry, Berlin, 16.-21. Juni 2002. submitted for publication

Antiparallel Ruthenium coupling in the doped Ruddlesden-Popper-Phase $La_{1.2}Sr_{1.8}Mn_{2-x}Ru_xO_7$

F. Weigand, S. Gold, A. Schmid, J. Geissler, and E. Goering
Max-Planck-Institut für Metallforschung, 70569 Stuttgart, Germany

K. Dörr, G. Krabbes, and K. Ruck
IFW Dresden, 01171 Dresden, Germany

X-ray magnetic circular dichroism measurements (XMCD) in the hard and soft X-ray region have been performed at Mn K and $L_{2,3}$ edges of the Ruthenium (with x=0.05, 0.1 and 0.5) doped Ruddlesden-Popper-Phase $La_{1.2}Sr_{1.8}Mn_{2-x}Ru_xO_7$. In combination with magnetometry a clear evidence for unexpected antiferromagnetic sublattice coupling between Manganese and Ruthenium has been found. A simple coupling model of Mn^{3+}/Mn^{4+} and Ru^{3+}/Ru^{4+} ions in high-spin state is proposed, which explains the antiparallel alignment and the technological interesting increase of the Curie temperature.

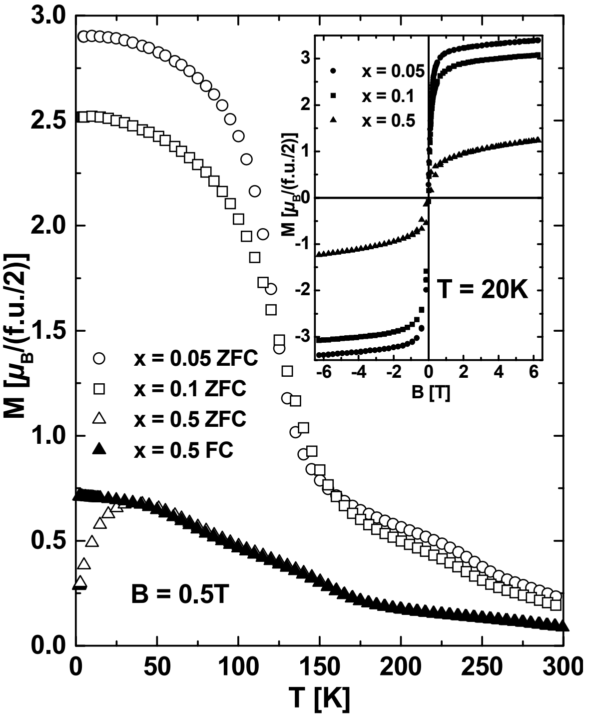

Figure 1: Mn L_2, L_3 edges for different Ru doping levels with an applied external field of B=0.5T. (a) Spin-averaged absorption coefficient μ_0; XMCD signal for (b) T=30K and (c) T=80K.

Since the discovery of the colossal magnetoresistance effect (CMR) near the ferromagnetic ordering temperature a lot of interest was attracted in manganese perovskite-like systems. To combine CMR of three-dimensional perovskites with two-dimensional giant magnetoresistance (GMR) behavior, homologous systems like (La, $Sr)_{n+1}Mn_nO_{3n+1}$ (n=1,2,3), called Ruddlesden-Popper-Phases, have been investigated in the last few years. For n=2 a natural stack of spin-valve devices has been revealed by neutron diffraction. For future technical applications of these systems, it is necessary to achieve Curie temperatures T_C near room temperature, but doping with transition metals usually results in decreased T_C.

In Figure 1 SQUID magnetization measurements are shown for different Ru doping levels, which results in slightly increased T_C, from 122K for Ru doping level of x = 0.05 to 128K for x = 0.1, and further increased T_C of 156K for x = 0.5, while the total magnetization strongly decreases. The maximal saturation magnetization varies from $3.39\mu_B$ to $1.25\mu_B$ per half stoichiometric formula-unit with increasing Ru concentration, measured at B = 6.5T and T = 20K (Fig. 1). To determine element-selective spin and orbital moments, XMCD measurements were performed at the Mn $L_{2,3}$ edges. Figure 2(a) shows the nonmagnetic ($2p \rightarrow 3d$ transitions), and the appropriate magnetic difference (XMCD) signals for the three doped samples at T = 20K (Fig. 2(b)) and 80 K (Fig. 2(c)) respectively. All spin averaged signals are very similar for all doping rates and temperatures, indicating nearly the same chemical environment at the Mn site [1]. For determination of the magnetic moments we fitted the Mn XMCD signal by a superposition of ground state moments to separate L_3 and

L_2 edge contributions, which could not simply be done by conventional sum rules due to the spectral overlap between L_3 and L_2 edges [2][3]. This analysis reveales Mn spin moments of 0.59 (x=0.05), 0.62 (x=0.1) and $0.35\mu_B$ (x=0.5) at T = 80K. By comparison of the spin values with other transition metal oxides we were able to identify a large fraction of this Mn 3*d* spin reduction to O 2*p* related hybridization effects, which are typical a factor of 1.5 to 3 in spin moment reduction [2][4][5]. In addition Mn K edge XMCD spectra have been measured in transmission mode, reflecting bulk properties of the samples. These results are consistend to the $L_{2,3}$ – XMCD data. Therefore, we conclude that relative changes observed at $L_{2,3}$ - edges reflect bulk Mn magnetization properties [1].

SQUID magnetization curves show a much stronger doping dependence as the XMCD results. Therefore, it is clearly necessary to introduce an additional negative magnetization respective to the Mn sublattice. We could clearly identify this antiparralell magnetic coupling of Ru to the Mn sublattice in a simple quantitative model [1].

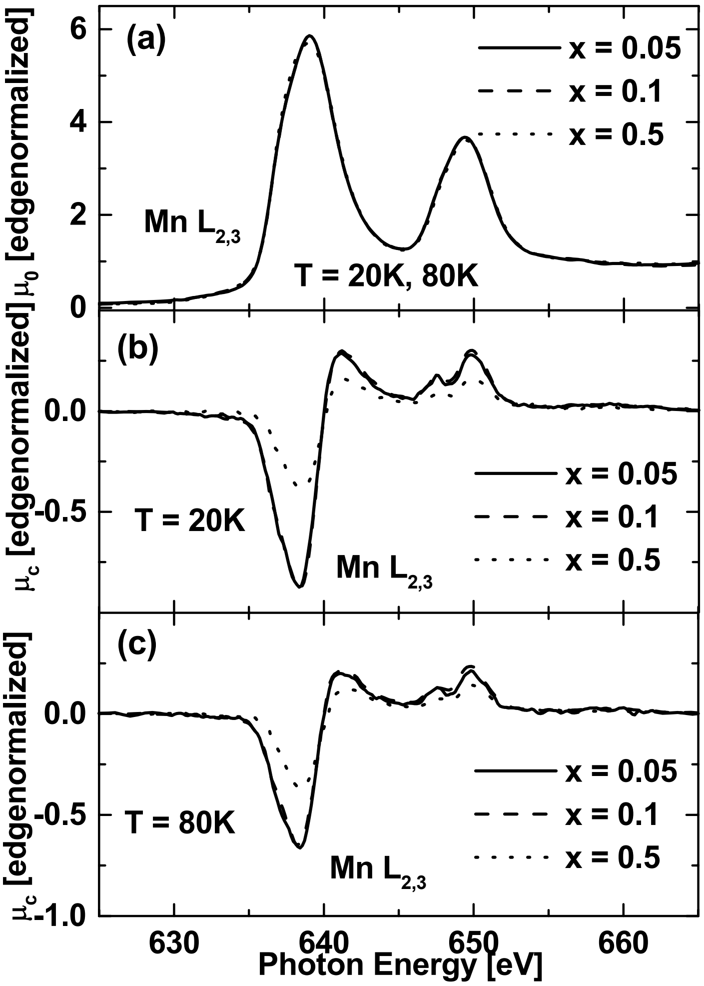

Figure 2: Mn L_2, L_3 edges for different Ru doping levels with an applied external field of B=0.5T. (a) Spin-averaged absorption coefficient μ_0; XMCD signal for (b) T=30K and (c) T=80K.

In conclusion, we have measured XMCD and SQUID magnetization of different Ru doped single phase $La_{1.2}Sr_{1.8}Mn_{2-x}Ru_xO_7$ samples. By a simple comparison of both methods, a clear antiferromagnetic coupled Ru sublattice has been identified. This has been explained quantitatively and consistently by Ru and Mn high-spin states. The enhanced Mn-Ru interaction leads to a higher T_C.

We would like to thank the BESSYII beamline staff for support and help, and S. Nagel and Mrs. G. Eazhilarasi for preparative work. This project is funded by the BMBF.

References:

[1] Weigand, F., Gold, S. et al.; Appl.Phys.Lett. 81, (2002) 2035 – 2037.

[2] Goering, E., Bayer, A. et al.; Phys.Rev.Lett. 88, (2002) 207203-1 - 207203-4.

[3] van der Laan, G.; Phys.Rev.B 55, (1997) 8086 – 8089.

[4] Goering, E., Gold, S., and Schütz, G.; J.Sync.Rad. 8, (2001) 422 – 424.

[5] Goering, E., Justen, M. et al.; Applied Physics A 74, (2002) 747 – 753.

Temperature dependence of CrO_2 magnetic moments and the magnetocrystalline anisotropy energy

S. Gold[1], E. Goering[1], G. Schütz[1], C. König[2], U. Rüdiger[2], and G. Güntherodt[2]
[1]Max-Planck Institut für Metallkunde, Heisenbergstr. 3, Stuttgart, 70569, Germany; [2]II. Physikalisches Institut der RWTH-Aachen, Huyskenweg, Aachen, 52056, Germany

Abstract

Soft X-ray magnetic circular dichroism (XMCD) spectra have been investigated in the temperature range from 25 K to 330 K and for different crystallographic projections for CrO_2 in the total electron yield (TEY) mode. For Fe the Bruno model suggested a relationship of projected orbital moments, spin-orbit coupling and the magnetocrystalline anisotropy energy (MCA) in a cubic crystal field. CrO_2 shows a strong anisotropic behaviour in the XMCD-spectra, for the projected orbital moment and the magnetic dipole term T_z. The T_z -term and the orbital moment favour different easy axes, and the T_z -term dominates the magnetic anisotropy. This has been interpreted quantitatively by the van der Laan model. Temperature dependent measurements of spin, orbital and T_z -moments simultaneously with the MCA, deduced from in situ hysteresis curves, confirms the van der Laan-model for the generation of L (T), T_z (T) and the MCA(T). A quantitative experimental consistency of projected magnetic moments and the MCA, especially as a function of temperature, has been given.

Introduction

In the last few years CrO_2 has attracted revived interest due to its remarkable high spin polarization at the Fermi energy, theoretically predicted to be 100% [1; 2] and recently verified by superconducting tunneling spectroscopy at T = 18K [3] and spin-polarized photoemission spectroscopy at T = 293K [4]. The reasons for this revival are mainly related to promising future technological applications on the basis of CrO_2-electrodes such as magnetic tunneling and spin injection devices. The oxygen mediated coupling and its half metallic nature are a challenging problem for theoretical investigations, originated by the presence of oxygen-hybridization, double exchange, self doping, and correlation effects [1]. The quantitative influence of orbital moments, inner 3d shell spin-orbit-coupling, and the T_z-term to MCA has been recently investigated. But its temperature dependence and the corresponding "generation" of orbital moments and the magnetic dipole term is still unknown.

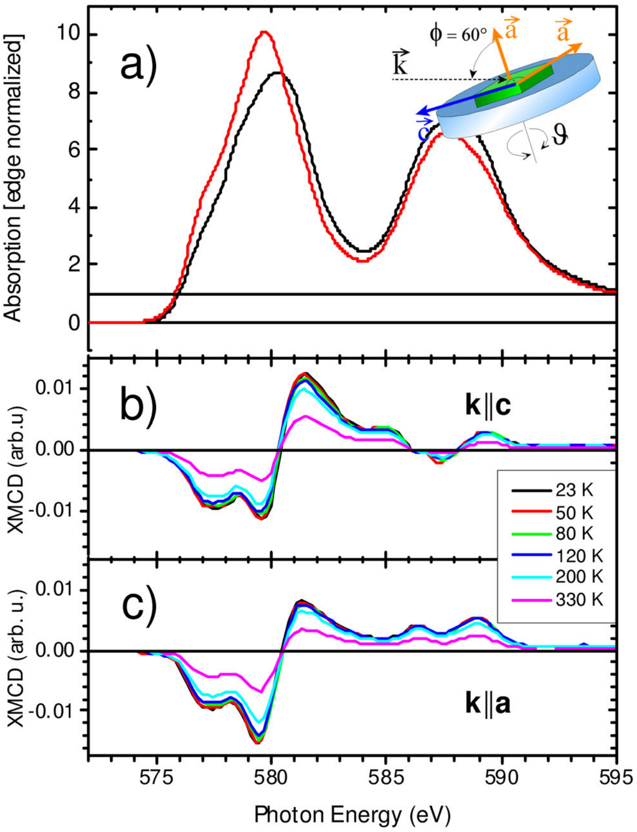

Figure 1: Cr $L_{2,3}$ XAS for parallel and antiparallel magnetization and measurement geometry (a). Temperature dependent XMCD signal for c-axis (b) and a-axis (c) enhanced projections.

Experimental and Discussion

We have investigated epitaxially grown (100) orientated CrO_2 - films, with a sample thickness of about 100nm. All spectra were recorded in total electron yield mode at the new high resolution bending-magnet-beamline PM I at BESSY II in an applied magnetic field of ≤5kOe (flipped at each data point). The degree of circular polarization was about 95%. We have measured with fixed angle of incidence of 60° and two azimuthal angles probing a- and c- axis projected magnetism. Further details of the experimental setup are reported elsewhere [5]. As an example, Fig. 1a shows normalized XAS spectra at intermediate (40deg) projected azimuthal sample orientation. We have measured at two different angles J for enhanced c-axis (Fig.1b) and a-axis (Fig.1c) projections.

By a fitting procedure, called moment analysis, we have extracted the isotropic spin moment **S** (Fig.2a), two orbital contributions **L** for different regions of the unoccupied density of states [5] and the magnetic dipole term $\mathbf{T_z}$. Fig.2b shows the mentioned two orbital contributions for a- and c-axis enhanced geometry, divided by the isotropic spin. Fig.2c shows the $\mathbf{T_z}$ moment divided by the isotropic spin. Orbital and $\mathbf{T_z}$ moments are proportional to the temperature dependent spin moment. This direct proportionality has been theoretically predicted by perturbation theory by Gerrit van der Laan [6]. Fig. 2d shows the hysteresis derived MCA divided by the squared spin moment, which is also constant as a function of temperature. This behavior is expected from the van der Laan model of the MCA, which includes two contributions $\propto \mathbf{L}\cdot\mathbf{S}$ and $\propto \mathbf{T}_z\cdot\mathbf{S}$ [5; 6]. Due to the proposed linear behavior of both moments to the temperature dependent spin moment, the MCA should be proportional to the squared spin moment, which has been proven for this system by our experiments (Fig. 2d).

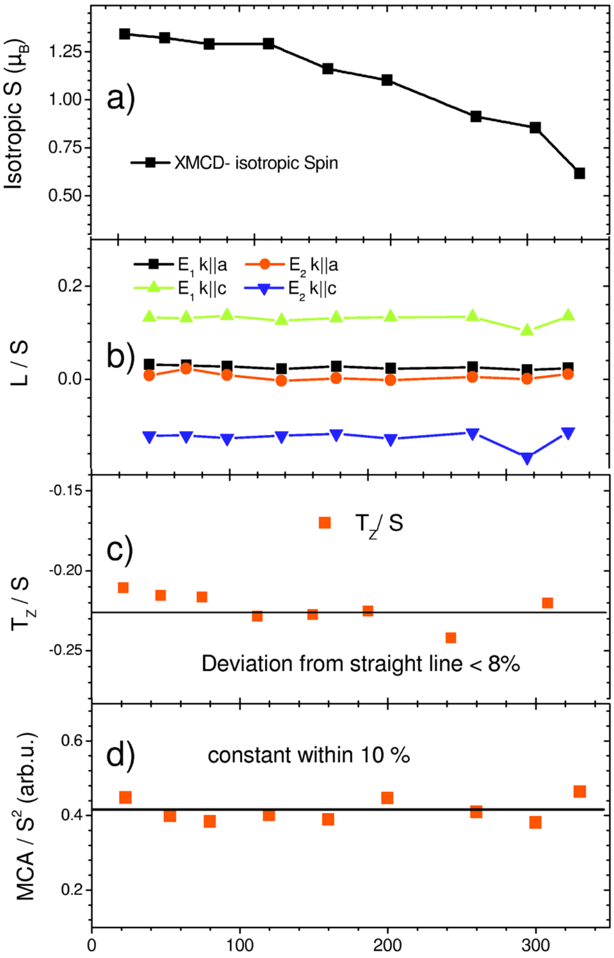

Figure 2: Moment analysis derived projected isotropic spin moment (a). The orbital moments along a- and c-axis (b) and the T_z-moment (c) have been normalized to the isotropic spin. MCA has been divided by the squared isotropic spin (d).

We grateful thank T. Kachel at BESSYII for very kind support during the measurement time.

References:
[1] Korotin, M. A., Anisimov, V. I., et al. Phys.Rev.Lett. 80, (1998) 4305 - 4308
[2] Schwarz, K.; J.Phys.F: Met.Phys. 16, (1986) L211
[3] Soulen, R. J., Byers, J. M. et al. ; Science 282, (1999) 85 - 88
[4] Dedkov, Yu. S., Fonine, M. et al. ; Appl.Phys.Lett. 80, (2002) 4181 - 4183
[5] Goering, E., Bayer, A. et al. ; Phys.Rev.Lett. 88, (2002) 207203-1 - 207203-4
[6] van der Laan, G.; J.Phys.: Condens.Matter 10, (1998) 3229 - 3253

Cobalt Growth on InGaP(001)(2x4): The Interface Formation

K. Lüdge[1], P. Vogt[1], B. Tepper[2], B. Winter[3], O. Rader[2], W. Braun[2], M. Zorn[4], M. Weyers[4],
W. Richter[1] and N. Esser[1]

[1] Technische Universität Berlin, Institut für Festkörperphysik, PN 6-1, Hardenbergstrasse 36, 10623 Berlin,
[2] BESSY GmbH, Albert-Einstein-Straße 15, 12489 Berlin,
[3] Max-Born-Institut, Max-Born-Str. 2a, 12489 Berlin
[4] Ferdinand Braun-Institut, Albert-Einstein-Str. 11, 12489 Berlin

Projekt: **Esser / Richter / Braun**
gefördert von der DFG, Förderkennzeichen: **Es127/4-3** und **Sfb 290 Teilprojekt B6**

For the development of novel spintronic devices based on the junction of ferromagnetic metals (Fe, Co, Ni) on semiconductors it is important to control the structure and composition of the interface and the growing layer. Spin randomizing scattering at non-ideal interfaces is believed to be the limiting factor for realizing spin polarized injection, in particular for devices that use the controlled spin injection into a semiconductor. Detailed knowledge and control of the interface structure and chemistry is thus mandatory. The growth of Fe, Co and Ni on III-V-semiconductors is known to be complicated by significant interfacial reactions. Recently we have demonstrated this, studying the interface formation between the Co and GaAs(001) substrate [1].

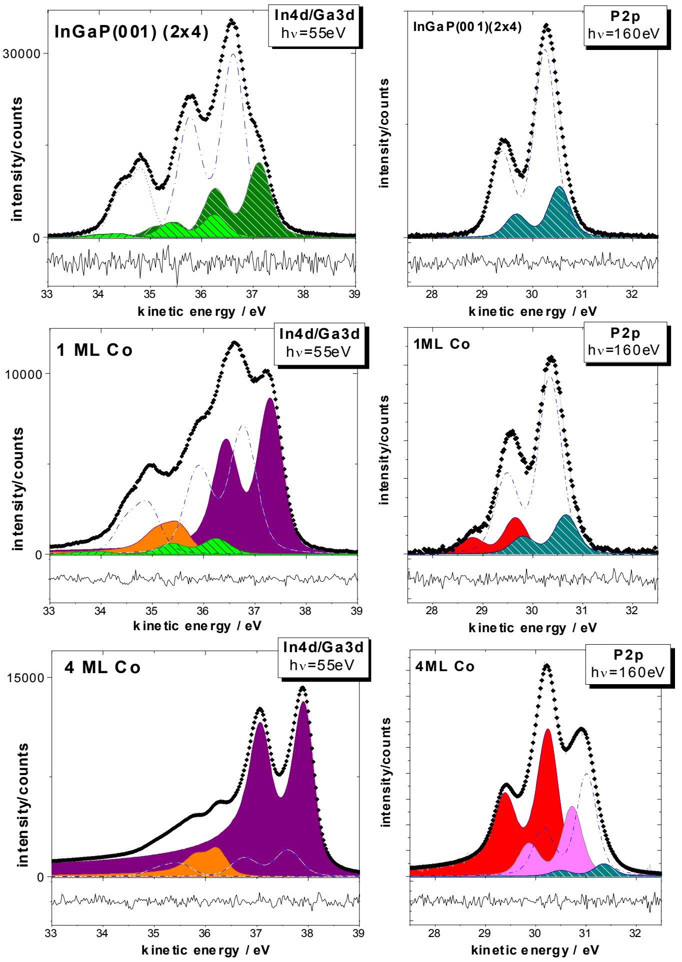

Fig. 1: In3d, Ga3d and P2p core level spectra for growth of Co on InGaP(001) (2x4) at 150°C. Upper, middle, and lower rows refer to clean, 1ML and 4ML of Co. Dashed-dotted lines are the bulk components, hatched and filled curves represent the surface and interface components.

Here we turn to Co on InGaP(001) substrates, a III-V material of the same lattice constant but different composition than GaAs. The objective of this work is to clarify the impact of substrate composition on the reactivity at the interface.

Soft X-ray photoemission spectroscopy (SXPS) measurements were performed at the U125/1 PGM and SGM beamlines with a total instrumental resolution (beamline plus analyzer) of 90meV. STM studies were performed in a separate UHV analysis system located at the TU Berlin. For all of these experiments, metal organic vapour phase epitaxy (MOVPE) grown InGaP samples capped by a P layer were used. In the UHV analysis vessels the protection layer was thermally desorbed at 420°C and subsequently annealed to 460°C to yield an InGaP(001) (2x4) surface, and Co was grown under UHV conditions directly on these surfaces. Surface conditions were checked by LEED and RAS after each preparation step.

A set of spectra obtained for Co growth at a substrate temperature of 150°C is shown in Fig. 1. Surface components arising at the clean surface are characteristic of the mixed-dimer surface structure [2]. With Co deposition strong interface reactions are evident. Metallic In and Ga components develop due to the formation of Co-In and Co-Ga compounds (colored emission components). Dominating is the Co-In reaction. For P two new components evolve, a strong one attributed to elemental P (red) and a small reacted one (pink). Thus, the interface reaction involves mainly the metallic elements In, Ga and Co while P is liberated to a large extent.

The relative intensities of In and Ga in the photoemission spectra can be strongly varied using the photon energy dependence of the cross section (see Fig. 2). By choosing an appropriate photon energy Ga or In components in the spectra can be suppressed or enhanced. The spectra shown in Fig. 1 were taken at 55eV, a photon energy where In is favored by a factor of 2 over Ga. This has to be kept in mind when discussing the relative intensity of the Ga and In peaks.

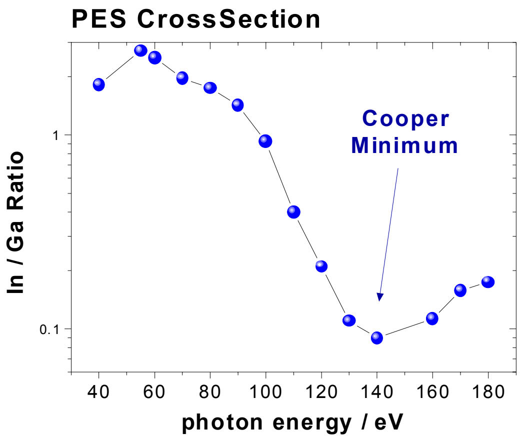

Fig. 2: *Ratio of In/Ga photoemission cross sections as a function of photon energy. Around 140eV photon energy the Cooper minimum of In occurs leading to a pronounced minimum.*

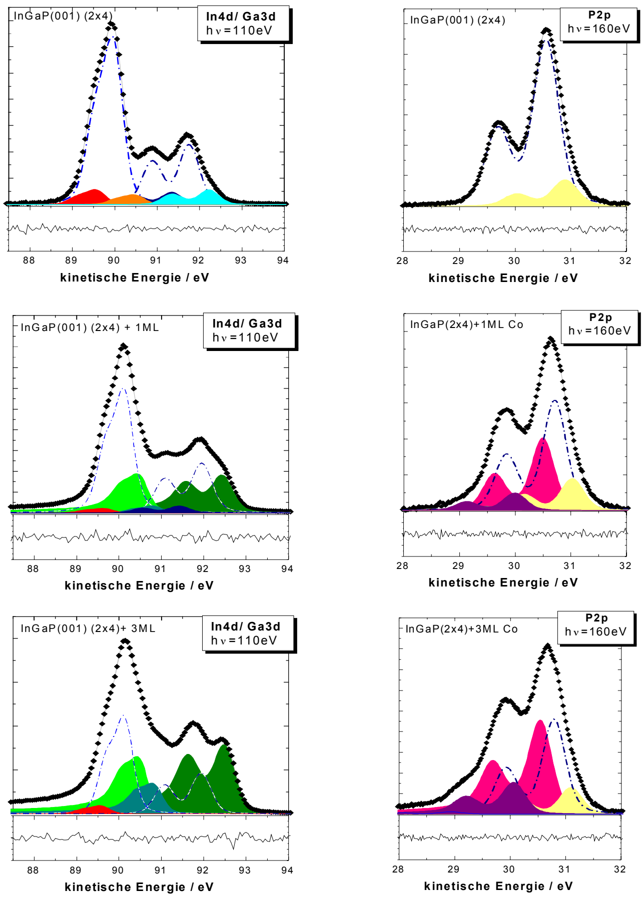

Fig. 3: *In3d, Ga3d and P2p core level spectra for growth of Co on InGaP(001) (2x4) at RT. Dashed lines are the bulk components, hatched and filled curves represent the surface and interface components. The bottom lines represent the residuum.*

In order to reduce the interface reaction Co deposition was performed at RT in a second set of experiments. Fig. 3 shows a set of according spectra taken at 110eV photon energy, where the Ga is favored by a factor of 2 over In, i.e. the ratio is approximately reversed.

Apart from the different cross sections changes of the interface reaction due to a lower growth temperature are minor. Still the strong reaction of the metallic elements shows up, but in contrast to the growth at 150°C at intermediate coverage (1ML) an elemental Ga compound appears in addition. Moreover, the Co-P compound is larger than the elemental P one. At large coverages (>10ML, not shown here) the spectra are similar to the ones of higher substrate temperature. We conclude that the Co-P and elemental Ga components refer to compounds which are thermodynamically unstable and thus less prominent for Co deposition at 150°C. Moreover, the preference of the Co-In reaction over the Co-Ga reaction is substantiated by the appearance of the elemental Ga.
STM images taken for RT (see Ref. [2]) and 150°C deposition temperatures show a disordered overlayer. Fig. 4 shows, as an example, 1ML Co on InGaP(001) for deposition at 150°C. For both deposition temperatures, any indication of epitaxial structures is not observable.

Summarizing, for Co on InGaP a strong interfacial reaction appears which is mainly driven by the reaction of In with Co. Evidence for epitaxial growth of Co was not found. According to the present results, a promising III-V-semiconductor material, leading to a low interface reactivity, might be GaP.

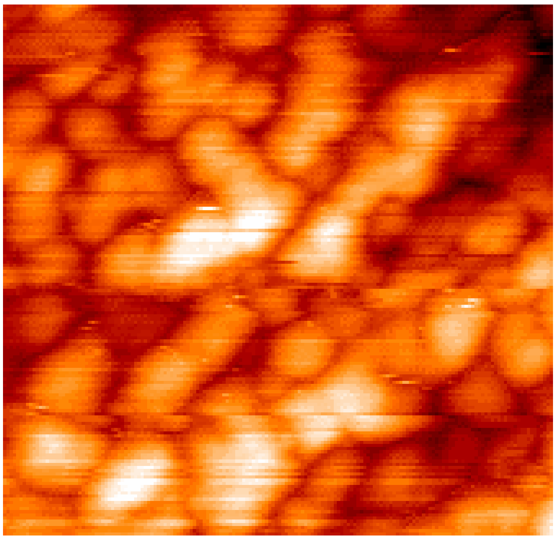

Fig. 3 *Filled state STM image of 8 ML of Co on InGaP(001) (2x4) deposited at RT, image size 50nm x 50nm*

For more details see:

[1] K. Lüdge, B. D. Schultz, M. M. Evans, P. Vogt, W. Braun, C. J. Palmstrøm, N. Esser and W. Richter, J. Vac. Sci. Technol. B **20**, 1591 (2002): *Structure and Interface Composition of Co Layers Grown on As-Rich GaAs(001) Surfaces*

[2] K. Lüdge, P. Vogt, B. Tepper, B. Winter, O. Rader, W. Braun, M. Zorn, M. Weyers, W. Richter and N. Esser, PCSI-30, J. Vac. Sci. Technol. B (2003), to be published.

Surface Crystallinity and Radiation-Amorphization of InP

N. Darowski, I. Zizak, G. Schumacher

Hahn-Meitner-Institute Berlin, Glienicker Strasse 100, D-14109 Berlin, Germany

When a swift heavy ion penetrates a solid, it slows down via the electronic S_e and nuclear energy loss S_n. If the electronic stopping power is sufficiently large (≥ 1 keV/nm), thermal spikes can be induced along the ion track. The energy is first deposited to the electronic system and subsequently transferred into the atomic system via various mechanisms. This transfer results in an increase in the temperature of the atomic system. For sufficiently large electronic excitations the temperature in the spike can exceed a critical temperature of the solid and a molten zone is formed in the wake of the projectile [1]. Quenching of the disorder of the molten zone leads to the formation of a latent track.

In predamaged InP ion tracks are formed when the electronic energy loss exceeds the critical value of about 13 keV/nm [2]. The cores of the tracks are amorphous and track overlap results in a homogeneous amorphous layer at sufficiently high fluences. At room temperature (RT) continuous tracks are generated while at liquid nitrogen temperature (T_{LN_2}) the tracks are discontinuous. At low temperatures 'melting' of the tracks is possibly suppressed by the high thermal conductivity which allows for a fast dissipation of heat [3]. Interestingly, Rutherford backscattering spectrometry [4] and cross-section transmission electron microscopy (TEM) analysis [3] of InP specimens irradiated up to $1.4 \cdot 10^{14}$ Xe/cm^2 point to a 40 nm thick surface layer which is almost defect-free while at depths larger than 40 nm complete amorphization was observed. X-ray diffraction on InP specimens irradiated with 390 MeV Xe ions confirm these findings [5].

On the other hand atomic force microscopy studies of InP after irradiation with 100 MeV Au ions and 180 MeV Ag ions by Singh and coworkers [6] suggested that the defect structure is caused by a cooperation of electronic and nuclear energy loss. Those authors argue that for intense ionization swift heavy ions create a high density of electron-hole pairs along their paths. Electronic excitation thus weakens the covalent bonds and results in an instability of the lattice structure. This instability enhances the damage efficiency of the nuclear energy loss. Because surface amorphization in InP is still poorly understood, it was the aim of this project to examine irradiation-induced surface amorphization in InP.

Pieces of commercially available InP(001) wafers with polished surfaces were irradiated with 350 MeV Au ions (S_n = 135 eV/nm, S_e = 25 keV/nm) at different temperatures up to a fluence of $\Phi t = 3 \cdot 10^{14}$ Au/cm^2. Some of the samples were covered by a 2 μm thick gold degrader foil to change the energy of the projectiles to 230 MeV Au ions (S_n = 150 eV/nm, S_e = 22 keV/nm). A part of the specimen was shadowed from the ion beam during irradiation and served as a reference. The irradiations with swift heavy ions have been carried out at the cyclotron of the ISL, Hahn-Meitner-Institute Berlin.

To study the lattice structure as well as the surface roughness and the thickness of the crystalline zone different x-ray scattering techniques have been combined. Conventional x-ray diffraction (XRD) yields information about the mean bulk properties of the crystal lattice, whereas x-ray reflectometry (XRR) measurements and grazing incidence x-ray diffraction (GID) are sensitive to the surface. The information about the lateral structure on atomic scale is obtainable only by means of GID. The incoming x-ray beam strikes the sample surface under a grazing angle of incidence, α_i, whereas the angle with respect to the diffracting lattice plane, ϑ_i, is measured in the surface. A diffracted beam occurs under a grazing angle of exit with respect to the sample surface, α_f at the detector position $\vartheta_i + \vartheta_f = 2\vartheta_{Bragg}$ whenever an in-plane Bragg reflection becomes adjusted by rotating the sample around its surface normal. By modifying α_i, the penetration depth Λ of the probing x-rays can be tailored and, therefore, enables a depth resolved study of structural changes.

As the disadvantageous ratio between incoming and scattered intensity demands the utilization of synchrotron radiation the scattering experiments have been performed at the KMC-2 bending magnet beamline at BESSY equipped with an (111) Si-Ge double crystal monochromator.

For the experiments a photon energy of $\mathrm{E} = 8.0\,\mathrm{keV}$ has been used, corresponding to a wavelength of $\lambda = 0.155\,\mathrm{nm}$. To enhance the spatial resolution small slits were mounted in front of the scintillation detector. All recorded curves were normalized to the intensity of the primary x-ray beam, which was monitored with an ionization chamber.

Figure 1 shows the diffraction curves recorded at the samples which were irradiated at room temperature with 350 MeV Au ions without degrader foil. $\Delta\theta_\mathrm{f}$ denotes the scattering angle with respect to the Bragg angle of the unirradiated sample. In case of the conventional x-ray diffraction (left) a decrease of the scattered intensity together with a broadening of the peak is observed with increasing fluences. No diffraction peak at all could be observed for the samples irradiated with $3 \cdot 10^{13}$ Au/cm^2 and $3 \cdot 10^{14}$ Au/cm^2. Thus complete amorphization is assumed for these fluences. In case of surface sensitive GID (right) the intensity decrease of the diffraction peak with increasing fluence is less pronounced. Thus the surface near lattice structure of the crystal is less affected by the irradiation than the bulk. This preliminary result points to a crystalline surface layer as observed in case of irradiation with 390 MeV Xe ions.

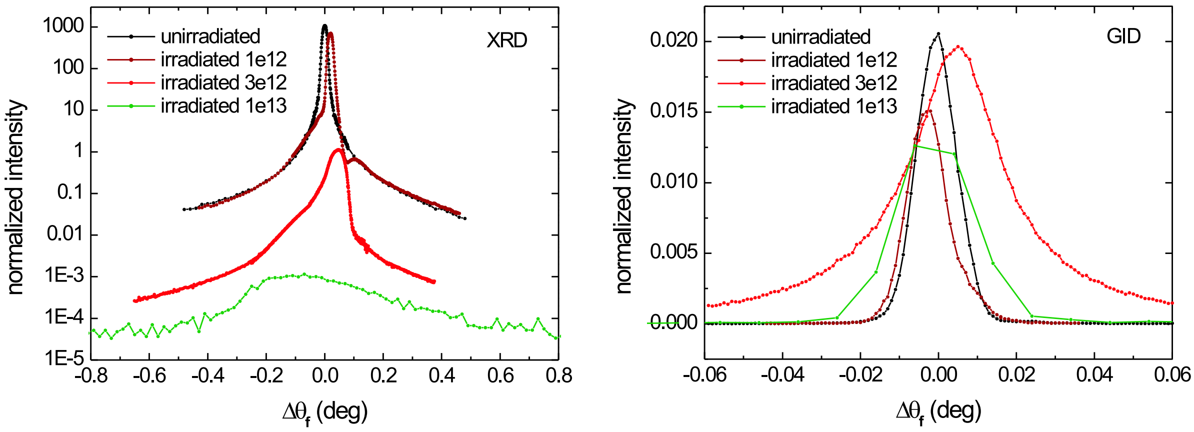

Figure 1 (002) diffraction curves (left) and (220) diffraction curves (right) recorded at InP irradiated with 350 MeV Au ions at room temperature. $\Phi\mathrm{t} = 1 \cdot 10^{12}, 3 \cdot 10^{12}, 1 \cdot 10^{13}$ Au/cm^2.

Figure 2 shows the diffraction curves recorded at samples irradiated at room temperature with 230 MeV Au ions (350 MeV Au ions with a $2\,\mu$m thick Au degrader foil). For the XRD diffraction curves (left) again a decrease of the scattered intensity together with a broadening of the peak is observed for the irradiated samples with increasing fluences. Comparing the GID measurements (right) with those of the samples irradiated without degrader foil no peak is observed for $\Phi\mathrm{t} = 1 \cdot 10^{13}$ Au/cm^2. A possible reason is an increase in surface roughness or Au surface contamination due to the degrader foil. Further investigations will clarify this point. The multi-peak structure of the GID diffraction curves recorded at the irradiated samples is due to a multi-peak primary beam profile. The fitted, individual half widths are comparable to the one of the unirradiated sample. Comparing the diffraction curves recorded at the samples irradiated with (Fig.2) and without (Fig.1) degrader foil in both cases significant amorphization occurs for $6 \cdot 10^{12} \leq \Phi\mathrm{t} \leq 1 \cdot 10^{13}$ Au/cm^2. For a detailed discussion of the contributions of nuclear and electronic energy loss, irradiation with 350 MeV Au ions in combination with a

5 μm thick Au degrader foil will be necessary. The increase in nuclear energy loss in case of a 2 μm thick Au degrader, i.e., the variation between $S_n/S_e = 5.4 \cdot 10^{-3}$ and $S_n/S_e = 6.8 \cdot 10^{-3}$ seems to has no significant effect.

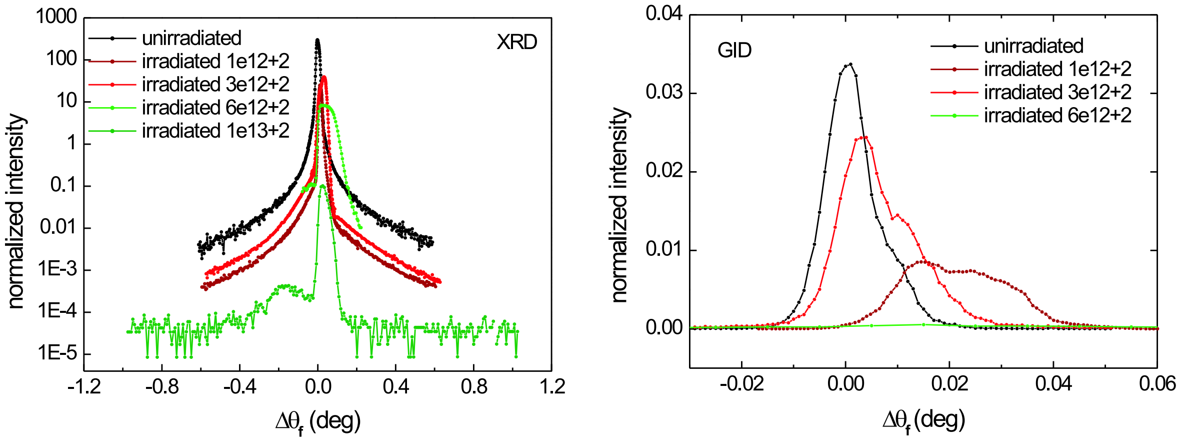

Figure 2 (002) diffraction curves (left) and (220) diffraction curves (right) recorded at InP irradiated with 230 MeV Au ions at room temperature. $\Phi t = 1 \cdot 10^{12}, 3 \cdot 10^{12}, 6 \cdot 10^{12}, 1 \cdot 10^{13}$ Au/cm^2.

Figure 3 shows the XRD diffraction curves recorded at two samples irradiated with a fluence of $1 \cdot 10^{13}$ Au/cm^2, one irradiated at room temperature and one held at liquid nitrogen temperature (80 K) during irradiation. Comparing the diffraction curves for both samples an increase of the intensity ratio between the signal of the unirradiated and the irradiated region is observed in case of the irradiation at low temperature. Thus for cooling to liquid nitrogen temperature the quality of the crystal lattice is improved, i.e. cooling renders amorphization more difficult.

It should be noted that this behaviour of InP is quite different from the amorphization behaviour of metallic alloys and insulators, in which amorphization is the easier the smaller the irradiation temperature is. The anomalous reduction of defect production in InP is tentatively attributed to the high thermal conductivity of the InP single crystal at low temperatures. Such an interpretation implies that the nucleation of disorder (or melting) in the track requires a critical time which will not be reached in InP volume cooled to 80 K. This anomalous defect production is reproduced for a second sample irradiated at low temperature with a fluence of $6 \cdot 10^{12}$ Au/cm^2.

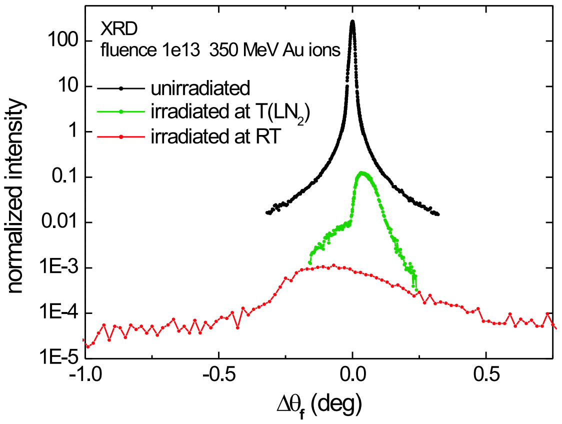

Figure 3 Comparison of the (002) XRD diffraction signal recorded at InP irradiated at room temperature and at liquid nitrogen temperature.

[1] H. Trinkaus, *Mater. Sci. Forum* **248-249** (1997) 3.
[2] W. Wesch *et al.*, *NIM* B **146** (1998) 341.
[3] P.I. Gaiduk *et al.*, *NIM* B **164-165** (2000) 377.
[4] O. Herre *et al.*, *Phys. Rev.* B **58** (1998) 4832.
[5] N. Darowski *et al.*,, *NIM* B (2003), in print.
[6] J.P. Singh *et al.*, *NIM* B **179** (2001) 37.

SY-XRF in certification of a reference material at the BAM*line*

A. Berger, W. Görner, S. Merchel, M. Procop, M. Radtke, H. Riesemeier
Bundesanstalt für Materialforschung und –prüfung (BAM), 12200 Berlin, Germany

In 2002 the BAMline participated with XRF measurements in the certification of the new reference material BAM-M387 (CuZn20Ni5). This material is one of the alloys which is used for the Euro coins.

The XRF investigations were performed with monochromatic radiation at an energy of 32 keV. At the BAMline two monochromators are available, a Double Multilayer Monochromator (DMM) and a Double Crystal Monochromator (DCM). For these measurements the DMM is used only. Beside the higher photon flux the DMM in contrast to the DCM has no relevant intensities in the higher harmonics. The last property is very important for the element quantification with high accuracy. Its limited resolving power E/ΔE of about 80 is acceptable for XRF applications.

To take part in the certification process of reference materials only primary methods are permitted. The Committee for Amount of Substance (CCQM) definition of a primary method of determination of amount of substance (i.e. an analysis) implies that the results of the measurement process is expressed without reference to a standard of the quantity being measured. These can be obtained experimentally by measuring one or more pure element reference samples under identical measuring conditions as those of the samples [1]. In our case we have measured thick polished samples of the material to be certified and thick polished pure element samples of the elements of interest. The quantity which was used to determine the elemental concentration in the BAM-M387 material was the ratio of the normalized count rate for the pure element sample and the BAM-M387 sample. This procedure has the advantage that the detector influence is eliminated and the influence of uncertainties in cross sections are minimized .

Because in XRF higher order effects must be taken into account, the calculations are based on an iterative approach. For the calculations the Monte Carlo program msim5d from Dr. L. Vincze, University of Antwerp, has been used. The simulated interaction types are the (i) photoelectric effect, followed by the emission of a fluorescence photon or Auger electron, (ii) Rayleigh (elastic) or (iii) Compton (inelastic) scattering and (iv) photo-electron bremsstrahlung.

Although the final results of the certification are not available up to now, preliminary evaluation shows, that the XRF measurements are in good agreement for the elements which can be determined undisturbed. I.e. the relative deviation for Cu (nominal value about 75.2%) is 0.1%, for Zn (19.5%) and Mn (790 ppm) they differences are about 1%, for Ni (5%) the deviation is 6%. This is caused by imprecise peak area determination due to the dominant Cu peak, which disturbes the evaluation of the Ni peak. For the used Si(Li) detector the Cu escape peaks overlaps with the Fe peak and therefore increase the determined count rates for iron. This results in a 27% to hig Fe (630 ppm) value.

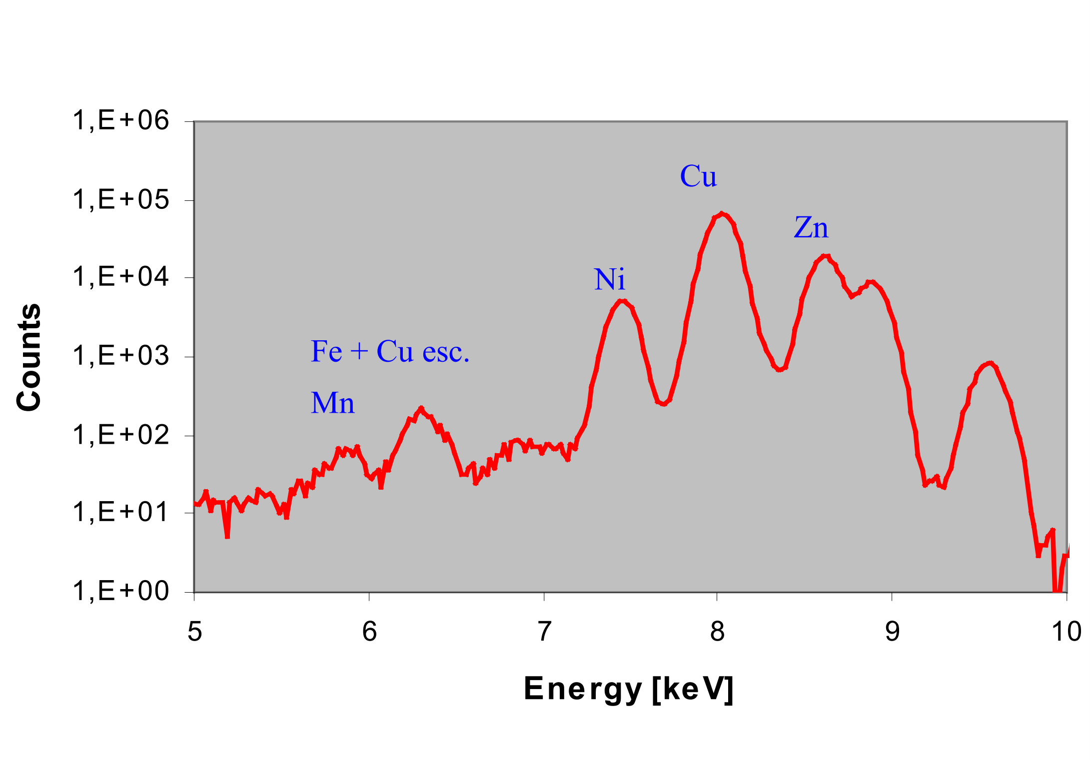

Fig.1: Spectra of the BAM-M387 reference material in the range of 5 to 10 keV. The spectra was collected for 300s with an excitation energy of 32 keV.

In the future the precision for the unsatisfactory elements will be improved by using different detectors, i.e. HpGe or WDX detector, and different excitation energies to suppress peak overlap.

[1] F. Adams, Synchrotron radiation micro-X-ray fluorescence analysis: A tool to increase accuracy in microscopic analysis, NIM B Corrected proof

Processing steps in $CuInSe_2$ solar cell technology: characterization by SXPS

R. Hunger[a*], T. Schulmeyer[a], M. Lebedev[a], A. Klein[a], W. Jaegermann[a], and S. Niki[b]

[a] Fachgebiet Oberflächenforschung, Institut für Materialwissenschaft, TU Darmstadt
[b] Thin Film Solar Cells Group, Energy Electronics Institute, AIST, Tsukuba, Japan

Introduction. For polycrystalline Cu(In,Ga)Se2 (CIGS) thin film solar cells, conversion efficiencies up to 18.8% have been achieved[1]. A recent efficiency improvement was associated with the change in preferred CIGS orientation from (112) to (110)[1]. We have investigated the effect of the surface orientation on the junction formation with CdS. To this end, we have explored the preparation of clean, contamination-free $CuInSe_2$ surfaces by means of a selenium capping and decapping process. Employing such decapped epitaxial $CuInSe_2$(001)/GaAs, we have characterized the junction formation with CdS. The photoemission characterization was performed at the U49/2-PGM2 beamline of the TU Cottbus/HMI/TU Darmstadt CRG in a UHV preparation and analysis system equipped with an Omicron EA 125.

Results and Discussion-1. Figure 1 shows the valence band spectra of epitaxial $CuInSe_2$(001) films 12 months after growth and storage in air. One of the samples was stored in air in the as grown state. The other epilayer that was covered with a protective amorphous Se cap immediately after growth and decapped prior to characterization by thermal annealing to 300°C. The valence band of the non-capped sample shows the typical broad, structureless features of surface oxides with hydrocarbon contamination. With $h\nu = 1050$ eV excitation a strong O1s signal is observed. Obviously, during the 12 months of storage in air, a surface oxide layer has formed. The decapped $CuInSe_2$(001) surface exhibits sharp valence band structures characteristic of Cu-poor CIS, and a nicely resolved In4d doublet with $E_B^{vbm}(In4d_{5/2}) = 17.22$ eV. The inset in Fig. 1 shows the relative contributions of Cu3d and S3s/p states to the valence band DOS of stoichiometric $CuInSe_2$ [2]. The pronounced dip in the valence band around 3.7 eV results from the reduced Cu-content compared to the stoichiometric surface. The high spectra quality of the decapped samples is accompanied by low surface contamination signals of O1s and C1s (not shown). It can be concluded that the selenium capping and decapping process is an efficient method to preserve at ambient and restore in UHV clean and well-defined $CuInSe_2$ surfaces.

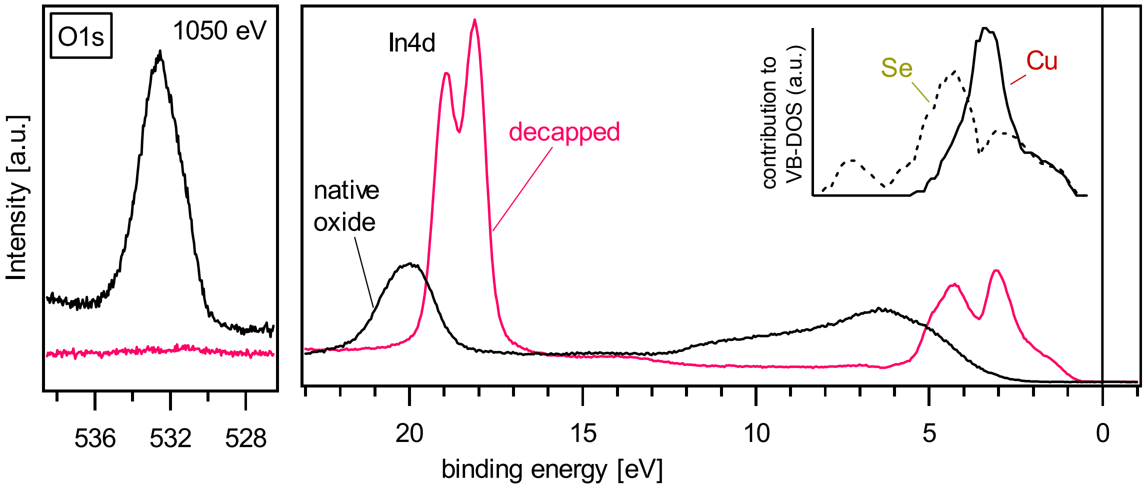

Figure 1: Comparison of the valence band spectra and the O1s core level of a Se-decapped $CuInSe_2$(001) epilayer and a non-capped, native oxide surface of $CuInSe_2$(001). The comparison demonstrates the effectiveness of the Se capping and decapping process for the conservation and preparation of clean, well-defined $CuInSe_2$ surfaces.

---

[*] E-mail: hunger@surface.tu-darmstadt.de

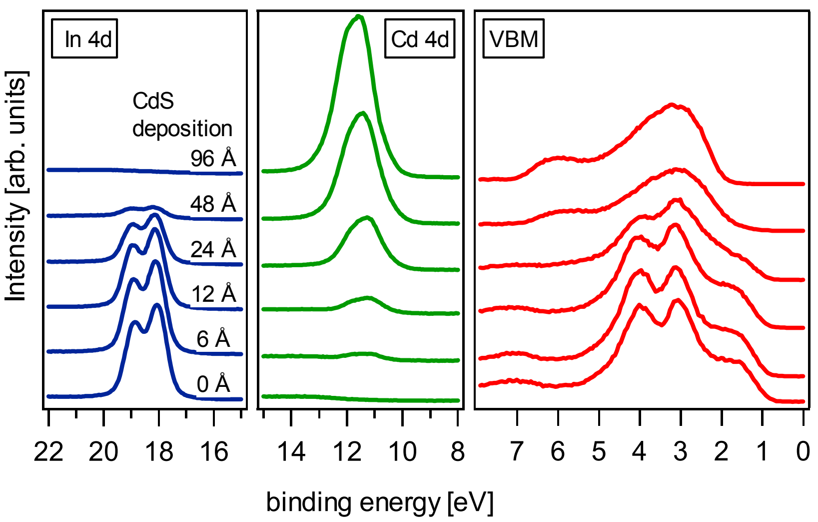

Figure 2: Monitoring of the $CuInSe_2(001)/CdS$ junction formation by stepwise deposition of CdS and subsequent photoemission characterization with hν = 95 eV.

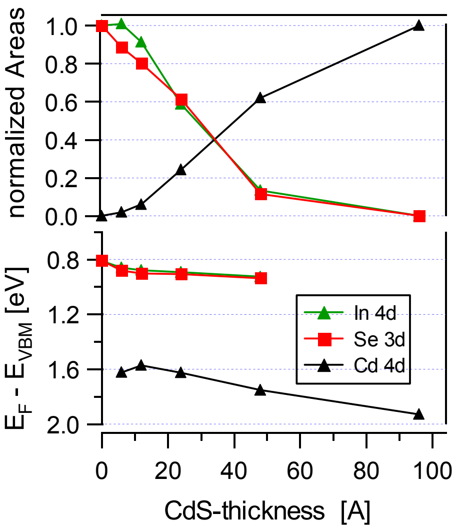

Figure 3: Development of the core level peak intensities and the positions of the valence band maximum of $CuInSe_2(001)$ and CdS with increasing CdS coverage. From the 48 Å coverage step, a valence band offset of 0.83 eV is obtained.

On decapped $CuInSe_2(001)$ surfaces, a heterojunction with CdS was formed by the stepwise vacuum evaporation of CdS. Photoelectron spectra taken after each deposition step are shown in Fig. 2. The In4d signal is continuously attenuated with the increase of the CdS overlayer thickness. The peak shifts of the shallow In4d and Cd4d core levels are due to the band banding induced by the junction formation. Taking the clean $CuInSe_2(001)$ surface and the thick CdS layers as reference points for the core level to valence band maximum separation, the evolution of the valence band maxima is extracted from the core level shifts, as plotted in Figure 3. As the junction formation is closed to completion for the 48 Å coverage, a valence band offset of 0.83 eV between Cu-poor $CuInSe_2(001)$ and CdS is extracted from the experimental data. A similar value, 0.85(15) eV, had been found for the band alignment of polycrystalline Cu-poor $CuIn_3Se_5$ with preferred (112) orientation with CdS[3], hence the surface orientation appears to have only a minor effect on the band alignment. We conclude that the reported solar cell efficiency increase from 17.7 to 18.8% when going from non-textured to preferred (110) orientation[1] appears not to be related to a change in band alignment.

Results and Discussion-2. Our second focus in the solar cell process technology was the wet chemical bath deposition of CdS. In order to understand the complex processes during the wet chemical junction formation, we have investigated the effect of a single component of the chemical bath, the ammonia base solution. The investigation was performed at the U49/2-PGM2 using the SoLiAS system, which allows for the wet chemical treatment of surfaces under the controlled conditions of an atmospheric pressure inert gas cell, combined with a direct and quick transfer to vacuum. Figure 4 shows a schematic sketch of this system. Mounted on the sample holder, the sample is transferred from the vacuum system to

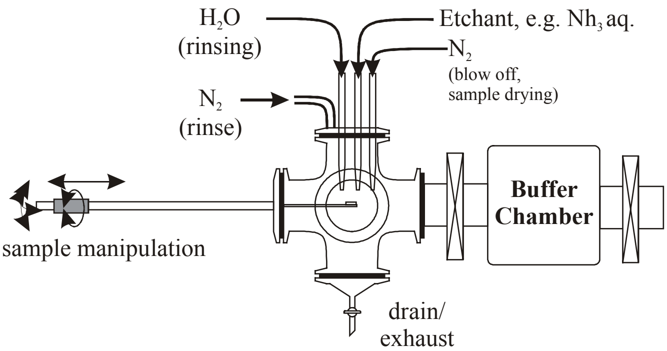

Figure 4: Schematic sketch of the atmospheric pressure electrochemistry cell for wet chemical treatments under controlled conditions and quick and direct transfer to the vacuum system via the so-called buffer chamber, a special-purpose load lock.

the electrochemistry cell, and exposed to a droplet of the etchant. The chemical treatment is terminated by blowing of the etchant droplet by nitrogen. Further details on our Solid-Liquid Interface Analysis System (SoLiAS) can be found in a separate contribution to this annual report.

Figure 5 shows the photoelectron spectra of a native oxide surface of epitaxial $CuInSe_2(001)$, and after etching in ammonia solution (25%, 1.5 min). For comparison the spectra of a decapped $CuInSe_2(001)$ surface are included as well. As the spectra evidence, the NH_3 etch leads to $CuInSe_2$ surfaces of remarkable quality: The spin-doublet splitting of the Se3d and In4d core levels are clearly resolved. A well-structured valence band is observed. Instead of a dip at 3.7 eV, a pronounced peak at 3.2 eV is found. This peak arises from the Cu3d contributions to the VB DOS and is caused by the much higher Cu content of the NH_3 etched film suface of [Cu]/[In]~0.8 compared to the decapped sample with [Cu]/[In]~0.4. It can be concluded that one of the functions of the chemical bath process of the solar cell technology is the removal of native surface oxides by the ammonia content of the process solution.

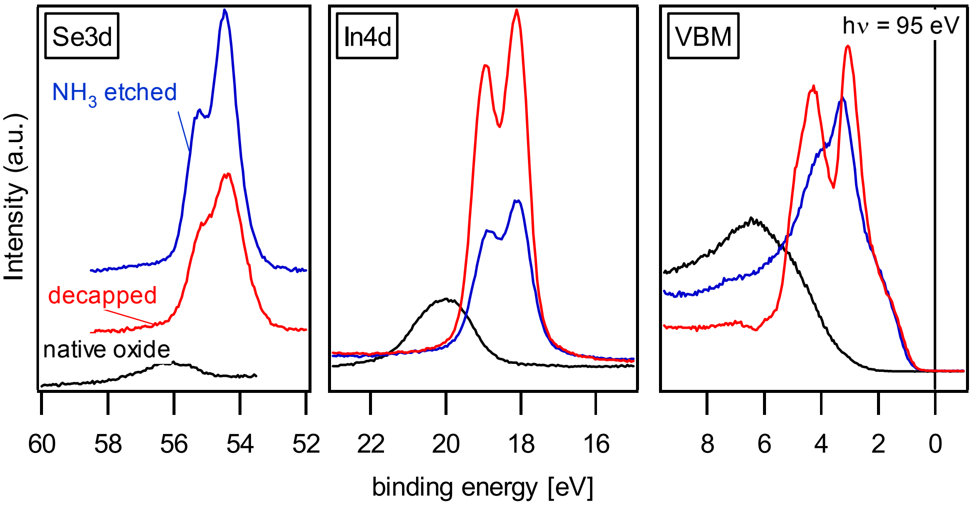

Figure 5: Comparison of the core levels and the valence band structure of a native oxide surface of epitaxial CuInSe2(001), and after etching in ammonia solution (25% NH_3) for 1.5 min. The NH_3 etch removes surface oxides effectively and photoelectron spectra with remarkable quality are obtained, as the comparison to the UHV-prepared, decapped $CuInSe_2(001)$ surface demonstrates.

For the future we plan to continue our studies and exploit the unique features of the SoLiAS system by stepwise increasing the complexity of the chemical treatment, including the remaining components of a Cd salt and thiourea. By comparison of these treatments to model systems of $CuInSe_2/CdS$ interfaces prepared in UHV, we want to get the complete picture and detailed understanding of the unique advantages of the chemical bath process.

[1] M. A. Contreras, B. Egaas, K. Ramanathan, J. S. Hiltner, A, F. Hasoon, and R. Noufi, Progress in Photovoltaics and Research Applications **7,** 311 (1999).

[2] T. Löher, A. Klein, C. Pettenkofer, and W. Jaegermann, Journal of Applied Physics **81,** 7806 (1997).

[3] D. Schmid, M. Ruckh, F. Grunwald, and H. W. Schock, Journal of Applied Physics **73,** 2902 (1993).

Commissioning of the Solid/Liquid Analysis System SoLiAS

R. Hunger, M. Lebedev, Th. Mayer, W. Jaegermann
Fachbereich Materialwissenschaften Technische Universität Darmstadt
C. Pettenkofer, Hahn-Meitner-Institut Berlin
D. Schmeißer, Brandenburgische Technische Universität Cottbus

BMBF 05 KS1RD / 0

The SoLiAS experimental station is a versatile preparation system dedicated to the investigation of solid/liquid interfaces with synchrotron radiation induced photoelectron spectroscopy SPS. During 2002 the system was installed at BESSY and succesfully commissioned at beamlines TGM 7 and U49/2. With the SPECS Phoibos 150 analyser a overall resolution below 200 meV is reached (Fig.1). The Phoibos 150 is retractable allowing free rotation of a VG ADES 500 ARUPS analyser installed in addition. In order to adapt the station to various beamlines it can be inclined horizontally versus its frame by 7°.

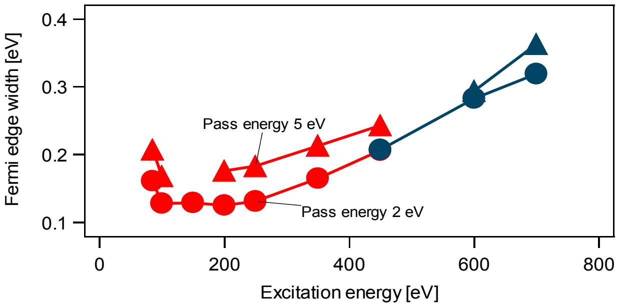

Fig.1:
Uncorrected width of Ag Fermi edge at RT measured with the Phoibos 150 analyser at beamline U49/2 with pinhole 1mm x 1mm. 1st harmonic red, 3rd harmonic blue.

The UHV analysis of solid/liquid interfaces may be performed with SoLiAS by three complementary routes:

i) synthesis of a model electrolyte in vacuo by coadsorption of solvent and redox species onto LN_2 cooled sample surfaces,
ii) emersion of a specimen from a liquid electrolyte and transfer to vacuum under inert (N_2) atmosphere,
iii) creation of frozen electrolytes by cooling emersed samples before pumping to UHV conditions.

Interface engeneering by means of electrochemical processes is of great technological interest. For the anylysis of solid/solid interfaces SoLiAS is equipped with

iv) vacuum preparation like heat treatment, sputtering, or PVD/CVD of contact materials.

Thus SoLiAS allows by emersion experiments ii) to analyse surfaces after technologically relevant wet preparation prozesses like etching [1,2], electrochemical oxidation and reduction [3], or electrodeposition of contact materials [4]. While wet chemical processes may be complex reaction sequences and ii) allows for the analysis of a final situation only, emersion experiments may be complemented by adsorption experiments i). By adsorption the interaction of a defined single electrolyte species with a surface may be investigated [5], by coadsorption of solvent and redox species the cooperative interaction with a specimen is accessible and may provide insight into intermediate reaction steps [1]. Furthermore the interaction of the solvent and an electrolyte species may be investigated by coadsorbing electrolyte constituents on inert surfaces [6]. Cooling of the sample before evacuation iii) allows to analyse soluble and volatile reaction products. In addition iii) allows to measure the occupied electron states of real (albeit) frozen electrolytes. Not only the impact of wet chemical processes on interface formation may be analyzed by UHV deposition iv), but also a comparision of wet chemically produced interfaces to vacuum deposited interfaces may be drawn [7]. The unique combination of integrated preparation options of SoLiAS is complemented by a fast entry load lock permitting high flexibility in sample usage.

While the data of the cited references were taken at different experimental systems with one of i)-iv) preparation facilities temporarily in use at a beamtime, all four are now permanently available at the same time. The presented data of fig. 1 to 5 were actually taken with SoLiAS, exemplifying its versatility. LN_2 cooled transfer between adsorption chamber and analysis chamber is demonstrated by H_2O adsorption onto a vacuum cleaved WSe_2 single crystal. Fig.2 shows the valence band emissions of orbitals $1b_2$, $3a_1$, and $1b_1$, the fingerprint of molecularly adsorbed water. The spectra were taken with a photon energy of hν=30 eV at beamline TGM7.

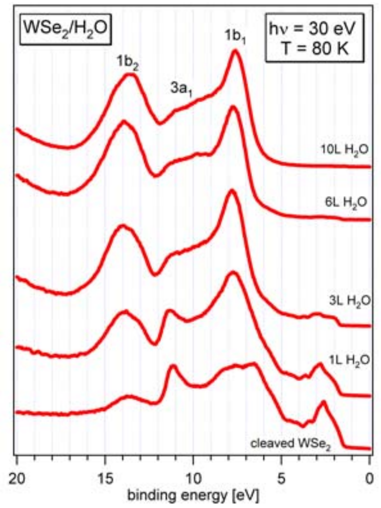

Fig.2
Valence aband spectra of H_2O adsorption on a LN_2 cooled WSe_2 crystal. The emissions $1b_2$, $3a_1$ and $1b_1$ indicate molecular adsorption. Spectra taken at beamline TGM7.

SPS on emersed samples is demonstrated by etching off the natural oxide of a GaAs (100) wafer surface in a solution of 3% HCl in water. The As and Ga 3d core level spectra of Fig.3a and b were taken at the U49/2 with highest surface sensitivity. The etched surface is covered with a layer of elementary As and As-H. Some remnants of intermediate AsCl and GaCl reaction products are found which can be rinsed off by deionized water as we have shown before.

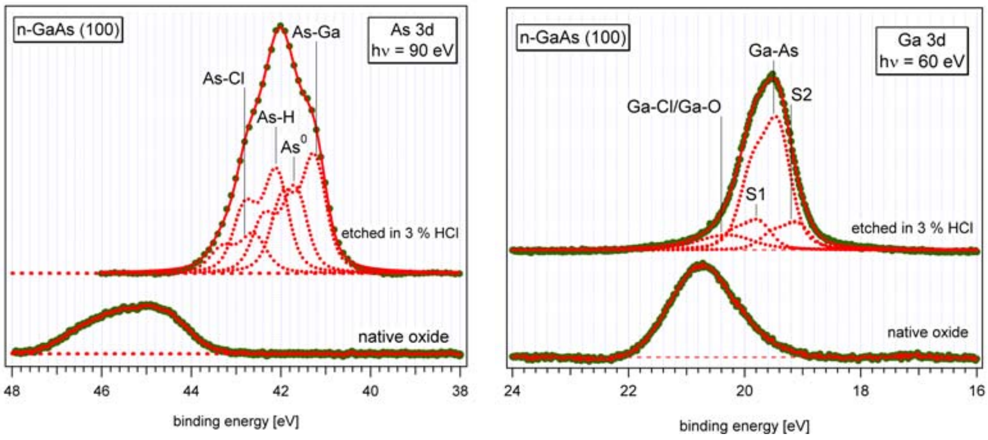

Fig.3 a,b
As and Ga 3d core levels of GaAs (100) native oxide and etched in 3% HCl in H_2O. Spectra taken at beamline U49/2.

Electrochemistry on defined vacuum-prepared surfaces immersed and emersed in clean N_2 atmosphere without contact to ambient air is demonstrated by a GaAs (100) surface vacuum cleaned by sputter-anneal cycles. Detailed comparison of the surface composition after contact to the solvents water or isopropanol is shown. In january 2003 also the freezing in of volatile reaction products by cooling of an emersed electrode was demonstrated.

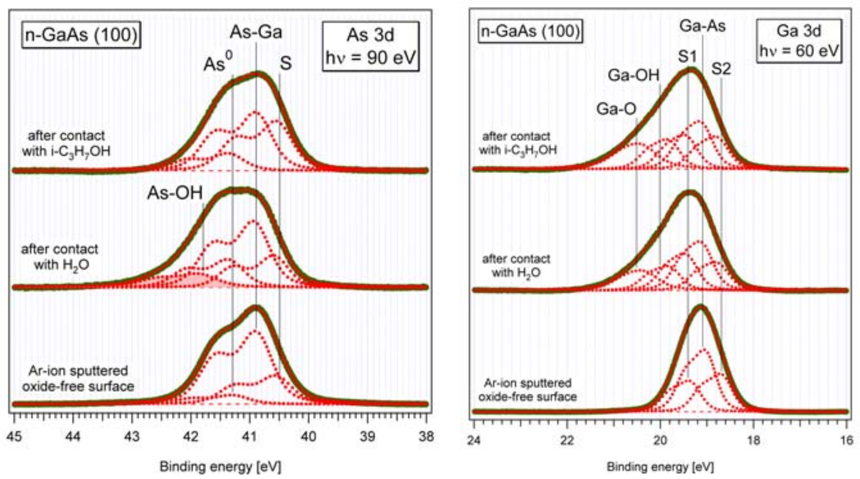

Fig.4 a,b
As and Ga 3d core level of sputter cleaned GaAs (100), and this surface after contact to liquid H_2O or isopropanol.

[1] M.Beerbom, O. Henrion, A.Klein, Th.Mayer, and W.Jaegermann
XPS analysis of wet chemical etching of GaAs by Br_2/H_2O: Comparison of emersion and model experiments.
Electrochimica Acta 45 (2000) 4663-4672.

[2] M.Beerbom, Th. Mayer, and W. Jaegermann
Synchrotron-Induced Photoemission of emersed GaAs Electrodes after ElectrochemicalEtching in Br_2/H_2O Solutions.
J. Phys. Chem. B 104 (2000) 8503

[3] M. Beerbom, Th.Mayer, W. Jaegermann TU-Darmstadt;
D.R. Batchelor, D. Schmeißer, BTU Cottbus
Synchrotron-Induced Photoemission of GaAs Electrodes after ElectrochemicalTtreatment in Aqueous Electrolytes.
Analytical and Bioanalytical Chemistry 374 (2002) 650-653

[4] D. Ensling, R. Hunger, D. Kraft, Th. Mayer and W. Jaegermann
Institute of Materials Science TU-Darmstadt
M. Rodriguez-Girones, V. Ichizli and H. L. Hartnagel
Institute of Microwave Engeneering TU-Darmstadt
Pulse Plating of Pt on n-GaAs (100) Wafer Surfaces: Synchrotron Induced Photoelectron Spectroscopy and XPS of Wet Fabrication Processes
Proc. of EMRS 2002; Nucl. Instrum. Meth.B, 200C (2003) 432

[5] Th. Mayer, A. Klein, O. Lang, C. Pettenkofer, and W. Jaegermann
H_2O adsorption on the layered chalcogenide semiconductors WSe_2, InSe, and GaSe
Surf. Sci. 269 / 270 (1992) 909

[6] Th. Mayer and W. Jaegermann
A Photoemission Study of the Solut-Solvent Interaction: Stepwise Solvation of Na^+ by Coadsorbed H_2O on a Semiconductor Surface Induced by the Synchrotron Photoemission Source.
J. Phys. Chem. B 104 (2000) 5945

[7] D. Kraft, A. Thißen, M. Campo, M. Beerbom, T. Mayer, A. Klein, and W. Jaegermann *Electronic Properties of Chemically Etched CdTe Thin Films: Role of Te for Back Contact Formation*
Materials Research Society Symposium (2001) Strasbourg Proceedings 668, H7.5

Texture modification in Ti layers with heavy ions

I. Zizak[1], N. Darowski[1], W. Assmann[2], J. Gerlach[3], A. Wenzel[4]

[1] *Hahn–Meitner–Institut, Glienicker Straße 100, D–14109 Berlin*
[2] *Sektion Physik der Univ. München, Am Coulombwall 1, D–85748 Garching*
[3] *Leibniz–Institut für Oberflächenmodifizierung, Permoserstr. 15, D–04318 Leipzig*
[4] *Univ. Augsburg, Universitätsstr. 1, D–86135 Augsburg*

Fast heavy ions interact with solid matter mainly via inelastic collisions with the target electrons. If the electronic stopping power of an ion penetrating the solid exceeds a specific critical value, a thermal spike is generated, i.e. the material "melts" in the volume of few nanometers around the ion path. Due to the small volume, this state lasts only few picoseconds. This effect can be used to modify the material properties, e.g. texture [1]. In the present report, the effect of the interaction of swift heavy ions on the orientation distribution of the crystals in polycrystalline hexagonal Ti is studied.

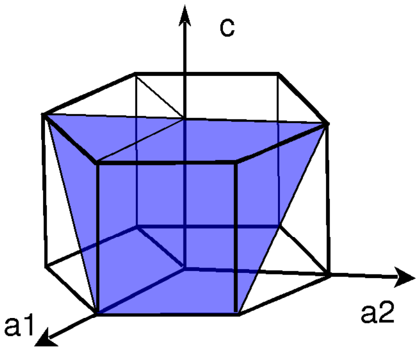

Fig. 1: *Hexagonal Ti lattice. The (101) plane is marked blue.*

Titanium films were prepared by vapor deposition at 400°C on commercial (001) Si wafers. Two Ti samples of different thicknesses (400 nm and 3μm) were examined. Both Ti samples were irradiated at the Tandem accelerator of the Maier–Leibnitz–Laboratory, Garching with 200 MeV Au ions. The fluence was about 10^{15}Au/cm^2. The angle between the ion beam direction and the surface was 19°. The beam spot size on the sample was only

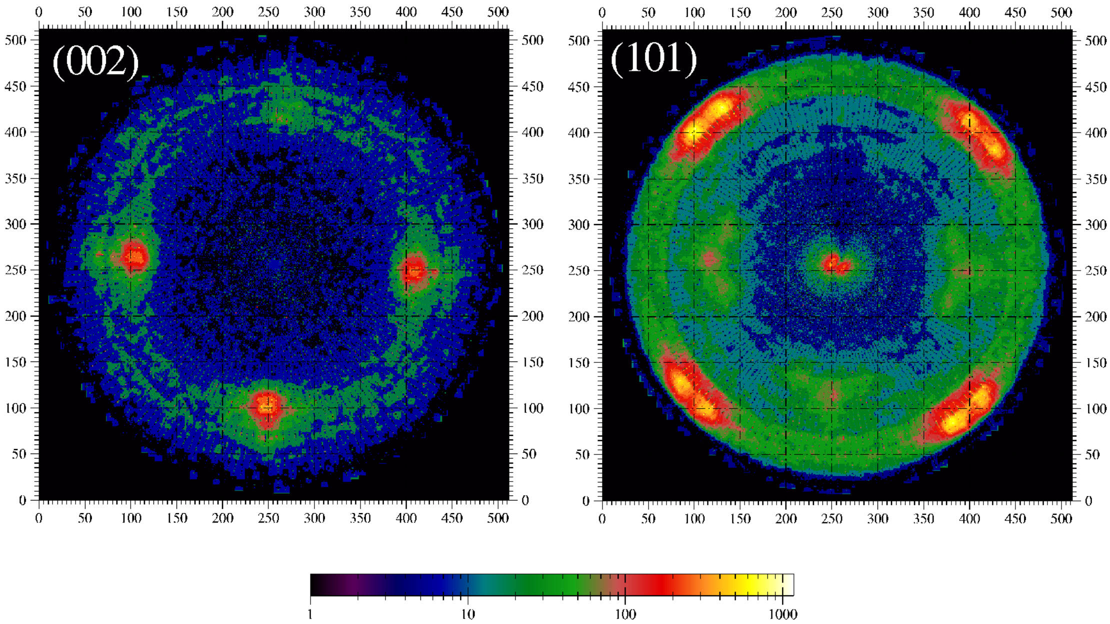

Fig. 2: *The (002) and (101) pole figure of the 400nm thick film. The pole figures did not change due to irradiation.*

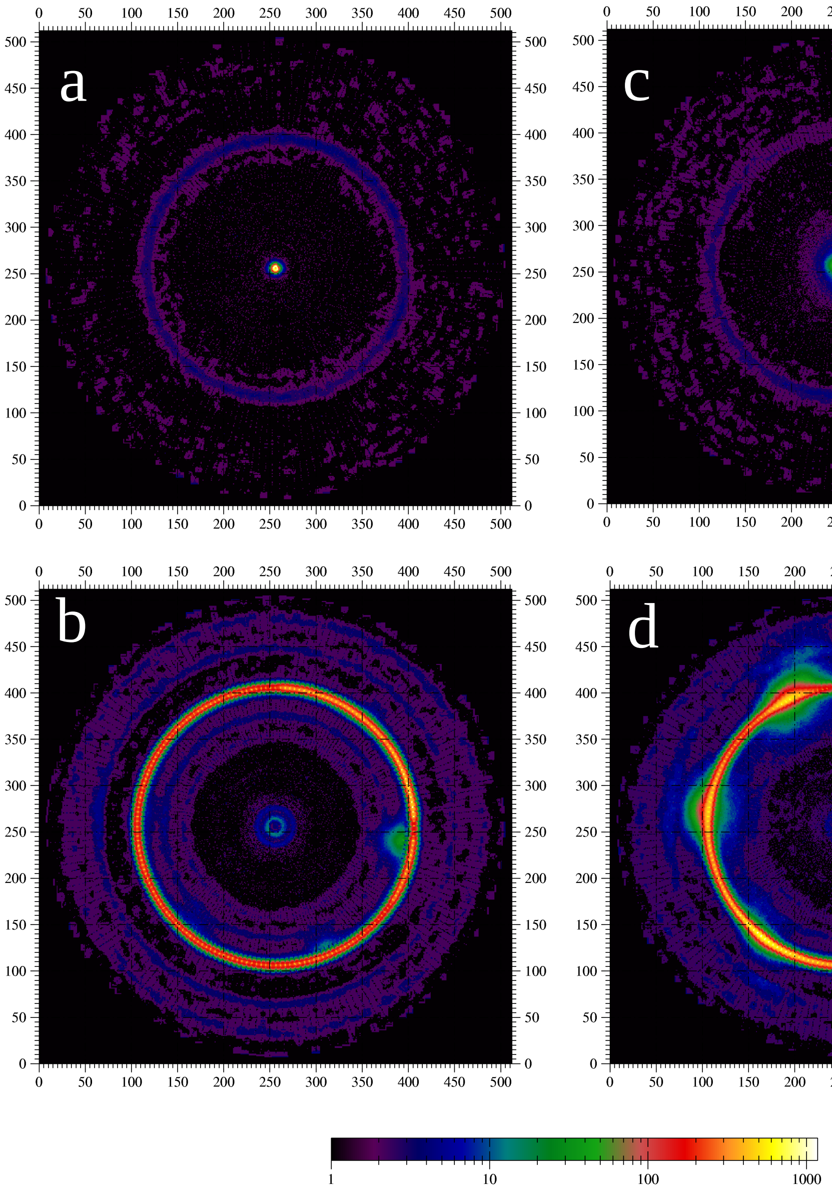

Fig. 3: *Comparison of the pole figures of the unirradiated (left) and irradiated (right) area of the 3µm thick sample. Although the c−axis (a and c) does not change the direction, there is an obvious difference between the (101) pole figures (b and d). The ion beam direction is marked with the red cross on the figures c and d.*

1×2 mm^2. The orientation distribution of the crystals, i.e. the texture of the irradiated Ti layers was studied at the bending magnet X−ray diffraction beamline KMC2 at BESSY using a 6−circle goniometer and a 2D position sensitive detector. The wavelength was λ=0.155nm. For each sample irradiated and unirradiated parts were examined.

The results of the measurements are presented as pole figure plots which is the standard visualization method for the description of the crystal orientation in a material. For data acquisition the X−ray detector is usually positioned at the 2θ angle where the scattering peak is expected, and the azimuthal (φ) and polar (χ) angles of the sample are varied between 0° and 360°, and from 0° to 90° respectively. φ denotes the rotation of the sample around the surface normal and χ denotes the tilt.

For the present experiments we used a position sensitive detector (Bruker AXS) for acquiring the pole figures, which had some advantages compared to a point detector. The area detector covered a very large region in χ angle allowing for a fewer steps in the polar angle scans of the sample. The second advantage was that all Bragg angles of interest could be acquired in the same frame. In our experiment, we measured (100), (101), and (002) Bragg reflections of Ti simultaneously (25°−45°). The step size for the measurement of the pole figures in χ direction was 15°, and in φ direction 2°. Utilizing the 2D detector also allowed for a simple background correction. The background was estimated by averaging the acquired intensities for 2θ values slightly larger and smaller than the scattering angle of the Bragg reflection.

In case of the thinner sample (400 nm) the orientation of the Ti layer was determined by the crystalline structure of the substrate (fig. 2). The Ti lattice is oriented with (101) plane parallel to the surface, and due to the 4−fold symmetry of the Si (001) substrate there are four different but equivalent orientations of the Ti lattice on the substrate. After irradiation the pole figure stayed unchanged.

In case of the 3 μm thick sample the layer is thick enough not to be influenced by the substrate, so the orientation of the unirradiated sample is [001] axis normal to the surface. As the surface is the only symmetry−breaking element, the crystals are randomly oriented in the azimuthal direction, which can be seen on the figure 3b as the circular intensity distribution at the polar angle 64°, corresponding to the angle between (001) and (101) plane normals in hexagonal Ti. After irradiation the (101) pole figure showed changes in the azimuthal distribution. The randomness is canceled, i.e. the crystals have a preferred azimuthal direction resulting in a 6−fold symmetry (see fig. 1). The direction of the incoming ion beam was 19° with respect to the surface (red cross in figure 3d). One of the (101) pole figure maxima points in the direction of the incoming ions.

One can conclude, that up to some critical thickness the lattice of deposited Ti matches to the lattice structure of the Si(001) substrate. The next neighbor distance in (101) Ti planes is similar to the lattice parameter of Si in the (001) planes. This matching of the lattices can be deduced from the 4−fold symmetry of the pole figures acquired from the thinner sample. The actual processes leading to the reorientation of the crystals is not yet investigated, and has to be studied further.

Due to the small irradiated area, it was not easy to separate the irradiated and unirradiated region of the sample. Thus, probably for some measurements both regions contribute to the recorded signal. The distinct peak on the (101) pole figure of unirradiated sample (fig. 3b), as well as the ring on figure 3d are attributed to this effect. The cyclotron of the ISL accelerator has lately the possibility to accelerate Au ions up to energies of 600 MeV with larger fluxes than the tandem accelerator in Garching. Using the ISL facility it will be possible to irradiate larger areas of the sample, so further X−ray measurements are going to be more accurate.

To our knowledge the recorded ordering after irradiation, which is interpreted as a recrystallization in direction of the incoming high−energy ion beam, was observed for the first time. A detailed study of the interaction process most probably will lead to a better understanding of the thermal spike model, which is still under discussion. For the future experiments are planned which will clarify the dependence of the texture on the angle of the impinging projectiles, the fluence, and the thickness of the Ti layer.

[1] K. Zhang *et al.*, *NIM* B **161−163** (2000) 1116.

Heusler-Alloys: Novel Materials for Magnetoelectronics

C. Felser[4], B. Heitkamp[1], F. Kronast[1], D. Schmitz[2], St. Cramm[3], H. A. Dürr[1], H. J. Elmers[4], G. H. Fechter[4], S. Wurmehl[4], T. Block[4], D. Valdaitsev[4], S. A. Nepijko[4], A. Gloskovki[4], G. Jakob[4], G. Schönhense[4], and W. Eberhardt[1]

[1]BESSY GmbH, Albert-Einstein-Straße 15, 12489 Berlin
[2]Hahn-Meitner-Institut Berlin GmbH, Glienicker Straße 100, 14109 Berlin
[3]Forschungszentrum Jülich GmbH, IFF, 52425 Jülich, Germany
[4]Universität Mainz, Duesbergweg 10-14, 55099 Mainz

Materials, which display large changes in resistivity in response to an applied magnetic field (magnetoresistance) are currently of great interest due to their potential for applications in magnetic sensors, magnetic random access memories, and spintronics [1]. Precondition for large effects seems to be a high degree of spin polarisation at the Fermi level. Guided by striking features in the electronic structure of several magnetic compounds, we prepared the Heusler compound $Co_2Cr_{0.6}Fe_{0.4}Al$. Based on our band structure calculations, we have chosen this composition in order to obtain a ferromagnetic half metal with a van Hove singularity in the vicinity of the Fermi energy in the majority spin channel and a gap in the minority spin channel. We find evidence for spin polarized transport at room temperature, showing up in a magnetoresistive effect of 30% in a small magnetic field of 0.1 Tesla (Fig. 1) [2].

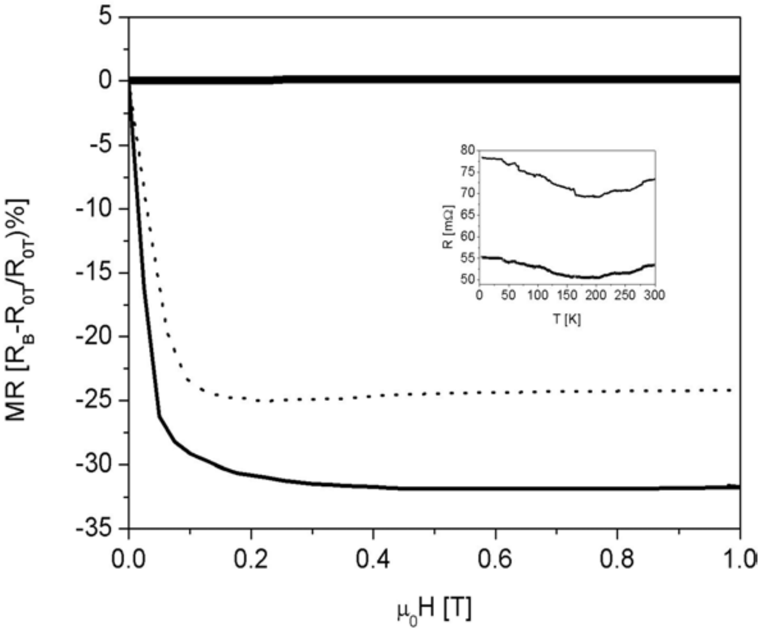

Fig. 1 Magnetoresistance of $Co_2Cr_{0.6}Fe_{0.4}Al$ and Co_2CrAl at room temperature as a function of an external field. Co_2CrAl shows no remarkable effect (thick line) Polycrystalline powder compacts show a larger effect (solid line) compared to annealed pressed pellets (dashed lines). The Inset shows the resistivity versus temperature curve of $Co_2Cr_{0.6}Fe_{0.4}Al$ at a zero field (solid line) and within an external field of 8 T (circles).

Heusler compounds are of the general formula X_2YZ. X and Y usually are transition metals and Z is either a non-magnetic metal or a a non-metal. Sometimes Y could be a rare earth element. The crystal structure of a Heusler compound is marked by four interpretating fcc-lattices. Ferromagnetic properties of Heusler alloys have been investigated experimentally and theoretically [3]. The Co-based Heusler alloys of particular interest because they show comparatively high Curie temperature.

The ordered Heusler alloy $Co_2Cr_{0.6}Fe_{0.4}Al$ was prepared by arc melting the constituent elements under an argon atmosphere. The samples were cooled down to romm temperature by rapidly shutting down the heating. Flat discs (8mm diameter by 1mm) were cut from the polycrystalline ingots and were mechanically polished. The measured ambient temperature neutron powder diffraction diagram of $Co_2Cr_{0.6}Fe_{0.4}Al$ reveals the well-ordered structure of a Heusler phase with a cubic lattice (Fm-3m) and a lattice constant of a = 5.737 Å. Using a SQUID magnetometer, we detected a saturation magnetic moment of 93 emu/g at T = 6.5 K and B = 1 T. The Curie temperature of $Co_2Cr_{0.6}Fe_{0.4}Al$ (27.8 valence electrons) was determined to be 760 K.The remnance of 2emu/g and coercitive field of 1 mT indicate that $Co_2Cr_{0.6}Fe_{0.4}Al$ is a soft magnet. This high magnetic moment corresponds to 3.3 μ_B per formula unit and is slightly reduced compared with the magnetic moment predicted by the LDA-band-structure calculation. The reduction may be explained by the presence of paramagnetic clusters in the solid solution alloy not visible via neutron diffraction but observable in the Mößbauer spectra [2].

For Co_2CrAl a ground state magnetic moment of 1.55 μ_B /formula unit has been reported by Bushow [4] and it was considered that Co atoms mainly carry the magnetic moment in this alloy whereas the contribution of Cr and Al atoms remains. Recent LMTO bandstructure calculations reveal a HMF character of the density of states, i.e. a gap at the Fermi level in the minority band and a high density of states in the majority band. According to our calculation all constituents of the alloy should possess a magnetic moment 0.77μ_B /atom for Co, 1.63μ_B /atom for Cr and -0.10μ_B /atom for Al. For the total moment a value of approximately 3μ_B /formula unit is obtained, in agreement with the thumb rule for the magnetic moment μ of halfmetallic Heusler alloys from 3d transition metals μ /μ_B =N-24, with N being the cumulated number of valence electrons (4s, 3d for the 3d-transition metals and 3s, 3p for Al). Reproducible magnetic moments could be obtained in agreement with the thumb rule if Cr is partly replaced by Fe. According to band structure calculations the electronic properties are mostly similar to Co_2CrAl. The replacement of Cr by Fe can be seen as a doping with electrons. Bandstructure calculations for the disordered variant confirm a strongly reduced magnetic moment (1~μ_B / formular unit) as well as a loss of the half-metallic character.

A photoelectron emission microsope (PEEM) magnifies the photoelectron distribution of the sample generated after excitation with synchrotron radiation. A spatial resolution of about 100 nm can be reached without energy analysis of the photoelectrons. Contrast of chemical, magnetic and topographic origin can be seen on the screen.

Although the sample is chemically almost homogeneous, spatially-resolved XAS-spectra are extracted by integrating over the outlined sections. There are areas that show an enrichment of Chromium at the expense of Iron and Cobalt.

Magnetic contrast is obtained by subtracting the images for the opposite light helicites. In Fig.3 a ferromagnetic coupling between Iron and Cobalt is seen by the similar magnetic contrast of the micrometer-sized domains measured at the corresponding absorption edges. At the Chromium Edge no contrast of magnetic origin is observed. On the nanometer-scale a more complicated domain pattern is resolved. These small domain pattern points to a small magnetic anisotropy energy. The magnetic properties depend very sensitively on the stoichiometry. On the Chromium-rich areas marked by the ellipses no magnetic domains can be found. Results obtained before Ar-ion bombardment of the sample show a much smaller magnetic contrast. However, the micrometer-size magnetic domains are clearly present (Fig. 2).

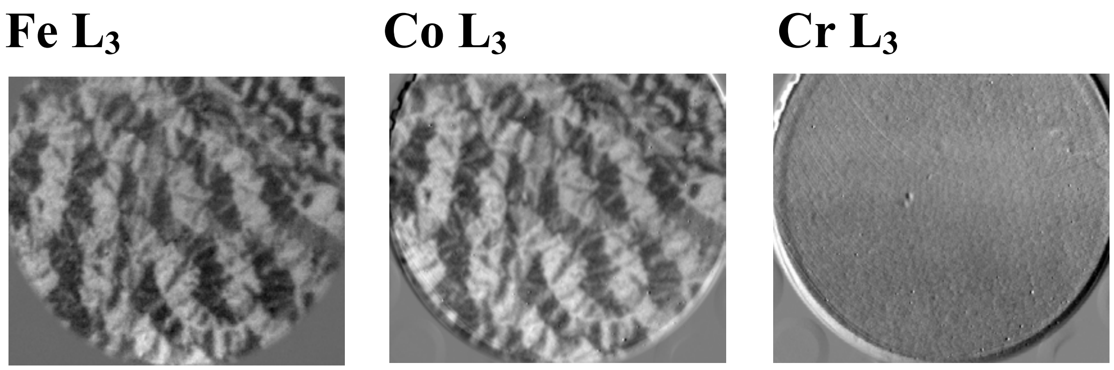

Fig. 2 shows magnetic contrast of $Co_2Cr_{0.6}Fe_{0.4}Al$ by photoelectron emission microsopy. A ferromagnetic coupling between Iron and Cobalt is seen by the similar magnetic contrast of the micrometer-sized domains measured at the corresponding absorption edges. At the Chromium Edge no contrast of magnetic origin is observed.

In order to investigate element specific magnetic properties and compare them with theoretical predictions, we have carried out measurements of the magnetic circular dichroism (MCD) in the soft X-ray core-level absorption of the Cr, Fe and Co 2p→3d excitation for $Co_2Cr_{0.6}Fe_{0.4}Al$.

MCD in Cr, Fe and Co 2p→3d XAS [5] (Fig. 3) was measured at the undulator beam line U56 / 1-SGM with a resolution of 80 meV at 800 eV. The XAS spectrum was obtained by the total electron yield method, measuring directly the sample current while scanning the photon energy. The magnetic field applied to the sample (0.3 Tesla) during the measurement was alligned with the surface normal and at an angle of 30 degrees with respect to the incident photon direction. We have observed a strong selective oxidation of Cr when polished surfaces on exposed air, therefore the surfaces were scrapped in situ in ultrahigh vacuum in order to remove the surface oxide layer.

We have evaluated element specific magnetic moments by magneto-optical sum rules. Absolute values of spin and orbital moments were estimated using values of the total magnetic moments obtained by SQUID magnetometry. For quenched samples we obtained spin magnetic moments in agreement with the band structure calculations for Co and Fe atoms, whereas Cr possess a reduced magnetic moment.
A clear difference is observed for the Cr XAS before and after removing the oxide layer. For clean surfaces of both the quenched and the annealed sample, the XAS spectra look similar to spectra obtained from metallic Cr samples. Resonant absorption lines are obtained at 575.9 eV and 584.6 eV for the L_{III} and L_{II} edge, respectively, with a full width at half maximum (FWHM) of ~3.5 eV, which is characteristic for Cr in the metallic state [6]. Contrarily, the Cr XAS spectrum of the oxidized surface shows two distinct peaks at the L_{III} edge (575.9 eV and 577.0 eV) and the peak at the L_{II} edge is accompanied by a shoulder. The peak positions and relative intensities are characteristic for the XAS spectrum obtained from Cr_2O_3 [7].

The XAS spectra at the Fe L_{III} and L_{II} edge show the resonant absorption lines at 707.7 eV and 721 eV, respectively, with a FWHM of ~2 eV, similar to the XAS spectra of metallic Fe [8]. In particular, the oxidized sample does not show an additional peak at the L_{III} edge, which could be expected at a photon energy shifted by 2 eV to higher binding energy [9].

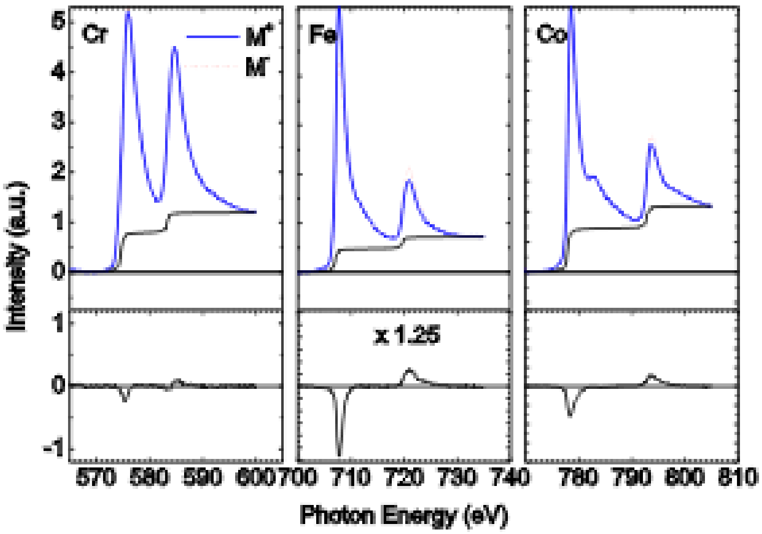

Fig. 3 Cr, Fe and Co 2p→3d XAS-MCD spectra in the quenched $Co_2Cr_{0.6}Fe_{0.4}Al$ *compound. Solid* (μ^-) *and dashed* (μ^+) *lines show the XAS spectra measured with external field applied parallel and antiparallel to the surface normal. The bottom panels represents the MCD spectra.*

As in the case of Fe, the XAS spectra at the Co L_{III} and L_{II} edge shows two prominent resonant peaks corresponding to the L_{II} and L_{III} component at 778.6 eV and 793.8 eV, similar to XAS spectra observed for metallic Co [8]. The FWHM is approximately 2 eV. No additional peaks can be recognized for the oxidized sample. In particular, no many-peak structures in the L_{III} region were observed as in the case of the Sn-based Heusler alloys Co_2YSn (Y=Ti, Zr, and Nb) [10]. The lack of these many-peak structures cannot be attributed to a limited energy resolution as can be concluded from the steep increase at 778 eV. Instead it must be explained by a different DOS which indicates a more metallic character of the Co d-band compared to the Co_2YSn alloys. For the quenched sample we observed a pronounced shoulder at the L_{III} peak shifted by 4 eV with respect to the maximum to a higher photon energy. A similar structure should be observed in the L_{III} region. A less pronounced shoulder can indeed be observed at the L_{II} peak. Less sharp structures in the L_{II} region can be ascribed to a lifetime broadening effect because the lifetime of the $2p_{1/2}$ core hole is much shorter than the $2p_{3/2}$ core hole due to the Coster-Kronig decay [8].

From the comparison of the XAS spectra of oxidized samples with clean surfaces it is obvious that the 3 elements Cr, Fe and Co react differently when exposed to air. This can be expected, because the metal - oxygen bond enthalpy is larger for Cr (430 kJ/mol) than for Fe (400 kJ/mol) and Co (385 kJ/mol). The strong selectivity, however, is surprising. Cr is selectively oxidized whereas the majority of Co and Fe remains in a metallic state. The information depth of XAS involves a surface layer of 1-2 nm thickness, i.e. 2-4 unit cells. Therefore, the selective oxidation of Cr involves a surface segregation process, which at least partially destroys the stoichiometry of the Heusler alloy in the surface region. Taking this into account, one may conclude that the near surface region of about 1-2 nm consists of metallic FeCo alloy mixed by Cr oxide, after exposure to air. From its chemical reactivity (Al-O bond enthalpy 511 kJ/mol) one might assume that Al is oxidized as well.

We have measured the MCD in Cr, Fe and Co 2p→3d XAS of the ferromagnetic Heusler alloy $Co_2Cr_{0.6}Fe_{0.4}Al$. We observed a strong selective oxidation of Cr when polished surfaces are exposed to air, involving a change of electronic properties at the surface. The differing properties of the surface compared to the bulk have to be taken into account for the interpretation of magneto-resistance effects in powder compacts [11,12] and of Andreev reflections [13] with respect to a potentially high spin polarization of the Heusler alloys. It is in particular important for the observed significant decrease of the magneto-resistance in pressed Heusler alloy powders or the possibility to verify a total spin polarization by means of Andreev reflections using HMF Heusler alloys [14]. A selective oxidation at the surface could potentially lead to a misinterpretation of the results using the latter method.

We have evaluated element specific magnetic moments by magneto-optical sum rules. Absolute values of spin and orbital magnetic moments were estimated using values of the total magnetic moment obtained by SQUID magnetometry. For quenched samples we obtained spin magnetic moments in agreement with band structure calculations for Co and Fe atoms whereas Cr atoms possess a reduced magnetic moment. Orbital magnetic moments are 10% (13%) of the spin moment for Cr (Co). For Fe the orbital moment is 14% of the spin moment, corresponding to the absolute value of 0.33 μ_B, which is considerable larger then the Fe bulk value (0.09 μ_B). We attribute the origin of the large orbital moment of Fe to the localization of the Fe 3d electrons. Annealing of $Co_2Cr_{0.6}Fe_{0.4}Al$ reduces magnetic moments at Fe and Cr drastically which tendatively attribute to increase atomic disorder. Atomic disorder seems to play a major role for the magnetic properties of Heusler alloys. Element specific magnetometry in combination with theoretical band structure calculations provides a key tool to the understanding of the influence of disorder and of the particular electronic properties of Heusler alloys. A careful preperation of the surface is necessary due to the selective oxidation.

[1] G. A. Prinz, *Science* **282**,1660 (1998).

[2] DE 10108760.8, T. Block, C. Felser, G. Jakob, J. Ensling, B. Mühling, P. Gütlich, R. J. Cava, submitted to *Appl. Phys. Letters*.

[3] Webster, P. J. *J. Phys. Chem. Solids* **32,** 1221-1231 (1971).

[4] K. H. J. Buschow and P. G. vanEngen, J. Magn. Magn. Mater. 25, 90 (1981).

[5] H. J. Elmers, G. H. Fechter, D. Valdaitsev, S. A. Nepijko, A. Gloskovki, G. Jakob, G.Schönhense, S. Wurmehl, T. Block, P.-C. Hsu, W. –L. Tsai, C. Felser, S. Cramm, *Phys. Rev. B* accepted.

[6] M.A. Tomaz, W.J. Antel, W.L. O'Brien, and G.R. Harp, Phys. Rev. B 55, 3716 (1997).

[7] C. Theil, J. van Elp, and F. Folkmann, Phys. Rev. B 59, 7931 (1999).

[8] C.T. Chen et al. *Phy*s. Rev. Lett, 75, 152 (1995).

[9] J.F. Hochepied, Ph. Sainctavit, and M.P. Pileni, J. Magn. Magn. Mater. 231, 315 (2001).

[10] A. Yamasaki, S. Imada, R. Arai, H. Utsunomiya, S. Suga, T. Muro, Y. Saitoh, T. Kanomata, and S. Ishida, Phys. Rev. B 65, 104410 (2002).

[11] A. Gupta, J.Z. Sun, J. Magn. Magn. Mater. 200, 24 (1999).

[12] J.M.D. Coey, A.E. Berkowitz, Ll. Balcells, F.F. Putris, A. Barry, Phys. Rev. Lett. 80 (1998) 3815.

[13] R.J. Soulen Jr., J.M. Byers, M.S. Osofsky, B. Nadgorny, T. Ambrose, S.F. Cheng, P.R. Broussard, C.T. Tanaka, J. Nowak, J.S. Moodera, A. Barry, J.M.D. Coey, Science 282, 85 (1998).

[14] N. Auth, G. Jakob, T. Block, and C. Felser, submitted to Phys. Rev. B (2002).

X-ray absorption spectroscopy on biological samples (BioXAS): The manganese complex of photosystem II

[1*]M. Haumann, [1]C. Müller , [1]M. Grabolle, [1]P. Liebisch, [2]M. Fieber-Erdmann, [2]A. I. Erko, and [1]H. Dau

[1]Freie Universität Berlin, FB Physik, Arnimallee 14, D-14195 Berlin, Germany
[2]BESSY II, Albert-Einstein-Straße 15, D-12489 Berlin, Germany
[*]Email: haumann@physik.fu-berlin.de

KMC-2 at BESSY II is a bending-magnet beamline equipped with a monochromator (Si111 crystal). X-ray absorption spectra of the tetra-manganese complex [1] of a photochemical enzyme, photosystem II (PSII), were measured with dried multilayers of PSII-containing membrane fragments. In these samples, the membrane normal is preferentially oriented in parallel to the sample normal resulting in orientation of the PSII proteins. PSII has been previously studied at room temperature by XAS [2,3] but for the first time, linear dichroism spectra were collected at a temperature where PSII is active [2].

XAS spectra at the Mn K-edge (XANES and EXAFS) were measured as fluorescence-detected absorption spectra (due to the low metal concentration of ~ 1 mM) using a large-area photodiode shielded with thin chromium and aluminium foils against scattered X-rays and ambient light [3]. An absolute energy calibration was obtained by the simultaneous measurement of the pre-edge peak (at 6543.3 eV) of a $KMnO_4$ standard. To investigate the linear dichroism, XAS spectra were measured at various angles between the electric field vector of the X-ray beam and the sample normal. The following results were obtained:

(1) Due to the new Si111 crystal of the monochromator the X-ray flux in the region of the Mn K-edge (~6550 eV) was significantly increased, a flux of about 10^{10} photons per second and mm^2 (beam size 900 x 240 µm) was determined using a calibrated photodiode. This beam intensity assures a reasonable signal-to-noise ration of XAS measurements within practicable total scan time.

(2) Unfortunately, relatively large monochromator glitches were observed in the region around 400 eV above the Mn K-edge although the monochromator was detuned to 70 % of maximal intensity. This effect limited the useful spectral range of EXAFS spectra.

(3) No photoreduction of the Mn complex (“radiation damage”, measured as a potential down-shift of the Mn K-edge on the energy scale) was observed during a single EXAFS scan (scan range 6500-7100 eV) within ~ 20 min at room temperature, the Mn K-edge energy remained constant (+/- 0.1 eV). Measurements of unperturbed EXAFS spectra of PSII are possible at KMC-2 at room temperature.

(4) Useful EXAFS spectra of the Mn complex (in the dark-stable so-called S_1-state) were obtained by averaging of about 40-50 scans. Linear dichroism Mn EXAFS spectra were measured at angles of 15°, 35°, 55°, and 75° (see Fig. 1).

(5) EXAFS spectra of the Mn complex revealed two major peaks, the first one being due to Mn-O vectors and the second one being mainly attributable to Mn-Mn interactions. Strong linear dichroism of Mn XAS spectra was observed under variation of the angle of the sample normal (about equivalent to the protein normal) (Fig. 1). XANES spectra (Fig. 1A) revealed a position of the Mn K-edge of 6551.2 eV and 6551.6 eV at 15° and 55°, respectively. A preliminary simulation (thick lines in Fig. 1B) of EXAFS spectra at 15° and 55° using 3 shells of backscatterers yielded an average angle of the two Mn-Mn vectors of 88 ° with respect to the membrane normal (Table 1) (using a mosaic spread parameter of $I_{ord} = 0.48$), comparable to previous results [4]. A more detailed analysis of these spectra is underway.

Simulations were made using the approach towards the linear dichroism of partially oriented systems described in [5].

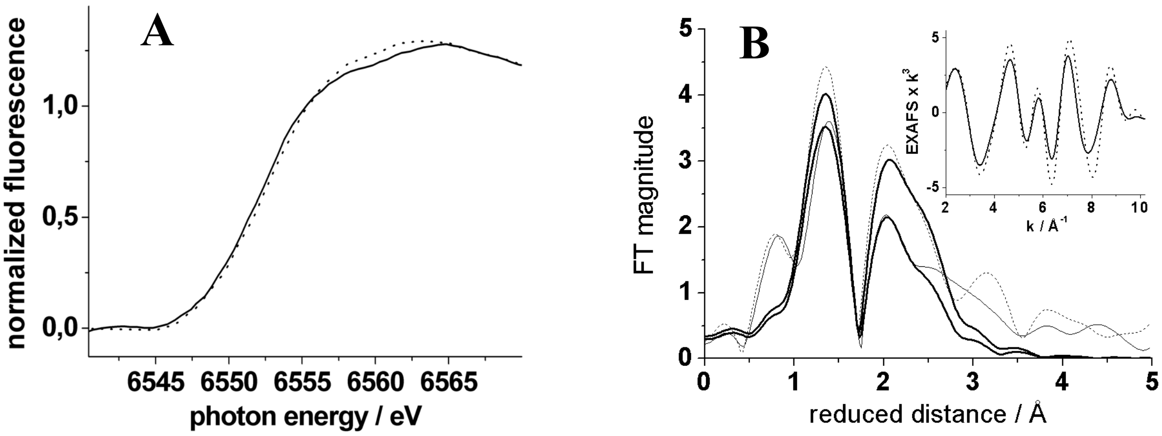

Figure 1: Linear dichroism XAS spectra of the tetra-manganese complex of photosystem II at room temperature (solid line, at 15°; dotted line, at 55°). (A) XANES spectra at the Mn K-edge. (B) Fourier transforms of EXAFS spectra (10-400 eV above E_0 = 6546 eV, cos windows extending over 10 and 30 % of the used K-space); thin lines, experimental spectra; thick lines, simulations. Inset: Backtransforms of FTs into the K-space (0.8-3.5 Å).

Table 1: Simulation parameters of the EXAFS spectra (S_1-state).

Shell, N_i	Vector	Coordination No. N_i [per Mn]	Distance, R_i [Å]	Debye-Waller parameter, $2\sigma^2$ [Å^{-1}]	Angle with membrane normal
I	Mn-O	4.00	1.88	0.019	58°
II	Mn-O	1.50	2.21	0.005	62°
III	Mn-Mn	1.15	2.71	0.005	88°

Conclusions:

(1) EXAFS measurements of biological samples with ultra-dilute (< 1 mM) metal concentrations yield an (almost) acceptable signal-to-noise ratio within reasonable data acquisition times at beamline KMC-2. Further improvements of the S/N ratio are desirable.

(2) For the first time, linear dichroism XAS spectra of the manganese complex of photosystem II have been successfully measured at room temperature (at four angles). Pronounced linear dichroism of spectra has been observed. A detailed analysis of spectra is currently underway.

(3) Future improvements of BioXAS measurements at KMC-2 will include, i.a., more elaborated data-acquisition protocols, minimization of air-travelling distances of the X-ray beam, minimization of "glitches", an improved detector, and the use of a cryostreamer or cryostat for temperature control of samples.

We thank the staff of KMC-2 for excellent technical support. Financial support from the BMBF (grant no. 05KS1KEA/6) and the SFB 498 is gratefully acknowledged.

[1] Dau, H., Iuzzolino, L. and Dittmer, J. (2001) Biochim. Biophys. Acta 1503, 24-39.
[2] Haumann, M., Grabolle, M., Neisius, T., and Dau, H. (2002) FEBS lett. 512, 116-120.
[3] Meinke, C., Sole, A., Pospisil, P., and Dau, H. (2000) Biochemistry 39, 7033-7040.
[4] Haumann, M., Grabolle, M., Werthammer, M., Iuzzolino, L., Dittmer, J., Meyer-Klaucke, W., Neisius, T., and Dau, H. (2001) Proc. 12th Int. Congr. Photosynthesis, http://www.publish.csiro.au/ps2001/cf/home/index.cfm.
[5] Dittmer, J. and Dau, H. (1998) J. Phys. Chem. B 102, 8196-8200.

Structural genomics at the BESSY light source: Crystal structure of human p14.5 reveals ligand binding site near the nine invariant residues of the Yjgf-like protein family

Babu A. Manjasetty[1,2,8], Heinrich Delbrück[3,4], Pham Dinh-Trung[4,5], Uwe Mueller[1,3], Martin Fieber-Erdmann[1,3], Volker Sievert[4,6], Konrad Büssow[4,6], Frank Niesen[4,7], Wilhelm Weihofen[3], Bernhard Loll[3], Wolfram Saenger[3] and Udo Heinemann[2,3,#]

[1]Protein Structure Factory, c/o BESSY GmbH, Albert-Einstein-Str. 15, 12489 Berlin, Germany.
[2]Forschungsgruppe Kristallographie, Max-Delbrück-Centrum für Molekulare Medizin, Robert-Rössle Str. 10, 13092 Berlin, Germany.
[3]Institut für Chemie/Kristallographie, Freie Universität, Takustr. 6, 14195 Berlin, Germany.
[4]Protein Structure Factory, Heubnerweg 6, 14059 Berlin, Germany.
[5]Alpha-Bioverfahrenstechnik GmbH, Heinrich-Hertz Str. 1b, 14532 Kleinmachnow, Germany.
[6]Max-Planck-Institut für Molekulare Genetik, Ihnestr. 73, 14195 Berlin, Germany.
[7]Universitätsklinikum Charité, Institut für Medizinische Physik & Biophysik, Ziegelstr. 5-9, 10096 Berlin, Germany.
[8]On leave from: Department of Physics, Government Science College, Bangalore 560012, India
[#]To whom correspondence should be addressed

Abstract. *Rapid protein structure determination for structural genomics projects requires full automation of all steps that are carried out at the synchrotron beamline i.e., from mounting crystals on a diffractometer to interpretable initial electron density maps. Such facilities have been developed at the BESSY electron storage ring, Berlin, under the auspices of the Protein Structure Factory structural genomics project. First successful experiments at the new facilities are described here. The experiment and analysis (from derivatization of the crystal to initial model with interpretable electron density) was completed within 24 hours. The crystal structure of human p14.5 was determined by the single wavelength anomalous dispersion method to 1.9 Å resolution. The most important finding in the structure is the binding of benzoate molecules in the conserved cleft on the protein surface. The two benzoate molecules are clearly visible within the cleft; their orientations suggest different ligand binding modes near the nine invariant residues of the Yjgf-like protein family.*

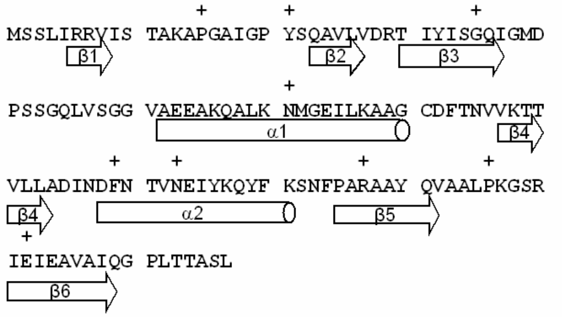

Figure 1. *Sequence of human p14.5. The nine invariant residues are shown as + mark above the sequence. The β-strands are depicted as arrows and α-helices as cylinders below the sequence.*

Investigations aimed at a complete understanding of the structure and function of genes and gene products in all life forms are rapidly progressing due to the availability of genome sequences [1]. Structural genomics initiatives all around the world begun to develop and implement technologies that will permit to determine three-dimensional protein structures at high throughput in a automated fashion [2]. The Berlin Protein Structure Factory (PSF) is a structural genomics project funded by BMBF, Germany. Within the PSF, the structure determination process includes target selection; cloning the coding sequence; protein expression and purification; biophysical characterization; identifying and optimizing crystallization conditions and incorporating suitable heavy atoms; collecting multiple or single wavelength anomalous dispersion (MAD or SAD) data at a synchrotron beamline; solving the phase problem; tracing the electron density map and building the model; refining the structure and finally, drawing functional

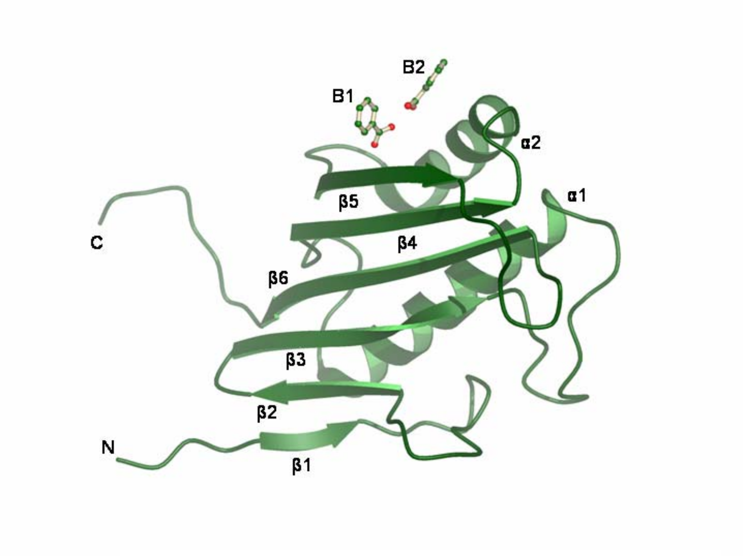

Figure 2. *Ribbon diagram of human p14.5 monomer. The benzoate anions are also shown as ball-and-stick representation.*

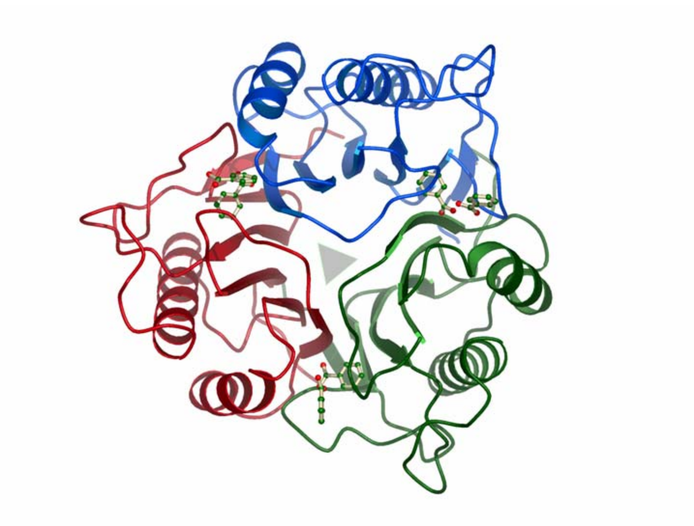

Figure 3. *Human p14.5 trimer. The view is along the non-crystallographic threefold symmetry axis.*

inferences from the solved structure. At this juncture, facilities for partial automation of all steps have been established at the BESSY electron storage ring, from crystal mounting to an interpretable initial electron density map, under the auspices of the PSF structural genomics project.

The Protein Structure Factory (http://www.proteinstrukuturfabrik.de) has set out to determine the three-dimensional structures of medically relevant human proteins by implementing and utilizing high-throughput technology. Initial successful experiments at BESSY new PSF beamline (PSF-ID14.2) are extremely encouraging. Here, we describe the crystal structure of human p14.5 (PID CAA64670) determined by single wavelength anomalous dispersion to 1.9 Å resolution.

Human trichloroacetic acid soluble protein, hp14.5, is a member of the large Yjgf-like protein family (matches 107 sequences represented in InterPro entry IPR006056) with unknown biological function. Although the molecular function of this protein family is not clear, previous studies suggest that it plays a role in the regulation of metabolic pathways and cell differentiation [3]. Human p14.5 is a translational inhibitor which was first isolated by Schmiedeknecht *et al*. in 1999 and shown to be significantly upregulated upon cellular differentiation from monocytes to macrophages [4]. Other previous studies suggest that hp14.5 strongly inhibits protein synthesis *in vitro* similar to a highly homologous perchloric acid soluble rat protein [5]. Recently, hp14.5 is identified as a tumor associated antigen derived from hepatocellular carcinoma [6].

Multiple sequence alignment with a large number of hp14.5 homologs does not reveal any invariant residues. On the basis of sequence identity, the hp14.5 homologs are divided into two groups. The high identity groups (> 30% identity), including hp14.5, has nine invariant residues (Figure 1). The three-dimensional structures of hp14.5 homologs from *Bacillus subtilis* Yabj and *E. coli* Yjgf are known and suggest that the nine invariant residues map to the narrow, deep cleft between the subunits [7, 8]. This conserved site has been proposed as substrate binding or catalytic site, but structures are unable to give a clue to the common biochemical mechanism for their variety of biological functions.

In order to elucidate the molecular mechanism of these protein family we have solved the crystal structure of human p14.5 by Hg-SAD methods. A Hg derivative was prepared by soaking the crystals in artificial mother liquor containing 15 mM ethyl-Hg phosphate (EMP) for 30 min. A characteristic Hg L_{III} spectrum has been observed by scanning the crystals for fluorescent photons at the Hg lines. For data acquisition, the crystal was flash-cooled to 100 K. Single wavelength anomalous diffraction data at the Hg L_{III} edge to 2.3 Å resolution on a

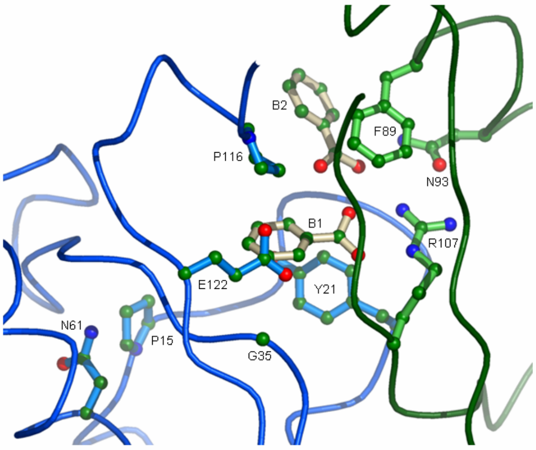

Figure 4a *The active site region around the tunnel 1.*

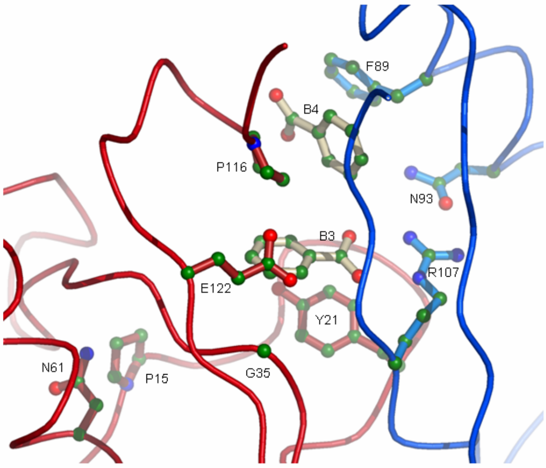

Figure 4b. *The active site region around the tunnel 2.*

Hg derivative and high resolution 1.9 Å native data were collected on the MAR345 imaging plate detector at the BESSY beamline PSF-ID14.2. The data were processed using the program DENZO [9]. The nine mercury atoms (9 molecules in asymmetric unit) were successfully located by the program SnB using the anomalous differences from the derivative dataset [10]. The anomalous phasing and refinement of the Hg locations were done with the program Solve [11]. The such obtained experimental phases were subjected to solvent flattening and automatic model building with the program RESOLVE [12]. The program was able to automatically trace 682 out of 1233 residues. To this stage, our experiment at the BESSY site, including heavy atom derivatization, data collection and initial structure determination was finished within 24

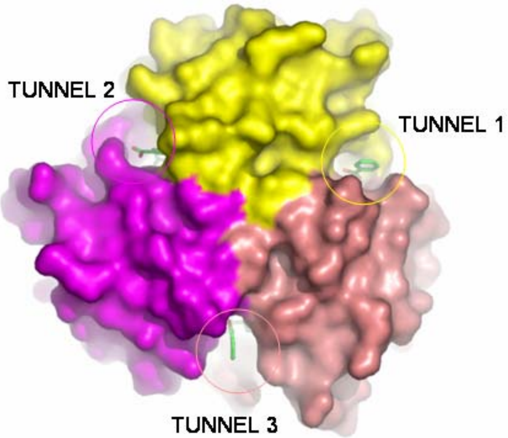

Figure 5a. *Molecular surface representation of the human p14.5 trimer. The surface was colored by chain. Three active tunnels are seen at the subunit interface.*

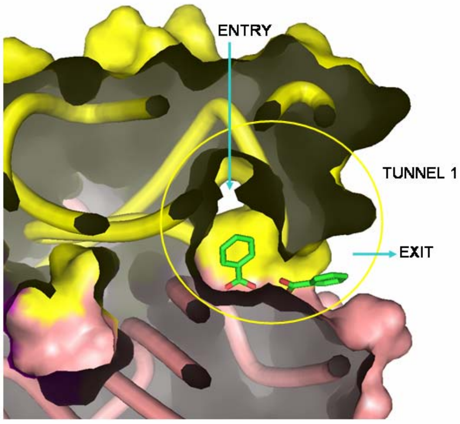

Figure 5b. *Zoom view of the ligand bound at the tunnel 1.*

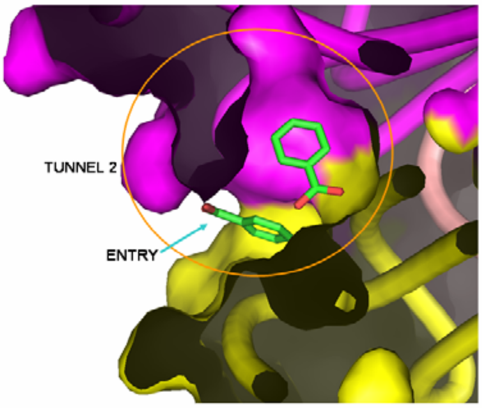

Figure 5c. *Zoom view of the ligand bound at the tunnel 2.*

hours. The phases were further improved by nine-fold non-crystallographic symmetry averaging along with automatic model building and refinement with the program RESOLVE in combination with REFMAC [15] which yielded 925 out of 1233 residues. For phase extension to 1.9 Å resolution the partial protein model was placed into the non-isomorphous unit cell for which native data had been collected by a molecular replacement approach using the program EPMR [13], and the remaining residues were built manually with the program O [14]. The final stages of model rebuilding and refinement with the program REFMAC (R_{free} = 25.6% and R = 20.6%) is underway.

The hp14.5 monomer chain, comprised of 137 residues, adopts a chorismate mutase-like fold (Figure 2). Like homologous structures, hp14.5 is present as a symmetric trimer in crystals (Figure 3). The hp14.5 trimers are related by non-crystallographic symmetry. There are three trimers (a total of nine hp14.5 molecules) in the asymmetric unit of the crystal. Detailed comparative studies of the hp14.5 structure with the homologous structures are in progress. The most important finding in the structure is the binding of two benzoate molecules per hp14.5 protein subunit. The interface between two hp14.5 monomers forms an approximately 12 Å deep and 8 Å wide conserved cleft on the surface of the trimer. Two benzoate molecules are clearly visible within the cleft (Figure 4). One is deeply buried in the cleft and adopts a similar orientation in all clefts. The other benzoate molecule is found in two distinct orientations, seemingly either entering or leaving the binding site. Sodium benzoate was present in the crystallization buffer at 35 mM concentration, indicating protein binding with a low dissociation constant. The nine invariant residues of the Yjgf-family proteins are arranged around the benzoate-binding cleft. The benzoate bound structure of hp14.5 will help us to derive the common biochemical mechanism and to understand the wide variety of biological functions of this protein family. Also, the structure could serve as target for diagnostic or therapeutic approaches.

References

1. Venter, J. C., Adams, M. D., Myers, E. W., Li, P. W., Mural, R. J., et al. (2001) *Science* **291**, 1304-1351.
2. Heinemann, U., Büssow, K., Mueller, U., and Umbach, P. (2003) *Acc. Chem. Res.*, in press.
3. Kim, J. M., Yoshikawa, H., and Shirahige, K. (2001) *Genes Cells* **6**, 507-517.
4. Schmiedeknecht, G., Kerkhoff, C., Orso, E., Stohr, J., Aslanidis, C., Nagy, G. M., Knuechel, R., and Schmitz, G. (1996) *Eur. J. Biochem.* **242**, 339-351.
5. Oka, T., Tsuji, H., Noda, C., Sakai, K., Hong, Y. M., Suzuki, I., Munoz, S., and Natori, Y. (1995) *J. Biol. Chem.* **270**, 30060-30067.
6. Stenner-Liewen, F., Luo, G., Sahin, U., Tureci, O., Koslovski, M., Kautz, I., Liewen, H., and Pfreundschuh, M. (2000) *Cancer Epidemiol. Biomarkers Prev.* **9**, 285-290.
7. Sinha, S., Rappu, P., Lange, S. C., Mantsala, P., Zalkin, H., and Smith, J. L. (1999) *Proc. Natl. Acad. Sci. USA* **96**, 13074-13079.
8. Volz, K. (1999) *Protein Sci.* **8**, 2428-2437.
9. Otwinowski, Z., and Minor, W. (1997) *Methods Enzymol.* **276**, 307-326.
10. Miller, R., Gallo, S. M., Khalak, H. G., and Weeks, C. M. (1994) *J. Appl. Crystallogr.* **27**, 613-621.
11. Terwilliger, T. C., and Berendzen, J. (1999) *Acta Crystallogr. D***55**, 849-861.
12. Terwilliger, T. C. (2001) *Acta Crystallogr. D* **57**, 1755-1762.
13. Kissinger, C. R., Gehlhaar, D. K., and Fogel, D. B. (1999) *Acta Crystallogr. D***55**, 484-491.
14. Jones, T. A., Zou, J. Y., Cowan, S. W., and Kjeldgaard. (1991) *Acta Crystallogr. A***47**, 110-119.
15. Murshudov, G. N., Vagin, A. A., and Dodson, E. J. (1997) *Acta Crystallogr. D***53**, 240-255.

Contact:

Udo Heinemann
Max Delbrück Center for Molecular Medicine
Robert-Rössle-Str. 10
D-13092, Berlin, Germany
Phone: +49 (30) 9406 3420
Fax: +49 (30) 9406 2548
E-mail: heinemann@mdc-berlin.de

Analysis of Metal- and Metalloid-Containing Proteins by SRXRF at the BAMline

M. Kühbacher[1], G. Weseloh[1], H. Bertelsmann[1], M. Özaslan[1],
M. Radtke[2], H. Riesemeier[2], A. Kyriakopoulos[1], D. Behne[1]

[1] *Hahn-Meitner-Institut Berlin, Department Molecular Trace Element Research in the Life Sciences, D-14109 Berlin, Germany*
[2] *Bundesanstalt für Materialforschung und -prüfung, Unter den Eichen 87, D-12200 Berlin, Germany*

ABSTRACT

Pilot studies have been carried out at the BAMline at BESSY II in collaboration with the Bundesanstalt für Materialforschung und -prüfung (BAM) on metal- and metalloid-containing compounds in biological samples after electrophoretic protein separation. After sodium dodecylsulfate polyacrylamide gel electrophoresis (SDS-PAGE) and transfer onto a blotting membrane the distribution of selenium among the proteins of testis homogenate of a rat and a wallaby was determined. The comparison with the autoradiogram of ^{75}Se-labeled proteins separated in the same way showed that of nine selenium-containing proteins found in rat testis homogenate by autoradiography four could be detected by synchrotron radiation X-ray fluorescence analysis (SRXRF).

INTRODUCTION

The species analysis of small amounts of metals and metalloids in biological samples and the determination of their spatial distribution within biological tissues is one of the major challenges of today's analytical chemistry. Nearly all of these elements are bound to proteins and peptides and may play a central role as catalytic or structural constituents. Most of these compounds are not yet known and their identification and the elucidation of their functions is of great interest in many fields of the life sciences. Selenoproteins play a central role in several redox processes in higher organisms. Testes are one of the major selenium-containing organs in mammals.[1] It has been shown that selenium is needed for testis development and especially for sperm maturation.[2,3,4] Disturbances in the selenoprotein metabolism may be related to male infertility. Information on the trace element-containing proteins can be obtained by isolation of these compounds and analysis of the elements in question. For this purpose gel electrophoretic protein separation methods have been combined with SRXRF, which is especially suited to the determination of the distribution of elements in samples with plane surfaces.

SRXRF MEASUREMENTS

After SDS-PAGE and transfer onto a blotting membrane the distribution of selenium among the proteins of testis homogenates was determined by SRXRF. The measurements were performed at the hard X-ray beamline (BAM*line*). The source of the beamline is a superconducting 7 Tesla wavelength shifter (WLS). For monochromatic excitation the double multilayer monochromator (DMM) was employed. The parameters for the measurement of the rat testis homogenate and for the wallaby testis homogenate (shown in brackets) were as follows: The incident X-ray beam had a 200 µm x 200 µm cross section (200 µm x 2000 µm) with an energy of 15 keV. The measurements were performed in air. The fluorescent X-rays were determined with a Si(Li) detector. It was placed in the plane of the storage ring perpendicular to the incident beam to allow efficient measurement of the characteristic fluorescent X-rays from the trace elements and minimize the X-ray Raleigh- and Compton scattering. The specimen was mounted onto a motorised X,Y,Z positioning stage moved by step pulse motors. A line scan with 560 µm (200 µm) step size and 198 (514) measuring points was taken. The spectra were obtained by using a digital signal processor. The measuring time was 200 s (60 s) real time for each spectrum. The spectra analyses were carried out using the fitting code “AXIL-QXAS”. The data acquired from the computer program were net peak areas of selenium K_α X-rays.

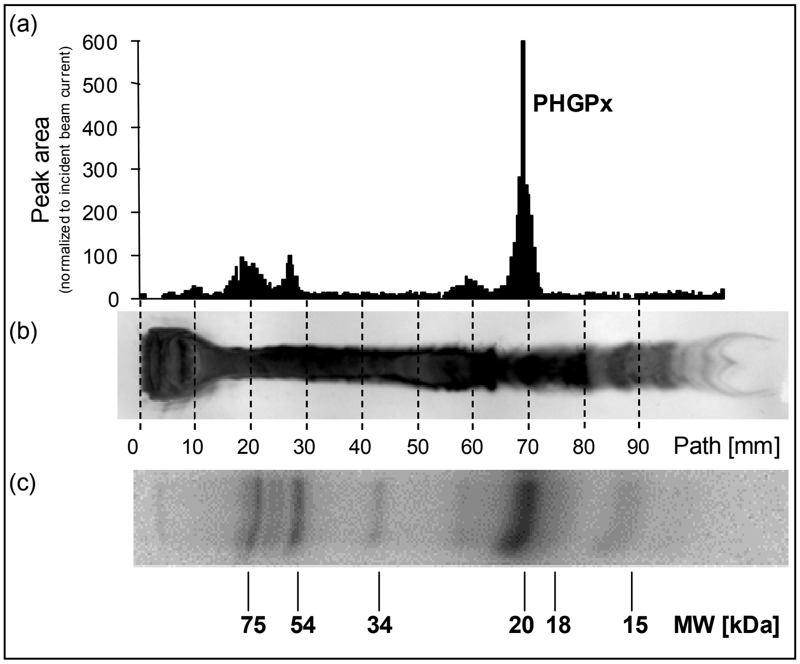

Figure 1. Line scan of rat testis homogenate with a total selenium amount of the sample of 5.2 ng.

(a) Distribution of selenium measured by SRXRF along the lane of proteins from rat testis homogenate separated by SDS-PAGE with phospholipid hydroperoxide glutathione peroxidase (PHGPx) as the major selenoprotein. Monochromatic excitation with the double multilayer monochromator: 15 keV; sampling time: 200 s real; beam dimensions: 200 µm x 200 µm.

(b) Coomassie-stained proteins of rat testis homogenate on the measured PVDF membrane.

(c) Autoradiogram of ^{75}Se-labeled proteins of rat testis homogenate separated in the same way.

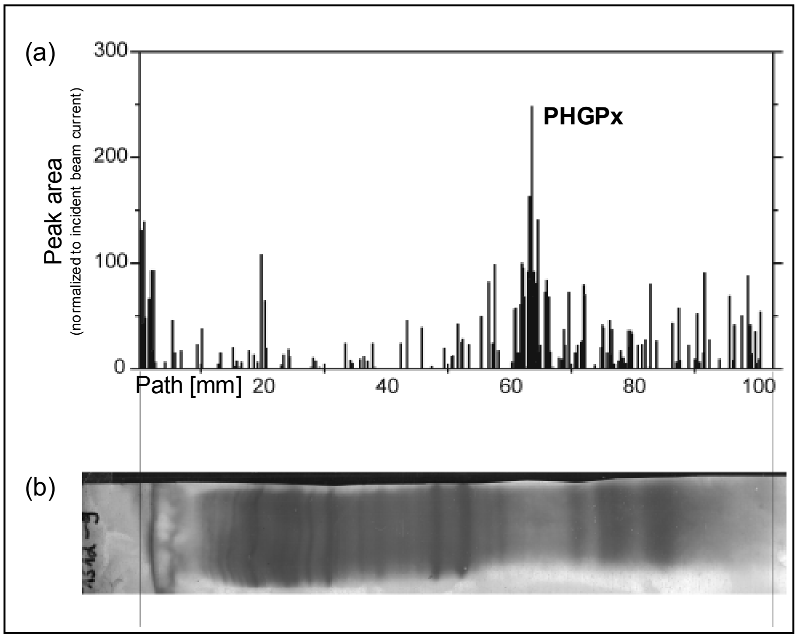

Figure 2. Analysis of selenium containing proteins in testis of a wallaby with a total selenium amount of the sample of 2.08 ng.

(a) Distribution of selenium measured by SRXRF along the lane of proteins from wallaby testis homogenate separated by SDS-PAGE with phospholipid hydroperoxide glutathione peroxidase (PHGPx) as the major selenoprotein. Monochromatic excitation with the double multilayer monochromator: 15 keV; sampling time: 60 s real; beam dimensions: 200 µm x 2000 µm.

(b) Coomassie-stained proteins of wallaby testis homogenate on the measured PVDF membrane.

RESULTS AND DISCUSSION

Figure 1 shows the results of the analysis of selenium in rat testis homogenate by SRXRF along the lane with the Coomassie-stained proteins which had been separated by SDS-PAGE and blotted onto a PVDF membrane. The total selenium amount of the sample was about 5.2 ng, with about 80% present in the dominant peak. By comparing this distribution pattern with the autoradiogram of ^{75}Se-labeled proteins of rat testis homogenate separated in the same way, this peak could be identified as the seleno-enzyme phospholipid hydroperoxide glutathione peroxidase (PHGPx). Glutathione peroxidases belong to the family of selenoproteins and play important roles in the defense mechanisms against oxidative damage by catalyzing the reduction of a variety of hydroperoxides, using glutathione as the reducing substrate. Of the nine selenium-containing proteins found in the autoradiogram, four could be detected by SRXRF. This experiment and the analysis of selenium containing proteins in a testis of a wallaby shown in figure 2 demonstrate the suitability of SRXRF for the determination of firmly bound trace elements in electrophoretically separated proteins for animal species which are not suited to radioactive tracer studies.

REFERENCES

[1] D. Behne, H. Hilmert, S. Scheid, H. Gessner, W. Elger, Biochim. Biophys.Acta., **966**, 12 (1988)

[2] E. Wallace, H.I. Calvin, G.W. Cooper, Gamete Research, **4**, 377 (1983)

[3] D. Behne, H. Weiler, A. Kyriakopoulos, J. Reprod. Fertil., **106**, 291 (1996)

[4] H. Pfeifer, M. Conrad, D. Roethlein, A. Kyriakopoulos, M. Brielmeyer, G.W. Bornkamm, D. Behne, FASEB J., **15**, 1236 (2001)

Characterization of Fibre Reinforced Metals by X-Ray Refraction CT

Bernd R. Müller, Manfred P. Hentschel, Axel Lange, Michael Harwardt
Bundesanstalt für Materialforschung und -prüfung (BAM), D-12200 Berlin, Germany

Introduction

X-ray refraction reveals the inner surface and interface concentrations of nanometer dimensions due to the short X-ray wavelength near 0,1 nm. Sub-micron particle, crack and pore sizes are easily determined by "X-ray refractometry" without destroying the structure by cutting or polishing for microscopic techniques. The physics of X-ray refraction is quite similar to the well-known refraction of the visible light by optical lenses and prisms, which is governed by Snell's law. However a major difference to the visible optics is, that the refractive index n of X-rays in matter is nearly one ($n < 1$) [1]. This causes deflections at very small angles in the order of a few seconds of arc. The X-Ray Refraction Technique is described elsewhere [2]. It localises the inner surface concentrations or individual edges of surfaces and interfaces such as sub-micrometer pores or cracks. The spatial resolution can be better than 10 µm.

Instrumentation

During the last year the SAXS instrumentation at the BAM*line* was upgraded by a 6-circle-goniometer (Fig. 1). Fig. 2 shows the delineation of the experimental set-up. To cover the whole object of investigation with the beam, the vertically narrow X-ray beam from the Double-Multilayer-Monochromator [3] is enlarged by an asymmetrical cut Si(022)-crystal (1st crystal). The sample is between the tow crystals and can be moved by an x-y-manipulator and rotated by a turntable for CT-measurements, respectively. The (analysing) 2nd Si(022)-crystal (symmetrical cut) reflects the beam toward an X-ray sensitive CCD-camera which has a lateral resolution of 6µm x 6µm.

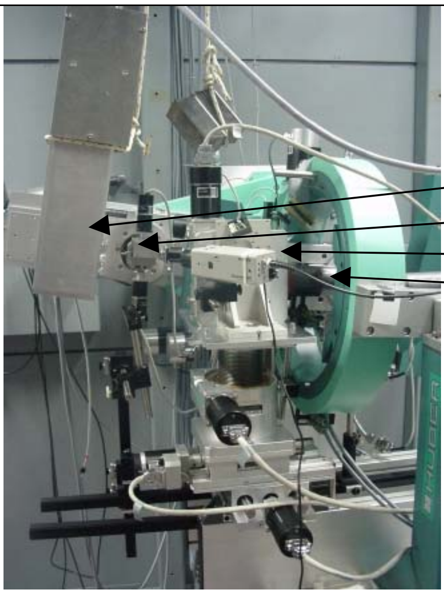	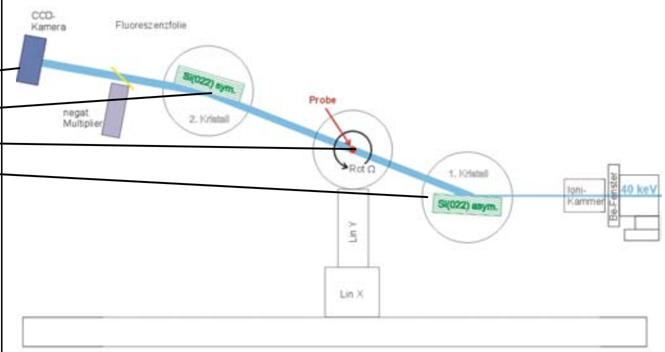
Figure 1: Photograph of the 6-circle-goniometer at the BAM*line.*	Figure 2: Experimental set-up of the SAXS-instrumentation at the BAM*line.*

Results

Fig. 3 shows the Rocking-Curve of the used crystals. The Curves are normalized to its area and therewith compensated for the sample absorption. It is clearly seen, that the inner structure (namely the interfaces) of the sample influences the shape of the curves noticeable. While the intensity is reduced at the maximum of the Rocking-Curve by refraction at the interfaces of the sample, the intensity is enhanced at the edges of the Rocking-Curve by the same effect.

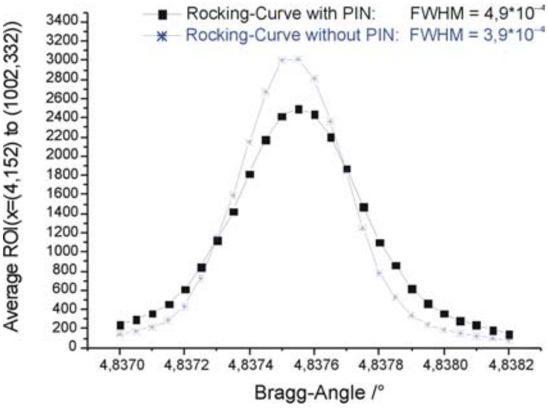

Figure 3: Rocking-Curve of the used crystals. Each point represents the average intensity over the given ROI. Filled squares: sample in the beam between the two crystals (FWHM=4,9*10^{-4}°); Stars: no sample in the beam (FWHM=3,9*10^{-4}°). Both graphs are normalized to its area.

Fig. 4 shows one reconstructed plane of the sample obtained from conventional (absorption based) CT-measurements. The main part of the picture shows a grey colour that represents the Titanium matrix of the sample. The light grey disks with the dark cores are the reinforcing SiC-fibres with its Tungsten core. For the same plane of the sample the result from Refraction-CT-measurements is given in Figure 5. The 2nd crystal was set to the maximum of the Rocking-Curve so that the X-rays, which are not fulfilling the Bragg-condition, due to refraction at the interfaces between fibre and matrix, as well as between the fibre and its core, are missing in the topography (dark rings).

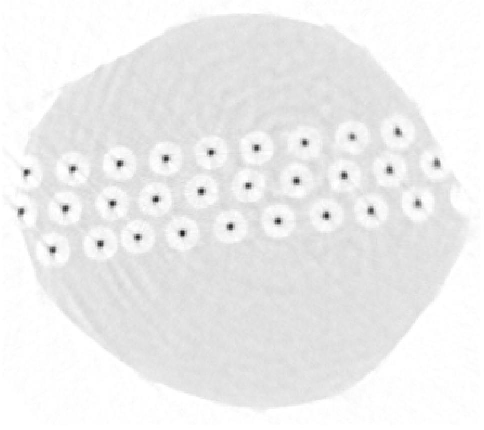

Figure 4: Reconstructed plane from CT-measurement where the 2nd crystal is not used (absorption of the sample).

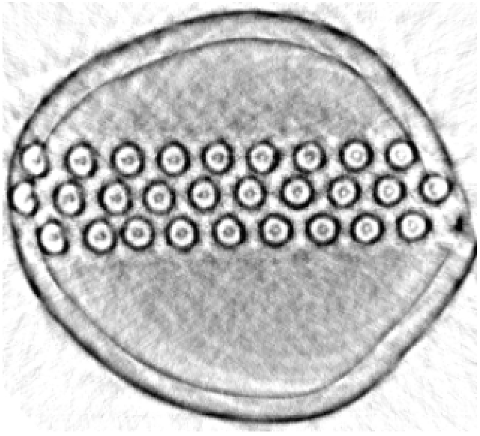

Figure 5: Reconstructed plane (the same as in Fig. 4) from Refraction-CT-measurement. The 2nd crystal was set to the maximum of the Rocking-Curve.

References

[1] A. H. Compton, S.K. Allison: “X-ray in Theory and Experiment”, Macmillan and Co. Ltd., London (1935).

[2] M.P. Hentschel, R. Hosemann, A. Lange, B. Uther, R. Brückner: “Röntgenkleinwinkelbrechung an Metalldrähten, Glasfäden und hartelastischem Polypropylen”, Acta Cryst. A 43 (1987) 506.

[3] W. Görner, M.P. Hentschel, B.R. Müller, H. Riesemeier, M. Krumrey, G. Ulm, W. Diete, U. Klein, R. Frahm; “The first hard X-ray beamline at BESSY II”, Nucl. Instr. and Methods in Phys. Res. A 467-468 (2001) 703-706.

Monocapillary Focusing System for Micro-EXAFS Micro-XANES and Micro-Fluorescence Analysis.

A. Erko, A. Firsov, BESSY GmbH, Berlin, Germany
A. Bjeoumikhov, N. Langhoff, IfG GmbH, Berlin, Germany

1. Abstract.

An elliptically shaped glass monocapillary with a spatial resolution of 5 µm has been used for the fine focusing of the pre-focused x-ray beam produced by the graded-crystal monochromator beamline KMC-2. The flux density gain of 50 was experimentally measured. The microprobe has been used in the energy range of 3.5 keV – 15 keV. XANES and EXAFS measurements for a large variety of samples were done.

2. Introduction.

The use of nanometer radiation as a tool for microscopy and nanometer technology is developing very rapidly. This can be attributed to the development of synchrotron radiation sources and on the progress in optics elements and methods for the X-rays beams control such as focusing and modulation. X-ray microprobes are widely used in combination with the most modern experimental technique, such as XANES, EXAFS and Micro-fluorescence analysis. These measurements required a large energy scan range, which is especially for EXAFS exceeds of 1000 eV. Therefore, x-ray polychromatic focusing optics is required to cover the necessary energy range.

X-ray optics systems based on total external reflection of radiation from metal surface are now most widely used. Such a mirror Kirkpatrick-Baez systems are able to focus x-ray beams to the spot ~ of 0.2 µm in diameter. However, the necessity of use a small grazing incidence angles leads to a small angular acceptance and limits substantially the performance of such optics, especially by the use with divergent banding magnet sources.

Development of the new methods of glass treatment enabled of elliptical mono-capillary fabrication with a micrometer spatial resolution. Such a mono-capillary can be placed into the preliminary focused beam at the end of conventional beamline. This provides a fine focusing of an x-ray beam into micrometer spot size.

3. Experimental set-up.

The graded-crystal monochromator beamline KMC-2 was used to set-up of the microprobe system[1]. The beam in the energy range of 3.5 keV- 15 keV is monochromatized by the double-graded-crystal monochromator and focused onto sample with the spot size of 150 µm horizontal and 700 µm vertical. The total flux in the spot is in the range of 10^9 – 10^{10} phot/sec/100 mA. The parameters of inner elliptical surface of the glass mono-capillary are shown in table 1.

Table 1. The Glass capillary ellipse parameters.

Large half-axis (mm)	Small half-axis (µm)	∅ of input aperture (µm)	∅ of output aperture (µm)	Focal Length (mm)	Focal Size (µm)
100	175	350	15	0.8	~ 5

The capillary is placed close to the focal position of the refocusing mirror of the beamline. In figure 1 is shown an optical scheme of the experimental set-up.

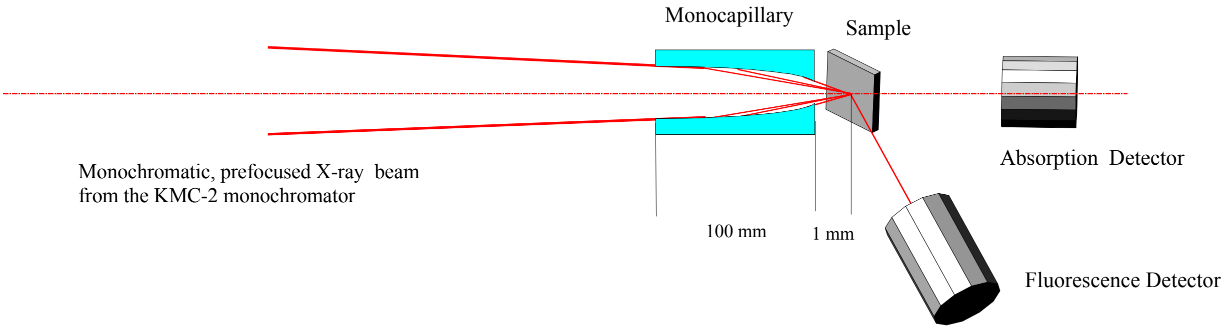

Figure 1. Optical scheme of the microprobe experimental set-up.
Energy range 3.5 keV - 15 keV.

The capillary holder is mounted on a special 5-axis goniometer with a remote control. High-resolution x-ray camera allows one to reduce an alignment time to several minutes and provides continuous control of the focused beam. Ionization chamber for the flux monitoring is located behind the slit system in front of capillary entrance aperture providing feedback signal for a intensity stabilization system and constant flux through the capillary aperture.

The microprobe-beamline provides an experimental set-up for EXAFS and XANES measurements in-air or He in the energy range of 3.6 keV – 15 keV. Beam intensity is stabilized by the MOSTAB electronics with an accuracy of 0.1 %. The detector system consists of a Si-PIN photodiode for fluorescence measurements, three ion chambers, a Scintillation counter and an energy-dispersive detector Röntec.

A sample stage and detectors are mounted on a θ -2θ goniometer. Precise X-Y-Z translation provides a 3-D scan with 1µ reproducibility of the sample position.

4. Experimental results.

Spatial resolution tests.

Knife-edge tests have been done to measure the size of a focal spot. Pt sharp-edge blades were used for these measurements. A two-dimensional mapping of a focal spot was performed using a Pt pinhole 5 µm in diameter. The results of measurements are shown in figure 2a, and 2b.

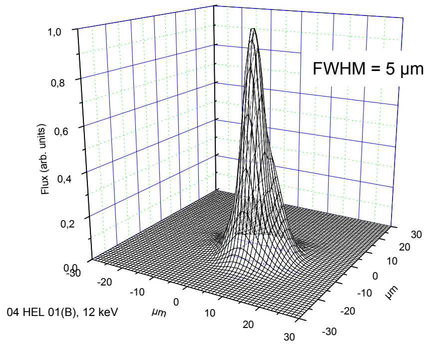

Figure 2a. Flux distribution in the focus of a monocapillary.

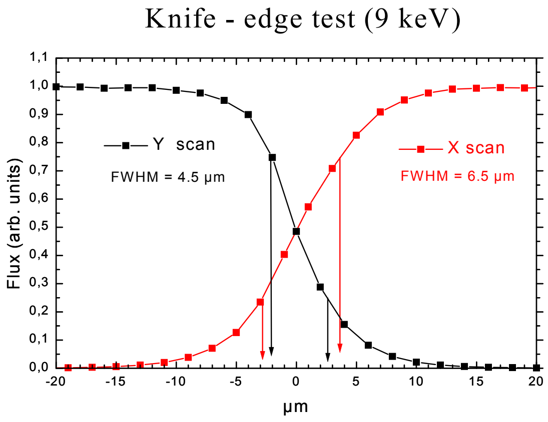

Figure 2b. Knife-edge test at the energy of 9 keV. vertical spotsize is 4.5 µm, horiszontal: 6,5 µm

Spatial resolution test in fluorescence mode was done using a e–lithography mask made with Ni pattern on the Si wafer. The pattern has Ni stripes of 4-6 μm in sizes thickness of the Ni layer of 0.12 μm. The results are shown in figure 3. Here are the image of a pattern, obtained in electron microscope (a) and two-dimensional fluorescence mapping of the same pattern in x-ray microprobe (b).

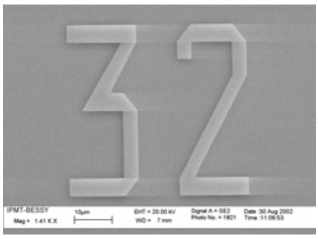

a)

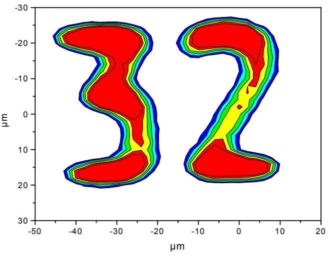

b)

Figure 3a. Spatial resolution test: Ni pattern on a Si substrate fabricated by e-beam lithography.Imagein a scanning electron microscopy

Figure 3b. Fluorescence image in a scanning X-ray microscope at 8.4 keV.

XANES measurements of Cu micro-particles.

As an example of XANES measurements of a test object consists of micro-particles of Cu and Fe mash was measured. Figure 4a shows a map of Cu K_α line in transmission. Than, the microprobe was placed in the position of Cu micro-particle and XANES measurements have been performed. The result is shown in figure 4b.

Figure 4a. 2D scan and XANES spectra of the Cu test-object. Measured in transmission.

Figure 4b. XANES spectrum of the Cu Micro-particle.

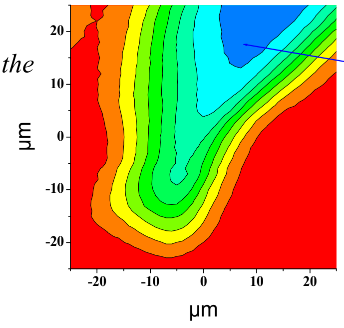

a)

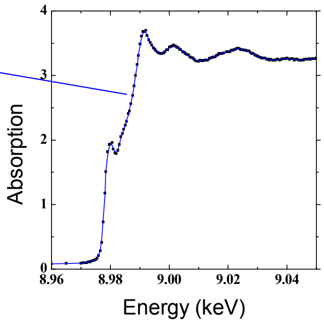

b)

Important practical measurements of the EXAFS spectra of Ge in Si matrix were done in cooperation with the Institute of Crystal Growth Berlin e.v. Ge micro-crystals in SiGe were an objects of investigations. The results: mapping and EXAFS spectra are shown in figure 5. Here are shown two spectra which correspond to the microprobe position on a Ge micro-crystal and on a Si matrix.

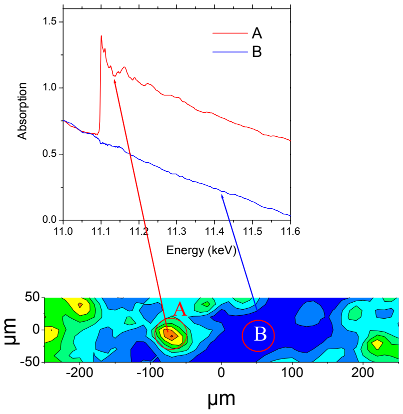

Figure 5. SiGe micro-crystals

5. Conclusions.

Monocapillary micro-focusing optics can be successfully used with the conventional EXAFS beamlines as an "add-on" system. Than, 5 μm spatial resolution can been achieved in a wide spectral range. XANES and EXAFS spectra of micro-objects have been measured in the range of 4 keV - 15 keV with energy resolution of ~ 2 10^{-4}.

---

[1] A. Erko, I. Packe, W. Gudat, N. Abrosimov, A. Firsov *"The Crystal Monochromator Based on graded SiGe Crystals"* Nuclear Instruments and Methods in Physics Research **A 467–468** (2001) 358–361

The Synthetic X-Ray Hologram: BESSY Experience.

A.A. Firsov, A. Erko, BESSY GmbH, Berlin, Germany.
A.A. Svintsov, S.I. Zaitsev, IMT RAS, Chernogolovka, Russia.

1. Abstract

We report the first successful fabrication and reconstruction of a synthetic x-ray hologram at BESSY GmbH. A hologram structure was calculated using computer software and fabricated on the surface of a Si (111) mono-crystal using e-beam lithography and a metal coating technique. A "white" broad-band synchrotron radiation beam from the BESSY bending magnet source was used for the hologram reconstruction. The image was obtained at the photon energy of 8 keV and the distance of 0.5 m from the hologram, which placed at the distance of 29 m from the source.

2. Hologram fabrication and results.

Here we show the first results of designing, optimization, fabrication and testing of synthetic x-ray hologram, produced at the BESSY microfabrication laboratory. The principle of x-ray hologram generation is the same as used in hologram generation published recently.

The word "X - RAY" composed of δ-function pixels has been chosen as the object (Figure. 1). The synthetic hologram has been designed as a phase shift mask placed on a polished surface of a Si (111) crystal (Figure 2). An initial hologram structure on resist was fabricated by an electron-beam lithography in the LEO-1560 e-beam writer controlled by the "Proxy for Windows" program package developed in the Institute of Microelectronics Technology Russian Academy of Sciences, Chernogolovka. After the development of the resist, a Ni layer was deposited, followed by the lift-off procedure. The thickness of the Ni layer was 340 nm, calculated to produce a π phase-shift at the energy of 8 keV and Bragg incidence angle of 14.2°.

Figure 1. The virtual object composed of δ-function pixels.

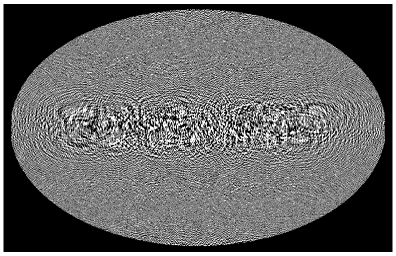

Figure 2. Synthetic hologram.

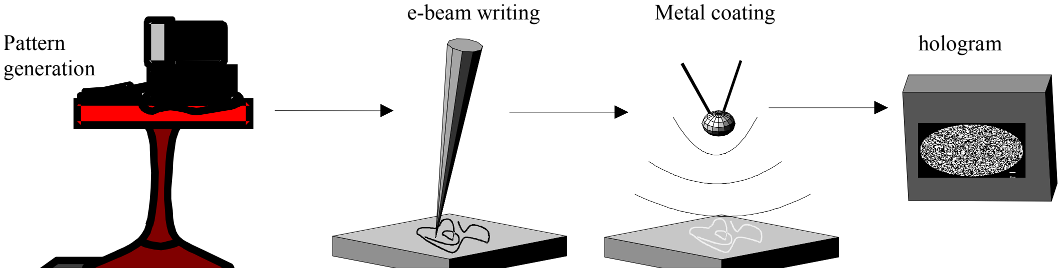

Figure 3. Fabrication of a synthetic hologram structure of Ni layer on the Si 111 substrate.

Thus, the hologram is a phase-shifting layer of a Ni film on a silicon substrate simultaneously serving both as a Bragg mirror and as an incident radiation monochromator (Figure 3).

Design parameters of the hologram are the following: photon energy 8 keV and 10 keV, apertures 400 µm, 270 µm and 120 µm, minimum period of interference fringes 0.2 – 0.3 µm, hologram-image distance 500 mm.

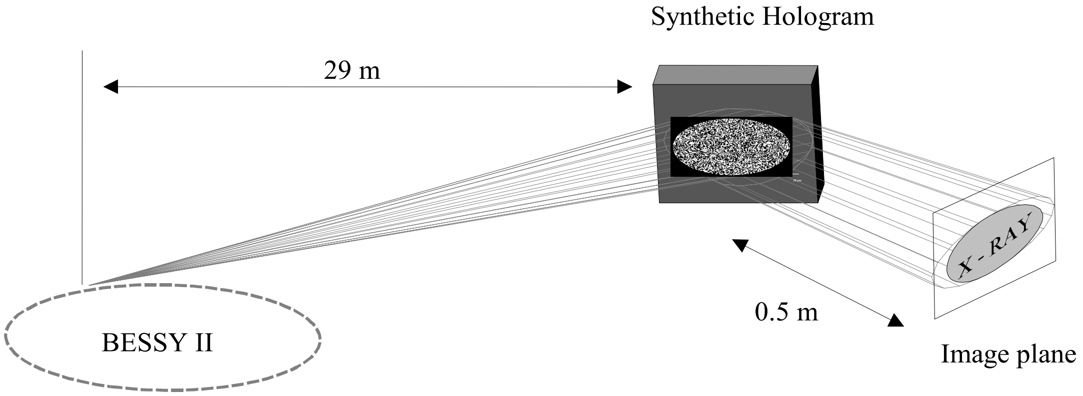

Figure 4. Experimental set-up. x-ray beam deflected in the horizontal plane.

Experimental tests of the hologram reconstruction were done at a BESSY white-beam beamline. The experimental arrangement is shown in Figure 4. A beam from the bending magnet was used. There were no optical elements except apertures between the source and the synthetic hologram. The distance between the source and the hologram was 29 m. The reconstructed image was recorded on a high-resolution x-ray film and enlarged using an optical microscope. The result of the reconstruction is shown in Figure 5.

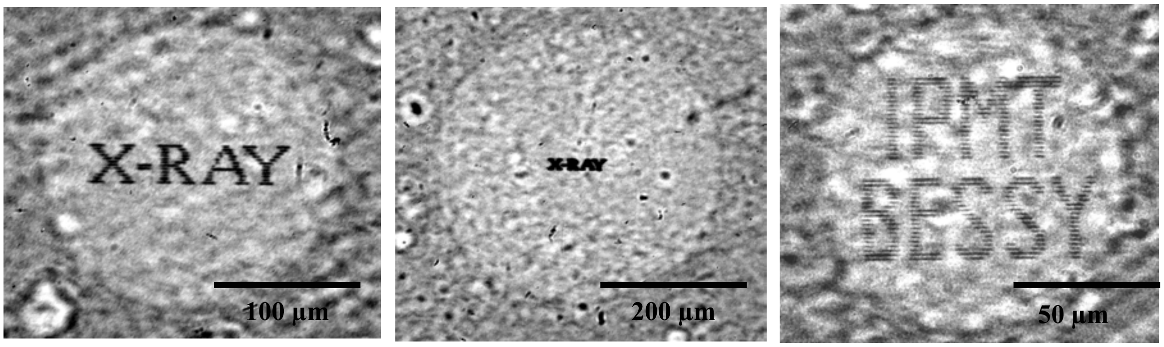

Figure 5. The images reconstructed from the synthetic hologram in a "white" synchrotron beam.

The image resolution was estimated to be on the order of 2.4 µm using micro-densitometery of the image edges. An estimated theoretical resolution is still better than the measured value.

The authors are very grateful to colleagues from BESSY and IMT RAS for their help in performing the experiment. We thank Prof. W. Eberhardt, Prof. W. Peatman and Dr. B. Löchel for support, discussion and encouragement. The work was partially supported by National (Russia) Program on “Physics of Nanostuctures” Grant 97-2021.

References.

1. A. Firsov, A. Svintsov, S.I. Zaitsev, A. Erko, V. Aristov *"The first synthetic X-ray hologram: results",* Optics Communications, **202** (2002) 55–59

Double Pinhole Diffraction of White Synchrotron Radiation

W. Leitenberger [a], H. Wendrock [b], L. Bischoff [c], T. Panzner [a], U. Pietsch [a], J. Grenzer [a], A. Pucher [a]

[a] Universität Potsdam, Institut für Physik, Am Neuen Palais 10, D-14469 Potsdam, Germany
[b] Institut für Festkörper- und Werkstoffforschung, P.O.B 270016,D-01171 Dresden, Germany
[c] Forschungszentrum Rossendorf e.V., P.O.B. 51 01 19, D-01314 Dresden, Germany

The coherence properties of hard X-rays can be exploited in a number of experiments in X-ray imaging, investigation of speckle pattern or time-correlation spectroscopy. The coherence properties of hard X-rays were already investigated using several experimental techniques [1 - 7]. Compared to other techniques the double slit experiment presented here needs a relatively simple set-up. It is a standard technique for probing the coherence properties of radiation in the visible spectral range provided by lasers, soft X-rays or even elementary particles and atoms. Recently this technique was applied at hard X-rays as well, probing the coherence properties of monochromatic radiation with large longitudinal coherence length [7].

This double-pinhole diffraction experiments using an incident white synchrotron radiation beam at the energy-dispersive reflectivity (EDR) beamline (bending magnet) at the BESSY II storage ring The aim of our activities was to characterize the coherence properties of the X-ray source.

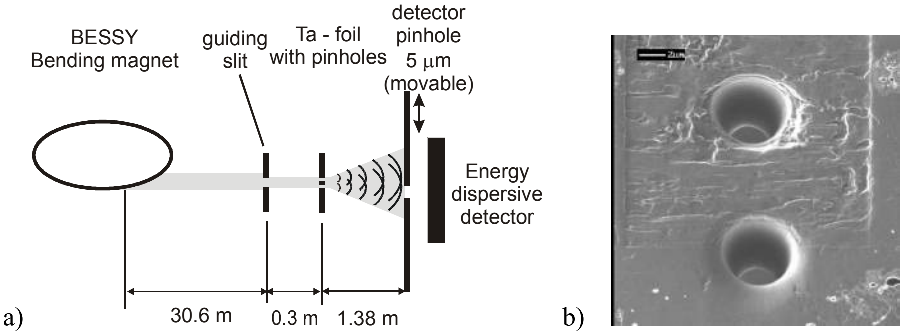

FIG. 1.a) Experimental set-up at the EDR-beamline at BESSY II b) Electron microscope image of the 30 μm tantalum foil containing the two micro pinholes 11 μm separated (exposure at 10 degree tilt angle).

In the experiment the two pinholes were separated in vertical direction. The energy-dispersive detector (XFlash by Fa. Roentec) was placed in 1.38 m distance behind the tantalum foil. The energy resolution of the detector was about 200 eV. A small pinhole of 5 μm in diameter was accurately scanned in vertical direction in front of the detector opening. By this the energy spectrum behind the pinhole mask could be recorded also with a good lateral resolution.

Some experimental results are shown in the following Fig. 2. The grey-scale map summarizes the normalized diffraction profiles over a large range of x-ray energies. The interference fringes are clearly visible between 5 keV and 16 keV. The fringe spacing decreases with increasing energy. Only in the region just below the Ta-absorption edge of 9.9 keV, the diffraction curves are not detectable caused by the low absorption of the tantalum foil.

A first evaluation of the data was done by fitting the experimental data to an analytical expression for the intensity distribution of the interference pattern in the far field.

$$I(x) = I_0 \left(\frac{\sin(k_d x)}{k_d x} \right)^2 \left(1 + V \cos(k_D x)\right) + I_b \qquad \text{with} \quad k_d \approx c \frac{Ed}{z} \text{ and } k_D \approx c \frac{ED}{z}. \quad (1)$$

x – co-ordinate in the diffraction plane, E - energy [keV], c – 5.07 [nm^{-1}] = 2π/1.239 [nm^{-1}] conversion factor from the wavelength to the energy domain, *L* - the source-to-pinhole distance, *D* - pinhole separation, *d* - diameter of the pinhole, *z* - pinhole-to-detector distance. The parameter *V* is the visibility of the interference fringes, given by [8]

$$.\,V=\frac{I_{\max}-I_{\min}}{I_{\max}+I_{\min}}=\frac{\sin(Y)}{Y}\quad with\quad Y=c\frac{sED}{4L}\tag{2}$$

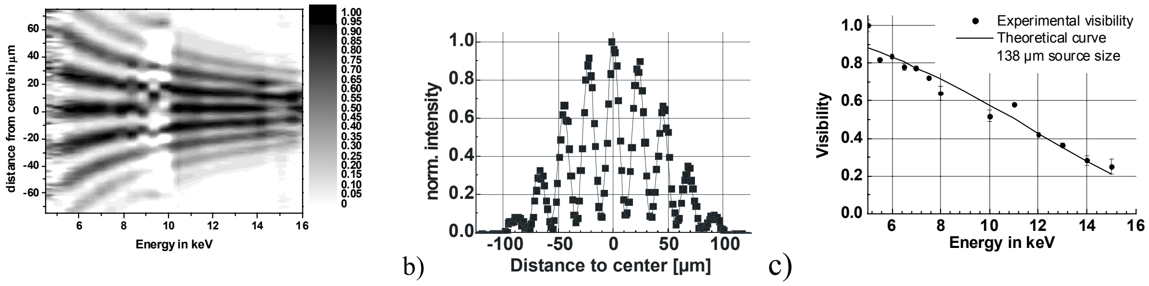

a) b) c)

FIG. 2. **a)** Normalized diffracted intensity as a function of energy and the distance from the optical axis. **b)** Normalized interference fringes at 6 keV, The squares are the measured data from Fig. 2a and the lines are the results of the best fit of eq. (1) **c)** measured frige visiilityas a fuction of energy

Here I_{max} and I_{min} are the maximum and the minimum intensities close to the central peak. Some single diffraction curves are shown in Fig. 2 b+c. Using eq. (1) the pinhole parameters were determined to *d*=2.0 µm, *D*=11.3 µm verifying the values determined by microscopy.

The energy dependence of the visibility should follow a sinc-function with the “effective source size” *s* as a parameter, which is qualitatively reproduced in Fig. 5. The calculated values for the fringe visibility are shown in the Fig. 5. As expected it becomes maximum for large wavelength and decreases to smaller wavelength. According to eq. (2) the source size *s* has a value of approximately 140 µm which is much larger compared to the values measured with a pinhole camera [9]. First, it is due to the insufficient consideration of the small detector distance which does not match the far field expression used by eq.1 and the relatively large size of the detector pinhole which influences the measurable visibility especially for smaller fringe distances. A numerical simulation of the experiment is done at the moment and will be presented in ear future.

Acknowledgement

The authors kindly acknowledge financial supports by the Max-Planck Institute of Colloids and Interfaces (Potsdam/Golm), the Hahn-Meitner Institute (Berlin) and the BESSY GmbH (Berlin).

References

[1] B. Lengeler, Naturwisssenschaften **88**, (2001) 249.

[2] A.R. Lang, A.P.W. Makepeace, J. Synchrotron Rad. **6**, (1999) 59.

[4] M. Yabashi, K. Tamasaku, T. Ishikawa, Phys. Rev. Lett. **87** (2001) 14080.1

[5] K. Fezzaa, F. Comin, S. Marchesini, et al. X-Ray Sci. and Techn. **7**, (1997) 12.

[6] C. Chang, P. Naulleau, E. Anderson, D. Attwood, Opt. Commun. **182**, (2000) 25.

[7] W. Leitenberger, S.M. Kuznetsov, A. Snigirev, Opt. Commun., **191**, (2001), 91.

[8] M. Francon, *Optical Interferometry* (Academic Press, New York and London, 1966).

M. Born, E. Wolf, *Principles of optics* (Cambridge Univ. Press, 1999).

[9] K. Holldack, J. Feikes, W.B. Peatman, Nucl. Instrum Meth. A **467-468** (2001) 235.

Coherence Experiment at the Energy-Dispersive Reflectometry Beamline at Bessy II

T.Panzner [a,b], W. Leitenberger [a], J. Grenzer [a], Y. Bodenthin [a], Th. Geue [a] and U. Pietsch [a]

H. Möhwald [b]

[a] Institut für Physik, Universität Potsdam, 14415 Potsdam, Germany
[b] MPI für Kolloid- und Grenzflächenforschung, 14476 Golm

1. Introduction

In recent years the technique of x-ray photon correlation spectroscopy (XPCS) has been developed exploiting the coherent properties of third generation synchrotron radiation sources. Many successful experiments have been done at bending-magnet- and undulator-beamlines using highly intense monochromatic radiation [1], [2], [3], [4].

Here we report on coherent scattering experiment which exploit white radiation provided by a bending-magnet-beamline [5]. The simultaneous use of a broad energy band pass can reduce the time of measurement and could allow to perform XPCS experiments at different q-values simultaneous [6].

For coherence experiments the most important parameters are the longitudinal and transverse coherence lengths. The longitudinal coherence length ζ_l at the wavelength λ is controlled by the energy-resolution of the experimental setup. The transverse coherence length ζ_t depends on the source size d_s and the source-sample-distance R_s [4].

$$\xi_l = \frac{\lambda^2}{2\cdot\Delta\lambda} \qquad (1) \qquad\qquad \xi_t = \frac{\lambda\cdot R_s}{2\cdot d_s} \qquad (2)$$

Applied on the condition of the EDR-beamline at BESSY II and considering the root-means-square source size $d_{s,vertical}$= (45 ± 5) µm and $d_{s,horizontal}$= (55 ± 5) µm [7], the source-sample distance R_s = 24360 mm and the energy resolution of $\Delta E/E = 10^{-2}$ (given by the energy resolution of our detector) the coherence lengths are calculated to:

ζ_l (6keV) = 10 nm

and

$\zeta_{t,vertical}$ (6keV) = 56 µm $\qquad$ $\zeta_{t,horizontal}$ (6keV) = 46 µm

Whereas the amount of ζ_t is comparable with that of a monochromatic experiment the second value, ζ_l , is much smaller. Nevertheless, the Fraunhofer figure should be measurable for small pinhole sizes.

2. Fraunhofer Diffraction Through a Pinhole

We performed an energy-dispersive diffraction experiment for qualitative verification of coherence properties of the beam, where the total intensity at the EDR- (bending-magnet) Beamline is a factor of 10^5 less compared to a typical undulator-beamline as ID 11 at ESRF, for example (see [8] and [9]).

The experimental setup for this Fraunhofer-diffraction is shown is figure 1.

The used pinholes were actually made for electron microscopy. The material is platinum and the pinholes have a conic shape into the beam direction. This conic shape and the different absorption lengths for different energies do to guess that we should see different pinhole diameters for different energies. But this two effects are so small that they did not make a visible effect during the measurements. This was verify after the measurement by calculating the fringes positions for different energies as a function of the pinhole diameter. The results of this calculations show that the same pinhole diameter can be used to explain the data within the energy band pass from 5 keV up to 15 keV.

The parallel white beam is guided through a 5µm pinhole and the Fraunhofer-diffraction is detected by a Röntec detector 1,34 m downstream. The Röntec-detector is an energy-dispersive detector with a resolution of $\Delta E/E$ =

10^{-2}. It is sensitive for energies between 0< E < 80 keV (divided into 4000 channels by a Multi Channel Analyser), and has an active area of 2mm x 2 mm.

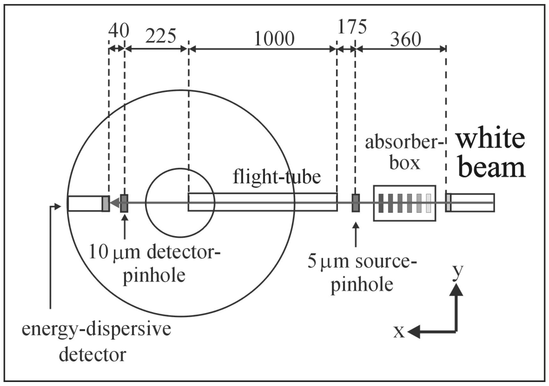

Fig. 1 : Experimental setup to measure the Fraunhofer diffraction at the EDR-beamline

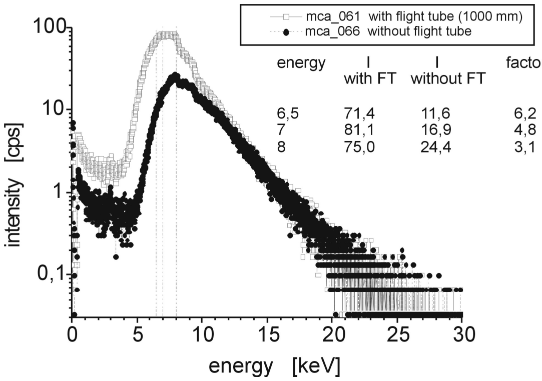

Fig. 2 : Measured incident spectrum at the EDR-beamline with and without a flight tube with two capton windows.

As an important parameter the counting response of the detector is linear up to 10^5 cps. For better spatial resolution of the Fraunhofer figure, a 10 µm pinhole was installed 40 mm in front of the detector. Both pinholes can be moved in y- and z-direction perpendicular to the beam with sub-micron accuracy. To reduce air-absorption an evacuated flight-tube was equipped between the two pinholes. Figure 2 shows the detected energy spectra of the incident beam with and without flight tube.

As shown, the implementation of the flight tube extends the radiation spectrum to lower energies and increases the total flux.

The center graph of figure 3 shows the measured Fraunhofer pattern. It was obtained by subsequent recording of diffraction spectra as a function of the detector height z by steps of $\Delta z = 2$ µm. Notice, that the shown range in z-direction is larger then the measured range. Due to a experimental problem the measurement could only performed between $-0.2 < z < 0.09$. Fig. 3 was obtained by mirrowing the data $-0.2 < z < 0$ onto the positiv z axis. This procedure should be correct, due to the rotational symmetry of the Fraunhofer fringes.

The total scan time was about 75 minutes. As demonstrated, the Fraunhofer fringes are well resolved in the energy space. The intensity distribution follows that of the incident spectrum (see fig.3, right). At E = 8 keV more than five fringes are resolved.

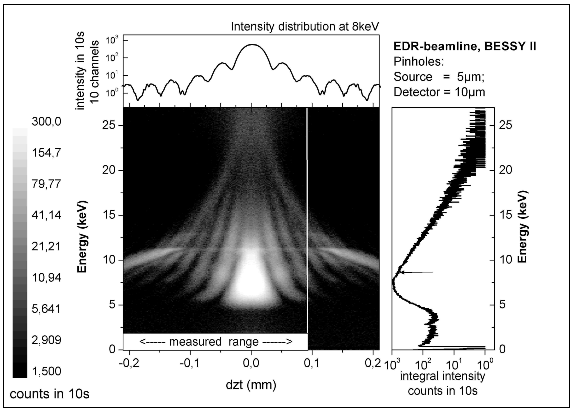

Fig. 3 : Fraunhofer pattern of a white incident Spectrum. Measured by using an energy-dispersive detector.

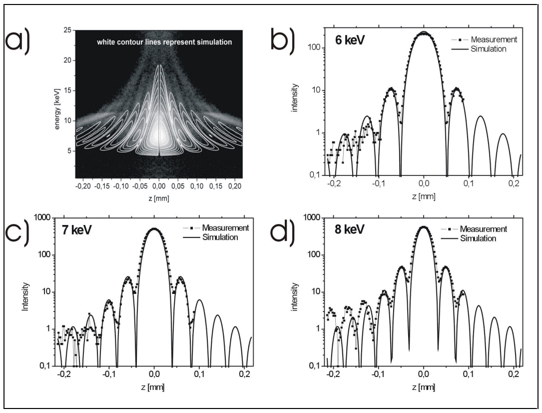

Fig. 4 : Simulated Fraunhofer pattern for the whole measured energy band pass and selected energies.

For fixed energy the diffracted intensity (Fraunhofer pattern) can be calculated by the following formula :

$$I_D = I_0 \left(\frac{2 \cdot J_1\left(\frac{2 \cdot \pi \cdot R \cdot \sqrt{y^2 + z^2}}{\lambda \cdot L} \right)}{\frac{2 \cdot \pi \cdot R \cdot \sqrt{y^2 + z^2}}{\lambda \cdot L}} \right)^2 \qquad (3)$$

where R is the radius of the incident pinhole, λ the wavelength, L the distance between diffracting pinhole and the detector and J_1 is the 1st order Bessel function.
At z=0 the measured intensity-distribution can be simmulated by :

$$I_0(E) = A \cdot e^{-B \cdot E} \cdot e^{-\frac{C}{E^3}} \qquad (4)$$

where A, B, C are the fitting parameters and E=12.398/λ is the energy in keV. This calculated intensity at z=0 was used as I_0 in equation (3) for the simulation of the measurement.
To consider the analyser pinhole size of 10 µm the calculated intensities (performed in steps of $\Delta z = 2$ µm) were convoluted with a recangular function of 10 µm width, i.e. the intensity at z_i was summerized by:

$$I_{D,AP=10} = \sum_{i-2}^{i+2} I_{D,j+i} \,. \qquad (5)$$

The results of simulation are shown in figure 4 (for selected energies (4b-d) and for the entire spectrum detected (4a)). The mismatch between the measured and calculated fringes positions below the 2nd orders for z < 0 in Fig. 4d corresponds to jump of 5 steps in z direction. To our mind it was a problem of the equiment during this scan. Fig.4 impressively demonstrates the appearance of coherent properties over a large energy band pass in this experiment.

3. Conclusion

The present experiment, performed at the EDR-Beamline at BESSYII, gives evidence for the fact that coherence experiments can be performed with a very small longitudinal coherence length in a white beam setup using an energy dispersive detector.
The measurement of the Fraunhofer-diffraction show a very good agreement with the calculated pattern. At the bending magnet of BESSY II and using a 5 µm pinhole the Fraunhofer-fringes are visible up to the 5. order.

4. References

[1] T. Thurn-Albrecht, G. Meier, P. Müller-Buschbaum, A. Patkowski W. Steffen, G. Grübel, D. L. Abernathy, O. Diat, M. Winter, M. G. Koch and M. T. Reetz , Phys. Rev. E 59 (1999) 642.
[2] D. O. Riese, W. L. Vos, G. H. Wegdam, F. J. Poelwijk, D. L. Abernathy and G. Grübel, Phys. Rev. E 61 (2000) 1676.
[3] A. Malik, A. R. Sandy, L. B. Lurio, G. B. Stephensoen, S. G. J. Mochrie, I. McNulty and M. Sutton, Phys. Rev. Letters 81 (1998) 5832.
[4] D. L. Abernathy, G. Grübel, S. Brauer, I. Mc Nulty, G. B. Stephenson, S. G. J. Mochrie, A. R. Sandy, N. Mulders and M. Sutton, J. Synchrotron Rad. 5 (1998) 37
[5] F. Livet, F. Bley, A. Létoublon, J. P. Simon and J. F. Bérar, J.Synchrotron Rad. 5 (1998) 1337.
[6] U. Pietsch, J. Grenzer, Th. Geue, F. Neissendorfer, G. Brezesinski, Ch. Symietz, H. Möhwald and W.Gudat, Nucl. Instr. Methods A 1077 (2001) 467.
[7] K. Holldack, J. Feikes, W. B. Peatman, Nucl. Instr. Methods A 467-468 (2001) 235.
[8] http://www.esrf.fr/exp_facilities/ID11/handbook/welcome.html
[9] http://www.bessy.de/users_info/beamlines/linespdf/D_13_2.pdf

Time-resolved magnetic domain imaging by X-ray photoemission electron microscopy

J. Vogel[1], W. Kuch[2], M. Bonfim[3], J. Camarero[1], F. Offi[2], Y. Pennec[1], K. Fukumoto[2], J. Kirschner[2], A. Fontaine[1], S. Pizzini[1]
[1]Laboratoire Louis Néel, CNRS, BP166, 38042 Grenoble, France
[2]Max-Planck-Institut für Mikrostrukturphysik, Weinberg 2, D-06120 Halle, Germany
[3]Departamento de Engenharia Elètrica, Universidade do Paraná, CEP 81531-990, Curitiba, Brazil

BMBF 05 KS1EFA6, EU HPRI-1999-CT-00028

Magnetization reversal dynamics at nanosecond timescales is an important subject for many technological applications of magnetic materials. In order to improve the performance of materials for fast magnetic applications, the fundamental understanding of magnetization reversal processes at high speed should be improved. This can be best done using imaging techniques, which allow the direct observation of the local magnetization direction in a sample as a function of time. The element selectivity of x-ray magnetic circular dichroism (XMCD) has recently been combined with the time structure of synchrotron radiation to separately study the magnetization reversal dynamics of the two ferromagnetic layers of a spin valve system [1]. The magnetic contrast provided by XMCD can also be used to obtain spatial resolution when combined with an appropriate imaging technique, like x-ray photoemission electron microscopy (X-PEEM). The time-resolved X-PEEM measurements that we present here add spatial resolution to the selective magnetization dynamics observations carried out by pump-probe XMCD.

The measurements were performed at the UE56/2-PGM2 helical undulator beamline. The set-up of the electrostatic photoelectron emission microscope (Focus IS-PEEM) is identical to that described in previous publications [2]. The spatial resolution selected for this experiment was of the order of 1 µm. In single bunch operation of BESSY, photon bunches are emitted with a repetition rate of 1.25 MHz (800 ns separation between bunches). Measurements were performed in pump-probe mode, by synchronizing nanosecond-short magnetic field pulses with the x-ray photon bunches. Magnetization reversal dynamics was then studied as a function of time, during and after the magnetic pulse, by changing the delay between magnetic and photon pulses.

The measurements were performed on the permalloy layer of a $Ni_{80}Fe_{20}$(5nm)/Cu(10nm)/Co(5nm) spin valve-like trilayer deposited on a step-bunched Si(111) substrate. The terraces of the substrate induce an in-plane uniaxial anisotropy in the magnetic layers, with the easy magnetization axis parallel to the steps. The magnetization dynamics of the two ferromagnetic layers of this sample has already been studied by time-resolved XMCD measurements [1]. The strength of the magnetostatic "orange-peel" coupling between the soft and the hard magnetic layers induced by the substrate topography decreases when going from quasi-static to nanosecond regimes. We tentatively explained this effect supposing that, while propagation of domain walls dominates in the quasi-static regime, nucleation of reversed domains dominates in the nanosecond regime. The coupling in these samples is strongly localized at the steps, and the domain walls have to overcome these strongly coupled regions in order to propagate. Nucleation can take place on all terraces in which case reversal does not require propagation of domain walls across the steps. By using time-resolved X-PEEM, we demonstrate here that nucleation processes indeed dominate the reversal in the nanosecond regime.

The sample was set at the inner surface of a double stripline copper coil, made of 12.5 µm thick Cu foil. The angle of incidence of X-rays on the sample was 60° from the surface normal. Magnetic pulses were provided by sending a fast current pulse through a low impedance coaxial cable made of two 12.5 µm thick and 15 mm wide copper strips connected to the microcoil.

The X-PEEM images of the $Ni_{80}Fe_{20}$/Cu/Co trilayer measured for different delays between field and photon pulses are shown in Fig. 1. The easy magnetization axis is vertical in the figure, and the field pulses are applied parallel to it. The photon energy was tuned to the maximum of the Fe L_3

absorption white line (707 eV), providing sensitivity to the magnetization of the permalloy layer only. The five images were taken with delays of 13, 15, 17, 20, and 22 nanoseconds after the maximum of the field pulse. The images, obtained at room temperature, represent the asymmetry (difference divided by the sum) of two measurements taken with opposite photon helicity. The contrast is due to the different absorption of regions of the sample having their magnetization parallel and anti-parallel to the incoming x-rays direction at that particular delay.

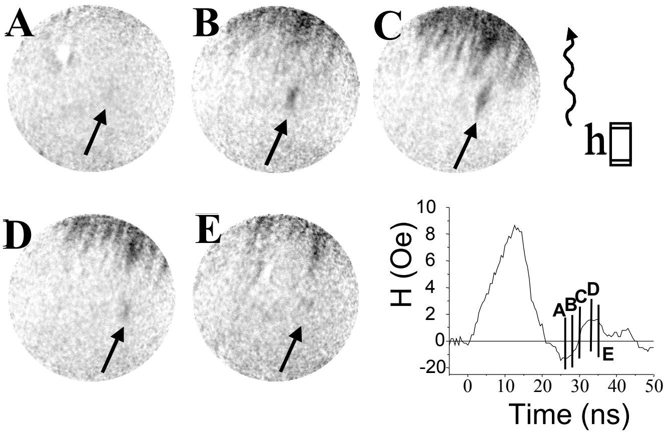

Fig. 1: Magnetic PEEM domain images of a NiFe layer, taken 13, 15, 17, 20 and 22 ns after the maximum of an 80 Oe field pulse. The shape of the pulse as well as the time position with respect to the pulse are given in the graph. The arrows inside the images indicate a nucleated and subsequently expanding reversed domain. The direction of the incoming photons is also indicated.

The first positive pulse was used to saturate the permalloy layer, while the dynamics was monitored during the negative and subsequent positive overshoot. Acquisition times were of the order of three minutes for each helicity, corresponding to over 100 million magnetic pulses. The magnetic contrast is limited principally because the nucleation of reversed domains for each magnetic pulse is probably not completely reproducible, but also because the nucleated domains are small with respect to the resolution of the image. In the first image, the nucleation sites which have been generated during the rise of the negative pulse are weakly visible and the clearest of them has been marked with an arrow. In the second and third image the nucleated sites have grown through propagation of the formed domain walls and the contrast becomes larger due to the larger size of the domains. The larger amount of nucleated reverse domains in the top of the image indicates that the field is not completely homogeneous. In the third image, several small, well-separated domains can be seen. The domains disappear during the positive overshoot. These results clearly show that for these short pulses the reversal takes place through nucleation of several reversed domains during the rise of the pulse and subsequent propagation of the formed domain walls.

In conclusion, we have shown that time-resolved X-PEEM measurements associated with nanosecond short magnetic field pulses can be used to probe the magnetization reversal dynamics in thin film samples. With the improvements in both synchrotron X-ray sources and X-PEEM microscopes, layer selective imaging of magnetization dynamics with picosecond time resolution and spatial resolution down to 2–5 nm can be foreseen in the near future.

J. C. acknowledges the European Union for a Marie-Curie Fellowship. We thank F. Petroff and A. Encinas for sample preparation.

[1] M.Bonfim et al., Phys.Rev.Lett. 86, 3646 (2001).
[2] W.Kuch et al., Surf.Rev ;Lett. 5, 1241 (1998).

NanoESCA: Imaging XPS with Resolution below 200nm

D. Funnemann[1], P. Bernhard[3], M. Escher[2], F. Forster[4], B. Krömker[1], M. Merkel[2], F. Reinert[4],
S. Schmidt[4], G. Schönhense[3], J. Westermann[1], C. Ziethen[3]

[1]Omicron NanoTechnology GmbH; [2]Focus GmbH; [3]Universität Mainz; [4]Universität des Saarlandes

Imaging XPS instruments with laboratory X-ray sources are currently limited to about 3 µm lateral resolution. In a cooperation between two university institutes and two companies we have developed the prototype of an instrument that is capable of a resolution below 100 nm. The instrument primarily consists of a newly designed band pass energy filter with negligible image aberrations (patent applied), combined with a suitably modified PEEM that is used as an entrance electron optics. Previous instruments of similar type had severe limitations when imaging electrons of high kinetic energy [1 (p. 235) and references therein], which restricted the useful kinetic energy range to less than 100 eV. These restrictions have been overcome as we show by various high photon energy and high kinetic energy measurements.

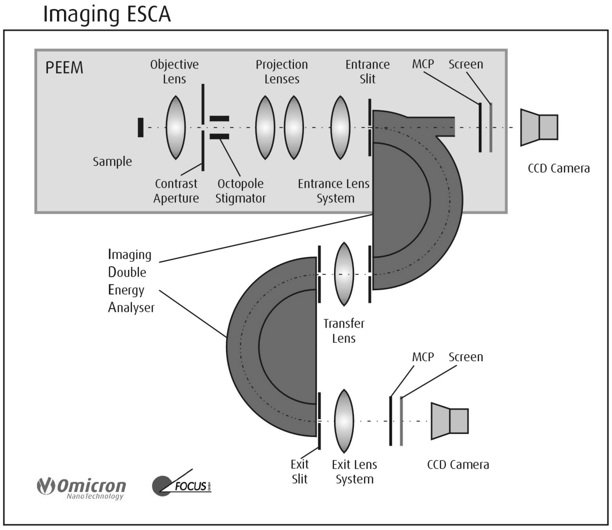

Fig.1: Schematic of the instrument

Characterisation measurements to determine the spatial and energy resolution limits of the current prototype instrument were carried out at the UE52 SGM beamline at Bessy II. Due to the high brightness and tuneable photon energies, experimental parameters such as lens focussing voltages could be optimised in a reasonable time. These parameters are required to be able to reproduce these measurements with laboratory XPS-sources at much lower excitation intensities.

Here, we present the results of these first measurements.

The energy resolution was tested on a microstructured Silver on Tantalum sample. The silver squares with a size of 6.7 x 6.7 µm² were generated by e-beam evaporation through a TEM copper grid. An area of about 3.3 x 3.3 µm² was selected in the images to extract the spectra which were taken at a photon energy of 700 eV (see Fig. 2).

a)

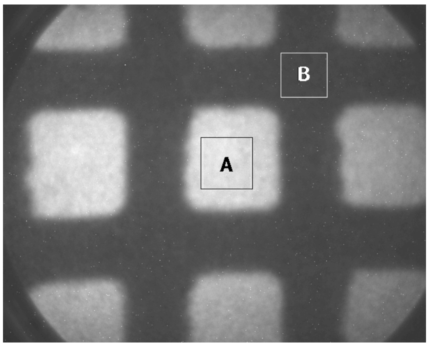

Fig. 2.

a) Photoelectron image of the Ag 3d5/2 intensity (331.7 eV kinetic energy) taken at 700 eV photon energy (Pass energy 100eV, ΔE=600meV)

b) Ag Spectrum corresponding to area marked A

c) Ta Spectrum corresponding to area marked B

b)

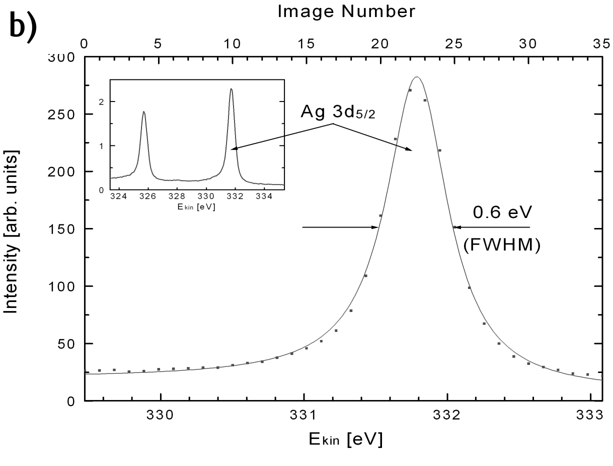

c)

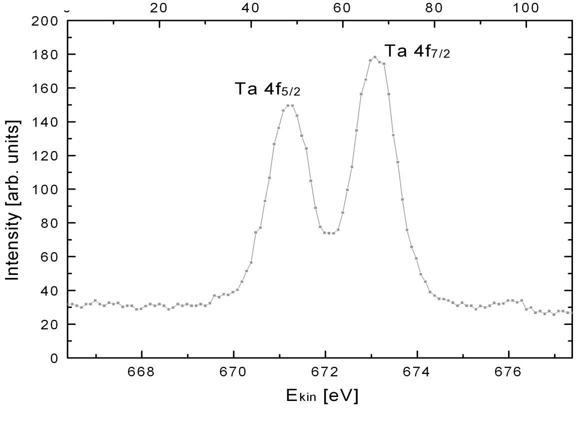

At an analyser pass energy of 100 eV and 1 mm slits, the measured energy resolution was better than 600 meV on the Ag $3d_{5/2}$ peak. However, this is not the resolution limit. It has been found that the energy resolution follows the theoretical calculations and is identical to the resolution of a single hemispherical analyser of the same radius at a given pass energy and slit width.

The spatial resolution was characterised using a test sample that was supplied by the Bundesanstalt für Materialforschung (BAM). This sample had been developed within the project "Qualitätssicherung in der Nanoanalytik" (Förderkennzeichen 13N 7698). It consists of alternating stripes of AlGaAs, InGaAs and GaAs with varying dimensions in the range between 500 nm and 0.5 nm (see Fig 3.).

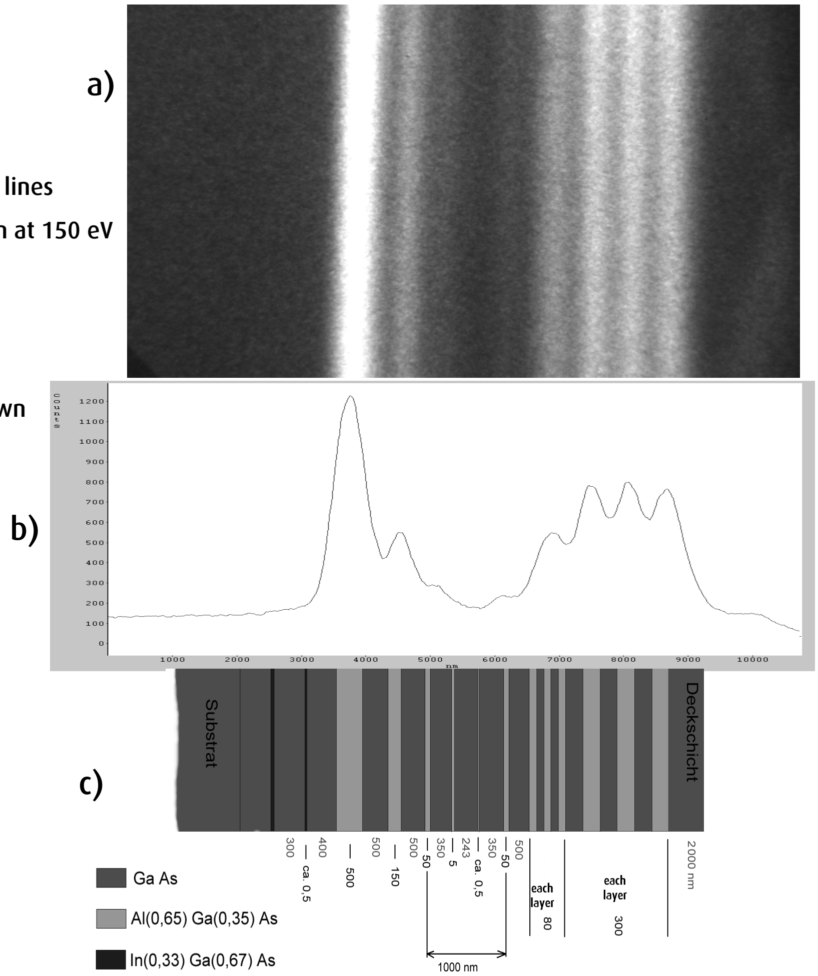

Fig. 3:

a) Photoelectron image of the Al 2p lines (about 70 eV kinetic energy) taken at 150 eV photon energy
(Pass energy 100eV, ΔE=600meV)

b) Corresponding line profile

c) Schematic of the test sample shown at the same scale as a) and b).

The series of 300 nm lines is clearly resolved. Structures of ≤ 50 nm are obviously distinguishable from the background, but the 80 nm periodic lines are not resolved. The resolution limit is about 140 nm as derived from the 16% to 84% width of an edge profile within the line scan. However, not only one result at minimum contrast is used to characterise the instrument, but also the complete modulation transfer function has been measured. Mechanical vibrations of the instrument are supposed to be the main reason for the observed resolution limit.

Further measurements at BESSY with a mechanically improved instrument are scheduled for February 2003.

The authors would like to thank the staff of BESSY for excellent cooperation.

Funding by the BMBF is gratefully acknowledged by all cooperation partners (FKZN 13N7865, 13N7863, 13N7864, 13N7847).

[1] S. Günther et al., Progress in Surface Science 70 (2002) 187-260
For further references see also:
H. Ade (Ed), “Spectromicroscopy” Special Issue: J. Electron Spectr. Relat. Phenom. 84, Vol.1-3 (1997)

Magnetic dichroism in angle-resolved photoelectron emission as contrast mechanism for magnetic domain imaging

W. Kuch, L. I. Chelaru, F. Offi, M. Kotsugi, J. Wang, K. Fukumoto, and J. Kirschner
Max-Planck-Institut für Mikrostrukturphysik, Weinberg 2, D-06120 Halle, Germany

BMBF 05KS1EFA6

The most frequently employed magnetic contrast mechanism for microscopic imaging of magnetic domains in a photoelectron emission microscope (PEEM) is the x-ray magnetic circular dichroism (XMCD) in the absorption of soft x-rays. In this method, the local intensity of emitted low-energy secondary electrons is imaged by a set of electrostatic lenses. Magnetic contrast is obtained from the dependence of the absorption of circularly polarized x-rays on the local magnetization direction for excitation at the maxima of elemental absorption edges.

If energy filtering of the photoelectrons that create the image is possible, a new class of dichroic effects is accessible for use as magnetic contrast mechanisms for magnetic imaging in PEEM. Magnetic dichroisms in photoelectron spectroscopy occur for various experimental geometries, involving circularly, linearly, or even unpolarized light, and can be observed in valence band or core level photoemission spectra. In contrast to XMCD, which (for a fixed helicity) depends only on the relative orientation between light incidence and magnetization direction, magnetic dichroism in photoemission depends on the relative orientation of three vectors, namely the direction of the incident x-ray beam, the magnetization direction, and the direction of the emitted electron. It is therefore also termed magnetic circular or linear dichroism in the angular distribution of photoelectrons (MCDAD or MLDAD). Angular resolution in the photoelectron detection is thus necessary to observe this kind of dichroism.

We report here the imaging of magnetic domains using MCDAD and MLDAD as magnetic contrast mechanisms in a PEEM equipped with a simple retarding field high-pass electron energy filter [1]. In this set-up, a grid is inserted in front of the imaging unit, which can only be passed by electrons with energies higher than the voltage applied to this grid [2]. An energy resolution better than 0.6 eV is achieved in this way. Sufficient angular resolution is provided by the contrast aperture in the back-focal plane of the objective lens of the microscope, which limits the range of accepted photoelectron emission angles to about 0.3° about the direction of normal emission.

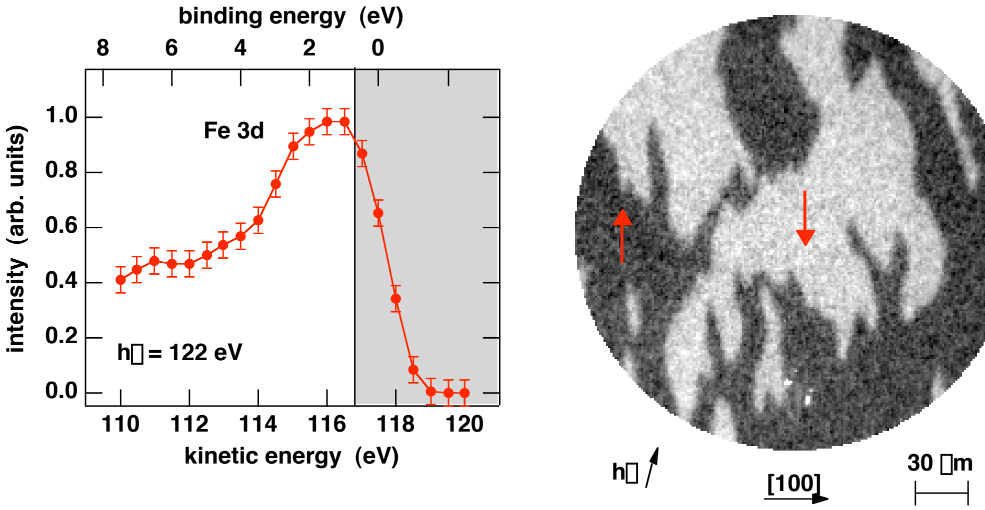

Fig. 1: *Left: Valence band photoemission spectrum of 10 ML Fe/W(001) for 122 eV photon energy. Right: Magnetic domain image using magnetic circular dichroism in valence band photoemission as contrast mechanism. Only electrons within the shaded area of the spectrum are used for the image. The image grayscale represents the change in photoelectron intensity upon helicity reversal. Arrows indicate the local magnetization direction.*

The measurements were performed at the beamline UE56/2-PGM2 on an Fe film of 10 atomic monolayers (ML) on a W(001) single crystal surface. Fig. 1 shows on the left a valence band photoemission spectrum for circularly polarized excitation with 122 eV photon energy (MCDAD). The data points are obtained from summing up the intensity over all image pixels of energy-filtered PEEM images. The right hand side shows the magnetic domain image obtained by accepting only photoelectrons within the shaded area of the spectrum. Analysis of domain images obtained by XMCD at the same sample position reveals that the magnetization direction in the bright and dark domains is along the plus and minus [010] crystallographic directions of the W(001) substrate, respectively [3]. MCDAD is thus sensitive to the longitudinal component of the magnetization, along the direction of incoming x-rays [4].

Fig. 2 shows on the left a core level photoemission spectrum of the Fe 3*p* region. Since MLDAD in Fe 3*p* photoemission is known to show up as a plus/minus modulation in intensity difference around the center of the photoemission peak [5], the normalized intensity difference image between the shaded regions “a” and “b” is calculated and shown on the right. Thin red lines indicate magnetic domains as observed by XMCD [3]. Although the noise level due to the subtraction of different high-pass energy filtered images is quite high, the contrast between the large domain with the magnetization vector pointing to the right and the domains pointing up and down is clearly recognized. In contrast to MCDAD, which is sensitive to the longitudinal component of the magnetization, MLDAD is sensitive to the transverse component [4], i.e., perpendicular to the light

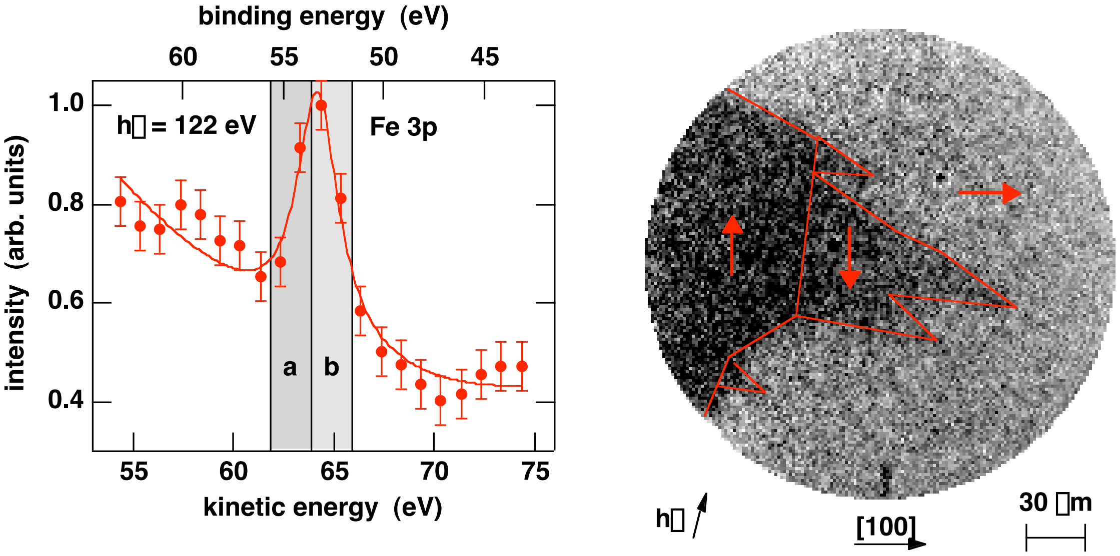

Fig. 2: Left: Fe 3p photoemission spectrum of 10 ML Fe/W(001) for 122 eV photon energy and linear p polarization. Right: Magnetic domain image using magnetic linear dichroism in Fe 3p core level photoemission. The grayscale represents the difference in photoelectron intensity between energy regions labeled "a" and "b". The red lines and arrows indicate magnetic domains observed by "conventional" domain imaging using magnetic circular dichroism in resonant x-ray absorption.

incidence. Appropriate combinations of magnetic dichroisms in photoemission have thus the potential for vectorial characterization of the local magnetization direction without rotating the sample.

[1] Focus Imaging Energy Filter (Omicron)

[2] M. Merkel, M. Escher, J. Settemeyer, D. Funnemann, A. Oelsner, C. Ziethen, O. Schmidt, M. Klais, and G. Schönhense, Surf. Sci. **480**, 196 (2001).

[3] W. Kuch, L. I. Chelaru, F. Offi, M. Kotsugi, and J. Kirschner, J. Vac. Sci. Technol. B **20**, 2543 (2002).

[4] D. Venus, Phys. Rev. B **48**, 6144 (1993).

[5] C. Roth, F. U. Hillebrecht, H. B. Rose, and E. Kisker, Phys. Rev. Lett. **70**, 3479 (1993).

Commissioning of the New Scanning Transmission X-Ray Microscope at the Undulator U41

U. Wiesemann[a], J. Thieme[a], P. Guttmann[a], R. Früke[b], S. Rehbein[c], B. Niemann[a], D. Rudolph[a] and G. Schmahl[a]

[a]Institute for X-Ray Physics, Georg-August-Universität Göttingen, Geiststr.11, 37073 Göttingen, Germany
[b]RheinAhrCampus Remagen, Südallee 2, 53424 Remagen, Germany
[c]Royal Institute of Technology/SCFAB, Biomedical & X-Ray Physics, SE-106 91 Stockholm, Sweden

The new scanning transmission X-ray microscope (STXM) at the undulator U41 [1] is now in the commissioning phase. It is operating in the soft X-ray energy region at approximately 200–600 eV. Planned spectromicroscopy research activities include environmental studies, water chemistry and geochemistry. Fig. 1 shows an overview of the STXM beamline.

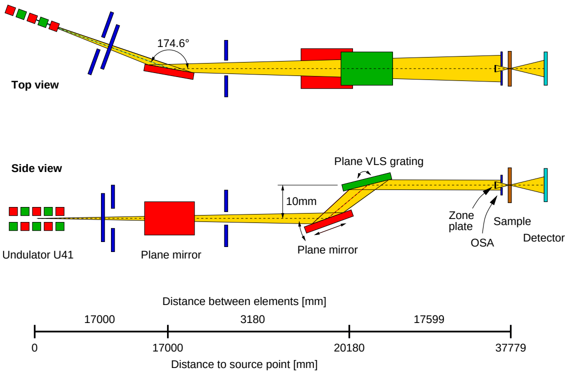

Figure 1: Overview of the STXM beamline

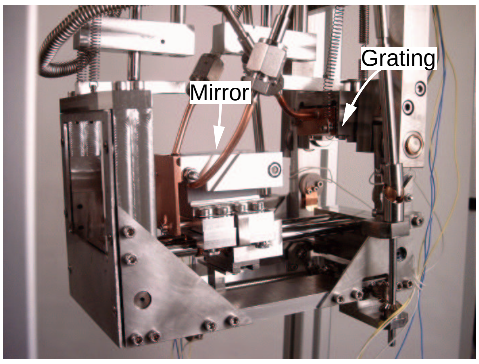

Figure 2: Side view of the monochromator

The STXM monochromator was designed for the particular requirements of a STXM, namely high flux throughput, the preservation of the beam coherence and ease of adjustment. It has a design similar to an earlier setup at BESSY I [2]. The monochromator consists only of a plane mirror and a plane grating (Fig. 2). It has no entrance or exit slits, which makes the alignment simple. Two separate areas of the mirror coated with nickel and chromium may be shifted into the beam for higher harmonics suppression at different wavelengths. The holographically exposed grating has a varied line density in order to get a vertically parallel beam in the -1^{st} diffraction order. The expected spectral resolution at the carbon K-edge, where most of the measurements will take place, is about 3500. A diffraction efficiency at the carbon K-edge of 3.0 % has been measured with a reflectometer at BESSY II.

The photon rate was measured with a photo diode in vacuum. The measured rate (Fig. 3) lies close to the design value calculated from the undulator brightness and the efficiencies of the optical elements. From the measured values, the expected photon rate in the focal spot was derived. At the carbon K-edge, the expected photon rate in the focal spot is about 10^7 phot./s.

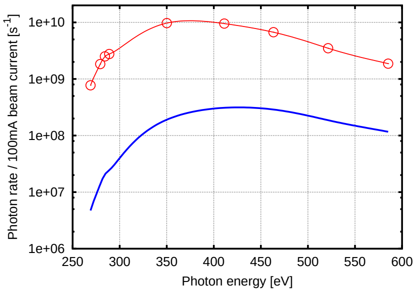

Figure 3: Measured photon rate of spatially coherent radiation on the zone plate (red line) and calculated photon rate in the focal spot (blue line)

First NEXAFS Spectra were acquired from a 300 nm thick polyimide foil in vacuum (Fig. 4). The photo diode used as a detector was masked with a 200 µm high slit aperture matching the zone plate diameter. At all energies NEXAFS features

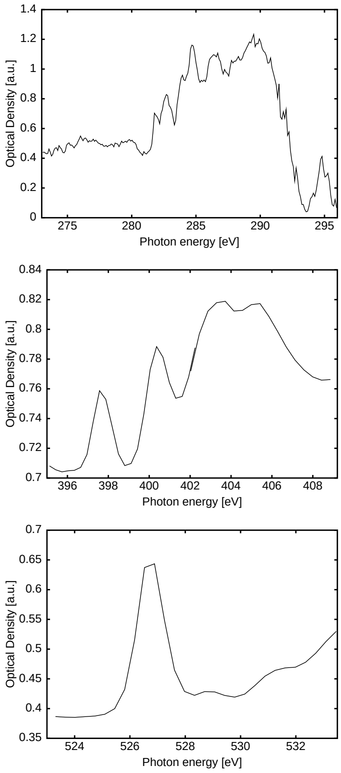

Figure 4: First NEXAFS spectra of a 300 nm thick polyimide foil in vacuum. Top to bottom: Carbon, nitrogen and oxygen absorption edge.

are clearly visible. The spectral resolution has not been determined for this proof of principle experiment. The decrease in optical density above 290 eV is probably due to a shift in the energy calibration for the I_0 spectrum.

The sample is situated in air between the zone plate and detector vacuum vessels. Fig. 5 shows a schematic of the optical path from zone plate to detector. High resolution images are acquired by scanning the zone plate with a piezoelectric flexure stage and recording the transmitted intensity with the detector. Larger, lower resolution scans are obtained by moving the sample with DC motors. The central stop of the zone plate and the order sorting aperture (OSA) prevent light of unwanted diffraction orders of the zone plate from reaching the sample. The OSA is formed by the holder for the vacuum exit window, which is not scanned together with the zone plate. This setup restricts the image field for a high resolution scan to about $25 \times 25\,\mu\text{m}^2$.

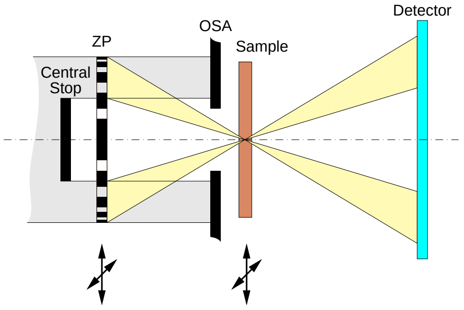

Figure 5: Optical path from zone plate to detector

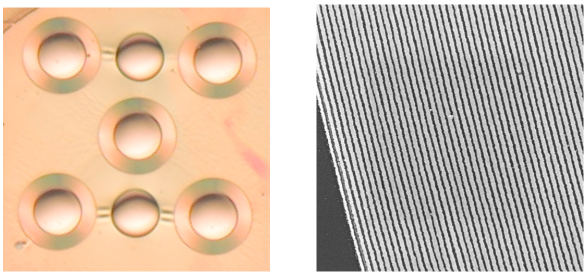

Figure 6: DIC image of a silicon membrane with a set of five zone plates (left) and EM image of outermost zones with 50 nm width (right)

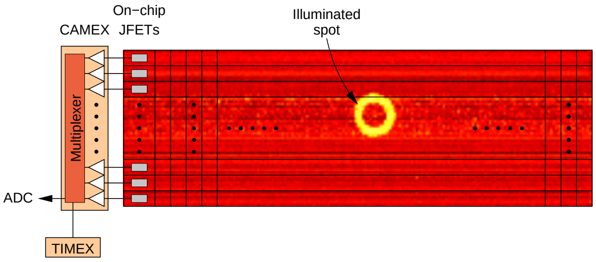

Figure 7: The pn-CCD detector

Nickel zone plates are made as a set of five on a 150 nm thick silicon membrane (Fig. 6) [3]. The zones are about 120 nm high, the outermost zone width is $\mathrm{d}\,r_\mathrm{n} = 50\,\text{nm}$ and the radius $r_\mathrm{n} = 100\,\mu\text{m}$. The diameter of the central stop is 130 µm. The zone plate parameters are optimized for working at the carbon K-edge, where the focal length is $f(283\,\text{eV}) = 2270\mu\text{m}$.

The detector employed in the STXM is a back-illuminated Ketek pn-CCD with 64×200 pixels of $150 \times 150\,\mu\text{m}^2$ size (Fig. 7). It has been developed by the MPI für Extraterrestrische Physik, München [4]. The signals of the 64 channels are amplified on the chip and read out in parallel leading to an extremely low noise of below 5 electrons / pixel. The detective quantum efficiency is higher than 50% in the water window energy range.

The read out of a whole frame takes 5 ms. The lines can also be read out continuously every 25 µs. The spot illuminated by hollow cone from zone plate has a diameter of about 10 pixels, so that the minimum dwell time of the raster scan is about 0.25 ms. Photon rates up to 10^9 phot./s can be measured. The position resolution of the CCD makes advanced contrast modes such as differential phase contrast or

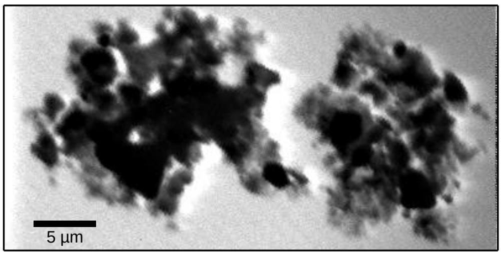

Figure 8: Chernozem dry sample imaged in absorption contrast, energy: 280 eV

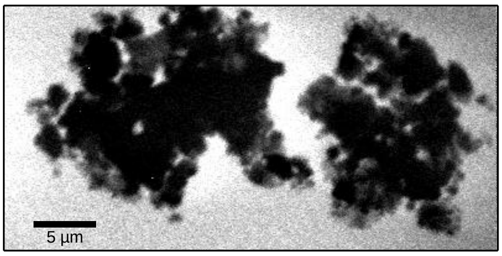

Figure 9: Absorption contrast, energy: 292 eV

dark field contrast possible [5].

Some of the first images are shown in Fig. 8 – 11. A chernozem dry sample on a Silicon Nitride membrane was imaged with a pixel size of $100 \times 100\,\mathrm{nm}^2$ at a dwell time of 6 ms. For the amplitude contrast images, the image intensity in each scan pixel is the sum of the intensity of all CCD pixels.

From the change in absorption by the sample below and above the carbon edge, the representative carbon thickness can be calculated (Fig. 10). A particle is indicated which is coated with an organic layer.

Fig. 11 shows the sample in differential phase contrast. The intensity of each scan pixel is the distance of the center of gravity of the diffraction pattern on the CCD from the optical axis, which corresponds to the phase gradient at the focal spot. This image is generated from the same data as Fig. 8; from the data recorded for a single scan, images in several different contrast modes can be calculated.

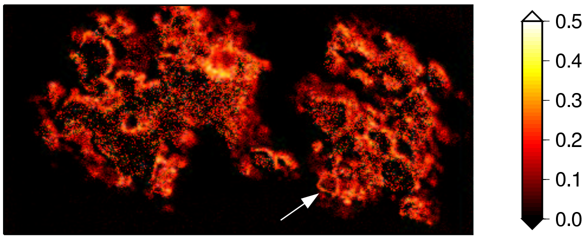

Figure 10: Representative carbon thickness in µm, see text

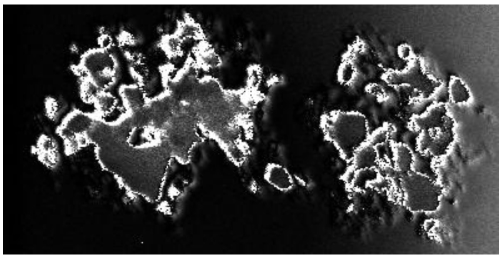

Figure 11: Differential phase contrast image at 280 eV

Acknowledgements

We would like to thank H. Düben, T. Gronemann, J. Herbst, P. Nieschalk, K.-H. Völker, M. Wedemeier, J. Wegner and D. Weinrich (IRP), H. Gorke (FZ Jülich), and R. Hartmann (Ketek). Thanks to the BESSY staff for providing excellent working conditions.

This project is a collaboration with the Engler–Bunte–Institut, University of Karlsruhe, and the Institut für Wasserchemie und Chemische Balneologie, TU München. This work has been funded by the German Federal Minister of Education and Research (BMBF) under contract number 02 WU 9893/0 and 05 KS 1MG1/9.

References

[1] U. Wiesemann, J. Thieme, R. Früke, P. Guttmann, B. Niemann, D. Rudolph, and G. Schmahl, NIM A **467-8** (2001) 861.

[2] A. Irtel v. Brenndorff, B. Niemann, D. Rudolph, and G. Schmahl, J. Synchrotron Rad. **3**, 197–198 (1996).

[3] S. Rehbein, "Nanofabrication of diffractive optics for soft X-ray and atom beam focusing", in D. Joyeux, F. Polack and J. Susini, eds., Proceedings of the 7th International Conference on X-Ray Microscopy (EDP Sciences), to be published.

[4] L. Strüder et al., NIM A **467-8** (2001) 861.

[5] G. R. Morrison and B. Niemann, "Differential Phase Contrast X-Ray Microscopy", in: J. Thieme, G. Schmahl, D. Rudolph and D. Umbach, eds., *X-Ray Microscopy and Spectromicroscopy* (Springer Verlag, Berlin, 1998) I-85–I-94.

Commissioning Results of the UE46-PGM Beamline

D. Schmitz, H. Rossner, P. Imperia, H. Maletta
Hahn-Meitner-Institut Berlin GmbH, Glienicker Str. 100, 14109 Berlin

J. Bahrdt, R. Follath, W. Frentrup, A. Gaupp, K. Holldack, H.-Ch. Mertins, F. Senf, S. Valencia
Berliner Elektronenspeicherring-Gesellschaft für Synchrotronstrahlung, Albert-Einstein-Str. 15, 12489 Berlin

During the year 2002 the beamline setup was finished. As a last step the refocussing chamber behind the exit slit was aligned and fixed beginning of February. During the shutdown end of February the undulator was put into the storage ring. Directly after this shutdown undulator commissioning was started so that it was possible to align the optical elements with undulator radiation from beginning of April. Flux, energy resolution and energy scale were systematically optimized with a photodiode and a gas ionisation chamber behind the exit slit. Then the refocussing mirrors were aligned by measuring and optimizing the focus using the BESSY CCD chamber [Hol00]. In addition, magnetic field parameter tables to move undulator and monochromator in parallel were optimized by comparing calculated values with measured values. Finally the polarization was measured with the small BESSY polarimeter [Sch99].

Nitrogen ionization spectra (Fig.1) were used to optimize the energy resolution of the beamline by aligning the first and third mirror and the exit slit. After alignment the energy resolution was best at the nominal exit slit position along the beam. This position was independent from the fixed focus constant c. With the 600 mm^{-1} grating and standard settings (1.4 mm (hor.) x 1.2 mm (vert.) beamline entrance aperture, c=2.25, 20 µm exit slit) an energy resolution E/ΔE of 4700 was reached at 400 eV. E/ΔE improved to 6300 when closing the aperture to 0.7 mm x 0.6 mm. From the raytracing simulations E/ΔE of 8000 was expected [Eng01]. The energy scale was also calibrated with Nitrogen ionization spectra which were measured for different orders of the grating and different fixed focus constants. The self consistent energy calibration procedure described in [Fol99] provided a photon energy of 400.78 eV for the first peak of the 1s -> 2pπ transition. The 1s -> np excitations of Neon were also measured and verified that the calibration of the energy scale was also valid at 867.1 eV.

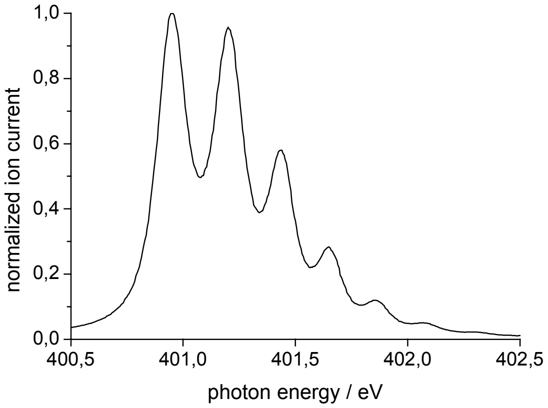

Fig.1: Typical ionization spectrum of Nitrogen.

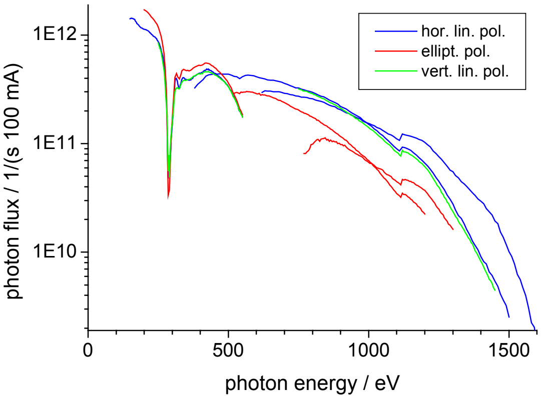

Fig.2: Photon flux for different polarizations and undulator harmonics.

After calibrating the energy scale the tables to move undulator and monochromator in parallel were optimized. The photon energy of the undulator harmonics were measured for different gaps and shifts. These values were then used to calculate a corrected version of the tables. With these tables photon flux measurements over the whole energy range for different polarizations and undulator harmonics were performed. The result of a flux measurement close to the focus is shown in Fig.2 where for the sake of simplicity a constant spectral sensitivity of the photodiode was assumed. Over a wide energy range the photon flux is between 10^{11} and 10^{12} (s 100 mA)$^{-1}$.

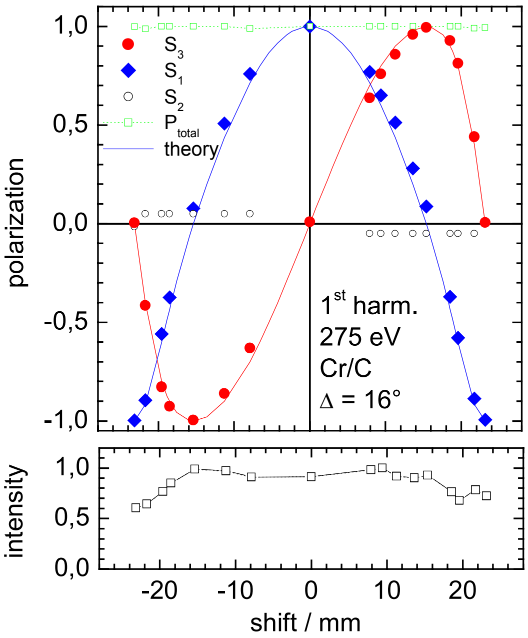

Fig.3: Polarization as a function of the symmetric shift of the undulator.

One of the main features of the UE46-PGM beamline is the variable polarization. Circular polarization of both helicities and linear polarization with various orientations of the polarization vector are possible. The polarization was measured with the small BESSY polarimeter at three photon energies using different undulator harmonics. At 275 eV the polarization was determined by a self calibrating analysis described in [Sch99]. The Stokes parameters which describe the circular (S_3) and linear (S_1, S_2) polarization are shown in Fig.3 as a function of the symmetric shift of the undulator. At 0 mm (±23.15 mm) the radiation is linearly polarized in the horizontal (vertical) direction and at +(-)15.38 mm it is circularly polarized with positive (negative) helicity. The experimental values (symbols) fully confirm the calculations [Fre] (lines).

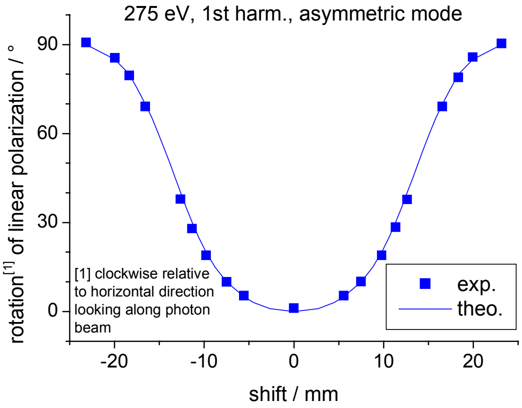

Fig.4: Rotation angle of the linear polarization vector as a function of the antisymmetric shift of the undulator.

The orientation of the linear polarization vector can be rotated by shifting two magnet rows of the undulator into opposite directions which is the so-called "antisymmetric mode". The resulting rotation angles of the linear polarization were also measured and are shown in Fig.4. The experimental values (symbols) again confirm the calculation (line). For both shift directions the linear polarization is rotated clockwise relative to the horizontal direction looking downstream.

The beamline has two refocussing mirrors behind the exit slit, M4a and M4b. M4a is used to focus the beam at a distance of 1 m and M4b to produce a collimated beam. Both beams were measured with the BESSY CCD chamber [Hol00] in order to align the refocussing mirrors by optimizing position and shape of the corresponding beams. The resulting intensity profiles and linescans for the focussed and collimated beam are shown in Fig.5 and Fig.6, respectively. The FWHM of the focus was 64 µm x 16 µm (horizontal x vertical) using an exit slit width of 20 µm. From raytracing simulations 40 µm x 10 µm were expected. The size of the collimated beam is about 1 mm x 1 mm and can be adjusted with beamline entrance aperture which in this case was 1.4 mm x 1 mm. The intensity distribution of the collimated beam shows vertical stripes. The stripe pattern does not change when the scattering angle of the last mirror is varied but it changes when different parts of the last mirror are illuminated. The stripe pattern can be explained by a surface roughness contribution on mirror M4b with a lateral wavelength of about 3 mm.

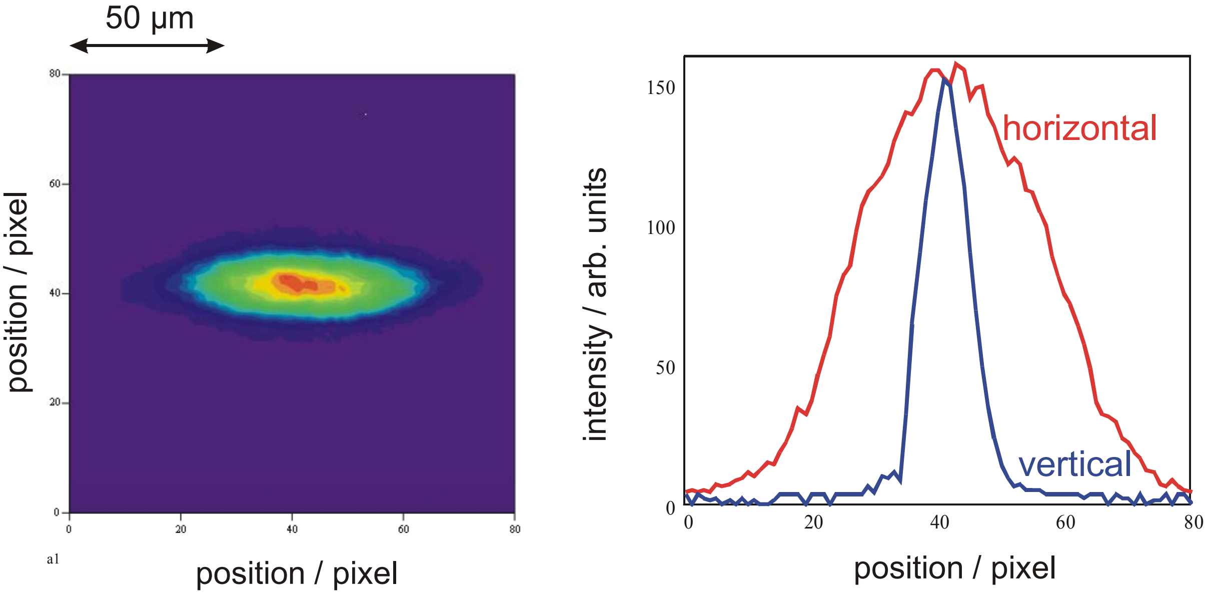

Fig.5: CCD image (left) and corresponding horizontal and vertical line scans (right) of the focus after alignment of the last mirror M4a.

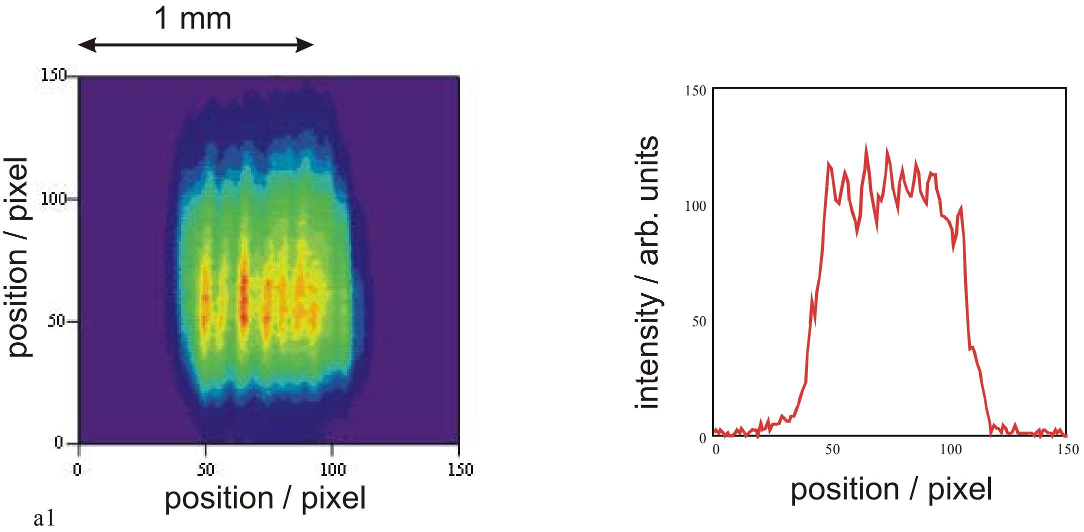

Fig.6: CCD image (left) and a corresponding horizontal line scan (right) of the collimated beam using M4b as the last mirror.

The beamline is equipped with an experimental end station which was successfully used to perform first experiments. The magnetization of *in-situ* prepared ultrathin Fe films on a V(110) single crystal was studied with XMCD. The measurements at UE46-PGM confirm the results which were obtained earlier [Sch01]. In addition, an X-PEEM was installed directly after the focus optimization to study the $Co_2Cr_{0.6}Fe_{0.4}Al$ Heusler alloy. These results are presented in a separate report [Fel02].

During the year 2003 it is planned to mount the 1200 mm^{-1} grating the delivery of which was delayed by the manufacturer because the specifications were not yet reached. This grating is going to improve the photon flux above 1600 eV and the energy resolution [Eng01]. It is also planned to install and test the high field reflectometer which combines high magnetic fields and low sample temperatures under ultra-high vacuum conditions.

[Hol00] K. Holldack *et al.*, BESSY annual report 2000, p. 336
[Sch99] F. Schäfers *et al.*, Applied Optics-OT **38**, 4074 (1999)
[Fre] W. Frentrup, private communication
[Eng01] U. Englisch *et al.*, Nuclear Instruments and Methods in Physics Research A, **467-468**, 541-544 (2001)
[Fol99] R. Follath *et al.*, BESSY annual report 1999, p. 481
[Sch01] D. Schmitz *et al.*, BESSY annual report 2001, p. 351
[Fel02] C. Felser *et al.*, BESSY annual report 2002

The new ALICE diffractometer for soft x-ray resonant magnetic scattering

J. Grabis, A. Nefedov, H. Zabel

Experimentalphysik IV, Ruhr-Universität Bochum, Universitätstrasse 150, 44780 Bochum Germany

Soft x-ray resonant magnetic scattering (XRMS) is a technique which allows element selective investigations of magnetic materials. The magnetic sensitivity is reached by tuning the energy of the incoming polarized photons close to an absorption edge of the particular material. Compared to methods like magnetic circular dichroism (XMCD) it is possible to gain additional information in the reciprocal space [1].

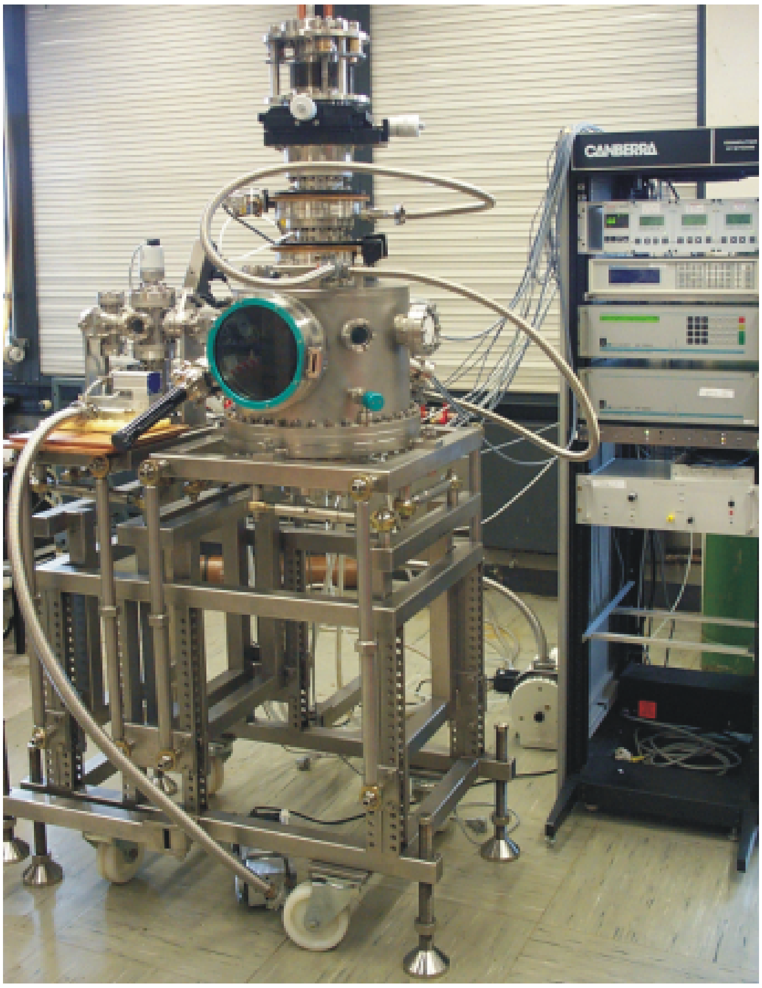

Figure 1: Picture of the experimental setup in the lab in Bochum: On top of the chamber are the two rotary feedthroughs for detector and sample movement and the sample manipulator. The differential pumping stage is on the left adjustable frame.

We report on the completion of the new two-circle diffractometer which has been constructed and built in Bochum during the last one and a half years [2]. Sample and detector are driven by differentially pumped rotary feedthroughs in a horizontal scattering geometry with stepper motors

Figure 2: Electromagnet: The poles inside the vacuum are mounted on a ball bearing (top). They are magnetically coupled to the rotatable coils in a cylindrical tube external to vacuum (bottom).

and worm gears external to the vacuum system. The angular resolution of the stepper motors is $0.005°$. The scattered beam is detected by a GaAsP avalanche photodiode and the corresponding photocurrent is measured by a Keithley 6514 electrometer. Typical currents are 100 nA in the direct beam decreasing to 0.01 pA at high scattering angles. The size of the slit in front of the detector is variable and was set to 500 μm during the experiments.

The sample can be linearly moved by a manipulator consisting of a XY table and a Z travel in each direction relative to the beam. The sample environment consists of a closed-cycle cryostat with the possibility of heating (temperature range 30 K - 500 K) and a rotatable electromagnet from AMACC, Sweden. The field can be applied in all directions parallel to the scattering plane. With two sets of poles which are different in gap size a maximum field of 1 kOe (for 40 mm gap) and 2.6 kOe (for 15 mm gap) can be reached, respectively.

The samples can be changed through a 200 mm-diameter load-lock window. The chamber is pumped by a 260 l/s turbo-molecular pump backed by a scroll-type dry roughing pump. At BESSY an oil-free vacuum of $< 1 \times 10^{-9}$ mbar is required at the last valve of the beamline. To fulfill this condition we installed a differential pumping stage consisting of a pinhole (1.5 mm diameter) and another turbo-molecular pump between our chamber and the beamline. That way we can start to measure at a pressure of 5×10^{-6} mbar in our chamber and the pumping time after sample change is below 30 minutes. For vacuum analysis a quadrupole mass spectrometer is contained in the setup.

Thin metallic foils for energy calibration, a gold mesh monitoring the incident beam, a pinhole and a pentaprism can be moved into the direct beam via two linear feedthroughs. The pentaprism in front of the pinhole can reflect a laser beam along the path of the x-ray beam. This provides a possibility of sample pre-alignement [3].

Goniometer chamber and differential pumping stage are mounted on two independently adjustable frames similar to the six-strut alignment systems commonly used e.g. at the Advanced Light Source in Berkeley. These frames are fixed to a rack each by seven struts - four vertical and three horizontal - with ball jointed end connections. By turning a strut the distance between the two ball joints can be varied. That way it is possible to move the frames in all six degrees of freedom.

Stepper motors, temperature and magnetic field are controlled via GPIB interface from a PC. Data acquisition is performed running standard SPEC software. For future experiments control of the BESSY monochromator via serial interface will be implemented in SPEC. This was done by another PC during the first experiments.

All functions of the setup have been successfully tested and first experiments have been carried out at the bending magnet beamline PM3 at BESSY II. Results of the first experiments are described elsewhere [4].

This project is funded by BMBF (Contract No.O3ZAE7BO). We thank J. Kortright (ALS, Berkeley), T. Hase (Durham), V. Leiner (ILL, Grenoble), F. Shäfers, H.-Ch. Mertins, I. Packe, T. Kachel (all BESSY) for useful hints and comments during the time of the chamber construction.

References

[1] C. Kao et. al., *Phys. Rev. Lett.* **65**, 373 (1990)

[2] J. Grabis, A. Nefedov, H. Zabel, *EP IV annual report 2001*

[3] M. Roper et. al., *Nucl. Instr. Meth. Phys. Res. A* **467-468**, 1101 (2001)

[4] A. Nefedov, J. Grabis, A. Bergmann, F. Radu, H. Zabel, *BESSY annual report 2002*

Application of time-resolved photoemission electron microscopy for real-time observation of magnetic processes

A. Krasyuk[1], A. Oelsner[1], S. Nepijko[1], A. Kuksov[2], C.M. Schneider[2], G. Schönhense[1]
[1]*Johannes Gutenberg – Universität, Institut für Physik, 55099 Mainz, Germany*
[2]*Institut für Festkörper- und Werkstoffforschung, 01099 Dresden, Germany*

In the present work, the time-dependence of magnetic field pulses and the field-induced magnetisation changes have been studied using time-resolved photoemission electron microscopy (PEEM). The experiment has been performed at the UE56/1-PGM at BESSY II (Berlin) in single-bunch mode providing photon pulses of about 100 ps width at a repetition rate of 1.25 MHz in the soft X-ray range. The time-dependence of the pulsed magnetic field generated above the surface of a microstrip device has been imaged in real time exploiting a stray-field induced ("Lorentz-type") contrast. The resulting field-induced changes in the magnetisation of cobalt micropatterns deposited on the microstrip line have been observed exploiting the MXCD contrast at the Co $L_{2/3}$ X-ray absorption edges.

The magnetization changes in the magnetic Cobalt micropatterns were induced by a fast magnetic field pulse generated by passing a short current pulse I through a copper microstrip line (see Fig.1) prepared lithographically on Si/SiO induces a magnetic field distribution H as indicated. Far away from the microstrip line the $H(r)$-distribution of the magnetic field decreases like $1/r$. The integral along a closed line of the magnetic field equals the current passing through the field loop, i.e. $\oint \vec{H} ds = I$. A measurement of the time profile of the pulser output is shown in Fig. 2. In our case, a fast magnetic pulser generates voltage pulses of up to 40 V at a rise time of about 500 ps. For the given pulse and the microstrip line geometry at the device (width b= 50 µm, thickness d about 100 nm) we obtain field pulses reaching a maximum of about 6.5 mT. The insulator material, its thickness, and the geometry of the microstrip line are chosen to achieve 50 Ohm impedance.

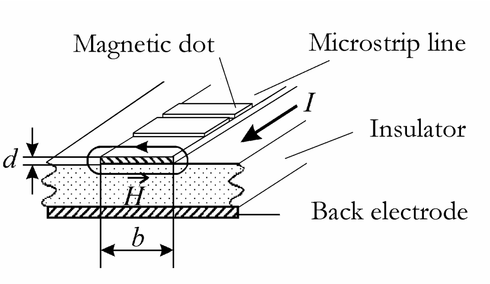

Fig.1: *Geometry of the magnetic microstrip line device consisting of a copper microstrip line on native-oxide-covered silicon with magnetic dots being deposited on the microstrip line*

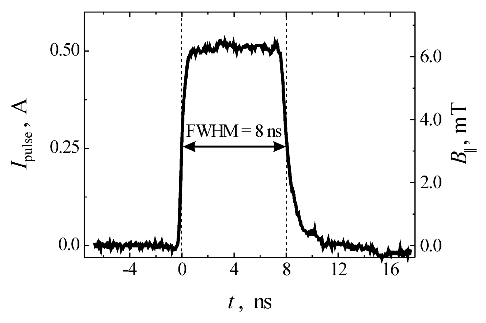

Fig.2: *Time structure of the current pulse measured at the output of the pulse generator and the expected magnetic field; the rise time is 500 ps*

The illuminating pulsed photon beam was synchronised with a fast electric pulser driving a microstrip line. Due to it we have a possibility to exploiting stroboscopic illumination of a periodic magnetization reversal processes. This basic approach is the same as was successfully used in previous magneto-optic Kerr effect experiments [1-3].

The time-dependence of the magnetic field in a pulsed microstrip line device has been imaged in real time (see Fig.3). This measurement exploited the stray-field induced ("Lorentz-type") contrast as known from the early experiments of Spivak et al. in the 1950s [4]. Quantitative evaluation of the field-induced image shift/distortion gives direct quantitative access to the corresponding magnetic fields on the microstrip line surface and their temporal behavior. This technique provides an easy and very fast local surface magnetometer with a lateral resolution in the 100 nm range. The field thus determined has a maximum amplitude of about 10 ± 2 mT being slightly larger than an estimation (6.5 mT) for the given microstrip line geometry and the measured pulser output. The measured field pulse appears broadened and exhibits a two-peak time profile (see Fig.4) followed by a pulse of reversed polarity arriving at a constant time delay. These findings give evidence of a reflection of the electrical pulse in the set-up. Comparison of the shape of the magnetic field pulse to the corresponding electrical pulse at the output of the pulse generator allows real-time observation

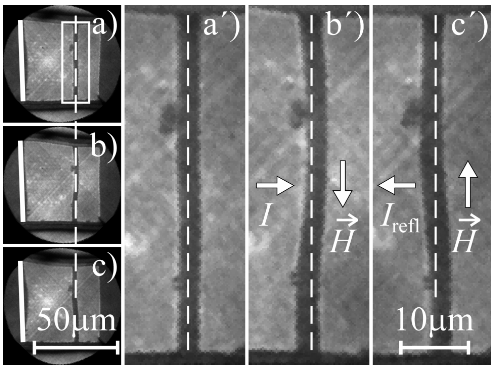

Fig.3: *Time-dependent image distortion used to determine the dynamical changes of the magnetic field driven by the current pulse and its reflections. a, a') field-free case; b, b') pulse towards the right (delay time 22 ns); c, c') pulse towards the left (delay time 28 ns).*

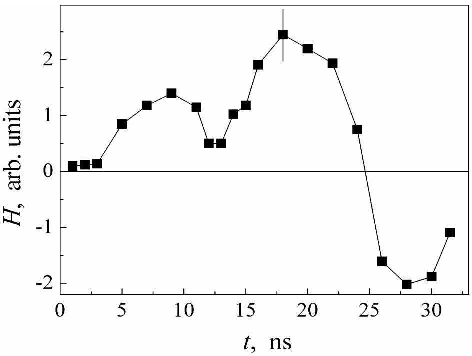

Fig.4: *Magnetic field vs time delay between field pulse and photon pulse determined from the distortion of the images like those shown in Fig. 3. Because of delays in the cables and the trigger the time zero does not correspond to the onset of the field pulse on the microstrip line.*

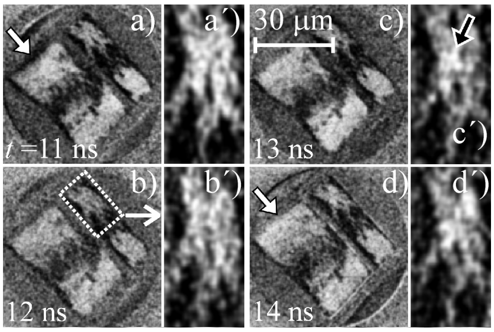

Fig.5: *Time dependence of MXCD contrast in two rectangular cobalt islands on the microstrip line, increment 1 ns. The series of images (a, b, c, d) were taken by means of a delayline detector and demonstrates the dynamics in magnetisation by relative changes in the grey levels of various regions in the cobalt islands. The detail series (a′,b′,c′,d′) shows the MXCD, magnified from the area indicated by the dotted rectangle in the 12-ns image. The white and black arrows mark two features with different periodicity*

of pulse broadening and reflection on it's way through the electrical set-up.

The resulting field-induced changes in the magnetisation of Cobalt microstructures deposited on the microstrip line have been observed exploiting the magnetic X-ray circular dichroism (MXCD) contrast at the Co $L_{2/3}$ X-ray absorption edges. The domain patterns of the rectangular Co islands (see Fig.5) with 45 μm width appear as dark and bright areas in the MXCD-PEEM images. The MXCD contrast method is sensitive to the projection of the local magnetisation vector on the helicity vector of the incoming synchrotron radiation. Systematic changes in the absolute grey levels of large domains as well as local changes of the domain patterns (shape and grey level) are observed. The applied field amplitude was obviously too small to induce a full switching of the magnetic patterns.

The temporal profile of the field pulse needs to be largely improved by better impedance matching, in order to get access to the intrinsic magnetic switching time. Magneto-optical measurements have reached time resolutions well below 100 ps [1-3]. In our first measurements the broadened pulse profile (cf. Fig.4) limits the time resolution to more than a ns. Lateral resolution in synchrotron-radiation excited X-PEEM is limited by the chromatic aberration of the PEEM's objective lens [5]. In the present experiment it is about 150nm with potential of considerable improvement in the future. The base resolution of the PEEM in threshold photoemission is better than 20 nm. Despite of the problem of impedance matching and the insufficient field amplitude in this first experiment, the results of Figs. 3 and 5 show that magnetic field- and domain- imaging with X-PEEM on a time scale of less than a ns is feasible.

We thank the BESSY staff for the good collaboration. Financial support by BMBF is gratefully acknowledged. (05KS1UM1/5 and 05KS1BDA/9)

[1] M. Bauer, R. Lopusnik, J. Fassbender, B. Hillebrands, Appl. Phys. Lett. **76**, 2758 (2000).

[2] M. Bauer, R. Lopusnik, H. Dötsch, B.A. Kalinikos, C.E. Patton, J. Fassbender, B.Hillebrands, J. Magn. Magn. Mat., in print.

[3] W. K. Hiebert, A. Stankiewicz, and M.R. Freeman, Phys. Rev. Lett. **97**, 1134 (1997).

[4] G.V. Spivak, T.N. Dombrovskaia and N.N. Sedov, Sov. Phys. Dokl. **2**, 120 (1957).

[5] C.M. Schneider and G. Schönhense, Rep. Prog. Phys. **65**, R 1785- R 1839 (2002)

Spatially resolved synchrotron-X-ray fluorescence analysis of geologic materials

M. Wilke, W. Leitenberger[*]

Institut für Geowissenschaften, Universtät Potsdam, Postfach 601553 , 14415 Potsdam, Germany
[*] *Institut für Physik, Universtät Potsdam, Postfach 601553 , 14415 Potsdam, Germany*

In Earth Sciences trace elements concentrations are used for understanding geological processes, such as genesis and development of the earth's crust including the magmatic processes involved.

Synchrotron-XRF measurements provide the possibility of determining the trace-element concentrations by using the intensity of the X-ray fluorescence emission lines (K- and L-lines). Since the incoming beam can be collimated down to a small spot size measurements of concentrations with spatial resolution are possible. Thus, enabling the determination of distributions of elements among different phases within a sample or the determination of concentration profiles within one phase.

Measurements were performed at beam line D-13-2 using the white beam for excitation and pinholes for beam collimation to test potential applications of the setup for various geological problems as well as the minimum beam size that is possible for such measurements. The pinhole size was varied between 10 µm and 35 µm. The energy-dispersive fluorescence detector (Si(Li)) was put at an angle of 90˚ to the incoming beam to minimize the background signal from scattering. The sample was set up at an angle of 45˚ to the beam and a camera attached to a microscope allowed imaging of the excited spot with high magnification. Samples used were glass standards fused from natural rocks (ATHO-G, T1-G, [1]) covering a typical concentration spectrum for natural rocks and a synthetic glass standard having a large suite of elements at low concentrations (NIST SRM 612, 30 – 80 ppm). In addition, a zircon sample ($ZrSiO_4$) containing a variety of rare earth elements (REE) and other elements with high atomic number (U, Th, Hf, Y) was used to test the possibility of trace element analysis in such a matrix.

Shown in Fig. 1a) and b) are spectra of the ATHO-G and T1-G standard acquired with pinhole sizes of 15, 25 and 35 µm and various sampling time. K-lines of elements with atomic numbers from 19 – 41 can be detected. The reference concentration levels are: ATHO-G: K: 2.22 wt%, Ca: 1.19 wt%, Ti: 0.147 wt%, Mn: 798 ppm, Fe: 2.5 wt%, Cu: 21 ppm, Zn: 139 ppm, Rb: 63 ppm, Sr: 96 ppm, Y: 94 ppm, Nb: 62 ppm, Zr: 524 ppm. T1-G: K: 1.61 wt%, Ca: 5.06 wt%, Ti: 0.44 wt%, Mn: 0.10 wt%, Fe: 4.99 wt%, Cu: 21 ppm, Zn: 84 ppm, Rb: 80 ppm, Sr: 283 ppm, Y: 23 ppm, Nb: 9 ppm, Zr: 147 ppm. NIST SRM 612: Ca 12 wt%, all other elements ca. 40 ppm, except Sr: 80 ppm.

Minimum detection limits determined from net peak intensities of these spectra are shown in Fig. 2. Spectra were processed using AXIL® software package The observations indicate that pinholes below 35 µm result in a beam intensity too low for feasible working conditions. For analysis of the geologically important elements Rb – Zr higher beam intensities, achieved by focussing instead of collimation, would be desireable. Another possibility to improve the signal-to-background ratio would be monochromatic excitation.

If no overlap with K-lines of major elements occurs L-lines of elements with atomic numbers greater than 47 can also be detected. Measurements on zircon would be a potential application. Zircon mainly fractionates heavy rare-earth elements as well as U, Th, Y, Hf. Values of U, Th and Pb (radiogenic) may be used for age determination, whereas the others are useful indicators for geologic fractonation processes. The spectrum is shown in Fig. 3. The peaks of U and Th are completely hidden by the strong background in that energy region although their amount in this sample is significant (xxx). Appropriate monochromatic excitation could potentially solve this problem. The fluorescence peaks of the REE and Pb, however, are almost completely overlapped by the signal from Hf that usually forms a major component in natural zircon. Therefore an analysis of these elements in this matrix is not possible in contrast to analyses in monazite (REE-Phosphate) as shown previously [2].

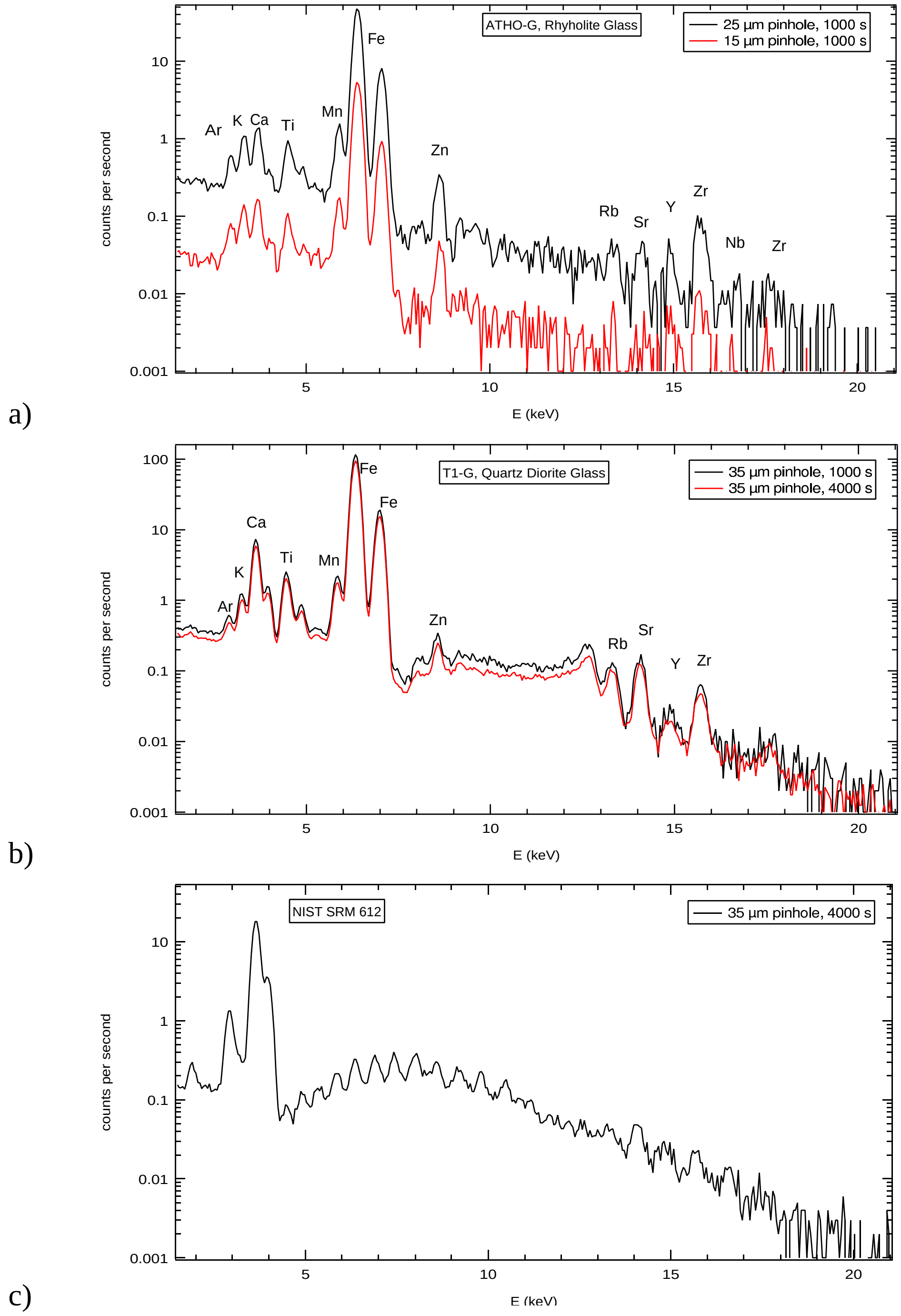

Figure 1: XRF spectra of glass standards acquired using a polychromatic beam collimated by pinhole.

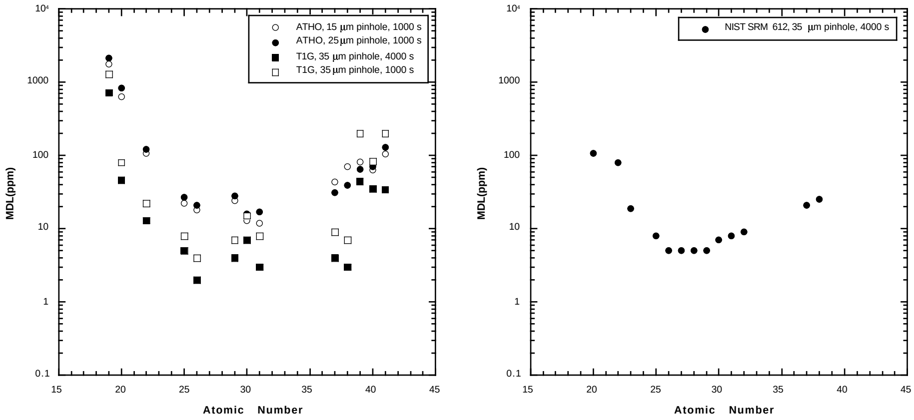

Figure 2: Minimum detection limits (MDL) calculated from shown spectra.

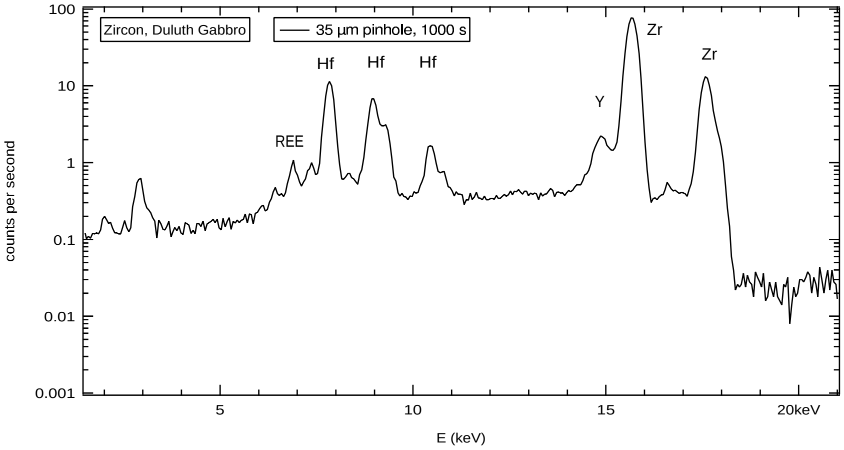

Figure 3: XRF spectrum of zircon acquired using a polychromatic beam collimated by pinhole..

References

[1] Jochum KP et al. Geostandards Newsletter, 24, 87-133 (2000)
[2] Wilke M et al. BESSY Annual Report (2001)

Reflectivity of Cr/Sc and Ni/V Multilayer Mirrors in the Soft X-ray Range

Fredrik Eriksson, Naureen Ghafoor and Jens Birch
Thin Film Physics Division, Department of Physics, Linköping University, S-58183 Linköping, Sweden

Göran Johansson
Biomedical and X-Ray Physics, Royal Institute of Technology/SCFAB, S-10621 Stockholm, Sweden

Franz Schäfers, Hans-Christoph Mertins and Dirk Abramsohn
BESSY GmbH, Albert Einstein Straβe 15, D-124 89 Berlin, Germany

Cr/Sc and Ni/V multilayer x-ray mirrors intended for use in the water window wavelength range have been grown by ion-assisted sputter deposition[1,2] at Linköping University, Sweden. The reflectivity of a multilayer is enormously enhanced due to an anomalous scattering close to the absorption edge of one of the constituting materials. The multilayers have therefore been investigated at the 2p absorption edges of Sc (398 eV) and V (512 eV), respectively.

Multilayer periods and layer thickness ratios were tailored to give maxium performance at either normal incidence, to be used as e.g. a microscope condensor mirror[3], or for reflection at the Brewster angle, e.g. as analyzers for polarized synchrotron radiation to distinguish between linearly and circularly polarized x-rays.[4,5] These requirements yielded extremely thin individual layer thicknesses down to about only 0.5 nm.

The measurements described here have been made using the polarimetry chamber[6] at beamlines U49/2 and UE56/1, both using plane grating monochromators. In Fig. 1 the obtained near-normal incidence reflectivity for a Cr/Sc multilayer with a period of Λ=1.57 nm containing 300 periods is shown. The reflectivity reaches 19.8% at an angle of incidence of θ=82.7°, which is 80% higher than reported elsewhere.[7] Included in the figure is also a simulation using the IMD software.[8] The deviation between the measurement and the simulation can be attributed to a constant layer thickness drift throughout the multilayer as a result of the deposition process. This layer thickness drift has, through simulations, been estimated to $\sim 1 \cdot 10^{-5}$ nm (10 femtometers!) per multilayer period. Although extremely small it clearly influences the appearance. Simulations, disregarding the constant layer thickness drift, implied an interface width of σ=0.31 nm.

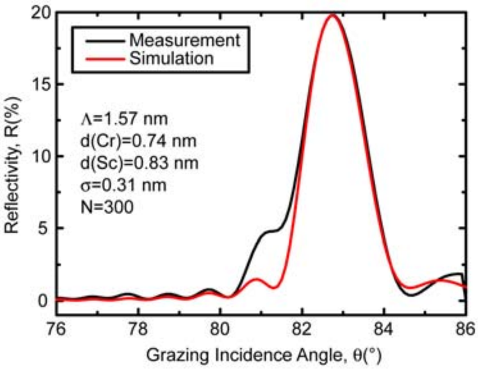

Fig. 1 Reflectivity of a Cr/Sc multilayer close to normal incidence. The reflectivity is 80% higher than reported elsewhere.

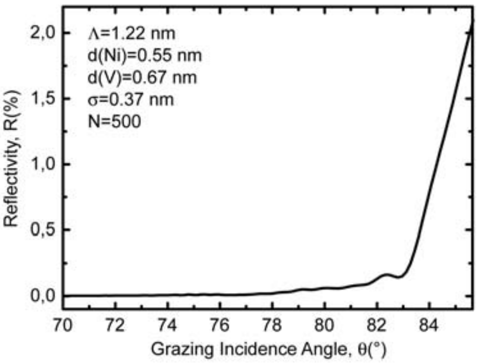

Fig. 2 Reflectivity of a Ni/V multilayer close to normal incidence. The reflectivity is at least 65% higher than reported elsewhere.

Fig. 2 shows an angular scan of a Ni/V multilayer measured, to see the optimum performance, at the V absorption edge (512 eV). At these high energies extremely thin layer thicknesses are required for normal incidence reflectance, and the demands on the interface quality becomes even more severe. Unfortunately, the polarimeter did not allow incidence angles above about 86°. However, it is clearly seen that an absolute reflectivity above 2% is achievable. Since the multilayer period is known, we estimate a peak to appear around 88°. This is, in fact, one of very few existing normal incidence multilayers for these energies, and the reflectivity is at least 65% higher than any other reported multilayers.[9]

In Fig. 3 the reflectivity of a Cr/Sc multilayer containing 100 periods, measured over the whole angular range, is shown. The reflectivity is plotted against the reciprocal scattering vector in order to have all Kiessig interference fringes equally distanced. The corresponding incidence angle is found above the graph. These oscillations are due to the interference of x-rays that have been reflected from different interfaces. Since each peak in the Fourier domain is associated with the distance between two interfaces, their highly regular presence is an evidence of very high layer conformity.

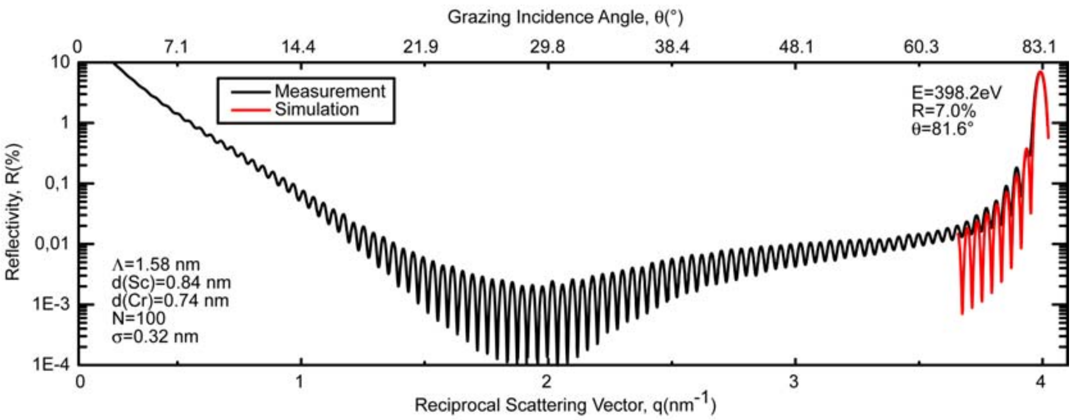

Fig. 3 Reflectivity of a Cr/Sc multilayer containing 100 bilayer periods.

In order to obtain information about the lateral interface structure, diffuse reflectivity measurements (Fig. 4) were made for 2θ-values corresponding to the Bragg peaks. These measurements reveal how much of the incoming intensity that is reflected in the specular and in other, diffuse, directions. In this particular example, there is very little diffuse reflectivity on each side of the specular peak, indicating flat interfaces. These measurements have been extremely powerful for qualitative comparisons between different multilayers to understand the influence of the deposition parameters and to improve the deposition process in order to minimize so called flare for these x-ray optical coatings.

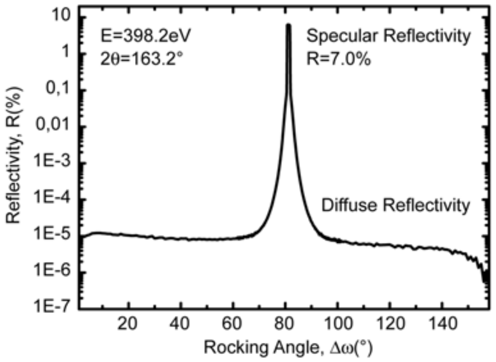

Fig. 4 Diffuse reflectivity measurement on the Bragg peak of the Cr/Sc multilayer shown in Fig. 3.

To investigate the polarization properties, Bragg scans (not shown), i.e. the peak reflectivity when simultaneously varying the incidence angle and the photon energy, were made for both s- and p-polarized light for a Cr/Sc and a Ni/V multilayer when operated at the Brewster angle, close to 45°. The peak reflectivities, for both s- and p-polarized light appear at the respective absorption edge of the spacer material. In the case of the Cr/Sc multilayer, which contains 150 bilayer periods, the maximum reflectivity was R=26.7% at an angle of incidence θ=43.7° and for Ni/V, also with 150 periods, the obtained value was R=10.1% at θ=43.4°. The polarizing power, i.e. the ratio between the reflectivities for s- and p-polarized light, showed maximum values at the Brewster angle where there is a minimum in the p-polarized light reflectivities, slightly below the absorption edge. For both the Cr/Sc and the Ni/V multilayer extraordinary high values of R_s/R_p=5450 and 4190, respectively, were found.

This work was supported by the European Community, contract HPP24/210102 and the Swedish National Research Council.

1. F. Eriksson, G. A. Johansson, H. M. Hertz, and J. Birch, "Enhanced soft x-ray reflectivity of Cr/Sc multilayers by ion-assisted sputter deposition," Optical Engineering **41** (11), 2903 (2002).
2. J. Birch, F. Eriksson, G. Johansson, and H. Hertz, "Recent Advances in Ion-Assisted Growth of Cr/Sc Multilayer X-Ray Mirrors for the Water Window," Vacuum **68** (3), 65-72 (2003)
3. M. Berglund, L. Rymell, M. Peuker, T. Wilhein, and H.M. Hertz, “Compact water-window transmission X-ray microscopy”, J. of Mic. **197**, 268-273 (2000)
4. S.S. Andreev, H.-Ch. Mertins, Yu.Ya Platonov, N.N. Salashchenko, F. Schäfers, E.A. Shamov, and L.A. Shmaenok, “Multilayer Dispersion Optics for X-ray Radiation”, Nucl. Instrum. Meth. A, **448**, 133-141 (2000)
5. F. Schäfers, “Multilayers for the EUV/Soft X-ray Range”, Physica B, **283**, 119-124 (2000)
6. F. Schäfers, H.-Ch. Mertins, A. Gaupp, W. Gudat, M. Mertin, I. Packe, F. Schmolla, S. Di Fonzo, G. Soullié, W. Jark, R. Walker, X. Le Cann, R. Nyholm, and M. Eriksson, “Soft X-ray Polarimeter with Multilayer Optics: Complete Analysis of the Polarization State of Light”, Appl. Opt. **38**, 19, 4074-4088 (1999)
7. F. Schäfers, M. Mertin, D. Abramsohn, A. Gaupp, H.-Ch. Mertins, and N.N Salashchenko, “Cr/Sc nanolayers for the water window: improved performance”, Nucl. Instrum. Meth. A, **467-468**, 349-353 (2001)
8. D.L. Windt, “IMD – Software for Modeling the Optical Properties of Multilayer Films”, Comput. Phys., **12**, 360-370, 1998
9. D.L. Windt, E.M. Gullikson, and C.C. Walton, “Normal-Incidence Reflectance of Optimized W/B_4C X-Ray Multilayers in the Range 1.4nm<λ<2.4nm”, Opt. Lett., **27**, 24, 2212- 2214 (2002)

Polarization dependent FTIR spectroscopy of anisotropic thin films and small samples: First measurements in the mid infrared at the IRIS beamline

M. Gensch, K. Hinrichs, A. Röseler and E.H. Korte
Institute of Spectrochemistry and Applied Spectroscopy – Department Berlin, Albert-Einstein-Str. 9, 12489 Berlin, Germany

K. Sahre, K.-J. Eichhorn
Institute of Polymer Research, Hohe Str. 6, 01062 Dresden, Germany

N. Esser
Institute of Solid State Physics, TU Berlin, Hardenbergstr. 36, 10623 Berlin, Germany

U. Schade
Berliner Elektronenspeicherring-Gesellschaft für Synchrotronstrahlung mbH, Albert-Einstein-Str. 15, 12489 Berlin, Germany

An experimental set-up for polarisation dependent and spectroscopic ellipsometric measurements (Fig. 1) was developed that utilizes the brilliance of synchrotron infrared radiation at the electron storage ring at BESSY II for investigations of small samples or sample areas. During commissioning of the beamline [1] and the experimental set-up a 1 mm^2 piece of a well characterized polyimide film was studied [2] to show the benefits of Fourier Transform Infrared (FT-IR) synchrotron ellipsometry. The band shapes are interpreted with respect to the anisotropic distribution of dipole moments within the film. In comparison to a globar source the signal intensity has been improved by more than one order of magnitude for this example.

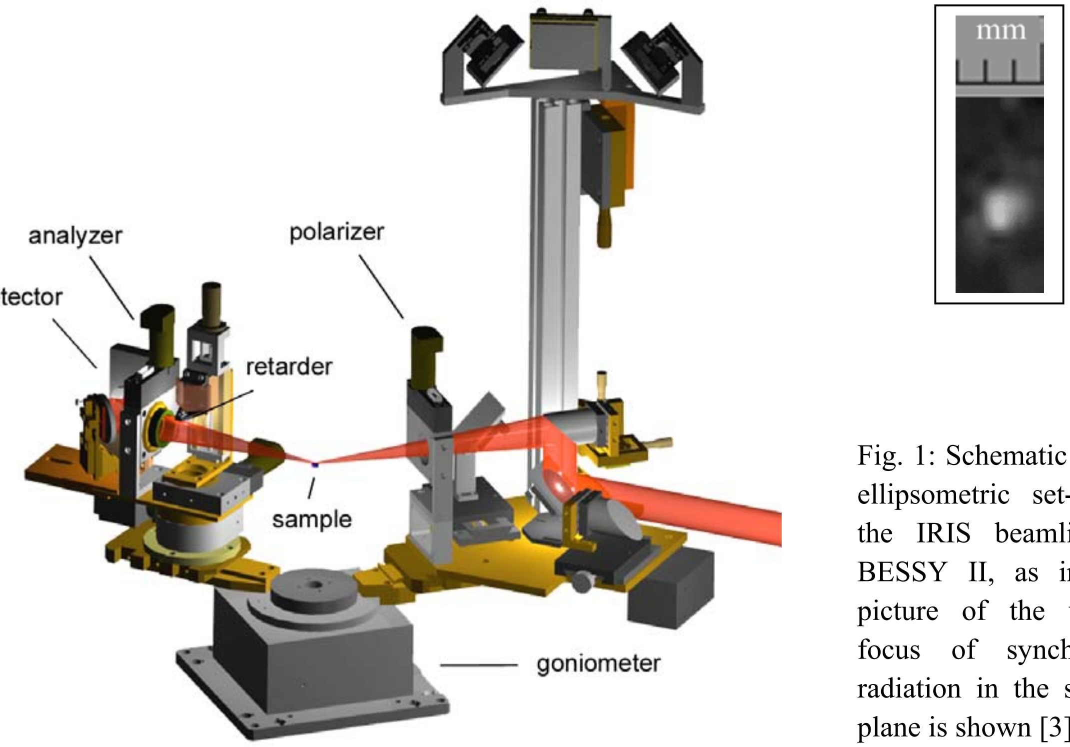

Fig. 1: Schematic of the ellipsometric set-up at the IRIS beamline at BESSY II, as inset a picture of the visible focus of synchrotron radiation in the sample plane is shown [3].

Fig. 2 presents the ratio of single beam spectra taken with the empty beam of the ellipsometric set up as if in transmission, using synchrotron radiation and thermal radiation of a globar (0.5 mm Jacquinot aperture). Significant bands are identified around 2000 cm^{-1} due to the multiphonon absorption of the diamond window separating the storage ring from the spectrometers. A Jacquinot aperture of 0.5 mm was used for comparison, since this size produces an about 1 mm^2 focus in the sample plane, because 1 mm corresponds to the longer side of the asymmetric shaped focus when using the synchrotron radiation. Comparing the radiation sources under these conditions an intensity advantage of a factor of 21 at 1000 cm^{-1} of the synchrotron over the globar is determined from our results[1].

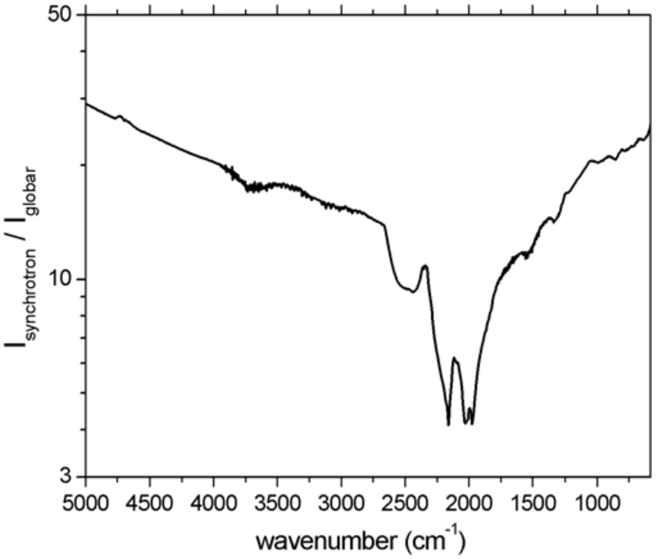

Fig. 2: Ratio (synchrotron/globar (Jacquinot aperture = 0.5 mm)) of polarized empty beam spectra of the ellipsometric set up measured with a MCT (from Ref. 2). For both sources the estimated focus area at 1000 cm^{-1} is about 1 mm^2. The azimuthal positions of the polarizer and analyser were set to 45°.

Neither in our standard lab ellipsometer attached at a BRUKER 55 or with the ellipsometer at the BRUKER 66 it was possible to take a measurement of the 1x1mm^2 piece of a 34 nm polyimide film with the globar, where it was possible to reveal the real bands. Instead the synchrotron measurement of the small sample is compared to the globar measurement of a larger piece of the same sample in order to check the results. In Figure 3 the $\tan\Psi$ spectrum of the mm^2 of the polyimide film measured with synchrotron radiation is compared to the spectrum of a probed area of about 100 mm^2 in a globar measurement. The synchrotron and globar spectra show similar band shapes and amplitudes. The minor offset of the $\tan\Psi$ spectra (0.025) can be explained by a difference of incidence angles of 0.8° or slightly different optical functions of the optical set up for globar and synchrotron. A structure in the globar spectrum around 1100 cm^{-1} is most likely caused by the absorption band of interstitial oxygen in the silicon bulk. In the synchrotron spectrum this peak is not observed because most likely the reflection from the silicon back surface does not reach the detector. In conclusion, the comparison shows that the synchrotron $\tan\Psi$ spectra of a 1 mm^2 small sample are as reliable as the globar ones of a 100 mm^2 large sample.

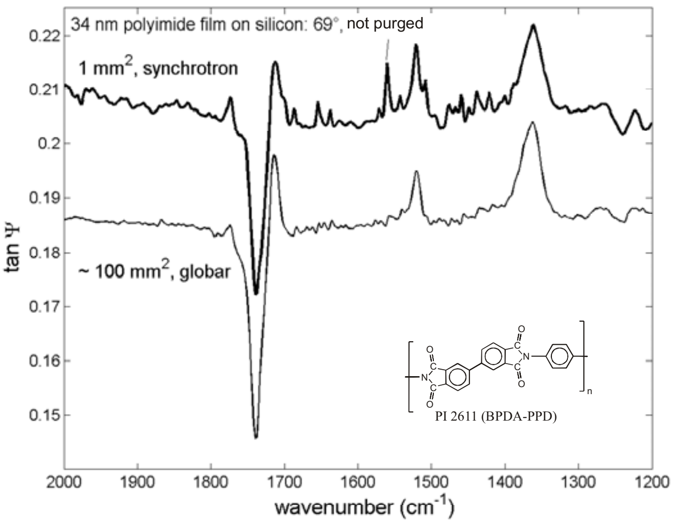

Fig. 3: Ellipsometric tanΨ spectrum of a 34 nm polyimide film ($1x1mm^2$) for an incidence angle of 69° taken with synchrotron radiation (from Ref. 2).
In comparison a globar spectrum (thin line) is shown, when the probed area was around 100 mm^2. As inset the molecular coordinate system and the structure of BPDA-PPD polyimide [poly(biphenyldianhydride-p-phenylenediamine)] is given.

Acknowledgements

The authors thank gratefully Ms I. Fischer, Mr. G. Hinte, D. Kutz and R. Herzlieb of ISAS and all the BESSY staff and IMPB at the Charité of the Humboldt University Berlin involved at the IR beamline for technical and construction assistance. We are indebted to Mr Hartmann of BRUKER for his help in technical and programming points and Ms M. Günther of TU Dresden for the film preparation. The financial support by the Senatsverwaltung für Wissenschaft, Forschung und Kultur des Landes Berlin and the Bundesministerium für Bildung und Forschung is gratefully acknowledged. Support of this work through the BMBF grant 05 SR8KK19 is gratefully acknowledged.

References:

[1] U. Schade, W.B. Peatman, Rev. Sci. Instr. **72,** 1620 (2001).

[2] K. Hinrichs, M. Gensch, K. Sahre, K.-J. Eichhorn, N. Esser, U. Schade, A. Röseler and E.H. Korte, submitted to Applied Spectroscopy.

[3] M. Gensch, K. Hinrichs, N. Esser, U. Schade, A. Röseler and E.H. Korte, to be published.

Electron Detectors for Experiments with combined Laser and Synchrotron Radiation

D. Bröcker[1], T. Gießel[1], P. Schmidt[1], W. Widdra[1,2]
[1]*Max-Born-Institut für nichtlineare Optik und Kurzzeitspektroskopie,*
Max-Born-Str. 2a, 12489 Berlin
[2]*Institut für Atomare Physik und Fachdidaktik, TU Berlin*

Introduction

We have developed two new electron detectors for photoelectron spectroscopy which have been tested in 2002 at the U125/1 SGM and U41/PGM beamlines at BESSY II.
One of the detectors has been designed for an angle-resolving toroidal electron analyser with an acceptance angle of greater than 90°. The angle information is read out by a multi-channel anode and connected to the counting electronics using a 128 channel stripe line and discrete preamplifiers and discriminators for each channel. The capacity of this new readout system reaches 20 MHz per channel as to be compared with 100 KHz for all channels using the former detection system of the toroidal electron analyser.
The second detector has been developed for the time-resolved measurement of the electron signal behind an energy dispersive analyser. The achieved time resolution of better than 2 ns enabled us to assign the photoelectron signal to specific synchrotron radiation pulses in multi-bunch mode at BESSY II. The purpose of this detection scheme is to set up a so-called pump multiple-probe experiment with combined laser and synchrotron radiation. This detection scheme allows us to perform experiments in multi bunch mode, which could be performed before only in single bunch mode. The overall time resolution in the pump multiple-probe experiment is limited to the time spread of the synchrotron radiation pulses (~30 ps).
In both detection systems, a serial readout scheme has been replaced by a parallel readout thereby using efficiently the high flux provided at undulator beamlines in multi buch mode.

Angle-Resolving 128-Channel Detector

The angle-resolving 128-channel detector has been designed for a toroidal analyser [1,2] in which the polar angle space (–20° to +90°) of the emitted photoelectrons is imaged onto an arc segment of the multi channel plate detector (see Fig. 1).

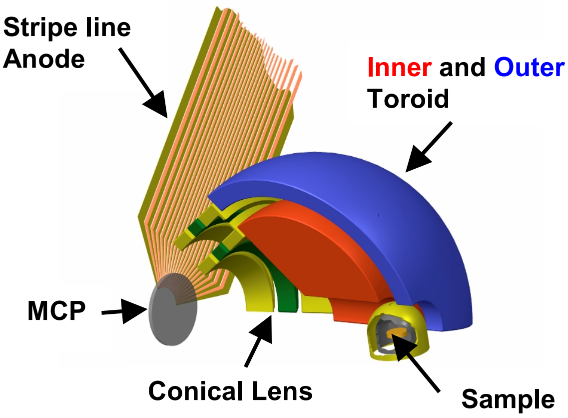

Fig.1: *Scheme of the toroidal analyser with stripe line anode.*

In order to increase the capacity of this detector we have replaced the formerly installed resistive stripe anode (capacity 100 kHz) by a 128-channel anode. This anode is the appropriately shaped end of a 128-channel stripe line which connects the anode with the pulse counting electronics. The pulse counting electronics consists of discrete preamplifiers and discriminators for each channel and programmable counter chips for every 16 channels. The capacity of the new detector reaches 20 MHz per channel. Results of the first test measurements at the U41/PGM are shown in Fig. 2. Displayed are EDCs showing the Si 2p core level measured simultaneously from an oxidized Si(100) surface for polar angles from –20° to +90° relative to the surface normal.

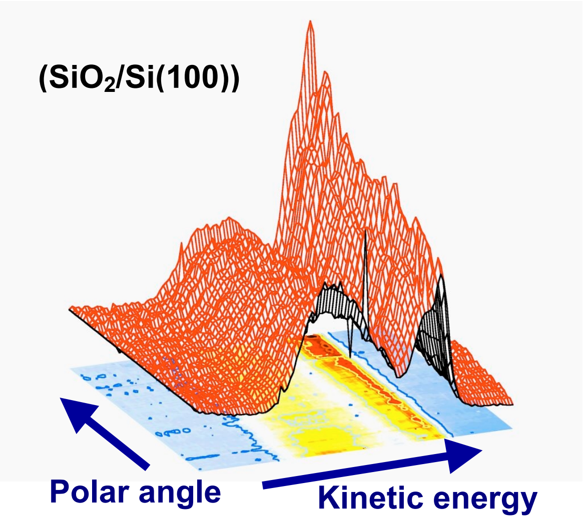

Fig. 2: Angular resolved Si 2p spectra measured simultaneously for a polar angle range of more than 90°.

As a first application photoelectron diffraction spectra from a monolayer C_6H_6 on Si(100) for the whole polar angle range have been measured simultaneously.

Time Resolving Detector for Pump Multiple-Probe Experiments with Laser and Synchrotron Radiation

In pump probe experiments with combined laser and synchrotron radiation as performed so far at the U125/1-SGM the laser pulses serve as pump pulses and create for example an excited electronic state which is probed after a certain delay time by synchrotron pulses via photoelectron spectroscopy. For such an experiment the repetition rates of laser and synchrotron radiation have to be the same and the phase between consecutive laser and synchrotron pulses has to be constant. The former of these two conditions is only fulfilled in single bunch mode using a Nd:YVO$_4$ laser with 1.25 MHz rep. rate. In multi bunch mode the time window of 2 ns between consecutive synchrotron pulses would be too small (given the synchrotron pulse time spread of 30 ps) for studying processes in the sub-nanosecond to nanosecond range. Apart from this, a 500 MHz laser system with pulse energies comparable to the Nd:YVO4 laser would be difficult to set up and probably damage the sample.

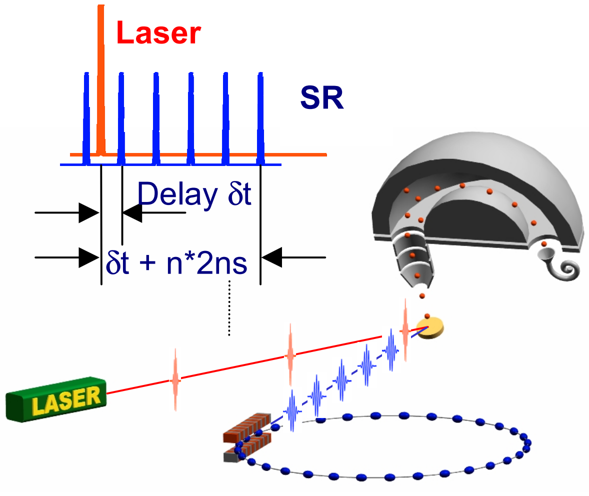

***Fig. 3:** Scheme of a pump multiple-probe experiment with laser and synchrotron radiation.*

In order to overcome the restriction of pump probe experiments to the single bunch mode we applied succesfully a so-called pump multiple-probe measuring scheme (see Fig. 3) which requires the separation of photoelectrons originating from two adjacent SR pulses, i.e. Δt= 2 ns. Although this is trivial for light detection, it needs special considerations for photoelectron detection due to the much longer electron time-of-flight through the energy-dispersive analyzer. Fig. 4 shows the time-resolved photoelectron probe signal at the exit of a 125 mm radius hemispherical energy analyzer triggered at the electronic SR bunch marker.

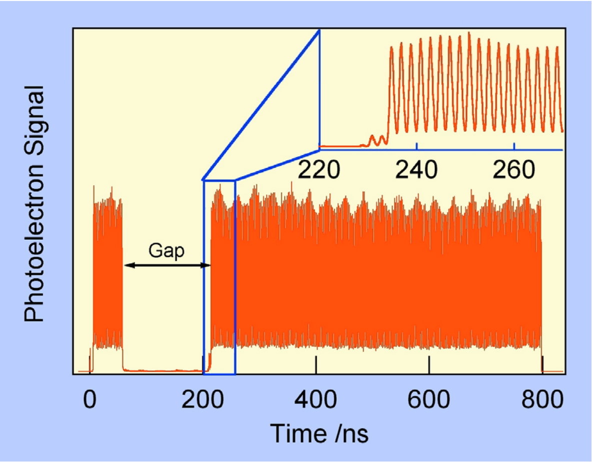

***Fig. 4:** Time-resolved SR photoemission signal at the exit slit of an energy-dispersive analyzer. The inset shows the signal on an enlarged time scale.*

Within the 800 ns bunch revolution time the non-uniform filling structure of the SR storage ring with a dark period of about 150 ns is clearly visible in the photoemission signal. Furthermore the signal from consecutive bunches, with a time interval of 2 ns, can be well separated as shown in the inset. This detection of individual bunches allows for an about two orders better overall time-resolution which is limited by the SR pulse length only.

We used the pump multiple-probe scheme for studying the recombination dynamics at the thermally-grown SiO_2/Si(100) interface. Fig. 5 shows high-resolution Si 2p core level spectra obtained for 130 eV photon energy from a 15 Å thick SiO_2 layer on Si(100).

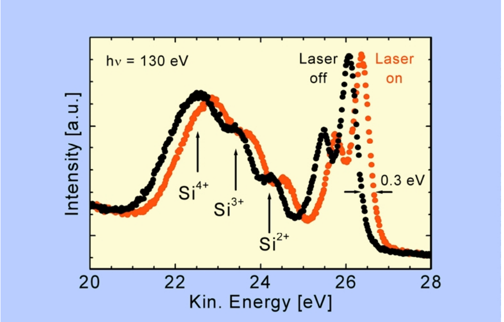

Fig. 5: *High-resolution Si 2p XPS spectra for a 15 Å thick SiO_2/Si(100) surface at a photon energy of 130 eV.*

The dominating feature corresponds to the atomic Si 2p doublet at binding energies around 100 eV. Additionally three shifted components due to the different Si oxidation states can be identified. Upon laser excitation at 1064 nm the core levels show a rigid shift of up to 300 meV to lower binding energy due to the surface photo voltage. The amount of the shift depends on the pump-probe delay. Fig. 6 shows the time-resolved photoemission signal as measured in the pump multiple-probe scheme for a fixed kinetic energy of 26.7 eV. This energy corresponds to the higher kinetic energy side of the atomic Si 2p core level peak. The lower trace exhibits the signal without laser. The upper trace (vertically shifted) indicates the photoemission signal with laser pulses at t=0 and every 40 ns.

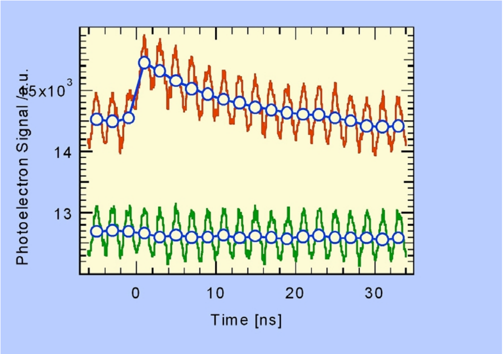

Fig. 6: *Time-resolved photoelectron detection for a fixed kinetic energy at the slope of the Si 2p core level. Spectra are shown with (upper trace) and without (lower trace) synchronized laser excitation at 1064 nm.*

[1] H.A. Engelhardt, A. Zartner and D. Menzel; Rev. Sci. instrum. **52**, 1161 (1981).

[2] H.A. Engelhardt, W. Bäck and D. Menzel; Rev. Sci. instrum. **52**, 835 (1981).

Surface sensitive scanning X-ray microprobe – gas microstrip detectors used as microscopes under ambient pressure conditions

A. Vollmer[1], J. D. Lipp[2], H. Weiss[3], A. Erko[4], and T. Rayment[1,*]

[1]Department of Chemistry, University of Cambridge, UK, [2]CLRC Rutherford Appleton Laboratory, UK, [3]Universität Magdeburg, Germany, [4]BESSY, Berlin, Germany

* *to whom correspondence should be addressed: email: tr22@cam.ac.uk*

Introduction

Gas Microstrip Detectors (GMSD) are widely used in particle physics (1-3), surface and material science (4,5), and catalysis (6). They function as very robust proportional counters, consisting of a pattern of interleaved metallic strips defined by micro-lithography upon a semiconducting glass plate, and can be operated with energy-, position- and time-resolution. In chemical applications and catalysis the advantage of GMSDs is their feasibility of energy selective electron detection under ambient conditions. It has been shown that energy selective x-ray absorption spectroscopy with gas microstrip detectors allows non-destructive depth profiling (5) at ambient pressure. Because of its efficiency, the technique is also suitable for low flux x-ray sources. Therefore, with a focussed incident X-ray beam and a high precision positioning system (x,y-piezo stage) the GMSD could be used as a scanning x-ray microprobe, which combines imaging with depth profiling and chemical state sensitive measurements. This would enable non-destructive, three dimensional mapping of a sample at ambient conditions.

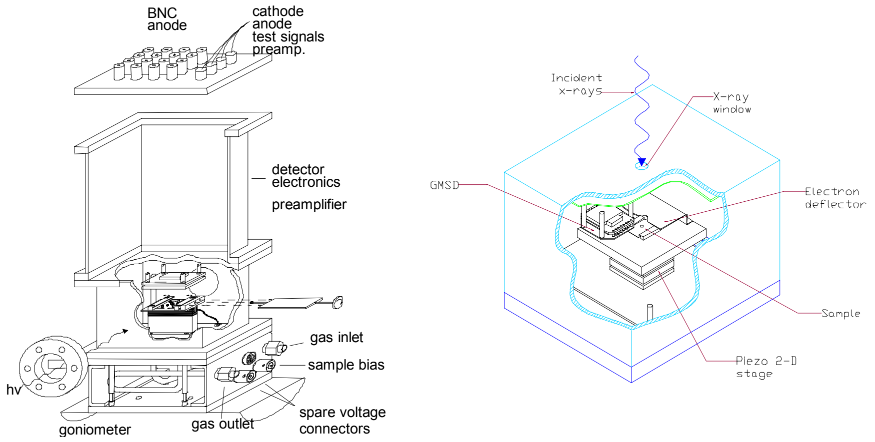

Fig 1: (a) design of the ‘standard’ Gas Microstrip Detector’ GMSD, grazing incidence beam, fixed sample and (b) design of the scanning x-ray microprobe, perpendicular beam, sample mounted on piezo stage

There are few limitations in terms of materials and measurement conditions in situ studies of reactions on surfaces, wear studies in lubricant oil, depth profiling of powder grains and experiments under electrochemical control have been performed (6). Possible applications include spatially resolved EXAFS of grains and clusters, catalysis of heterogeneous materials, corrosion studies, mineralogy and many more.

Design of the scanning x-ray microprobe

The 'conventional' design of the GMSD used in material science and catalysis is described in greater detail elsewhere (7), but it is worth noting that in the standard geometry the sample is fixed at grazing incidence while the detector plate is mounted above the sample in a distance of 10 to 20mm. For scanning experiments the incident beam has to be perpendicular to the surface in order to minimize the spot size and maximize the spatial resolution. Figure 1 shows a schematic drawing of both the conventional and prototype Scanning x-ray microprobe.

Experimental

The scanning x-ray microprobe studies were performed at the electron storage ring, BESSY 2 in Berlin on beamline KMC-2, the beam size being 250 µm by 600µm. To create a microfocus of 5µm in diameter, a Pt pinhole was used.

A 150 mesh Cu microscope grid glued onto a Si wafer was used as a test sample The measurements were carried out at fixed energy above the Cu edge by monitoring the electron yield depending upon the sample position with respect to the beam.

The data were collected with the station data acquisition system configured to count events after pre-amplification, shaping and discrimination whilst a parallel system simultaneously recorded the amplitude (energy) of every event, using a FAST COMTEC multi channel analyser system.

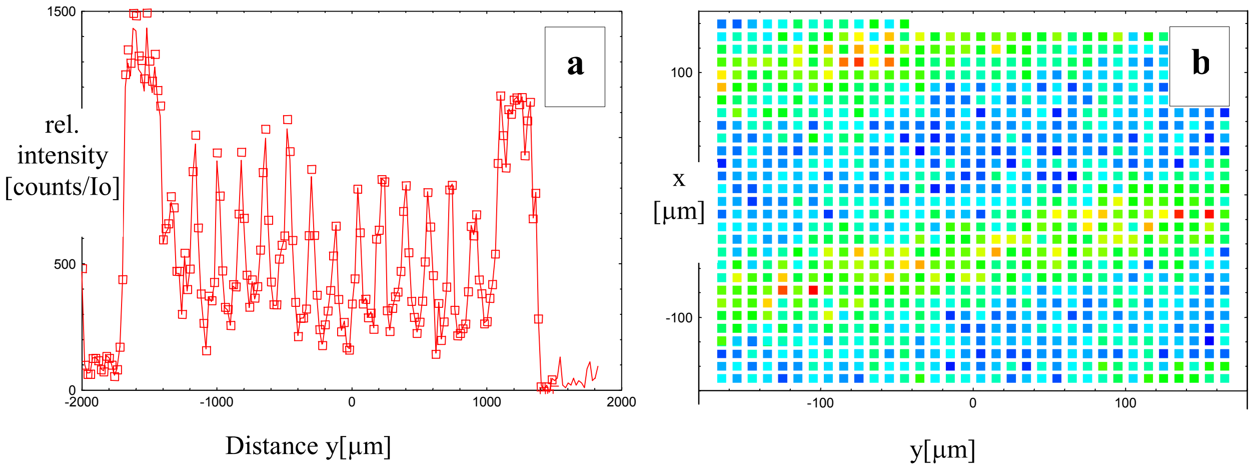

Fig 2: (a) scan of a 150 µm mesh Cu microscope grid, 5µm beam width, 10µm step size, hν=8900eV and (b) pixel image in x,y direction, lighter colour indicates Cu.

Results

The x-ray beam was rastered over the copper microscope grid by moving the sample in steps of one micron. The results presented in figure 2 show the pattern of the grid in one direction and as a two-dimensional plot. Due to the very low beam intensity of only 10^5 photons per second through the pinhole only a low count rate could be obtained. Nonetheless it was possible to map the grid. For further investigations into a sample's electronic structure, depth profile or oxidation state a much higher flux of initial photons is required. This can be achieved by either using a micro-focus beamline or capillary optics in the detector neither of which was accessible for these experiments.

Conclusions

It has been shown previously that oxidation state sensitive measurements as well as depth profiling experiments are feasible using gas microstrip detectors. In these experiments on KMC-2 a new type of scanning probe has been investigated. With an appropriate focussed x-ray source it allows mapping of microstructures in terms of their chemical composition as well as their geometrical structure. Within certain limits three-dimensional imaging should be possible.

References

1. R. Lewis, *J. Synchrotron Rad.* **1**, 43 (1994).
2. 2 .J. E. Bateman et al*, Nucl. Instrum. Methods A* **348**, 372 (1994).
3. A. Oed, *Nucl. Instrum. Methods A* **263**, 351 (1988).
4. M. Glew et al, Physics B, (2002)
5. T. Rayment et al, Rev. Sci. Instrum. 71, 3640 (2000).
6. to be published
7. A. Vollmer et al, submitted to *Analytical Chemistry*

PM3: Back to operation with a new optical design

T. Kachel, F. Eggenstein, BESSY

PM3 is one of several BESSY monochromators that have been transferred from BESSY I to BESSY II. The performance of the beamline has been strongly improved by a new optical design. The original layout[1] was such that the PM plane pre - mirror / plane grating unit was placed in the direct beam and an elliptical mirror served for focusing of the divergent beam. The resolution was never higher then about 3000 in this configuration and namely the refocusing mirror was suspected to be its limiting factor. The new layout consists of a toroidal pre - mirror in front of and a refosussing cylindrical mirror behind the monochromator.

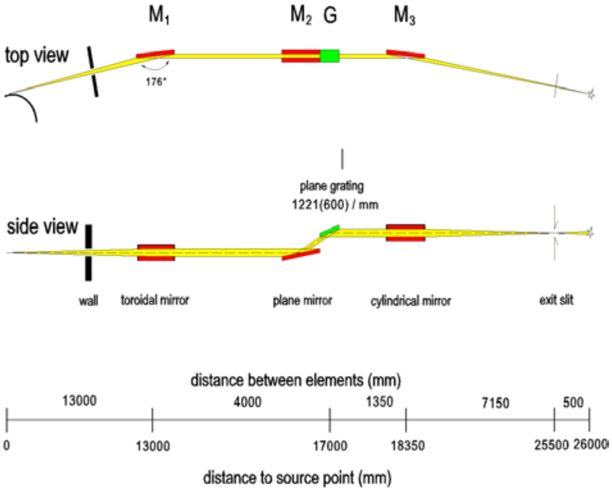

Fig. 1: The optical layout of PM3

The water cooled pre - mirror is placed at 13,000 mm in the direct beam. While in horizontal direction the beam is focused at 26,000 mm, the beam is vertically collimated behind M1. A major advent-age of the vertical collimation is the independence of the focal point position on the c_{ff} – factor. This advantage is paid for by a reduced vertical acceptance of the grating at higher photon energies. The plane mirror (M2) / plane grating (G) configuration is still the original Zeiss design. The grating G is placed at 17,000 mm. Behind the grating the collimated beam is vertically focused onto the exit slit at 25,500 mm by a cylindrical refocusing mirror.

The main test of the beamline properties during the commissioning period was the determination of the resolution. Shortly, using $c_{ff} = 12$ we achieved a width of the He $(2,-1_3)$ emission line at about 64 eV photon energy of minimum 1.9 meV. That corresponds to a resolving power of about 32,000. This is, to our knowledge, the best value reported so far for an SX700 type monochromator including those which are adapted to undulator sources.

Circularly polarized dipole radiation can in principle be utilized by moving an aperture through the incoming SR beam, thus transmitting only the upper or lower part of the dipole emission cone. Here, however, this is not possible because of the limited vertical acceptance of the grating. The transmitted part of the collimated SR beam would not hit the grating but shine below or above. This drawback can be overcome by a small tilt of the premirror M1 along its z – axis (= direction of the light). The rotation leads to a reflected beam below or above the SR emission plane and, in turn, for a fixed grating height to light accepted above or below the plane.

The tilt of M1 produces rotated images of the source on the succeeding optical elements including the exit slit. This should, as calculated, result in a reduced resolution for the circularly polarized SR modus as long as the slit remains in the storage ring plane. Particularly, the rotation is large for lower photon energies, i.e. below about 50 eV. However, until now we were not able to observe such a clear loss of resolving power. In contrast, we measured the N 1s emission as a resolution test for both, in plane (red dots) and out of plane (black line) light. The spectra are hardly distinguishable.

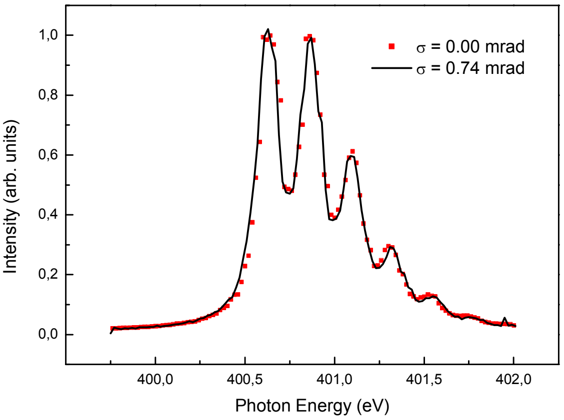

Fig.2: The N1s emission line for in plane (dots) and out of plane (line) acceptance. 3rd peak to 1st valley ratio is 0.69.

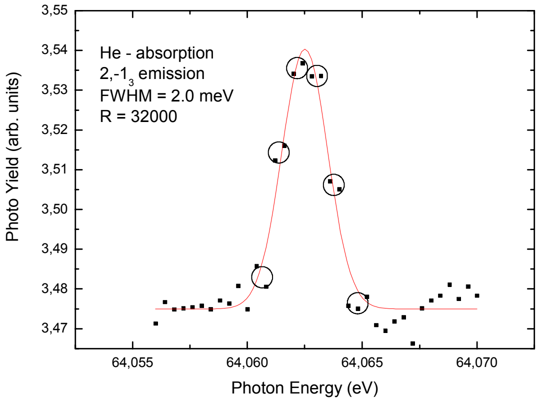

Fig. 3: The figure shows the He $(2,-1_3)$ – emission line. The smallest linewidth obtained was 1.9 meV. The circles demonstrate the smallest stepwidth of the monochromator.

A further result of tilting M1 around its long axis is a shift of the real photon energies compared to the nominal ones. This shift appears whenever the light impinges on the grating unit with an angle off the storage ring plane. But it is easy to correct for this error by either an additional tilt of M2 or by rescaling the photon energy axis following the $E^{3/2}$ – law.

The beamline is equipped with a permanent small in – line polarimeter. It is set up by a foil of 50 nm permalloy on 1 µm mylar which is used in transmission. The foil can be brought into the light in front of the exit slit, while the absorption spectra of the Fe and Ni lines can be detected on a Au – diode behind. The foil stands under 45° to the beam and can be magnetized within its surface plane. Thus, spin dependent absorption spectra of these absorption lines can be taken without opening the last beamline valve. The asymmetry in the absorption spectra gives us a direct independent measure of the actual degree of helicity at the respective photon energies. The calibration of the measured asymmetries to the absolute degree of helicity has been done via user experiments on well known CrO_2 samples by Goering, Gold, et al. At the Fe 2p edge we have obtained a circular polarization of 92.5 % with a relatively moderate tilt of M1.

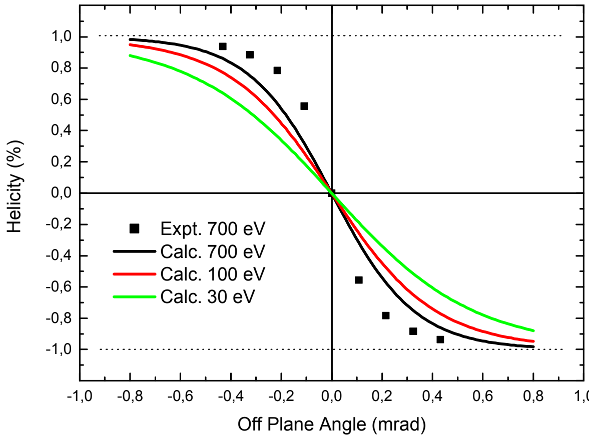

Fig. 4: Values of the circular polarization as a function of the off plane angle as measured (squares) at the

Experiments at higher photon energies were not completely successful until now. Experiments at the S 1s edge in ZnS cited only broad features with low signal to background ratio. In contrast, experiments on the Si 1s level on a natively oxidized Si sample could be successfully carried out. EXAFS – measurements at the Si 1s edge should be possible.

Special thanks to H. Gundlach and M. Willmann who have worked on the design and setup of PM3 at earlier stages of the development. Fruitful discussions with R. Follath and W. Peatman are acknowledged.

References: 1) H. Petersen, C. Jung, C. Hellwig, W.B. Peatman, and W. Gudat, Rev. Sci. Instrum. **66,** 7 (1995)

Polycapillary lens as a condenser of synchrotron radiation

S. Shcherbinin [a,b] , W. Leitenberger [c], A. Erko [d], S. Dabagov [a,e]

[a]- *P.N. Lebedev Physical Institute RAS, 119991 Moscow, Russia*
[b]- *Moscow State University, Vorobjovy Gory, 119899 Moscow, Russia*
[c]- *University of Potsdam, Institute of Physics, Am Neuen Palais 10, D-14469 Potsdam, Germany*
[d]- *BESSY GmbH, 12489 Berlin, Germany*
[e]- *INFN Laboratory Nazionali di Frascati, I-00044 Frascati (RM), Italy*

1. Introduction

For the last years capillary/polycapillary optics has been developing very fast, that's why for more than fifteen years, originating from the splendid and simple idea, it became an independent branch of optics intensively studied. In difference of the conventional focusing techniques for X-rays new capillary optics enables effectively governing of the X-ray beams. The various samples of capillary optics allow a beam of radiation to be deflected through the large angles [1], the radiation to be focused (condensed) with the increase of radiation density in 2-3 orders [2], etc. Due to these features, capillary optics applications cover various areas, where there is a necessity to increase the density of X-ray flux, and generally saying, where there is a necessity to handle X-rays, namely, these are medicine [3], various fields of X-ray physics, for instance, spectroscopy and diffractometry, etc. [4]. Moreover, by means of capillary structures (specially designed deflectors - benders), good results on the deflection of the beams of thermal neutrons were obtained in a set of experiments [5].

Nowadays we have well developed technology for manufacturing both monocapillaries and polycapillaries, and also both assembled and monolithic capillary systems, so at present one counts four generations of capillary optical elements [6]. Hence, the appearance of new samples requires developing a testing procedure and studying the characteristics of new generations lenses. In this work the results on condensing of X-rays (increasing in the density of radiation) by the polycapillary lens of the 3d generation are presented.

2. Experimental

The measurements have been done for the energy range of 5-25 keV at the beamline EDR of the BESSY II storage ring. For the lens alignment purposes a goniometer of the HUBER company was utilized that allows us to use a complete set of freedom degrees, namely, short XYZ movements plus two orthogonal rotations.

A plane with a 35 μm hole, which was placed behind the lens, was used to make scanning of the radiation spot. Because of the high intensity of SR radiation, after this plane we were induced to put a scatterer of X-rays, the radiation from which was detected by a detector situated perpendicularly to the direction of the SR beam. Such techniques of registration was also necessary due to the high sensitivity of the detector used, moreover, putting the Al-filters essentially suppresses intensity of the soft component of X-radiation on the sample. Similar scheme of the radiation detection was already used during previous experiments on focusing of radiation by means of capillary structures [6]. A Si multichannel analyzer *Roentec Xflash 1201* with 4096 channels (energy resolution of ~ 200 eV) was utilized as a detector. The registered values of radiation intensity at various energies correspond to a number of photons detected by the defined channel. After the alignment procedure a linear scanning of the total spot area was organized in the focal plane.

Polycapillary lens tested in our experiment, had the following parameters: the length – 47 mm, the inlet and outlet diameters of lens – 8.5 and 6.3 mm, respectively, the focal length – 74 mm, the convergence angle of the lens outlet – 0.09 rad.

Processing data, the obtained distributions of radiation density were normalized by the value of the storage ring current during the measurements. The gain factor was calculated comparing the values of radiation density with and without polycapillary lens.

3. Results

One of the main research subjects of experiments on propagation of X-rays in capillary structures is a problem of its use for the increase of radiation density. In our experiment we also studied focusing features of a lens for various energies of the falling radiation in the range of 5-20 keV. The dependence of amplification in radiation density versus a radiation energy that was obtained by scanning of a spot of transmitted radiation in the focal plane of the lens, is presented in Fig. 1. The maximum of the gain factor has been observed in the range of 7-8 keV, the density of falling radiation increases in about 150 times for this interval. As expected, for higher energies of radiation the falling down in the gain has been detected as well as for lower energies. The latter is in a good agreement with a point that each capillary lens works effectively only for optimal energy range.

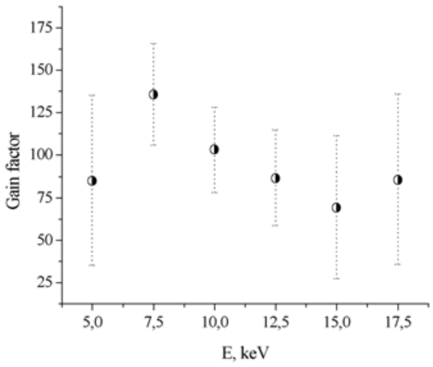

Figure 1. The gain in X-radiation density for various energies.

Moreover, for selected energy we have measured the spatial distribution of radiation density in the mean focus. Fig. 2 shows the distribution of X-radiation density in the focal plane at the energy of 7.5 keV. Evidently, in order to be more precise, for such experiments, one requires shifting a focal distance in accordance with the real focal distance for selected energy.

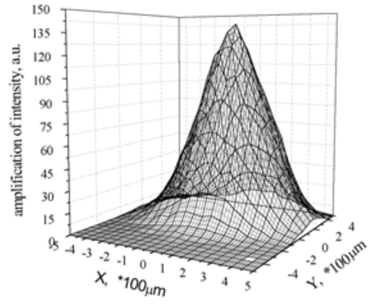

Figure 2. The spatial distribution of the gain in X-radiation density for 7.5 keV energy at the focus of polycapillary lens.

4. Acknowledgements

We are grateful to Dr. V.A. Murashova for her attention and many fruitful discussions. The lens tested was fabricated in the Institute for Roentgen Optics (Moscow).

References

1. S.B.Dabagov, V.A.Murashova, R.V.Fedorchuk, and M.N.Yakimenko, *Proc. SPIE: X-Ray Optics, Instruments and Missions*, **3444** (1998) 493-497.
2. D.H. Bilderback, S.A. Hoffman, and D.J. Thiel, *Synchr. Rad. News* **7** (1994) 27-31.
3. Kumakhov Optics and Application. *SPIE Selected Papers* **4155** (2000).
4. V.N. Makhov, S.B. Dabagov, A. Marcelli, N.Yu.Kirikova, V.A. Murashova, R.V. Fedorchuk, and M.N. Yakimenko, *Synchrotron Radiation News*, **13** (2000) 20-23.
5. A.Ioffe, S.B.Dabagov, M.A.Kumakhov, *Neutron News*, **6** (1995) 20-21.
6. B.Kanngiesser, N.Kemf, and W.Malzer, *Nucl. Instr. Meth. **B*** **198** (2002) 230-237.

At-wavelength Metrology on Sc-based Multilayers for the UV and Water Window

F. Schäfers*, S. Yulin, T. Feigl, N. Kaiser

*BESSY mbH, Albert-Einstein-Str. 15, D-12489 Berlin

Fraunhofer Institut Angewandte Optik und Feinmechanik, Winzerlaer Str. 10, D-07745 Jena

Application of EUV and Soft X-rays in material science, microscopy, plasma diagnostic, microlithography and development of X ray - lasers strongly depends on the advance of the multilayer optics which is used for manipulation of X-ray beams, focusing and imaging. In the wavelength range λ = 3.1 nm – 30 nm multilayer mirrors are widely used as an effective interference reflectors. Up to now the reflectivities of 15% at the λ = 3.1 nm [1], 13% at the λ = 4.5 nm [2] and 70% at the λ = 13.5 nm [3] were achieved by material combinations of Cr/Sc, Cr/C and Mo/Si, respectively.

Due to the unusual behaviour of its optical constants Sc is a very attractive candidate for multilayers optimised for the anomalous dispersion region of the 3p [4] and 2p absorption edges [1] around 28 eV (45 nm) and 398 eV (3.12 nm), respectively.

At the 2p edge normal incidence reflectances of up to 20 % employing Cr/Sc multilayers have been established in the last years which opened the way towards microscopy applications employing normal incidence optics. The optical performance is strongly influenced by the interface quality because the single layer thicknesses are in the atomic range of about one nanometer. Cr/Sc is the most promising material combination for application in the “water window” due to its good growth properties

In this contribution new experimental data for Sc/Si multilayers are presented also for the 3p region between 35 and 50 nm to understand its optical performance.

This long-wavelength range is a difficult spectral range for optical coatings and has so far not been considered systematically because of the high absorption for all materials. This has prevented so far the development of attractive multilayer coatings because the radiation is absorbed in the outermost layer and the performance is sensitively dependent on surface contamination. Thus, single layer coatings are generally used here. Furthermore the knowledge of the optical constants of suitable reflective materials is very limited due to the same reasons, which makes a systematic development and optimisation of multilayer coatings difficult.

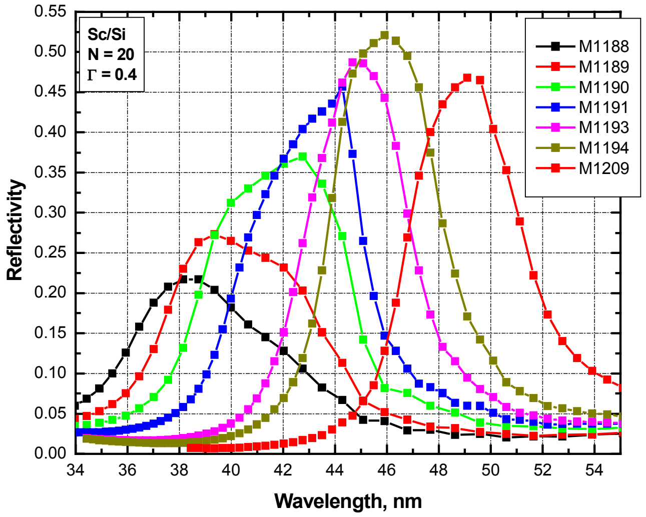

Fig. 1 Normal-Incidence reflectivity (θ=85°) of Sc/Si multilayers with different periods.

Light sources and monochromators in this range suffer from intensity and higher orders, since this range is intermediate between the classical normal incidence and grazing incidence working range for monochromators where both types do not reach their optimum performance.

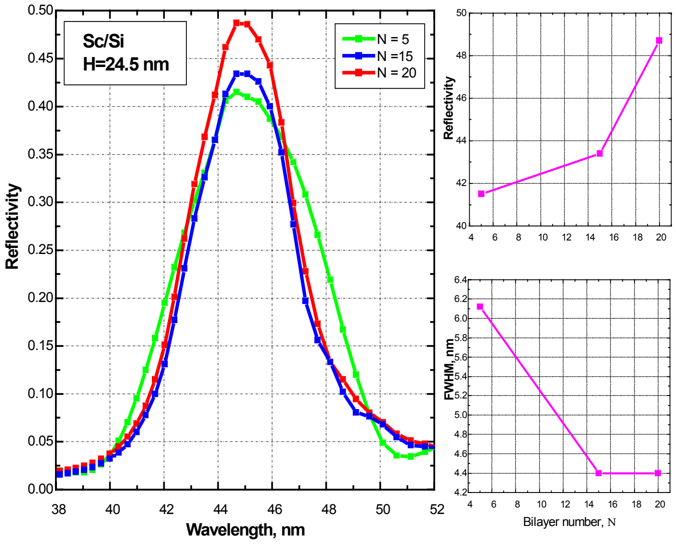

Fig. 2 Reflectivity improvement and change of FWHM for Sc/Si mirrors with increasing number of periods

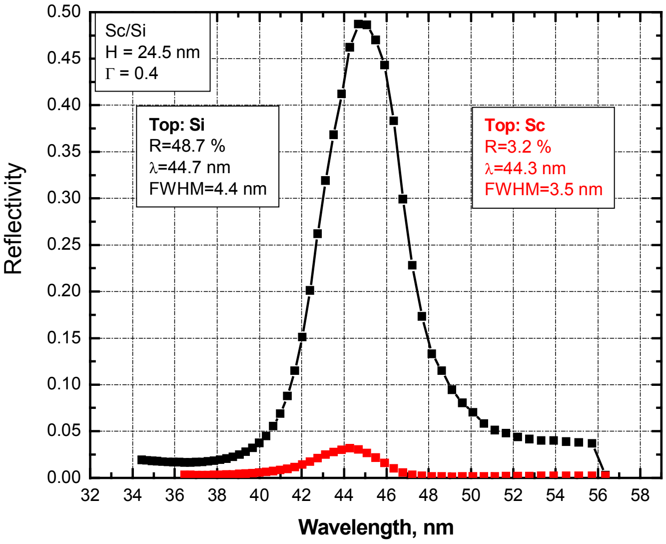

Fig. 3 Comparison of two similar Sc/Si multilayers with different by top layer coating

The Sc/Si and Cr/Sc multilayers were deposited by DC magnetron sputtering in an industrial sputtering system Kenotec MRC 903. This system is equipped with rectangular magnetrons with the size 120 mm x 360 mm. The Cr, Sc and Si targets were operated at a power of 150 W. The system works at a base pressure of ≈ $1 \cdot 10^{-7}$ mTorr that is achieved by a cryopump and the deposition is performed under Ar atmosphere of 1 mTorr. During the deposition process the samples are moved beyond the targets and the film thickness scales with the inverse velocity. A high accuracy speed control ensures a good reproducibility of film thickness even at high speeds that are necessary to prepare films with thicknesses below 1 nm. All samples were characterized with small angle x-ray reflection on a Siemens D5005 diffractometer with Cu K_α-radiation at λ = 0.154 nm.

The at-wavelength reflectivity measurements of the Sc/Si multilayers were done on BESSY U125/1-PGM beamline using the BESSY polarimeter experimental chamber [5], for the Cr/Sc multilayers the UE52-SGM was used.

Fig 1 shows the normal-incidence reflectivity as function of wavelength (R=f(λ)) for 20-periodic Sc/Sc multilayers with different periods and a constant thickness ratio Γ = 0.4. Unusually large reflectivities of up to 50 % have been found.

The improvement of reflectivity and change of FWHM for Sc/Si mirrors with increasing number of periods is shown in Fig. 2. The reflectivity of 41.3% was achieved by the use of 5 bilayers.

A convincing argument for the necessity of at-wavelength metrology is demonstrated in Fig. 3. Shown is a comparison of two Sc/Si multilayers with identical parameters designed for a working wavelength of 45 nm. The only difference is the top layer which is silicon (black curve) and scandium, respectively (red curve). This reflectivity is completely suppressed due to catastrophic oxidation of top Sc and corresponding catastrophic influence of surface effects on optical performance in this wavelength range! A Cu-Kα reflectivity test gave no difference in the performance of both multilayers.

The normal incidence reflectivity of two similar Cr/Sc multilayers operating in the water window close to the Sc-2p edge is shown in Fig. 4.

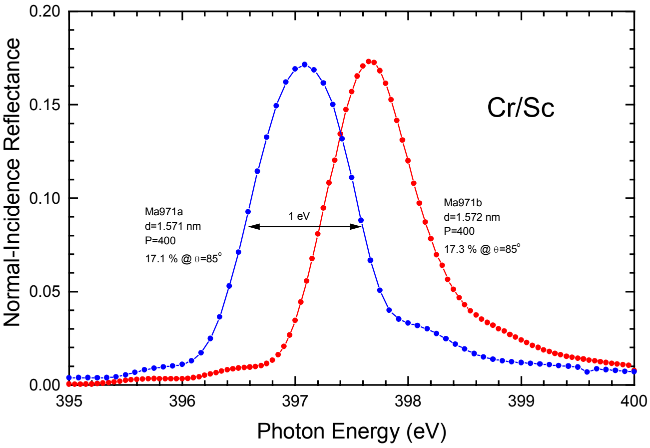

Fig. 4 Normal incidence reflectivity θ = (85^o) of Cr/Sc multilayers (d_1 = 1.571 nm and d_2 =1.572 nm) as function of photon energy. Both multilayers have N = 400 periods.

These promising and still not limited results on multilayer coatings in the UV and water window are believed to satisfy today's demands in various application fields such as astrophysics, microscopy in the water window, plasma diagnostics, spectroscopy, etc.

References

1. F. Schäfers et al., *Cr/Sc nanolayers for the water window: improved performance,* Nucl. Instrum. Meth. in Phys. Res. **A467-8**, 349-353 (2001)
2. N.N. Salashenko et al., *Multilayer X-ray optics for synchrotron radiation*, Nucl. Instrum. Meth. **A359**, 114-120 (1995)
3. Bajt S et al, *Improved reflectance and stability of Mo/Si multilayers*. Proc SPIE **4506**, 65-67 (2001)
4. V.E. Levashov, *Sc/Si Normal Incidence Mirrors for a VUV interval of 35-50 nm,* Proceedings of X-Ray Laser Conf., Kyoto, Japan, in: Inst. Phys. Conf. Ser. No. 159; IOP publishing Ltd., 593 - 599 (1999)
5. F. Schäfers et al., *A Soft Soft X-Ray Polarimeter using Multilayer Optics: Complete Analysis of the Polarization State of Light,* Applied Optics **38**, 4074-4088 (1999)

CP-NIM
The Circular Polarised Normal Incidence Monochromator Beamline

F.Neißendorfer, M.Mertin, F.Schäfers
BESSY GmbH, Albert-Einstein-Str. 15, D-12489 Berlin, Germany

In order to fullfill the user demands for circularly polarised UV radiation the former BESSY I 6.5 m NIM has been re-set into operation as CP-NIM. The Monk-Gillieson type optical layout of a plane grating in a convergent light beam remained unchanged, but due to space limitations and the three times larger distance to the source point at BESSY II the focussing geometry had to be modified. The radius of the premirror is now 10.3 m making a 2:1 demagnification of the source on to the exit slit. Off-plane bending magnet radiation is used for acceptance of circularly polarised radiation, which is horizontally dispersed to conserve the polarisation. The circular polarisation (left- right helicity) can be selected by vertical apertures. Thus the resolving power is expected to benefit from the considerably reduced horizontal beam size as compared with BESSY I.
The optical layout is sketched in Figure 1. EXIT 1 is now equipped with a BIRD&TOLE exit slit chamber equipped with vertical baffles and beam diagnostics, while on EXIT 2 (not shown in Fig. 1) the focus/exit slit is outside the beamline vacuum system to be incorporated into the experimentalist's vacuum chamber.
The monochromator-control has been realised according to the BESSY II standard using a PC with operating system OS/2 and the EMP/2 measuring program.

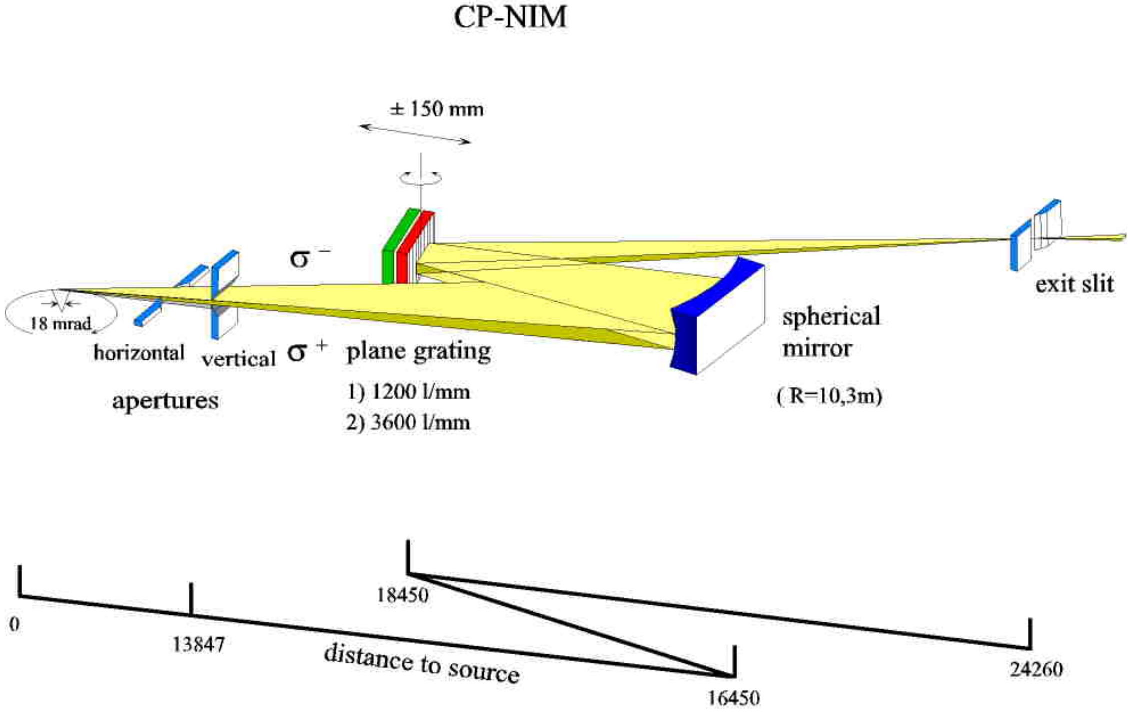

Fig. 1 **Optical layout of the CP-NIM**

The optical properties of the CP-NIM have been simulated with raytracing calculations and were confirmed experimentally in the last months. Part of the results are displayed here in terms of photon flux, resolving power and polarisation.

Fig. 2 shows the photon flux for both 1200 and 3600 l/mm grating as function of the photon energy. Three polarisation settings with the circular polarisation variing between Pc=0.7 and 0.84 are shown for an exit slit setting of 1 mm. The flux is in the 10^{10} range, which is despite of the smaller horizontal acceptance of 18 mrad comparable to the BESSY I data (50 mrad).

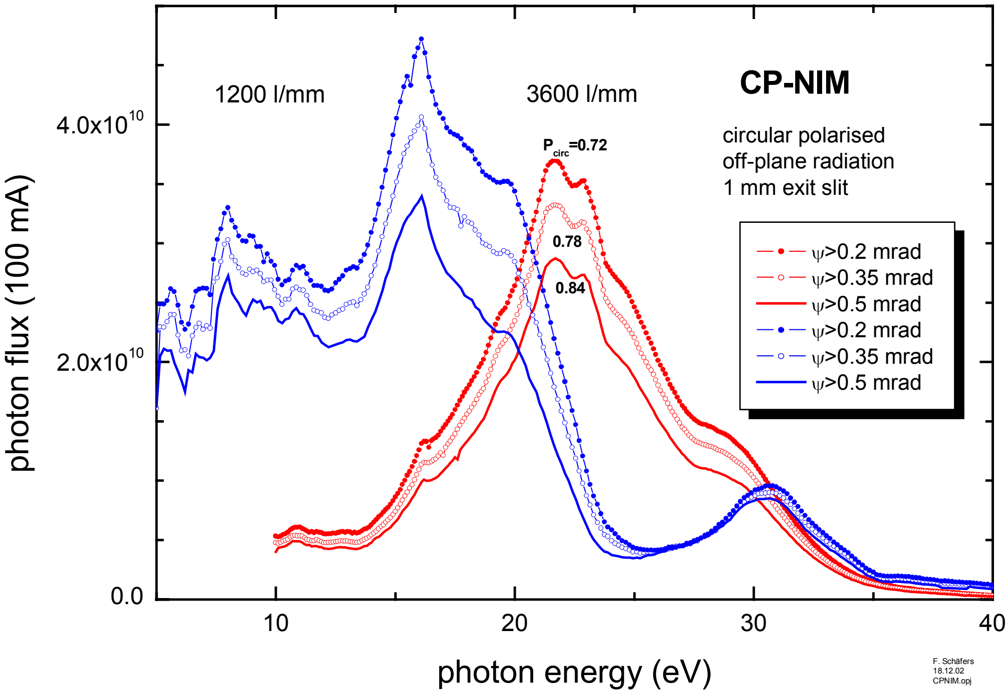

Fig. 2 **Photon flux, for both gratings, for 3 polarisation settings**

The energy resolution has been checked by an ionisation chamber filled with Xe gas and recording the autoionisation range between the $5p_{3/2}$ and $5p_{1/2}$ photoionisation threshold (Fig.

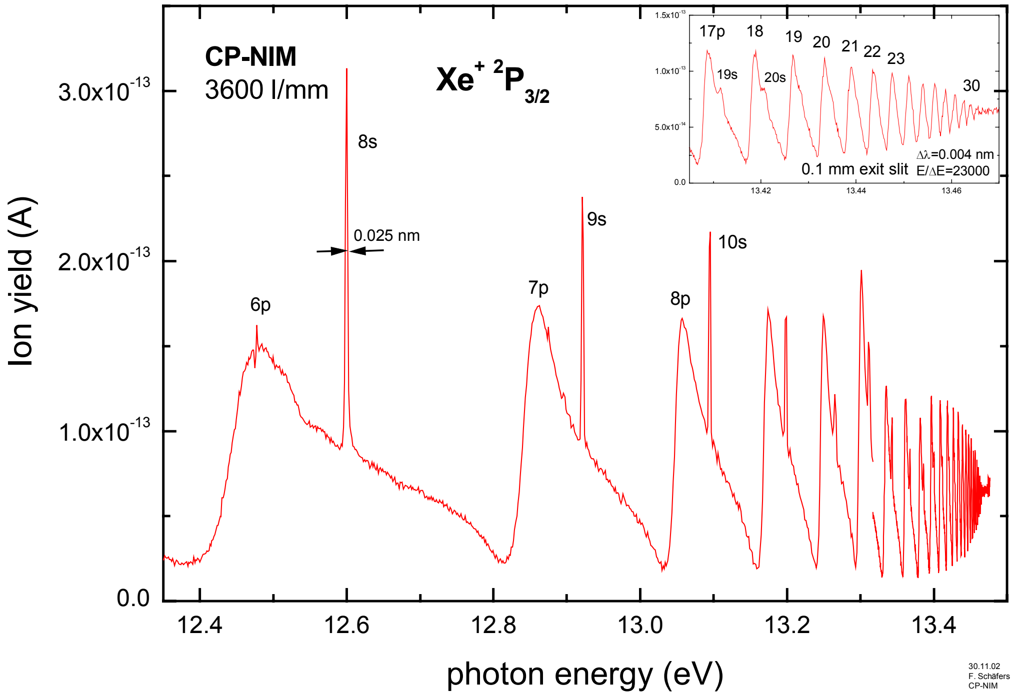

Fig. 3 Autoionisation resonances of atomic Xenon between the $5p_{3/2}$ and $5p_{1/2}$ thresholds.

3). The np series could be traced up to at least n=30, corresponding to a resolving power of at least 0.004 nm at an exit slit of 100 um. This corresponds to a resolution of λ/Δλ of 23.000 which exceeds the available BESSY I data by a factor of 50. Thus this beamline has turned into a high resolution monochromator.

The resolving power as function of the slit width measured using atomic Xe is shown in Fig. 4a for both gratings, while the calculated dependence on photon energy is plotted in Fig. 4b. The calculated dependence of circular polarisation as function of the polarisation slit setting shows Fig. 4c. The polarisation will be measured in spring 2003.

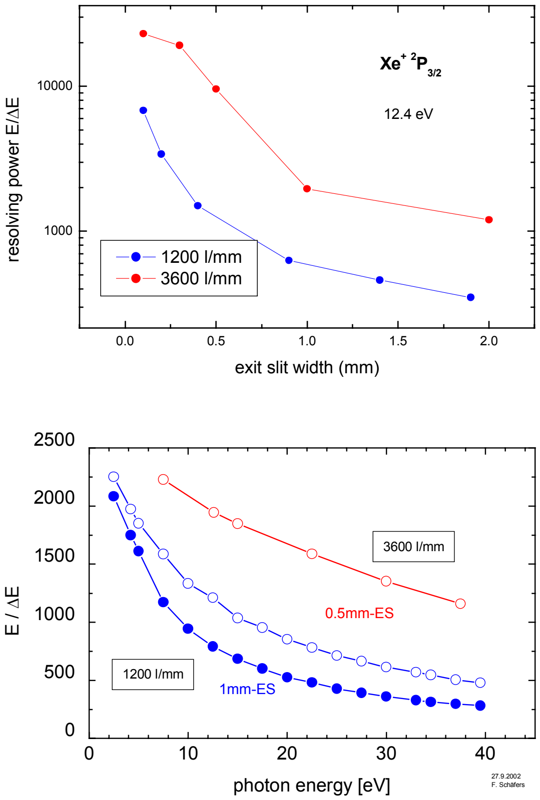

Fig.4a,b **Resolving power as function of exit slit width (4a) and energy, respectively (4b).**

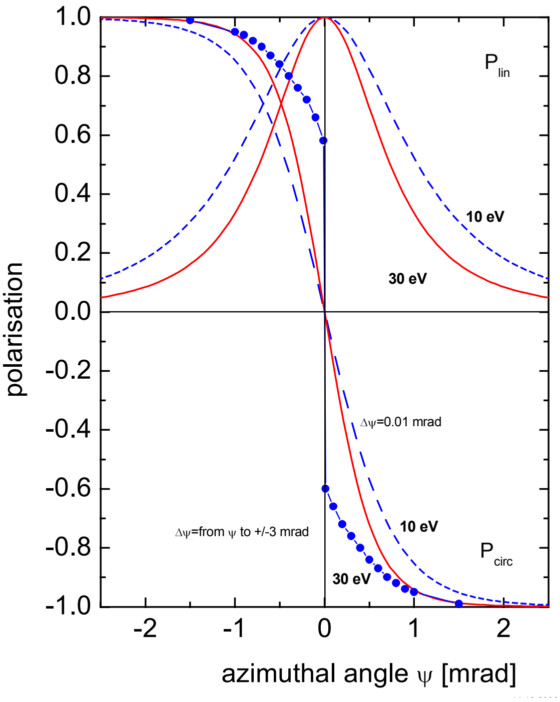

Fig. 4c **Degree of polarisation as function of the off-plane angle**

References
1. F. Schäfers, W.Peatman, A.Eyers, Ch.Heckenkamp, G.Schönhense, U.Heinzmann, Rev.Sci.Instr. **57**, 1032-1041 (1986)
2. http://www.bessy.de/users_info/beamlines/linespdf/D_16_1B.pdf

Transmission Photoelectron Microscopy of Diatoms at the Multilayer Monochromator Beamline U125-1/ML at BESSY II

M. Pohl, U. Kleineberg, U. Heinzmann (University of Bielefeld, Physik, 33615 Bielefeld)
M. Wieland (RheinAhrCampus, University of Applied Sciences, 53424 Remagen)
A. Oelsner, G. Schönhense (University of Mainz, Institute of Physics, 55099 Mainz)

Photoelectron Microscopy utilizing photoemission by energy-tunable soft x-ray radiation (X-PEEM) has been proven to be a valuable tool for spectromicroscopic imaging of surface structures (chemical, topographic or magnetic contrast) on a mesoscopic size scale (spatial resolution < 100 nm, energy resolution < 1 eV).

While almost all experiments performed so far have been carried out by *directly illuminating the sample surface* under oblique angles of incidence (typ. 20 deg to the surface) only very few experiments have been reported about photoelectron microscopy *in transmission geometry* [1-3]. The transmission setup requires the use of thin samples attached to ultrathin silicon membranes (thickness 100-200 nm), both being (semi-) transparent for the incident soft x-ray radiation.

Although Transmission Photoelectron Microscopy (T-PEEM) is similar in construction to the X-PEEM technique (using the same electron emission microscope) it is functionally different in that it images the secondary electrons produced by the *x-ray shadowgraph* of the sample on the backside of the transparent photocathode and not the photoelectron yield of the sample surface itself.

Transmission spectromicroscopy has considerable applications beyond material sciences e.g. in life sciences where a major advantage is the compatibility to sealed environmental sample cells where the sample can be held under controlled (e.g. hydrated) conditions. Furthermore electrical charging effects which may cause image distortions in photoemission microscopy of non-conducting samples do not play any role in T-PEEM if the photocathode is sufficiently conducting.

Transmission Photoelectron Microscopy is related to Transmission X-ray Microscopy (TXM) or Scanning Transmission X-ray Microscopy (STXM) the latter methods using the soft x-radiation transmitted through the sample for imaging by means of high resolution soft x-ray imaging or focusing optics.

Our T-PEEM setup at the BESSY undulator beamline U125-1/ML is displayed in Fig. 1.

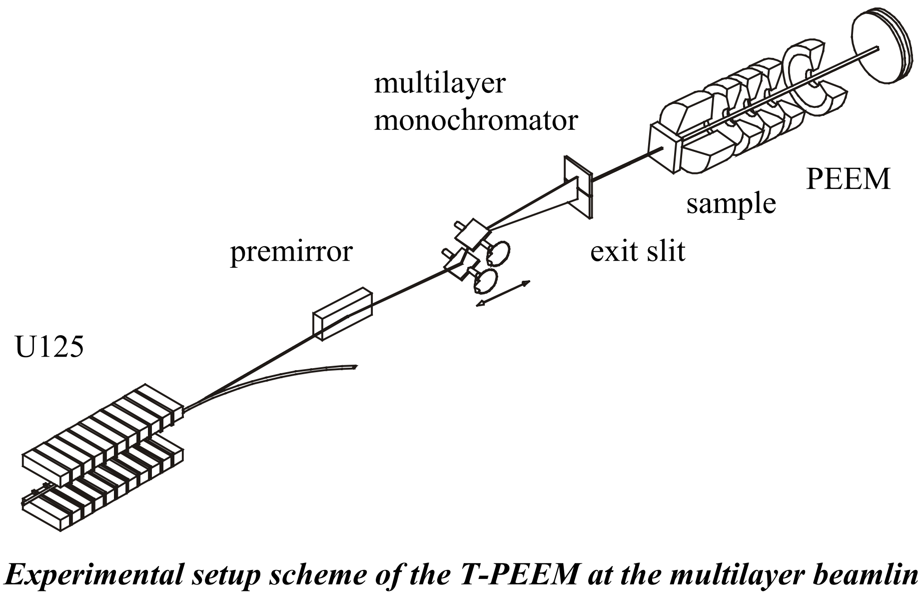

Fig. 1 : Experimental setup scheme of the T-PEEM at the multilayer beamline U125-1/ML

Undulator radiation emitted from the U125 is deflected by a plane Ni-coated Si-premirror at a deflection angle of 6 deg (resulting in a high energy cutoff photon energy at about 500 eV) and monochromized by a multilayer monochromator. The multilayer monochromator is equipped with a concave spherical multilayer mirror and a plane 3600 L/mm multilayer grating both operating at non-grazing incidence angles. Wavelenght tuning is achieved by simultaneously varying the angle of incidence on both elements in a 15-65 deg angular range. Three sets of multilayer optics are available and can be exchanged in vacuo. A set of Mo/Si multilayer mirror [4] and grating is used for the 95-100 eV photon energy range while a second set of C/Ti multilayer optics is used in the 410-456 eV range.

A conventional electrostatic photoelectron microscope with a piezo-driven integrated sample stage (Focus IS-PEEM) has been used for T-PEEM imaging. The images have been recorded by means of a peltier-cooled 1024*1024 pixel slow-scan CCD camera (Photometrics Coolsnap).

First transmission spectromicroscopy imaging experiments have been performed on silicate algae (Diatoms) using the Transmission Photoelectron Microscope setup. The dried algae have been dissolved and diluted in ultrapure water and spread onto the frontside of a silicon membrane (membrane thickness about 150 nm). The samples are loaded into a preparation chamber via a loadlock system where the flat backside of the membrane samples can be coated insitu with a CsI photocathode film to enhance the secondary electron yield from the membrane.

Finally the samples are transferred *in vacuo* from the preparation chamber into the PEEM instrument.

Figure 2 shows two examples of T-PEEM images recorded at 95 eV photon energy from different sample areas. The images have been recorded with an image field size of about 16 µm in diameter. Differently shaped diatoms and diatom fragments have been found, rod-shaped and circular forms being the most prominent species. A finestructure consisting of a number of filaments is clearly visible within the diatoms (marked by white arrows). The lateral resolution of the recorded images has been determined from slope of the intensity linescans across the marked areas to be better than 65 nm.

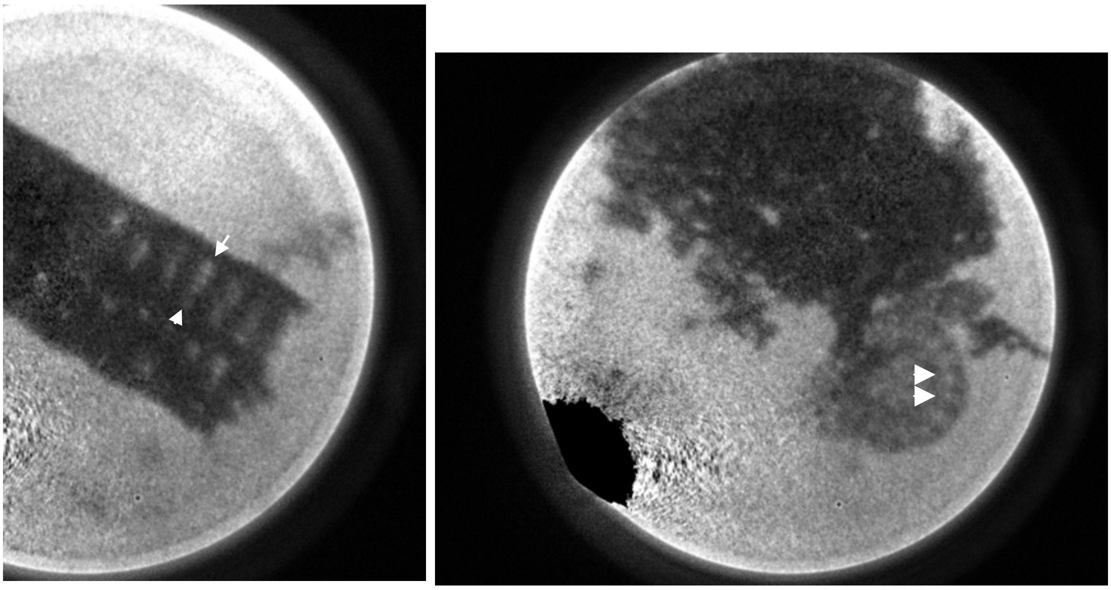

Fig. 2 : T-PEEM images (image field size 16 µm in diameter) of differently shaped diatom species at a photon energy of 95 eV.

The theoretical proximity resolution of the shadowgraph limited by diffraction is determined by the illuminating wavelenght (13 nm) and the proximity distance of the object and the photocathode (approx. thickness of the membrane 150 nm) and can be estimated to be about 45 nm. Our experimentally achieved resolution has thus been found to be close to the theoretical limit and a further improvement may be achieved by reducing the membrane thickness (50-100 nm possible) and by imaging at higher photon energies. The abberation-limited resolution of the microscope sets a theoretical limit at about 20 nm.

Spectromicroscopic T-PEEM images of diatoms have been recorded at different photon energies just below the Si-L edge (99.2 eV) and at a photon energy of 456 eV which is in the vicinity of the O-K edge (500 eV). Figure 3 shows two images of identical sample areas with an image field size of 32 µm being selected for both images. While the diatom in the image center appears as strongly absorbing species at 99 eV photon energy and a high intensity contrast between the silicate skeleton of the diatom and the Si-membrane is clearly visible, the contrast almost vanishes at 456 eV photon energy. The oxygen-containing silicate skeleton shows a strong absorption at 99 eV while the Si membrane is transparent. At a higher photon energy of 456 eV the absorption of the Si membrane is enhanced while the silicate shows a lower absorption due to the vicinity of the O-K edge at 500 eV. Surprisingly, a new image feature of higher electron yield (bright structure) located close to the diatom ocurrs at 456 eV which has not been visible at 99 eV. This may be explained by a local additional oxidation of the Si-membrane resulting in a lower absorption of this area compared to the non-oxidized membrane at 456 eV. It is feasible to assume that the silicate algae has induced a chemical oxidation reaction with the Si membrane leaving a "fingerprint' of its original shape.

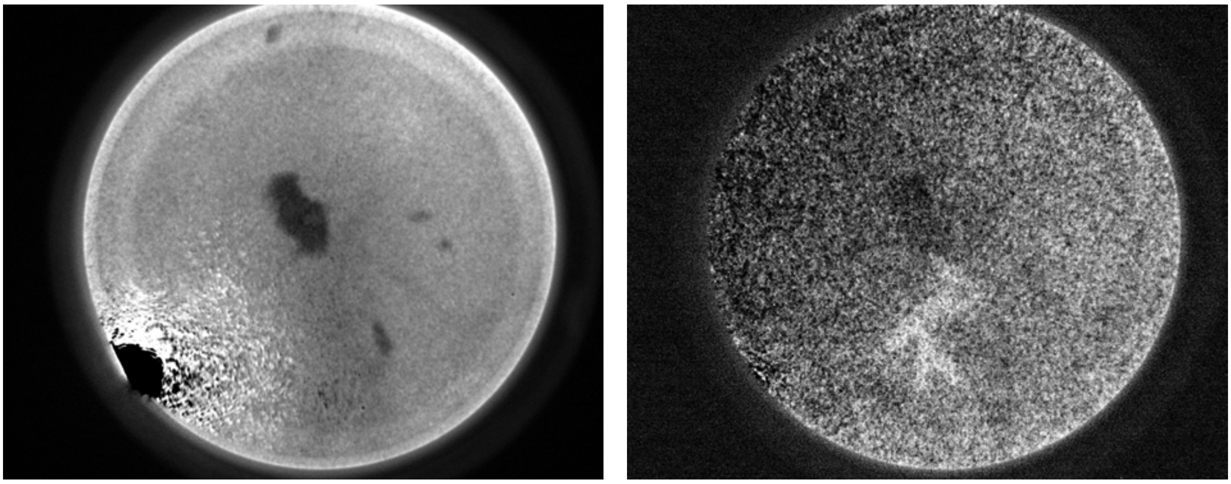

Fig. 3 : T-PEEM images (image field 32 µm in diameter) of a diatom species at two different photon energies; left image : E = 99 eV right image : E = 456 eV

Acknowledgments :

The authors would like to thank Prof. G. Schmahl for providing the non-comercial Si membranes and the excellent techical and scientific support at the U125-1 provided by the BESSY staff. BMBF project funding under grant number 05KS1PBA-8 is acknowledged.

References :

1. G. De Stasio et.al.; Rev. Sci. Instrum. 67(3), 737-741 (1996)
2. R.N. Watts et.al.; Rev. Sci. Instrum. 68(9), 3464-3476 (1997)
3. G. De Stasio et.al.; Rev. Sci. Instrum. 69(9), 3106-3108 (1998)
4. U. Kleineberg et.al. ; Thin Films (2003, in press)

GROWTH DYNAMICS OF ULTRATHIN ORGANIC FILMS MONITORED BY THE SMART SPECTROMICROSCOPE

SMART collaboration (coordinator: E. Umbach, authors: Th. Schmidt, R. Fink)

(Univ. Würzburg - Fritz-Haber-Institut der Max-Planck Gesellschaft Berlin - TU Darmstadt - TU Clausthal – LEO Oberkochen – BESSY)

The worldwide spectromicroscopy activities based on both, the photon and the electron imaging are steadily increasing. XPEEM (x-ray photoelectron emission microscopy) has become a routine technique to study e.g. magnetic or organic films, especially using the linear or the circular dichroism for imaging contrast. The XPEEM technique, in particular in combination with an imaging energy analyzer [1] - as it is the case for the SMART microscope [2] - hass a manifold of advantages: (a) surface sensitivity (about 1nm when imaging electrons with 30 to 100 eV kinetic energy and about 5 – 10 nm using secondary electrons), (b) different image contrasts due to elemental sensitivity, chemical or electronic state or due to magnetic or geometric (e.g. orientation) structure, (c) *in situ* study of dynamic processes like film growth, phase transition, desorption etc. due to the fast acquisition of the parallel detection system, and – as a last example – (d) the combination of three fundamental methods in one instrument [3]: microscopy – spectroscopy – diffraction for comprehensive characterization of an identical microspot of a size of 1 μm or even only a few tens of a nm. XPEEMs equipped with an electron gun are additionally able to utilize elastically or inelastically reflected or emitted electrons: LEEM microscopy to visualize atomic steps, superstructures, facets etc. due to electron diffraction at the surface, LEED (low energy electron diffraction) or ELS (electron loss spectroscopy) or Auger Electron Emission Spectroscopy (AES) or Microscopy. The actual version of the SMART microscope is an energy filtered XPEEM, quasi permanently installed at the UE52-PGM beamline. In summer 2003 the final version will be set up by incorporating the aberration corrector consisting of an electrostatic tetrode mirror in combination with a highly symmetric magnetic beam splitter, as proposed by Rose and Preikszas [4], and a high-brilliance electron gun. The aberration correction will improve both, the resolution limit down to values of 2 - 5 nm and the transmission by a factor of 10 to 100.

Though being in a test phase the microscope has been successfully used to investigate the growth of organic layers on metal surfaces, in particular the model systems PTCDA and NTCDA on Ag(111) and Au(111) single crystals. The photoelectrons were excited either by the UV-light of a Hg short arc lamp with a photon energy of 4.9eV (Hg-PEEM) or by the polarized, highly monochromatized ($\Delta E \approx 0.1$eV) synchrotron radiation (XPEEM) in an photon energy range between about 150 and 600eV.

The *in situ* growth dynamics of PTCDA on Ag(111) using Hg-PEEM is shown in Fig.1. The contrast in these images is not dominated by the work function – what is usually the case in Hg-PEEM. In fact, the image intensity mainly results from the strongly emitting Ag substrate, so the contrast is caused by attenuation of the covering organic layer: the thicker the layer the darker the intensity. The thickness difference of only one monolayer can be determined. Above room temperatures the growth is of Stranski-Krastanov type: after two nearly perfectly closed layers three-dimensional (3D) islands are formed (see 4 ML image in Fig1.). That can be explained by thermodynamics: a strain in the first 2 layers forces the additional material to create 3D islands in order to reduce the contact area to this strained layers. It should be pointed out: before the 3rd layer is completed, the 4th layer starts growing and 3D islands are created. These islands compete with 3rd and 4th layer, which both turn out

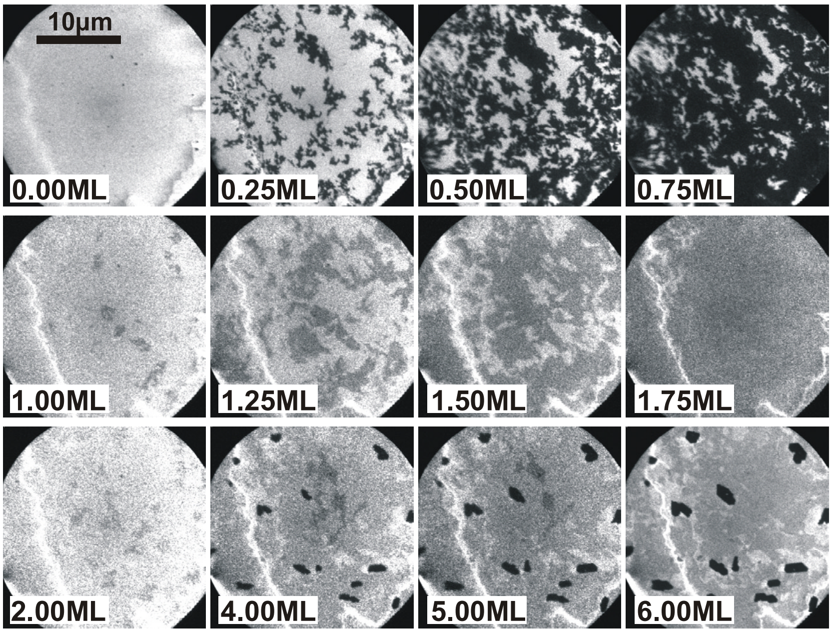

Fig 1: Growth of PTCDA on Ag(111) at 400 K, deposition rate = 0.2ML/min. Images were taken with Hg-PEEM during deposition. The intensity is rescaled at 1 and 2 ML.

to be metastable, because after termination of deposition these layers disappear, if the sample is not rapidly cooled down.

The growth kinetics (e.g. diffusion) causes on the one hand the density of the 3D islands to decrease with increasing temperature. On the other hand the limited diffusion at lower temperatures results in a transition from this 3D to the layer-by-layer growth mode which we observe at room temperature: more than seven (not perfectly closed) layers are involved in the growth. Furthermore the substrate morphology has an influence on both, the island density and the growth mode: keeping the deposition temperature constant, the concentration of 3D islands on substrate areas with high step densities or with step bunches is increased, while on flat, large substrate terraces the tendency to layer-by-layer growth is promoted. This indicates a strong influence of the substrate step edges on the diffusion (steps act as a barrier) and/or on the nucleation process (steps act as a nucleation centre).

One of the most important properties of organic films is the orientation of the molecules. From integral NEXAFS investigations on perfectly closed films (deposition temperatures below room temperature) it is known that the PTCDA molecules in the film are flat lying on the substrate [5]. In the case of a film with 3D islands the interpretation of the integral data concerning the molecular orientation in these islands would be difficult because the 3D islands cover only a few percent of the overall surface area and therefore contribute insufficiently to the integral NEXAFS signal. However, spectromicroscopy allows local probing and is therefore the ideal method to investigate these inhomogeneous samples. In order to analyse clearly the linear dichroism in NEXAFS, the angle between the surface normal and the polarization of the light has to be varied. The well-established procedure "rotation of the sample surface with respect to polarization" can usually not be applied in PEEMs because the sample geometry is fixed (the surface normal has to be parallel to the electron optical axis). But the installation of the new UE52 undulator in April 2002 has enabled the free choice of the orientation of linear polarization or of the helicity of circular polarization. In this way we imaged with PEEM, for the first time worldwide, the identical sample spot with two linear polarization orientations, standing perpendicular to each other. Figure 2 shows a nominal 5 ML thick PTCDA film with 3D islands for two polarizations at different photon energies. Clearly, the two sequences show different behaviour in the image

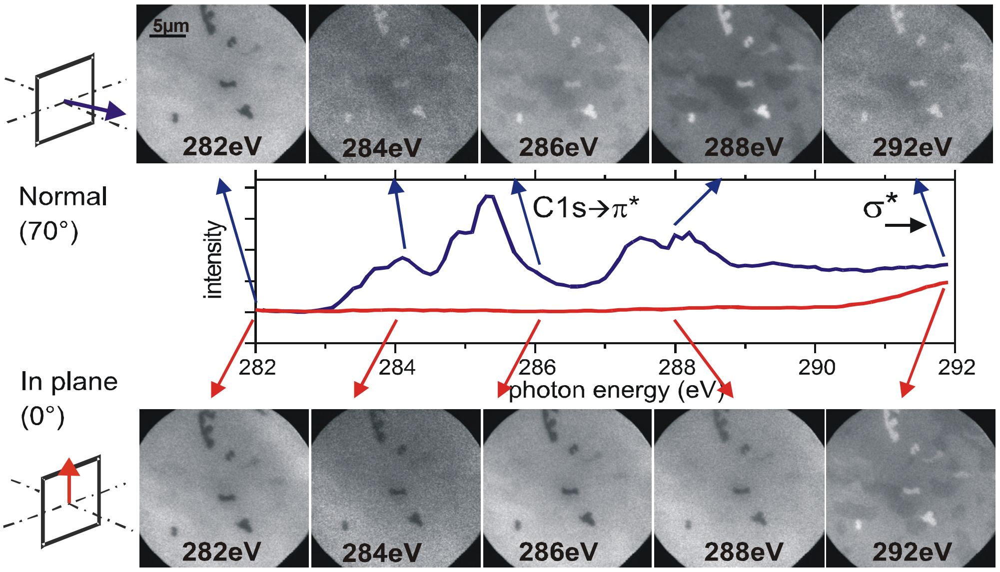

Fig. 2: XPEEM images of a 5 ML thick PTCDA film on Ag(111) at out-of-plane (top) and in-plane (button) polarization at different photon energies. The integral NEXAFS spectra (center) show a clear linear dichroism concluding that all the molecules are perfectly flat lying on the substrate.

contrast: for in-plane polarization the contrast does nearly not change, except for the 292 eV image, when excitation into σ* orbitals starts. However, the images with the out-of-plane polarization show a strong change in contrast: the dark islands in the 282 eV image appear bright in the energy range of the π* resonance (284 - 288 eV). The intensities in the images have two major contributions:

(a) Electrons emitted from the organic layer by the C1s to π* excitation (strongly polarization dependent) and to σ* (polarization independent)
(b) Electrons emitted from the underlying Ag substrate.

The latter electrons have to surpass the organic layer. As a consequence the attenuation results in a thickness contrast: the thick islands in the 282 eV images appear dark. Case (a) behaves just the opposite: the thicker the organic film the more the C1s excitation contributes to the image intensity. That results in bright islands in the 284 - 288 eV images for the out-of-plane polarization and for the σ* emission for both polarization. For the in-plane polarization the π* resonance is missing, which can be seen also in the NEXAFS spectrum in the middle of Fig. 2 which was generated from a stack of 150 images. Due to the high photon energy resolution even the vibronic fine structure can be seen in the spectrum. From the image contrast behaviour we can clearly conclude, that the molecules are flat lying in both, the 3D islands and in the underlying layer, which is partly a tri- and partly a bi-layer (= dark grey areas in the 284-288eV images for out-of-plane polarization).

This project is funded by the Federal German Ministry of Education and Research (BMBF) under contracts 05 SL8 WW8-1 and 05 KS1WW2-0.

References:

[1] Th. Schmidt et al., Surf. Rev. Lett. **5** (1998) 1287
[2] R. Fink et al., J. Electr. Spectrosc. Rel. Phen. **84** (1997) 231.
[3] Th. Schmidt et al., Surf. Rev. Lett. **9** (2002) 223
[4] D. Preikszas and H. Rose, J. Electr. Micr. **1** (1997) 1; D. Preikszas, Dissertation D 17, Technische Hochschule, Darmstadt, Germany (1995)
[5] A. Schöll et al, in preparation

First SPECS PHOIBOS 150 performance tests

D. R. Batchelor[1], S. Mähl[2], O. Schaff[2], P. R. Bressler[1]
[1]BESSY, Albert-Einstein-Str. 15, 12489 Berlin
[2]SPECS Voltastraße 5, 13355 Berlin

We present first photoemission tests of the PHOIBOS 150 hemispherical analyser for the BESSY end station PHOENEX. These tests were carried out on the former SIFES end station. The nine channeltron electron energy analyser will become part of the new PHOENEX experimental station available for external use in 2003.

Figure 1 shows a Xe $5p_{3/2}$ photoemission peak obtained using a SPECS gas cell (UGC10) on the 3m NIM-2 monochromator. Acquiring data with the total set up was fast, the count rate sufficiently high. The FWHM of the peak obtained by curve fitting is 4.54meV. Assuming monochromator, Doppler broadening, and lifetime contributions of 1.30, 1.45 and 0.09meV (2Γ), respectively, we estimate an analyser contribution of ~ 3.65meV in figure 1.

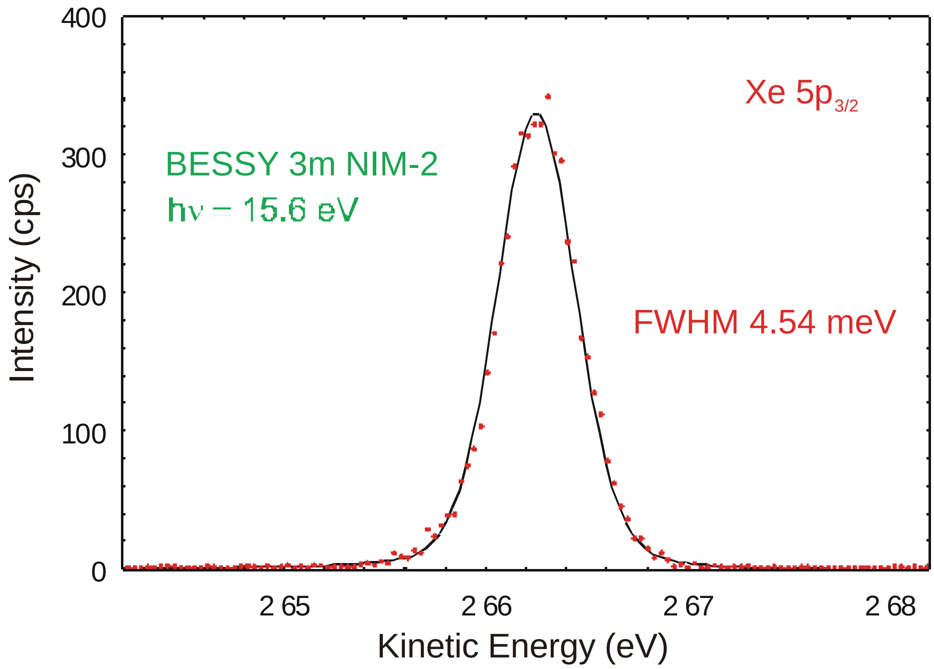

Figure 1: Xe $5p_{3/2}$ photoemission excited by 15.6 eV photons on 3m NIM 2.

This result was obtained by optimising the gas cell electrodes to compensate for potential variations within the cell [1]. Figure 2 shows the FWHM as a function of the pass energy without optimisation of the cell electrodes.

To test the analyser's performance at high kinetic energies photoemission spectra were also recorded on the KMC-2 beamline. Figure 3 shows spectra from a freshly evaporated gold film using 3.0 keV photon energy. Both, a wide scan as well as a detailed scan of the Au 4f region are displayed. The monotonic step-like form of the wide scan indicates a good alignment of sample and that the lens voltages/analyser transmission are correct. The solid line in the inset is the curve fit of the spectrum with Shirley background. The monochromator resolution is ~ 5500. The Lorentzian width for Au 4f peaks obtained, 0.18eV, is in good agreement with literature [2].

The analyser will be set up on the PHOENEX station. The new system has optimised magnetic shielding and was specifically designed for high resolution ARPES-type experiments. More conclusive performance tests will be carried out early next year.

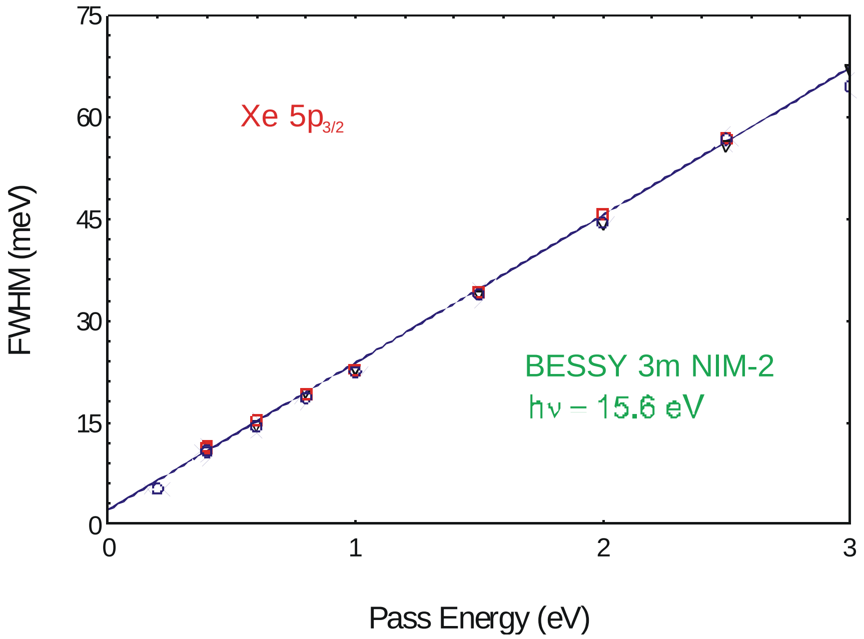

Figure 2: FWHM as a function of pass energy.

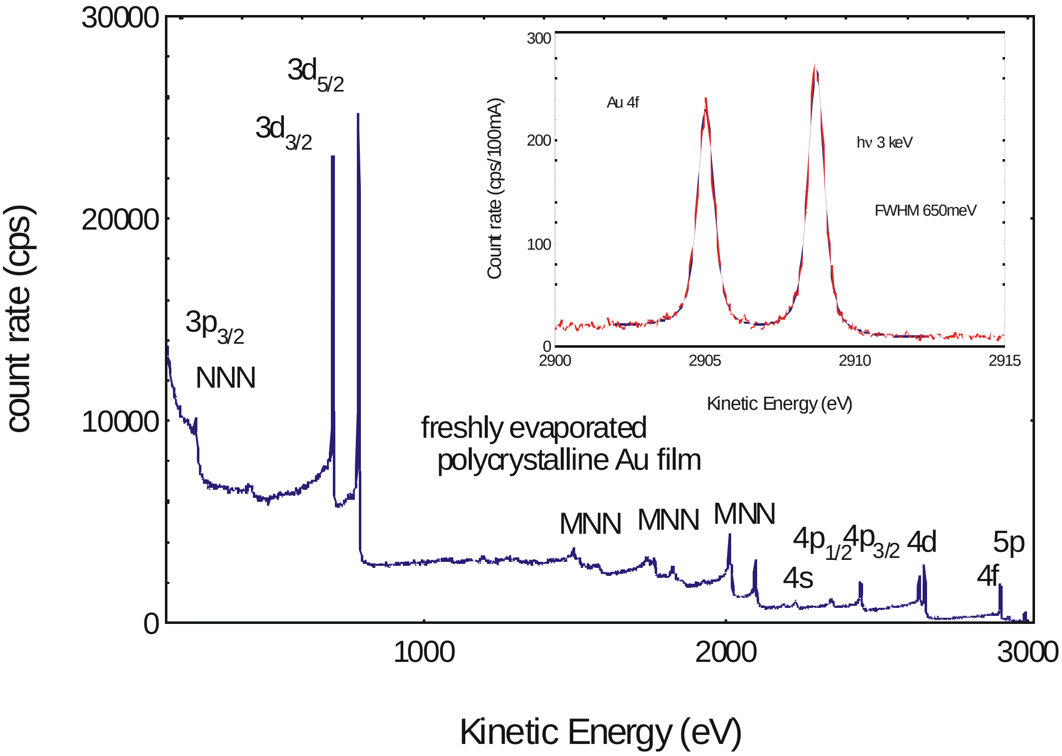

Figure 3: Wide photoemission scan of an evaporated Au film excited by 3 keV photons. Insert shows Au 4f peaks with the fitted curve.

We wish to thank A. Erko, G. Reichardt and W. Braun for their support during the tests and for the fruitful discussions.

References

[1] P. Baltzer, L. Karlsson, M. Lunddqvist, B. Wannberg. Rev. Sci. Instrum. 64(1993)2179

[2] I. Lindau et al., Nature 250, 214 (1974)

The Nanometer Optical Component Measuring Machine - NOM - at BESSY

Heiner Lammert, Tino Noll, Thomas Schlegel, Frank Siewert, Thomas Zeschke
Berliner Elektronenspeicherring-Gesellschaft für Synchrotronstrahlung - BESSY -
Albert Einstein Straße 15, D 12489 Berlin
e-mail: Lammert@Bessy.de

BESSY Annual Report 2002, Berlin

Introduction

The cooperative research project, named Nanometer-Optikkomponenten - NOK - [1] and coordinated by BESSY, with it's 11 partners from German industries and science was established with the goal to provide optical components for use in synchrotron radiation research with an exactness that exceeds the present technological limit of 0.1 arcsec rms for the slope error of mirrors and grating substrates for use in experiments with Synchrotron Radiation [2]. The necessity of more exact components, their generating processes and measuring methods and the goal of the cooperative project NOK are subject of the present activities within the scope of this cooperative research project. One half of the cooperative project complex aims at the production of optical components with higher accuracy than the present technological limit of the above- mentioned 0.1 arcsec rms. The other half of the complex is expended on the development of measurement methods and their applications. One partner in the NOK-cooperative research project in respect to measurement development is the Physikalisch-Technische Bundesanstalt in Braunschweig, where the so called ESAD method (Extended shear Angles Difference) integrated in one autocollimator is developed. The other measurement development in the project has been implemented at BESSY with the compilation of the Nanometer-Optical component-Measuring Machine (NOM) since the beginning of 2001.

The principle of the Nanometer-Optical component-Measuring Machine - NOM -

In the BESSY Optical Lab we have gained many experiences in measurement of optical synchrotron radiation components with the Long Trace Profiler (LTP) [3];[4] for many years. The limit of the LTP accuracy we could possibly overcome with a differentiated temperature regime and with the application of some different methods of autocalibration in case that the accuracy of the surfaces, which are to be measured, were higher than the systematical deviations of the LTP. So, for example, we were able to achieve a measuring result of a spherical surface of 0.07 arcsec rms slope deviation with a multitude of different scans witch correspond to another coordinate measuring machine result of 0.03 arcsec rms. This result of a measurement uncertainty, clearly higher than 0.1 arcsec rms was an exception. As a general rule the measurement uncertainty of the LTP is not much better than 0.1 arcsec rms. For us that was the main reason to develop a new measurement equipment with the goal to decrease the measurement uncertainty in the range of 0.01 arcsec rms, that is about the decuple accuracy. The main problem is a multitude of systematic measurement deviations, which are not or very hardly observable in the measurement result. Such systematically “errors”, for example, may be found in the inhomogeneity of the optical glass or in system calibration. To find in the measurement result without the observable systematic deviations of higher order, it is the best method to compare one measurement equipment with another one. However in all the special differences of the samples in respect of their forms, surfaces, materials, or in respect of the different environmental conditions there is not always a chance to utilize another measurement equipment of the needed accuracy. To meet this problem it is our idea to integrate a second measurement principle into one unit, in order to be able to measure the same slope deviation of a sample as possible on the same area and/or at the same time with two sensors at the same measurement machine. So the principle of the NOM is to need a hybrid system.

The hybrid system NOM unites two different sensors: one LTP-head [5] and one Autokollimator (AKF) [6]. They are fixed opposite each other, the measurment beams arranged nearly aligned see fig. 1. The measuring principle is non-contact deflectometry. The LTP operates like a common LTP principle with a double beam, which comes to interference after focusing at the face of the electronic sensor. The LTP-head has been developed especially for BESSY by the inventor Peter Takacs and produced by Ocean Optics Ltd. The used Autokollimator is a special development by Möller Wedel Optical GmbH with a small aperture of less than 2 mm. Slope deviations of the sample are registered in both sensors. The LTP gives sample slope deviations in the main (tangential-) direction in the long axis, the AKF gives sample slope values in the same direction and in the orthogonal direction (saggital slope deviation of the sample, short axis).

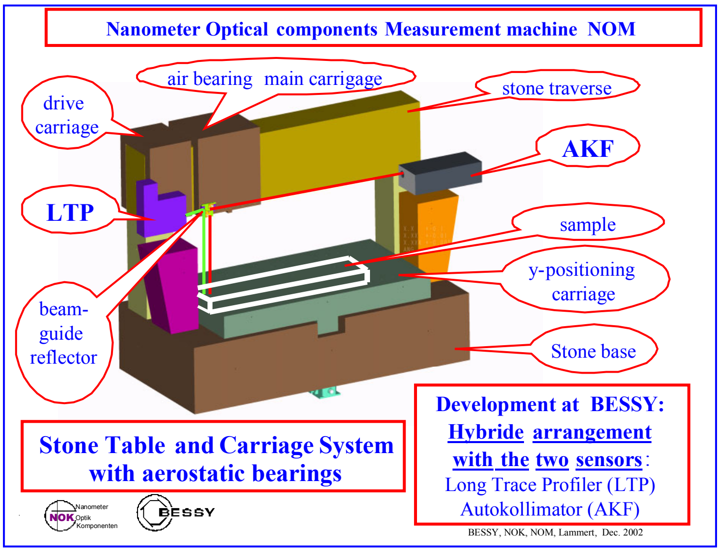

Nanometer Optical components Measurement machine NOM

Stone Table and Carriage System with aerostatic bearings

Development at BESSY:
Hybride arrangement with the two sensors:
Long Trace Profiler (LTP)
Autokollimator (AKF)

Fig. 1: Principle of the NOM: On the compact stone base the two sensors are mounted: the LTP-head and die AKF. The surface under test on the sample is placed on the table of the y-positioning carriage. The beams of the sensors are guided by the beam guide reflectors. These are moved by the main carriage and die sample is scanned. The beams from the LTP are reflected back into the LTP-head and AKF-beam back into the AKF. So the sample may be scanned in the same trace at the same time. The different values of the LTP- and AKF-measurement results comprise among other things the systematic otherwise not observable deviations of the sensors. An analysis of this deviation allows to separate and eliminate these deviations. An average of the LTP- and AKF-results leads to a minimization of the measuring errors.

Fig.2 Picture of the NOM in the stage of the development in December 2002 in the optical Lab at BESSY. At the measuring table a 1000 mm long toroidal mirror with alignment implement is positioned to adjust the sample in two directions: to rotate around the vertical axis and to translate orthogonal to the measurement direction with the help of the stone carriage. This air bearing carriage also allows to measure parallel traces in the range of 300 mm.

The measurement range of the NOM is up to 1200 mm in length; 300 mm in depth; 12 mrad view angle. The compact stone parts weigh about 4.000 Kilograms. The air bearing main carriage is on its way of 1,2 m of a very high accuracy of the slope moves. Especially the pitch influence (on the main direction) moreover is compensated by a double reflector and consequently invariant in this main carriage pitch tilts. The stone table and carriage system is also constructed for this special tasks. The NOM is enclosed of a temperature stable housing in a temperature controlled measurement Lab.

Measurment results with the NOM

We are sure, that the accuracy of the NOM will be very high. In some special cases we could demonstrate a measurement uncertainties in the range of < 0,01 arcsec rms or lower. Also the reproducibility is accordingly low.

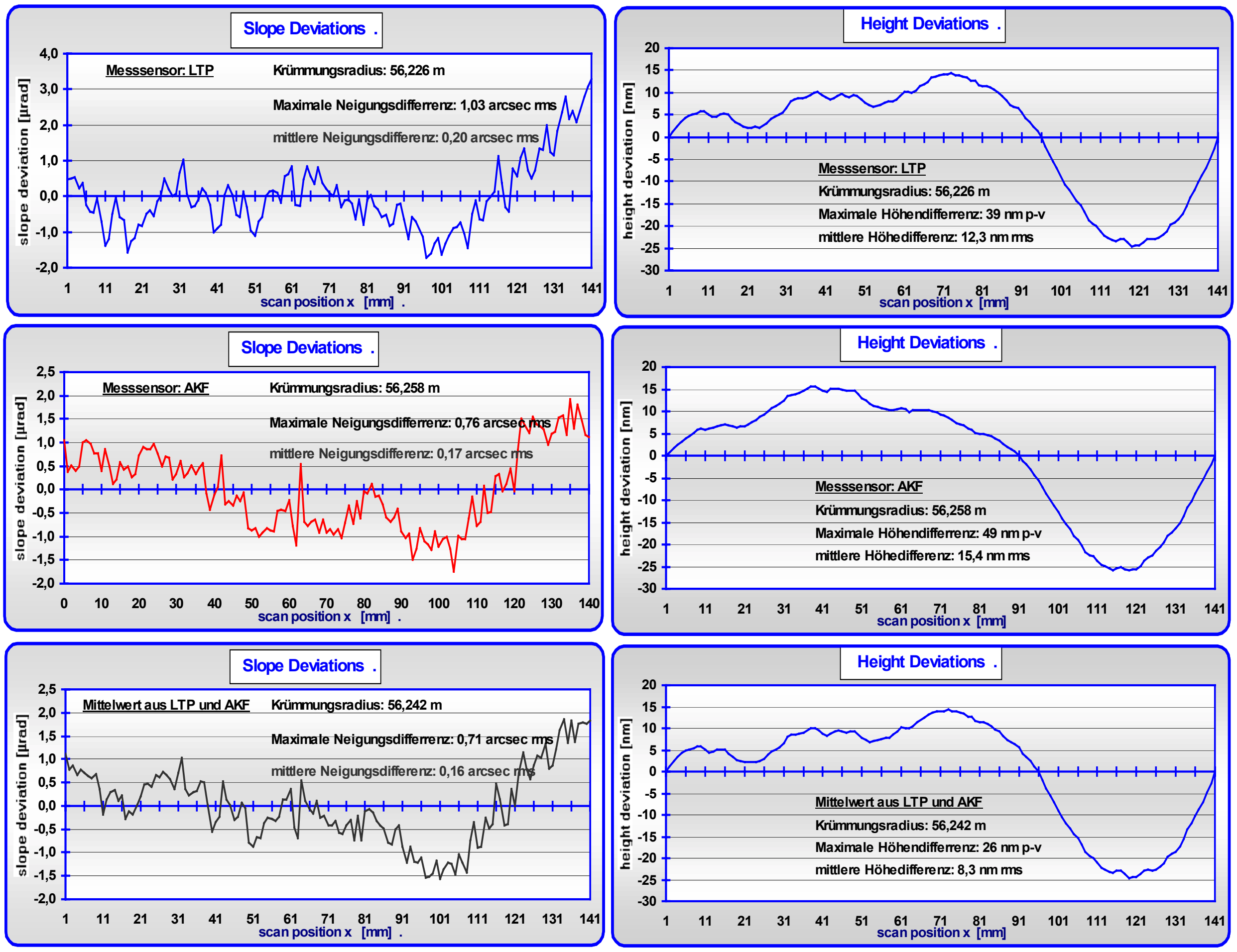

Fig.3 The 6 diagrams show the comparison and the subsumption of measurement with the common LTP at BESSY and with the NOM with Autokollimator (AKF) with a same sample. The sample is a spherical mirror, 150 mm long, R = 56.2 m in the slope error range of 0.1 arcsec rms. The two diagrams right at the top show the LTP, those in the middle the AKF and at the bottom the average of slope error (left side) and hight deviations (right side). The results of this demonstrated measurement correspond to the framing uncertainties of the two different measurement methods in the range of 0,015 arcsec rms and 1,5 nm rms and for the radius in the range of +/- 0,3 %.

The difference of the two LTP- and AKF- results primarily represents the systematical measurement deviations (errors) whereas the high rate of the random measurement deviations (errors) is already compensated in the respective measurements with the used LPT- and AKF-measurement strategies. These discrete systematical measurement deviations of the LTP and of the AKF measurement are not visible in the respective result. But the difference of the two results of the two different measurement methods gives a general picture of the summery of the most different systematical measurement deviations and we are able to evaluate the range of the systematical measurement deviations. The measuring uncertainties are with the utmost probably lower than the difference of the two measurement results of the two different methods. As shown in fig. 3 the sum of the invisible systematical measurement deviations of both measurement methods are lower as above-mentioned of the different values 0,015 arcsec rms ore 1,5 nm rms. The average of these two results in the diagrams at the bottom is consequently saved with a measurement uncertainty of this range of 10 milli-arcsec rms.

Another NOM-measurement result is shown in fig. 4. a Zerodur™ mirror in dimensions of 510 mm x 118 mm.

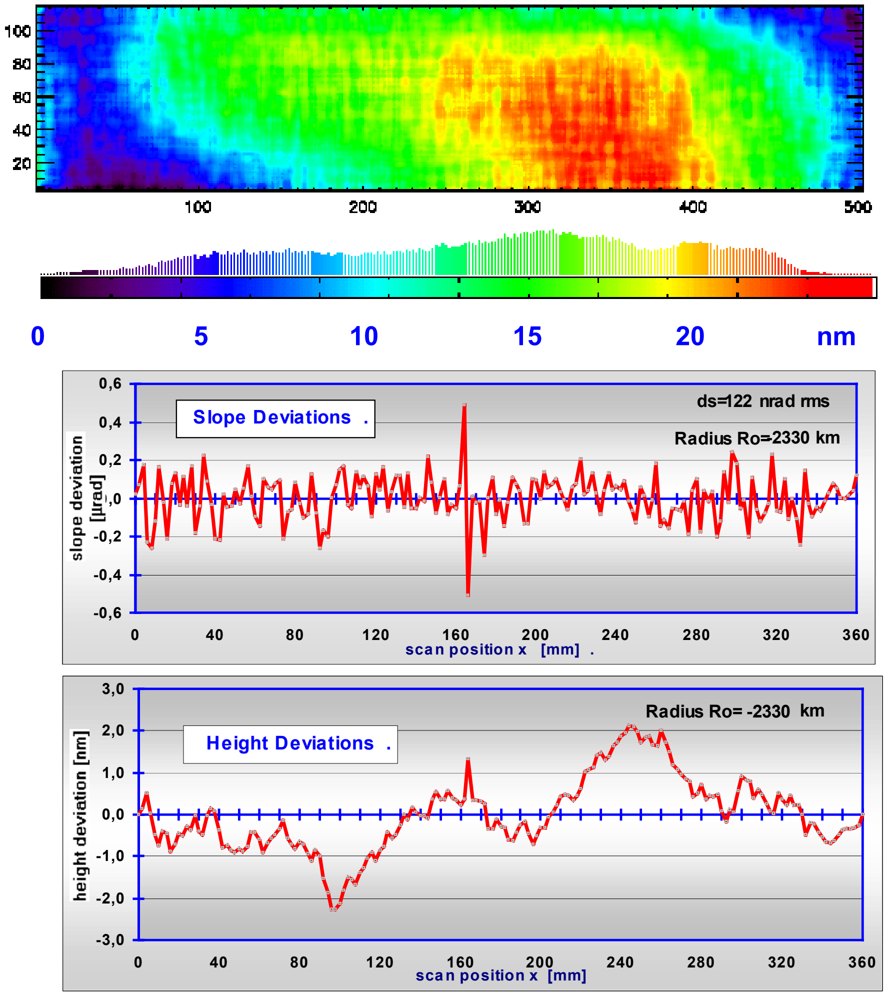

Fig.4: NOM - measurement results of a 2D-scan of the 510 mm x 118 mm Zerodur-mirror.

Fig. 4a: Landscape-diagram over a 550 cm² expanded plane surface with measured hight deviations less than 25 nm p-v. 400 cm² of this surface are in range of +/- 10 nm p-v with slope deviation of 0.04 arcsec rms.

Fig. 4b.: Slope deviation of a 360 mm long line scan in a central region of this surface. The result of the fitted scan is 0.025 arcsec rms with a slope optimized radius of 2330 km. The estimated uncertainty is in the range of < 0.01 arcsec rms.

Fig. 4c: Linescan in the same central region like Fig. 4b. The result displays 4.4 nm p-v and 0.9 nm rms. The estimated measurement uncertainty is less than 0.5 nm p-v or 0.2 nm rms.

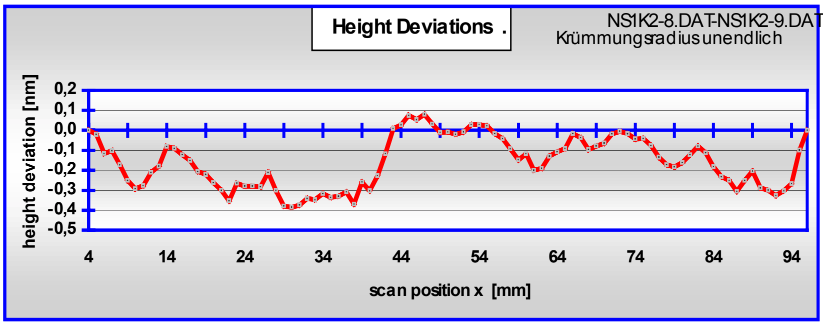

Fig. 5: Measured result of reproducibility of a 100 mm Silicon plane substrate for a grating. The reproducibility is in the range of 0.1 nm rms or 0.01 arcsec rms without optimized environmental conditions.

The results of fig. 4a-c shows that the NOM is able to acquire cognizance about slope and height deviations of the sample in large Dimensions up to 1200 mm in format of linescans and in display format of two dimensions. In this case a 400 cm² surface is detected with the high accuracy with estimated measurement uncertainty in range of < 0.01 arcsec rms. The reproducibility as shown in fig. 5 was reached under the present stage of development of the NOM with not optimized conditions of temperature, and other environment terms. It is planned, to isolate the NOM with a special housing construction. So we can anticipate a reduction of the measurement uncertainty trough a stabilization of environmental conditions and especially an extensive minimization of a quota random influences to the measurement reproducibility.

Conclusion

The presented hybrid principle of the NOM allows a higher measurement accuracy than the today common usual accuracy. The shown results of the measurements can be improved. Our development of the NOM measurment system is not finished at present time. For higher measurement accuracy it is possible to consider the influence of the yet provisional recorded environmental conditions with special measures for thermal stabilization and isolation, reduction of vibration and suppression of air convection. Finally the reached status of the NOM will be able to measure with an accuracy in the range of < 0,01 arcsec rms for optical components with large extended surfaces.

Acknowledgments

This work has been supported by the Bundesministerium für Bildung und Forschung and the Verein Deutscher Ingenieure VDI (No. 13 N 7929). We thank Möller-Wedel-Optical GmbH, Wedel , Berliner Glas KGaA, Berlin and IOM Institut für Oberflächenmodifizierung e.V. Leipzig for the scientific cooperation.

References

[1] Lammert, Heiner, Nanometer Optical Components for Synchrotron Radiation Beamlines. BESSY Annual Report 2001, BESSY Berlin, p. 301, http://www Bessy.de/

[2] Lammert, H, F. Senf, F. Eggenstein, U. Flechsig, R. Follath, S. Hartlaub, T. Noll, G. Reichardt, J.S. Schmidt, M. Weiss, T. Zeschke, W.B. Peatman, and W. Gudat; Nucl. Instr. and Meth. A 467-468 (2001) 488 - 491

[3] Lammert, H., Senf, F.; Berger M.; Improvement of Synchrotron Radiation Mirrors below the 0.1 arcsec rms Error Limit with the Help of a Long Trace Profiler: SPIE (San Diego 1997), Vol. 3152, p. 168-179

[4] Lammert, H., Int. Workshop Metrology for X-ray and Neutron-Optics, APS Argonne US, March 2000

[5] Takacs, P.Z., K. Furenlid; Measurement of Surface Finish and Figure Accuracy; Proc. of the Int. Workshop High Performance Monochromators and Optics for Synchrotron Radiation in the Soft X-Ray Region, held at BESSY GmbH, Berlin, 1991

[6] Möller-Wedel Optical GmbH, Wedel; htpp://www.moeller-wedel-optical.com/

NOK
Nanometer
Optik
Komponenten

GENERATION OF FEMTOSECOND SYNCHROTRON RADIATION PULSES AT BESSY II

H.-J. Bäcker, J. Bahrdt, H. A. Dürr, V. Dürr, W. Eberhardt, A. Gaupp,
K. Holldack, E. Jaeschke, S. Khan, D. Krämer, H.-C. Mertins, W. B. Peatman,
G. Reichardt, T. Quast, M. Scheer, F. Senf, G. Wüstefeld

BESSY, Albert-Einstein-Str. 15, 12489 Berlin, Germany

1. Introduction

Probing atomic motion or magnetic properties with x-rays on a sub-picosecond time scale offers exciting scientific opportunities. While contemporary synchrotron radiation sources are limited in pulse duration to tens of picoseconds, optical laser pulses can be three orders of magnitude shorter. The generation of femtosecond x-ray pulses by combining femtosecond lasers with electron bunches of a third-generation synchrotron light source was proposed [1] and experimentally demonstrated [2] at the Advanced Light Source in Berkeley. It is planned to use this technique, now commonly known as "bunch slicing", at BESSY II to study ultrafast magnetic phenomena by probing element-specific spin and orbital properties of magnetic materials with a time resolution below 100 fs.

The principle of bunch slicing is sketched in figure 1: In the field of a wiggler ("modulator") a femtosecond laser co-propagating with an electron bunch modifies the energy of electrons in the overlap region ("slice"). To extract their radiation, the energy deviation is translated into a transverse parallel shift (figure 1, top) or angular displacement (bottom) in a subsequent undulator ("radiator").

While laser-driven energy modulation has been demonstrated experimentally, sufficient separation of the ultrashort x-ray pulse is another challenging task. For spatial separation, the source must be imaged onto an aperture by a mirror which causes a strong background of non-specularly reflected photons. This can be avoided by employing angular separation where the short radiation component can be extracted by an aperture, provided the angular dispersion is large enough. Synchrotron radiation simulations indicate that the bending angle between modulator and radiator should be at least 100 mrad (5.7°).

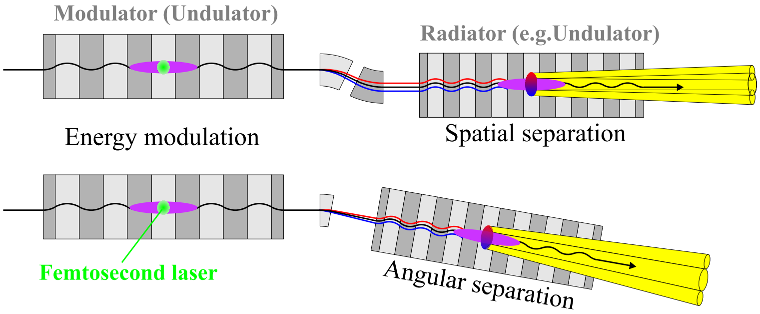

Figure 1: Principle of bunch slicing with spatial (top) and angular (bottom) displacement of energy-modulated electrons. Spatial separation requires a mirror to image the short radiation component that is emitted parallel to the main pulse. In the angular separation scheme, the short pulses are emitted at an angle and can be extracted just by an aperture.

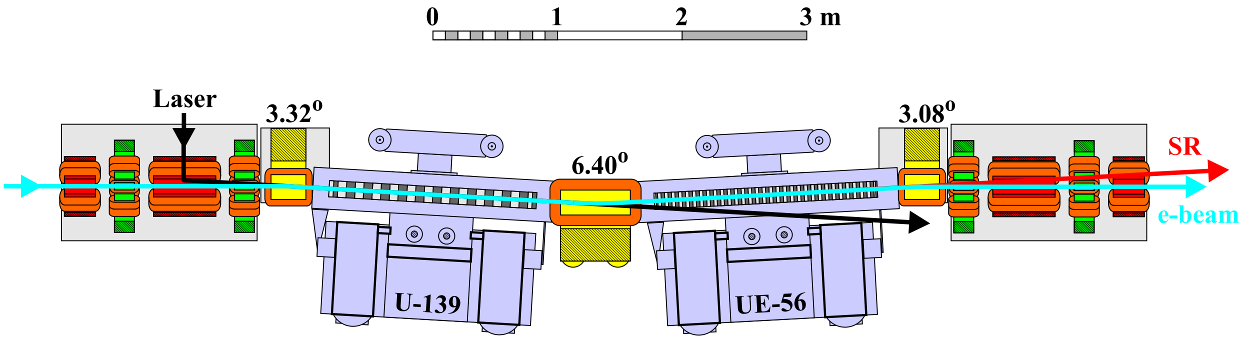

Figure 2: Top view of the magnetic components of the femtosecond source including two undulators (U-139 and UE-56) and three dipole magnets (yellow) with a total length of 5.4 m. The adjacent quadrupole (red) and sextupole magnets (green) are unchanged. The black and blue arrows are the laser and the electron beam, respectively, the red arrow symbolizes synchrotron radiation (SR) from the UE-56.

2. Layout of the Femtosecond Radiation Source

The shortest possible pulse duration is achieved by placing the modulator and the radiator in the same straight section since an achromat between them would cause significant path length differences (e.g. 400 fs for 1% energy deviation). The layout shown in figure 2 fulfills this constraint with minimum impact on the storage ring performance. A closed bump formed by three bending magnets encloses modulator and radiator with an angle of 6.40° between them. Here, the radiator frontend and beamlines are rotated by 3.08° away from the straight section axis. Other arrangements with more elaborate bumps were ruled out because they would intolerably modify the electron beam optics and the machine circumference.

The modulator is a planar undulator of $\lambda_U = 139$ mm period length with sufficient field to match the condition that its wavelength

$$\lambda = \frac{\lambda_U}{2\gamma^2}\left(1 + \frac{K^2}{2}\right)$$

equals the laser wavelength. Here, K is the field parameter, and γ is the electron Lorentz factor. For the laser, a Ti:sapphire system with 800 nm wavelength is the obvious choice. The laser beam enters the vacuum vessel 2 m upstream of the modulator center through a set of remotely adjustable mirrors. Behind the radiator, the laser beam and modulator radiation are both monitored in order to ensure the spatial and temporal laser-electron overlap. Apart from traditional methods, coherent infrared radiation [3] is a potential diagnostics tool which is very sensitive to the density modulation within the electron bunch.

The radiator is the downstream module of the presently installed UE-56/1 [4] which allows one to select any degree of elliptical polarization. Since the angular separation scheme does not involve optical elements, the beamline requirements in this respect are greatly relaxed, but high transmission and minimum pulse lengthening in the beamline must be ensured.

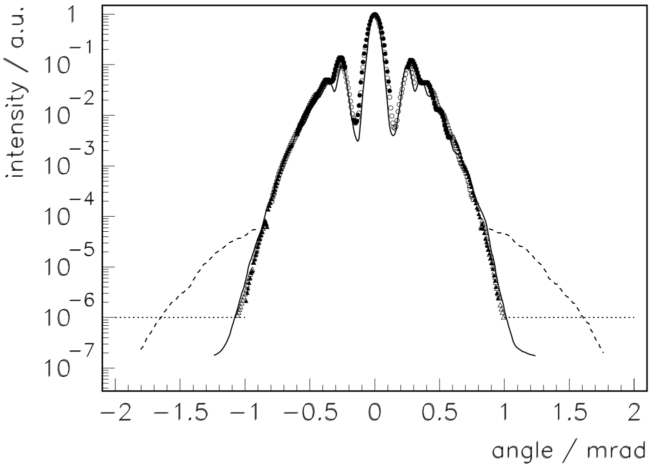

Figure 3: Measured (points) and calculated (solid line) angular radiation characteristics of a UE-56 undulator at 708 eV. Also shown is the calculated short-pulse component (dashed) and the expected background level (dotted) from dipole radiation.

3. Study of Angular Radiation Characteristics

In order to verify the feasibility of angular separation, synchrotron radiation from the downstream part of the UE-56/1 undulator has been studied experimentally and by simulation using the code WAVE [5]. The angular radiation characteristics were measured by horizontal movement of a pinhole 12 m downstream of the source point and changing the electron beam angle in steps of 0.2 mrad. The photodiode signal behind a PGM monochromator tuned to a photon energy of 708 eV was recorded over a dynamic range of 10^6 limited by artefacts from the adjacent bending magnets (figure 3, dotted line). The measured angular distribution closely resembles the simulation result obtained for an idealized undulator folded with an electron beam profile of $6 \cdot 10^{-9}$ radm horizontal emittance (solid line) and with a distribution of energy-modulated electrons (dashed line). The latter was produced by a detailed simulation of the interaction between the electrons and the laser field in the modulator.

The short-pulse photon rate depends on the position and width of the separating aperture, the laser and electron bunch parameters, and on the undulator settings. Assuming a bunch current of 10 mA and a laser with 1 kHz repetition rate and 50 fs pulse duration, the calculation yields typically 10^6 photons per second and 0.1% bandwidth entering the beamline. With a background level of 10^{-6} due to dipole radiation, a signal:background ratio of 10:1 can be expected.

References

[1] A. A. Zholents, M. S. Zoloterev, Phys. Rev. Lett. 76 (1996), 912.

[2] R. W. Schoenlein et al., Science 287 (2000), 2237.

[3] M. Abo-Bakr et al., Phys. Rev. Lett. 88 (2002), 254801.

[4] M. R. Weiss et al., Nucl. Inst. Meth. A467-8 (2001), 449.

[5] M. Scheer, BESSY, unpublished.

A novel fast detector for determining the horizontal source position in dipole beamlines

K.Holldack, D.Ponwitz, W.B.Peatman
BESSY,Albert Einstein-Str.15, 12489 Berlin

Usually dipole beamlines make an optical image of the electron beam on the sample at the experiment. Hence, a horizontal position shift of the e-beam causes a travel of the focus on the sample. Despite the high quality of the rf-BPM based global orbit correction [1] there are residual drifts of the horizontal orbit caused by long term load dependent motion of machine components and other current dependent effects. In addition, there are relatively fast internal sources like the compressors of the He-cryostats of the wavelength shifters which cause a relatively faster residual jitter of the global orbit at about 1.5 Hz. Much faster beam motion at multiples of the 50 Hz line frequency may influence the final signal to noise at the experiment.
Here we present the design and performance of a detector which meets the requirement to measure the horizontal position and motion of the electron beam and enable corrections to be made. It is called TPM (**T**riangular **P**osition **M**onitor): and located in an unused portion of (~4 mrad out of 22 mrad) a standard dipole front end.

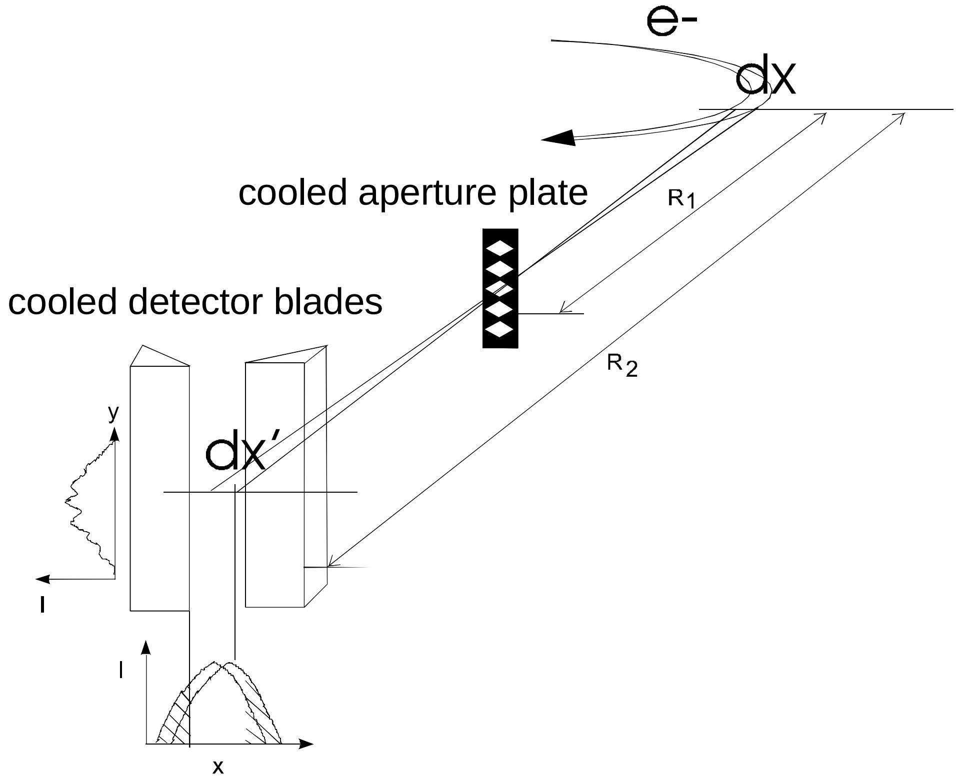

Fig.1 Layout and operation principle of a TPM-monitor. Vertical blades are mounted in the front end on the base of an existing SPM-monitor off-axis at R_2=8.53 m away from the source point. The aperture plate consisting of a vertical array of 31 laser-ablated rhombic structures is upstream at 5m and mounted on water cooled copper frame.

As depicted in figure 1 the detector works by a projection of the source point through a thermally stabilized aperture array located between source point and a blade detector which probes the projection further downstream by photo-emission. The blades are machined from OFHC-copper and withstand the heat load of <1W/100mA as expected at BESSY II dipole magnets for the acceptance of <0.4 mrad transmitted through the apertures. For crosstalk suppression they have to float on -300V to ground.

One easily finds from the geometry in figure 1 that vertical position and displacements and angular changes of the electron beam do not lead to an intensity asymmetry at the detector. This is valid for the case that the vertical dimension of the individual apertures *b* is much smaller than the vertical opening angle of the broadband SR detected by the blades. Only a horizontal displacement *dx* of the electron beam causes a shift *dx'* of the center of gravity of the projection at the detector.

In addition, the TPM exploits the fact that the low emittance of the storage ring leads to a horizontal source dimension of about σ_h~50µm at this location producing a sharp shadow (σ_h<<a , a~2-3mm) of the array of rhombic apertures at the detector. Furthermore, the apertures are machined with an edge accuracy <10µm. Therefore, the position response, which can be measured by a standard difference over sum technique of the two photo emission signals of both blades, depends exclusively on the geometry of the rhombic apertures and its distance to the source point, as derived below for $R_1=R_2$ t.e. $dx=dx'$.

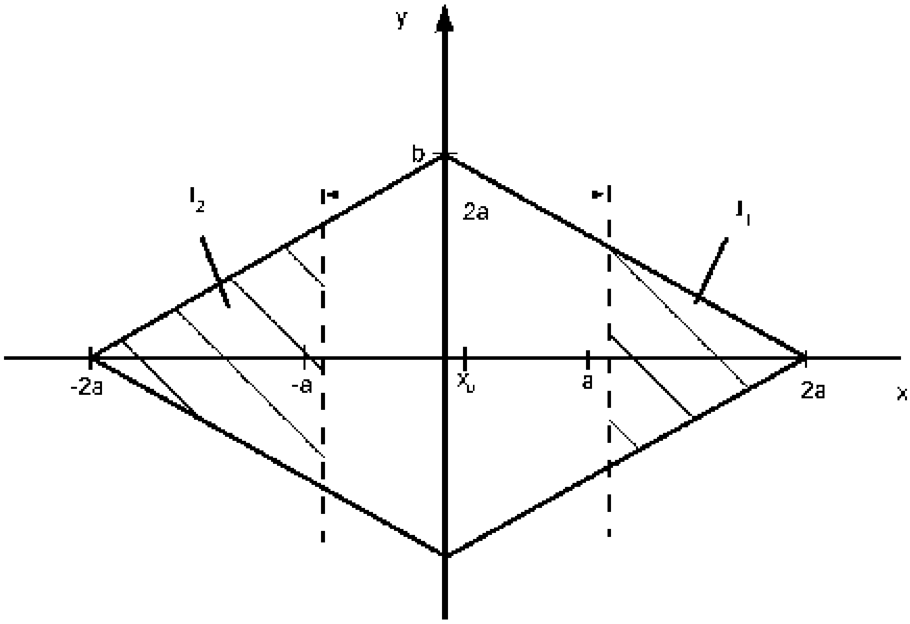

Fig.2 Geometry of the projection of one of the rhombic apertures at the detector distance. The blades integrate the horizontal fan outside a gap of 2a. The photo currents I_1 and I_2 change when the beam is horizontally displaced away from the alignment axis at x_o.

After a short derivation its easy to find that the difference over sum A of both intensities is given by:

$$A=\frac{I_1-I_2}{I_1+I_2}=\frac{-2x_oa}{x_o{}^2-3a^2}=\frac{-2x_o/a}{(x_o/a)^2-3}$$

After substituting $z=x_o/a$ one obtains:

$$\underline{\underline{A=\frac{2z}{3-z^2}}} \qquad x_o << a \Rightarrow \qquad \underline{\underline{A=\frac{2z}{3}}}$$

These quantities are plotted in figure 3 showing the linear range being ~*a*. One finds that in the linear range the position x_o is simply given by $\boldsymbol{x_o=(3/2)aA}$. For a typical value of a=2 mm and the fact that the quantity A is measured with an accuracy $dA \sim 10^{-4}$ a source point shift dx_o of down to 0.3µm can be theoretically detected.

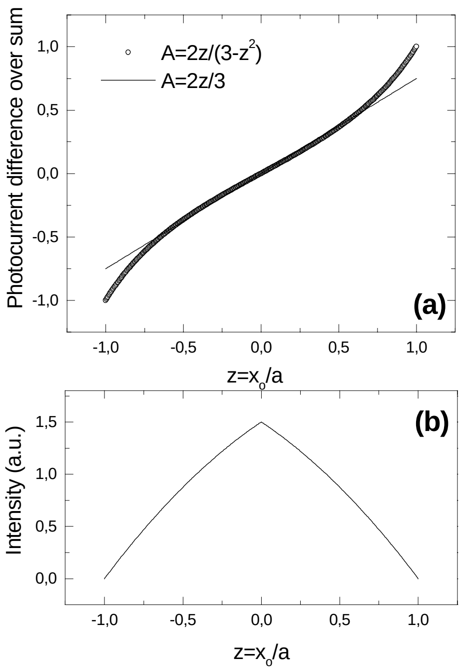

Fig. : (a) Calibration function of the TPM- and (b) SR-intensity distribution at the blades.

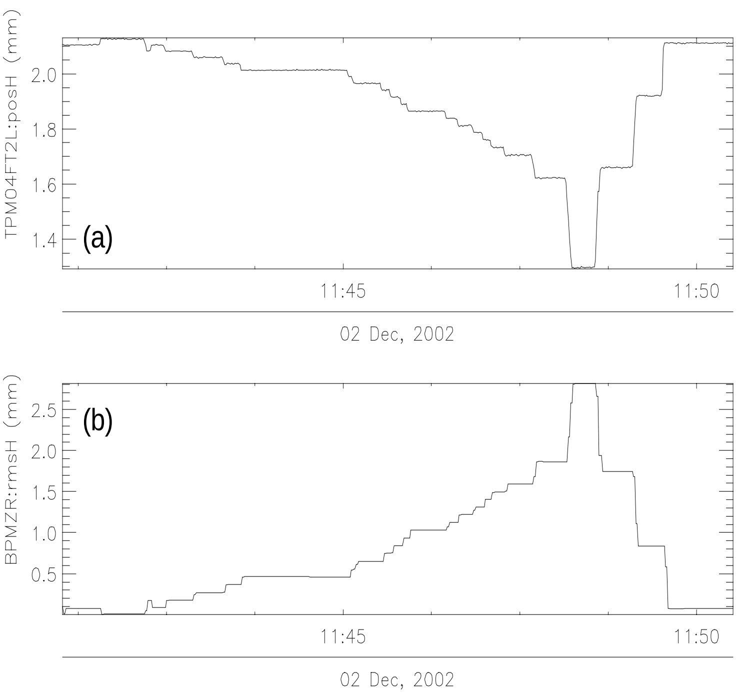

Fig. 4: Cross- calibration example of the TPM (a) with BPMs in the storage ring (b). A strict linear correlation over 2 mm has been confirmed by stepwise variation of a horizontal steering magnet. [2]

A prototype monitor was installed at a 6.7° dipole at section H04 of the BESSY II storage ring using standard optical alignment methods. Here the distance of the aperture array is R_1=5.3 m from the source and the blades are mounted at R_2=8.5 m. The thermal stabilization and electronics as well as the implementation into the control system was done in the same way as for the SPM- and XBPM-monitors [3] around the ring such that the position signal is monitored online at least with the 10Hz sampling rate as given by the control system electronics [4]. Using other electronic hardware a position signal up to 2kHz or even up to 100 MHz can be obtained. The monitor is as reliable and simple as expected and required for front end monitors. It yields a current independent direct information on the horizontal position of the electron beam regardless of the beamshutter status with <1µm resolution. Because it is designed to augment the conventional SPM monitors [3] its installation in all possible dipole front ends is planned. Using two identical monitors at horizontally staggered locations in the SR fan even the angle of the electron beam track being an issue for edge radiation acceptance in the dipole can be determined.

References:

[1] R. Mueller et al. Proc. EPAC 2000, Vienna, Austria, pp.668
[2] the assistance of the machine operators (esp. J.Feikes) is greatly appreciated
[3] K.Holldack et al., Nucl.Instr.Meth. A 467-468 (2001) 213-220
[4] K.Holldack, EPICS-Meeting 2002, Berlin ,http://www-csr.bessy.de/control/Epics02/

XANES Investigations of Baroque Tin-Amalgam Mirrors

Jens Bartoll*, Stefan Röhrs* and Alexei Erko²

*Technische Universität Berlin, Institut für Chemie, Straße des 17. Juni 135, 10623 Berlin
²Bessy GmbH, Albert-Einstein-Str.15, 12489 Berlin

Introduction

Mirrors made of glass and a reflective coating of tin-mercury amalgam were the dominating mirrors from the sixteenth to the nineteenth century. They were made by pressing glass plates onto a tin foil that was covered with a thin layer of mercury before [1]. These mirrors can be found in almost all Baroque castles.

Unfortunately, many of these mirrors suffer from corrosion. The corrosion processes usually start with small black dots within the amalgam layer reaching states where larger areas of the mirror lose their reflective properties. Until now, the mechanisms of these corrosion processes are not fully understood. This is mainly due to the fact that a chemical analysis of the participating components is problematic. Most analytical methods do not have the necessary local resolution to analyse the small spots (µm-range) that represent the beginning of corrosion.

The KMC-2 beam line offers possibilities for XRF mapping and XANES measurements with a resolution in the micrometer range. It is therefore a suitable technique to study the corrosion processes of amalgam mirrors non-destructively.

It was the **aim** of this investigation to analyse spots (µm-range) that represent the beginning of corrosion processes of tin-mercury amalgam mirrors. Micro XRF and XANES measurements were performed in order to identify the elements and compounds (Sn, Hg, Sn-Hg alloys, SnO, SnO_2, HgO) possibly involved in the corrosion processes. The knowledge of these mechanisms will help to find measures to better preserve these art objects.

Materials

Baroque mirror fragments from the former castle in Dresden were studied. Figure 1 shows the backside of one piece with a typical corrosion pattern.

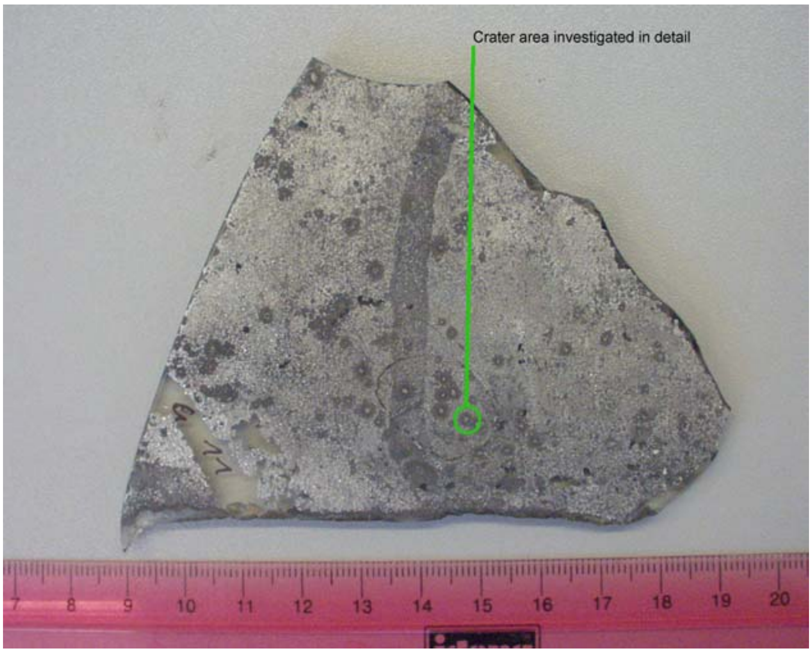

Figure 1: Backside of a shred of an investigated tin-amalgam mirror. The area (corrosion "crater") investigated in more detail is marked by the circle. The scale at the bottom is in cm.

Methods

Two different absorption edges were scanned at the KMC-2 beam line. Energies matching with the Sn L_{III} and Hg L_{III} were used. Measurements at the Sn L_{III} edge were carried out in He environment to prevent absorption of the x-ray by air. Standard materials were measured for the interpretation of the results. Among others the adsorption edges of Sn, SnO, SnO_2, Hg, Sn-Hg amalgam, HgO, and HgS were analysed.

Results

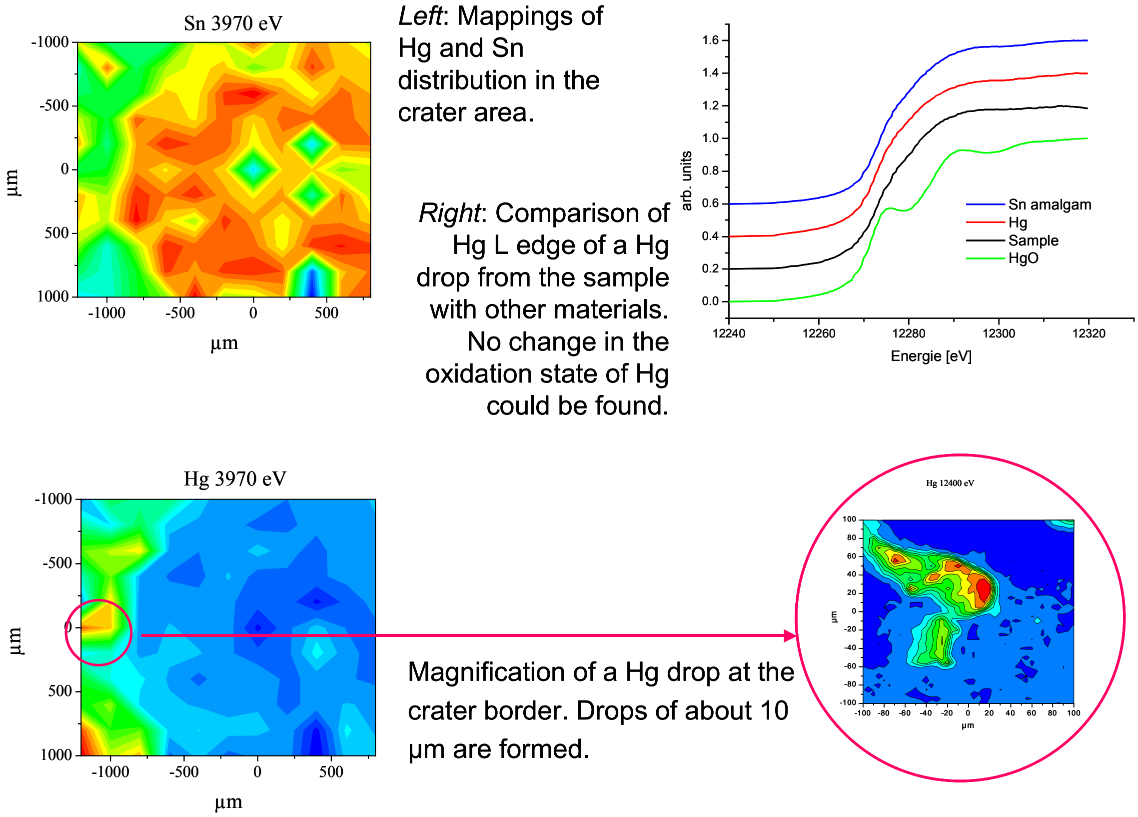

Left: Mappings of Hg and Sn distribution in the crater area.

Right: Comparison of Hg L edge of a Hg drop from the sample with other materials. No change in the oxidation state of Hg could be found.

Magnification of a Hg drop at the crater border. Drops of about 10 µm are formed.

Figure 2: Results of the µ-XRF and µ-XANES investigations at the Hg-L edge.

Using the XRF mapping facility of KMC-2 it was possible to get mappings of the tin and mercury distribution within the corrosion spots of the mirrors in high resolution (see Figure 2 left).

The absorption edges (XANES) of mercury measured for the corrosion areas of the mirrors show that there is no oxidation of mercury involved in the corrosion processes (compare Figure 2, uppermost right). Mercury occurs either as a component of the amalgam or elemental forming small drops.

Figure 3 shows the absorption edges (XANES) of tin measured on different sites within a corrosion area of a mirror. The comparison of the absorption patterns of standard compounds or their superposition to those of the mirror samples allows the identification of Sn-Hg alloys, SnO_2 and possibly SnO. No elemental tin (β-Sn) was identified.

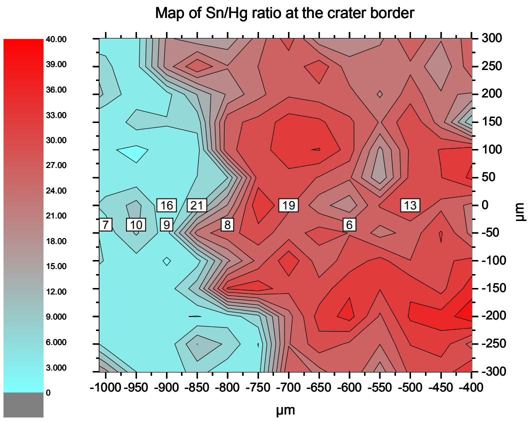

Map of the Sn/Hg ratio with spots investigated marked by numbers

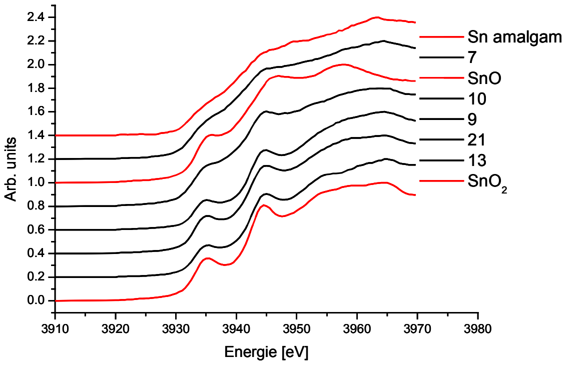

Various different absorption edge spectra were found. Mainly dominated by SnO_2 adsorption edge shapes some spectra show also amalgam or SnO like adsorption edge features.

Figure 3: Results of the µ-XANES investigations of the Sn-L edge at various spots.

Conclusions

Micro-XRF and XANES are suitable tools to investigate corrosion processes of amalgam layers on a microscopical scale.

Sn-Hg alloys, Hg and SnO_2 (possibly SnO, too) could be identified within the corrosion areas studied. Therefore, the corrosion process most probably starts with the escape of Hg from the alloy forming drops on the surface of the alloy layer. The next step would be the oxidation of the Sn remaining behind and still in contact with Hg drops. Most probably, first SnO, then SnO_2 is formed. The mercury drop eventually evaporates leaving behind a "crater" surrounded by SnO and SnO_2, and filled with a thin layer of SnO_2 crystals, which eventually fall out of the "crater".

Taking into account these results a useful measure to prevent the corrosion of tin-mercury mirrors could be the suppression of the evaporation of mercury, e.g., by sealing the back of the mirrors.

The formation of the α-modification of tin at low temperatures (below 13 °C) might be another trigger process for the corrosion. This possibility will be investigated in future.

References

[1] Hadsund P.: Studies in Conservation **38** (1993) 3-16.

NANOMETER-SIZED INCLUSIONS OF SHEET SILICATES IN NATURAL CLINOPYROXENES

Koch-Müller, M.(1), Matsyuk S.(2) and Wirth R.(1)
(1) GeoForschungsZentrum Potsdam, Telegrafenberg, 14473 Potsdam, Germany (mkoch@gfz-potsdam.de),
(2) Institute of Geochemistry, Mineralogy and Ore Formation,
Ukrainian Academy of Science, Pr. Palladina 34, Kiev-252 142, Ukraine

Beside in nominally hydrous minerals such as amphibole, serpentine, mica and talc hydrogen may be stored in nominally anhydrous minerals (NAMs) such as pyroxene, garnet and olivine. NAMs can dissolve traces of OH as point defects. Although the amount of water in these minerals is generally very low (up to 0.1 wt % H_2O), the water content that can be dissolved in NAMs in the upper mantel is large and may exceed the amount of water in the hydrosphere. The presence of water in the earth's crust and mantle has enormous effects on the dynamic of processes of the earth, because the incorporated hydrogen changes the physical properties of the minerals such as the melting point, rheological behavior (hydrolytical weakening) and the transformation kinetics.

An appropriate method for detecting traces of hydrogen in minerals is IR spectroscopy. IR spectroscopy using a conventional laboratory source needs a comparatively large beam size to get an acceptable signal to noise ratio (about 60 µm). However, transmission electron microscope analyses of olivine, showed that the presence of nm-sized hydrous phase inclusions might influence the IR-spectra. To check for the presence of such inclusions in nominally anhydrous minerals, we used the new facilities of the infrared synchrotron beamline at Bessy II. An infrared microscope and interferometer is coupled to the synchrotron beam and allowed us to collect IR spectra with a spatial resolution of 5 x 5 µm.

Clinopyroxene is a major constituent of the earth's crust and mantle. Infrared spectra of clinopyroxenes (cpx) from eclogites exhibit three groups of absorption bands in the OH-region: : group (a) 3445-3465 cm^{-1}, groups (b) 3500 – 3540 cm^{-1} and group (c) 3600 – 3624 cm^{-1}. The bands of group (a) are usually the strongest in the spectra, and they are related to vacancies in the M2 sites (Smyth et al., 1991). To understand what causes the absorption bands of group (b) and (c) we investigated a series of mantle-derived cpx from eclogites by FTIR spectroscopy and transmission electron microscopy. The IR spectra of all our samples showed absorption bands of all three groups with different intensity ratios (Fig. 1).

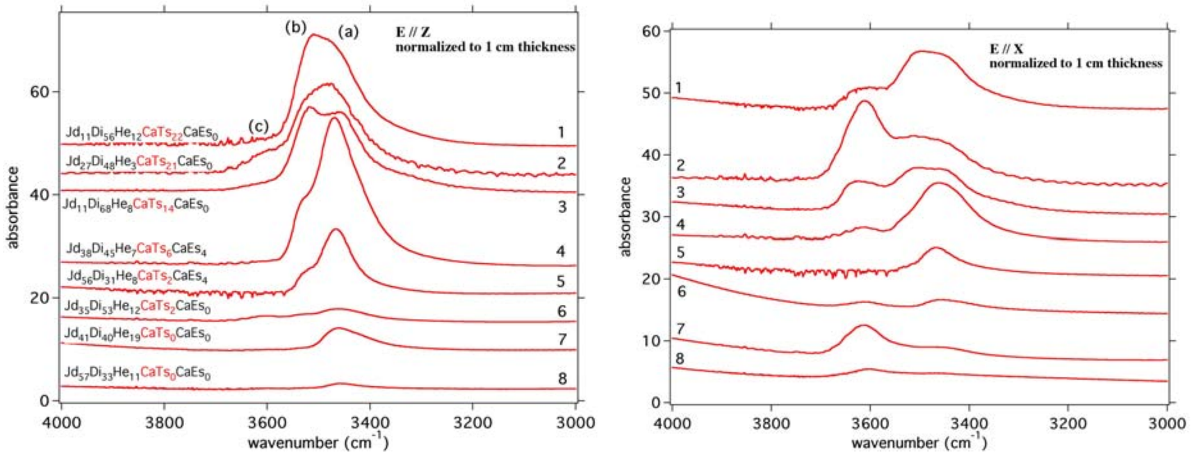

Fig. 1: Polarized infrared spectra of natural clinopyroxenes in the OH stretching region

The intensities and peak positions of the bands of group (b) correlate with the amount of tetrahedrally coordinated Al^{3+} for a series of cpx from three different kimberlite pipes of Yakutia, Russia (Fig. 2).

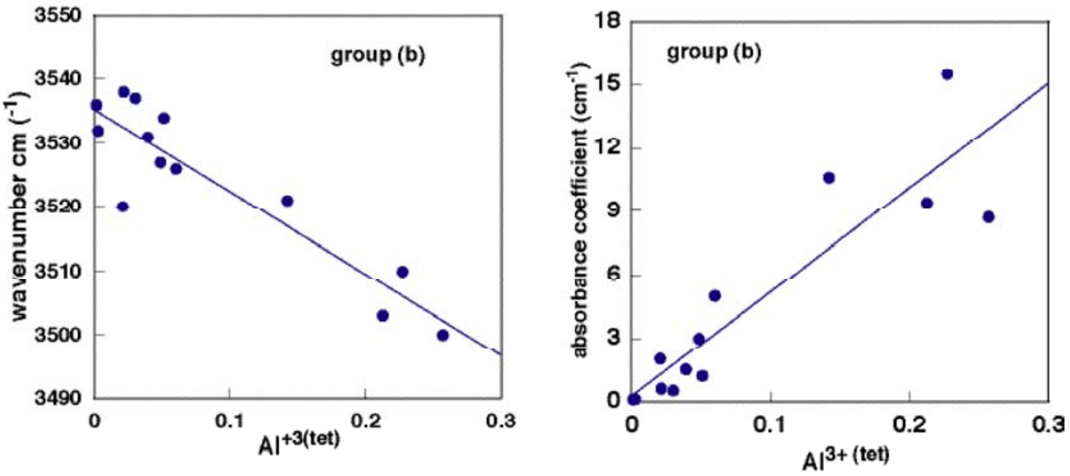

Fig. 2: Correlation of tetrahedrally coordinated Al^{3+} pfu with the absorbance coefficients (cm^{-1}) of the OH bands of group (b).

However, for the bands of group (c), we did not find any relationship between the absorption bands and chemical composition. In seven out of 15 samples the intensities of bands (c) were rather high. When applying synchrotron IR radiation, we realized that the intensities mostly of the absorption bands of group (c) vary extremely within one crystal. The strongest intensities correlate with micrometer to nanometer sized crystalline inclusions in the clinopyroxenes (Fig. 3), but they do also occur in optically clear parts of the crystals. With TEM we identified the inclusions as biotite and clinochlore.

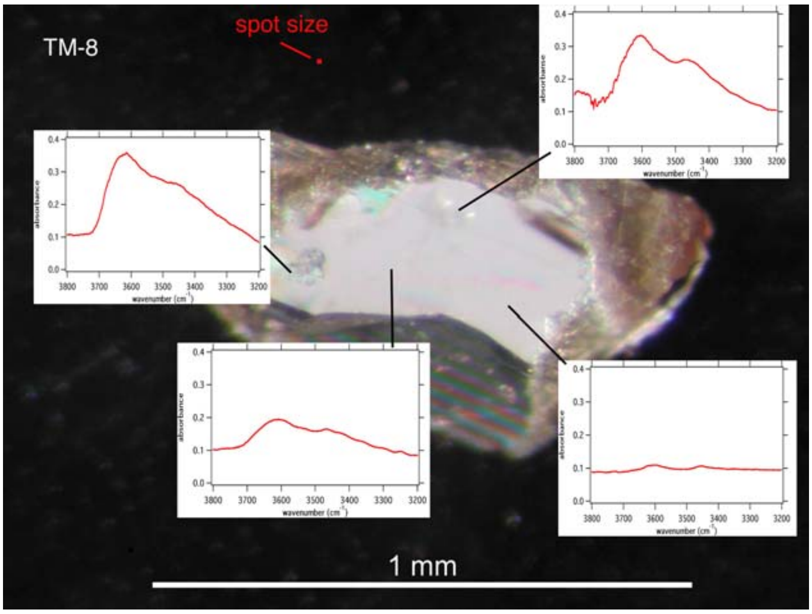

Fig. 3: Picture of the cpx sample TM-8 (0.22 mm thick) showing the position and spot size of the synchrotron IR measurements and the corresponding infrared spectra indicating that at least the OH band of group (c) do not belong

Thus, we could show that the OH groups, which cause the absorption bands of group (c) in clinopyroxene, are not intrinsic. Reported amounts of hydrogen solved in the clinopyroxene structure (e.g., Katayama and Nakashima, 2002) were overestimated. Before speculating about the water budged of the earth, the incorporation mechanism of H and the true amounts of water solved in the minerals need to be known. The results encourage us to setup further investigations of nominally anhydrous minerals using sychrotron IR radiation with its fantastic spatial resolution.

Katayama I., and Nakashima S. (2002) American Mineralogist, 88, 229 –234.
Smyth J.R., Bell, D.R. and Rossman G.R., 1991, Nature 351, 732-735.

BAM*line* meets Dürer and van Eyck: Multi-disciplinary investigation of Renaissance silver point drawings by µ-SR-XRF

I. Reiche[1], A. Berger[2], S. Buck[3], W. Görner[2], T. Ketelsen[4], S. Merchel[2],
M. Radtke[2], J. Riederer[1], H. Riesemeier[2]
[1]Staatliche Museen zu Berlin, Rathgenforschungslabor, 14059 Berlin, Germany
[2]Bundesanstalt für Materialforschung und -prüfung, 12200 Berlin, Germany
[3]Städelsches Kunstinstitut und Städtische Galerie, 50596 Frankfurt/M., Germany
[4]Staatliche Kunstsammlungen Dresden, Kupferstich-Kabinett, 01307 Dresden, Germany

Introduction

Silver point drawings belong to the most precious and rarest treasuries of graphical art collections. They were essentially created during the Renaissance and are characterised by extremely thin grey-brownish strokes on paper necessarily coated before use [1].

Art historical investigations generally allow the attribution of a drawing to a certain artist or school. If their authenticity cannot be identified unambiguously, further information on the works of art can only be obtained by physico-chemical analyses.

These analyses of drawings permit the characterisation of artists' materials and techniques, support restoration and conservation strategies, can help to date and to determine their authenticity and provenance. However, artists' materials used for drawings are poorly known because of mainly two reasons: investigations must be absolutely non-destructive and realised without any direct contact. Furthermore, very little material is deposited on the paper support. For silver point drawings, the areal density is below 100 $\mu g/cm^2$; the total detected mass is below 50 ng of silver. That is the reason why sophisticated analytical methods using synchrotron radiation (or ion beams, i.e. PIXE) are necessary for the study of drawings as they are extremely sensitive, non-destructive and can be realised in air using an excitation spot in the micrometer range [2,3].

The aim of this research project is to obtain a better knowledge of artists' materials to study alteration phenomena and to define a chemical fingerprint for silver point drawing materials of well-known artists in order to create a database for the identification of uncertain drawings. The study is performed by spatially resolved Synchrotron Radiation induced X-ray fluorescence analysis (µ-SR-XRF) at the BAM*line* at BESSY II. So far, results of a few silver point drawings of Albrecht Dürer (1471-1528) were reported earlier [1,2]. Now, we investigated additional drawings from Dürer, and for the first time Jan van Eyck (approx. 1395-1441) and his school. We especially focus in the case of the drawings "Willibald Pirckheimer" (A. Dürer) and "Niccolò Albergati" (J. van Eyck) on the comparison between the silver point used for inscriptions and for the drawing itself. Their comparison can be helpful for the art historical interpretation of these works of art.

Drawings

We studied silver point drawings attributed to Albrecht Dürer:

- "Lazarus Ravensburger und das Türmchen von Liere", "Zwei Mädchen", "Zwei Löwen", "Paul Topler und Martin Pfinzing" from the sketchbook of his journey to the Netherlands in 1520/21 conserved in the Kupferstichkabinett Berlin,
- "Marx Ulstat, die schöne Jungfrau von Antwerpen" and "Der Chor der Groote Kerk in Bergen op Zoom" from the sketchbook of his journey to the Netherlands in 1520/21 conserved in the Graphische Sammlung Städelsches Kunstinstitut Frankfurt am Main,
- "Willibald Pirckheimer" from the Kupferstichkabinett Berlin,
- "Sebastian Brant" from the Kupferstichkabinett Berlin

and to Jan van Eyck:

- "Niccolò Albergati" conserved in the Kupferstich-Kabinett Dresden (Fig. 1a),
- the school of Jan van Eyck "Jacobäa von Bayern" from the Graphische Sammlung Städelsches Kunstinstitut Frankfurt am Main.

Experimental set-up at BAM*line*

We determined major and minor element contents in the silver point lines of the drawings by means of μ-SR-XRF at the BAM*line* [4]. At the BAM*line* set-up a super conducting wavelength shifter with a maximum field of 7 Tesla is used as an X-ray source. For the actual measurements, a W/Si Double-Multilayer-Monochromator (DMM) was used to produce an X-ray beam with an energy of 30 keV with a beam size of 200 x 400 μm^2 . The drawings were fixed on a sample frame in air on a motorized xyz-stage at an angle of 45° to the X-ray beam. Fluorescence signals were detected for 300 s each with a Si(Li)- or HPGe-detector covered with an Al filter at 90° with respect to the incident beam. During measurements drawings could be supervised by a video system and a long-distance microscope. Data evaluation was performed by means of AXIL. Relative concentrations of the silver points were determined after background subtraction using a thin layer approximation.

Results and discussion

Up to 20 points per drawing were successfully analysed using the μ-SR-XRF set-up described above. All drawings are revealed to be realised with silver points. The strokes contain different amounts of other constituents such as Cu, Zn, Sr, Hg, and Pb. Gold was also found in the strokes in some drawings from the school of van Eyck. This element has never been detected in a silver point drawing before. The presence of mercury, a phenomenon that was already evidenced in all the other ancient silver point drawings analysed up to now [1-3], is more likely attributed to an alteration process than to the original composition of the silver point used by the artist.

Drawings attributed to Albrecht Dürer:

All analysed silver point drawings from the Netherlands sketch book by A. Dürer show a similar element composition of the silver strokes corresponding to a silver alloy containing between 4 and 12 wt.% of Cu and traces of Zn. Only one drawing is revealed to have a different composition, the partial drawing of the "man with a fur cap" [2,3].

Preliminary evaluation of the experimental results of the drawing "Willibald Pirckheimer" by Dürer showed that probably the same silver point was used for the realisation of the Greek inscription and the drawing itself. The Dürer monograms are executed with another drawing material as ink for instance. However, the similitude of the composition of the inscription and the portrait indicates that the inscription was created simultaneously to the drawing. Therefore, the inscription can be also attributed to Dürer himself.

Drawings attributed to Jan van Eyck and his school:

Two different types of silver points can be evidenced on the drawing "Niccolò Albergati" (Fig. 1). One stylus corresponding to the strokes of the drawing contains relatively pure silver and only traces of Cu (and Hg). Another silver stylus was probably used for the inscription on the left, above and below the drawing. These strokes contain a relatively large amount of gold. The drawing of "Jacobäa von Bayern" shows a silver point with a typical composition. It contains minor amounts of Cu, but also traces of Hg and Au. In contrast to "Niccolò Albergati", in this drawing the detection of gold could be attributed by microscopic investigations to the presence of extremely small gold particles dispersed on the paper surface.

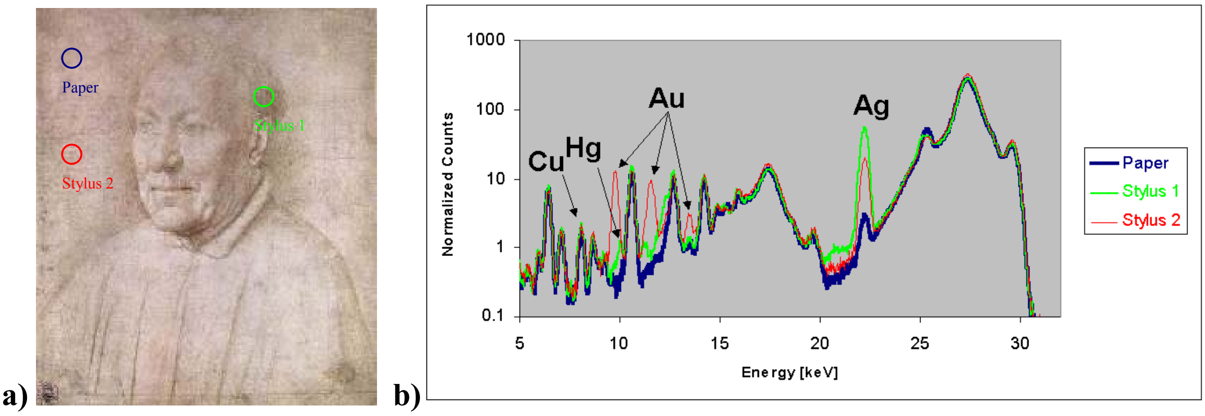

Figure 1. *a) Jan van Eyck drawing "Niccolò Albergati" from the Kupferstich-Kabinett Staatliche Kunstsammlungen Dresden (Inv.n°: C 775) and b) SR-XRF-spectra (30 keV excitation energy) of a silver point line of the portrait and of the inscription on the left compared to the paper backing.*

Conclusion and outlook

µ-SR-XRF investigations are a powerful tool for the non-destructive study of precious silver point drawings. First results of A. Dürer's drawings from his sketch book [2,3] were supplemented by the study of further drawings of the same book conserved in the Kupferstichkabinett Berlin and the Städelsche Kunstinstitut Frankfurt/M. Furthermore, another important complex of drawings attributed to Jan van Eyck and his school was analysed. These investigations evidenced different characteristics of the silver point used by each artist. The results show the potential of physico-chemical analyses for the unambiguous attribution of works of art to a certain artist, a workshop or a particular school, but can also be helpful for the distinction between doubtful parts of a drawing and original ones. Finally, this study illustrates the importance to continue this project for the conservation and understanding of these precious art objects. For the very next future, we are planning to work on more complex drawings of another German artist, Hans Holbein the Ancient.

References

[1] A. Duval, PIXE analysis of metalpoint drawings, 6th International Conference on non-destructive testing, microanalytical methods and environmental evaluation for study and conservation of works of art, 17-20 May 1999, Rome, 1007-1022.

[2] I. Reiche A. Berger, W. Görner, S. Merchel, M. Radtke, J. Riederer, H. Riesemeier, Non-destructive investigation of Dürer's silver point drawings by Sy-XRF, BESSY Annual report (2001) 292-293.

[3] I. Reiche, A. Berger, W. Görner, S. Merchel, M. Radtke, J. Riederer and H. Riesemeier, A closer look at Albrecht Dürer's drawings (1471-1528), BESSY Highlights Annual Report (2001) 32-33.

[4] W. Görner, M.P. Hentschel, B.R. Müller, H. Riesemeier, M. Krumrey, G. Ulm, W. Diete, U. Klein, R. Frahm, BAM*line*: The first hard X-ray beamline at BESSY II, *Nucl. Instr. and Meth.* A 467-468 (2001) 703-706.

Acknowledgements

We gratefully acknowledge the help and support during beam time of H. Bevers, M. Roth, E. Alex, C. Severit, R. Fricke and R. Wittich (Staatliche Museen Berlin, Kupferstichkabinett), Martin Sonnabend and Ruth Schmutzler (Graphische Sammlung, Städelsches Kunstinstitut, Frankfurt am Main) and Olaf Simon (Staatliche Kunstsammlungen Dresden, Kupferstich-Kabinett) as well as the fruitful discussions with A. Duval and H. Guicharnaud (C2RMF, Paris). We would also like to thank BESSY for beam time at BAM*line*. This work was supported by the German Academic Exchange Service (DAAD) and the French Ministry of Research and Education under the contract number (D/0122896).

Fe in silicate glass and melt

M. Wilke, F.Farges[*], R. Bernhardt[**] and G.M. Partzsch[**]

Institut für Geowissenschaften, Universtät Potsdam, Postfach 601553 , 14415 Potsdam, Germany
[*]*Laboratoire des Geomateriaux, Université Marne-la-Vallée, 77454 Marne la Vallée Cedex 2, France*
[**]*Mineralogisches Institut, Universität Heidelberg, INF 236, 69120 Heidelberg, Germany*

In natural magmatic systems, Fe is the most abundant transition element. Due to its heterovalent nature and the different crystal-chemical behaviour of the two Fe species, the ferric-ferrous ratio affects a wide number of physical and chemical properties of melts, such as viscosity, nucleation during crystallization, stability of phases and hence the differentiation trend of magmatic rocks. This study explores the structural environment of Fe in silicate glass and melt by using XANES (pre-edge) and EXAFS. The structure found in the glass represents the structure of the melt as it is frozen in at the glass transformation temperature (T_g). Usually it is assumed that the melt structure at T_g is similar to the one found at higher temperature. Previous studies, however, have found evidence that this assumption may be not be true indicating that relaxation kinetics around T_g may be sufficient to re-organize the melt structure even at high quench rates ([1], [2], [3]). Therefore, XAFS spectra at the Fe K-edge measured on glasses are compared to those measured under in-situ conditions on the melt.

<u>Resolution of spectrometer</u>

For a reliable interpretation of XANES spectra use of a spectrometer with apropriate resolution is certainly needed, i.e. a resolution that is able to significantly deconvolute the Lorentzian peak shape given by the core-hole live time limit. This is especially needed for investigations using the pre-edge region due to the small energy differences of the transitions on one hand and also a better separation of pre-edge features and main edge. As shown in Fig. 1, a Si (220) two-crystal (KMC2, BESSY) or a Si (111) four-crystal monochromator (A1, HASYLAB, E/ΔE=12200) are able to separate all features present in the pre-edge. The spectrum taken with the Si (111) two-crystal monochromator that is now available at KMC2 (BESSY, E/ΔE=4200) is , however, significantly less resolved and does not reveal all pre-edge features.

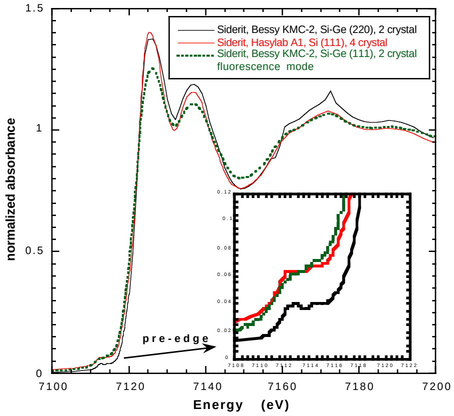

Figure 1: XANES spectra of siderite ($FeCO_3$, octahedrally co-ordinated $Fe^{2=}$) acquired using various spectrometer setups as indicated. Note the effect of spectrometer resolution on the spectra, especially in the pre-edge region. Dotted spectrum is probably affected by self absorption (this should not affect resolution).

<u>High temperature measurements of model compounds</u>

High temperature measurements of model compounds are needed to better evaluate temperature-dependent changes observed in glass/melt systems, i.e. changes in pre-edge intensity and/or position as well as anharmonic effects in the EXAFS region. In-situ high-temperature XANES measurements of silicate melts carried out in air have shown strong changes in the pre-edge indicating changes in redox state and co-ordination of Fe with temperature [4] (Fig. 2), unless these observed changes are not related to any temperature effects on the electronic transitions recorded in the pre-edge region. Therefore, high temperature investigations of model compounds are performed to look at the pre-edge of Fe in a constant co-ordination geometry as a function of temperature. Samples were heated using a Pt-Loop furnace and spectra were recorded in fluorescence mode using the Si-Ge (111) two-crystal monochromator and a photo diode as fluorescence detector. The high temperature XANES of six-fold co-ordinated Fe^{2+} in olivine is shown in Fig. 2. If any temperature effects are present in the pre-edge region they have to be very small as they cannot be revealed using this spectrometer setup. A confirmation of these observations by measurements with a better energy resolution and a fluorescence detector covering a larger solid angle for better signal-to-noise ratio would be desireable.

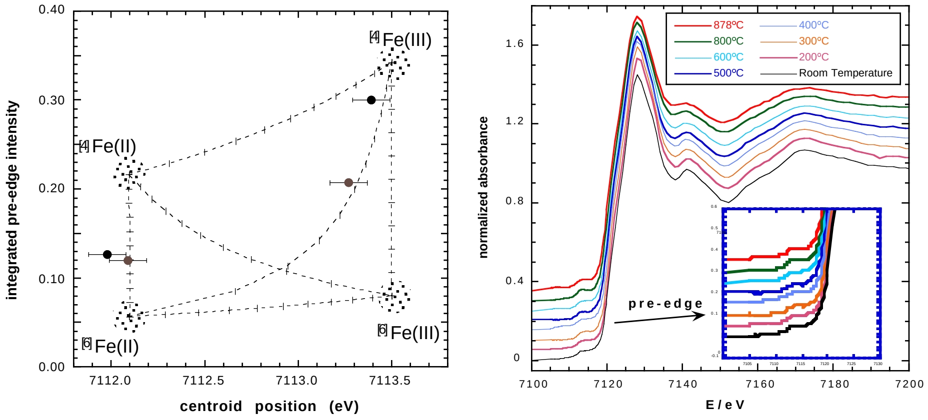

Figure 2: (left) pre-edge intensity and centroid position of Fe in $Na_2Si_3O_7$-glass (grey symbols) and melt at 950˚C (black symbols) on a graph showing the change of pre-edge intensity and position with Fe-co-ordination and redox state as developed from model compounds [5]. (right) XANES of Fe in San Carlos olivine ($Mg_{1.8}Fe_{0.2}SiO_4$) acquired at the indicated temperatures.

Effect of P on Fe in silicate glass

Even in its natural concentration range (< 2-3 wt%) P is known to have considerable effects on Fe speciation in melt as well as on phase stability of iron bearing phases (e.g. Titanomagnetite [9]) and therefore influences liquid-phase relations of basaltic magmas. ([6], [7], [8], [9]). This part of the study explores effects of dissolved phosphorus on the Fe speciation in depolymerized silicate glasses and melts. The pre-edge, analyzed on high-resolution XANES spectra that were collected in parallel, indicates decrease of the Fe-redox state by dissolution of P into the glass, even for samples with high Fe/P ratio [10]. EXAFS measurements performed on the same samples are meant to provide further constraints on possible changes in the co-ordination environment of Fe invoked by P.

We investigated synthetic basaltic glasses (7159V), transitional alkaline in composition, using Fe K-edge XAS spectroscopy to gain information on the local surrounding of iron, and to reveal any changes invoked by dissolution of P. Samples were equilibrated at 1350°C and oxygen fugacities from air to $\Delta FMQ = -1$ (FMQ: fayalite-magnetite-quartz buffer). FeO_{tot}-contents were 14.4 wt% and 6 wt% in order to compare samples with high and low Fe/P ratios. P-free glasses were compared to glasses with P_2O_5 contents of 2.5 wt% (high Fe/P) and 6 wt% (low Fe/P). The oxygen fugacity was controlled by CO/CO_2 gas mixtures. After run duration of 5 hours, the samples were drop-quenched in distilled water. EXAFS spectra were collected at BESSY, beamline KMC2, using the Si-Ge gradient two-crystal (111) monochromator ($E/\Delta E=4200$) and at HASYLAB, beamline A1, using the Si (111) two-crystal setup.

Fourier transforms of the k^3-weighted EXAFS are shown in Fig. 2. For the samples with high Fe-content, only the oxidized show slight changes in the second co-ordination shell upon incorporation of P. Fourier transforms for reduced samples are virtually identical. In contrast, changes related to P for samples with low Fe-content are much stronger. In this case changes for both, first and second co-ordination shell, are significant. The peak of the first co-ordination shell decreases and shifts towards longer distance for both redox conditions. This change may just reflect the change in oxidation state and therefore change of amplitude and phase shift. Currently, it is not clear if these differences may even indicate changes in the topology of the oxygen-environment of Fe. Results of pre-edge analysis do not indicate such changes. Changes in the second co-ordination shell might indicate association of P with Fe as previously suggested by [9].

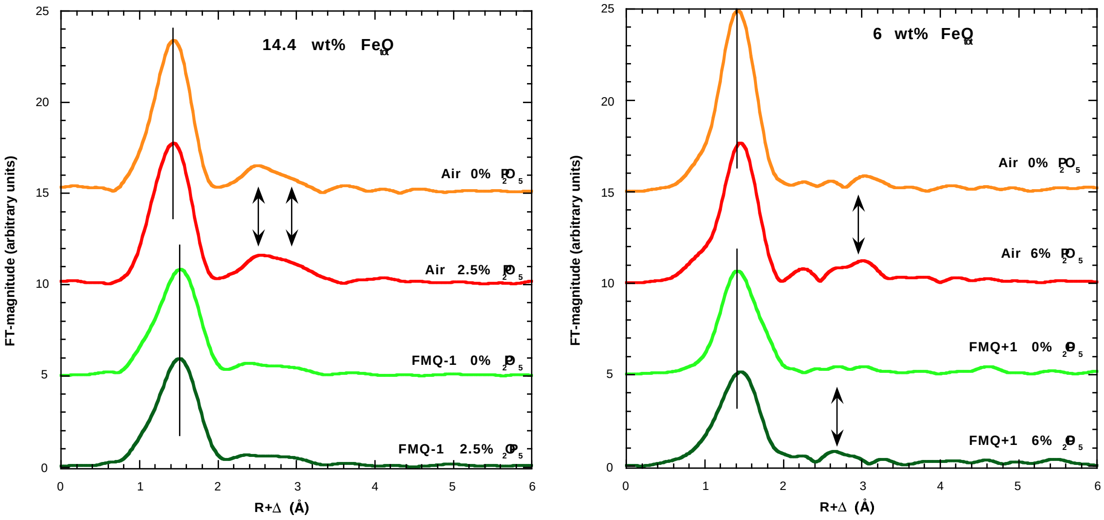

Figure 3: Fourier transforms of k^3-weighted EXAFS for basaltic glasses with varying Fe/P ratio (left high Fe/P, right low Fe/P).

The technical support by A. Erko during beamtime is highly appreciated.

References

[1] Farges, F., Hao Gan, Rehr J.R., Brown G.E. Jr, Navrotsky A. Geochim. Cosmochim Acta 60, 3055-3065 (1996)

[2] Farges, F., Waychunas, G.A., Brown Jr G.E., Calas G., Galoisy L. Geophys. Res. Letters 21, 1931-1934 (1994)

[3] Jackson W.E., Mustrede Leon M., Brown G.E. Jr., Waychunas G.A., Conradsen SD, Combes J.M. Science 262, 229-233 (1993)

[4] Wilke, M. Partzsch G.M., Farges F., Bernhardt R. HASYLAB Annual Report (2002)

[5] Wilke, M., Farges, F., Petit, P.E., Brown, Jr., G.E., Martin, F. Am. Mineral., 86, 714-730 (2001)

[6] Mysen BO, Chem. Geol., 98, 175-202 (1992)

[7] Gwinn R, Hess PC, Contrib. Mineral. Petrol., 113, 424-435 (1993)

[8] Toplis MJ, Dingwell, DB, Libourel G, Contrib. Mineral. Petrol., 117, 293-304 (1994)

[9] Toplis MJ, Libourel G, Carroll M, Geochim. Cosmochim. Acta., 58, 797-810 (1994)

[10] Wilke, M., Bernhardt, R., Partzsch G., HASYLAB Annual Report (2002)

Biological Experiments with the Transmission X-ray Microscope

C. Knöchel, P. Guttmann, S. Gleber and G. Schmahl

Institute for X-Ray Physics, Georg-August-Universität Göttingen,
Geiststr.11, D-37073 Göttingen, Germany

Introduction

In this work, we present biological experiments performed with the new designed transmission X-ray microscope installed at the undulator U41 at BESSY II [1]. For these experiments, a micro zone plate of 25 nm outermost zone width and a rotating condenser for dynamical aperture synthesis [2] are used to image biological samples in the soft X-ray range. Biological investigations, which started at the BESSY I bending magnet microscpe, are continued to proof the capabilities of the new system, especially the higher resolution and the more homogeneously illuminated field of view.

PtK2-Cells

Kidney cells from a rat kangoroo (PtK2 cell line) were imaged at BESSY I to study the cell cycle and the cytoskeleton [3]. Using the BESSY II microscope, chemically and cryogenically fixed PtK2 cells have been investigated. Figure 1 shows X-ray micrographs of glutaraldehyde fixed cells imaged at room temperature.

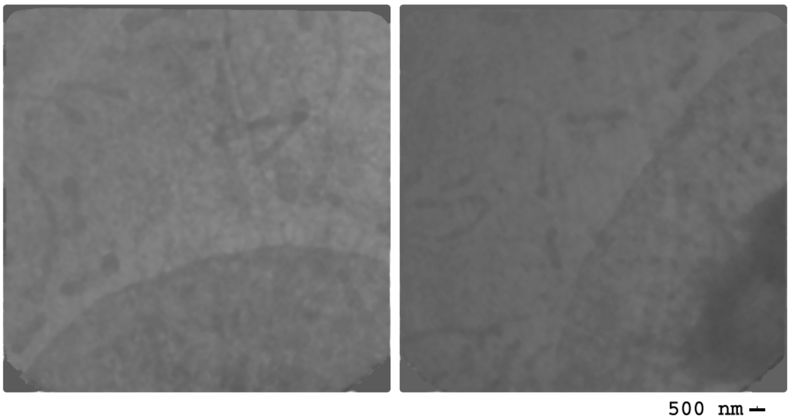

Fig 1: Chemically fixed PtK2-cells

The cell nucleus and parts of the endoplasmatic reticulum and the cytoskeleton are resolved without staining. A power spectrum analysis of the X-ray micrographs shows a cutoff frequency corresponding to smallest structures of under 25 nm in the object.

Drosophila Melanogaster Cells

Embryotic Drosophila Melanogaster cells (SL2 cell line) were studied at BESSY I in respect of the dosage compensation complex [4]. At BESSY II unfixed, initially living SL2 cells, chemically fixed SL2 cells and cryogenically fixed SL2 cells have been investigated.

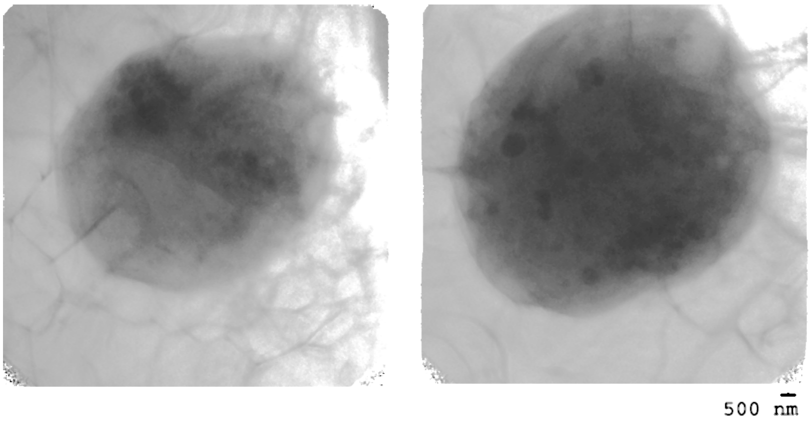

Fig 2: Cryogenically fixed SL2 cells

In figure 2, X-ray micrographs of cells fixed in liquid nitrogen and imaged at cryogenic temperature are shown. Salt structures in the ice occur due to the freezing process. The nucleus, vesicles and membranes are visible and there is no structural damage as in X-ray micrographs taken at room temperature apparent.

Diatoms

Using stereo imaging techniques, further spatial information can be derived from images taken at different angles. Three dimensional distances can be calculated from the displacement of characteristic structures in the images of tilted objects. Figure 3 shows X-ray micrographs of Diatoms imaged under an angle of 17° at BESSY II.

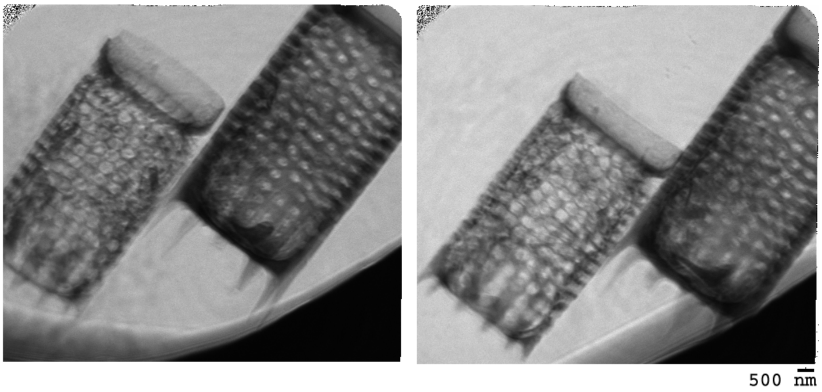

Fig 3: Diatoms imaged under different angle

Conclusion

Experimental techniques developed at BESSY I have been adapted to the new transmission X-ray microscope with its better optical properties. The better resolution, the more homogeneously illuminated field of view and the higher monochromaticity have been demonstrated.

Acknowledgements

We would like to thank T. Gronemann, J. Herbst, P. Nieschalk and J. Wegener for expert technical help and the staff of BESSY II for excellent working conditions. This work has been funded by the German Federal Minister of Education and Research (BMBF) under contract number 05KS1MG1/9.

References

[1] P. Guttmann et al “The transmission X-ray microscope at BESSY II”, XRM 2002 proceedings, Journal de Physique IV, Vol 104 (2003)
[2] B. Niemann et al “Concept and Realization of the novel rotating condenser-monochromator at the Göttingen TXM at BESSY II”, XRM 2002 proceedings, Journal de Physique IV, Vol 104 (2003)
[3] O. Methe et al “Transmission X-ray microscopy of intact hydrated PtK2 cells during the cell cycle”, Journal of Microscopy, Vol. 188, Pt 2 (1997), 125 – 135
[4] S. Vogt et al “X-Ray Microscopic Studies of the Drosophila Dosage Compensation Complex”, Journal of Structural Biology, 132, (2000) 123 – 132

Bond breaking by inner shell excitations

B. Naydenov, K. Eberle, R. Schneider, S. Rohrmoser, D. Menzel, P. Feulner
Physikdepartment E20, Technische Universität München, D-85747 Garching
S. Wada and K. Tanaka,
Department of Physical Science, Hiroshima University, 1-3-1 Kagamiyama, Higashi-Hiroshima 739-8526, Japan

In this contribution we report three selected results obtained in 2002 at the U41-PGM beamline, using the single bunch as well as the multiple bunch modes. In the single bunch period we focused on photon stimulated ion desorption by core electron excitations from chemisorbates, and on spectroscopy of threshold electron. The multi bunch studies were dedicated to the determination of kinetic energy distributions (KEDs) of photodesorbed ions under both high photon and high KE resolution, and to photon stimulated desorption of neutrals from self assembled monolayers (SAMs).

In previous investigations we have shown that inner shell excitations of chemisorbates on metals stimulate desorption of ions and neutrals. Whereas neutrals dominate for all one electron excitations and are therefore important products for any kind of bond tailoring, ions can be useful probes for multi electron states /1,2/. Because the electronic character as well as the energy of these highly excited states is only weakly affected by adsorption, PSD of ions can provide important information on molecular properties. In particular the KEDs turned out to be useful fingerprints of the excitation types /1/. Using a previously described linear TOF assembly for their discrimination /3/, we have extended the database for the molecules N_2 and CO for different substrates and a wide energy range. As an example, we show in Figs.1,2 data obtained for perpendicularly chemisorbed N_2 by N1s excitation (A_z light). This polarization is interesting because the σ^* resonance, a one electron state, and multi electron states appear in the same energy range. Fig.1 shows the N^+-yield as a function of $h\nu$ for isolated /4/ and chemisorbed N_2, and Fig.2 the KEDs of the N^+ ions from the chemisorbate. For the isolated molecule, the polarisation resolved N^+ yield /4/ is dominated by the [N1s]σ^* transition (Fig.1). For chemisorbed N_2, the ion signal in this energy range is extremely low. Only for photon energies beyond 20 eV we find a strong increase with weak maxima around 22 and 33 eV (Fig.1). From the shape of these spectra no clear discrimination of electronic states is possible. An analysis of the KEDs helps to entangle them. Below the N1s threshold N^+-PSD is due to multiple valence excitations. In the KED, they appear as a broad peak with a maximum around 3 eV and a tail extending up to 15 eV. These valence contributions do not show strong dependences on photon energy. Because we are not interested in them in our present study, we have subtracted their contributions from all other curves in Fig.2. Within the range of the σ^* resonance, 3 different core induced features of the KEDs remain after this subtraction. A maximum around 10eV KE is the signature of one electron core excitations. A very similar spectrum is obtained for excitation of the π-resonance by A_{xy} light (not shown). With respect to the large photon absorption cross section it is very weak, reflecting the strong quenching of ionic products by rapid electron transfer from the substrate. The high KE indicates that only highly dissociative decay states contribute (satellites or states with inner valence holes – coincidence measurements are presently not possible due to the small signals). At 14 eV above the π-resonance and beyond we find a second contribution in the KEDs with very low kinetic energy. It is due to two electron excitations appearing in this energy range. Majority channels of core decay provide sufficient positive charge for ionic final state products. The very different shape of the one and two electron contributions allows to untangle them. Between 19 and 24 eV the N^+ yield (Fig.1), as well as the width of the maximum at low KE increase (Fig.2). We explain this as due to the onset of three electron excitations. A very similar behavior has been observed for A_{xy} light. For even higher photon energies excitations of more than 3 electrons become possible and the widths of the KEDs increase further (Fig.2). The change, however, is gradual. Distinct thresholds cannot be discriminated. At very high photon energies, in the range of multiple shake-off processes, we obtain a KED resembling that of the subthreshold region, although with larger yield.

As shown, KEDs of ions desorbed by innershell excitations can vary drastically reflecting different mixtures of contributiong states. But even the KED for a single primary state can vary as a function of the photon energy. Our examples are the threshold resonances of ammonia and water. Both resonances are of the type core-to-4a_1, and for both molecules these states show ultrafast dissociation (UFD) in the gas phase, i.e. bond breaking before core decay, as demonstrated by the appearance of atomic lines in the decay spectra /5,6/. If for a system exhibiting UFD the excitation energy is varied across the resonance, the KE of the fragments resulting from late decay varies simultaneously, as determined from Doppler shifts of atomic lines in the decay spectrum (see, e.g., /7/).

For chemisorbed and condensed molecules the situation is more complicated. To the best of our knowledge, no atomic lines have been found as yet for these systems, although numerous efforts have been made. For chemisorbates this may be due to the very fast electron transfer which modifies the core state before decay, leading to overlapping channels and very broad spectral features. For condensed water and ammonia the deviations from the gas phase are less clear. UFD due to core-to-LUMO excitations would create neutral hydrogen atoms. However, no enhanced emission of H was found from condensed H_2O and NH_3 /8/. Instead, increased emission of H^+ occurs, which by AEPICO was shown to be coincident with spectator electrons, i.e., core decay precedes dissociation /9,10/. These findings have been explained by condensation induced modifications of the excited state, which reduce its antibonding character with respect to the gas phase /9,10/. Even if the core decay occurs before dissociation, however, tuning over the resonance will vary the fragment energy if $\Delta h\nu$ is neither exclusively transferred into the energy of the decay electrons, nor into excitations of the matrix. Fig.3 shows results for ammonia. Scanning the excitation energy across the core-to-LUMO resonance we find a continuous shift of the H^+ KE. Results for water (not shown) are very similar.

The last experiment which we report here was dedicated to site selective bond breaking. Methyl and ethyl ester terminated SAMs exhibit dramatic site selectivity in photon stimulated ion desorption (PSID). For the [C1s]σ^*(O-CH_3, O-C_2H_5) state, the desorption of CH_n^+, CD_n^+ (for partly deuterated molecules), and $C_2H_m^+$, respectively, is strongly enhanced /11/. The large photon flux of the U41-PGM and our sensitive detector for neutrals /8/ made investigations of PSD of neutrals possible for the first time, The results are surprising. For all samples under investigation (the same as in ref.11), decreased site selectivity, and increased desorption by primary and secondary valence excitations was found in the neutral channel. Although further investigations are needed, the importance of neutral products even for these - in comparison with chemisorbates on metals - weakly coupled systems is evident.

Acknowledgement

We thank the staff of BESSY, in particular C. Jung, for help during the experiments, and Z.W. Gortel for helpful discussions. Support by the Deutsche Forschungsgemeinschaft (project Me 266/21-2) and by the German Israeli Foundation (GIF; project I-557-217.05/97) is gratefully acknowledged.

1. P. Feulner et al., Surface Rev. Lett. 9 (2002) 759.
2. D. Menzel and P. Feulner, J. Phys.: Condens. Matter 13 (2001) 11249.
3. Weimar et al., Surf. Sci. 451 (2000) 124.
4. E. Shigemasa et al., Phys. Rev. A66 (2002) 022508.
5. I. Hjelte et al., Chem. Phys. Lett. 334 (2001) 151.
6. I. Hjelte et al., Maxlab Activity Report 1999.
7. see, e.g., for the HF, DF case: K. Wiesner et al., Chem. Phys. Lett 354 (2002) 382, and references therein.
8. R. Romberg et al, Surf. Sci. 451 (2000) 116.
9. K. Mase et al., Surf. Sci. 451 (2000) 143.
10. M. Nagasono et al., Surf. Sci. 390 (1997) 102.
11. S. Wada et al., Surf. Sci, (in press, SUSC 13264)

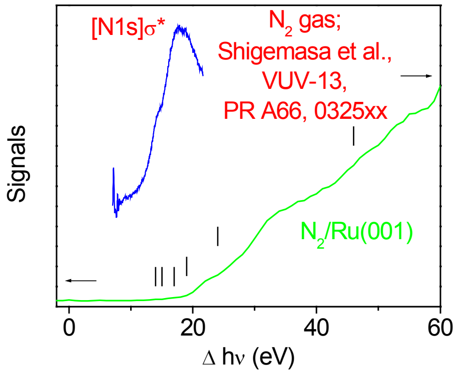

Fig.1 (top): N$^+$ yield for [N1s] excitation by A$_z$ light from isolated N$_2$ molecules (blue) /4/, and from N$_2$ chemisorbed on a Ru(001) surface (green). Excitation energies are given with respect to the π-resonance. Kinetic energy distributions (KEDs) obtained for the photon energies indicated by vertical bars are displayed in Fig.2.

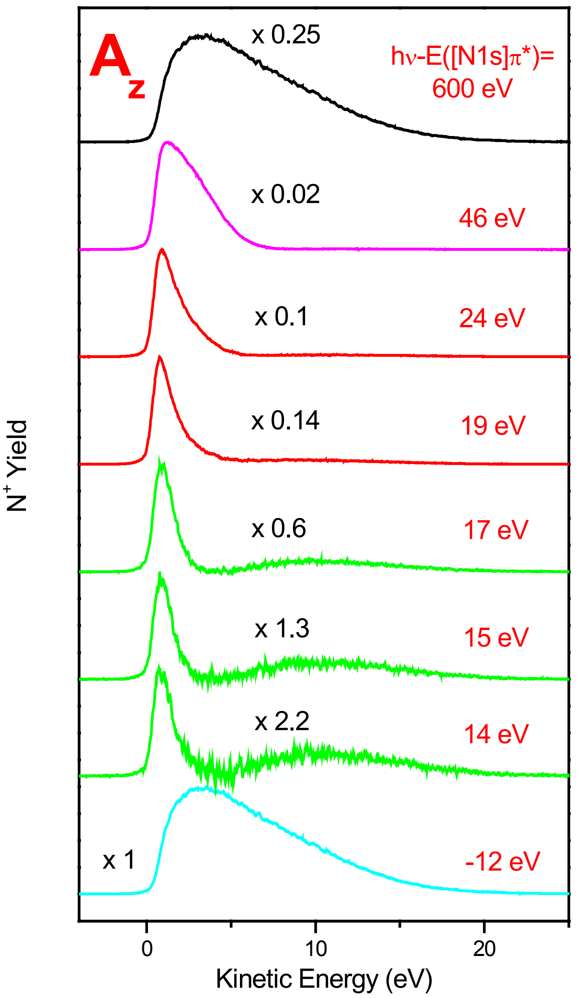

Fig.2 (right): KEDs obtained from N$_2$/Ru(001) for selected photon energies. The background due to multiple valence excitation (cyan trace) has been subracted from the data obtained beyond the N1s threshold.

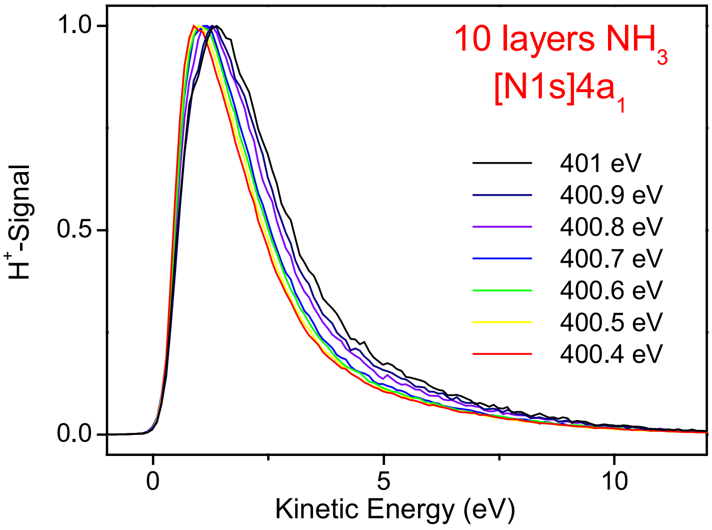

Fig.3: KEDs of H$^+$ ions from multilayers of ammonia desorbed by the [N1s]4a$_1$ core-to-LUMO transition as a function of the photon energy. The spectra have been normalized.

Studies of Clay and Soil Samples with the New Transmission X-Ray Microscope at BESSY II

J. Thieme, P. Guttmann*, S.-C. Gleber

Institut für Röntgenphysik, Georg-August-Universität Göttingen, Geiststraße 11, 37073 Göttingen, Germany
*Institut für Röntgenphysik, Georg-August-Universität Göttingen, c/o BESSY, Albert-Einstein-Straße 15, 12489 Berlin, Germany

1. Introduction

Soils are penetrated by lithosphere, hydrosphere and atmosphere and therefore very heterogeneous media. Its fabric consists of a pore system, which determines the inner surface within a soil. Pore radii range from mm to sub-µm, where radii of some µm or less are the most frequent, thus contributing to the largest part of the inner surface. These micro pores are mainly built up by colloidal particles such as clays, quartz particles, iron and aluminium oxides, or organic particles as bacteria, fungi, humic substances, xenobiotica etc. The inner surface affects many important soil parameters as turnover of nutrients, adsorption of toxicants, bioavailability of these substances, water storage capacity and water flow. Therefore, it is of great importance to have a close look at the microstructure built up by these colloids. Due to the size of the particles and as nearly all chemical reactions occur in aqueous phase, X-ray microscopy is a technique very well suited for these purposes [1].

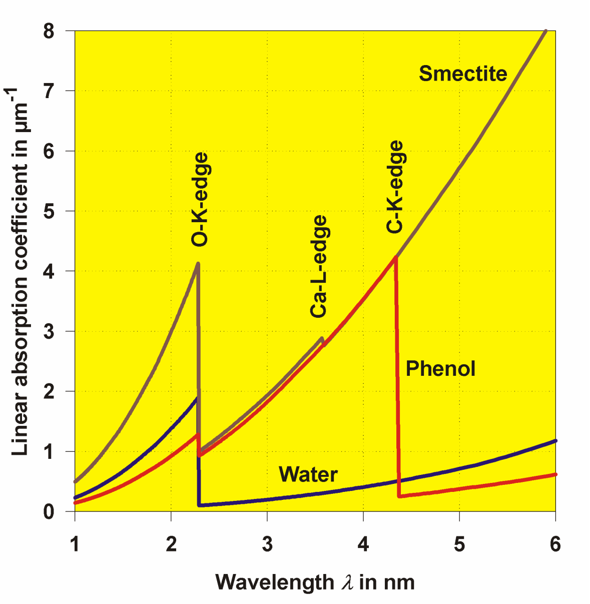

Figure 1: The linear absorption coefficient µ is plotted as a function of wavelength for three different substances, i.e. water, the clay mineral smectite and phenol as an organic molecule. Important absorption edges of oxygen, calcium, and carbon are indicated.

2. Results

Clay and soil samples have been imaged with the new transmission X-ray microscope (TXM) at the undulator U41 [2]. The aim of this study was to prove, that imaging of specimens from the environment in aqueous dispersions is possible with this new design. Two clay samples, Na^+-montmorillonite and nontronite, and three soil samples, chernozem, gleysol, and luvisol, have been imaged. The images clearly show the new, high quality of X-ray images taken with this new TXM. Using the rotating mirror condenser the monochromaticity of the radiation has been improved to $\lambda/\Delta\lambda = 2000$, which results in a better clarity of the images [3]. A micro zone plate with $dr_n = 25$ nm has been used as microscopic objective, improving the resolution noticeable. As a result, single particles within the flocks can easily be identified.

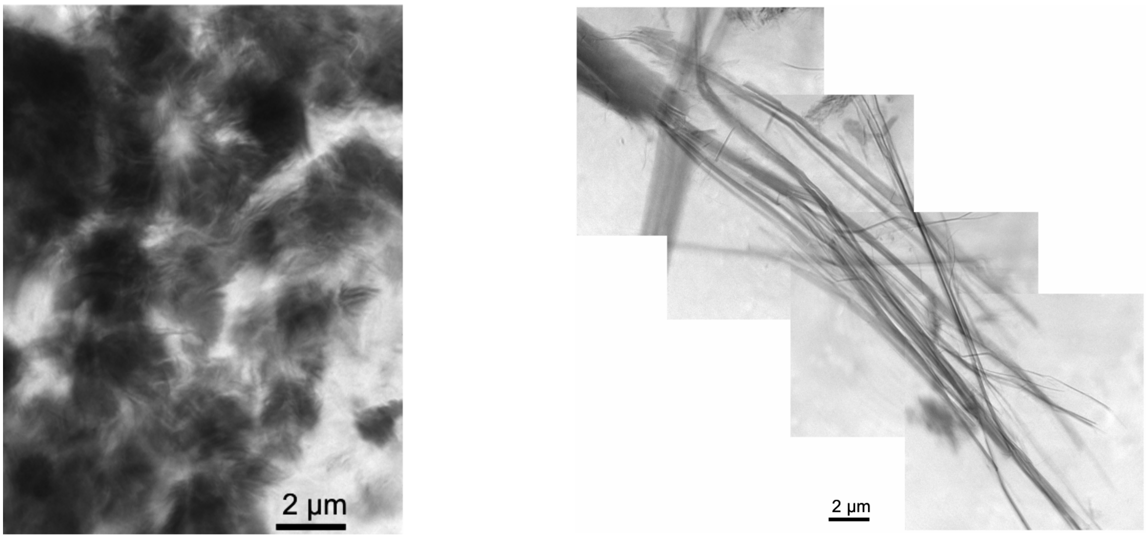

a)

b)

Figure 2: X-ray micrographs of flocks of two clay samples, Na^+-montmorillonite (a) and nontronite (b), both in aqueous dispersion. Figure 1b is composed of four X-ray micrographs

The clay samples have been chosen to demonstrate the great variety in shape of clay particles. Na^+-montmorillonite consists of small particles stacked together whereas nontronite particles are much larger in size, forming structures much more open.

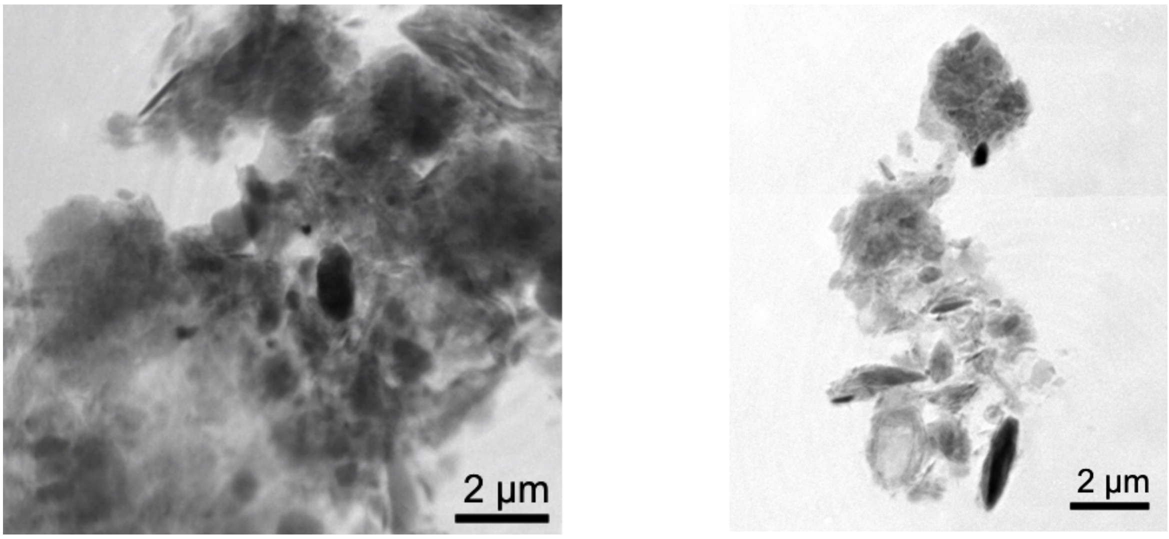

Figure 3: X-ray micrographs of flocks of a Chernozem soil.

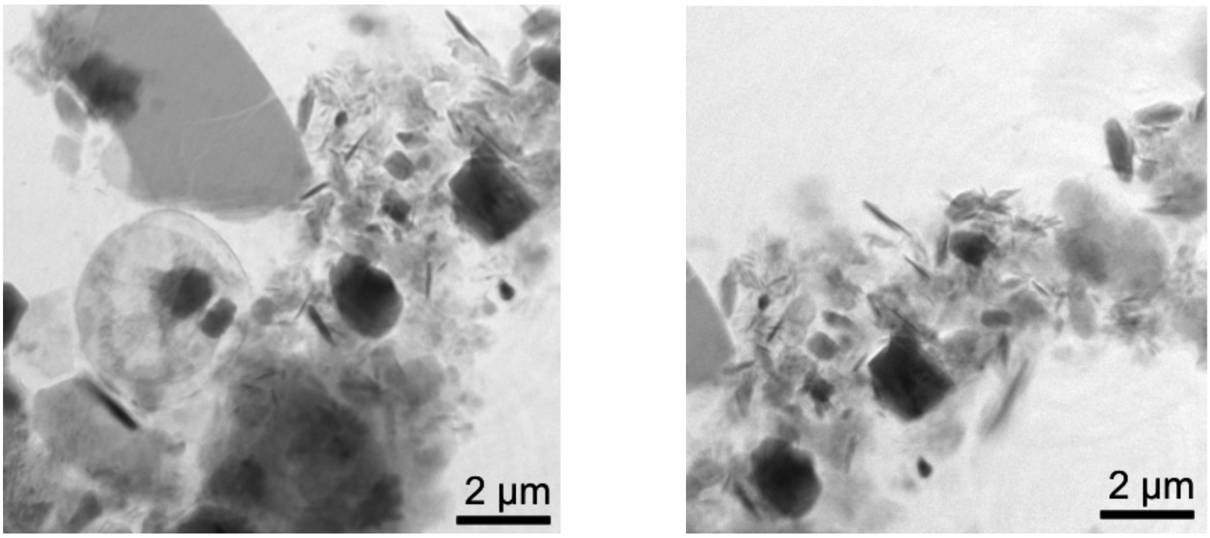

Figure 4: X-ray micrographs of flocks of a Gleysol soil.

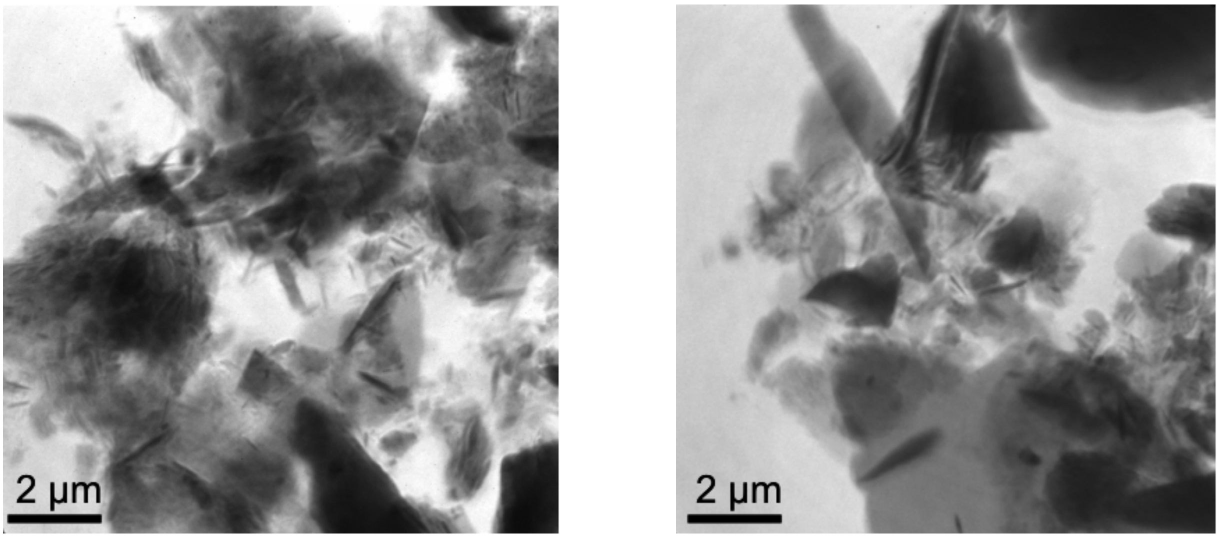

Figure 5: X-ray micrographs of flocks of a Luvisol soil.

The soil samples show that in the colloidal range flocks of particles feature many different appearances. The trained eye, however, quickly identifies in each sample particles of similar shapes. In this size range all samples mainly consist of clay particles making these similarities comprehensible. In addition, micro organisms are very often attached to the flocks. They can be found in the images as ellipsoidal or round shapes with a distinct membrane.

3. Outlook

The proof of principle has been achieved successfully. Therefore, the following projects from the fields of soil science, hydrogeology, and water technology will be addressed with X-ray microscopy in the future: The interaction of organic and inorganic colloids will be studied. Here, the new scanning transmission X-ray microscope will play an important additional role due to its capability of obtaining spatially and spectroscopically resolved data at the same time [4, 5]. The study of colloid bound transport processes will help to address issues of transport of substances in soils and groundwater aquifers. Soils build complex environments with large amounts of microorganisms. Especially soil colloids form together with bacteria the so-called micro-habitats. Viability, activity and mobility of bacteria are strongly dependent on their attachment to surfaces of soil particles. This adhesion leads to a flocculation of soil components, which again influences the soil structure and its stability. X-ray microscopy is a well suited method to study these processes. Last but not least, there is a great variety of anthropogenic influences on these ecosystems, which also can be examined by X-ray microscopy.

4. Acknowledgments

This work has been supported by the Federal Minister of Education and Research (BMBF) under contract number 05KS1MG1/9. We would like to thank the staff of BESSY for providing excellent working conditions.

5. References

[1] Thieme, J., Schmidt, C., Abbt-Braun, G., Specht, C., Frimmel, F.H., „X-ray microscopy studies of refractory organic substances“, in: Refractory Organic Substances in the Environment, Frimmel, F.H. et al. Eds. (Wiley-VCH, Weinheim, 2002) 239-248

[2] Guttmann, P., Niemann, B., Rehbein, S., Knöchel, C., Rudolph, D., Schmahl, G., “The transmission X-ray microscope at BESSY II“, J. Phys. IV, Vol 104 (2003)

[3] Niemann, B., Guttmann, P., Rehbein, S., Knöchel, C., “Concept and realization of the novel rotating condenser-monochromator at the Göttingen TXM at BESSY II”, J. Phys. IV, Vol 104 (2003)

[4] Wiesemann, U., Thieme, J., Guttmann, P., Früke, R., Rehbein, S., Niemann, B., Rudolph, D., Schmahl, G., “First results of the new scanning transmission X-ray microscope at BESSY II“, J. Phys. IV, Vol 104 (2003)

[5] Wiesemann, U., Thieme, J., Guttmann, P., Früke, R., Rehbein, S., Niemann, B., Rudolph, D., Schmahl, G., „Commissioning of the new scanning transmission X-ray microscope at the undulator U41”, this report

Magnetization profiles of single Co layer in a Cu/Co/Pt sandwich

E. Goering, J. Geissler, S. Gold, and G. Schütz
Max-Planck-Institut für Metallforschung, Stuttgart, Germany
D. Schmitz, and H. Maletta
Hahn-Meitner-Institut, Glieniker Strasse, Berlin

Abstract

The magnetization depth profiles at the Cu and Pt site of a single Co layer have been investigated by X-ray resonant magnetic reflectivity. By the use of the Parratt algorithm in combination with an artificial slicing method. A quantitative determination of the Co magnetization profile at both interfaces could be extracted from the measured magnetic asymmetry ratio at the Co L_3 edge. The observed asymmetry ratios in the order of 40% are in excellent agreement with the simulated Co L_3 asymmetry, which quantitatively takes into account π and σ scattering channels for circular polarized light in a large angle scattering regime. The experimentally determined magnetization profiles are in agreement with complementary experimental results and with theoretically determined magnetization profiles. The shown method is a new tool for systematic investigations of the influence of magnetization properties at interfaces as a function of roughness or ligand layer composition for layered systems like MRAMS, GMR or TMR sensors.

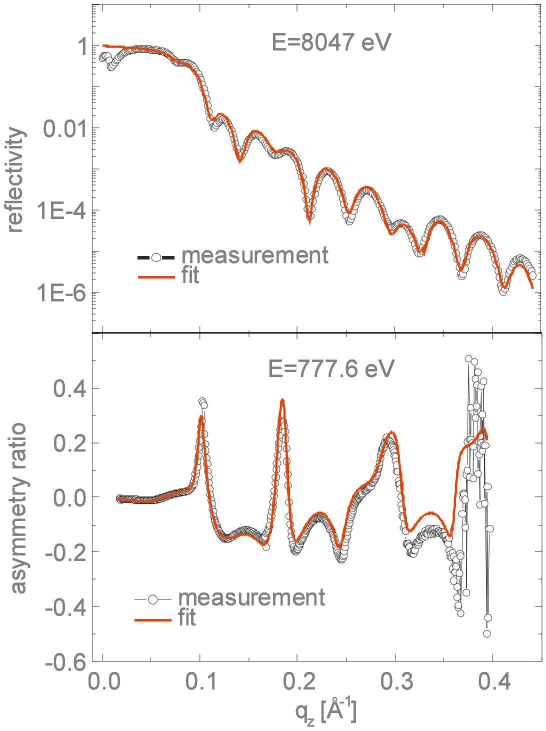

Figure 1: Non resonant Cu Kα -reflectivity curves of the sample and best Parratt simulation (top). Magnetic asymmetry and magnetization profile related simulation (bottom).

Layered systems, consisting of magnetic and non magnetic components, are of substantial technical interest from fundamental physical aspects as well as for technical applications. Famous examples are for a class of magnetic sensors and magneto- and spin-electronic devices are magnetic random access memories (MRAMs) and giant magneto resistive (GMR) read heads in hard disc applications. The reliable determination of magnetic and chemical interface properties in combination with element specificity and its influence to magneto transport properties is crucial for further improvements and optimization.

X-ray magnetic circular dichroism (XMCD) absorption spectroscopy in the soft and hard X-ray region is a well established method to determine element- and symmetry-selective quantitative values of projected average magnetic moments. Recent magnetic resonant reflectivity measurements in the hard X-ray range have given detailed element-specific and quantitative insight into the induced Pt magnetization profile of a single Pt/Co interface [1], in excellent agreement with previous XMCD measurements and full relativistic band structure calculations. Changes in shape and strength of induced magnetization profiles corresponding to differently prepared interfaces and roughness could be identified [2]. Nevertheless, the mentioned X-ray resonant magnetic reflectometry (XRMR) measurements at the Pt L_3 edge have been performed at very small scattering angles, where the magnetic asymmetry ratio is the same for π and σ scattering channels and the magnetic scattering amplitudes have a simple linear influence to the charge scattering amplitudes [1; 2]. In the soft X-ray region large scattering angles are present and the hard X-ray small angle approximation in dipole approximation breaks down [2; 3]. In this report we show the first quantitative determination of polycrystalline Pt magnetization profile of a single Pt layer with different interfaces at each site, taking into account magnetic scattering amplitudes for π and σ scattering channels in a cinematic approximation. Soft x-ray reflectivity measurements have been performed in θ-2θ geometry at the BESSY II undulator beamlines UE56/1 and UE52, utilizing circular polarized light and providing a large dynamic range of about 7 orders of magnitude. The reflected intensity, measured with a diode has been normalized to the photocurrent of an Au coated Copper mesh, which monitors the incoming photon beam intensity.

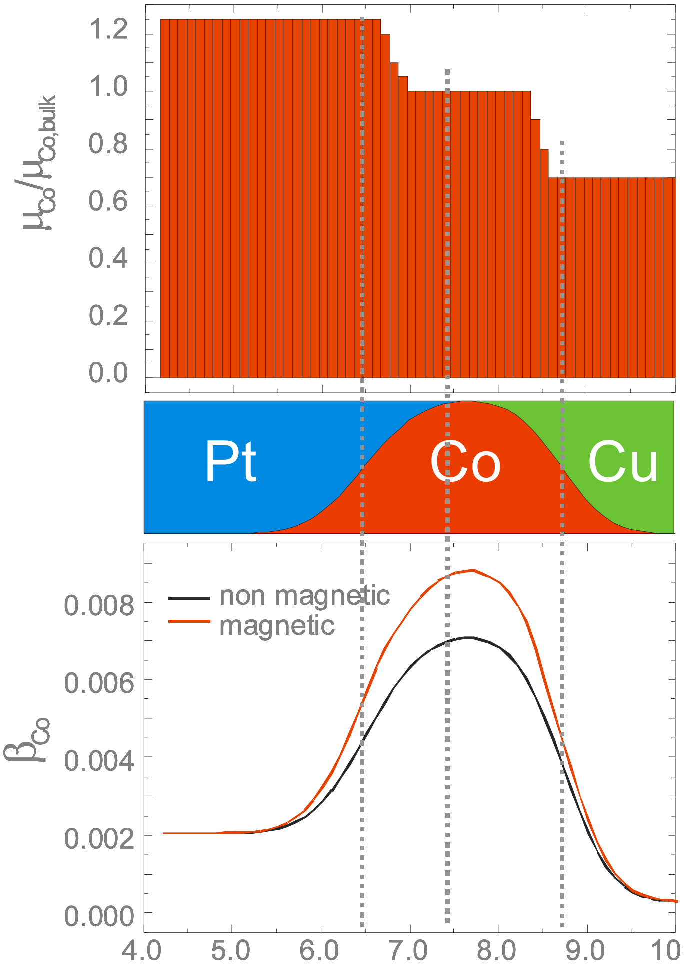

Figure 2: Top: Derived Co magnetization per Co ion. Middle: Chemical profile and layer thickness extracted from conventional non resonant Cu Kα reflectometry. Bottom: Absorptive charge scattering (black line) and total (charge + magnetic) scattering amplitudes.

In Fig.1 the non resonant Cu K_α reflectivity and the corresponding Parratt simulation are shown, providing detailed information about layer thickness and interface roughness, which are shown in the middle part of Fig.2. The magnetic asymmetry ratio and the best theoretical simulation at the Co L_3 edge are shown in the lower part of Fig.1, while the corresponding Co magnetization profile is shown in the upper part of Fig.2. The dispersive and absorptive parts of the magnetic and charge scattering amplitudes have been determined via Kramers-Kronig-relation, by scaling absorption spectra to tabulated values. The resulting charge and total absorptive scattering amplitudes are shown in the lower part of Fig.2.

The enhancement of the Co magnetization [4] at the Pt and the reduction at the Cu site [5] are in agreement with complementary experimental results. Further details of the simulation procedure and the experimental results will be presented elsewhere [6].

We would like to thank F. Senf and the BESSYII beamline staff for very kind support and R. Mattheis for the sample preparation.

References:

[1] Geissler, J., Goering, E. et al.; Phys.Rev.B 65, (2001) 020405(R)-1 - 020405(R)-4
[2] Geissler, J., Goering, E., Weigand, F., and Schütz, G.; Z.Metallkd. 93, (2002) 946 - 952
[3] Seve, L., Jaouen, N. et al. ; Phys.Rev.B 60, (1999) 9662 - 9674
[4] Canedy, C. L., Li, X. W., and Xiao, G.; Phys.Rev.B 62, (2000) 508 - 519
[5] Ney, A., Poulopoulos, P., and Baberschke, K.; Europhysics Letters 54, (2001) 820 - 825
[6] Goering, E., Geissler, J. et al. ; in preparation, (2003)

Projects in Basic Research
(January 2003)

Projektleiter	Institution	Projekttitel	Förderung	Förder-kennzeichen
Adamchuk	St. Petersburg State University	Lateral quantum-size effects in photoemission spectra from stepped graphite surface formed by thermal treatment of SiC	DLRIB	RUS00/219
Adamchuk	St. Petersburg State University	Electronic structure of two-dimensional intercalation-like systems on Ni(111)/W(110)	DLRIB	RUS00/219
Babanov	Institute of Metal Physics, RAS, Ekatarinenburg	Investigation of oxide half-metallic ferromagnets by means fo angle-resolved photoemission spectroscopy with high energy resolution and EXAFS	DLRIB	RUS00/219
Bakker/Knobloch	BESSY	Planung und Entwicklung eines Freie Elektronen Lasers bei BESSY	Zukunftsfonds Land Berlin	
Banhart	Hahn-Meitner-Institut Berlin	Investigation of pore formation in metallic forms by synchrotron computer tomography		
Bansmann/Meiwes-Broer	Universität Rostock	Magnetismus von Inselschichten und Clustern auf Oberflächen	DFG	ME 835/14-3
Bartoll	Technische Universität Berlin	Untersuchung von Korrosionserscheinungen an historischen Spiegeln		
Batchelor/Bressler/Winter	BESSY MBI Berlin	Change transfer in a family of Cu porphyrazines		
Baumgärtel	Freie Universität Berlin	Photoanregung von gasförmigen Molekülen im Bereich 5-25 eV		
Baumgarten	FZ Jülich	Photoemission on Cu nanowires on stepped W-surfaces		
Becker/Prümper	Fritz-Haber-Institut Berlin	Vollständige Experimente zur Photoionisation mittels Koinzidenzspektroskopie oder Targetpräparation	DFG DFG	BE 860/18-2 ZI 183/11-2
Becker/Püttner	Fritz-Haber-Institut Berlin	Doppelanregungszustände in Helium	BMBF	05KS1 KED/0

Projektleiter	Institution	Projekttitel	Förderung	Förder-kennzeichen
Becker/Viefhaus	Fritz-Haber-Institut Berlin	Coherence properties in atomic and molecular photoionization	BMBF DFG	05 KS1 EB1/2 BE 860/18-2
Behne	Hahn-Meitner-Institut Berlin	Identifizierung und Analyse von metallhaltigen Proteinen aus dem Zentralnervensystem und dem männlichen Reproduktionsorganen mit Hilfe der Röntgenfluoreszenzanalyse		
Bertagnolli	Universität Stuttgart	EXAFS Untersuchungen an organometallischen Nickel (II) Komplexen		
Birch	University of Linköping	Characterization of reflectivity and interfaces of Ni/V and Cr/Sc soft X-ray multilayer mirrors grown by ion assisted magnetron sputter deposition	EU	
Bluhm/Schlögl	Fritz-Haber-Institut Berlin	Investigation of catalytic reactions using high pressure XPS		
Boscherini	University of Bologna	Structural origin of the electronic and optical properties of InGaAsN quantum wells	EU	
Boyen/Ziemann	Universität Ulm	Elektronische, strukturelle und chemische Eigenschaften geträgerter Nanoteilchen	BMBF	05 KS1VUA/8
Bradshaw/Polcik	Fritz-Haber-Institut Berlin	Photoelektronenbeugung an adsorbierten Atomen, Molekülen und dünnen Schichten	MPG	
Braun/Jenichen/ Kaganer/ Schulz/Ploog	Paul-Drude-Institut Berlin	Oberflächenstrukturanalyse mittels Dreistrahlinterferenz; Stepbunching auf Vizinalflächen: Kinetik und Thermodynamik Nitride, Antimonide, Phosphide und ferromagnetische Metalle auf GaAs		
Brezesinski/Möhwald	MPI f. Kolloid und Grenz-flächenforschung Golm	Organic monolayers on water and on solid support		
Bürgler/Cramm	FZ Jülich	SXE on semiconductor / metal/seminconductor layers		
Cramm/Freiwald/ Eberhardt	FZ Jülich BESSY	SXA and SXE on liquids		

Projektleiter	Institution	Projekttitel	Förderung	Förder-kennzeichen
Cramm/Zimina/ Eberhardt	FZ Jülich BESSY	Soft X-ray emission and absorption on the organic semiconductors P30T and P3HT and on Fe/Si/Fe GMR multilayers		
Dabagov	Lebedev Physicsl Institute of RAS, Moskau	Study on effects of synchrotron radiation passage through capillary structures	DLRIB	RUS00/219
Dähne-Prietsch	Technische Universität Berlin	Photoemission at MIS structures with external gate bias	BMBF	05 KS1 KTA/4
Darowski	Hahn-Meitner-Institut Berlin	Investigation of crystallisation behaviour of amorphous alloys at the surface and in thin layers		
Darowski	Hahn-Meitner-Institut Berlin	Analysis of lateral nanostructures defined by ion implantation		
Dau/Haumann	Freie Universität Berlin	X-ray absorption spectroscopy on biological samples: The Manganese complex of photosystem II	BMBF DFG	05 KS1 KEA/6 SFB 498/C6
de Groot	Utrecht University	Oxidation/reduction behaviour of low-loading and high-loading Fe/ZSM5 systems	EU	
Domashevskaya	Voronezh State University	Investigations of electron structure specificity and the nature of photoluminescence in porous materials and quantum points for indirect band-gap and direct gap semiconductors	DLRIB	RUS00/219
Dürr/Kronast/ Eberhardt/ Schmitz/Maletta	BESSY HMI Berlin	Manganmagnetisierungs-dynamik in (Ga, Mn)As		
Dürr/Schondelmaier/ Cramm/Eberhardt	BESSY FZ Jülich	Chemical and magnetic structure of exchange biased interfaces probed by soft X-ray standing waves		
Ehresmann/ Schmoranzer	Universität Kaiserlautern	Resonante magnetische Streuung an NiFe/NiO und CrMnPt/NiFe/Ta Exchange-Bias-Systemen nach vorheriger Mokfikation durch He-Ionenbeschuss	DFG	Eh187/2-1
Ehresmann/ Schmoranzer	Universität Kaiserlautern	Autoionisation der N_2(1s-->π^x). Resonanz in die Zustände N_2^+ B und C	DFG	SCH379/11
Ehresmann/ Schmoranzer	Universität Kaiserlautern	Nachweis von Dissoziationsprozessen molekularer Rydbergzustände in N_2 in atomare Rydbergzustände	DFG	SCH379/11

Projektleiter	Institution	Projekttitel	Förderung	Förder-kennzeichen
Ehresmann/ Schmoranzer	Universität Kaiserlautern	Besetzung von metastabilen 01 $3s^5$ S-Zuständen nach Anregung und Prädissoziation von O_2	DFG	SCH379/11
Eisebitt/Freiwald/ Eberhardt	BESSY	Soft X-ray spectroscopy in liquid environnment: Towards an understanding of the electronic structure in active centers of biomolecules		
Eisebitt/Lörgen/ Cramm/Eberhardt/ Stöhr	BESSY FZ Jülich SSRL Stanford	Coherent resonant soft X-ray scattering from magnetic domain pattern		
Eisebitt/Zimina/ Eberhardt	BESSY	Orientation and electronic structure in polymers for integrated plastic circuits		
Erko	BESSY	Investigation of the properties of capillary micro optics		
Esser/Hinrichs/Korte	Technische Universität Berlin ISAS Berlin	In situ IR-Ellipsometrie: Elektronische und vibronische Anregungen an adsorbatmodifizierten Oberflächen	BMBF DFG	05 SR8KK19 Es127/4-3 SFB290TPB6
Esser/Richter	Technische Universität Berlin	Aufbau und Betrieb eines VUV-XUV Ellipsometers mit Synchrotronstrahlung	BMBF	05KS1KTB/2
Esser/Richter/Braun	Technische Universität Berlin BESSY	Epitaktisches Wachstum von Kobalt, Nickel und Eisen auf GaAs(001), InP(001) und In_{a-x} $Ga_xP(001)$	DFG	ES 127-4/3 SFB 290TPB6
Fauth/Schütz	Universität Würzburg/MPI f. Metallforschung Stuttgart	XMCD experiments on the magnetism of 3d transition metal clusters		
Fauth/Schütz	Universität Würzburg/ MPI f. Metallforschung Stuttgart	Charakterisierung von deponierten Übergangsmetallclustern mittels (resonanter) Photoemission		
Felsch	Universität Göttingen	Elektronic structure and magnetism of GdN thin layers	DFG	SFB 602TPA1
Felser	Universität Mainz	XANES und XMCD-PEEM Untersuchungen an Halbheusler und Heusler Verbindungen		
Fink/Borisenko	IFW Dresden	Superconductivity of Bi-based cuprates		
Fink/Knupfer	IFW Dresden	Einfluss von Grenzflächenphänomemen auf die Funktion organischer Feldeffekttransistoren	EU	ERB FMRXCT 970 1551

Projektleiter	Institution	Projekttitel	Förderung	Förder-kennzeichen
Fink/Umbach	Universität Erlangen Universität Würzburg	NEXAFS Feinstruktur in quinon-basierenden Ladungstransfersalzen	BMBF	05KS1WWA-5
Firsov	BESSY	Tests of diffraction microoptics		
Föhlisch/Wurth	Universität Hamburg	Resonante Rumpfelektronenspektroskopie als Sonde für ultraschnelle Elektronendynamik an Oberflächen	DFG	WU 207/1-2
Freund/Kuhlenbeck	Fritz-Haber-Institut der MPG Berlin	Elektronische Struktur molekularer Schichten auf reinen und modifizierten Oxid-, Karbid- und Nitridsubstraten		
Funnemann	Omicron Taunusstein	Nano ESCA: Imaging XPS with resolution below 200nm	BMBF	13N7865
Getzlaff	Universität Mainz	Elementspezifische Untersuchungen zum temperaturabhängigen Spinorientierungsübergang in Doppellagensystemen		
Gießel/Widdra	Max-Born-Institut Berlin	Temperaturabhängige Photoelektronenbeugung an dünnen Metallfilmen		
Glass-Maujean	Université P. et M. Curie Paris	Decay dynamics of doubly excited states in molecular hydrogen investigated by time resolved fluorescence analysis	EU	
Goebbels/Riesemeier	BAM Berlin	Charakterisierung von Strukturkeramiken und Bauteilen aus der Mikro-Strukturtechnik mittels Mikrocomputertomographie	DFG	GO 530/1-3
Goering/Schütz	MPI f. Metallforschung Stuttgart	XMCD-Untersuchungen und Reflektometrie an $La_{0.7}$ $Sr_{0.3}$ $MnO_3/SrTiO_3$ Vielfachschichten		
Goering/Schütz	MPI f. Metallforschung Stuttgart	Temperaturabhängigkeit projizierter Bahnmomente am Modellsystem CrO_2 und Einfluss von Bahnmoment und magnetischem Dipolterm auf den Reorientierungsübergang		
Goering/Schütz	MPI f. Metallforschung Stuttgart	Ferro- und Antiferromagnetisches Wechselspiel in Ruthenium dotierten Bi-Lagenmanganaten		

Projektleiter	Institution	Projekttitel	Förderung	Förder-kennzeichen
Golden	University of Amsterdam	Alcaline earth hexaborides and borocarbides: new materials for room temperature spintronics	EU	
Golden	University of Amsterdam	K-space microscopy of high temperature superconductors	EU	
Gomoyunova	Ioffe Physico-Technical Institute, St. Petersburg	Electronic and atomic structure of cobalt silicides at initial stages of their formation	DLRIB	RUS00/219
Gonzalez-Elipe	Instituto de Ciencia de Materiales de Sevilla	Resonant photoemission and Augeremission of M/TiO_2 structures	EU	
Görner/Radtke/Procop	BAM Berlin	Zertifizierung von Referenzmaterialien, Oberflächen- und Ultraspurenanalyse mit (μ-)RFA	BMBF	13N7704
Grunze/Zharnikov	Universität Heidelberg	Röntgenspektroskopie an organischen Grenzflächen und Biomaterialien in Kontakt mit Lösungen	BMBF	05 KS1VHA/3
Grunze/Zharnikov	Universität Heidelberg	Neutronensteu- und Synchrotronstrahlungsexperimente an biologisch relevanten organischen Monoschichten. Teilprojekt: Homogene und heterogene organische Schichten als Substrate für Anwendungen in der Biosensorik	BMBF	03 GRE1HD
Güntherodt	RWTH Aachen	Hochauflösende spinpolarisierte Photoemission von Ferromagnet-Oxid-Grenzflächen und oxidischen halbmetallischen Ferromagneten	BMBF	05 KS1PAA/7
Haibel	Hahn-Meitner-Institut Berlin	Synchrotron tomography on aluminium and zinc foams		
Haevecker/Schlögl	Fritz-Haber-Institut der MPG Berlin	Charakterisierung der katalytisch relevanten Oberflächenzustände von Vanadium-Pyrophosphat-Oxid Katalysatoren für die n-Butanoxidation		
Heberle	FZ Jülich	Testmessungen an Proteinen mit THz Strahlung		
Heinzmann/ Drescher	Universität Bielefeld	Spinpolarisationstransfer an Auger-Elektronen aus freien Atomen	DFG	HE 1049/7UP2

Projektleiter	Institution	Projekttitel	Förderung	Förder-kennzeichen
Heinzmann/ Kleineberg	Universität Bielefeld	In-vitro Transmissions-Photoelektronenemissions-Mikroskopie im Wasserfenster am Messplatz U125/1-ML bei BESSY II	BMBF	05 KS1PBA/08
Held	University of Cambridge	Charakterisierung der Adsorption chiraler Moleküle auf glatten und gestuften Oberflächen	EU	
Herein	ACA Berlin	XAS measurements at the BAMline	BMBF	03 C3013
Hergenhahn	Fritz-Haber-Institut der MPG Berlin	Elektronenspektroskopie an einem freien Clusterstrahl		
Hergenhahn	Fritz-Haber-Institut der MPG Berlin	Hochaufgelöste Photoelektron-Auger-Elektron Koinzidenzspektren von gasförmigen Molekülen	DFG	HE 3060/3-3
Heske/Umbach	Universität Würzburg	Charakterisierung der elektronischen Struktur von II-VI und organischen Halbleitern mit resonanter inelastischer Röntgenstreuung: Volumeneigenschaften und Grenzflächeneffekte	BMBF DFG	05 KS1WW1/6 SFB410TPB3
Heske/Umbach	Universität Würzburg	Elektronische und chemische Eigenschaften nasschemisch präparierter II-VI Nanopartikel	DFG	SFB410TPC5
Hinrichs	ISAS Berlin	IR-Ellipsometrie für die Untersuchung der Struktur und der optischen Eigenschaften anisotroper Proben und Schichten	BMBF	05 SR8KK19
Hofmann	Humboldt Universität zu Berlin	Infrarotspektroskopische Untersuchungen am Rhodopsin	BMBF	O5 KS1KK1/4
Horn	Fritz-Haber-Institut der MPG Berlin	Magnetism and quantum size effects in metallic layers on semiconductor surfaces		
Horn	Universität Augsburg	Untersuchung zeitlicher und räumlicher Korrelationen mittels Neutronen- und Röntgenstreuung	BMBF DFG	05 SB8WAA8 SFB484TPA3

Projektleiter	Institution	Projekttitel	Förderung	Förder-kennzeichen
Ionov	Institute of Solide States, RAS, Chernogolovka, Moskau	Investigation of electronic structure and quantization effects in low-dimensional 1D, 2D systems: quasi 2D single-crystalline W/Mo epitaxial structures and quasi 1D Ni/Re wires on vicinal W(110) surfaces)	DLRIB	RUS00/219
Jaegermann	Technische Universität Darmstadt	Grenzflächen polykristalliner leitender Oxide	BMBF	01 SF0034
Jaegermann	Technische Universität Darmstadt	Elektronische Struktur von van der Waals-Epitaxiequanten-Schichten	DFG	JA 859/7-1
Jaegermann/Klein	Technische Universität Darmstadt	Potentialinhomogenitäten an Halbleiteroberflächen und -grenzflächen	BMBF	0329857
Jaegermann/Mayer	Technische Universität Darmstadt	Charakterisierung von Festkörper-Elektrolyt-Grenzflächen	BMBF DFG	05 KS1RD1/0 JA 859/3-1
Kaindl/Püttner	Freie Universität Berlin	Doppelanregungszustände in Helium	BMBF DFG	05 KS1KED/0 DO 561/1-3
Kanngießer	Technische Universität Berlin	Depth sensitive micro-X-ray fluorescence analysis	DFG	KA 925/1-4
Kanngießer/Hahn	Technische Universität Berlin BAM Berlin	Untersuchung von Migrations- und Oxidationsprozessen anorganischer Verbindungen in Tintenfraß-geschädigten Manuskripten		
Kanngießer/ Zimmermann	Technische Universität Berlin	Bestimmung von Fluoreszenz- und Augerausbeuten im weichen Röntgenenergiebereich mit Hilfe der Photoelektron-Photoion Koinzidenztechnik		
Kisker	Universität Düsseldorf	Investigation of domain structures of ferromagnetic thin films grown on antiferromagnetic substrates	BMBF	05 KS1PFA/3
Knop-Gericke/ Conrad	Fritz-Haber-Institut der MPG Berlin	Charakterisierung der Sauerstoffzustände im Volumen der sauerstoffreichen Ru(0001) Oberfläche		
Knop-Gericke / Schlögl	Fritz-Haber-Institut der Max-Planck-Gesellschaft	Katalytische Oxidation: Röntgenabsorptionsuntersuchungen im weichen Röntgenbereich (250 eV < hv < 1000 eV) unter Reaktionsbedingungen		

Projektleiter	Institution	Projekttitel	Förderung	Förder-kennzeichen
Knop-Gericke/ Schlögl	Fritz-Haber-Institut der MPG Berlin	Von Einkristallsystemen zu realen Katalysatoren am Beispiel der Hydrierung an Silberkatalysatoren		
Koch-Müller	Geoforschungszentrum Potsdam	Location and quantification of OH in nominally anhydrous minerals	BMBF	05 KS1KK1/4
Kuch/Kirschner	Max-Planck-Institut für Mikrostrukturphysik Halle	Elementspezifische Abbildung magnetischer Domänen in gekoppelten magnetischen Dünnschichtsystemen	BMBF	05 KS1EFA/6
Kuch/Kirschner	Max-Planck-Institut für Mikrostrukturphysik Halle	Time and layer resolved magnetic imaging of spin valve structures using PEEM		
Kuch/Kirschner	Max-Planck-Institut für Mikrostrukturphysik Halle	Magnetic linear dichroism of metallic ferromagnetic and antiferromagnetic ultrathin films		
Kühbacher	Hahn-Meitner-Institut Berlin	Lokalisation von Proteinablagerungen im biologischen Geweben mit Hilfe der Synchrotron FT-IR Spektroskopie	BMBF	05 KS1KK1/4
Lammert	BESSY	Verbundprojekt zu Arbeiten zur hochgenauen Vermessung von Nanometer-Optikomponenten	BMBF	13 N7929
Lamont	University of Huddersfield	Structural determination of maleic anhydride on Si(100)	EU	
Lasch	Robert-Koch-Institut Berlin	Infrared microspectroscopy of tissue sections	BMBF	05 KS1KK1/4
Laubschat/Molodtsov	Technische Universität Dresden	Band mapping by high energy angle resolved resonant photoemission of solids	BMBF DFG	KS10DA/2 SFB463TPB04
Leitenberger	Universität Potsdam	Characterization of homepitaxial 4H-SiC layers by X-ray white beam diffraction topography		
Leitenberger	Universität Potsdam	Nondestructive characterization of SiC ingots by high energy white beam diffraction topography		
Lewerenz	Hahn-Meitner-Institut Berlin	Phototelectron spectroscopy on electro-chemically prepared silicon surfaces		
Ley/Seyller	Universität Erlangen-Nürnberg	Wechselwirking von Mn mit GaAs Oberflächen		

Projektleiter	Institution	Projekttitel	Förderung	Förder-kennzeichen
Ley/Seyller	Universität Erlangen-Nürnberg	Photoemissionsuntersuchungen am SiC		
Locht	Universität Lüttich	High resolution photoabsorption spectroscopy of CH_3X and C_2H_3X (X= F, Cl and Br)	EU	
Lux-Steiner	Hahn-Meitner-Institut Berlin	Synchrotron diagnostics to support material and technology development of cost efficient Cu (In, Ga) (S, Se)$_2$ photovoltaic modules	BMBF	01 SF0007
Makhov	Lebedev Physical Institute, RAS, Moscow	Photoemission study of core hole relaxation and related phenomena in crossluminescence crystals	DLRIB	RUS00/219
Manzke	Humboldt Universtität zu Berlin	Röntgenabsorptions-Spektroskopie (XAS) an kondensierter Materie mit Synchrotronstrahlung	BMBF	05 KS1KHA/0
Manzke	Humboldt Universtität zu Berlin	Photoelektronenspektroskopie höchster Auflösung an kondensierter Materie	BMBF	05 KS1KH1/1
Martins/Wurth	Universität Hamburg	Correlations in free atoms and molecules		
Menzel/Feulner	Technische Universität München	Elektronisch stimulierte Desorption: Energieaufgelöstes PSDIAD und atomselektiver Bindungsbruch	DFG DFG	SFB 338C10 Me 266/21-2
Mertins/Dürr	BESSY	Test von Zonenplatten		
Mertins/Gudat	BESSY Universität Potsdam	Magnetooptische Polarisationsspektroskopie mit Synchrotronstrahlung an magnetischen Schichtsystem	BMBF	05 KS1IPB/8
Mikheeva	Kurchatov Institute Moskau	Angle resolved photoemission study of partially oxidated yttrium surfaces near the Y3d threshold	DLRIB	RUS00/219
Mikoushkin	Ioffe Physico-Technical Institute St. Petersburg	Fullerite modification by synchrotron radiation	DLRIB	RUS00/219
Mittsev	Ioffe Physico-Technical Institute St. Petersburg	Yb adsorption and silicide formation on Si(100)	DLRIB	RUS00/219
Müller	Freie Universität Berlin und PSF	Röntgendiffraktion an medizinisch relevanten Proteinen	BMBF	Leitprojekt PSF

Projektleiter	Institution	Projekttitel	Förderung	Förder-kennzeichen
Müller/Hentschel	BAM Berlin	Synchrotron Refraktions Topographie an heterogenen Hochleistungswerkstoffen		
Naumann	Robert-Koch-Institut Berlin	Infrared microspectroscopy of tissue from scrapie-infected Syrian hamsters	BMBF	05 KS1KK1/4
Netzer	Karl-Franzens-Universität Graz	Wechselwirkung von Aminosäuren mit Oxidoberflächen - hochaufgelöste NEXAFS und XPS Spektroskopie	EU	
Neumann	Universität Osnabrück	Untersuchung der elektronischen Struktur von Perowskiten mittels XES, XAS und RIXS		
Niehus	Humboldt Universität zu Berlin	Untersuchung der Oxidationszustände von epitaktisch gewachsenen Vanadiumoxidfilmen auf Cu_3Au		
Okotrub	Institute of Inorganic Chemistry Novosibirsk	Electronic structure investigation of nanocomposite materials based on cage carbon	DLRIB	RUS00/219
Paloura	Aristotle University of Thessaloniki	Ga-K-XAFS measurements on In GA N and Al Ga N alloys	EU	
Pettenkofer	Hahn-Meitner-Institut Berlin	Untersuchung der elektronischen Struktur der initiellen Wachstumsphase von heteroepitaktischen $CuInS_2$ Filmen		
Piancastelli	University "Tor Vergata" Rom	Surface-induced circular dichroism in adsorbates	EU	
Pietsch	Universität Potsdam	Energiedispersive Röntgenstreuung an organischen dünnen Filmen auf festen und flüssigen Trägern		
Pietsch	Universität Potsdam	Spectroscopic investigation of molecular orientation of azobenzene in polymer films with surface relief gratings	DFG	Pi 217-1
Pietsch	Universität Potsdam	Aufbau eines Experiments zur kohärenten Röntgenstreuung		
Ploog	Paul-Drude-Institut Berlin	Combined PES, XAS, XMCD study of Mn-containing III-V-based magnetic semiconductors		

Projektleiter	Institution	Projekttitel	Förderung	Förder-kennzeichen
Powis	University of Nottingham	Circular dichroism in the photoionisation of free chiral molecules	EU	
Rader/Gudat	BESSY Universität Potsdam	Interface states at stepped monolayers		
Rader/Gudat	BESSY Universität Potsdam	Quantendrähte auf gestuften Substraten		
Rader/Gudat	BESSY Universität Potsdam	Elektronische Struktur von Spin-Gapmaterialien an Grenzflächen	BMBF	05 KS1IPA/0
Rader/Gudat	BESSY Universität Potsdam	Quantisierung von seltenen Erden und Mn Filmen auf W und Mo Substraten		
Rader/Gudat	BESSY Universität Potsdam	Temperature dependence of quantum well states of Gd selforganized chains of Gd		
Rader/Shikin/Gudat	BESSY Universität Potsdam	Ground state electronic structure of Ni metal probe through quantum well states		
Reiche	Rathgen-Forschungslabor Berlin	Ortsaufgelöste Ultraspurenanalyse an mittelalterlichen Gemälden und Metallstiftzeichnungen mit RFA	DAAD	PROCOPE D/0122896
Reinert	Universität des Saarlandes	Nano ESCA-Entwicklung eines abbildenden Photoelektronenspektrometers zur hochauflösenden Material- und Defektanalyse	BMBF	13 N7847
Rettig	Humboldt Universität zu Berlin	Fluorescence decay of model compounds for the primary process of vision	DFG	SFB 448TPB3
Riesemeier	BAM Berlin	Glaskapillaroptiken als röntgenoptische Systeme einer neuen Generation	BMWA	VI A2-17/02
Rühl	Universität Würzburg	Experimelle und theoretische Untersuchungen zur hochaufgelösten Anregung der Rumpfniveaus von Molekülen, Clustern und Adsorbaten	DFG	RU 420/5-1
Rühl (Koordinator)	Universität Würzburg	Aufbau und Test eines Messstandes zur Untersuchung gespeicherter Nanopartikel mit Synchrotronstrahlung	BMBF	05 KS1MPA/8
Ruts	Physical-Technical Institute Izhevsk	Local atomic structure of Fe-C and Co-C systems	DLRIB	RUS00/219

Projektleiter	Institution	Projekttitel	Förderung	Förder-kennzeichen
Sacchi	Université de Paris-Sud	Field dependent magnetic coupling in Co/Cu multilayers investigated by specular and diffuse resonant scattering of polarized soft X-rays	EU	
Saenger	Freie Universität Berlin	Struktur-/Funktionsbeziehungen von HLA-B27	DFG	
Schade	BESSY	IR-Ellipsometrie an planetaren Analogmaterialien		
Schäfers	BESSY	Charakterisierung von Cr/Sc Multilayern im weichen Röntgengebiet		
Schäfers	BESSY	Vorexperiment zu reflektometrischen Untersuchungen mit einem Industriepartner		
Schartner/ Schmoranzer	Universität Gießen/ Universität Kaiserslautern	Radiative Zerfälle doppelt angeregter He- und Ne-Atome	DFG	Scha 235/16 Schm 379/12
Schartner/ Schmoranzer	Universität Gießen/ Universität Kaiserslautern	Transfer von Orientierung beim resonanten Augerzerfall des Kr $3d^9{}_{5/2}5p^1P$-Zustandes: Ein Zugang zur vollständigen Partialwellenanalyse	DFG	Scha /235/16 Schmo 379/12
Schartner/ Schmoranzer	Universität Gießen/ Universität Kaiserslautern	Orientierung O10 und Alignment A20 von Kr^+ $4p^45p$-Zuständen bei Inteferenz resonanter Raman-Auger-$3d^95p$-Prozesse nach Anregung mit zirkular polarisierter Synchrotronstrahlung	DFG	Scha 235/16 Schmo 379/12
Schmahl	Georg-August-Universität Göttingen	Weiterentwicklung des röntgenmikroskopischen Messplatzes am Undulator U41 am BESSY II und röntgenmikroskopische Experimente	BMBF	05 KS1MG1/9
Schmeißer	Brandenburgische Technische Universität Cottbus	Al-Fe Legierungsbildung durch Reibschweißen	BMBF	03 N3052 2
Schmeißer	Brandenburgische Technische Universität Cottbus	ZnS-$CuInS_2$ Legierungen	DFG	GEP-SCHM745/3
Schmeißer	Brandenburgische Technische Universität Cottbus	Studium der Wechselwirkung von Gold und Silber mit Polypyrrol und Poly (3-Hexylthiophen)-2,5 diyl	BMBF	03 N50209

Projektleiter	Institution	Projekttitel	Förderung	Förder-kennzeichen
Schmeißer	Brandenburgische Technische Universität Cottbus	Charakterisierung von $Si0_2/Si_{1-x-y}Ge_xC_y$ und $Si/Si_{1-x-y}Ge_xCy$ Heterogrenzflächen		
Schmeißer	Brandenburgische Technische Universität Cottbus	Photoelektronen-spektroskopische Untersuchungen zur Pr_3O_3/Si(001)-Grenzfläche		
Schmidt-Böcking	Johann Wolfgang Goethe Universität Frankfurt(M)	Elektronenkorrelation in doppelt hoch angeregten Heliumzuständen nahe der Kontinumsgrenze untersucht mit Elektron-Ion-Photon-Koinzidenz		
Schneider	IFW Dresden	Elektronische und mikromagnetische Struktur in neuen magnetoelektronischen Materialien	BMBF	05 KS1BD1 0
Schneider	IFW Dresden	Magnetic domains and magnetization dynamics in nanostructured materials	BMBF	05 KS1BDA/9
Schneider	IFW Dresden	Soft X-ray MOKE and magnetic scattering on exchange-coupled films	BMBF	05 KS1BD1/0
Schneider	IFW Dresden	Magnetooptic effects at the 3p edges of transition metal compounds	BMBF	05 KS1BD1/0
Schneider	IFW Dresden	Spin-resolved electronic states in ferromagnetic transition metal compounds	BMBF	05 KS1BD1/0
Schoenes/Barkow	Technische Universität Braunschweig	Ellipsometrische Messungen an einem System mit helikaler magnetischer Struktur: UPtGe		
Schönhense	Johannes-Gutenberg-Universität Mainz	Abbildung magnetischer Domänen in eisenhaltigen natürlichen Mineralien in Kombination mit spektromikroskopischen Untersuchungen und µSpot-CDAD-Holographie	BMBF	05 SC8UMA0
Schönhense	Johannes-Gutenberg-Universität Mainz	Picosekunden PEEM. Photoemissionsmikroskop für die zeitaufgelöste Beobachtung dynamischer Prozesse	BMBF	05 KS1UM1/5

Projektleiter	Institution	Projekttitel	Förderung	Förder-kennzeichen
Schönhense	Johannes-Gutenberg-Universität Mainz	Innovative Reaktoren und in-situ Analytik für Nano-Schutzschichten. Chemisch selektive Schichtabbildung mit höchster Ortsauflösung	BMBF	13N 7759
Schönhense	Johannes-Gutenberg-Universität Mainz	Nano-ESCA-Entwicklung eines abbildenden Photoelektronenspektrometers zur hochauflösenden Material- und Defektanalyse	BMBF	13N 7863
Schumacher	Hahn-Meitner-Institut Berlin	Lattice misfit in single crystal superalloy SC16	DFG	Ne 645/5-2
Schüßler-Langeheine	Universität zu Köln	Resonant soft X-ray scattering from transition metal compounds	DFG	SFB 608TPC4
Schwentner	Freie Universität Berlin	Lichtinduziertes Trockenätzen	DFG	Schw 230/12-2
Selcuk	PSI Villigen	Strain state and interface roughness of silicon-germanium quantum cascade laser structures		
Soriano	Universidad Autonoma de Madrid	Study of the electronic structure of small particles and ultra-thin films of metal oxides, nitrides and carbides	EU	
Starke/Kaindl	Freie Universität Berlin	Röntgenmagnetooptik und Magnetismus von nanostrukturierten Lanthanidmaterialien		
Steinrück	Universität Erlangen-Nürnberg	Charakterisierung und Veränderung molekularer Schichten auf dünnen Metallschichten	DFG	STE 620/2-2
Steinrück/Denecke	Universität Erlangen-Nürnberg	Höchstaufgelöste Photoelektronenspektroskopie mit Synchrotronstrahlung zur in-situ Untersuchung von Oberflächenreaktionen	DFG	STE 620/4-1
Stöhr/Eisebitt/ Eberhardt	SSRL Stanford BESSY	Critical fluctuations in thin magnetic films and polymers investigated by resonant soft X-ray scattering		
Svensson	University of Uppsala	Investigation of Fano type interference patterns in resonant Raman Auger spectra and in VUV photoelectron spectra of hydrogenhalogenide molecules in the gas phase	EU	

Projektleiter	Institution	Projekttitel	Förderung	Förder-kennzeichen
Szargan	Universität Leipzig	Resonante Phtoemission und Röntgenfluoreszenz von Dünnschichtmaterialien auf ZCIS- und CIGSS Basis	BMBF	05 KS1 OL1/3
Tepper/Kachel	Universität Kassel BESSY	Spectroscopic studies of poisoning of catalytical metalized oxide surfaces		
Tiedje	University of British Columbia Vancouver	High-resolution X-ray emission spectroscopy in dilute nitride semiconductors		
Titov	Insitute of Metal Physics Ekatarinenburg	ARPES study of electronic structure of intercalation compounds Cr_xTiSe_2, Fe_xTiSe_2 and Co_xTiSe_2	DLRIB	RUS00/219
Umbach (Koordinator)	Universität Würzburg	Höchstauflösende Spektromikroskopie mit dem abberationskorrigierten Niederspannungs-Elektronenmikroskop SMART	BMBF	05KS1WW2/0
Umbach/Fink	Universität Würzburg Universität Erlangen	Elektronische und vibronische Feinstruktur in grenzflächenmodifizierten organischen Dünnschichten	BMBF	05 SF8 WWA/5
Umbach/Heske/Fink	Universität Würzburg Universität Erlangen	Elektronische, chemische und strukturelle Eigenschaften nasschemisch präparierter Nanopartikel	DFG	SFB 410TPC5
Umbach/Fink	Universität Würzburg Universität Erlangen	Spektroskopische Charakterisierung bioverträglicher Titanoxid-Oberflächen	DFG	UM6/9-1
Unger	Bundesanstalt für Materialforschung und -prüfung	Untersuchung dünner, im Pulsplasma hergestellter Polymer- und Blockcopolymerfilmen mit der Röntgenabsorptions-spektroskopie		
Unger	Bundesanstalt für Materialforschung und -prüfung	Charakterisierung neuartiger Kohlenstoffschichten mit der Röntgenabsorptions-spektroskopie (NEXAFS) unter Berücksichtigung der Anforderungen industrieller QM Systeme	BMBF	MIQN03 114600
Vinogradov	St. Petersburg State University	Covalency effects in the electronic structure of 3d metal compounds by high resolution X-ray absorption		

Projektleiter	Institution	Projekttitel	Förderung	Förder-kennzeichen
Vogel	Laboratoire Louis Néel Grenoble	Time and layer resolved magnetic imaging of spin valve structures using PEEM	EU	
Vollmer	University of Cambridge	Electron yield X-ray absorption spectroscopy using gas microstrip detectors	EU	
Wende/Baberschke	Freie Universität Berlin	Röntgenabsorptionsuntersuchung an magnetischen Schichtsystemen und Naonstrukturen	BMBF	05 KS1 KEB4
Weschke/Kaindl	Freie Universität Berlin	Grenzflächenbedingte Materialmodifikation von Lanthanidmetallen	BMBF	05 KS1KEE/8
Weschke/Kaindl	Freie Universität Berlin	Magnetic effects in the band structure of thin metal films	BMBF	05 KS1KED/0
Weschke/Kaindl	Freie Universität Berlin	Resonante magnetische Streuung an in situ präparierten Lanthanidmetallfilmen	BMBF	05 KS1/KEE/8
Westphal	Universität Dortmund	Photoelektronenbeugungs-Untersuchungen an der SiO_2/Si Grenzschicht	BMBF	05 SE8PMB-9
Widdra/Gießel/Hertel	Max-Born-Institut Berlin	Bestimmung der lokalen Adsorptionsgeometrie von Stufenkantenadsorbaten auf vizinalen Halbleiteroberflächen		
Widdra/Hertel	Max-Born-Institut Berlin	Pump-Probe Untersuchungen zur Dynamik von Halbleiteradsorbat- und Oberflächenzuständen		
Wilke	Universität Potsdam	XAFS of Fe in silicat glasses and melts	DFG	WI 2000/1-1
Wilke	Universität Potsdam	Spatially resolved determination of trace element concentrations with SR X-ray fluorescence analysis		
Winter/Widdra/Hertel	Max-Born-Institut Berlin	Electron spectroscopy from liquid water surfaces		
Winter/Widdra/Hertel	Max-Born-Institut Berlin	Electronic structure of organic thin films		
Wöll	Ruhr-Universität Bochum	Charakterisierung organischer Dünnschichten und Oberflächen mittels Absorptionspektroskopie im weichen Röntgenbereich	DFG	SFB 558TP15
Wöll	Ruhr-Universität Bochum	Tiefendifferenzierende XPS-Analyse der Oberflächenregion heterogener Katalysatoren	DFG	GR 1447/9-1

Projektleiter	Institution	Projekttitel	Förderung	Förder-kennzeichen
Woodruff	University of Warwick	Scanned-energy mode photoelectron diffraction	EU	
Wurth	Universität Hamburg	Magnetische Eigenschaften kleiner, größenselektierter, deponierter Übergangsmetallcluster	BMBF	05 KS1GUB/5
Zabel	Ruhr-Universität Bochum	Study of magnetic superlattices by soft X-ray resonant magnetic scattering	BMBF	03 ZAE7BO
Zahn/Kampen/ Braun	Technische Universität Chemnitz/ BESSY	Organisch modifizierte Metall/Halbleiterkontakte	BMBF	05 KS1OCA/1
Zahn/Kampen/ Braun	Technische Universität Chemnitz/ BESSY	VUV-XUV-Ellipsometrie an molekularen Halbleitern		
Zheludeva/Kovalchuk	Shubnikov Institute of Chrystallography Moskau	Studies of liquid crystal monolayers	DLRIB	RUS00/219
Ziemann/Boyen	Universität Ulm	Electronic properties of size selected supported nanoparticles	BMBF	05 KS1VUA/8
Zimmermann	Technische Universität Berlin	Hochauflösende Elektronenspektroskopie an freien Atomen der 3d-Übergangselemente	DFG	Zi 183/16-1
Zimmermann	Technische Universität Berlin	Dichroismusexperimente mit laserpolarisierten freien Atomen der 3d-Übergangsmetalle	DFG	183/16-1

LIST OF PUBLICATIONS 2002

M. Aggour, U. Störkel, C. Murrell, S.A. Campbell, H. Jungblut, P. Hoffmann, R. Mikalo, D. Schmeißer
Electrochemical Interface Modification of CuInS2 Thin Films
Thin Solid Films, **403**, 57-61, (2002)

Ch. Ammon, A. Bayer, G. Held, B. Richter, Th. Schmidt, H.-P. Steinrück
Dissociation and oxidation of methanol on Cu(110)
Surface Science, **507-510**, 845, (2002)

Ch. Ammon, G. Held, J. Pantförder, H.-P. Steinrück
Growth and electronic properties of thin Zn layers on Cu(111)
Surface Science, **482-485**, 886, (2001)

Ch. Ammon
Elektronenspektroskopische Untersuchungen zu Herstellung und Eigenschaften ultradünner Schichten auf Kupferoberflächen
Dissertation (2002)

B. Beckhoff, G. Ulm
Determination of Fluorescence Yields using Monochromatized Undulator Radiation of High Spectral Purity
Advances in X-ray Analysis, **44**, 349-354, (2001)

R. Bernhardt, G.M. Partzsch, M. Wilke
Fe in synthetic basaltic glass: An Fe K-XANES and 57Fe Mössbauer study
Eur. Jour. Mineral., **14, Beih. 1**, 19, (2002)

A. Borgschulte
Elektronenbeugungs- und Photoemissionsstudien an magnetischen und optischen Funktionsschichten
Dissertation, TU-Braunschweig, (2002)

A. Borgschulte, D. Zur, D. Menzel, J. Schoenes, P.M. Oppeneer
Effects of the stoichiometry and chemical order on the electronic structure and magnetic properties
Phys. Rev. B, **66**, 144421, (2002)

S.V. Borisenko, A.A. Kordyuk, T.K. Kim, S. Legner, K.A. Nenkov, M. Knupfer, M.S. Golden, J. Fin
Superconducting Gap in the Presence of Bilayer Splitting in Underdoped (Pb,Bi)2Sr2CaCu2O8+d
Physical Review B, **66**, 140509 (R), (2002)

S. Brünken, Ch. Gerth, B. Kanngießer, T. Luhmann, M. Richter, P. Zimmermann
The decay of the Ar 2s-1 and 2p-1 and Kr 3p-1 and 3d-1 holes
Phys. Rev. A, **65**, 042708, (2002)

R. Claessen, M. Sing, U. Schwingenschlögl, P. Blaha, M. Dressel, C.S. Jacobsen
Spectroscopic signatures of spin-charge separation in the quasi-1-dimensional organic conductor TTF
Physical Review Letters, **88**, 096402, (2002)

A. Dallmeyer, K. Maiti, O. Rader, L. Pasquali, C. Carbone, W. Eberhardt
Magnetism and interlayer coupling in fcc-Fe/Co films
Phys. Rev. B, **63**, 104413, (2000)

Yu.S. Dedkov, U. Rüdiger, G. Güntherodt
Evidence for the half-metallic ferromagnetic state of Fe3O4 by spin-resolved photoelectron spectroscopy
Physical Review B, **65**, 064417, (2002)

R. Denecke, M. Kinne, C.M. Whelan, and H.-P. Steinrück
In-situ core-level photoelectron spectroscopy of adsorbates on surfaces involving a molecular beam – general setup and first experiments
Surface Review and Letters, **9**, 797, (2002)

W. Eberhardt
Clusters as new materials
Surface Science, **500**, 242-270, (2002)

A. Ehresmann
Photodissociation processes of small molecules investigated by high resolution VUV-fluorescence spectrocopy
Photonic, Electronic & Atomic Collisions
Proc. 22nd ICPEAC (Eds.J. Burgdörfer, J.S. Cohen, S. Datz, C.R. Vane), 113-23, (2002)

T. Eimüller, M. Scholz, P. Guttmann, M. Köhler, G. Bayreuther, G. Schmahl, P. Fischer, G. Schütz
Undulation instabilities in laterally structured magnetic multilayers
J. Appl. Phys., **91, No. 10**, 7334-7336, (2002)

P. Feulner, M. Ecker, R. Romberg, R. Weimar, A. Föhlisch
Core-excitation-induced bond breaking of chemisorbed molecules probed by emission of ions, neutrals, and electrons
Surface Rev. Lett., **9**, 759, (2002)

A. Firsov, A. Svintsov, S.I. Zaitsev, A. Erko, V. Aristov
The first synthetic X-ray hologram: results
Optics Communications, **202**, 55-59, (2002)

R. Flesch, W. Tappe, E. Rühl
Highresolution near-edge spectroscopy of molecules and molecular van der waals clusters
Surface Review and Letters, **9**, 99-104, (2002)

S. Frey, H.-T. Rong, K. Heister, Y.-J. Yang, M. Buck, M. Zharnikov
Response of biphenyl-substituted alkanethiol self-assembled monolayers to electron irradiation: Damage suppression and odd-even effects
Langmuir, **18**, 3142-3150, (2002)

K. Fukumoto, H. Daimon, L. Chelaru, F. Offi, W. Kuch, J. Kirschner
Micromagnetic properties of the Cu/Ni crossed-wedge film on Cu(001)
Surface Science, **514**, 151, (2002)

P. Gambardella, A. Dallmeyer, K. Maiti, M.C. Malagoli, W. Eberhardt, K. Kern, C. Carbone
Ferromagnetism in one-dimensional monatomic metal chains
Nature, **416**, 301-304, (2002)

G.A. Garcia
Molecular Photoionization
Dissertation, University of Nottingham, (2002)

A. Gerlach, K. Berge, T. Michalke, A. Goldmann, C. Janowitz, R. Müller
High-resolution photoemission study of long-lived d-holes in Ag
Surf. Sci., **497**, 311, (2002)

O. Geßner, Y. Hikosaka, B. Zimmermann, A. Hempelmann, R.R. Lucchese, J.H.D. Eland,
P.-M. Guyon, U.Becker
The 4sigma-1 inner valence photoionization dynamics of NO derived from photoelectron-photoion angular correlations
Physical Review Letters, **88**, 193002, (2002)

O. Geßner
Untersuchung der Photoionisationsdynamik räumlich orientierter Moleküle in der Gasphase
Dissertation, Wissenschaft und Technik Verlag Berlin, **D 83**, (2002)

Th. Gleim et al.
Energy level alignment at zincblende Cd(Mn)Se/ZnTe/InAs(100) interfaces for spintronic devices
Appl. Phys. Letters, **81**, 3813, (2002)

Th. Gleim
Einfluß von Zwischenschichten auf d. elektronische Struktur v. II-VI/III-V,II-VI /IV –Halbleiter
Dissertation, Universität Würzburg, (2002)

K. Godehusen, T. Richter, P. Zimmermann, M. Martins
On the photoionization of atomic Ni – a comparison with Ni metal and NiO photoionization
Phys. Rev. Lett., **88**, 217601, (2002)

J. Goebbels, G. Weidemann, H. Riesemeier, A. Nitschke
Charakterisierung keramischer Mikrobauteile mittels Computertomographie-Vergleich von Laboranlagen und Synchrotronstrahlung
DGZfP, **BB 80-CD**, (2002)

E. Goering, M. Justen, J. Geissler, U. Rüdiger, M. Rabe, G. Güntherodt, G. Schütz
Magnetic anisotropy of textured CrO2 thin films investigated by X-ray magnetic circular dischroism
Applied Physics A, **74**, 747-753, (2002)

E. Goering, A. Bayer, S. Gold, G. Schütz, M. Rabe, U. Rüdiger, G. Güntherodt
Direct correlation of Cr 3d orbital polarization and O 2p X-ray magnetic circular dichroism of epitaxial CrO2 films
Europhysics Letters, **58**, 906-911, (2002)

E. Goering, A. Bayer, S. Gold, G. Schütz, M. Rabe, U. Rüdiger, G. Güntherodt
Strong anisotropy of projected 3d moments of epitaxial CrO2- films
Physical Review Letters, **88**, 207203, (2002)

E. Goering, J. Will, S. Gold
Surface magnetization reversal of sputtered CrO2
Zeitschrift für Metallkunde, **93/5**, 372-376, (2002)

H. Grimmer, O. Zaharko, M. Horisberger, H.-Ch. Mertins, F. Schäfers
Optical components for polarization analysis at the vanadium L3 edge and the carbon K edge
Surf. Rev. Lett., **9**, 481-485, (2002)

H. Grimmer, O. Zaharko, M. Horisberger, H.-Ch. Mertins, F. Schäfers
Optical Components for Polarization Analysis at the Vanadium L3 Edge and the Carbon K Edge
Surf. Rev. Lett., **9**, 481, (2002)

M. Zharnikov and M. Grunze
Modification of thiol-derived SAMs by electron and x-ray irradiation: Scientific and lithographic aspects
J. Vac. Sci. Technol. B, **20**, 1793-1807, (2002)

P. Grübling, J. Hollandt, G. Ulm
Topography of an electron cyclotron resonance plasma in the vacuum-ultraviolet spectral range
Rev. Sci. Instrum., **73**, 614-616, (2002)

R. den Hartog, A. Kozorezov, D. Martin, G. Brammertz, P. Verhoeve, A. Peacock, F. Scholze, D.J. Goldie
Large-Format Distributed Read-Out Imaging Devices for X-ray Imaging Spectroscopy
Proc. SPIE, **4497**, 50-60, (2002)

R. den Hartog, A. Kozorezov, D. Martin, G. Brammertz, P. Verhoeve, A. Peacock, F. Scholze, D.J. Goldie
Large-Format Distributed Read-Out Imaging Devices for X-ray Imaging Spectroscopy
AIP. Conf. Proc., **605**, 11-14, (2002)

K. Hasche, G. Ulm, K. Herrmann, M. Krumrey, G. Ade, J. Stümpel, K. Busch, P. Thomsen-Schmidt,
S. Schädlich, A. Schindler, W. Frank, M. Procop, U. Beck
About calibration of thickness standards on the nanometre scale
Proc. of 3rd euspen International Conference, Eindhoven, 26-30 May, 549-552, (2002)

M. Hecker, U. Muschiol, C.M. Schneider, H.-Ch. Mertins, D. Abramsohn, F. Schäfers
Effect of Annealing on Structural and Magnetic Properties of Co/Cu Multilayers investigated by Reson
J. Magn. Magn. Mater, **240**, 520, (2002)

U. Hergenhahn, O. Kugeler, E. E. Rennie, A. Rüdel, S. Marburger
Vibrational excitation in the C 1s spectrum of ethane
Surface Reviews and Letters, **9**, 13, (2002)

P. Hoffmann, R.P. Mikalo, D. Schmeißer
Si(001) Surface Oxidation by N2O
Journal of Non-Crystalline Solids, **303**, 6-11, (2002)

P. Hoffmann, R.P. Mikalo, D. Schmeißer
PEEM – a spectromicroscopic tool for mc-Si surface evaluation
Solar Energy Material & Solar Cells, **72**, 517-523, (2002)

M. Hülsmeyer, R.C. Hillig, A. Volz, M. Rühl, W. Schroder, W. Saenger, A. Ziegler, B. Uchanska-Ziegler
HLA-B27 Subtypes Differentially Associated with Disease Exhibit Subtle Structural Alterations.
J. Biol. Chem., **277 (49)**, 47844-47853, (2002)

C. Janowitz, R. Müller, L. Dudy, A. Krapf, R. Manzke, C. Ast, H. Höchst
Unusual electronic ground state of a prototype cuprate: band splitting of single CuO2-plane Bi2 Sr2-xLaxCuO6+d
Europhys. Lett., **60 (4)**, 615, (2002)

B. Kanngießer, N. Kemf, W. Malzer
Spectral and Lateral Resolved Characterisation of X-ray Micro-Beams
Nucl. Instr. and Meth. B, **3-4**, 3-4, (2002)

P. Kavouras, M. Katsikini, Th. Kehagias, E.C. Paloura, Ph. Komninou, J. Antonopoulos, Th. Karakosas
A parametric study of implantation induced variations on the mechanical properties of epitaxial GaN
Journal of Physics: Condensed Matter, **14**, 12953-12959, (2002)

N. Kawahara, T. Shoji, T. Yamada, Y. Kataoka, B. Beckhoff, G. Ulm, M. Mantler
Fundamental parameter method for the low energy region including cascade effect and photoelectron excitation
Advances in X-ray Analysis, **45**, 511-516, (2002)

N. Kempf
Ortsaufgelöste Bestimmung leichter Elemente mittels Mikro-Röntgenfluoreszenzanalyse
Diplomarbeit, Technische Universität Berlin, (2002)

T. Kerkau, B. Krässig, O. Schwarzkopf, H. Kossmann, B. Kämmerling, V. Schmidt
Calibration procedures to study molecular fragmentation by electron-ion coincidences
Nuclear Instruments and Methods in Physics Research A, **479**, 555-567, (2002)

T. Khalil, B. Schmidtke, M. Drescher, N. Müller, U. Heinzmann
Experimental Verification of Quardrupole-Dipole Interference in Spin-Reolved Photoionization
Physical Review Letters, **89**, 053001-1, (2002)

M. Kinne, T. Fuhrmann, C.M. Whelan, J.F. Zhu, J. Pantförder, M. Probst, G. Held, R. Denecke, H.-P. Steinrück
Kinetic parameters of CO adsorbed on Pt(111) studied by in-situ high resolution x-ray photoemission
Journal of Chemical Physics, **117(23)**, 10852, (2002)

R. Klein, F. Scholze, R. Thornagel, J. Tümmler, M. Wedowski, R. Jansen, B. Mertens,
A. van de Runstraat, G. Ulm
Irradiation of EUV multilayer optics with synchrotron radiation of different time structure
Proc. SPIE, **4782**, 292-299, (2002)

R. Klein, P. Kuske, R. Thornagel, G. Brandt, R. Görgen, G. Ulm
Measurement of the BESSY II electron beam energy by Compton-backscattering of laser photons
Nucl. Instr. and Meth. A, **486**, 545-551, (2002)

R. Klein, M. Krumrey, M. Richter, F. Scholze, R. Thornagel, G. Ulm
Radiometry with Synchrotron Radiation at the PTB Laboratory at BESSY II
Synchrotron Radiation News, **15**, 23-29, (2002)

R. Klingeler, N. Pontius, G. Lüttgens, P.S. Bechthold, M. Neeb, W. Eberhardt
Photoelectron spectroscopy of GdO
Phys. Rev. A, **65**, 032502, (2002)

A.A. Kordyuk, S.V. Borisenko, M.S. Golden, S. Legner, K.A. Nenkov, M. Knupfer, J. Fink, H. Berge
Doping dependence of the Fermi surface in (Bi,Pb)2Sr2CaCu2O8+d
Physical Review B, **66**, 014502, (2002)

A.A. Kordyuk, S.V. Borisenko, T.K. Kim, K.A. Nenkov, M. Knupfer, J. Fink, M.S. Golden, H. Berge
Origin of the Peak-Dip-Hump Line Shape in the Superconducting-State (p,0) Photoemission Spectra of Bi2SrCaCu2O8
Physical Review Letters, **89**, 077003, (2002)

K.H. Korte, U. Schade, W.B. Peatman, A. Röseler, D. Tsankov, K. Hinrichs
Infrared ellipsometric view on monolayers: towards resolving structural details
Anal. Bioanal. Chem., **374**, 665-671, (2002)

H. Koschel, U. Birkenheuer, G. Held, H.-P. Steinrück
Correlation between chemical properties and electronic structure of pseudomorphic Cu monolayers on Ni(111) and Ru(0001)
Surface Science, **477**, 113, (2001)

W. Kuch, F. Offi, L.I. Chelaru, M. Kotsugi, K. Fukumoto, J. Kirschner
Magnetic interface coupling in single-crystalline Co/FeMn bilayers
Physical Review B, **65**, 140408, (2002)

W. Kuch, Xingyu Gao, J. Kirschner
Competition between in-plane and out-of-plane magnetization in exchange-coupled magnetic films
Physical Review B, **65**, 064406, (2002)

W. Kuch, L.I. Chelaru, F. Offi, M. Kotsugi, J. Kirschner
Magnetic dichroisms in absorption and photoemission for magnetic characterization in x-ray photoelectron emission microscopy
Journal of Vacuum Science and Technology B, **20**, 2543, (2002)

W. Kuch, J. Gilles, Xingyu Gao, J. Kirschner
Layer-resolved magnetic imaging of spin-reorientation transitions in Ni/Cu/Co trilayers
Journal of Magnetism and Magnetic Materials, **242-245**, 1246, (2002)

J. Kunes, P. Nowák, P.M. Oppeneer, C. König, M. Fraune, U. Rüdiger, G. Güntherodt, C. Ambrosch-Draxl
Electronic structure of CrO2 as deduced from its magneto-optical Kerr spectra
Physical Review B, **65**, 165105, (2002)

J. Kunes, P.M. Oppeneer, H-Ch. Mertins, F. Schäfers, A. Gaupp, W. Gudat, P. Novák
X-ray Faraday effect of ferromagnetic films: contribution of the core exchange splitting
Journal of Magnetism and Magnetic Materials, **240**, 454-456, (2002)

J.T. Lau, A. Föhlisch, M. Martins, R. Nietubyc, M. Reif, W. Wurth
Spin and orbital magnetic moments of deposited small iron clusters studied by x-ray MCD
New J. Phys., **4**, 98, (2002)

J.T. Lau, A. Föhlisch, R. Nietubyc, M. Reif, W. Wurth
Size-Dependent Magnetism of Deposited Small Iron Clusters Studied by X-Ray MCD
Phys. Rev. Lett., **89**, 057201, (2002)

J.T. Lau
Magnetische Eigenschaften kleiner massenselektierter Übergangsmetallcluster
Dissertation, Universität Hamburg, (2002)

H.J. Lewerenz, M. Aggour, Chr. Murrel, M. Kanis, P. Hoffmann, H. Jungblut, D. Schmeißer
Interface engineering of photo electrochemically prepared Si surfaces
Journal of Non-Crystalline Solids, **303**, 1-5, (2002)

H. Liebel, A. Ehresmann, H. Schmoranzer, Ph.V. Demekhin, B.M. Lagutin, V.L. Sukhorukov
Deexcitation dynamics of Rydberg states in O2: I. Total cross sections for OI fluorescence emission
J. Phys. B: At. Mol. Opt. Phys, **35**, 895-905, (2002)

R. Locht, B. Leyh, A. Hoxha, D. Dehareng, H.W. Jochims, H. Baumgärtel
The Vacuum UV photoabsorption spectrum of Methyl chloride (CH3Cl) and its perdeuterated isotopomer CD3Cl II. A vibrational analysis
Chem. Phys., **272**, 277-292, (2001)

R. Locht, B. Leyh, A. Hoxha, H.W. Jochims, H. Baumgärtel
The Vacuum UV photoabsorption spectrum of Methyl chloride (CH3Cl) and its perdeuterated isotopomer CD3Cl II. A Rydberg series analysis
Chem. Phys., **272**, 259-275, (2001)

K. Lüdge, B.D. Schultz, M.M. Evans, P. Vogt, W. Braun, C.J. Palmstrøm, N. Esser, W. Richter
Structure and Interface Composition of Co Layers Grown on As-Rich GaAs(001) Surfaces
J. Vac. Sci. Technol. B, **20**, 1591, (2002)

G. Lüttgens, N. Pontius, P.S. Bechthold, M. Neeb, W. Eberhardt
Photon-induced thermal desorption of CO from small metal-carbonyl clusters
Phys. Rev. Lett., **88**, 076102, (2002)

M. Martins, K. Godehusen, Ch. Gerth, P. Zimmermann, J. Schulz, Ph. Wernet, B. Sonntag
Core hole induced degeneracy of the valence subshells in the 5p photoemission of atomic Europium
Phys. Rev. A, **65**, 030701, (2002)

M. Martins
On the 3p scandium photo excitation of atomic scandium
J. Phys. B, **35**, L223, (2002)

E. Meltchakov, H.-Ch. Mertins, M. Scheer, S. DiFonzo, W. Jark, F. Schäfers
Soft X-Ray Resonant Magnetic Reflectivity of Gd/Fe Multilayers
J. Magn. Magn. Mater., **240**, 550, (2002)

E. Meltchakov, W. Jark, S. Di Fonzo, H.-Ch. Mertins, M. Scheer, F. Schäfers
Two-Band Magneto-Optical Elements for Soft X-Ray Polarization Analysis at the Fe,Co2p and Gd 3d edge
Surface Review and Letters, **9**, 925-930, (2002)

H.-Ch. Mertins, O. Zaharko, A. Gaupp, F. Schäfers, D. Abramsohn, H. Grimmer
Soft X-Ray Magneto-Optical Constants at the Fe 2p Edge Determined by Bragg Scattering and Faraday Effect
J. Magn. Magn. Mater., **240**, 451, (2002)

H.-Ch. Mertins, D. Abramsohn, A. Gaupp, F. Schäfers, W. Gudat, O. Zaharko, H. Grimmer, P.M. Oppeneer
Resonant magnetic reflection coefficients at the Fe 2p edge obtained with linearly and circularly polarized soft x rays
Phys. Rev. B, **66**, 184404, (2002)

R.-P. Methling et al.
Magnetic Studies on Mass-selected Iron Particles
Eur. Phys. J. D., **16**, 173, (2001)

M. Meyer, A. Marquette, A. Grum-Grzhimailo, R. Flesch, E. Rühl
Alignment of Ar+ Ions produced after resonant auger decay Ar 2p5 3d resonances*
Surface Review and Letters, **9**, 141-146, (2002)

S. Mickat
Multiplex-Fluoreszenz-Spektroskopie an doppelt angeregten Edelgaszuständen
Diplomarbeit, Universität Gießen, (2002)

R. Müller, C. Janowitz, A. Krapf, M. Schneider, R.-St. Unger, L. Dudy, H. Dwelk, R. Manzke, H. Höchst
Photon energy dependence of ARPES-spectra of single layer Bi2Sr2-xLaxCuO6+d
Physica B, **312-313**, 91, (2002)

R. Müller, M. Schneider, R. Mitdank, C. Janowitz, R.-St. Unger, A. Krapf, H. Dwelk, W. Frentrup, R. Manzke
Systematic X-ray absorption study of hole doping in BSCCO-phases
Physica B, **312-313**, 94, (2002)

R. Müller, C. Janowitz, M. Schneider, R.-St. Unger, A. Krapf, H. Dwelk, A. Müller, L. Dudy, R. Manzke
Fermi surface and superconducting gap of triple-layered Bi2Sr2Ca2Cu3O10+d
Journal of Superconductivity, **15**, 147, (2002)

A. Ney, A. Scherz, P. Poulopoulos, K. Lenz, H. Wende, K. Baberschke, F. Wilhelm, N.B. Brookes
Clarification of contesting results for the total magnetic moment of Ni/Cu(001)
Phys. Rev. B, **65**, 024411, (2002)

B. Obst, J.E. Hansen, B. Sonntag, Ph. Wernet, P. Zimmermann
Photoionisation studies of the 2p resonances of atomic Calcium
Phys. Rev. A, **65**, 062716, (2002)

F. Offi
Magnetic interaction between antiferromagnetic and ferromagnetic films:
Co/Fe50Mn50 bilayers on Cu(001)
Dissertation, Martin-Luther-Universität Halle-Wittenberg, (2002)

A. Owens, M. Bavdaz, A. Peacock, H. Andersson, S. Nenonen, M. Krumrey, A. Puig
High-resolution X-ray spectroscopy using a GaAs pixel detector
Nucl. Instr. and Meth. A, **479**, 531-534, (2002)

A. Owens, M. Bavdaz, G. Brammertz, M. Krumrey, D. Martin, A. Peacock, L. Tröger
The hard X-ray response of HgI2
Nucl. Instr. and Meth. A, **479**, 535-547, (2002)

A. Owens, M. Bavdaz, H. Andersson, T. Gagliardi, M. Krumrey, S. Nenonen, A. Peacock, I. Taylor, L. Tröger
The X-ray response of CdZnTe
Nucl. Instr. and Meth. A, **484**, 242-250, (2002)

A. Owens, A. Peacock, M. Bavdaz, G. Brammertz, F. Dubecky, V. Gostilo, D. Gryaznov,
N. Haack, M. Krumrey, A. Loupilov
The X-ray response of InP: Part B, synchrotron radiation measurements
Nucl. Instr. and Meth. A, **491**, 444-451, (2002)

S. Park, T.U. Kampen, T. Kachel, P. Bressler, W. Braun, D.R.T. Zahn
Interaction of metals with an organic semiconductor: Ag and In on PTCDA
Applied Surface Science, **190**, 376-381, (2002)

S.H. Payne, H.J. Kreuzer, M. Kinne, R. Denecke, H.-P. Steinrück
Strong repulsion and site exclusion in a system with ontop and bridge sites on a
one-dimensional lattice: equilibrium and kinetics
Surface Science, **513**, 174, (2002)

P. Poulopoulos, A. Scherz, F. Wilhelm, H. Wende, K. Baberschke
Direct probe of induced magnetic moments at interfaces via x-ray magnetic circular dichroism
Physica Status Solidi (a), **189**, 293, (2002)

M. Probst, R. Denecke, C. Whelan, M. Kinne, D. Borgmann, H.-P. Steinrück
Electron spectroscopic studies of iron and iridium silicides
Surface and Interface Analysis, **34**, 744, (2002)

M. Procop, M. Radtke, M. Krumrey, K. Hasche, S. Schädlich,W. Frank
Electron probe microanalysis (EPMA) measurement of thin-film thickness in the nanometre range
Anal. Bioanal. Chem., **374**, 631-634, (2002)

H. Rabus, R. Klein, F. Scholze, R. Thornagel, G. Ulm
Validation of the uncertainty budget for soft X-ray radiant power measurement using a cryogenic radiometer
Metrologia, **39**, 381-389, (2002)

O. Rader, C. Pampuch, A.M. Shikin
Direct and resonant photoemission study of ultrathin Gd on W(110)
Surf. Rev. Lett., **9**, 1113, (2002)

A. Rahmim, S. Tixier, T. Tiedje, S. Eisebitt, M. Lörgen, R. Scherer, W. Eberhardt, J. Lüning, A. Scholl
Interference between magnetism and surface roughness in coherent soft x-ray scattering
Phys. Rev. B, **65**, 235421, (2002)

E.E. Rennie, U. Hergenhahn, O. Kugeler, A. Rüdel, S. Marburger, A.M. Bradshaw
A core level photoionisation study of furan
J. Chem. Phys., **117**, 6524-32, (2002)

E.E. Rennie, I. Powis, U. Hergenhahn, O. Kugeler, T.M. Watson, S. Marburger
Valence and C 1s core level photoelectron spectra of Butan-2-ol
J. Phys. Chem. A, **106**, 12221-8, (2002)

E.E. Rennie, I. Powis, U. Hergenhahn, O. Kugeler, G. Garcia, T. Lischke, S. Marburger
Valence and C 1s core level photoelectron spectra of camphor
J. Electron Spectrosc. Relat. Phenom., **125**, 197-203, (2002)

M. Richter, U. Kroth, A. Gottwald, Ch. Gerth, K. Tiedtke, T. Saito, I. Tassy, K. Vogler
Metrology of pulsed radiation for 157-nm lithography
Appl. Opt., **41**, 7167-7172, (2002)

U. Schade, A. Röseler, E.H. Korte, F. Bartl, K.P. Hofmann, T. Noll, W. Peatman
New Infrared Spectroscopic Beamline at BESSY II
Rev. Sci. Instr., **72**, 1568-1570, (2002)

A. Scherz, P. Poulopoulos, H. Wende, G. Ceballos, K. Baberschke, F. Wilhelm
Thickness dependence of the V induced magnetic moment in Fe/V/Fe(110) trilayers
J. Appl. Phys., **91**, 8760, (2002)

A. Scherz, H. Wende, K. Baberschke, J. Minar, D. Benea, H. Ebert
Relation between L2,3 XMCD and the magnetic ground-state properties for the early 3d element V
Phys Rev. B, **66**, 184401, (2002)

Michael Schlüter
Untersuchung der Photodissoziation von CO über VUV-Fluoreszenzemissionsquerschnitte der Fragmente
Diplomarbeit, Universität Kaiserslautern, (2002)

Th. Schmidt, U. Groh, R. Fink, E. Umbach, O. Schaff, W. Engel, B. Richter, H. Kuhlenbeck, R. Schlögl
XPEEM with energy-filtering: advantages and first results from the SMART project
Surf. Rev. Lett., **9**, 223-232, (2002)

F. Scholze, G. Brandt, P. Müller, B. Meyer, F. Scholz, J. Tümmler, K. Vogel, G. Ulm
High-accuracy detector calibration for EUV metrology at PTB
Proc. SPIE, **4688**, 680-689, (2002)

D. Schondelmaier, S. Cramm, R. Klingeler, J. Morenzin, Ch. Zilkens, W. Eberhardt
Orientation and self-assembly of hydrophobic fluoroalkylsilanes
Langmuir, **18**, 6242-6245, (2002)

J. Schulz, Ph. Wernet, K. Godehusen, R. Müller, P. Zimmermann, M. Martins, P. Zimmermann, B. Sonntag
Linear dichroism in the 4d photoionisation of atomic Europium
J. Phys. B, **35**, 1, (2002)

C. Schüßler-Langeheine, H. Ott, A.Yu. Grigoriev, Z. Hu, C. Mazumdar, G. Kaindl, E. Weschke
Oxygen-induced magnetic surface states on the (0001) surfaces of heavy lanthanide metals
Phys. Rev. B, **65**, 214410, (2002)

C. Schüßler-Langeheine, E. Weschke, R. Meier, A.Yu. Grigoriev, H. Ott, C. Mazumdar
Resonant Magnetic X-Ray Scattering From In-Situ Grown Holimium Metal Films
in: Speciation, Techniques and Facilities for Radioactive Materials at Synchrotron Light Sources,
T, 295-302, (2002)

V. Senz, A. Kleibert, J. Bansmann
Transverse Magneto-optical Kerr-effect in the soft X-ray regime of ultrathin iron films and islands
Surf. Rev. Lett., **9**, 913, (2002)

A.M. Shikin, O. Rader, G.V. Prudnikova, V.K. Adamchuk, W. Gudat
Quantum well states of sp- and d-character in thin Au films on W(110)
Phys. Rev. B, **65**, 075403, (2002)

A.M. Shikin, O. Rader, W. Gudat, G.V. Prudnikova, V.K. Adamchuk
Quantum well states of sp and d character in ultrathin epitaxial Ag and Au films on W(110)
Surf. Rev. Lett., **9**, 1375, (2002)

N. Sieber, Th. Seyller, R. Graupner, L. Ley, R. Mikalo, P. Hoffmann, D. Batchelor, D. Schmeißer
Wetchemical preparation of silicate adlayer terminated SiC(0001) surfaces studied by PES and LEED
Mater. Sci. Forum, **389-393**, 717-720, (2002)

N. Sieber, Th. Seyller, L. Ley, M. Polcik, D. James, J.D. Riley, R.G.C. Leckey
A high resolution photoemission study of hydrogen terminated 6H-SiC surfaces
Mater. Sci. Forum, **389-393**, 713-716, (2002)

N. Sieber
Wasserstoff- und sauerstoffstabilisierte 6H-SiC{0001}
Dissertation, Universität Erlangen-Nürnberg, (2002)

R. Stuik, F. Scholze, J. Tümmler, F. Bijkerk
Absolute calibration of a multilayer-based XUV diagnostic
Nucl. Instr. and Meth. A, **492**, 305-316, (2002)

J. Thieme
Studies of soil colloids with X-ray microscopy
European Microscopy and Analysis, **Juli 2001**, 9-11, (2001)

J. Thieme, C. Schmidt, G. Abbt-Braun, C. Specht, F.H. Frimmel
X-ray microscopy studies of refractory organic substances
in: Organic Substances in the Environment, F.H. Frimmel et al. (Eds.), Wiley-VCH, Weinheim, 239-248, (2002)

J. Tümmler, F. Scholze, G. Brandt, B. Meyer, F. Scholz, K. Vogel, G. Ulm, M. Poier, U. Klein, W. Diete
New PTB reflectometer for the characterization of large optics for the extreme ultraviolet spectral region
Proc. SPIE, **4688**, 338-347, (2002)

M. Veldkamp, B. Beckhoff, R. Fliegauf, G. Ulm, M. Frank, S. Friedrich, S.E. Labov
Characterization of superconducting tunnel junction X-ray detectors by means of monochromatized undulator radiation
Nucl. Instr. and Meth. A, **487**, 450-456, (2002)

A.S. Vinogradov, S.I. Fedoseenko, D.V. Vyalikh, S.L. Molodtsov, V.K. Adamchuk, C. Laubschat, G. Kaindl
High resolution F 1s absorption spectra of solid fluorides of 3d elements
Optika i Spektroskopija (in Russian) [Optics and Spectroscopy (English translation)],
93, N6, 935-943 [862-869], (2002)

A.S. Vinogradov, A.B. Preobrajenski, S.A. Krasnikov, T. Chasse, R. Szargan,
A. Knop-Gericke, R. Schloegl, P. Bressl
X-ray absorption evidence for the back-donationin in iron cyanide complexes
Surface Review and Letters, **9, N1**, 359-364, (2002)

A.S.Vinogradov, S.I. Fedoseenko, D.V. Vyalikh, S.L. Molodtsov, V.K. Adamchuk, C. Laubschat, G. Kaindl
High resolution F 1s absorption spectra of solid fluorides of 3d elements
Optika i spektroskopija (in Russian) [Optics and Spectroscopy (English translation)],
93, N6, 935-943 [862-869], (2002)

P. Voigt
Atomic Structure of the (001) Surfaces of InP, GaP and InGaP
Dissertation, TU Berlin, (2002)

O. Vormoor
Aggregation kolloidaler Teilchen: Ein Vergleich von Röntgenmikroskopie und Streumethoden
Dissertation, (2002)

M.-C. Wang, J.-D. Liao, C.-C. Weng, R. Klauser, S. Frey, M. Zharnikov, M. Grunze
The effect of the substrate on response of thioaromatic SAMs to free radical-dominated plasma
J. Phys. Chem. B, **106**, 6220-6226, (2002)

M.-C. Wang, J.-D. Liao, C.-C. Weng, R. Klauser, S. Frey, M. Zharnikov, M. Grunze
Modification of alkanethiolate self-assembled monolayers by free radical-dominant plasma
J. Phys. Chem. B, **106**, 77-84, (2002)

F. Weigand, S. Gold, A. Schmid, J. Geissler, E. Goering
Antiparallel Ruthenium coupling in the doped Ruddlesden-Popper-Phase La1.2Sr1.8Mn2-xRuxO7
Applied Physics Letters, **81/11**, 2035-2037, (2002)

Ph. Wernet, A. Verweyen, J. Schulz, B. Sonntag, K. Godehusen, R. Müller, P. Zimmermann, M. Martins
Combining High Resolution Photoelectron Spectroscopy and Laser Polarization for a Study of the 4f and 5p Photoionization of Atomic Thulium
J. Phys. B, **35**, 3887, (2002)

M. Wilke, R. Bernhardt, G.M. Partzsch,
Fe in synthetic basaltic glass: Effect of Phosphorus – An X-ray absorption spectroscopic study
European Journal of Mineralogy, **14/Beih. 1**, 174, (2002)

D. Wollert
Untersuchung der Einsatzmöglichkeiten hochauflösender supraleitender Tunneldiodendetektoren
Diplomarbeit, Technische Universität Berlin, (2002)

Xingyu Gao, W. Kuch, F. Offi, S.S. Kang, S. Imada, J. Kirschner
Search for multi-atom resonant photoemission in magnetic thin films
Journal of Electron Spectroscopy and Related Phenomena, **123**, 11, (2002)

O. Zaharko, P.M. Oppeneer, H. Grimmer, M. Horisberger, H.-Ch. Mertins, D. Abramsohn,
F. Schäfers, A. Bill, H.-A. Braun
Exchange Coupling in Fe/NiO/Co Film Studied by Soft-X-Ray Resonant Magnetic Reflectivity
Phys. Rev. B, **66**, 134406, (2002)

M. Zharnikov, H.-P. Steinrück
Holography with photoelectrons: a direct approach
J. Physics: Condens. Matter, **13**, 10533, (2001)

M. Zharnikov, S. Frey, K. Heister, M. Grunze
An extension of the mean free path approach to X-ray absorption spectroscopy
J. Electron Spectrosc. Relat. Phenom., **124**, 15-24, (2002)

A.V. Zimina, A.S. Shulakov, S. Eisebitt, W. Eberhardt
Depth-resolved soft X-ray emission spectroscopy of Si-based materials
Surf. Rev. Lett., **9**, 461-467, (2002)

Keyword Index

(click on page number to open selected page)

Authors Index

(click on page number to open selected page)